

AD-A142 573

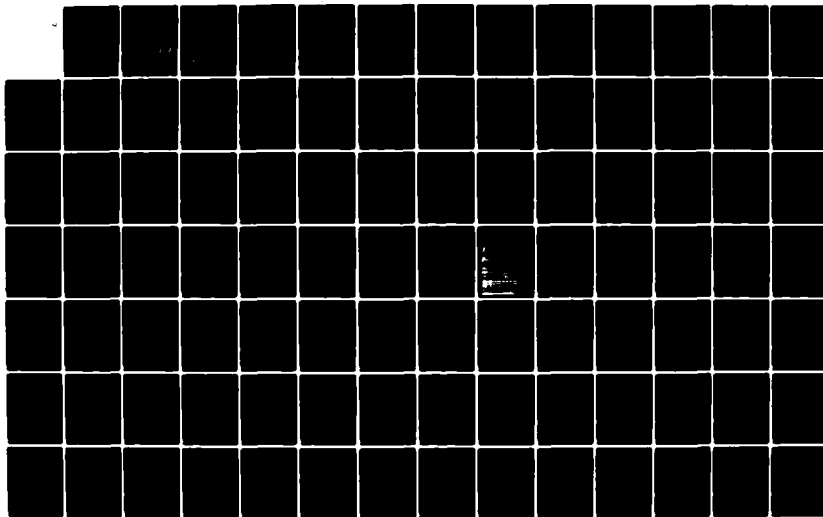
GEOPHYSICAL PLASMAS AND ATMOSPHERIC MODELING(U) SCIENCE
APPLICATIONS INC MCLEAN VA E HYMAN ET AL. MAR 84
SAI-84/1554 SBI-AD-E001 718 N00014-83-C-2034

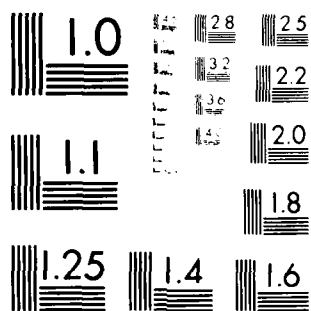
1/8

UNCLASSIFIED

F/G 4/1

NL





MICROCOPY RESOLUTION TEST CHART
NATIONAL BUREAU OF STANDARDS-1963-A

AD-A142 573

DTIC FILE COPY

GEOPHYSICAL PLASMAS
AND ATMOSPHERIC MODELING
FINAL REPORT
SAI 84/1554
MARCH 1984

(L.C.)

ADE001718

DTIC
ELECTE
JUN 27 1984
S A D

This document has been approved
for public release and sale; its
distribution is unlimited.

SCIENCE APPLICATIONS, INC.

ADA 142573

(10)

GEOPHYSICAL PLASMAS
AND ATMOSPHERIC MODELING
FINAL REPORT
SAI 84/1554
MARCH 1984

DTIC
ELECTE
S JUN 27 1984 D
A



SCIENCE APPLICATIONS, INC.

Post Office Box 1303, 1710 Goodridge Drive, McLean, Virginia 22102, (703) 821-4300

This document has been approved
for public release and sale; its
distribution is unlimited.

GEOPHYSICAL PLASMAS
AND ATMOSPHERIC MODELING

FINAL REPORT

SAI 84/1554

March 1984

Submitted to:

Dr. Joseph Huba
Geophysical and Plasma Dynamics Branch
Plasma Physics Division
Naval Research Laboratory
Washington, D.C. 20375

Prepared by:

Ellis Hyman with
Pradeep Chaturvedi, James Chen, Jim Drake, Guruḍas Ganguli,
Supriya Ganguli, Charles Goodrich, Adil Hassam, Y.C. Lee,
John Lyon, Horace Mitchell, Dennis Papadopoulos,
Harvey Rowland, Keith Sashegyi, Punyamurthula Satyanarayana,
George Schmidt, and Robert Smith

Prepared Under:

Contract No. N00014-83-C-2034

SCIENCE APPLICATIONS, INCORPORATED

1710 Goodridge Drive, McLean, Virginia 22102 (703) 734-5840

TABLE OF CONTENTS

<u>Section</u>	<u>Page</u>
I. TECHNICAL DISCUSSION.	I-1
REFERENCES.	39
APPENDIX A - Tearing Instability in an Anisotropic Neutral Sheet	A-1
APPENDIX B - Fast Collisionless Tearing in an Anisotropic Neutral Sheet	B-1
APPENDIX C - A Dynamic Model for the Auroral Field Line Plasma in the Presence of Field-Aligned Current	C-1
APPENDIX D - Electromagnetic Ion-Cyclotron Waves in Magnetospheric Plasmas: Non-Local Aspects. .	D-1
APPENDIX E - Velocity Shear Stabilization of the Current Convective Instability.	E-1
APPENDIX F - Influence of Magnetic Shear on the Collisional Current Driven Ion Cyclotron Instability	F-1
APPENDIX G - Rayleigh-Taylor Instability in the Presence of a Stratified Shear Layer.	G-1
APPENDIX H - Finite Temperature Effects on the Evolution of Ionospheric Barium Clouds in the Presence of a Conducting Background Ionosphere.	H-1
APPENDIX I - Saturation of the Lower-Hybrid-Drift Instability by Mode Coupling.	I-1
APPENDIX J - Nonlinear Mode Coupling Theory of the Lower-Hybrid-Drift Instability.	J-1
APPENDIX K - Parameter Survey for Collisionless Coupling in a Laser Simulation of HANE. . . .	K-1
APPENDIX L - Preliminary Report on UVDEP and PRODEP Results for the NRL Laser/HANE Experiment . .	L-1

Page

2210
COPY
INSPECTED
2

1
 2
 3
 4
 5
 6
 7
 8
 9
 10
 11
 12
 13
 14
 15
 16
 17
 18
 19
 20
 21
 22
 23
 24
 25
 26
 27
 28
 29
 30
 31
 32
 33
 34
 35
 36
 37
 38
 39
 40
 41
 42
 43
 44
 45
 46
 47
 48
 49
 50
 51
 52
 53
 54
 55
 56
 57
 58
 59
 60
 61
 62
 63
 64
 65
 66
 67
 68
 69
 70
 71
 72
 73
 74
 75
 76
 77
 78
 79
 80
 81
 82
 83
 84
 85
 86
 87
 88
 89
 90
 91
 92
 93
 94
 95
 96
 97
 98
 99
 100
 101
 102
 103
 104
 105
 106
 107
 108
 109
 110
 111
 112
 113
 114
 115
 116
 117
 118
 119
 120
 121
 122
 123
 124
 125
 126
 127
 128
 129
 130
 131
 132
 133
 134
 135
 136
 137
 138
 139
 140
 141
 142
 143
 144
 145
 146
 147
 148
 149
 150
 151
 152
 153
 154
 155
 156
 157
 158
 159
 160
 161
 162
 163
 164
 165
 166
 167
 168
 169
 170
 171
 172
 173
 174
 175
 176
 177
 178
 179
 180
 181
 182
 183
 184
 185
 186
 187
 188
 189
 190
 191
 192
 193
 194
 195
 196
 197
 198
 199
 200
 201
 202
 203
 204
 205
 206
 207
 208
 209
 210
 211
 212
 213
 214
 215
 216
 217
 218
 219
 220
 221
 222
 223
 224
 225
 226
 227
 228
 229
 230
 231
 232
 233
 234
 235
 236
 237
 238
 239
 240
 241
 242
 243
 244
 245
 246
 247
 248
 249
 250
 251
 252
 253
 254
 255
 256
 257
 258
 259
 260
 261
 262
 263
 264
 265
 266
 267
 268
 269
 270
 271
 272
 273
 274
 275
 276
 277
 278
 279
 280
 281
 282
 283
 284
 285
 286
 287
 288
 289
 290
 291
 292
 293
 294
 295
 296
 297
 298
 299
 300
 301
 302
 303
 304
 305
 306
 307
 308
 309
 310
 311
 312
 313
 314
 315
 316
 317
 318
 319
 320
 321
 322
 323
 324
 325
 326
 327
 328
 329
 330
 331
 332
 333
 334
 335
 336
 337
 338
 339
 340
 341
 342
 343
 344
 345
 346
 347
 348
 349
 350
 351
 352
 353
 354
 355
 356
 357
 358
 359
 360
 361
 362
 363
 364
 365
 366
 367
 368
 369
 370
 371
 372
 373
 374
 375
 376
 377
 378
 379
 380
 381
 382
 383
 384
 385
 386
 387
 388
 389
 390
 391
 392
 393
 394
 395
 396
 397
 398
 399
 400
 401
 402
 403
 404
 405
 406
 407
 408
 409
 410
 411
 412
 413
 414
 415
 416
 417
 418
 419
 420
 421
 422
 423
 424
 425
 426
 427
 428
 429
 430
 431
 432
 433
 434
 435
 436
 437
 438
 439
 440
 441
 442
 443
 444
 445
 446
 447
 448
 449
 450
 451
 452
 453
 454
 455
 456
 457
 458
 459
 460
 461
 462
 463
 464
 465
 466
 467
 468
 469
 470
 471
 472
 473
 474
 475
 476
 477
 478
 479
 480
 481
 482
 483
 484
 485
 486
 487
 488
 489
 490
 491
 492
 493
 494
 495
 496
 497
 498
 499
 500
 501
 502
 503
 504
 505
 506
 507
 508
 509
 510
 511
 512
 513
 514
 515
 516
 517
 518
 519
 520
 521
 522
 523
 524
 525

Section I

TECHNICAL DISCUSSION

The work performed by Science Applications, Inc. (SAI) on this contract, "Geophysical Plasmas and Atmospheric Modeling," Contract Number N00014-83-C-2034, SAI Project Number 1-157-13-588, encompasses a wide range of topics in space plasma physics and atmospheric modeling in support of the programs of the Geophysical and Plasma Dynamics Branch of the Naval Research Laboratory (NRL). This report covers the period 16 December 1982 to 15 February 1984. In this section we will summarize the various subjects studied and the results obtained. Details will be included in Appendices which will document reports and publications resulting from our work.

In the following subsections we will describe the major accomplishments in each of the following research efforts: (A) 3D magnetospheric modeling, (B) tearing instability in an anisotropic neutral sheet, (C) auroral plasma transport, (D) magnetic shear effects on the current driven ion cyclotron instability, (E) instability mechanisms causing high latitude ionospheric irregularities, (F) auroral instability studies, (G) nonlinear saturation of the lower-hybrid-drift instability and anomalous plasma transport, (H) laser/HANE theory support, (I) early time HANE phenomena, (J) uranium vapor release, (K) late

time HANE striation models, (L) quasi-steady state multi-plasma cloud configurations in the ionosphere, (M) chaotic behavior in ionospheric processes, (N) linear dynamics of tropical heat sources and interactions with mid-latitudes, (O) the large scale dynamics of the Indian summer monsoon, (P) collective particle acceleration (CPA), and (Q) plasma behavior in crossed electric and magnetic fields.

(A) 3D Magnetospheric Modeling

During the past year, the bulk of the effort in the magnetospheric modeling program has gone into the development of a new 3-D simulation code involving better numerics and better modeling of the magnetosphere-ionosphere (MI) coupling. The code is not yet completed, but the individual modules involved have been debugged. The improved numerics include high-order spatial differencing and an extension of the partial donor cell method to conservative hyperbolic systems. Initial tests with the coded algorithms indicate improvements of about a factor of two can be expected in the final code. The improved model of MI coupling uses the assumption of constant field aligned current per flux tube to map the currents from the near earth magnetosphere to the ionosphere. The ionospheric load on the magnetosphere is then calculated using a very simple electrostatic model containing only a constant Pedersen conductivity.

This MI coupling model was used with data from the old simulation runs to see what sort of ionospheric current and convection patterns would arise. It was found that the old runs gave clear Region 1 currents in the ionosphere and less clear but visible Region 2 currents. Using a reasonable ionospheric conductivity, the polar region convection had a symmetric two cell pattern, but the polar cap potential drop was about a factor of ten too low. Since there was no explicit ionospheric load on the old simulation models, this is not surprising. However, the fact that the proper qualitative pattern did arise indicates that the new simulation code should be able to answer many questions about energy transfer from the solar wind to the ionosphere.

The above results have been presented at the Chapman Conference on Magnetic Reconnection at Los Alamos National Laboratory, October 3-7, 1983. An abstract for the meeting follows.

"Modeling the Global Interaction Between the Solar Wind
and the Magnetosphere"

J.G. Lyon, Science Applications, Inc.
J.A. Fedder, J.D. Huba, J.L. Giuliani, Jr.
Naval Research Laboratory

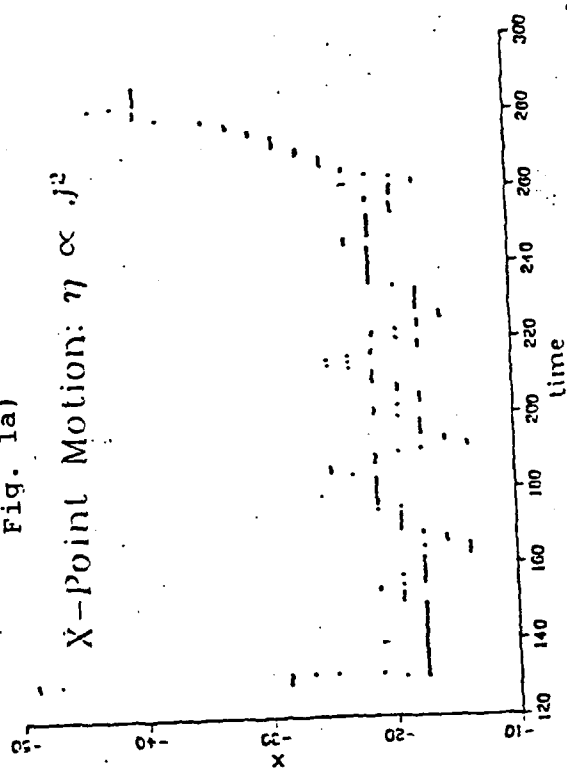
We would like to discuss two areas in the simulation of the interaction of the solar wind and the magnetosphere that have been of particular interest to us recently. The first is the effect of microphysical effects upon the dynamics of tail reconnection. The second is the structure of the three-dimensional current systems in our simulations.

In our 2D simulations we have been able to suppress numerical reconnection in the magnetotail by use of the equatorial symmetry plane. A number of runs have been made with different resistivity models along with a southward IMF. The results from the different resistivities are quite similar and somewhat surprising. Fig. 1a shows the position of the x-point in the tail for a case with resistivity $\propto J^2$. The x-point oscillates quite a bit, but does not go tailward large distances until the end of the run when a northward magnetic field is introduced. The cause of the oscillations is not clear but appears to be related to the electric field imposed on the tail magnetopause. By contrast, Fig. 1b shows the case where the Joule heating has been removed. This might correspond to the case where thermal conduction is so high that the heat is carried away as it is generated. In this case the x-point does move a large distance down tail at a speed of about 100 km/s. This increased response to what appears to be an external driving force is not too surprising, since the absence of Joule heating should decrease the pressure - and resistance to external pushing -- in the reconnection region. These 2D simulations may not be too realistic but they do show clearly that the microphysics in the simulation model can lead to global consequences.

We have also looked at the 3D current distribution in our simulations when reconnection is taking place in the tail. We find that the cross tail current appears to be diverted in a tailward direction. It also strengthens during the reconnection event. The parallel current structure found in the simulation is shown schematically in Fig. 2. The region 1 currents are coupled to the magnetopause, flowing downward into the ionosphere on the dawn side and upward on the dusk side. The region 2 currents close to the interior of the magnetosphere and, on the night side, to the plasma sheet boundary. The tailward diversion of the current sheet mentioned above has the sense of the region 2 currents.

An important limitation on these simulations is the boundary condition at the ionosphere. We will discuss some progress in improving the treatment of this boundary and the mapping of magnetospheric phenomena to the ionosphere.

Fig. 1a)



X-Point Motion: No Joule Heat, $\eta \propto j^2$

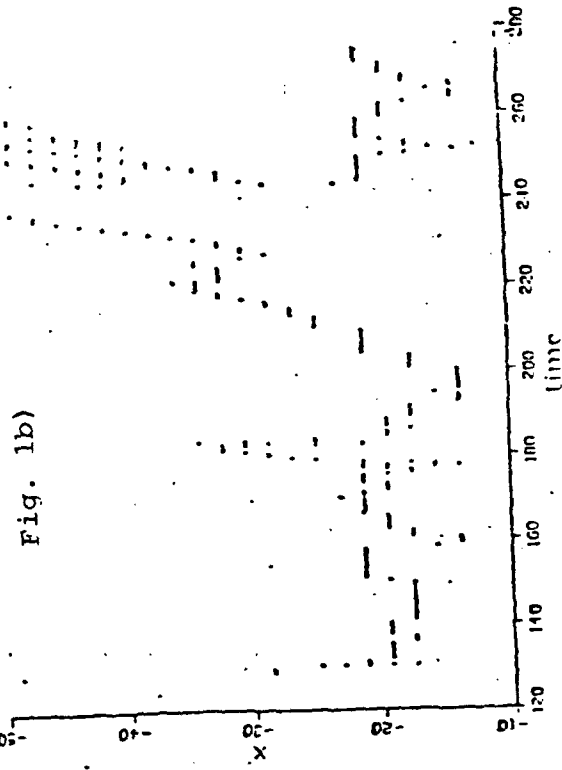
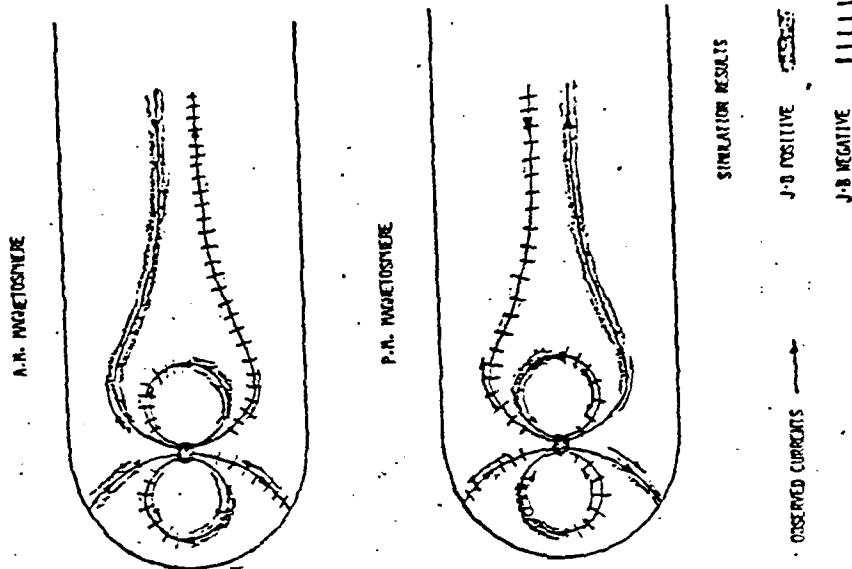


Fig. 2



These results have also been presented at the fall meeting of the American Geophysical Union. The abstract for that presentation follows.

Simulation of Magnetospheric Current Systems*

J.A. FEDDER, J.L. GIULIANI, JR., P.J. PALMADESSO, (all at the Naval Research Laboratory, Washington, D.C. 20375) and J.G. LYON (Science Applications, Inc., McLean, VA 22102)

In previous work, we have been able to identify Birkeland current systems in the MHD magnetosphere simulation results.¹ Using a new higher resolution simulation code, which includes magnetosphere-ionosphere coupling effects, we are presently studying magnetospheric current systems. In this paper we will present simulation results for magnetospheric current systems. We will discuss their source regions, coupling to the ionosphere, and driving mechanisms.

1. J.G. Lyon, and J.A. Fedder, "Current and electric fields during substorms from 3D MHD simulations," presented at Chapman Conference on Magnetospheric Currents, 1983.

*This work is supported by National Aeronautics and Space Administration and the Office of Naval Research.

(B) Tearing Instability in an Anisotropic Neutral Sheet

We have recently completed a work to investigate quantitatively the tearing instability properties of an anisotropic neutral sheet. We have found that the tearing-mode growth rate can be enhanced by one to two orders of magnitude in the presence of modest ion temperature anisotropy ($T_{i\perp}/T_{i\parallel} \lesssim 1.5$; electrons are assumed to be isotropic). The detailed analysis is given in Appendix A, entitled "Tearing Instability in an Anisotropic Neutral Sheet." This work is contained in NRL

Memorandum Report 5178, September 1983, and has been accepted for publication in Phys. Fluids where it will appear in May 1984.

An application of this study to the magnetotail has been completed. It is found that the linear e-folding time for the growth rate of the collisionless tearing instability is reduced to a small fraction of the time delays believed to precede the onset of reconnection. A report on this work is included in Appendix B, entitled "Fast Collisionless Tearing in an Anisotropic Neutral Sheet" and has been published in Geophys. Res. Lett. 11, 12 (1984).

(C) Auroral Plasma Transport

We have used a previously developed, one-dimensional multi-moment multi-fluid model of the auroral field line plasma to investigate the behavior of turbulence and non-equilibrium effects in the presence of field-aligned current in this region. Our initial simulation results were published in the Journal of Geophysical Research this year (H.G. Mitchell, Jr., and P.J. Palmadesso, J. Geophys. Res. 88, 2131, 1983) and are included in this report in Appendix C, entitled "A Dynamic Model for the Auroral Field Line Plasma in the Presence of Field Aligned Current."

We have expanded this model by the inclusion of a hotter magnetospheric electron population at high

altitudes in order to better model the transient effects of field-aligned current onset in the auroral plasma. Simulations performed with this expanded model have revealed that the existence of multiple timescales in the plasma for reaction to the current onset can create the macroscopic plasma configurations necessary for the growth of plasma instabilities. At current onset, the magnitude of the hot precipitating electron flux is increased, resulting in a locally enhanced ambipolar electric field at the altitude where the majority ion specie changes from oxygen to hydrogen (about 4000 km altitude). This enhanced electric field accelerates the hydrogen ions upward, creating a transient region of lower ion density. The precipitating electrons must accelerate in this region to maintain the field-aligned current, and so a region of high electron-hydrogen ion relative drift is created, the condition necessary for hydrogen cyclotron turbulence. This region is transient, but persists for times on the order of the time for significant changes in the field-aligned current. This work has been presented at the Chapman Conference on Magnetospheric Currents (April 1983), an abstract of which follows.

Dynamic Auroral Field Line Plasma Behavior in the Presence of Field-Aligned Current*

H.G. MITCHELL, JR. (Science Applications, Inc., McLean, VA 22102)

P.J. PALMADESSO (Naval Research Laboratory, Washington, D.C. 20375)

A simulation model of the auroral magnetic field line plasma has been developed in order to study the dynamic response of this plasma to a current parallel to the magnetic field, both with and without mechanisms for anomalous transport and resistivity. This simulation is one-dimensional and contains three particle species (e^- , H^+ , O^+), which are each characterized by five distribution function moments (density, velocity and heat flow along the field line, temperatures perpendicular and parallel to the field) treated dynamically. The model includes a region beginning at about 800 km altitude in the topside ionosphere and extending out $10 R_E$ along the diverging magnetic field. Simulations with this model indicate the importance of both the spatial gradients and dynamic interactions in the behavior of the field line plasma. Although the electrons react to changes in the parallel current on a short timescale, their behavior is coupled to the dynamics of the two ion species by charge neutrality, current conservation, and the ambipolar electric field. As a result, two and three species interactions can force density and thermal oscillations to persist along the field for times comparable to that for changes in the field-aligned current. Simulations have also been performed with various forms of resistivity included in order to judge the effects of anomalous heating and momentum transfer on the plasma.

*This work was supported by ONR and NASA.

Our attempts to simulate realistic auroral currents and plasma configurations have led us to use the auroral plasma flux tube model at the boundary of the fluid approximation included in the model. Large temperature gradients and energy fluxes parallel to the magnetic field have prompted us to an investigation of the theoretical and computational aspects of such a problem and have led

to new results in the interpretation and use of multi-moment fluid models. We have reported on these results and the subsequent plasma simulations at the Fall, 1983 meeting of the American Geophysical Union and the abstract of this presentation follows.

Simulating Energy Transport Along High-Latitude Field Lines*

H.G. MITCHELL, JR. (Science Applications, Inc., McLean, VA 22102) and P.J. PALMADESSO (Naval Research Laboratory, Washington, D.C. 20375)

The interaction of magnetospheric and ionospheric plasmas along high latitude magnetic field lines is a highly dynamic process and is very dependent on the details of plasma transport along the magnetic field. We have previously modeled this transport with the goal of studying mechanisms of parallel electric field generation in a dynamic simulation.¹ The plasma specie in this model were treated in a multi-moment fluid approximation derived from that of Schunk² in which each species is characterized by number density, temperatures parallel and perpendicular to the magnetic field, and velocity and heat flow along the field. As we have extended our simulation to include hot magnetospheric particles, we find that heat flows on the order of the specie thermal velocities are very often generated in the dynamic interaction of these particles with the ionospheric plasma. Such large heat flows strain the bounds of the original approximation, and, since the time scale for energy transport along the field has important consequences for the field line dynamics, we have compared our original approximation with several others in order to simulate this transport as accurately as possible. We will describe the results of this investigation for the dynamics of hot magnetospheric particles in the converging high-latitude magnetic field.

1. Mitchell, H.G., Jr. and P. Palmadesso, J. Geophys. Res., **88**, 2131, 1983.
2. Schunk, R.W., Rev. Geophys. Space Phys. **15**, 429, 1977.

*This work supported by the Office of Naval Research and the National Aeronautics and Space Administration.

Various models have been developed in the past in order to study the behavior of plasma on the auroral magnetic field lines. The dynamics of the upward current on the auroral field line and the current free polar wind case has been studied by Mitchell and Palmadesso. The dynamics of the return current remains an interesting question.

Return currents play an important role in the study of magnetosphere-ionosphere coupling. We have performed simulations using the dynamics of the large scale return current on auroral field lines. The model is a multi-moment multi-fluid approximation of a gyrotropic plasma consisting of three species (electrons, hydrogen ions, oxygen ions) along a segment of the auroral magnetic field lines extending from an altitude of 800 km to 10 earth radii. Field aligned currents of different magnitudes were introduced into the system and the effects were noted. Interesting results have emerged. Unlike the polar wind and upward current simulations, here, the preliminary results show that the electron velocity increases with the onset of the return current and the electron temperature gradient decreases. Also, the ambipolar electric field decreases, thereby, decreasing the hydrogen ion velocity at the lower end of the tube. To maintain constant current the electron velocity then decreases. The primary effects displayed by the temperature are (i)

adiabatic cooling due to the expansion of the cross sectional flux tube area with height and (ii) anisotropy, which may be viewed as the fluid model manifestation of the mirror effect.

The behavior of small scale return currents in steady state, the effects of anomalous resistivity on heat flow, electron and ion velocities, and the electron and ion temperatures is currently under investigation.

(D) Magnetic Shear Effects on the Current Driven Ion Cyclotron Instability

Earlier studies have established the importance of self consistent magnetic shear due to field aligned currents (G. Ganguli and P. Bakshi, "Nonlocal Aspect of Electrostatic Current Driven Ion-Cyclotron Instability Due to Magnetic Shear", *Phys. Fluids* 25, 1830, (1982)) and the finite current channel length (P. Bakshi, G. Ganguli and P. Palmadesso, "Finite-Width Current, Magnetic Shear, and the Current-Driven Ion-Cyclotron Instability", 26, 1808 (1983)). These results have been applied to magnetospheric plasmas and various implications regarding satellite observations of ion cyclotron waves have been discussed. (G. Ganguli, P. Bakshi and P. Palmadesso, "Electrostatic Ion-Cyclotron Waves in Magnetospheric

Plasmas: Non-Local Aspects", J. Geophys. Res. (to appear) (1984): NRL Memorandum Report 5197) This work is included in this report as Appendix D.

All the earlier work so far deals with nonlocal effects on temporal growth rates alone. Ion-cyclotron waves are convective. Thus, in order to draw definitive conclusions regarding the ion cyclotron instability in a bounded plasma (e.g. the magnetospheric plasmas) one must also investigate the effects of nonlocality, if any, on spatial growth rates. A start has been made to study nonlocal aspects of the convective properties of the current-driven ion cyclotron instability. Initial results are very interesting, (G. Ganguli, P. Bakshi and P. Palmadesso, "Nonlocal Effects on the Convective Aspects of the Current Driven Ion Cyclotron Modes (CDICM)", Transc. AGU, 64, 820 (1983)). The abstract from the above paper follows.

Nonlocal Effects on the Convective Aspects of the Current Driven Ion Cyclotron Modes (CDICM)*

G. GANGULI (Science Applications, Inc., McLean, VA 22102), P. BAKSHI (Boston College, Chestnut Hill, MA 02167 and Science Applications, Inc., McLean, VA 22102) and P. PALMADESSO (Naval Research Laboratory) Washington, D.C. 20375

Previously^{1,2} we have reported that the nonlocal effects of the finite width current channel and the magnetic shear can significantly modify the normal mode structure of the CDICM and introduce subtleties not accessible using the local approach. We now report the nonlocal effects on the convective aspects of CDICM. The local theory predicts a finite parallel group velocity, $V_{g\parallel}$. The nonlocal theory

reproduces the local theory results for V_g if L_c (the current channel size) $\ll L_s$ (the magnetic shear length). As L_c is increased V_g decreases; and for $L_c > L_s$ becomes negligible. Thus for $L_c > L_s$ the instability becomes absolute in the direction of the magnetic field. The group velocity perpendicular to the magnetic field is only marginally affected by the nonlocality. Implications to the magnetospheric plasmas will be discussed. Effects of the smaller scale substructures in the current profile are also considered.

1. P. Bakshi, G. Ganguli and P. Palmadesso, Phys. Fluids 26, 1808 (1983).
2. G. Ganguli, P. Bakshi and P. Palmadesso, J.G.R., (to be published).

*This work is supported by NASA and ONR.

As the current channel length L_c becomes equal to or greater than the magnetic shear length L_s we find that the ion cyclotron instability undergoes a rather drastic change in its propagation characteristics in the direction along the external magnetic field. The group velocity parallel to the external magnetic field vanishes, thereby making the instability absolute rather than convective as is usually believed. An in depth analysis of the general propagation properties of the current driven ion cyclotron instability is currently ongoing.

Energetic electron precipitation from the radiation belt has been of considerable interest. The possibility of exciting whistler mode turbulence by injection of cold plasma in the quiet time radiation belt has been around for sometime (N.M. Brice, "Artificial Enhancement of Energetic Particles Precipitation through Cold Plasma Injection: A Technique for Seeding Substorms?", J.

Geophys. Res. 75, 25 (1970): Brice, N.M. and C. Lucas, "Influence of Magnetospheric Convection and Polar Wind Loss of Electrons from the Outer Radiation Belt", J. Geophys. Res. 76, 900 (1971)). We have investigated the possibility of whistler mode turbulence in the AMPTE cold plasma release experiment by using a realistic time dependent cold plasma model and proper boundary conditions prevailing in the magnetosphere (P.J. Palmadesso, J.A. Fedder, and G. Ganguli, "Temporal Evolution of Whistler Growth in a Cold Plasma Injection Experiment," Trans. AGU 64, 798 (1983); (Manuscript in preparation for publication)). The abstract follows.

Temporal Evolution of Whistler Growth in a Cold Plasma Injection Experiment*

P.J. PALMADESSO and J.A. FEDDER (both at Naval Research Laboratory, Washington, D.C. 20375) and G. GANGULI (Science Applications, Inc., McLean, VA 22102)

Profiles of the temporal evolution of whistler growth following the injection of cold plasma into the magnetosphere have been calculated with parameters appropriate to AMPTE. Simple models of the spatial spreading of the injected plasma were used to generate profiles of the variation with time of the plasma density within the expanding cloud and the effective length of the interaction region. The gain factor for amplification of a whistler wave packet traversing the cloud was taken to be $G(t) = \exp[\gamma(t) L(t)/V_g(t)]$, where γ is the spatially averaged temporal growth rate, L is the effective length of the interaction region and V_g is the group velocity. It appears that strong amplification and strongly enhanced pitch angle diffusion can be achieved and maintained for substantial periods of time in practical cases.

*This work supported by the Office of Naval Research.

We conclude that in the parameter range of the AMPTE cold plasma release experiment a strong amplification and a strongly enhanced pitch angle diffusion can be achieved and maintained for substantial periods of time in practical cases.

(E) Instability Mechanisms Causing High Latitude Ionospheric Irregularities

In our continuing effort to understand the mechanisms that generate scintillation causing irregularities in the high latitude ionosphere, we have carried out a linear stability analysis by including the dominant sources of free energy, namely, the field aligned currents, velocity shear and density gradients. First, the effects of velocity shear on the current convective instability was investigated using techniques similar to those used in the studies on Rayleigh-Taylor instabilities ("Rayleigh-Taylor Instability in the Presence of a Stratified Shear Layer", P. Satyanarayana et al., to appear in the Journal of Geophysical Research). The results shows that velocity shear preferentially excites a long wavelength mode and possibly leads to the large scale structure in the east-west direction in the so called plasma blobs. Detailed analysis is given in Appendix E, in a paper entitled "Velocity Shear Stabilization of the Current Convective Instability." This paper has been accepted for publication in the Journal of Geophysical Research.

Recent observations report strong field-aligned currents of $500 \mu\text{A}/\text{m}^2$ in the high latitude ionosphere at the same time that irregularities of various scale sizes are observed. Since the field-aligned currents introduce a shear in the magnetic field, we studied the effects of magnetic shear on the collisional current-driven ion cyclotron instability conjectured to be operating in the E region of the ionosphere. Our results show that magnetic shear has a stabilizing influence on the instability. However, the field-aligned currents in the ionosphere are not strong enough to produce sufficient magnetic shear to have any significant stabilizing influence. Currents of $\sim \text{mA}/\text{m}^2$ are needed to produce noticeable effects. The details are given in Appendix F, entitled "Influence of Magnetic Shear on the Collisional Current Driven Ion Cyclotron Instability." This paper is currently being reviewed by "Plasma Physics".

The paper pertaining to the study of effects of velocity shear on Rayleigh-Taylor instability has been accepted by the Journal of Geophysical Research. This paper contains an extensive parametric study in a continuation of our previous effort, "Influence of Velocity Shear on Rayleigh-Taylor Instability," by P.N. Guzdar, P. Satyanarayana, J. Huba and S.L. Ossakow, Geophys. Res. Lett. 9, 547, 1982. The results were applied

to large scale phenomena observed during equatorial spread F and to the structuring in barium releases. The new results are: (i) strong stabilization of short wavelength modes when the velocity reversal point is in the Rayleigh-Taylor localization region, and (ii) significant reduction in the growth rate when the collision frequency is considered to be inhomogeneous which is usually the case in the ionosphere. The detailed analysis is given in Appendix G, entitled "Rayleigh-Taylor Instability in the Presence of a Stratified Shear Layer."

(F) Auroral Instability Studies

We have carried out a study of the nonlinear saturation of the current-driven collisional electrostatic ion-cyclotron instability based on resonance broadening theory. This instability is likely to be excited at ionospheric altitudes in the auroral zone corresponding to the upper E- and the F- regions where field-aligned currents are known to flow. The theory of Dum and Dupree, developed for the collisionless current-driven electrostatic ion-cyclotron wave instability, is extended to take collisional electrons into account. The nonlinear saturated amplitudes are computed and a comparison of these with the experimental observations is made. A draft paper reporting on this work has been completed and will

be submitted for publication under the title "Stabilization of the Collisional Current-Driven Ion Cyclotron Instability" by Chaturvedi, Huba and Ossakow.

An earlier study investigating the effect of magnetic field shear on the current-convective instability (Huba and Ossakow)¹, has been extended to include in the treatment $E \times B$ and gravitational instabilities with applications to the diffuse auroral situation. It is shown that the reduction in the growth rates for these instabilities is greater at longer wavelengths. It is also found that at the long wavelengths (comparable to the density gradient scalelength), the contribution to the growth of the perturbations comes largely from the current-convective mechanism.

This study does not take velocity shear effects into account such as have been studied by Satyanarayana and Ossakow² for a stream-free field case. The two effects will be combined in a future study. A draft paper reporting on this work has been completed and will be submitted for publication under the title "Convective Fluid Instabilities in a Sheared Magnetic Field in Diffuse Aurora" by Chaturvedi, Huba, and Ossakow.

Finite temperature effects have been included in a multilayer barium cloud study to investigate the behavior of the cloud striation growth rate as a function of the relative compressibility of the background and cloud. The

numerical studies performed show that relatively incompressible backgrounds are stabilizing while relatively compressible backgrounds are destabilizing. This work will appear in the Proceedings of the DNA sponsored Late Time HANE/Polar Physics Meeting at SRI International, Menlo Park, CA, October 4-7, 1983. It is, also, being submitted to the J. Geophys. Res. and will appear as an NRL Memo Report. It is included in this report as Appendix H under the title, "Finite Temperature Effects on the Evolution of Ionospheric Barium Clouds in the Presence of a Conducting Background Ionosphere" by Zalesak, Chaturvedi, Ossakow, and Fedder.

(G) Nonlinear Saturation of the Lower-Hybrid-Drift Instability and Anomalous Plasma Transport

In collisionless or nearly collisionless plasma cross field transport associated with classical transport is small. In plasma configurations where the scale lengths of density, L_n , are comparable to the ion Larmor radius ρ_i , the lower hybrid drift instability can cause transport greatly exceeding the classical levels. During the past year we have completed an in depth study of the nonlinear saturation of the lower hybrid drift instability and the associated particle transport. This work represents the first fully self-consistent nonlinear theory of a "drift

wave" instability and therefore represents a significant milestone in our understanding of anomalous transport of plasma across a magnetic field.

In the linear phase of the instability, the resonant interaction of ions with the wave leads to instability of long wavelength modes with wavevector $k \sim \rho_{es}^{-1}$, where ρ_{es} is the electron Larmor radius based on T_i . The electrons stabilize short wavelength modes with $k \gg \rho_{es}^{-1}$ either by classical collisional damping or the damping associated with their cross-field B resonant interaction with the wave. An equation describing the nonlinear coupling of stable and unstable modes has been derived. This nonlinear equation was solved numerically by modifying an existing pseudo-spectral code developed by Fyfe, Joyce and Montgomery (1977)³.

A detailed study of the saturation of the lower-hybrid-drift instability has been completed for a range of parameters and with a variety of mechanisms for dissipating the energy in the wavelength modes. The linearly unstable spectrum in k space grows and then saturates as the modes nonlinearly spread their energy over a broad region of k space. The saturation level of potential fluctuations $\tilde{\phi}$ is given by

$$e\tilde{\phi}/T_i \sim 2-3(2m_e/m_i)^{1/2} v_{di}/v_i$$

with V_{di} the diamagnetic velocity and V_i the ion thermal velocity. This saturation amplitude is relatively insensitive to either the force or strength of the dissipation. The self-consistent cross field transport coefficient D is given by

$$D = 2.4 c_{es}^2 (V_{di}/V_i)^2 \omega_{lh}$$

where ω_{lh} is the lower hybrid frequency. The calculated saturation amplitude is found to be consistent with both laboratory measurements of lower hybrid drift turbulence and with recent particle simulations of this instability.

The above studies have been documented initially in Phys. Fluids under the title "Saturation of the Lower-Hybrid-Drift Instability by Mode Coupling" a copy of which is included in this report as Appendix I. A more recent report entitled "Nonlinear Mode Coupling Theory of the Lower-Hybrid-Drift Instability" has been published as NRL Memorandum Report 5209, November 1983, will be published in Phys. Fluids, May 1984, and appears in this report as Appendix J.

(H) Laser/HANE Theory Support

A preliminary study of short-scale-length coupling mechanisms was initiated in support of the NRL experiment, conducted by B. Ripin, on laboratory simulation of HANE by an expanding laser-produced plasma. The KLYSMA code,

which includes coupling criteria for the instabilities studied by Lampe, Manheimer, and Papadopoulos (1975)⁴ in a multi-fluid anomalous transport model intended for simulation of the early-time HANE regime, was resurrected and run with parameters appropriate to the laboratory experiment. A run with the nominal design parameters of the experiment (as of mid-autumn 1982) was conducted. This run exhibited no short-scale-length coupling; it was concluded that for the nominal experiment parameters the debris shell was too narrow to contain significant exponentiation of any instability in a transit time. Although this run included no chemistry and utilized the thin-shell initialization built into the then-existing KLYSMA for HANE applications, further analytical study indicated that this conclusion would be valid even with more appropriate initialization, for the nominal experiment parameters. These considerations led to re-examination of the design parameters with respect to coupling criteria for the various instabilities. It was concluded that the magnetized ion-ion (MII) instability was the process most likely to yield observable coupling in the experiment, but that it would be necessary to abandon "faithful" scaling of the laboratory simulation in favor of "qualitative" scaling. A study was made of the design parameter regimes in which coupling by the MII

instability would be indicated according to the criteria of Lampe et. al. Criteria for instability turn-on, non-stabilization by EM effects, high-beta expansion, and system size were expressed in terms of the design parameters: these included the ambient magnetic field strength, ambient density, target yield, expansion velocity, and characteristic system dimension. Results of this study were presented at the DNA experiment review at NRL on 27-29 January 1983, and are documented in R.A. Smith and J.D. Huba, "Parameter Survey for Collisionless Coupling in a Laser Simulation of HANE" (NRL Memo Rpt. 5092). This report appears here as Appendix K.

A series of numerical simulations of the high pressure regime of the NRL laser experiment were performed to try to determine the source of the bubbles in the expanding shock front. A number of possibilities were tried to reproduce this phenomenon; a rippling of the position of the debris shell, a perturbation of the mass within the debris shell, and a slug of more slowly moving material behind the debris shell. None of these reproduced the experimental results. In all cases the shock front proved stable. However, it was found that within the shocked region, perturbations of internal structure did grow. This result could be applicable to the late time structure of a HANE. These results have been presented at the Early Time High Altitude Nuclear

Effects Meeting at NRL, October 18-20, 1983, and will appear in the Proceedings of that meeting.

Using the NRL codes, UVDEP and PRODEP, developed for HANE studies we have obtained estimates for ionization in the NRL laser/HANE experiment. The effects on the background N_2 gas of (1) x-rays emitted following laser irradiation of an aluminum target, (2) debris ions moving out from the target, and (3) deposition of uv radiation resulting from interaction between the debris ions and the background gas were calculated. This work was documented in NRL Memorandum Report 5146 entitled "Preliminary Report on UVDEP and PRODEP Results for the NRL Laser/HANE Experiment", August 1983, and appears here as Appendix L.

(I) Early Time HANE Phenomena

The role of collective effects in HANE was examined assuming that Larmor coupling is the dominant coupling process and neglecting the role of NRL's short coupling instabilities. It was shown that the ion distributions generated following Larmor coupling are unstable to electrostatic loss cone type instabilities. A preliminary assessment indicated that these instabilities affect the temperatures of the air and debris ions so that Larmor coupling resembles closely short length coupling. Estimates of minimum electron and ion temperatures were presented for Starfish, Checkmate and Spartans at typical

altitudes. The results have been submitted as an NRL Memorandum Report entitled "The Role of Collective Interactions Following Larmor Coupling in HANE" by K. Papadopoulos.

The modified two stream instability (MTSI) is an important anomalous transport process in the early time development of HANE. A summary of the conditions for its development and the appropriate energy transport coefficients can be found in Lampe et. al.⁴. The coefficients derived in this memorandum were used in multifluid codes such as KLYSMA which determined the early time coupling phenomenology. Since in KLYSMA the electrons are treated as a single one temperature fluid, the energy transfer to electrons was in the form of bulk heating. As first discussed in Lampe and Papadopoulos⁵ the energy transfer to electrons from the MTSI is often dominated by energetic tail formation rather than bulk electron heating. Recent simulations by Tanaka and Papadopoulos⁶ have confirmed these results and clarified the physics underlying the electron energization process. Whether it is necessary to incorporate the energy transfer to suprathermal tails rather than bulk electron heating in the HANE codes depends critically on the phenomenology aspect under consideration. If ionization processes play an important role the presence of non Maxwellian tails is usually important. The same is true if one is interested

in line radiation signatures for diagnostic purposes. Both of the above considerations are relevant to the NRL experiment. In nuclear test cases such as STARFISH or SPARTAN in the 150-400 km altitude range the location and properties of the energetic electron patches depends quite critically on the partition of the energy transfer to electrons during coupling between bulk heating and tail formation. A note was published giving some simple prescriptions in the spirit of Lampe et. al.,⁴ which allow incorporation of the effects of tail formation in multifluid codes, such as KLYSMA, and examined some of the HANE aspects affected by such considerations. These results appeared in the High Altitude Newsletter No. 2, October 1983 edited by Walter Chestnut of SRI. A copy of this report is reproduced here in Appendix M.

A comparison between models of energetic particle generation following HANE and observations of particle energization in high M_A flows in the earth's bow shock was performed. Many similarities were apparent. The same was true for debris jetting and observations of interplanetary clouds following coronal mass ejections from the sun. The results and their impact on HANE phenomenology were presented at the Early Time HANE meeting at NRL, October 18-20, 1983, and will appear in the Proceedings of that meeting.

In addition, the status of the chemistry routines in CYLWHAT and KLYSMA was evaluated and recommendations for changes and improvements for the new early time codes were made. This work is continuing.

(J) Uranium Vapor Release

We have completed a numerical simulation to model the release of uranium vapor at an altitude of 200 km. We used a 1D hydrocode incorporating the chemistry and realistic diffusion coefficients. We calculate motion along the magnetic field, in which ions can diffuse, and motion perpendicular to the field, in which the ions do not diffuse. We determine the spatial and temporal distribution of U, UO^+ , and UO_2^+ . The purpose of the prospective release is to evaluate the infrared emission (LWIR) due to oxides of uranium that may be important in HANE events. If these ions emit large amounts of ir and striate, there could be adverse effects on the operation of optical detectors used in defense systems. This work has been published as NRL Memorandum Report 5193, entitled "Simulation of a Uranium Vapor Release in the High Altitude Atmosphere," November 1983, and appears in this report as Appendix N.

(K) Late Time HANE Striation Models

Optical detectors used as part of U.S. defense against missile attack may be severely degraded for hours following a HANE occurrence, depending on properties of

the detector and on the nature of ionospheric spatial irregularities in the disturbed atmosphere. Currently large scale codes exist to predict visible and ir emission following a nuclear burst (ROSCOE and derivatives, NORSE and NADIR). A model has been incorporated into ROSCOE to provide an estimate of the power spectral density (PSD) of the spatial irregularities. It is essentially a trivial model, however, which incorporates no angular dependence with the magnetic field direction and relative ion-neutral wind directions and assumes a universal falloff of k^{-2} in the PSD.

We are developing a first order model for high altitude nuclear induced striations and the resulting PSD, based on what is known from plasma instability theory and simulations at NRL and elsewhere and on comparison with the high altitude data that is available. This model, while a substantial improvement over current use in the above codes, should be considered only a step in the longer range goal of understanding the striating disturbed ionosphere more completely than we currently do. This is because of the very limited data available and the incomplete nature of our understanding of the processes that induce striations.

The spatial PSD depends on the size or sizes of nuclear induced striations, their shape, i.e.,

distribution of ions, the sharpness of edges, whether the emission is due to plasma recombination or debris, and the direction from which we view the striation. At this stage of development of the theory it is possible to estimate sizes, shapes, and edge properties for some "candidate" mechanisms that cause striation growth. Spectral properties of the model we are developing have been reported on at the DNA Late Time HANE/Polar Physics Meeting, 4-7 October 1983 at SRI International and, also, at the ROSCOE/NORSE/NADIR-C/LAMP Community Meeting, 15-17 November 1983. A copy of the presentation made at the ROSCOE Meeting with notes is included in this report as Appendix O. It has appeared in the Proceedings of the ROSCOE Meeting and will appear in the Proceedings of the SRI Meeting.

In another paper we treat the theory of the spectral properties of optical data scans. Entitled "Estimating Spectral Indices from Transforms of Discrete Representations of Density Functions" we determine limitations on extracting meaningful spectral indices in terms of the complexity of the spatial emission profile, the adequacy of resolution, and aliasing errors. The paper has been submitted as an NRL Memorandum Report.

(L) Quasi-steady State Multi-Plasma Cloud Configurations
in the Ionosphere

It has been observed that kilometer-scale size structures can persist in both barium and nuclear cloud striation phenomena. Beyond a certain point in late times after the release of such plasma clouds, the bifurcation of clouds appears to stop. This so-called "freezing" phenomenon results in an array of closely spaced plasma cloud striations which tend to drift in unison for an extended period of time. The possible mechanisms for causing the cessation of bifurcation have attracted considerable attention in the literature. However, there is another necessary ingredient for the freezing phenomenon. After bifurcation has stopped, the multiple striation fingers appear to undergo quasi-steady state $E \times B$ drift across the geomagnetic field. We have considered the nature and properties of closely spaced multiple plasma striations in quasi-steady state. The neutral electrical interaction of the striations is included exactly. Using the technique developed in a previous paper (Chen, et. al.: J. Geophys. Res. 88, 5528, 1983), we have been able to demonstrate the existence of quasi-steady state multiple plasma cloud configurations. We have shown that the influence of neighboring clouds on the electric field inside nearby clouds decreases as K^{-1} for any x_0/a so that the cloud interior is effectively

shielded from the intercloud interaction. Here, $K \equiv \sigma_{in}/\sigma_{out}$, the Pedersen conductivity ratio and $2x_0$ is the center-to-center distance of striations (modeled by cylinders of radius a). As a result, the electric field inside all the clouds is essentially uniform and equal so that such a system would be seen to drift in unison across the magnetic field while maintaining the overall geometrical shape.

The above results have been described in an NRL Memorandum Report, in press, and have, also, been accepted, in a more compressed version, for publication in J. Geophys. Res. under the title "Quasi-Steady State Multi-Plasma Cloud Configuration in the Ionosphere". It appears here as Appendix P.

(M) Chaotic Behavior in Ionospheric Processes

A series of detailed studies of the transition from orderly to chaotic behavior in a simple dynamical system were conducted in 1983. Orbits of particles acted on by the field of a standing wave structure, an idealized representation of wave structures which can arise on auroral field lines or in ionospheric density depressions, exhibited Feigenbaum period doubling as the amplitude parameter has increased, and stochastic behavior at the limit of the period doubling cycle. At higher amplitudes a band structure was observed in surface-of-section plots

of the particle motion, and this in turn evolved into a strange attractor at very large wave amplitude.

(N) Linear Dynamics of Tropical Heat Sources and Interactions with Mid-Latitudes

A two dimensional linear model has been developed to investigate the response of a stratified atmosphere to prescribed tropical heat sources in the presence of a new zonal flow. The heat sources of interest are those that arise from warm sea surface temperature anomalies (SST's) that occur in the central and western tropical Pacific during an El Nino event. During such events the convection is greatly increased over the region of the SST anomaly, greatly changing the atmospheric circulation in the region. The anomalous convection due to the warm SST anomaly influences the atmospheric circulation far from its origin in mid-latitudes. It is hoped that this model will aid in the understanding of the structure of such teleconnection responses.

In this model, the primitive equations on a sphere in log-pressure coordinates are linearized about a basic state with a near zonal flow which can depend on latitude and height. The stratification of the model basic state atmosphere can be varied with height and latitude. The model variables are Fourier amplitudes for each zonal wavenumber. The motion is presently forced by a prescribed heating function of given frequency, which

represents the latent heating due to large-scale tropical convection. The model is damped by eddy diffusion, Rayleigh friction and Newtonian cooling. Damping through the vertical transport of horizontal momentum by deep convection is also parameterized. The boundary layer is formulated using an eddy diffusion coefficient K with the surface stress formulated using a drag coefficient. The same formulation is used for the surface heat flux generated by warm SST anomalies. The model domain is global with a rigid upper boundary at 22.5km. The model equations are finite differenced on a staggered grid and the resulting finite difference equations form a block matrix system which is solved by standard techniques.

The model has been tested for the case of steady latent heating in a basic state at rest and the same result obtained as the Walker circulation solution of Geisler (1981).⁷ The model will be used to compare the response forced by a prescribed cumulus heat source in a realistic mean zonal flow to that forced by a warm SST anomaly. The cumulus heating initiated by the warm SST anomaly will be found by an iterative process through a number of solutions. The boundary layer convergence from the previous solution will be used to calculate the vertical flux of moisture at the top of the trade wind inversion (at $z = 2\text{km}$). The vertical moisture flux is then matched to a new cumulus heating rate and a new

solution found. A one-dimensional model, which uses Fourier modes in longitude and modes in the vertical in a constant mean flow, will be converted to a fully modal model. The normal modes excited by the above heat sources will then be calculated and compared to the two-dimensional model solutions for realistic mean zonal flows. This work is described in more detail in Appendix Q entitled "Model of Linear Response to Tropical Heat Sources."

(O) The Large-Scale Dynamics of the Indian Summer Monsoon

The large-scale dynamics of the summer monsoon in the region of India is currently being investigated. The research is a follow on from the author's Ph.D. thesis research on the linear dynamics of the East African low-level jet. A paper on this thesis work (see Appendix R) was presented at the 15th Technical Conference on Hurricanes and Tropical Meteorology, January 9-13, 1984, in Miami, Florida. The title is "A Linear Dynamic Model of the East African Jet in a Stratified Atmosphere." The following is the abstract for this paper:

A Linear Dynamic Model of the East African Jet in a Stratified Atmosphere, K.D. Sashegyi and J.E. Geisler

Relative effects of prescribed summer monsoon heat sources and the topographic barrier of East Africa on the maintenance of the East African jet were investigated using a linearized primitive equations models in a stratified atmosphere. The topographic barrier, modeled as a rigid wall, concentrated the broad cross-equatorial flow

forced by the large-scale latent heating over India into a boundary jet. Low-level sensible heating over Somalia and Saudi Arabia increased the cross-equatorial flow, created a local wind maximum along the coastline of Somalia and a more gradual turning of the jet from the topographic barrier.

At present, the three dimensional regional area model of Chang and Madala (1980) is being adapted to study the nonlinear aspects of the large scale Indian monsoon. The model includes realistic topography and will be driven as in the linear model by a prescribed latent heat source representing the large scale monsoon convection in the region of India. The model domain runs from 20S to 40N and 30°E to 110°E. Sigma coordinates (normalized pressure P/P_s , where P_s is the surface pressure) are used as the vertical coordinate. The model has 5 sigma levels in the vertical, 31 grid points in latitude and 81 grid points in longitude. The horizontal resolution of the model is 1° in longitude and 2° in latitude. The solution obtained with this nonlinear model will be compared to the linear solutions.

(P) Collective Particle Accelerator (CPA)

A collective particle accelerator (CPA) is a device in which an intense relativistic electron beam (IREB) gives rise to an axial electric field which in turn accelerates a solid beam injected along the axis. A previous study of the stability of a solid charged beam propagating inside a hollow relativistic electron beam (H. Uhm, Phys. Fluids 25, 1908 (1982)) concluded that such a configuration is unstable to transverse oscillations.

We have studied both the normal mode approach (as in Uhm (1982)) and the convective aspects of the transverse oscillations (G. Ganguli and P. Palmadesso, "Finite Geometry Effects on the Stability of a Charged Beam Propagating Through a Relativistic Annular Electron Beam", to appear

in *Journal of Applied Physics*, (1984) and NRL Memo Report 5191), and conclude that it is possible to achieve successful acceleration of a portion of the axial beam. Thus, the transverse oscillation is not fatal to CPA operation.

Further studies of the CPA particle orbits are now under investigation. This work is included in this report in Appendix S.

(Q) Plasma Behavior in Crossed Electric and Magnetic Fields

The behavior of plasmas subject to crossed electric and magnetic fields has been the subject of considerable study under this task. The particular case of interest is shown in Figure 3. A large amplitude electro-magnetic pulse traveling between two highly conducting regions is incident upon a plasma slab. If the pulse amplitude is large enough, then electrons from the negative conducting region (the cathode side) are magnetically constrained and cannot enter the plasma slab to provide current carriers, hence the current must be carried via the plasma ions. After a sufficient time has passed, the plasma ions represent the only current carriers.

The problem is complicated by the fact that the magnetic field must diffuse into the plasma slab. Thus, the current is initially carried in a very thin region, Figure 4, whose thickness is equal to the skin depth of

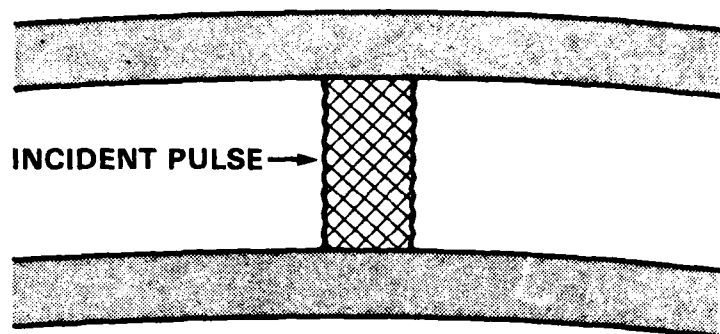


FIGURE 3

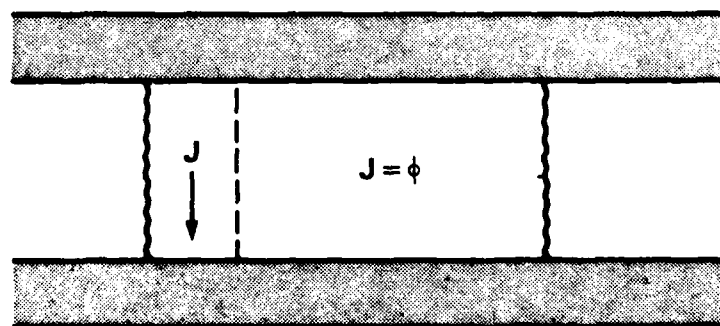


FIGURE 4

the plasma. The high current density in this region quickly depletes the electrons near the cathode and then attempts to draw the full current in this region as space-charge limited ion current (Figure 5). If the ion density is such that a sufficient number of ions are supplied to the electron depleted region, then the vacuum gap will grow larger. As the space charge limit is proportional to $v^{3/2}d^{-2}$, this means that the voltage across the vacuum gap must increase. Another way of looking at it is that the impedance of the region must increase. This means that the skin depth increases and a new region of plasma is available for carrying the current. The process continues until the whole plasma slab has eroded and the pulse is finally allowed to pass to the right.

As this problem is inherently a 2-dimensional problem, many different length scales must be considered: (1) the magnetic skin-depth; (2) the plasma sheaths; and (3) the vacuum gap. As noted above, the gap affects the plasma impedance which affects the skin depth; it also affects the ion current which affects the plasma sheath. Thus all of these length scales are inter-related.

The current work under this contract has been an attempt to understand the global physics of this problem and how the various parts are inter-connected. Figure 6 shows the global structure of the plasma; much work needs

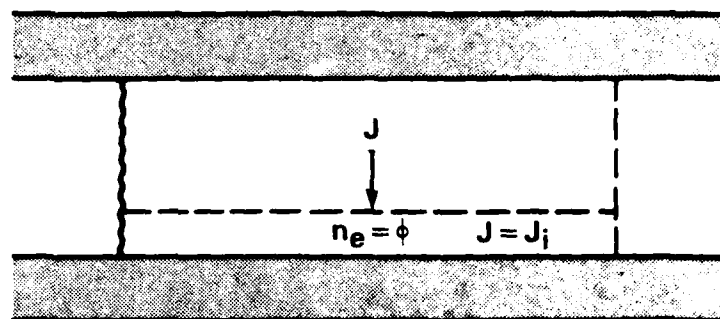


FIGURE 5

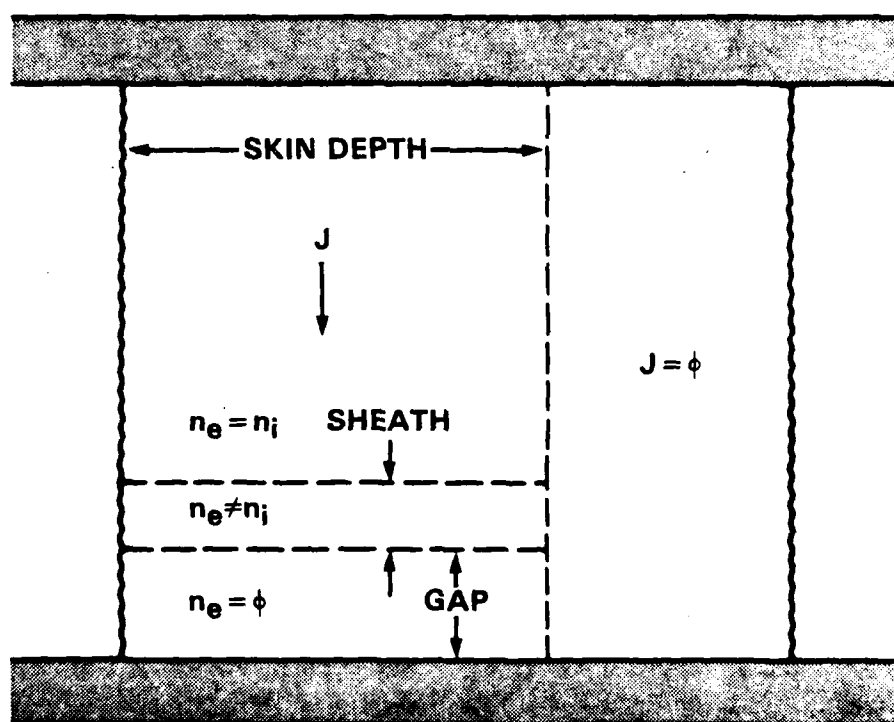


FIGURE 6

to be performed to understand the dynamic interplay
between the various regions.

REFERENCES

1. Huba, J.D. and S.L. Ossakow, Influence of magnetic shear on the current-convective instability in the diffuse aurora, J. Geophys. Res 85, 6874 (1980).
2. Satyanarayana, P. and S.L. Ossakow, Velocity shear stabilization of the current-convective instability, accepted for publication by J. Geophys. Res. (1984).
3. Fyfe, D., G. Joyce and D. Montgomery, J. Plasma Phys. 17, 317 (1977).
4. Lampe, M., W.H. Manheimer, and K. Papadopoulos, "Anomalous transport coefficients for HANE applications due to plasma microinstabilities," NRL Memo Report 3076, 1975.
5. Tanaka, M. and K. Papadopoulos, Phys. Fluids 26, 1697, (1983).
6. Lampe, M. and K. Papadopoulos, Astrophys. J. 212, 886 (1977).
7. Geisler, J.E., "A linear model of the Walker circulation," J. Atmos. Sci. 38, 1390 (1981).

APPENDIX A
TEARING INSTABILITY IN AN
ANISOTROPIC NEUTRAL SHEET

J. Chen
Science Applications, Inc.

and

P. Palmadesso
Naval Research Laboratory

Tearing Instability in an Anisotropic Neutral Sheet

J. CHEN* AND P. PALMADESSO

*Geophysical and Plasma Dynamics Branch
Plasma Physics Division*

**Science Applications, Inc.
McLean, VA 22102*

September 7, 1983

This research was supported by the Office of Naval Research and
the National Aeronautics and Space Administration.



NAVAL RESEARCH LABORATORY
Washington, D.C.

Approved for public release; distribution unlimited.

A-3

PRECEDING PAGE BLANK-NOT FILLED

SECURITY CLASSIFICATION OF THIS PAGE (When Data Entered)

REPORT DOCUMENTATION PAGE		READ INSTRUCTIONS BEFORE COMPLETING FORM
1. REPORT NUMBER NRL Memorandum Report 5178	2. GOVT ACCESSION NO.	3. RECIPIENT'S CATALOG NUMBER
4. TITLE (and Subtitle) TEARING INSTABILITY IN AN ANISOTROPIC NEUTRAL SHEET		5. TYPE OF REPORT & PERIOD COVERED Interim report on a continuing NRL problem.
		6. PERFORMING ORG. REPORT NUMBER
7. AUTHOR(s) J. Chen* and P. Palmadesso		8. CONTRACT OR GRANT NUMBER(s)
9. PERFORMING ORGANIZATION NAME AND ADDRESS Naval Research Laboratory Washington, DC 20375		10. PROGRAM ELEMENT PROJECT, TASK AREA & WORK UNIT NUMBERS 61153N; RR033-02-44; 47-0884-0-3; NASA 14365
11. CONTROLLING OFFICE NAME AND ADDRESS Office of Naval Research, Arlington, VA 22203 National Aeronautics and Space Admin., Washington, DC 20546		12. REPORT DATE September 7, 1983
		13. NUMBER OF PAGES 37
14. MONITORING AGENCY NAME & ADDRESS (if different from Controlling Office)		15. SECURITY CLASS (of this report) UNCLASSIFIED
		15a. DECLASSIFICATION DOWNGRADING SCHEDULE
16. DISTRIBUTION STATEMENT (of this Report) Approved for public release; distribution unlimited.		
17. DISTRIBUTION STATEMENT (of the abstract entered in Block 20, if different from Report)		
18. SUPPLEMENTARY NOTES *Present address: Science Applications, Inc., McLean, VA 22102 This research was supported by the Office of Naval Research and the National Aeronautics and Space Administration.		
19. KEY WORDS (Continue on reverse side if necessary and identify by block number) Tearing instability Anisotropic neutral sheet Kinetic instability		
20. ABSTRACT (Continue on reverse side if necessary and identify by block number) A study is made of the collisionless tearing-mode stability properties of a field-reversed plasma layer whose temperature distribution is anisotropic. The plasma is confined by its self magnetic field with no external field. A kinetic description is used for both ions and electrons. The wavevector k of the perturbation is taken to be parallel to the equilibrium magnetic field B_0 and perpendicular to the equilibrium current J_0 . The analysis is carried out for the low-frequency perturbation ($ \omega \ll$ (Continues)		

DD FORM 1473
1 JAN 73EDITION OF 1 NOV 65 IS OBSOLETE
S/N 0102-014-6601

SECURITY CLASSIFICATION OF THIS PAGE (When Data Entered)

A-5

PRECEDING PAGE BLANK-NOT FILMED

20. ABSTRACT (Continued)

ω_{ci}) using simplified particle orbits. The effects of the axis-crossing and nonaxis-crossing orbits are discussed. It is found that the conventional technique of matching the inner and outer asymptotic solutions at the electron inner region is inadequate for the anisotropic case. An intermediate region in which the axis-crossing ion orbits are important is identified. The eigenvalue equation is solved using both analytic approximations and numerical methods to obtain the eigenmode structure and the linear dispersion relation. It is found that the collisionless tearing-mode growth rate is significantly enhanced for $T_{\perp} > T_{\parallel}$ and that the mode is strongly stabilized for $T_{\perp} < T_{\parallel}$, showing that the anisotropic tearing-mode dominates the conventional isotropic tearing-mode instability.

CONTENTS

I. INTRODUCTION.....	1
II. FORMULATION.....	4
A. Linear Eigenvalue Equation.....	4
B. Anisotropic Plasma Layer in Thermal Equilibrium.....	7
III. Stability Properties for an Anisotropic Neutral Sheet.....	8
A. Model Orbits.....	8
B. Linear Dispersion Relation.....	14
IV. SUMMARY.....	26
Acknowledgments.....	28
References.....	29

TEARING INSTABILITY IN AN ANISOTROPIC NEUTRAL SHEET

I. INTRODUCTION

In this paper, we investigate the tearing-mode stability properties of a field-reversed plasma layer whose temperature distribution is anisotropic ($T_{\perp} \neq T_{\parallel}$). The symbols \perp and \parallel refer to directions perpendicular and parallel to the equilibrium magnetic field, respectively. Figure 1 shows a schematic drawing of the geometry and the coordinate system. The equilibrium magnetic field $\underline{B}_0(z) = B_x^0(z)\hat{x}$, indicated by the solid lines, is generated self-consistently by the current $\underline{J}_0(z) = J_0(z)\hat{y}$ with no external magnetic field. The magnetic field reverses its direction in the plane $z = 0$ and $J_0(z)$ is symmetric in z . Both ions and electrons are assumed to contribute to the equilibrium current. The number density $n_0(z)$ is also shown in the figure. In this one-dimensional equilibrium, all physical quantities depend on z alone. The plasma is assumed to consist of collisionless ions and electrons so that Vlasov equations are used for both species.

It is well-known that inertia of the current carriers can lead to collisionless tearing instability in a system such as the one described above. Considerable work has been done on the basic collisionless tearing-mode properties of the neutral sheet configuration¹⁻⁸. An example of physical systems that may be modelled by this configuration is the earth's magnetotail⁹. Subsequent to the early work, tearing-mode results have been considered in connection with the magnetotail^{10,11}. In these studies, the neutral sheets are generally assumed to have isotropic temperature distributions ($T_{\perp} = T_{\parallel}$). However, in a collisionless plasma, the motion of particles parallel to the magnetic field is decoupled from the perpendicular motion and temperature anisotropy can be maintained even in thermal equilibrium. Laval and Pellat¹² used an energy principle analysis to show that collisionless tearing-mode properties can be strongly modified by weak temperature anisotropy. In particular, it was found that the $k \parallel B_0$ mode can be stabilized by a very small degree of electron temperature anisotropy: $T_{e\perp}/T_{e\parallel} < (1 - a_e/\delta)$ where a_e is the electron gyroradius and δ is the layer half-thickness. In this work, neither the dispersion relation nor the marginal condition for the anisotropic case was given. Recently, Chen and Davidson¹³ carried out a Vlasov-fluid analysis of a field-reversed ion layer at marginal stability using approximate

Manuscript approved July 14, 1983.

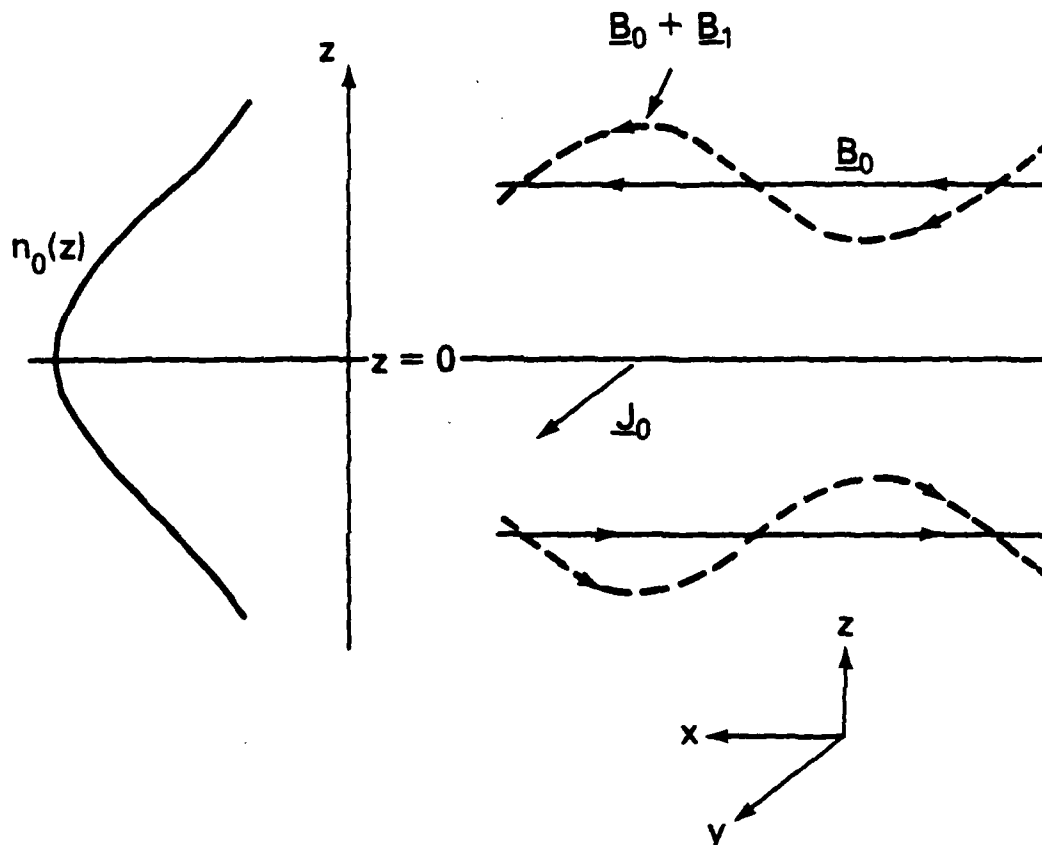


Fig. 1 Schematic drawing of a neutral sheet and the coordinate system. The magnetic field $B_0(z)$ reverses direction at $z = 0$. The dashed lines indicate the magnetic field configuration including the perturbation.

orbits in a cylindrical coordinate system. It was found that relatively small temperature anisotropy in ions significantly modified the stability boundaries. Consistent with the results of Ref. 12, the range of unstable wavenumbers is reduced for $T_{i\perp}/T_{i\parallel} < 1$ and is increased for $T_{i\perp}/T_{i\parallel} > 1$. More recently, Basu and Coppi¹⁴ studied a fluid-like "field swelling" instability in an anisotropic plasma in which the magnetic pressure is comparable to the particle pressure and in which there is no equilibrium current. This analysis is local and is based on the fluid equations. However, in the neutral sheet configuration, the instability is intrinsically nonlocal and the plasma β is much greater than unity in the field-null region so that the fluid equations are invalid. Thus, the treatment of Ref. 14 is not applicable to the tearing-mode instability which is due to resonant particles crossing the field-null region.

A difficulty in treating the neutral sheet configuration is the complicated particle orbits¹⁵. In order to make the problem tractable analytically, "straight-line" approximations have often been used^{8,10} for the particle orbits crossing the null plane. Numerically, the problem is also difficult. In a noteworthy but rarely referenced work, Holdren¹⁶ utilized an integrodifferential equation formalism to show the feasibility to treat the various orbits exactly. In order to minimize the numerical errors, relativistic electrons with large orbits were used and no definitive comparison can be made between the relativistic numerical results and the previous nonrelativistic, approximate results⁵. In addition, the numerics required are prohibitive and it is in general difficult to use this method.

In the present model, we will adopt the straight-line orbits but improve the treatment of the ion orbits. The effects of the small Larmor radius orbits will also be considered. The anisotropic collisionless tearing-mode analysis is carried out for perturbations of the form $\psi(x, z, t) \equiv \hat{\psi}(z) \exp(ikx - i\omega t)$ where the wavevector \underline{k} is taken to be parallel to the equilibrium magnetic field. In Fig. 1, the dashed lines indicate schematically the magnetic field lines including the mirror-like perturbation given above. As a general remark, the problem treated here is different from that of tearing instabilities in tokamak discharges¹⁸ because the tokamak geometry would have an applied magnetic field in the y-

direction (Fig. 1). This alters the particle orbits significantly. The configuration studied here is more closely related to certain θ -pinches and ion layers.

In Section II, we present the basic linear analysis of the perturbation. In Section III, simplified particle orbits are used to obtain the eigenvalue equation. This equation is solved to give the linear anisotropic dispersion relation. Section IV discusses the results.

II. FORMULATION

Figure 1 shows a schematic drawing of a neutral sheet. We assume that there is no equilibrium electrostatic field and no bulk motion of the plasma (i.e., $\underline{E} \times \underline{B} = 0$). We consider a class of equilibria described by $f_{0j} = f_{0j}(\underline{H}_{1j} - V_j P_{yj}, H_{1j})$ where $j = e, i$ and (H_{1j}, P_{yj}, H_{1j}) are the single-particle constants of the motion in the equilibrium magnetic field. Here, $H_{1j} = (m_j/2)(v_y^2 + v_z^2)$, $P_{yj} = m_j v_y + (q_j/c)A_y^0(z)$, $H_{1j} = (m_j/2)v_x^2$ and $A_y^0(z)$ is the vector potential for the equilibrium magnetic field, where q_j is the electric charge, m_j is the mass, and $V_j =$ constant is the mean drift velocity of the species j .

A. Linear Eigenvalue Equation

The analysis is carried out for perturbations of the form $\psi(x, z, t) = \hat{\psi}(z)\exp(ikx - i\omega t)$ where the wavevector $\underline{k} = k\hat{x}$ is parallel to the equilibrium magnetic field. The magnetic field configuration including this perturbation is indicated by dashed lines in Fig. 1. The characteristic frequency is low with $|\omega| \ll \omega_{ci}$ where $\omega_{ci} = eB_0/m_i c$ is the ion cyclotron frequency in the asymptotic magnetic field $B_0 \equiv B_x^0(z = \infty)$. Moreover, we consider the case where $kv_e \sim \omega_{ci}$ which is true for a wide range of parameters of interest so that we also have typically $|\omega| \ll kv_e$, where v_e is the electron thermal velocity. This will be verified a posteriori.

Using the standard method of characteristics, the first-order Vlasov distribution function for each species is

$$f_{1j} = -\frac{q}{m} \int_{-\infty}^t dt' (\underline{E}_1 + \frac{1}{c} \underline{v}' \times \underline{B}_1) \cdot \frac{\partial}{\partial \underline{v}'} f_0, \quad (1)$$

where $(\underline{x}', \underline{v}')$ represents the particle orbits in the equilibrium field with the conditions $\underline{x}'(t' = t) = \underline{x}$, $\underline{v}'(t' = t) = \underline{v}$ and $\psi(t \rightarrow -\infty) = 0$ for all perturbation quantities. The time integration is carried out along the unperturbed orbits. In the above equation and in the remainder of the paper, the species index $j = e, i$ is suppressed where no confusion arises. The perturbed fields are given by

$$\underline{B}_1 = \nabla \times \underline{A}_1, \quad (2)$$

$$\underline{E}_1 = -\nabla\phi - \frac{1}{c} \frac{\partial \underline{A}_1}{\partial t}, \quad (3)$$

$$\nabla \times \underline{B}_1 = \frac{4\pi}{c} \underline{J}_1, \quad (4)$$

and

$$\nabla \cdot \underline{E}_1 = 4\pi\rho_1, \quad (5)$$

where \underline{A}_1 and ϕ are the perturbed vector and scalar potentials. In this paper, we choose the Coulomb gauge ($\nabla \cdot \underline{A}_0 = 0$). Because the characteristic frequency of the perturbation is low, $\omega \ll \omega_{ci}$, we assume charge neutrality to first order. Note that $B_{1y}(x, z, t) = 0$ for the mirror-like perturbations so that $\underline{J}_1 = J_{1y}(x, z, t)\hat{y}$ and $\underline{A}_1 = \psi(x, z, t)\hat{y}$.

For the general form $f_0 = f_0(H_1 - V_j P_y, H_1)$, note that

$$\frac{\partial f_0}{\partial \underline{v}} = m(\underline{v} - \hat{v}\hat{y}) \frac{\partial f_0}{\partial H_1} + m\left(\frac{\partial f_0}{\partial H_1} - \frac{\partial f_0}{\partial H_1}\right) \underline{v} \cdot \hat{x}.$$

Using Eqs. (2) and (3) in Eq. (1), straightforward calculation yields

$$f_{1j} = q_1 \frac{\partial f_0}{\partial H_1} [(\phi - \beta_j \psi) + i\omega S_y] - ikq_1 \left(\frac{\partial f_0}{\partial H_1} - \frac{\partial f_0}{\partial H_1}\right) \underline{v} \cdot \hat{x} S_y, \quad (6)$$

where S_y is the orbit integral along the unperturbed orbits given by

$$S_y \equiv \int_{-\infty}^t dt' (\phi - \frac{1}{c} \underline{v}' \cdot \hat{y} \psi) \quad (7)$$

and

$$\beta_j \equiv \frac{v_j}{c}$$

is the uniform mean drift velocity normalized to the speed of light c . Here, use has been made of $\partial/\partial t \rightarrow -i\omega$ and $\partial/\partial x \rightarrow ik$. For the isotropic case, the last term in Eq. (6) vanishes and we trivially recover the previous results⁸. For the anisotropic case, estimating v_x by the typical thermal velocity v_{th} , we note that the ratio of the second term to the third term is of the order of $\omega/(kv_{th})$ which makes the last term in Eq. (6) small in comparison with the first two terms for low frequency perturbations except for a very small degree of anisotropy. This means that the marginal state¹³ and the growth rate can be significantly modified in comparison with the isotropic case. It is the purpose of this paper to give a quantitative illustration of this point.

Another consequence of the low-frequency nature of the perturbation is that the perturbed scalar potential ϕ is much smaller than $(v_y/c)\psi$ ⁸. This can be seen by noting that the electric field E_{1x} along the magnetic field is at most comparable to the components perpendicular to the magnetic field, say, E_{1y} . That is to say, $E_{1x} \leq E_{1y}$. This implies

$$\phi \leq \left(\frac{\omega}{kv_{th}}\right)\left(\frac{v_{th}}{c}\right)\psi.$$

For the low frequency case ($\omega \ll kv_{th}$), ϕ is much less than $(v_y/c)\psi$ where $v_y \sim v_{th}$ for the typical thermal particle. Physically, this is simply a statement of quasi-neutrality at low frequencies. Although it is theoretically straightforward to include ϕ , we will adopt the simplification of neglecting ϕ in comparison with $(v_y/c)\psi$. Then, the approximate perturbed distribution function is

$$f_{1j} = -q\beta \frac{\partial f_0}{\partial H_{\perp}} \psi + i\omega q \frac{\partial f_0}{\partial H_{\perp}} S_y - ikq \left(\frac{\partial f_0}{\partial H_{\perp}} - \frac{\partial f_0}{\partial H_{\parallel}} \right) v_x S_y, \quad (8)$$

where the orbit integral [Eq. (7)] has been simplified to

$$S_y = -\frac{1}{c} \int_{-\infty}^t dt' v_y' \psi. \quad (9)$$

The first term in Eq. (8) is the usual adiabatic term which does not depend on the detailed particle orbits. The second term represents the change in

momentum and the third term represents the change in energy of the particles. In particular, $ikqS_y$ is the time-integrated Lorentz force acting on the particles in the x-direction.

B. Anisotropic Plasma Layer in Thermal Equilibrium

In the preceding section, we have described the general theoretical framework appropriate for equilibria of the type $f_{oj}(H_{\perp j} - V_j P_{yj}, H_{\parallel j})$. To examine the stability properties in detail, we specialize to the case where the plasma layer consists of two species (electrons and ions), both satisfying the two-temperature Maxwellian distribution given by

$$f_{oj} = \frac{\hat{n}_o}{2\pi T_{\perp j}/m_j} \frac{1}{\sqrt{2\pi T_{\parallel j}/m_j}} \exp\left[-\frac{1}{T_{\perp j}} (H_{\perp j} - V_j P_{yj})\right] \exp\left(-\frac{1}{T_{\parallel j}} H_{\parallel j}\right), \quad (10)$$

where $H_{\perp j} = (m_j/2)(v_y^2 + v_z^2)$, $P_{yj} = m_j v_j + (q_j/c)A_y^o(z)$, $H_{\parallel j} = (m_j/2)v_x^2$, $V_j = \text{constant}$ is the mean velocity of the species j , and $A_y^o(z)$ is the vector potential for the equilibrium magnetic field. As stated before, the electrostatic field is taken to be zero in the frame of the layer.

The equilibrium particle density and magnetic field profiles corresponding to Eq. (10) depend only on the perpendicular temperature and are well-known¹⁷

$$n_o(z) = \hat{n}_o \operatorname{sech}^2\left(\frac{z}{\delta}\right), \quad (11)$$

and

$$B_x^o(z) = \frac{2cT_{\perp}/\delta}{e(V_i - V_e)} \tanh\left(\frac{z}{\delta}\right), \quad (12)$$

where δ is the characteristic half-thickness of the plasma layer given by

$$\delta \equiv \left(\frac{c^2 T_{\perp}}{2\pi \hat{n}_o}\right)^{1/2} \frac{1}{e(V_i - V_e)}. \quad (13)$$

Here, $T_{\perp} \equiv T_{i\perp} + T_{e\perp}$, and \hat{n}_o is the maximum number density at $z = 0$ for both species. For $z \rightarrow \infty$, we have $B_x^o(z \rightarrow \infty) = B_o$ with

$$B_o \equiv \sqrt{8\pi \hat{n}_o T_{\perp}}, \quad (14)$$

where $B_0 > 0$ is chosen without loss of generality. This choice implies $(V_i - V_e) > 0$ so that the total current is in the $+y$ -direction, given by

$$\underline{J}_0(z) = e(V_i - V_e)n_0(z)\hat{y}. \quad (15)$$

Because of charge neutrality, the equilibrium ion and electron densities are equal. It is easy to show that the zero electrostatic field condition is equivalent to

$$T_{i\perp}V_e + T_{e\perp}V_i = 0. \quad (16)$$

If we denote the gyroradius of the thermal particles by $a_j \equiv v_{j\perp}/\omega_{cj}$ where $v_{j\perp} \equiv \sqrt{2T_{j\perp}/m_j}$ and $\omega_{cj} = eB_0/m_jc$ with B_0 given by Eq. (14), then it is easy to show by using Eqs. (13) and (16) that

$$\frac{a_j}{\delta} = \frac{|V_j|}{v_{j\perp}} \quad (17)$$

and

$$\frac{q_j V_j}{c T_{j\perp}} = \frac{2}{B_0 \delta}. \quad (18)$$

As a general remark, the equilibrium configuration described above is obtained by balancing the Lorentz force $c^{-1}(\underline{J}_0 \times \underline{B}_0)$ with the perpendicular pressure gradient $-(\partial/\partial z)[n_0(z)T_{\perp}]$.

III. Stability Properties for an Anisotropic Neutral Sheet

A. Model Orbits

In order to determine the stability properties of the system described by Eqs. (10)-(18), the orbit integral S_y [Eq. (9)] must be evaluated. Generally, the orbits in the equilibrium field are complicated.¹⁵ In the previous calculations on the isotropic neutral sheets, "straight-line" orbits^{8,10} have been used to evaluate the orbit integral. In these approximations, the neutral sheet is divided into two regions. In the inner region, $|z| \leq d_j \sim \sqrt{a_j \delta}$ where the magnetic field is weak, the orbits

are taken to be straight lines across the null-plane ($z = 0$) and reflected from the surfaces at $|z| = d_j$. Thus, v_y is nearly constant in this region. In addition, the perturbed vector potential $\psi = A_{1y}$ is assumed to be constant in the inner region (constant- ψ approximation). In the outer region, $|z| \geq d_j$, the particles are assumed to execute nonaxis-crossing small Larmor radius orbits and these orbits are neglected. In particular, in Ref. 8, the dispersion relation is obtained by matching the inner and outer solutions at $z = \sqrt{2a_e\delta}$. This approximation neglects the axis-crossing ion orbits that extend far beyond the electron inner region since $d_i/d_e \sim (m_i/m_e)^{1/4}$. Although the effects of the axis-crossing electrons are greater than those of the axis-crossing ions, the ion effects dominate in the intermediate region $d_e \leq |z| \leq d_i$, as will be shown in this section. In the isotropic case, it will turn out that the neglect of the intermediate region does not change the dispersion relation substantially. However, in the anisotropic case, the ion orbits in the intermediate region affects the dispersion relation significantly. In the present analysis, we include the three regions (Fig. 2) and define the boundary surfaces at

$$d_e \equiv \sqrt{2a_e\delta} \quad (19)$$

for the electrons and

$$d_i \equiv \sqrt{a_i\delta/2} \quad (20)$$

for the ions, where $a_j = v_{j1}/\omega_{cj}$ is the Larmor radius of a thermal particle with $v_{j1} = \sqrt{2T_{j1}/m_j}$. Physically, d_e is the distance where the local electron Larmor radius $a_e(d_e) \equiv v_{e1}/\omega_{ce}(d_e)$ is equal to $d_e/2$. Here, $\omega_{ce}(d_e) = eB_x^0(d_e)/m_e c$. d_i is the distance where the local ion Larmor radius $a_i(d_i) \equiv v_{i1}/\omega_{ci}(d_i)$ is equal to d_i . The factor of $\sqrt{2}$ is somewhat arbitrary and is chosen to avoid overestimating the large ion orbits. Moreover, this choice allows the use of the constant- ψ approximation in the region $|z|/\delta \leq d_i/\delta \ll 1$.

The orbit integral S_y [Eq. (9)] will now be evaluated for the three regions as shown in Fig. 2. In the respective inner region for each species, the orbits consists of nearly straight segments^{8,10} and v_y is

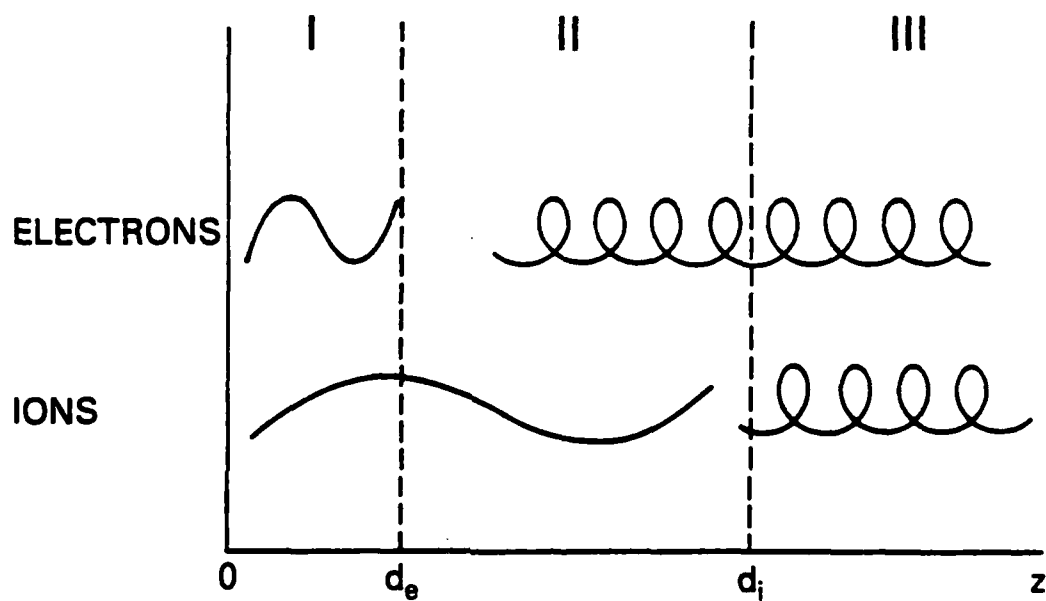


Fig. 2 Schematic drawing of electron and ion orbits.

nearly constant. Then, from Eq. (9), the approximate orbit integral is

$$S_y^{\text{in}} = ic^{-1} v_y \psi(x, z, t) (kv_x - \omega)^{-1}, \quad (21)$$

where v_x is an exact constant of the motion and the constant- ψ approximation has been used. Using Eq. (21) in the first velocity moment of f_{1j} , we obtain the perturbation current densities for the inner regions (region I for electrons and regions I and II for ions),

$$J_{1i}^{\text{in}} = \frac{c}{4\pi n_0 \delta^2} \frac{2T_{1\perp}}{T_1} \left[1 + \left(\frac{\omega}{kv_{1\parallel}} \right) \left(\frac{1}{2} \frac{\delta^2}{a_1^2} + 1 \right) Z \left(\frac{\omega}{kv_{1\parallel}} \right) \right. \\ \left. - \alpha_1 \left(\frac{1}{2} \frac{\delta^2}{a_1^2} + 1 \right) W \left(\frac{\omega}{kv_{1\parallel}} \right) \right] n_0(z) \psi, \quad (22)$$

and

$$J_{1e}^{\text{in}} = \frac{c}{4\pi n_0 \delta^2} \frac{2T_{e\perp}}{T_e} \left[1 + \left(\frac{\omega}{kv_{e\parallel}} \right) \left(\frac{1}{2} \frac{\delta^2}{a_e^2} + 1 \right) Z \left(\frac{\omega}{kv_{e\parallel}} \right) \right. \\ \left. - \alpha_e \left(\frac{1}{2} \frac{\delta^2}{a_e^2} + 1 \right) W \left(\frac{\omega}{kv_{e\parallel}} \right) \right] n_0(z) \psi. \quad (23)$$

where the anisotropy parameter is defined by

$$\alpha_j \equiv 1 - \frac{T_{j\perp}}{T_{j\parallel}}. \quad (24)$$

The dispersion function is given by

$$Z(\xi) \equiv \frac{1}{\sqrt{\pi}} \int_{-\infty}^{\infty} dx \frac{\exp(-x^2)}{x - \xi}$$

and

$$W(\xi) \equiv -\frac{1}{2} Z'(\xi).$$

In deriving Eqs. (22) and (23), use has been made of the equilibrium properties, Eqs. (13), (14), (16) and (18), and $v_{j\parallel} = \sqrt{2T_{j\parallel}/m_j}$.

In the outer regions, regions II and III for electrons and region III for ions, the particles mainly execute ∇B drift motion with the drift

velocity \underline{v}_D^j given by

$$\underline{v}_D^j = - \underline{\hat{y}} \frac{mc v_{\perp}^2}{2qB_0 \delta} \sinh^{-2}\left(\frac{z}{\delta}\right), \quad (25)$$

where $v_{\perp}^2 \equiv v_y^2 + v_z^2$ is a constant of the motion. This expression is a good approximation for the guiding center motion in the outer regions for most particles ($a_j \ll \delta$) except for the ones with kinetic energy much greater than the thermal energy. Note that, for thermal particles ($v_{\perp} \approx v_{j\perp}$), $v_D^j/v_{j\perp}$ is of the order of $(a_j/\delta) \sinh^{-2}(z/\delta)$ so that $v_D^j/v_{j\perp}$ is of order unity near $z = d_j$. The actual motion of a particle is then

$$v_y \approx v_D^j + \tilde{v} \cos(\omega_{cj}t + \lambda)$$

and

$$v_z \approx \tilde{v} \sin(\omega_{cj}t + \lambda),$$

where ω_{cj} is the local cyclotron frequency, \tilde{v} is the gyration velocity in the V_D frame and λ is the phase angle. Then, the approximate orbit integral S_y for the outer regions is

$$S_y^{\text{out}} = ic^{-1} v_D^j (kv_x - \omega)^{-1} \psi - c^{-1} \tilde{v} \int_{-\infty}^t dt' \cos(\omega_{cj}t' + \lambda) \psi.$$

The second term represents the oscillatory motion in the guiding center frame. Taking the phase average over λ for the low frequency perturbation, it is easy to see that the second term averages to zero and we have

$$S_y^{\text{out}} = ic^{-1} v_D^j (kv_x - \omega)^{-1} \psi(x, z, t). \quad (26)$$

Integrating over the velocity space and after some algebra, we obtain

$$J_{11}^{\text{out}} = \frac{c}{4\pi n_0 \delta^2} \frac{2T_{\perp}}{T_{\parallel}} \left[1 - \left(\frac{\omega}{kv_{i\parallel}} \right) \frac{Z(\omega/kv_{i\parallel})}{\sinh^2(z/\delta)} \right]$$

$$+ \alpha_i \frac{W(\omega/kv_{i\parallel})}{\sinh^2(z/\delta)}] n_o(z) \psi, \quad (27)$$

and

$$J_{le}^{out} = \frac{c}{4\pi n_o \delta^2} \frac{2T_{e\perp}}{T_{e\parallel}} \left[1 - \left(\frac{\omega}{kv_{e\parallel}} \right) \frac{Z(\omega/kv_{e\parallel})}{\sinh^2(z/\delta)} \right. \\ \left. + \alpha_e \frac{W(\omega/kv_{e\parallel})}{\sinh^2(z/\delta)} \right] n_o(z) \psi. \quad (28)$$

In obtaining these expressions, use has been made of the equilibrium relationships Eqs. (17) and (18), and $a_j^2/\delta^2 \ll 1$ has been dropped.

The third term in the square brackets of each equation is the anisotropy term. In Ref. 8, where the isotropic case is treated, the second term in each equation is neglected by using the ordering $(\omega/kv_{j\parallel}) \sim (a_j/\delta)^{3/2} \ll 1$ and the ion contribution J_{li}^{in} is neglected in region II. Galeev and Zelenyi¹⁹ estimated the drift velocity by V_D^j [Eq. (25)] without the factor $\sinh^{-2}(z/\delta)$ and concluded that this contribution is small. However, as the discussion following Eq. (25) shows, this term can be of order unity in Eqs. (27) and (38) near $z = d_e$. Moreover, Dobrowolny⁸ and Galeev and Zelenyi¹⁹ matched the interior ($|z| < d_e$) and exterior ($|z| > d_i$) solutions at $z = d_e$ by arguing that the interior electron contribution to the perturbed current density [Eq. (23)] is much greater than the external ion contribution [Eq. (27)] for $|z| > d_e$. This argument overlooks the fact that the axis-crossing ion orbits extend far beyond the electron inner region ($|z| = d_e$) so that the relevant comparison in the intermediate region (region II) is between the exterior electrons [Eq. (28)] and interior ions [Eq. (22)]. For the case in which ions and electrons are both anisotropic, the ratio J_{li}^{in}/J_{le}^{out} at $z = d_e$ in region II is approximately $(\alpha_i/\alpha_e)(m_e/m_i)(\delta/a_e)$ which is typically of order unity. For the case in which only ions are anisotropic ($\alpha_e = 0$), the ratio is approximately $\alpha_i(\delta/a_e)^{5/2}(m_e/m_i)$ which is much greater than unity. As z increases to d_i , the ratio increases because of the factor $\sinh^{-2}(z)$ in the electron contribution. Thus, in general, the ion contribution is not negligible in the intermediate region. Moreover, this intermediate region is wider than the electron inner region by a factor of

$d_i/d_e = (T_{i\perp}/T_{e\perp})^{1/4} (m_i/m_e)^{1/4}/2$. For comparable $T_{i\perp}$ and $T_{e\perp}$, this quantity is roughly 4. The intermediate region is in turn thinner than the sheet thickness δ by a factor of $\sqrt{a_i/2\delta} \ll 1$. In this paper, we treat the three-region matching problem (see Fig. 2); in region I, the total current density is $J_{1T} = (J_{1i}^{\text{in}} + J_{1e}^{\text{in}})$; in region II, $J_{1T} = (J_{1i}^{\text{in}} + J_{1e}^{\text{out}})$; in region III, the current density is $J_{1T} = (J_{1i}^{\text{out}} + J_{1e}^{\text{out}})$.

B. Linear Dispersion Relation

The linear eigenvalue equation is obtained by substituting Eqs. (22), (23), (27) and (28) into Eq. (4) according to the three-region scheme described in the preceding section. The equation is then solved subject to the following conditions. The solution ψ must be such that its first derivative ($\partial\psi/\partial z$) vanishes asymptotically ($|z| \rightarrow \infty$) and that the logarithmic derivative is continuous at $|z| = d_e$ and $|z| = d_i$. For the inner region (I), the eigenvalue equation is found to be

$$\frac{d^2 \hat{\psi}}{dz^2} = \Lambda^2 \hat{\psi}(\bar{z}) \quad (29)$$

where $\psi(x, z, t) = \hat{\psi}(z) \exp(ikx - i\omega t)$ and

$$\begin{aligned} \Lambda^2 \equiv \bar{k}^2 - 2 \left\{ 1 + \frac{T_{i\perp}}{T_{i\parallel}} \left(\frac{1}{2} \frac{\delta^2}{a_i^2} + 1 \right) \left[\left(\frac{\omega}{kv_{i\parallel}} \right) Z \left(\frac{\omega}{kv_{i\parallel}} \right) - \alpha_i W \left(\frac{\omega}{kv_{i\parallel}} \right) \right] \right. \\ \left. + \frac{T_{e\perp}}{T_{e\parallel}} \left(\frac{1}{2} \frac{\delta^2}{a_e^2} + 1 \right) \left[\left(\frac{\omega}{kv_{e\parallel}} \right) Z \left(\frac{\omega}{kv_{e\parallel}} \right) - \alpha_e W \left(\frac{\omega}{kv_{e\parallel}} \right) \right] \right\}, \end{aligned} \quad (30)$$

with $\text{sech}^2(z/\delta) \approx 1$ for $|z| < d_e \ll \delta$. Here, $\bar{k} \equiv k\delta$ and $\bar{z} = z/\delta$. By setting $\alpha_i = \alpha_e = 0$, Eqs. (29) and (30) reduce to the inner equation of Ref. 8. In general, Λ is independent of z and the solution is

$$\hat{\psi}^{\text{in}}(z) = C \cosh(\Lambda \bar{z}) \quad (31)$$

where C is an integration constant and the symmetric solution has been chosen.

In the intermediate region II, the eigenvalue equation takes on the form

$$\frac{d^2 \hat{\psi}}{dz^2} = \bar{k}^2 \hat{\psi} - 2 \left\{ 1 + \frac{T_{i\perp}}{T_{i\parallel}} \left(\frac{1}{2} \frac{\delta^2}{a_i^2} + 1 \right) \left[\left(\frac{\omega}{kv_{i\parallel}} \right) Z \left(\frac{\omega}{kv_{i\parallel}} \right) - \alpha_i W \left(\frac{\omega}{kv_{i\parallel}} \right) \right] \right\}$$

$$\begin{aligned}
& - \frac{2T_{e\perp}}{T_{\perp}} \left[\left(\frac{\omega}{kv_{e\perp}} \right) Z \left(\frac{\omega}{kv_{e\perp}} \right) - \alpha_e W \left(\frac{\omega}{kv_{e\perp}} \right) \sinh^{-2}(\bar{z}) \right] \\
& \times \operatorname{sech}^2(\bar{z}) \hat{\psi}.
\end{aligned} \tag{32}$$

It is easy to see that the inner ion orbit contribution dominates the small gyroradius electron contribution in this region.

In the exterior region $|z| > d_i$, the orbit of both species are mainly of the small gyroradius drifting type and the eigenvalue equation takes on the form

$$\begin{aligned}
\frac{d^2 \hat{\psi}}{d\bar{z}^2} = & [\bar{k}^2 - 2 \operatorname{sech}^2(\bar{z})] \hat{\psi} + 2 \left\{ \frac{T_{i\perp}}{T_{\perp}} \left[\left(\frac{\omega}{kv_{i\parallel}} \right) Z \left(\frac{\omega}{kv_{i\parallel}} \right) - \alpha_i W \left(\frac{\omega}{kv_{i\parallel}} \right) \right] \right. \\
& \left. + \frac{T_{e\perp}}{T_{\perp}} \left[\left(\frac{\omega}{kv_{e\parallel}} \right) Z \left(\frac{\omega}{kv_{e\parallel}} \right) - \alpha_e W \left(\frac{\omega}{kv_{e\parallel}} \right) \right] \right\} \sinh^{-2}(\bar{z}) \operatorname{sech}^2(\bar{z}) \hat{\psi}.
\end{aligned} \tag{33}$$

Asymptotically, where the ∇B contribution vanishes due to near uniformity of the equilibrium magnetic field, the solution of the above equation is²⁰

$$\hat{\psi}_e(z) = D \left(1 + \frac{1}{\bar{k}} \tanh|\bar{z}| \right) \exp(-\bar{k}|\bar{z}|), \tag{34}$$

where the even solution is chosen and D is an integration constant. As required, the first derivative is proportional to $\exp(-\bar{k}|\bar{z}|)$ and vanishes as $|\bar{z}| \rightarrow \infty$.

If we set $\alpha_i = \alpha_e = 0$ in Eq. (30) and match the inner and asymptotic solutions [Eqs. (31) and (34)] at $z = d_e$, then the isotropic results of Ref. 8 are recovered. Equating the logarithmic derivatives of Eqs. (31) and (34) at $z = d_e$, we obtain the linear dispersion relation

$$\Lambda \tanh(\Lambda \bar{d}_e) = (1 + \bar{k}^{-1} \tanh \bar{d}_e) [\bar{k}^{-1} \operatorname{sech}^2 \bar{d}_e - \bar{k}^{-1} (1 + \bar{k}^{-1} \tanh \bar{d}_e)], \tag{35}$$

where Λ is given by Eq. (30) and $\bar{d}_e \equiv d_e/\delta$. This is equivalent to the series representation in terms of generalized Legendre functions given in Ref. 8. Neglecting terms of order $\bar{d}_e \ll 1$, the right hand side can be simplified and we have approximately

$$\Lambda \tanh (\Lambda \bar{d}_e) = \frac{1}{\bar{k}} - \bar{k}. \quad (36)$$

Using the small-argument expansion of Z function in Eq. (32), we find $(\Lambda \bar{d}_e) \ll 1$ for the low-frequency perturbations. Then, keeping only the leading terms in Eq. (36), we find that the instability is primarily due to the resonant electrons and

$$\frac{\gamma}{kv_{e\parallel}} \approx \left(\frac{a_e}{\delta}\right)^{3/2} \frac{1}{\sqrt{2\pi}} \left(1 + \frac{T_i}{T_e}\right) \left(\frac{1}{\bar{k}} - \bar{k}\right), \quad (37)$$

which is identical to the isotropic result⁸. It shows that $(\gamma/kv_{e\parallel}) \ll 1$ scales as $(a_e/\delta)^{3/2}$ and that $\gamma > 0$ (unstable) for $\bar{k} < 1$ and $\gamma < 0$ (stable) for $\bar{k} > 1$. By setting $\gamma = 0$ and neglecting terms of order \bar{d}_e , we find the marginal condition

$$0 = \frac{1}{\bar{k}_0} - \bar{k}_0,$$

and the marginal wavenumber $\bar{k}_0 = 1$, recovering the previous result^{1,2}.

For the anisotropic case, the approximate dispersion relation is still given by Eq. (36) with $\alpha_j \neq 0$ in Λ [Eq. (30)]. As we can see from Eq. (30), the electron anisotropy effects are large because of the small gyroradius ($a_i^2/a_e^2 \approx m_i/m_e$, $\delta^2/a_e^2 \gg 1$). As a result, it is likely that nonlinear effects become important for electrons on a time scale comparable to ω_{ci}^{-1} . This makes the present analysis unsuitable except for very small degrees of electron anisotropy, viz., $|T_{e\perp}/T_{e\parallel} - 1| \ll a_e/\delta$. Thus, in the remainder of this paper, we will primarily consider the case with anisotropic ions and isotropic electrons. Then, keeping only the leading terms, we have

$$(\Lambda \bar{d}_e)^2 \approx 2\sqrt{\pi} \left(\frac{\delta}{a_e}\right) \left(1 + \frac{T_{i\perp}}{T_{i\parallel}}\right)^{-1} \left(\frac{\gamma}{kv_{e\parallel}}\right) + 2\alpha_i \left(1 + \frac{T_{i\perp}}{T_{i\parallel}}\right)^{-1} \left(\frac{\delta}{a_e}\right) \frac{m_e}{m_i}, \quad (38)$$

where $\alpha_i = (1 - T_{i\perp}/T_{i\parallel})$. In marginal state, $\gamma = 0$ and

$$(\Lambda \bar{d}_e)^2 = 2\alpha_i \left(1 + \frac{T_{i\perp}}{T_{i\parallel}}\right)^{-1} \left(\frac{\delta}{a_e}\right) \frac{m_e}{m_i}.$$

For systems in which (a_e/δ) and (m_e/m_i) are comparable such as the

magnetotail, $(\Lambda d_e)^2 \ll 1$. Then, the marginal wavenumber \bar{k}_0 is given by

$$\frac{1}{\bar{k}_0} - \bar{k}_0 = \sqrt{2} \alpha_1 \left(1 + \frac{T_{i\perp}}{T_{e\perp}}\right)^{-1} \left(\frac{m_e}{m_i}\right) \left(\frac{\delta}{a_e}\right)^{3/2}. \quad (39)$$

Using Eqs. (38) and (39) in Eq. (36) and keeping only the leading terms, we find

$$\frac{\gamma}{kv_{e\parallel}} = \frac{1}{\sqrt{2\pi}} \left(\frac{a_e}{\delta}\right)^{3/2} \left(1 + \frac{T_{i\perp}}{T_{e\perp}}\right) \left[\left(\frac{1}{\bar{k}} - \bar{k}\right) - \sqrt{2} \alpha_1 \left(1 + \frac{T_{i\perp}}{T_{e\perp}}\right)^{-1} \left(\frac{m_e}{m_i}\right) \left(\frac{\delta}{a_e}\right)^{3/2}\right]. \quad (40)$$

This is the approximate anisotropic dispersion relation obtained by matching the inner and asymptotic solutions at $z = d_e$. From Eq. (40), we find that the normalized growth rate γ/ω_{ci} has a maximum at

$$\bar{k}_c \equiv -\frac{1}{2} \left(\frac{1}{\bar{k}_0} - \bar{k}_0\right),$$

and

$$\left(\frac{\gamma}{\omega_{ci}}\right)_{\max} = \frac{1}{\sqrt{2\pi}} \left(\frac{a_e}{\delta}\right)^{5/2} \left(\frac{m_i}{m_e}\right) \left(1 + \frac{T_{i\perp}}{T_{e\perp}}\right) (1 + \bar{k}_c^2). \quad (41)$$

Equation (36) is obtained to show the basic properties of the isotropic and anisotropic dispersion relations. One noteworthy property of this equation is that Λ is either purely real or purely imaginary. Using small-argument expansion of Z and W functions, it is easy to see that ω is nearly purely imaginary for the low-frequency perturbations being considered, as we assumed in the preceding discussion of approximate solutions. In the remainder of the paper, we specialize to the case of imaginary frequency with $\omega \equiv i\gamma$ so that $\gamma > 0$ corresponds to instability. The transcendental equation (36) has also been solved numerically to obtain the dispersion relation in detail. Figures 3 and 4 show the growth rate γ normalized to the asymptotic ion cyclotron frequency ω_{ci} versus the normalized $\bar{k} \equiv k\delta$. The dispersion curves are shown for several values of $T_{i\perp}/T_{e\perp}$ and two values of (α_1/δ) , 0.03 and

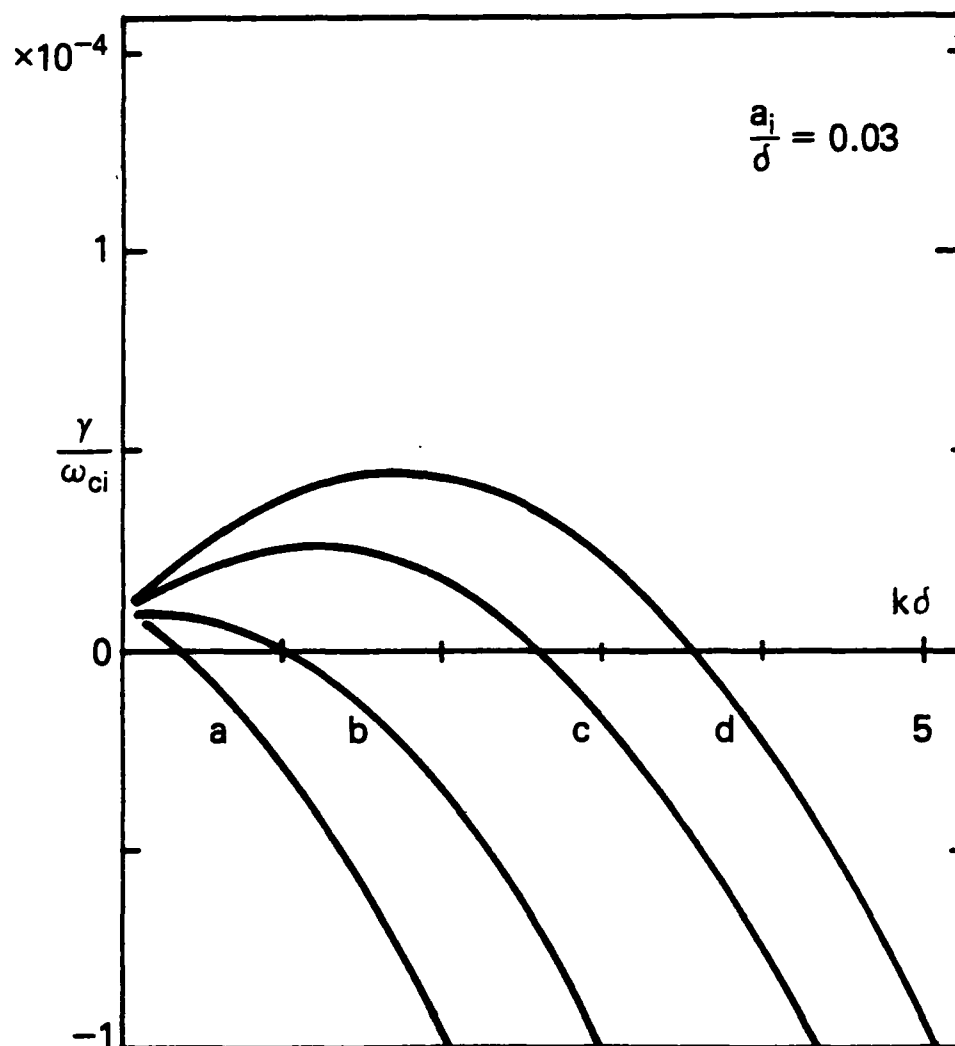


Fig. 3 Normalized growth rate (γ/ω_{ci}) versus $k\delta$ for $a_i/\delta = 0.03$ using the two-region approximation [Eq. (37)]. The value of $T_{i\perp}/T_{i\parallel}$ is (a) 0.9, (b) 1.0, (c) 1.1 and (d) 1.15. ($T_{e\perp}/T_{e\parallel} = 1$).

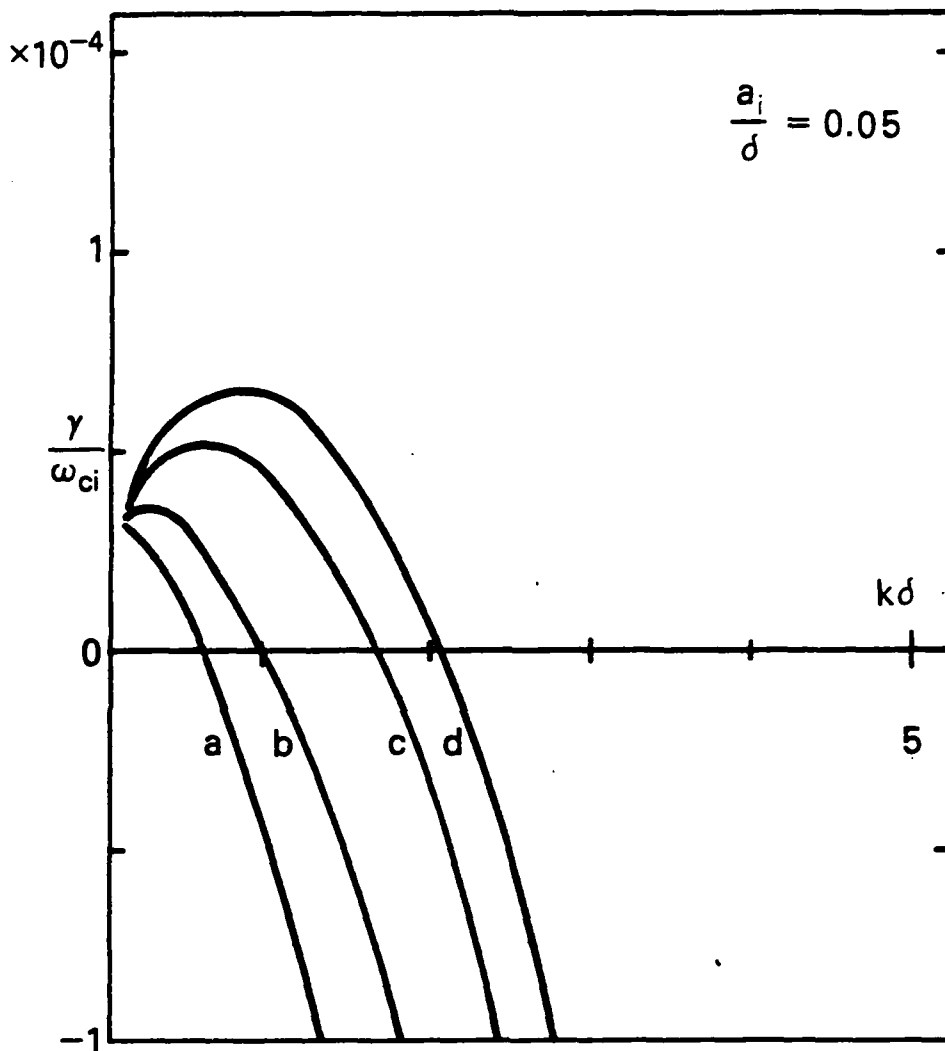


Fig. 4 Normalized growth rate (γ/ω_{ci}) versus $k\delta$ for $a_i/\delta = 0.05$ using Eq. (37). The value of $T_{i\perp}/T_{i\parallel}$ is (a) 0.9, (b) 1.0, (c) 1.1 and (d) 1.15. ($T_{e\perp}/T_{e\parallel} = 1$).

0.05. In particular, the value $a_i/\delta = 0.03$ roughly corresponds to the quiescent magnetotail parameters. In addition, we have used $T_{i\perp}/T_{e\perp} = 2$. In this case, $a_e/\delta = 5 \times 10^{-4}$.

The curve b in each figure corresponds to the isotropic result⁸ with the marginal wavenumber $k\delta = 1$ independently of (a_i/δ) . Consistent with the previous conclusions¹³, we find that temperature anisotropy with $T_{i\perp}/T_{i\parallel} > 1$ is destabilizing while anisotropy with $T_{i\perp}/T_{i\parallel} < 1$ is stabilizing. Here, \underline{k} is parallel to \underline{B}_0 so that the case with the greater temperature perpendicular to \underline{k} is more unstable. These figures also show that Eq. (39) describes the stability boundary accurately. For example, for $T_{i\perp}/T_{i\parallel} = 1.1$ and $a_i/\delta = 0.03$, we have $\bar{k}_0 = 2.67$. For $a_i/\delta = 0.05$, we have $\bar{k}_0 = 1.68$, in agreement with these figures. In addition, Eq. (40) is a good approximation for all the curves shown in these figures. In comparing Figs. 3 and 4, note that the two values of a_i/δ correspond to different values of δ and ω_{ci} so that γ and k are normalized to different scales [see Eqs. (14), (17) and (18)]. The curves are not completed for $k\delta = 0$ because the theory breaks down as $k \rightarrow 0$. Comparing curves a, c and d with curve b in each of Figs. 3 and 4, we see that the effect of anisotropy is substantial. This is expected because the anisotropy term, the third term in Eq. (8), is greater than the isotropic term by a factor of $(kv_{j\parallel}/\omega) \gg 1$. In this regard, we point out that Laval and Pellat¹² used an energy method to show that the mode treated here is completely stabilized for

$$\frac{T_{e\perp}}{T_{e\parallel}} < 1 - \frac{a_e}{\delta}. \quad (42)$$

For the parameter used in Fig. 3, the right hand side is approximately 0.9995. Using this value of electron temperature anisotropy in Eq. (37), we find that the mode is in fact completely stabilized. With electron anisotropy, the square brackets in Eq. (40) would contain another term identical to the second term except for the replacement $e \rightarrow i$ and $m_e/m_i \rightarrow 1$. [See the discussion preceding Eq. (38)]. The reason for the extremely sensitive dependence on the electron anisotropy described above is that the electron term without the small mass ratio enhances the anisotropy effects discussed above. As a general remark, we note that γ/ω_{ci} is typically of the order of 10^{-4} . In addition, $\gamma/kv_{j\parallel}$ is also

of the order of 10^{-4} for the unstable parameter regimes for both species. Thus, the low frequency approximation used to derive Eq. (8) is justified a posteriori.

So far, we have examined anisotropic tearing-mode properties using the two-region matching method following a number of previous works. However, examination of Eq. (32) shows that, in the intermediate region, it is the ion orbits that dominate. Furthermore, because $d_i \gg d_e$, the effect of these ions is expected to be large. In order to study the anisotropic properties including the intermediate region, we have numerically integrated Eqs. (32) and (33) in regions II and III. The physically acceptable solution must have the asymptotic behavior given by Eq. (34) and the logarithmic derivative must be continuous at $z = d_i$ and $z = d_e$. At $z = d_e$, the derivative is matched to that of the analytic solution, Eq. (31). The matching condition then gives the linear anisotropic dispersion relation. The results are plotted in Figs. 5 and 6 for several values of $T_{i\perp}/T_{i\parallel}$ and for two values of a_i/δ , 0.03 and 0.05. Here, the electrons are isotropic.

Comparing Figs. (3) with (5) and (4) with (6), we see that inclusion of the ion orbits in the intermediate region modifies the growth rate and the stability boundary significantly. In general, the anisotropy effects are further enhanced by the inclusion of the intermediate region (region II). That is, for $T_{i\perp}/T_{i\parallel} < 1$, the mode is more strongly stabilized with the intermediate region than without it. For $T_{i\perp}/T_{i\parallel} > 1$, the instability is more strongly enhanced with the intermediate region than without it. However, the isotropic dispersion curves obtained using the "three-region" matching method are nearly identical to the corresponding ones obtained using the two-region approach. The absolute value of (γ/ω_{ci}) of curve b in Fig. 3 is greater than that of curve b in Fig. 5 by approximately 3% to 4% ($a_i/\delta = 0.03$). The absolute value of (γ/ω_{ci}) of curve b in Fig. 4 is also greater than that of curve b in Fig. 6 by similar amounts ($a_i/\delta = 0.05$). This agreement is nontrivial since Eq. (32) shows that the dominant ion orbits in the intermediate region modifies the eigenvalue equation significantly and indicates that the isotropic dispersion relation is indeed determined primarily by the resonant electrons in the inner region $|z| < d_e$. The above behavior can be

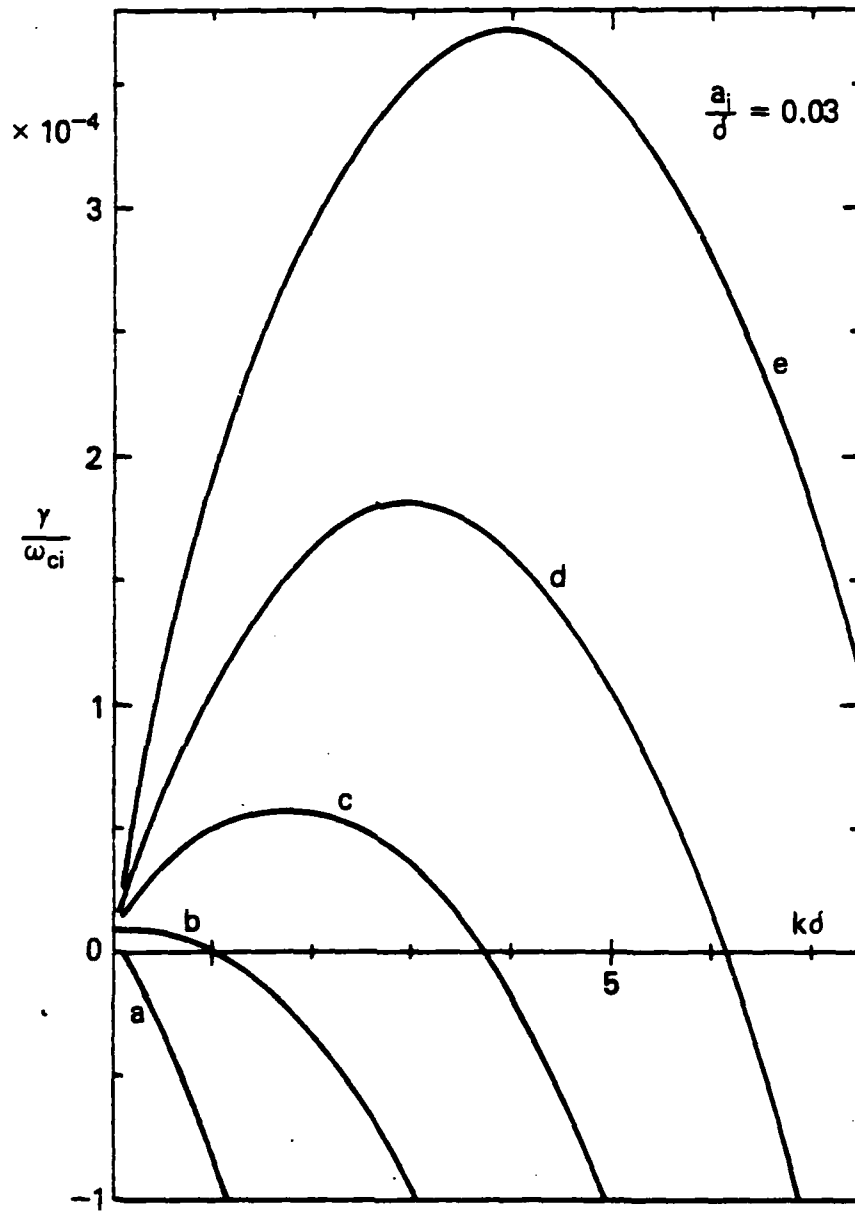


Fig. 5 Normalized growth rate (γ/ω_{ci}) versus kd for $a_i/\delta = 0.03$ including the intermediate ion region. The value of $T_{i1}/T_{i||}$ is (a) 0.9, (b) 1.0, (c) 1.05, (d) 1.1 and (e) 1.15. ($T_{e1}/T_{e||} = 1$).

understood from Eqs. (6) or (8) by noting that $ikqS_y$ is the time-integrated Lorentz force in the x-direction causing the particles to bunch. Since the ion orbits are larger than the electron orbits by approximately $d_i/d_e = 4$, the accumulated influence is also increased. It is evident that the Lorentz force term is zero in the isotropic case. It is of interest to note that the force responsible for the anisotropic effects is similar to that in the mirror instability²⁰. However, unlike the mirror instability, there is no threshold value of $T_{i\perp}/T_{i\parallel}$ that is required for the onset of the anisotropic effects.

Figures 5 and 6 show that for $T_{i\perp}/T_{i\parallel} > 1$ the maximum growth rate is enhanced by one order of magnitude or more from the isotropic case and that the marginal wavenumber is increased. For $T_{i\perp}/T_{i\parallel} < 1$, the instability is essentially stabilized. Note that, as before, (γ/ω_{ci}) is typically of the order of 10^{-4} so that the low frequency approximation is justified. The results are shown for $T_{i\perp}/T_{i\parallel}$ up to 1.15. For higher $(T_{i\perp}/T_{i\parallel} \geq 1.3)$ degrees of anisotropy, the increasing value of (γ/ω_{ci}) would render the low frequency and constant- ψ approximations invalid. The dashed line (e) in Fig. 6 shows the dispersion curve for $T_{i\perp}/T_{i\parallel} = 1.1$ with the ∇B contribution neglected. We see that the qualitative behavior is not significantly changed and that the ∇B drift has the opposite, albeit small, effect from the axis-crossing orbits. This is easy to understand since the guiding center of a drifting particle is opposite to the mean drift velocity of the plasma layer [Eq. (25)].

Figure 7 shows the maximum growth rate $(\gamma/\omega_{ci})_{\max}$ as a function of temperature anisotropy $(T_{i\perp}/T_{i\parallel})$. In Fig. 8, we have plotted the eigenfunction $\hat{\psi}(z)$ for $|z| > d_e$ for two values of $T_{i\perp}/T_{i\parallel}$. Both curves correspond to the respective maximum growth rates $(\gamma/\omega_{ci})_{\max}$. The matching surfaces at $|z| = d_e$ and $|z| = d_i$ are also shown. We see that the constant- ψ approximation is reasonable for the values of $T_{i\perp}/T_{i\parallel}$ used here. However, for $T_{i\perp}/T_{i\parallel} \geq 1.3$, the variation in $\hat{\psi}$ within the ion layer becomes substantially greater.

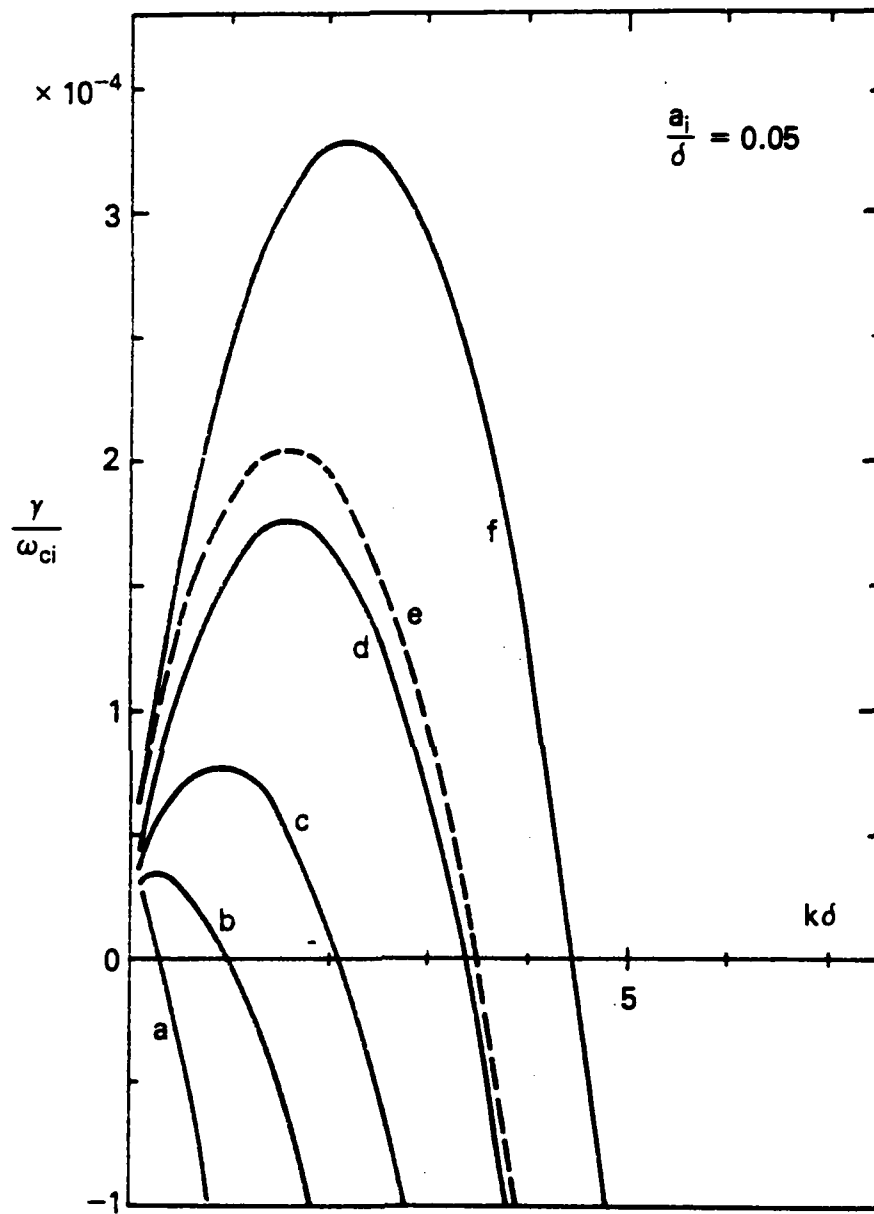


Fig. 6 Normalized growth rate (γ/ω_{ci}) versus $k\delta$ for $a_i/\delta = 0.05$ including the intermediate ion region. The value of $T_{i\perp}/T_{i\parallel}$ is (a) 0.9, (b) 1.0, (c) 1.05, (d) 1.1, (e) 1.1 with ∇B neglected and (f) 1.15. ($T_{e\perp}/T_{e\parallel} = 1$).

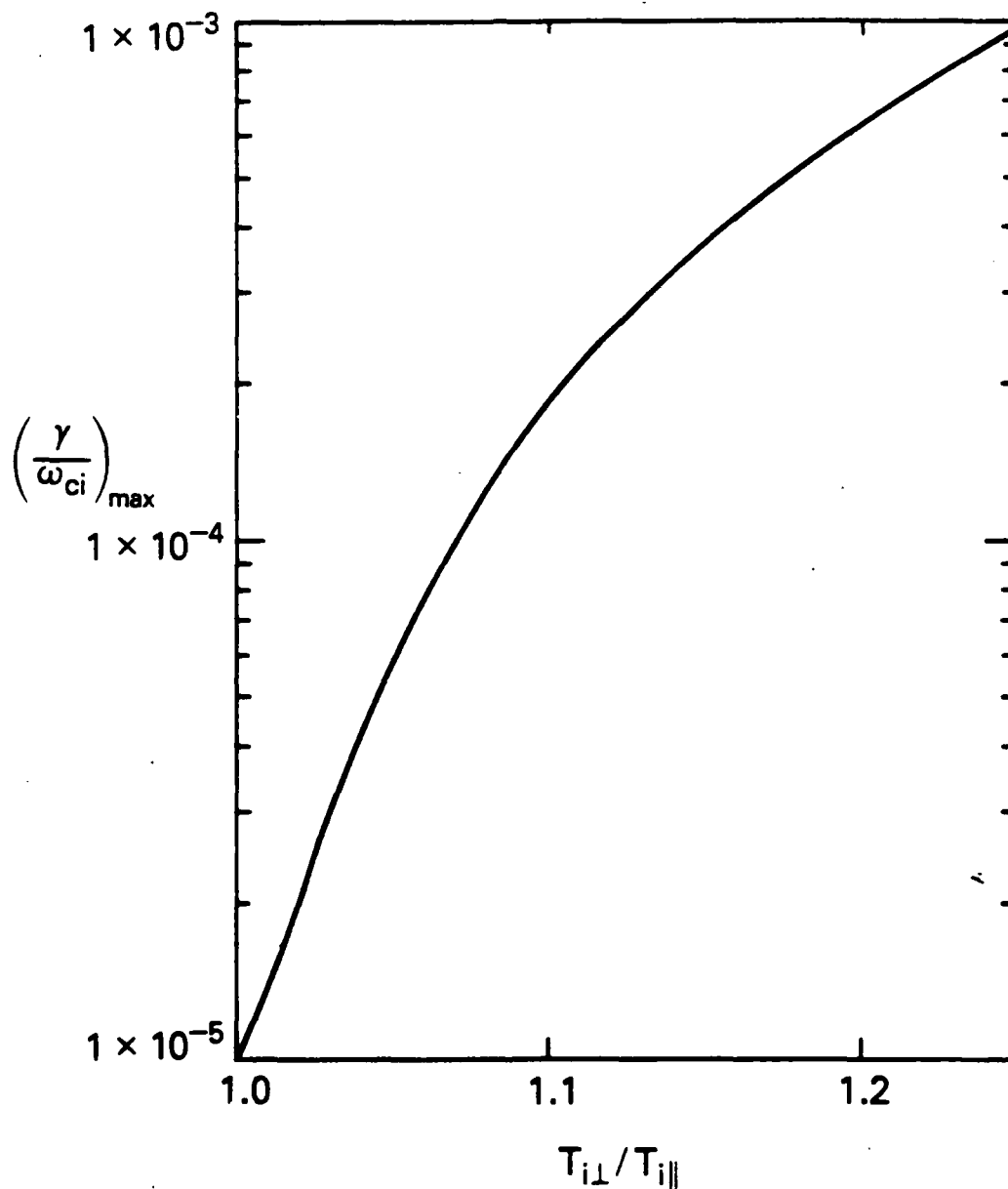


Fig. 7 Maximum growth rate $(\gamma/\omega_{ci})_{\max}$ versus $T_{i\perp}/T_{i\parallel}$ for $a_1/\delta = 0.03$ and $T_{e\perp}/T_{e\parallel} = 1$.

IV. SUMMARY

In this paper, we have investigated the collisionless tearing-mode properties of an anisotropic ($T_{\perp} \neq T_{\parallel}$) neutral sheet. Both ions and electrons are described by Vlasov distribution functions. Using simplified particle orbits and constant- ψ approximation, the perturbed distribution function is evaluated for low frequency perturbations ($\gamma/\omega_{ci} \ll 1$) with $\underline{k} \parallel \underline{B}_0$. The first-order current densities are explicitly found [Eqs. (22), (23), (27) and (28)] and eigenvalue equation is obtained for the three regions [Fig. 2 and Eqs. (29), (32) and (33)]. The equation is solved using both analytic approximations and numerical methods to obtain the linear dispersion relation (Figs. 3, 4, 5 and 6) and the eigenmode structure (Fig. 8). First, by neglecting the ion intermediate region (region II), the conventional two-region matching method is used to find the approximate anisotropic dispersion relation [Eq. (40) and Figs. 3 and 4] as well as other dispersion properties [Eqs. (39) and (41)]. Then, the full eigenvalue equation is numerically integrated in regions II and III. The three-region matching condition then gives rise to the anisotropic dispersion relation illustrated in Figs. 5 and 6 for a number of parameter values. It is shown that temperature anisotropy with $T_{i\perp}/T_{i\parallel} > 1$ enhances the growth rate by as much as an order of magnitude or more while anisotropy with $T_{i\perp}/T_{i\parallel} < 1$ strongly stabilizes the mode. This is consistent with previous results based on energy principle¹² and marginal stability¹³ calculations. It is also found that the conventional approach of matching the inner and outer solutions at the electron inner region ($|z| < d_e$) is not adequate in the anisotropic case. An intermediate region ($d_e < |z| < d_i$) is identified in which the axis-crossing ion orbits are dominant. It is the ions in this region that account for the substantial differences as exhibited by Figs. 3, 4, 5 and 6. The use of simplified orbits also allows evaluation of the effects of different orbits explicitly. In particular, it is found that the inner orbits and outer orbits (the \sqrt{B} drift orbits) have the opposite effects on the growth rate: where the inner orbits are destabilizing, the outer orbits are stabilizing and vice versa in the anisotropic case.

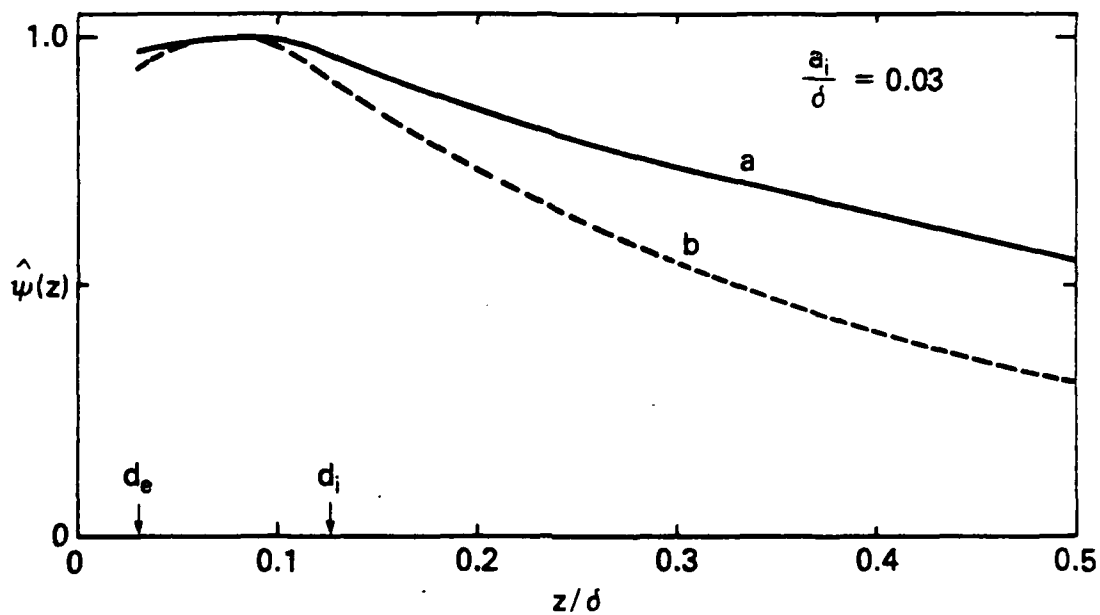


Fig. 8 Eigenfunction $\hat{\psi}(z)$ versus z/δ corresponding to $(\gamma/\omega_{ci})_{\max}$ for (a) $T_{i\perp}/T_{i\parallel} = 1.05$ and (b) $T_{i\perp}/T_{i\parallel} = 1.1$. $a_i/\delta = 0.03$. The matching boundaries are indicated: $|\bar{z}| = d_e$ and $|\bar{z}| = d_i$. ($T_{e\perp}/T_{e\parallel} = 1$).

A physical system for which the present analysis may be applicable is the earth's magnetotail. The previous works on the tearing-mode stability of such a system have studied isotropic neutral sheets (see, for example, Refs. 8, 10 and 11). In light of the fact that the magnetotail is highly collisionless, it is reasonable to expect the temperature distribution to be generally anisotropic. Our present results suggest that the linear tearing-mode properties of the magnetotail and similar physical systems are dominated by the anisotropic tearing-mode. In fact, the $\mathbf{k} \parallel \mathbf{B}_0$ mode can grow significantly faster than previously predicted if temperature anisotropy is present ($\alpha_i > a_i/\delta$). Thus, the particle temperature distribution is a critically important quantity for understanding the linear tearing-mode stability properties.

The present analysis utilized simple approximate orbits in evaluating the orbit integrals. In the isotropic case, the two-region approach⁸ yielded results in agreement with numerical results,⁴ indicating that the stability properties are not critically dependent on the precise orbits. In the anisotropic case, however, the large ion orbits are important so that a more accurate calculation of the orbit integrals is desirable. In the present analysis, the orbits that are neglected are mainly those of particles with energy substantially greater than the typical velocities, constituting a relatively small fraction of the total particles. In conjunction with the fact that the low frequency and constant- ψ approximations are well satisfied by the results, we expect the present results to be a good first approximation for understanding the essential physics of the collisionless anisotropic tearing-mode properties.

Acknowledgments

We are grateful to Drs. J. F. Drake, J. M. Finn, and Y. C. Lee for insightful discussions. This research was supported by NASA W-14365 and ONR.

References

1. H. P. Furth, Nucl. Fusion Suppl. Pt. 1, 169 (1962).
2. D. Pfirsch, Z. Naturforsch. 17a, 861 (1962).
3. G. Laval and R. Pellat, Compt. Reud. 259, 1706 (1964).
4. F. C. Hoh, Phys. Fluids 9, 277 (1966).
5. G. Laval, R. Pellat, and M. Vuillemin, in Plasma Physics and Controlled Nuclear Fusion Research (International Atomic Energy Agency, Vienna, 1966), 2, 259.
6. K. Schindler, in Proceedings of the Seventh International Conference on Phenomena in Ionized Gases (Gradevinska Knjiga, Beograd, Yugoslavia, 1966), Vol. II, 736.
7. K. Schindler and M. Soop, Phys. Fluids 11, 1192 (1968).
8. M. Dobrowolny, Nuovo Cimento B 55, 427 (1968).
9. N. F. Ness, J. Geophys. Res. 70, 2989 (1965).
10. B. Coppi, G. Laval, and R. Pellat, Phys. Rev. Lett. 16, 1207 (1966).
11. K. Quest and F. V. Coroniti, J. Geophys. Res. 86, 3299 (1981).
12. G. Laval and R. Pellat, ESRO SP-36, 5 (1968).
13. J. Chen and R. C. Davidson, Phys. Fluids 24, 2208 (1981).
14. B. Basu and B. Coppi, Phys. Rev. Lett. 48, 799 (1982).
15. B. U. Ö. Sonnerup, J. Geophys. Res. 76, 8211 (1971).
16. J. P. Holdren, Ph.D. thesis, Stanford University IPR Report No.351 (1970)
17. E. G. Harris, Nuovo Cimento 23, (1962).
18. J. F. Drake and Y. C. Lee, Phys. Fluids 20, 1341 (1977).
19. A. A. Galeev and L. M. Zelenyi, Sov. Phys. JETP 42, 450 (1975).
20. This form of solution was pointed out to us by J. M. Finn.
21. See, for example, G. Schmidt, Physics of High Temperature Plasmas, 2nd ed., Academic Press, New York (1979).

APPENDIX B
FAST COLLISIONLESS TEARING IN AN
ANISOTROPIC NEUTRAL SHEET

J. Chen and J.G. Lyon
Science Applications, Inc.

and

P.J. Palmadesso and J.A. Fedder
Naval Research Laboratory

FAST COLLISIONLESS TEARING IN AN ANISOTROPIC NEUTRAL SHEET

J. Chen¹, F. J. Palmadesso², J. A. Fedder² and J. G. Lyon¹

¹ Science Applications, Inc. McLean, VA 22101.

² Naval Research Laboratory, Washington, DC 20375.

Abstract: The collisionless tearing mode in a neutral sheet is studied in the presence of ion temperature anisotropy using Vlasov description for both ions and electrons. It is found that the growth rate of the instability is significantly enhanced if $T_{\perp i}/T_{\parallel i} > 1$ where the symbols \perp and \parallel refer to the directions perpendicular and parallel to the equilibrium magnetic field. For typical magnetotail parameters with modest temperature anisotropy, it is shown that the linear e-folding time is reduced to a small fraction of the time delays believed to precede the onset of reconnection. This enhancement of the growth rate is due to the Lorentz force acting on the ions that cross the neutral plane, traversing beyond the conventional electron tearing layer.

Introduction

The isotropic collisionless tearing mode (Furth, 1962; Pfirsch, 1962) has been under extensive investigation for the past few decades (Coppi et al., 1966; Laval et al., 1966; Schindler, 1966; Dobrowolny, 1968). In particular, it was suggested (Coppi et al., 1966) as a possible mechanism for magnetic field line reconnection in the magnetosphere (Dungey, 1961). The tearing mode may also be relevant to the dayside magnetopause (e.g., Greenly and Sonnerup, 1981; Quest and Coroniti, 1981). Figure 1 shows schematically the geometry and the coordinate system.

The central importance of the tearing mode is that the growth rate of the instability is believed to provide a measure of the time delay for the onset of reconnection after the interplanetary magnetic field turns southward. One difficulty in identifying the conventional isotropic collisionless tearing mode as a possible mechanism for reconnection is that the instability is a weak one. For example, using the results of Dobrowolny (1968), the electron tearing growth time is estimated to be of the order of 1 hour for the tail region, which is too long to have any role. However, in a collisionless plasma, the motion of particles parallel to the magnetic field is decoupled from the perpendicular motion and temperature anisotropy is likely to exist (Crooker and Siscoe, 1977). Laval and Pellat (1968) used an energy principle analysis to show that collisionless tearing mode properties can be strongly modified by weak anisotropy. In this work, however, the eigenmode structure was not studied and quantitative

estimates of the growth rate were not given. Recently, Chen and Davidson (1981) carried out a Vlasov-fluid analysis for a field-reversed ion layer at marginal stability using approximate orbits. It is found that slight anisotropy ($T_{\perp i}/T_{\parallel i} > 1$) can increase the range of unstable wavenumbers of the tearing mode in an ion layer, indicating that the magnetopause and magnetotail properties may be affected significantly by anisotropy. Here the symbols \perp and \parallel refer respectively to the directions parallel and perpendicular to the equilibrium magnetic field. More recently, Basu and Coppi (1982) studied a fluid-like "field swelling" instability in an anisotropic plasma. This analysis is local and is based essentially on the fluid equations so that it is not applicable to the tearing mode which is due to the large orbits crossing the neutral line.

In this paper, we calculate the anisotropic dispersion relation and show that the tearing mode growth rate for a collisionless neutral sheet can be strongly enhanced if the particle distribution is anisotropic $T_{\perp} > T_{\parallel}$. In light of the new results, we reconsider some aspects of the reconnection processes in the open magnetosphere. However, the detailed treatment of the plasma physics aspects is not appropriate here and the reader is referred to a previous paper (Chen and Palmadesso, 1983). As a general remark, we note that the real magnetotail has a small normal component of the magnetic field which may be stabilizing to collisionless tearing mode because the electrons can be magnetized (Galeev and Zelenyi, 1976; Lembège and Pellat, 1982). However, ions may still be unmagnetized, giving rise to an "ion tearing mode" (Schindler, 1974). In addition, pitch angle scattering may tend to destabilize the mode (Coroniti, 1980) as well as isotropize electron anisotropy. In the present work, we do not include the normal field or pitch angle scattering. Because the above effects tend to affect primarily the electrons, we will take the electrons to be isotropic and include only anisotropic ions.

Anisotropic Tearing-mode Instability

Consider a perturbation given by $\psi(x, z, t) = \hat{\psi}(z)\exp(ikx - i\omega t)$ with the wavevector $\mathbf{k} = k\mathbf{x}$ parallel to the equilibrium magnetic field $\mathbf{B}_0(z) = B_0(z)\mathbf{x}$ which is generated self-consistently by the current density $\mathbf{J}_0 = J_0\mathbf{x}$. For the tearing mode, we have $\omega \ll \omega_{ci}$ where ω_{ci} is the ion cyclotron frequency in the asymptotic field $B_0 = B_0(z = \infty)$. In addition, for the parameters of interest, we also have $\omega \ll kv_{th}$ where v_{th} is the thermal velocity of the particles. In this paper, we adopt for both ions and electrons ($j = i, e$) Harris-type

Copyright 1984 by the American Geophysical Union.

Paper number 3L1782.

0094-8276/84/003L-1782\$3.00

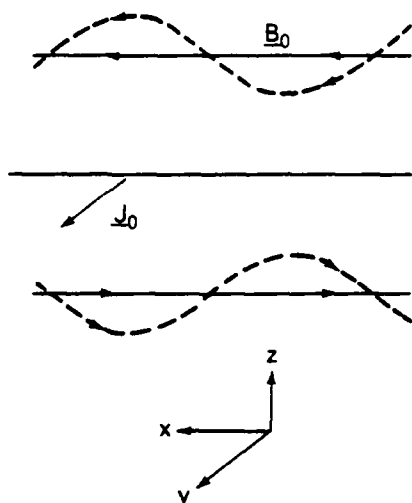


Fig. 1. A schematic drawing the geometry. B_0 is the equilibrium magnetic field and $(B_0 + B_1)$, represented by the dashed lines, is the total magnetic field including the perturbation.

equilibrium distribution functions given by

$$f_{0j}(H_{\perp j} - v_j p_{yj}, H_{\parallel j}) = \frac{n_{0j}}{2\pi T_{j\perp}/m_j} \frac{1}{\sqrt{2\pi T_{j\parallel}/m_j}} \times \exp\left[-\frac{1}{T_{j\perp}}(H_{\perp j} - v_j p_{yj})^2\right] \exp\left[-\frac{1}{T_{j\parallel}} H_{\parallel j}\right]. \quad (1)$$

Here $H_{\perp j} = (m_j/2)(v_y^2 + v_z^2)$, $p_{yj} = m_j v_j + (q_j/c)A_y^0(z)$, $H_{\parallel j} = (m_j/2)v_x^2$, v_j is the mean velocity of the species j , and $A_y^0(z)$ is the vector potential for the equilibrium magnetic field. The electrostatic field is taken to be zero in the frame of the neutral sheet and charge neutrality will be assumed. The self-consistent equilibrium quantities are well-known and are given by $n_0(z) = n_0 \text{sech}^2(z/\delta)$ and $B_x^0(z) = B_0 \tanh(z/\delta)$, where $B_0 \equiv (8\pi n_0 T_1)^{1/2}$, $T_1 \equiv T_{1\perp} + T_{1\parallel}$ and

$$\delta \equiv \left(\frac{c^2 T_1}{2\pi n_0}\right)^{1/2} \frac{1}{e(V_1 - v_e)}. \quad (2)$$

Using the method of characteristics, the linearized Vlasov distribution function for each species can be written as

$$f_{1j} = \frac{q_j \beta_j}{T_{j\perp}} f_{0j} \psi - \frac{i\omega q_j}{T_{j\perp}} f_{0j} Q_y + \frac{ik q_j}{T_{j\perp}} \left(1 - \frac{T_{j\perp}}{T_{j\parallel}}\right) f_{0j} v_x Q_y \quad (3)$$

where

$$Q_y \equiv -\frac{1}{c} \int_{-\infty}^{\infty} dt v_y \psi. \quad (4)$$

Here, $\beta_j \equiv v_j/c$, c is the speed of light, and $\psi \equiv A_y$ is the perturbed vector potential. In equation (3), use has been made of $\partial/\partial t \rightarrow -i\omega$ and $\partial/\partial x \rightarrow ik$. In obtaining equations (3) and

(4), we have used $\omega \ll \omega_{ce}$, $\omega \ll \omega_{ci}$, which is a consequence of charge neutrality at low perturbation frequencies (Dobrowolny, 1968). Here, ω is the perturbed scalar potential. Using equation (3) in Ampere's law, we obtain

$$\frac{d^2 \psi}{dz^2} - k^2 \psi = -\frac{4\pi}{c} \sum_j q_j \int_{-\infty}^{\infty} dz v_y f_{1j}. \quad (5)$$

In the isotropic limit, $T_{j\perp}/T_{j\parallel} = 1$, the last term of equation (3) vanishes and the isotropic results are recovered. For the anisotropic case, estimating v_x by the typical thermal velocity v_{th} , we see that the second term is smaller than the last term by approximately $\omega/(kv_{th}) \ll 1$ so that the anisotropy term is dominant unless the degree of anisotropy is small. In order to evaluate Q_y and f_{1j} quantitatively, we note that the component v_y is nearly constant for a typical particle in the inner regions ($|z| < d_i$) where the magnetic field is weak. Here, we take $d_i \equiv \sqrt{a_i \delta}/2$ and $d_o \equiv \sqrt{2a_i \delta}$, where a_i is the Larmor radius of a thermal particle. In the outer regions ($|z| > d_i$), a typical particle executes the usual ∇B drift motion. These approximations are intended to model the various particle orbits (see, for example, Sonnerup, 1971). In addition, $\psi(z)$ is assumed to be nearly constant in the inner regions.

Using the above approximations, after some algebra, we obtain for each species in the respective inner regions and outer regions,

$$Q_y^{\text{in}} = ic^{-1} v_y \hat{\psi}(z) (kv_x - \omega)^{-1} \exp(ikx - i\omega t), \quad (6)$$

$$Q_y^{\text{out}} = ic^{-1} v_D \hat{\psi}(z) (kv_x - \omega)^{-1} \exp(ikx - i\omega t). \quad (7)$$

The quantity v_D is the usual ∇B drift velocity in the y -direction. Using equations (3), (5), (6) and (7), it is clear that equation (5) is an eigenvalue equation for $\hat{\psi}(z)$, subject to the conditions that its first derivative ($\partial \hat{\psi}/\partial z$) vanish asymptotically ($|z| \rightarrow \infty$) and that the logarithmic derivative be continuous at $|z| = d_o$ and $|z| = d_i$. However, unlike the conventional isotropic tearing mode calculations in neutral sheets (see, for example, Dobrowolny, 1968) in which the "inner" solution for $|z| < d_o$ is matched to the "outer" solution for $|z| > d_i$, it is found that the dispersion relation for the anisotropic tearing mode is critically affected by the ion orbits in the "intermediate" region $d_o \leq |z| \leq d_i$. Therefore, the eigenvalue equation (5) must be solved in the above three regions. For the inner region, an analytical solution can be obtained. In the intermediate and outer regions, the equation is solved numerically. The resulting dispersion relation, obtained by matching the logarithmic derivative of $\hat{\psi}$ at $z = d_o$ and $z = d_i$ (three-region approximation), is shown in Figure 2 for several values of $T_{1\perp}/T_{1\parallel}$ with $a_i/\delta = 0.1$.

Note first that v/ω_{ci} and the associated values of v/kv_i and v/kv_e are all substantially less than unity, justifying the low frequency approximations *a posteriori*. Another point to note is that curve b for the isotropic case is

nearly equal to the conventional two-region result with the present three-region growth rates being slightly smaller. This reduction in γ can be traced to the TS drift. As $\alpha_i \equiv T_{i1}/T_{i2}$ is increased, the growth rate and the range of unstable k -numbers both increase substantially. For example, the maximum growth rate for $\alpha_i = 1.5$ is $\gamma = 2.2 \times 10^{-3} \omega_{ci}$ compared with the isotropic maximum growth rate $\gamma = 1.9 \times 10^{-3} \omega_{ci}$ for the same parameters, an enhancement by a factor of 10. The wavelength at maximum γ is reduced to roughly 2.7 from 27.5. For $\alpha_i < 1$, even a small deviation from isotropy strongly stabilizes the mode as shown by curve a of Figure 2. This latter behavior is consistent with the qualitative conclusion of Laval and Pellat (1968). Physically, the anisotropy effects are due to the Lorentz force which is similar to the mirror forces (the third term of equation (3)). Note that Hill (1975) also found that the magnetic merging is enhanced if $p_{\perp} > p_{\parallel}$.

Discussion

Two regions where the preceding results may be relevant are the neutral regions of the magnetotail and the dayside magnetopause. In this regard, we note that the need to consider temperature anisotropy in these regions has been pointed out (Crooker and Siscoe, 1977; Cowley, 1978). We will use some parameters suitable for the tail neutral region for illustration. For example, for 1 keV ions, $a_1/\delta = 0.1$, $T_{i1}/T_{i2} = 2$ and $B_0 = 20$ G, we have $\omega_{ci} = 1.9 \text{ sec}^{-1}$ and Figure 2 (curve b) yields the minimum e-folding time $(\gamma_{\max})^{-1} = 45$ minutes for the isotropic case. If $\alpha_i = 1.25$, then $(\gamma_{\max})^{-1} = 12$ minutes. For $\alpha_i = 1.5$, we have $(\gamma_{\max})^{-1} = 4$ minutes, a reduction by more than one order of magnitude. This shows that, in the presence of even small to modest ion temperature anisotropy, the e-folding time scale is a small fraction of the delay time of ~ 30 minutes for the onset of reconnection. We, therefore, conclude that the anisotropic collisionless tearing mode may indeed play an important role in reconnection processes in the magnetosphere. It is important to note that no classical or anomalous resistivity is used in our calculation. Further increase in α_i yields even greater enhancement in the growth rate. However, the approximations used in the analysis begin to break down for much larger α_i so that we are not able to make quantitative statements for large degrees of anisotropy.

So far, the anisotropic tearing mode results have been considered in the context of the tail region. In the neutral region of the dayside magnetopause, a_1/δ may be nearly unity, which is outside the regime of validity of the present analysis. However, we expect qualitatively similar effects to occur. Note also that only the linear regime has been investigated and we cannot draw definitive conclusions concerning the possible magnetic island formation. We speculate that the saturation level in the presence of anisotropy is greater than in the absence of anisotropy. As a general remark, it can be shown (Chen and Palmadesso, 1983) that the linear growth rate (γ/ω_{ci}) has an overall scaling factor of $(a_e/\delta)^{5/2}$ in the low frequency regime. Therefore, as the neutral sheet thickness δ

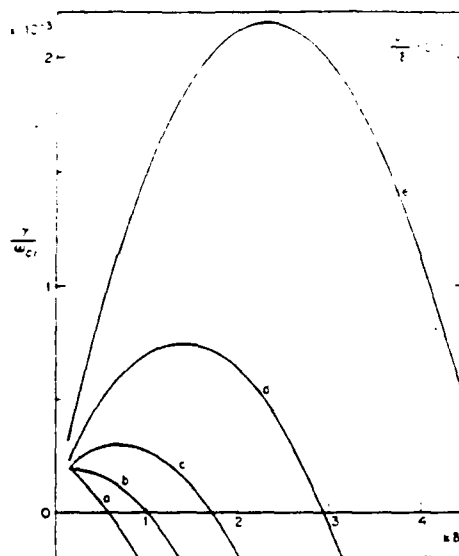


Fig. 2. Normalized growth rate (γ/ω_{ci}) versus $k\delta$ for $a_1/\delta = 0.1$ and isotropic electrons. The value of T_{i1}/T_{i2} is (a) 0.9, (b) 1.0, (c) 1.1, (d) 1.25 and (e) 1.5. The curves are not completed near $k\delta = 0$ because a number of approximations break down for $k \rightarrow 0$.

decreases, the growth rate increases rapidly while the enhancement due to temperature anisotropy increases only as (a_e/δ) .

As discussed in Section 1, the magnetotail possesses a number of features such as the weak normal component of the magnetic field and pitch angle scattering that are not included in the present analysis. So far, these modifications have been applied to the isotropic tearing mode in the literature. In view of the fact that anisotropic tearing mode completely dominates the isotropic case, we suggest that tearing instability in the presence of anisotropy is the more relevant perturbation to investigate and that the above modifications should be considered for the anisotropic case. Moreover, since the enhancement of the growth rate is primarily due to the large ion orbits, we expect qualitatively similar effects to persist even if the above refinements are included.

Acknowledgments. This research was supported by National Aeronautics and Space Administration and the Office of Naval Research.

References

- Basu, B. and S. Coppi, Field-swelling instability in anisotropic plasmas, *Phys. Rev. Lett.*, **48**, 799, 1982.
- Chen, J. and R.C. Davidson, Tearing-mode stability properties of a diffuse anisotropic field-reversed ion layer at marginal stability, *Phys. Fluids*, **24**, 2208, 1981.
- Chen, J. and P. Palmadesso, Tearing instability in an anisotropic neutral sheet, *NRL Memo. Report 5178*, Naval Res. Lab., Washington, DC., 1983.

- Coppi, B., G. Laval, and R. Pellat, Dynamics of the geomagnetic tail, Phys. Rev. Lett., 16, 1207, 1966.
- Coroniti, F.V., On the tearing modes in quasineutral sheets, J. Geophys. Res., 85, 6719, 1980.
- Cowley, S.W.H., The effect of pressure anisotropy on the equilibrium structure of magnetic current sheets, Planet. Space Sci., 1037, 1978.
- Crooker, N.U. and G.L. Siscoe, A mechanism for pressure anisotropy and mirror instability in the dayside magnetosheath, J. Geophys. Res., 82, 185, 1977.
- Dobrowolny, M., Instability of a neutral sheet, Nuovo Cimento B, 55, 427, 1968.
- Dungey, J.W., Interplanetary magnetic field and the auroral zone, Phys. Rev. Letts., 6, 47, 1961.
- Furth, H.P., The "mirror instability" for finite particle gyroradius, Nucl. Fusion Suppl. Pt. 1, 169, 1962.
- Galeev, A.A. and L.M. Zelenyi, Tearing instability in plasma configurations, Sov. Phys. JETP, 43, 1113, 1976.
- Greenly, J.B. and B.U.Ö. Sonnerup, Tearing modes at the magnetopause, J. Geophys. Res., 86, 1305, 1981.
- Hill, T.W., Magnetic merging in a collisionless plasma, J. Geophys. Res., 80, 4689, 1975.
- Laval, G., R. Pellat and M. Viullemin, Instabilities electromagnetiques des plasmas sans collisions, in Plasma Physics and Controlled Nuclear Fusion Research (International Atomic Energy Agency, Vienna), Vol. II, 259, 1966.
- Laval, G. and R. Pellat, Stability of the plane neutral sheet for oblique propagation and anisotropic temperature, ESRO SP-36, 5, 1968.
- Lembege, B. and R. Pellat, Stability of a thick two-dimensional quasineutral sheet, Phys. Fluids, 25, 1995, 1982.
- Pfirsch, D., Mikroinstabilitäten vom Spiegeltyp in inhomogenen Plasmen (Mirror type instabilities in inhomogeneous plasmas), Z. Naturforsch., 17a, 861, 1962.
- Quest, K.B. and F.V. Coroniti, Tearing at the dayside magnetopause, J. Geophys. Res., 86, 3289, 1981.
- Schindler, K., in Proceedings of the Seventh International Conference on Phenomena in Ionized Gases (Gradevinska Knjiga, Beograd, Yugoslavia), Vol. II, 736, 1966.
- Schindler, K., A theory of the substorm mechanism, J. Geophys. Res., 79, 2803, 1974.
- Sonnerup, B. U. Ö., Adiabatic particle orbits in a magnetic null sheet J. Geophys. Res., 76, 8211, 1971.

(Received September 19, 1983;
accepted October 25, 1983.)

APPENDIX C

A DYNAMIC MODEL FOR THE AURORAL FIELD LINE PLASMA
IN THE PRESENCE OF FIELD-ALIGNED CURRENT

H.G. Mitchell, Jr.
Science Applications, Inc.

and

P.J. Palmadesso
Naval Research Laboratory

A Dynamic Model for the Auroral Field Line Plasma in the Presence of Field-Aligned Current

H. G. MITCHELL, JR.

Science Applications, Inc., McLean, Virginia 22102

P. J. PALMADESSO

*Geophysical and Plasma Dynamics Branch, Plasma Physics Division, Naval Research Laboratory,
Washington, D. C. 20375*

We have developed a dynamic numerical model of the plasma along an auroral field line in order to provide a vehicle for studying ionosphere-magnetosphere coupling processes. The model is a multimoment, multifluid approximation of a gyrotropic plasma consisting of three species (electrons, hydrogen ions, oxygen ions) along a segment of auroral magnetic field line extending from an altitude of 800 km to 10 earth radii. We have performed simulations for the case of a current-free polar wind equilibrium of the field line plasma and the case in which a large upward field-aligned current is applied to the field line. In the former case, the agreement between our model and previous static results is reasonable given the differing boundary conditions inherent in the two cases. In the case of a field-aligned current, we note that the flux tube plasma responds to the current on several time scales. After an initial rapid heating of the electrons due to precipitation in a converging magnetic field, electric field coupling of the electrons to the ions causes thermal oscillations of the flux tube plasma to persist on time scales of the order of 1 hour, illustrating the complicated nature of the response of a collisionless plasma when heat flow transport is treated in a dynamic manner.

INTRODUCTION

It is a well-established fact that currents flow along the magnetic field lines which link the auroral ionosphere with the earth's magnetosphere, and it is becoming increasingly clear that these currents play an important role in the coupling of the magnetosphere and ionosphere (see, for example, *Potemra [1979]*). Early theories of the plasma along the field lines above the aurora assumed that the collisionless nature of this plasma would imply an effectively infinite conductivity along the magnetic field so that no significant parallel electric fields could be supported by the plasma. This conclusion has since been disputed by observational evidence of field-aligned acceleration, first in the 'inverted V' events [*Frank and Ackerson, 1971, 1972; Burch et al., 1976*] and more directly in the S3-3 satellite observations [*Shelley et al., 1976; Mizera and Fennel, 1977*]. It is now fairly well established that at certain times a large (1-10 keV) and relatively stable electric potential difference exists between the topside ionosphere and an altitude of several earth radii along auroral field lines, although the specific process by which large parallel electric fields are maintained in the auroral plasma in the absence of appreciable collisional resistivity has not been determined.

A number of mechanisms have been proposed to account for these parallel electric fields. One avenue of research has been devoted to the plasma instabilities which might disrupt the flow of the Birkeland currents along the magnetic field by scattering the current-carrying particles in wave-turbulent fields. The existence of instability in this region is supported by the observations of terrestrial kilometric radiation emission from the auroral field line plasma [*Gurnett, 1974*] and by the S3-3 observations of electrostatic hydrogen cyclotron waves in this region [*Kintner et al., 1978*]. Reviews of the

theory of plasma instabilities and turbulence in the auroral plasma can be found in the work of *Papadopoulos [1977]* and *Mozer [1976]*, while specific mechanisms are set forth in works of *Papadopoulos and Coffey [1974]*, *Hudson et al. [1978]*, and *Rowland et al. [1982]*. Another view is that the parallel potential drop may be confined to a small parallel scale and supported by charge imbalances due to density gradients in particle populations reflected or accelerated by the large electric field present in the region. Such a structure is called either a double layer [*Shawhan et al., 1978; Quon and Wong, 1976*] or an electrostatic shock [*Swift, 1975; Kan, 1975; Hudson and Mozer, 1978*] depending on the configuration of the plasma, and there is evidence to suggest that such regions of large dc electric field and large gradients in plasma parameters exist on auroral field lines [*Mozer et al., 1977; Torbert and Mozer, 1978*]. It has also been proposed [*Alfvén and Fälthammar, 1963; Block and Fälthammar, 1976; Lennartsson, 1976*] that the divergence of the auroral magnetic field is sufficient by itself to support a large parallel potential. In this model, hot magnetospheric electrons are prevented from free streaming down the magnetic field line by the magnetic mirror force due to the converging field.

It is difficult to say in many cases whether a specific process for maintaining the auroral electric field agrees or disagrees with observation. Processes dependent on microscopic interactions tend to be developed for simplified configurations such as a homogeneous plasma or a constant magnetic field and so do not yield clear predictions for the auroral plasma. Further, the details of the energy balance are not well understood along the auroral field line even in the absence of current, and these strongly affect the behavior of the particle distributions involved in any resistive mechanism. Clearly, a more global approach to the problem of field line acceleration for the auroral plasma would be useful. The plasma configuration along high latitude field lines has been investigated in the hydrodynamic models of *Banks and Holzer [1968]* and *Schunk and Watkins [1981, 1982]* and in

This paper is not subject to U.S. copyright. Published in 1983 by the American Geophysical Union.

Paper number 3A0001.

the kinetic models of *Lemaire and Scherer* [1973], *Chiu and Schulz* [1978], and *Chiu and Cornwall* [1980], among others. These models tend to be static models of steady-state auroral plasma configurations. There has been a significant amount of research done on the form and behavior of auroral particle distribution functions in the presence of parallel electric fields [*Evans*, 1974; *Whipple*, 1977; *Lyons et al.*, 1979; *Fridman and Lemaire*, 1980], and static kinetic models do a good job of reproducing these results. Such models can say little concerning the stability and temporal evolution of the field line plasma or the relative importance of the parallel field mechanisms, e.g., the question of whether the parallel electric field has a double layer or magnetic mirror configuration, or the question of the importance of anomalous resistivity in inhibiting a cold magnetospheric electron current.

We will describe in this paper a dynamic model we have been developing for the purpose of understanding the behavior of the auroral field line plasma in the presence of field-aligned current and auroral acceleration mechanisms. This model is a numerical model of a segment of auroral field line beginning in the topside ionosphere and extending well out into the magnetosphere, encompassing the transition of the auroral plasma from collisional to collisionless behavior and employing a multimoment multifluid approximation of the type developed by *Schunk* [1977]. The details of this model will be given here along with the results of our early simulations of the auroral plasma both with and without field-aligned current. We intend in the future to investigate particular mechanisms of auroral field line acceleration with this model by adjusting the anomalous transport terms in the model's plasma transport equations to simulate the effects of plasma turbulence and by introducing modifications designed to model other proposed acceleration processes. In this way we hope to gain a better understanding of the behavior of these mechanisms in the context of the global behavior of the auroral plasma.

THE FIELD LINE MODEL

The field line model is designed to dynamically simulate the behavior of the plasma in a flux tube encompassing an auroral field line. The field line is assumed to be radial with no curvature and to extend from an altitude of about 800 km in the topside ionosphere out to a distance of 10 R_E . The cross-sectional area of the flux tube diverges as r^2 , where r is the geocentric distance, and the model is essentially one-dimensional, with all quantities functions of r . The actual region of interest in this model is the lower four earth radii or so, including the region in which the plasma changes from collisional to collisionless behavior (about 800–3000 km altitude) and the region in which the plasma is significantly affected by the flux tube divergence.

The flux tube plasma consists of three particle species: electrons, hydrogen ions, and oxygen ions. In the present version of the model, the oxygen ions are a static background population at a constant temperature. They are present in the model in order to approximate the behavior of the plasma in the topside ionosphere by providing a thermal reservoir and the correct electron scale height at the lower end of the flux tube. The electrons and hydrogen ions are the dynamic species in the model. The distribution functions for these two species are assumed to be gyrotropic about the field line direction and are characterized by five moments:

number density, temperatures parallel and perpendicular to the field line, and species' velocity and heat flow along the field. Including the heat flow as a dynamic quantity rather than calculating it by means of a thermal conduction approximation allows a reasonable treatment of thermal wave effects in the collisionless region of the model.

The moments of the distribution function are treated dynamically using a set of transport equations derived from the 13-moment equations of *Schunk* [1977]. For a gyrotropic plasma, these equations are

$$\frac{\partial n_s}{\partial t} = -v_s \frac{\partial n_s}{\partial r} - n_s \frac{\partial v_s}{\partial r} - \frac{n_s v_s}{A} \frac{\partial A}{\partial r} + \frac{\delta n_s}{\delta t} \quad (1)$$

$$\begin{aligned} \frac{\partial v_s}{\partial t} = & -v_s \frac{\partial v_s}{\partial r} - \frac{k}{m_s} \frac{\partial T_{s\parallel}}{\partial r} - \frac{k T_{s\parallel}}{m_s n_s} \frac{\partial n_s}{\partial r} - \frac{k(T_{s\parallel} - T_{s\perp})}{m_s A} \frac{\partial A}{\partial r} \\ & - \frac{e_s}{m_s} E - \frac{GM}{r^2} + \frac{\delta v_s}{\delta t} \end{aligned} \quad (2)$$

$$\begin{aligned} k \frac{\partial T_{s\parallel}}{\partial t} = & -v_s k \frac{\partial T_{s\parallel}}{\partial r} - 2k T_{s\parallel} \frac{\partial v_s}{\partial r} - \frac{6}{5 n_s} \frac{\partial q_s}{\partial r} \\ & - \frac{2}{5} \frac{q_s}{n_s A} \frac{\partial A}{\partial r} + k \frac{\delta T_{s\parallel}}{\delta t} \end{aligned} \quad (3)$$

$$\begin{aligned} k \frac{\partial T_{s\perp}}{\partial t} = & -v_s k \frac{\partial T_{s\perp}}{\partial r} - \frac{2}{5 n_s} \frac{\partial q_s}{\partial r} \\ & - \left(\frac{4}{5} \frac{q_s}{n_s} + v_s k T_{s\perp} \right) \frac{1}{A} \frac{\partial A}{\partial r} + k \frac{\delta T_{s\perp}}{\delta t} \end{aligned} \quad (4)$$

$$\begin{aligned} \frac{\partial q_s}{\partial t} = & -v_s \frac{\partial q_s}{\partial r} - \frac{16}{5} q_s \frac{\partial v_s}{\partial r} - \left(\frac{11}{18} T_{s\parallel} - \frac{8}{9} T_{s\perp} \right) \frac{n_s k^2}{m_s} \frac{\partial T_{s\parallel}}{\partial r} \\ & - \left(\frac{17}{9} T_{s\parallel} - \frac{8}{9} T_{s\perp} \right) \frac{n_s k^2}{m_s} \frac{\partial T_{s\perp}}{\partial r} - \frac{4k^2}{9m_s} (T_{s\parallel} - T_{s\perp})^2 \frac{\partial n_s}{\partial r} \\ & + \left[\frac{n_s k^2}{m_s} (T_{s\parallel} - T_{s\perp}) \left(\frac{1}{3} T_{s\parallel} - \frac{4}{3} T_{s\perp} \right) \right. \\ & \left. - \frac{7}{5} v_s q_s \right] \frac{1}{A} \frac{\partial A}{\partial r} + \frac{\delta q_s}{\delta t} \end{aligned} \quad (5)$$

where n_s is the number density, v_s is the velocity, $T_{s\parallel}$ is the parallel temperature, $T_{s\perp}$ is the perpendicular temperature, q_s is the heat flow, m_s is the mass, and e_s is the charge of species s . A is the cross-sectional area of the flux tube, E is the electric field parallel to the field line, k is Boltzmann's constant, G is the gravitational constant, and M is the mass of the earth. For a given moment F of the distribution function, $\delta F/\delta t$ is the change in F due to resistive and plasma turbulence effects. The present version of the field line model includes only resistivity due to Coulomb collisions among the three particle species in the model. Once the behavior of this simulation is understood for this case, the turbulence terms will be altered to reflect the behavior of the particle distribution functions in the presence of plasma

microprocesses. The specific resistive terms used in the present simulation are *Burgers'* [1969] collision terms for the case of Coulomb collisions with corrections for finite species velocity differences, given by

$$\frac{\delta n_i}{\delta t} = 0 \quad (6)$$

$$\frac{\delta v_i}{\delta t} = \sum_j v_{sj}(v_i - v_j)(1 - \phi_{sj}) \quad (7)$$

$$k \frac{\delta T_i}{\delta t} = \sum_j \frac{m_i v_{sj}}{(m_i + m_j)} \left\{ \frac{6}{5} k T_i - \left[2 - \frac{4 m_i}{5 m_j} \right] k T_j + \frac{4}{5} k T_{i,j} + \frac{4 m_i}{5 m_j} k T_{s,j} + \left[2 k T_i + \left(4 + 6 \frac{m_i}{m_j} \right) k T_j \right] \phi_{sj} \right\} \quad (8)$$

$$k \frac{\delta T_{s,i}}{\delta t} = \sum_j \frac{m_i v_{sj}}{(m_i + m_j)} [3 k T_i - 3 k T_j - m_i (v_i - v_j)^2 (1 - \phi_{sj})] - \frac{k}{2} \frac{\delta T_s}{\delta t} \quad (9)$$

$$\frac{\delta q_s}{\delta t} = \sum_i \frac{n_i m_i v_{si}}{(m_s + m_i)^2} \left[\frac{27}{10} m_i \frac{q_i}{n_i} - \left(3 m_s + \frac{8}{5} m_i + \frac{13}{10} \frac{m_i^2}{m_s} \right) \frac{q_i}{n_i} + \frac{3}{2} \frac{m_i}{m_s} (m_i + m_s) k T_s (v_i - v_s) \right] (1 + \phi_{si}) \quad (10)$$

where each sum includes all charged particles species in the simulation. v_{sj} is a velocity-corrected Coulomb collision frequency,

$$v_{sj} = \frac{n_j (32\pi)^{1/2} e_i^2 e_j^2 (m_i + m_j) \ln \Lambda \exp(-x_{sj}^2)}{3 m_s^2 m_i \alpha_{sj}^3} \quad (11)$$

($\ln \Lambda$ is the Coulomb logarithm), and

$$T_s = \frac{1}{3} T_{s,e} + \frac{2}{3} T_{s,i}$$

$$\alpha_{sj}^2 = \frac{2 k T_i}{m_i} + \frac{2 k T_j}{m_j}$$

$$x_{sj}^2 = \frac{(v_i - v_j)^2}{\alpha_{sj}^2}$$

$$\phi_{sj} = \frac{2}{5} x_{sj}^2 + \frac{4}{35} x_{sj}^4 + \frac{8}{315} x_{sj}^6$$

The scale of this model is large compared to the electron Debye length, so the transport equation (1) for electron number density may be replaced by an expression for charge neutrality:

$$n_e = n_p + n_o \quad (12)$$

(The subscripts *e*, *p*, and *o* represent electrons, hydrogen ions, and oxygen ions, respectively.) Further, the assumption

will be made that the total flux tube current remains constant at some fixed value *I* during a simulation (i.e., the auroral current generator is not strongly affected by the behavior of the flux tube plasma), which implies that the electron velocity transport equation (2) is replaced by

$$v_e = \frac{1}{n_e} \left(n_p v_p - \frac{I}{eA} \right) \quad (13)$$

The assumption of charge neutrality and constant current along the field line allows the parallel electric field *E* to be calculated from a generalized Ohm's law constructed from the electron and ion velocity transport equations (2):

$$E = \frac{m_s}{en_e A} \frac{\partial}{\partial r} (n_p v_p^2 A - n_e v_e^2 A) - \frac{1}{e} \left[\frac{\partial T_e}{\partial r} - \frac{T_e}{n_e} \frac{\partial n_e}{\partial r} + \frac{(T_e - T_{e-})}{A} \frac{\partial A}{\partial r} \right] - \frac{n_o m_o G M}{n_e e r} - \frac{m_e}{e} \left[\frac{\delta v_e}{\delta t} - \frac{n_e}{n_i} \frac{\delta v_i}{\delta t} \right] \quad (14)$$

where terms on the order of m_e/m_i have been neglected. By using Poisson's equation, the divergence of this electric field provides a value for the charge density along the field line which can be used to verify the assumption of charge neutrality. In the future, we intend to treat the field line current in a more general manner by including the flux tube in an auroral current circuit, in which case the flux tube would become a nonlinear circuit element in that circuit, and the magnitude of the field line current would be determined self-consistently by the behavior of the circuit.

The field line model, therefore, uses equations (1)–(5) for hydrogen ions and equations (3)–(5) for electrons to step the values of these distribution moments forward in time, while calculating the electric field and electron density and velocity self-consistently at each time with equations (12)–(14). The simulation calculates transport using the simple partial donor cell method [Hain, 1978] on an unequally spaced grid. The segment of the field line being modelled is divided into about 100 cells. The cell size at the lower end of the segment is small, around 50 km, in order to properly deal with the transport in the presence of the large density gradients due to the small oxygen scale height. The cell size increases with altitude until it reaches roughly 1500 km at an altitude of 10 earth radii (R_E), the upper boundary of the model. The time step for this simulation is determined primarily by the transit time of a thermal electron in a cell at the lower end of the field line and is set at about .06 seconds.

By using equations (1)–(5) to model the behavior of the auroral plasma, we are assuming a particular form for the auroral particle distribution functions, specifically that they are roughly displaced Maxwellian distributions. This would not be a good approximation in the case in which a distribution is composed of particles of widely differing character, as in a distribution containing both cold ionospheric electrons and hot magnetospheric electrons. In such a case, it is appropriate to separate the electrons into two species, each modeled by a set of transport equations. We intend to do this in the future, but, for the simulations presented here, we are assuming that the magnetospheric electrons are cold and are treating the electrons as a single species. There are several reasons for this. First, the dynamic behavior of the flux tube plasma can be quite complex, and we believe it necessary to

understand the dynamics in the absence of hot magnetospheric particles in order to proceed to the more realistic case. More importantly, certain theories of the field line plasma rely on the absence of a cold magnetospheric electron current [Lennartsson, 1976, etc.]. It is not clear that there is no significant cold particle population in the magnetosphere [Olsen, 1982], and simulations such as these may illustrate the behavior of a current carried by such particles.

THE POLAR WIND SIMULATION

The first simulations with the field line model were performed to construct a steady state configuration of the field line plasma in the current-free case. We began by initializing the flux tube in a polar wind configuration similar to that of Banks and Holzer [1968]. In the polar wind, hydrogen ions are accelerated upwards in the flux tube to supersonic velocities due to the flux tube divergence and the small partial pressure of H^+ at the upper end of the field line. The outward H^+ flux depletes the hydrogen ion population at lower altitudes, and, as a result, oxygen ions are the dominant ion species up to an altitude of around 4000 km. The O^+-e charge separation electric field in this region provides the initial H^+ acceleration up the field line. In the model of Banks and Holzer, the population of H^+ is maintained against depletion by O^+-H charge exchange at the altitudes below 1000 km, and the hydrogen ion escape flux is limited to about $1 \times 10^8 \text{ cm}^{-2} \text{ s}^{-1}$ at 1000 km. In the field line model, there are no neutral species at this point, so the hydrogen ion flux is maintained by a fixed density and upward velocity for H^+ at 800 km, the lower boundary of the model. As a result, the hydrogen ion number density tends to be somewhat greater in the lowest few cells of the field line model than would be expected in the presence of O^+-H charge exchange.

The model of Banks and Holzer assumed that the charged particle species in the flux tube had uniform temperatures and, therefore, heat flow was neglected. We assumed the same, initializing the three flux tube particle species at a constant temperature of 2000 K with no heat flow. To begin our simulations, the transport of thermal energy density and heat flow were suppressed in the field line model in an attempt to duplicate the results of Banks and Holzer. The model achieved a steady state polar wind under these conditions, with the number density and velocity profiles shown in Figures 1a, 1b. Once this equilibrium had been reached, the thermal energy density and heat flow transport were "turned on," and the simulation was run until a new steady-state was achieved. The lower boundary temperature was held fixed at 2000 K during the simulation. The upper boundary temperature was determined by an outflow condition in that thermal gradients propagating up the field line were allowed to propagate out of the simulation.

The temperature profiles from the new steady-state are shown in Figures 2a, 2b. The primary effect displayed by the electron temperatures in this equilibrium is adiabatic cooling due to the expansion of the cross-sectional flux tube area with height. At the lower end of the field line, the high rate of expansion causes rapid cooling, and the resulting temperature gradient is maintained by low thermal conductivity due to high particle density. The electron temperature profiles tend to flatten out in the upper regions of the tube as both the rate of expansion and the particle densities decrease. In

addition, the electron temperatures develop a small anisotropy at 3000–4000 km altitude due to unequal rates of cooling in the perpendicular and parallel directions. This may also be viewed as the fluid model manifestation of the mirror effect, with perpendicular energy being transferred into parallel energy as the electrons are accelerated upwards in the diverging magnetic field.

The hydrogen ion temperatures, on the other hand, increase with increasing altitude at the lower end of the flux tube, before beginning to exhibit adiabatic cooling at higher altitudes. The temperature increase is caused by the Joule heating of the hydrogen from collisions with the oxygen ions. The strength of this effect decreases rapidly with altitude due to the small scale height of the oxygen, allowing the adiabatic cooling to become dominant at about 4000 km altitude. The anisotropy of the cooling is much more evident in the hydrogen ions than in the electrons because of the supersonic hydrogen velocities and the fact that, in the collisionless region, heat transport along the field line is less efficient for the hydrogen than for the electrons. As a result, the hydrogen temperature profiles maintain significant gradients at higher altitudes than the electron profiles and exhibit large temperature anisotropies at the upper end of the flux tube.

It is instructive to compare these results with those of Schunk and Watkins [1981, 1982]. These works model current-free steady state configurations of the auroral field line plasma by integrating up the field line the steady state form of a set of transport equations for a three-species (e , H^+ , O^+) plasma similar to the ones in equations (1)–(5). The steady state configurations which result are a function of the lower boundary (1500 km altitude) conditions, specifically, the values of the species density, velocity, temperature, and temperature gradient. Comparing the results of our simulations with those of Schunk and Watkins [1982] for the hydrogen ion profiles in the case of supersonic polar wind, a number of similarities can be seen. For low electron temperatures, both exhibit an anisotropic hydrogen ion cooling resulting in a larger parallel than perpendicular temperature at the upper end of the field line. Also, both have a region in which the parallel temperature increases with altitude before adiabatic cooling dominates. The rate of cooling for the hydrogen ions is less in our simulation, most likely because both the oxygen ions and the electrons are hotter at the lower end of the field line (2000 K in our simulation versus 1000 K in that of Schunk and Watkins). The highly anisotropic cooling of the hydrogen ions is also a feature of another steady state polar wind model, that of Holzer *et al.* [1971], which also attempted to realistically deal with the ion heat flow in the collisionless region. The heat flow for hydrogen ions is upward and monotonically decreasing in these models, implying that the polar wind requires an outward flow of heat from the ionosphere. The magnitude of the heat flow is roughly the same in our simulation as in that of Schunk and Watkins.

The electron profiles of Schunk and Watkins [1981] cannot be directly compared to our simulation results. By assuming a positive electron temperature gradient at an altitude of 1500 km, they achieve an equilibrium in which the electron temperatures are monotonically increasing with altitude and the electron heat flow is down the field line. Further, the temperature anisotropy is reversed in the upper region of the field line, with the perpendicular temperature being the larger. Thus the positive temperature gradient boundary

condition for the electrons forces the upper boundary of the field line to act as a heat source for the flux tube. The outflow condition in our model, on the other hand, treats the upper boundary as an electron heat sink, resulting in a monotonically decreasing electron temperature with altitude. As long as the electron species velocity is less than the electron thermal velocity, the assumed electron temperature of the upper boundary plasma has a strong effect on the electron temperature profiles in the flux tube. The supersonic outflow of hydrogen ions in the polar wind implies that the energy flux must be outward for the hydrogen ions, with the result that only the ionosphere can provide a heat source for H^+ regardless of the assumed temperature of the upper boundary protons. Schunk and Watkins [1982] note that the upper boundary plasma can provide a proton heat source in the case of a subsonic H^+ outflow.

A FIELD-ALIGNED CURRENT SIMULATION

Simulations have been performed with the field line model in the presence of current parallel to the magnetic field and

we would like to briefly describe one of these simulations. In this case, a constant upward current of $1.0 \times 10^{-6} \text{ A.m}^{-2}$ at an altitude of 800 km was assumed for the duration of the simulation. This value was chosen to be physically reasonable and to illustrate the effect of a large downward electron energy flux on the flux tube plasma. The initial state of the flux tube is assumed to be the steady state polar wind described in the previous section.

The electron temperature profiles are shown in Figures 3a, 3b, and 3c for times of 2, 8, and 20 min after current onset. Initially, the now-precipitating electron distribution sees a converging magnetic field, and the temperature rises in the lower regions of the flux tube. Below about $2 R_E$ altitude, the strong mirror force causes the perpendicular temperature to increase at the expense of the parallel temperature, creating a strong temperature anisotropy around 4000 km. Below 4000 km, the electron number density increases sharply, and the effect of the precipitating electrons is mitigated. As the electrons are heated in the lower end of the flux tube, the temperature gradient results in a large upward electron heat

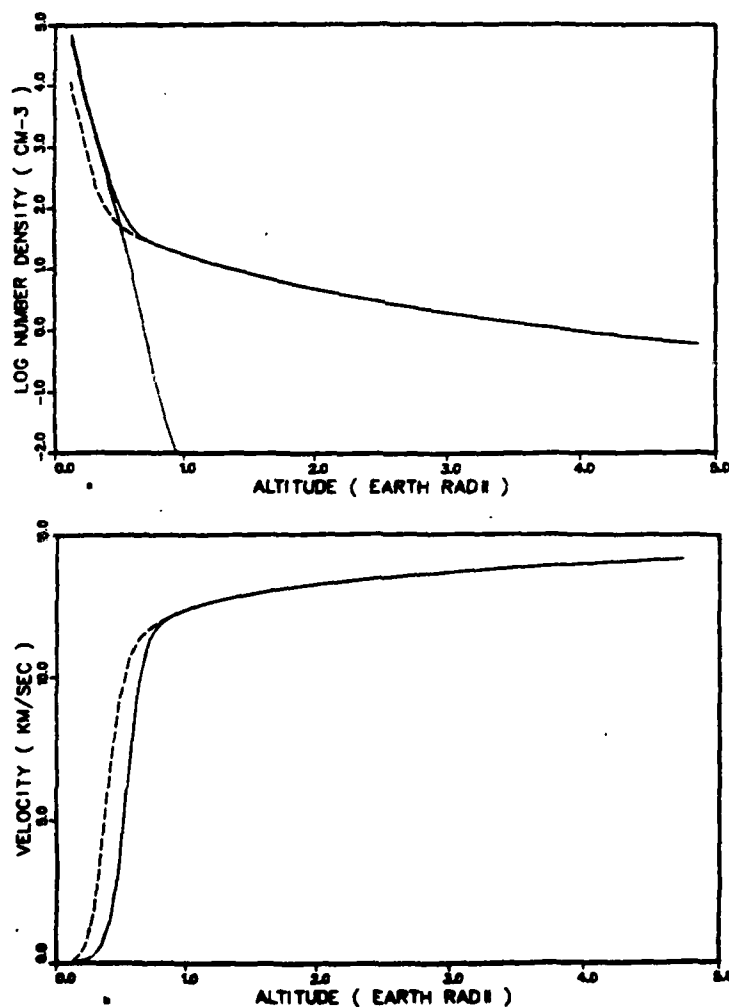


Fig. 1. (a) Number densities for the steady state polar wind with no field-aligned current: n_e (solid curve), n_p (dashed curve), n_o (dotted curve). (b) Velocities for the steady state polar wind with no field-aligned current: v_e (solid curve), v_p (dashed curve). The oxygen ion velocity is uniformly zero.

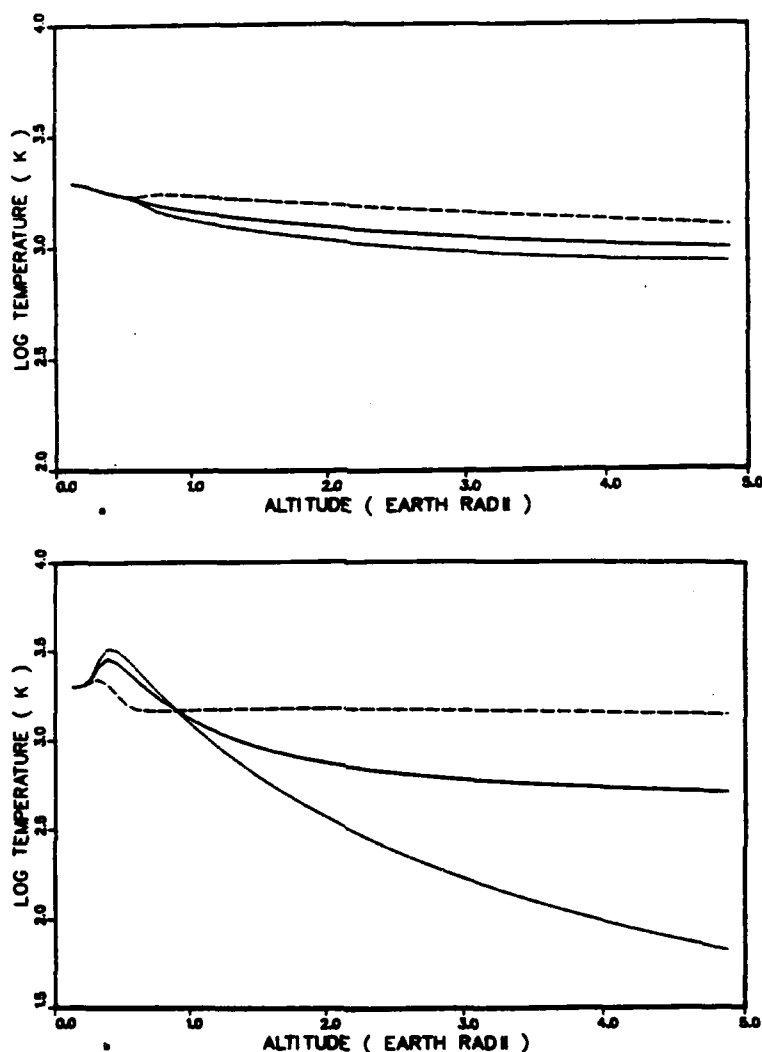


Fig. 2. (a) Electron temperatures for the steady state polar wind with no field-aligned current: T_e (solid curve), $T_{e\perp}$ (dashed curve), $T_{e\parallel}$ (dotted curve). (b) Hydrogen ion temperatures for the steady state polar wind with no field-aligned current: T_p (solid curve), $T_{p\perp}$ (dashed curve), $T_{p\parallel}$ (dotted curve). The oxygen ion temperature is uniformly 2000 K.

flow and electron thermal wave propagating up the field line. This wave can be seen at about $4 R_E$ in Figure 3a. The rate of electron heating is greater than the rate of heat loss due to the upward heat flux until about 8 min after current onset (Figure 3b). At this time, there exists a large, anisotropic electron temperature maximum between 4000 and 6000 km altitude. The large upward heat flow in the upper altitudes has cooled the electrons in the perpendicular direction resulting in a strong anisotropy at high altitudes also. After eight minutes, the temperature maximum at 4000 km collapses as the thermal energy is transported out of this region by the strong upward heat flux. By 20 min after current onset, the electron temperature has achieved a rough equilibrium between downward convecting electron energy and upward heat flux (Figure 3c).

During the existence of the electron temperature peak at 5000 km, the ambipolar electric field in this region has increased by about an order of magnitude from the polar wind value, accelerating the hydrogen ions upwards. The

resulting velocity gradient creates an upward-propagating pulse of hydrogen ions with higher temperature and density, as illustrated in a plot of the hydrogen ion temperature profiles at 20 min after current onset (Figure 4). The pulse is at about $2 R_E$ altitude in this figure. The electron density and velocity are tied to the hydrogen ion density and velocity at high altitudes by charge neutrality and current conservation, so such a density pulse is also visible in the electron profiles. Since the electric field eventually settles down to approximately its original value, the hydrogen ion profiles return to the polar wind values as the electrons reach equilibrium.

We have performed simulations with larger field-aligned currents than the one described here. In such cases, the transient electron thermal effects in the flux tube are larger and persist for longer times. In addition, the electric field coupling of the electrons to the ions induces ion density and thermal waves, which achieve equilibrium slower than the electrons. The point that we wish to stress here is that the flux tube plasma seems to have a rapid initial response to the

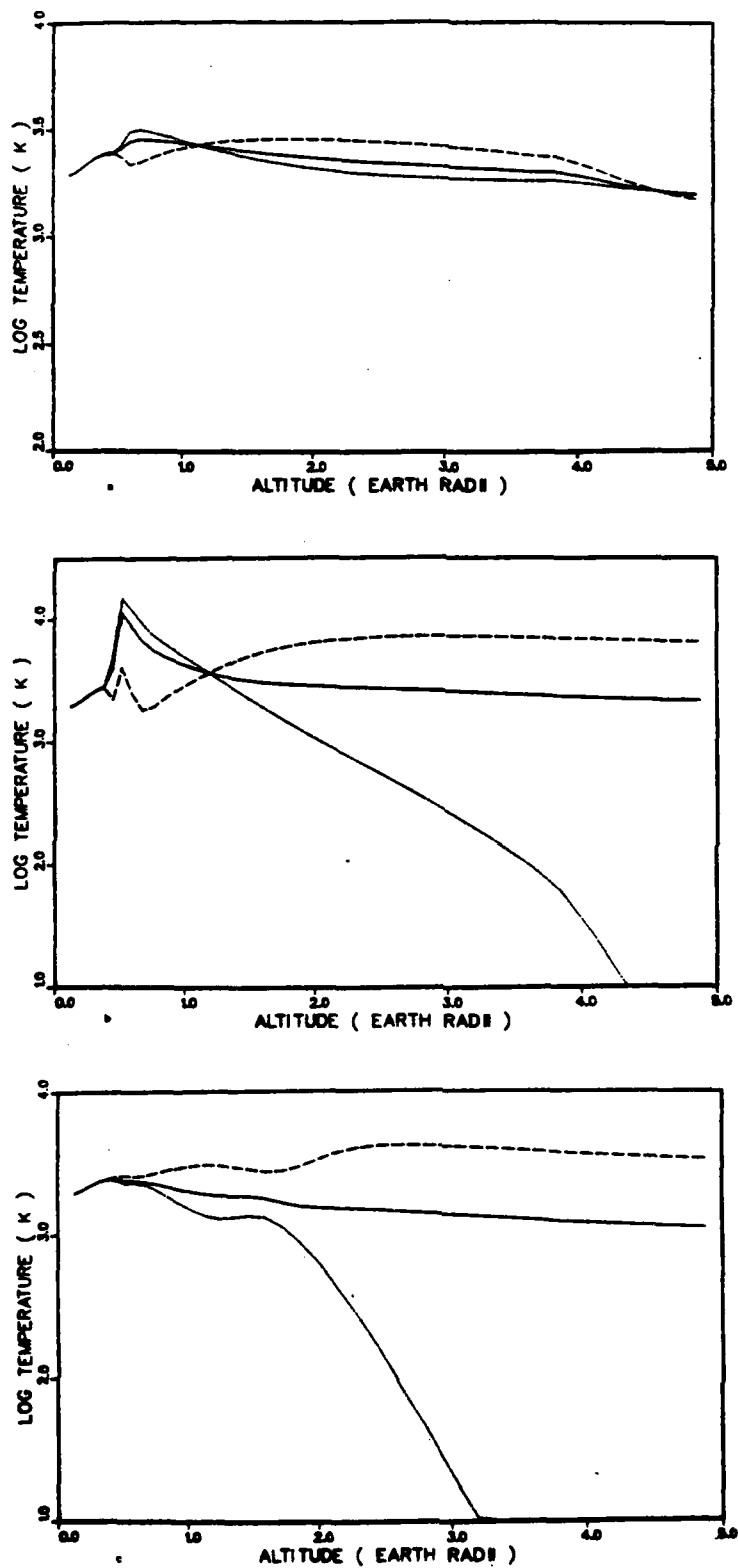


Fig. 3. Electron temperatures after the onset of a current of $1.0 \mu\text{A}/\text{m}^2$ at 800 km: T_e (solid curve), T_i (dashed curve), T_{ei} (dotted curve). (a) Two min after current onset; (b) 8 min after current onset; (c) 20 min after current onset.

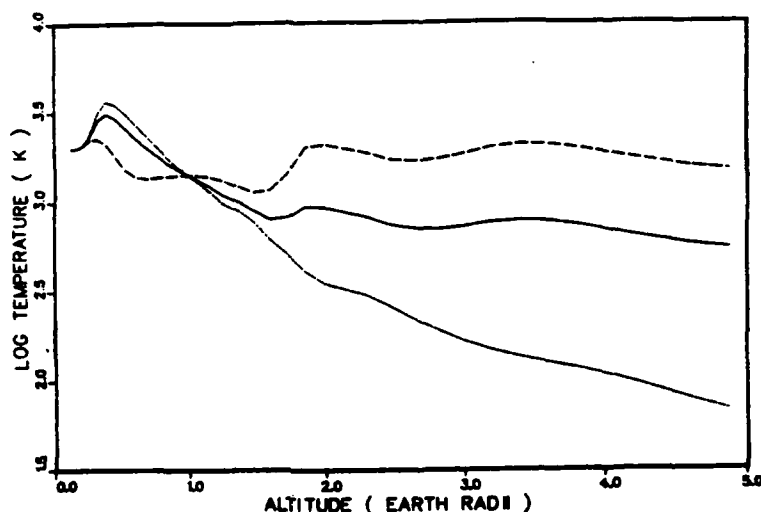


Fig. 4. Hydrogen ion temperatures at 20 min after the onset of a current of $1.0 \mu\text{A}/\text{m}^2$ at 800 km: T_e (solid curve), T_p (dashed curve), T_p (dotted curve).

onset of current, one affecting the electron temperature and energy flux predominantly. After this response, it is not clear that the plasma 'settles down' to some equilibrium configuration in a reasonable time. Large electron and ion thermal waves can persist for relatively long times when the heat flows are treated dynamically. One of our future goals is to use this model to investigate the behavior of these thermal waves for a range of currents and upper boundary configurations.

SUMMARY

We have described here some of the results of our model for the behavior of the auroral field line plasma. Our results for equilibrium in the current-free case are in reasonable agreement with the previous work in this area, illustrating the important role that the upper boundary layer plays in determining the temperature profile of the electron population in contrast to the relative insensitivity of the supersonic hydrogen ion population to this layer. The simulations with current which we have performed suggest that the time scale on which the field line plasma achieves equilibrium is highly dependent on the behavior of the energy transport in the collisionless region. In fact, there may exist no equilibrium on the field line in the presence of a current varying on the time scale of interest in this problem.

The results presented here are meant to illustrate the kinds of behavior the field line model manifests and to point the way for future improvements in the model. Because of the importance of hot magnetospheric electrons in the dynamics of the field line, one of our first steps will be to include these particles in our simulation. Also, we feel that there is more to be done in order to understand the effect the upper field line configuration has on the behavior of the flux tube plasma. It is our intention to proceed in these areas in addition to our main goal, that of investigating the effect of anomalous resistivity and electric field mechanisms in the collisionless region of our model.

Acknowledgments. This work was supported by the Office of Naval Research and by NASA contract W-14365.

The editor thanks R. Schunk and J. Lemaire for their assistance in evaluating this paper.

REFERENCES

- Alfvén, H., and C.-G. Fälthammar. *Cosmical Electrodynamics. Fundamental Principles*. 2nd ed., pp. 162-167. Oxford University Press, New York, 1963.
- Banks, P. M., and T. E. Holzer. The polar wind. *J. Geophys. Res.*, **73**, 6846-6854, 1968.
- Block, L. P., and C.-G. Fälthammar. Mechanisms that may support magnetic-field-aligned electric fields in the magnetosphere. *Ann. Geophys.*, **32**, 161-174, 1976.
- Burch, J. L., S. A. Fields, W. B. Hanson, R. A. Heelis, R. A. Hoffman, and R. W. Janetzke. Characteristics of auroral electron acceleration regions observed by Atmospheric Explorer C. *J. Geophys. Res.*, **81**, 2223-2230, 1976.
- Burgers, J. M., *Flow Equations for Composite Gases*, pp. 108-159. Academic, New York, 1969.
- Chiu, Y. T., and J. M. Cornwall. Electrostatic model of a quiet auroral arc. *J. Geophys. Res.*, **85**, 543-556, 1980.
- Chiu, Y. T., and M. Schulz. Self-consistent particle and parallel electric field distributions in the magnetospheric-ionospheric auroral region. *J. Geophys. Res.*, **83**, 629-642, 1978.
- Evans, D. S., Precipitating fluxes formed by a magnetic field aligned potential difference. *J. Geophys. Res.*, **79**, 2853-2858, 1974.
- Frank, L. A., and K. L. Ackerson. Observations of charged particle precipitation into the auroral zone. *J. Geophys. Res.*, **76**, 3612-3643, 1971.
- Frank, L. A., and K. L. Ackerson. Local time survey of plasma at low altitudes over the auroral zone. *J. Geophys. Res.*, **77**, 4116-4127, 1972.
- Fridman, M., and J. Lemaire. Relationship between auroral electron fluxes and field aligned electric potential difference. *J. Geophys. Res.*, **85**, 664-670, 1980.
- Gurnett, D. A., The earth as a radio source: terrestrial kilometric radiation. *J. Geophys. Res.*, **79**, 4227-4238, 1974.
- Hain, K., The partial donor cell method. *NRL Memo. Rep.*, 3713, 18 pp., Nav. Res. Lab., Washington, D. C., 1978.
- Holzer, T. E., J. A. Fedder, and P. M. Banks. A comparison of kinetic and hydrodynamic models of an expanding ion-exosphere. *J. Geophys. Res.*, **76**, 2453-2468, 1971.
- Hudson, M. K., and F. S. Mozer. Electrostatic shocks, double layers, and anomalous resistivity in the magnetosphere. *Geophys. Res. Lett.*, **5**, 131-134, 1978.
- Hudson, M. K., R. L. Lysak, and F. S. Mozer. Magnetic field-aligned potential drops due to electrostatic ion cyclotron turbulence. *Geophys. Res. Lett.*, **5**, 143-146, 1978.
- Kan, J. R., Energization of auroral electrons by electrostatic shock waves. *J. Geophys. Res.*, **80**, 2089-2095, 1975.
- Kintner, P. M., M. C. Kelley, and F. S. Mozer. Electrostatic hydrogen cyclotron waves near one earth radius altitude in the polar magnetosphere. *Geophys. Res. Lett.*, **5**, 139-142, 1978.

- Lemarie, J., and M. Scherer. Kinetic models of the solar and polar wind. *Rev. Geophys. Space Phys.*, **11**, 427-468, 1973.
- Lennartsson, W. On the magnetic mirroring as the basic cause of parallel electric fields. *J. Geophys. Res.*, **81**, 5583-5586, 1976.
- Lyons, L. K., D. S. Evans, and R. Lundin. An observed relation between magnetic field aligned electric fields and downward electron energy fluxes in the vicinity of auroral forms. *J. Geophys. Res.*, **84**, 457-461, 1979.
- Mizera, P. F., and J. F. Fennell. Signatures of electric fields from high and low altitude particle distributions. *Geophys. Res. Lett.*, **4**, 311-314, 1977.
- Mozer, F. S. Anomalous resistivity and parallel electric fields, in *Magnetospheric Particles and Fields*, edited by B. M. McCormac, pp. 125-136. D. Reidel, Hingham, Mass., 1976.
- Mozer, F. S., C. W. Carlson, M. K. Hudson, R. B. Torbert, B. Parady, J. Yatteau, and M. C. Kelley. Observations of paired electrostatic shocks in the polar magnetosphere. *Phys. Rev. Lett.*, **38**, 292-295, 1977.
- Olsen, R. C. The hidden ion population of the magnetosphere. *J. Geophys. Res.*, **87**, 3481-3488, 1982.
- Papadopoulos, K. A review of anomalous resistivity for the ionosphere. *Rev. Geophys. Space Phys.*, **15**, 113-127, 1977.
- Papadopoulos, K., and T. Coffey. Anomalous resistivity in the auroral plasma. *J. Geophys. Res.*, **79**, 1558-1561, 1974.
- Potemra, T. A. Current systems in the earth's magnetosphere. *Rev. Geophys. Space Phys.*, **17**, 640-656, 1979.
- Quon, B. H., and A. Y. Wong. Formation of potential double layers in plasmas. *Phys. Rev. Lett.*, **37**, 1393-1396, 1976.
- Rowland, H. L., K. Papadopoulos, and P. J. Pammadesso. Anomalous resistivity on auroral field lines. *NRL Rep. 5227*, 6 pp., Naval Res. Lab., Washington, D. C., 1982.
- Schunk, R. W. Mathematical structure of transport equations for multispecies flows. *Rev. Geophys. Space Phys.*, **15**, 429-445, 1977.
- Schunk, R. W., and D. S. Watkins. Electron temperature anisotropy in the polar wind. *J. Geophys. Res.*, **86**, 91-102, 1981.
- Schunk, R. W., and D. S. Watkins. Proton temperature anisotropy in the polar wind. *J. Geophys. Res.*, **87**, 171-180, 1982.
- Shawhan, S. D., C.-G. Falthammar, and L. P. Block. On the nature of large auroral zone electric fields at 1-R_E altitude. *J. Geophys. Res.*, **83**, 1049-1054, 1978.
- Shelley, E. G., R. D. Sharp, and R. G. Johnson. Satellite observations of an ionospheric acceleration mechanism. *Geophys. Res. Lett.*, **3**, 654-656, 1976.
- Swift, D. W. On the formation of auroral arcs and the acceleration of auroral electrons. *J. Geophys. Res.*, **80**, 2096-2108, 1975.
- Torbert, R. B., and F. S. Mozer. Electrostatic shocks as the source of discrete auroral arcs. *Geophys. Res. Lett.*, **5**, 135-138, 1978.
- Whipple, E. C., Jr. The signature of parallel electric fields in a collisionless plasma. *J. Geophys. Res.*, **82**, 1525-1531, 1977.

(Received April 5, 1982;
revised November 10, 1982;
accepted December 21, 1982.)

UNCLASSIFIED

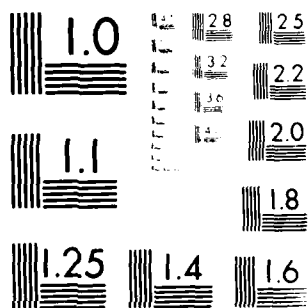
APPLICATIONS INC MCLEAN VA E HYMAN ET AL. MAR 84

SAI-84/1554 SBI-AD-E001 718 N00014-83-C-2034

F/G 4/1

NL

2/6



MICROCOPY RESOLUTION TEST CHART
 NATIONAL BUREAU OF STANDARDS-1963-A

APPENDIX D
ELECTROSTATIC ION-CYCLOTRON WAVES IN MAGNETOSPHERIC
PLASMAS: NON-LOCAL ASPECTS

G. Ganguli and P. Bakshi
Science Applications, Inc.

and

P. Palmadesso
Naval Research Laboratory

Electrostatic Ion-Cyclotron Waves in Magnetospheric Plasmas: Non-Local Aspects

G. GANGULI,* P. BAKSHI,* AND P. PALMADESSO

*Geophysical and Plasma Dynamics Branch
Plasma Physics Division*

**Science Applications, Inc.
McLean, VA 22102*

October 14, 1983

This research was sponsored by the Office of Naval Research and
the National Aeronautics and Space Administration.



NAVAL RESEARCH LABORATORY
Washington, D.C.

Approved for public release; distribution unlimited.

SECURITY CLASSIFICATION OF THIS PAGE (When Data Entered)

REPORT DOCUMENTATION PAGE		READ INSTRUCTIONS BEFORE COMPLETING FORM
1. REPORT NUMBER NRL Memorandum Report 5197	2. GOVT ACCESSION NO.	3. RECIPIENT'S CATALOG NUMBER
4. TITLE (and Subtitle) ELECTROSTATIC ION-CYCLOTRON WAVES IN MAGNETOSPHERIC PLASMAS: NON-LOCAL ASPECTS	5. TYPE OF REPORT & PERIOD COVERED Interim report on a continuing NRL problem.	
7. AUTHOR(s) G. Ganguli,* P. Bakshi,* and P. Palmadesso	6. PERFORMING ORG. REPORT NUMBER	
8. PERFORMING ORGANIZATION NAME AND ADDRESS Naval Research Laboratory Washington, DC 20375	9. CONTRACT OR GRANT NUMBER(s)	
11. CONTROLLING OFFICE NAME AND ADDRESS Office of Naval Research Arlington, VA 22203	10. PROGRAM ELEMENT PROJECT TASK AREA & WORK UNIT NUMBERS 61153N; RR033-02-44; W-14365; 47-0884-0-3; 47-1447-0-3	
14. MONITORING AGENCY NAME & ADDRESS (if different from Controlling Office)	12. REPORT DATE October 14, 1983	
	13. NUMBER OF PAGES 36	
	15. SECURITY CLASS (for this report) UNCLASSIFIED	
	15a. DECLASSIFICATION/DOWNGRADING SCHEDULE	
16. DISTRIBUTION STATEMENT (of this Report) Approved for public release; distribution unlimited.		
17. DISTRIBUTION STATEMENT (of the abstract entered in Block 20, if different from Report)		
18. SUPPLEMENTARY NOTES *Present address: Science Applications, Inc., McLean, VA 22102 P. Bakshi - permanent address: Department of Physics, Boston College, Chestnut Hill, MA 02167 This research was sponsored by the Office of Naval Research and the National Aeronautics and Space Administration.		
19. KEY WORDS (Continue on reverse side if necessary and identify by block number) EIC waves Non-local effects Magnetospheric plasma		
20. ABSTRACT (Continue on reverse side if necessary and identify by block number) The importance of the effect of the magnetic shear and the finite size of the current channel on the electrostatic ion-cyclotron instability for the space plasmas is illustrated. A non-local treatment is used. When the channel width L_c is larger than the shear length L_s , there is a large reduction in the growth rate along with a noteworthy reduction of the band of the unstable perpendicular wave- lengths. For $L_c < L_s/10$ the growth rate is not much altered from its local value; however for L_c $\rho_i \leq 10^2$ the growth rate starts falling below the local value and vanishes for $L_c \sim \rho_i$. The non- local effects lead to enhanced coherence in the ion cyclotron waves.		

DD FORM 1 JAN 73 1473

EDITION OF 1 NOV 65 IS OBSOLETE
S/N 0102-014-6801

SECURITY CLASSIFICATION OF THIS PAGE (When Data Entered)

D-5

PRECEDING PAGE BLANK-NOT FILMED

CONTENTS

I.	INTRODUCTION.....	1
II.	THEORY.....	2
	a. Assumptions.....	2
	b. Dispersion Relation.....	3
	c. Finite Slab Effects.....	5
III.	RESULTS.....	7
IV.	DISCUSSIONS.....	10
V.	OUTLOOK.....	14
	ACKNOWLEDGMENTS	15
	REFERENCES.....	28

ELECTROSTATIC ION-CYCLOTRON WAVES IN MAGNETOSPHERIC PLASMAS: NON-LOCAL ASPECTS

1. INTRODUCTION

The current driven ion-cyclotron instability (CDICI) has been of considerable interest to space plasma physicists. Recent observations by Kintner (1980) and Kintner et al. (1978) have made it very topical. Drummond and Rosenbluth (1962) were first to examine this instability analytically while Kindel and Kennel (1971) studied it in the context of space plasmas in the earth's magnetosphere. The results from Kindel and Kennel have frequently been applied to observations involving the electrostatic CDICI in space. It should be noted, however, that the analysis of both Drummond and Rosenbluth and Kindel and Kennel is a local analysis. They consider a uniform zeroth order magnetic field (i.e., $\underline{B} = B_0 \hat{z}$), thereby neglecting the self-consistent magnetic field generated by the field aligned currents. This magnetic field (usually small) will give rise to a shear in the zero order magnetic field (see Figure 1) and consequently make the zero order field space dependent (i.e., $\underline{B}(x) = B_0(x) \hat{y} + B_z \hat{z}$, where shear is in the x-direction).

In general, magnetic shear is a damping agent and can significantly alter the local mode structure (e.g., it was shown by Ross and Mahajan, (1978) that an infinitesimal shear can completely damp the universal drift instability). Recently Waltz and Dominguez (1981), motivated by the TFR (1978) tokamak experiment, have provided numerical results for the behavior of CDICI in a sheared magnetic field pertinent to the TFR (1978) parameters. Ganguli and Bakshi (1982) have given a detailed analytical treatment of the CDICI in a sheared magnetic field and have concluded that even a small shear can give a significant reduction in the growth rates. It also greatly reduces the region of unstable perpendicular wavelengths.

The above mentioned treatments of shear implicitly assume that a uniform shear prevails over a large enough region of space. A finite current channel size, of width L_c , may introduce important modifications when L_c becomes comparable to or smaller than the shear length L_s . Recently Bakshi, Ganguli and Palmadesso (1983) have developed the theory for the effects of shear on CDICI, taking into consideration the role played by a finite width current channel. The main result of that

Manuscript approved August 9, 1983.

investigation shows that the growth rate is given by the pure shear theory when $L_c > L_s$ and reverts to the local growth rate if $L_c \ll L_s$, with a smooth transition as a function of (L_c/L_s) . There is another non-local effect, due to the variation of the current profile across the slab, which leads to quenching of the instability if the slab width is reduced to only a few ion gyro radii.

In this paper we illustrate the importance of these non-local treatments of the CDICI for the space plasmas. We show that the non-local theory can, under certain circumstances, lead to enhanced coherence in the electrostatic CDICI.

II. THEORY

a. Assumptions

We consider a slab geometry where both the electrons and the ions have a Gaussian distribution function. The plasma has a negligible β ($\beta \equiv \frac{8\pi nkT}{B^2} \ll 1$), and the electrons drift with respect to the ions along the magnetic field with a velocity V_d . Both species have a finite non-zero temperature $T_\alpha = m_\alpha v_\alpha^2 / 2 k_B$, α denoting the species, m_α is the mass, v_α is the thermal velocity and k_B is the Boltzmann's constant. We neglect the term $(k\lambda_D)^2 \ll 1$ where k is the wavevector in arbitrary direction while λ_D is the Debye length. Since for most space plasmas of interest, the ion and electron temperatures are of the same order, we shall restrict the analysis here for the temperature ratio $\tau \equiv T_i/T_e = O(1)$. The ambient magnetic field is in the \hat{y} - \hat{z} plane and contains a shear in the \hat{x} -direction. Let us first consider a simple model for a sheared magnetic field, given by

$$\underline{B} = B_0 \{ \hat{z} - (x/L_s) \hat{y} \}, \quad (1)$$

with $x/L_s \ll 1$ and $L_s = (\partial\theta/\partial x)^{-1}$ where $\theta = \tan^{-1}(B_y/B_z)$. Thus L_s is the scale length characterizing the magnetic shear. In the absence of shear the field configuration is $\underline{B} = B_0 \hat{z}$.

In a shear free field the plasma is unstable to the CDICI when $\omega - k_{\parallel} V_0 < 0$ for ω and k_{\parallel} consistent with the dispersion relation. The waves at maximum growth (for $T_e = T_i$) are characterized by $\omega_r \sim \Omega_i$, $\Omega_i = eB_0/m_i c$, the ion Larmour frequency; $v \ll \omega_r$; and $k_{\perp} = 0(1)$ where $\rho_i = (2k_B T_i / m_i)^{1/2} / \Omega_i$, is the ion Larmour radius. Electron Landau and ion-cyclotron damping reduce the growth rate depending on the magnitude of k_{\parallel} (see Ganguli and Bakshi (1982)).

The above description of the plasma gets significantly modified by the introduction of a shear in the magnetic field as given in expression (1). The magnetic field rotates in the ϕ - z plane (see Figure 1) as a function of x . If at $x = 0$ we have $k_{\parallel} = 0$ then at $x = x_1$ we see that $k_{\parallel} \neq 0$ since at x_1 the magnetic field has rotated by an angle $\theta_1 = x_1 / L_s$. Thus the dispersive properties of the plasma are also a function of x . It is this effect which changes the boundary condition from plane waves to outgoing energy flux condition and which the local theory fails to account for, thereby giving incomplete results.

We introduce shear (i) locally, by replacing k_{\parallel} by $k_{\parallel}^0 + sk_y x$, where $s = 1/L_s$ and (ii) globally by replacing ik_x by " $\frac{\partial}{\partial x}$ ". Since the magnitude of the magnetic shear of interest to us is quite small, we neglect the orbital effects of shear [Bakshi, Bellew, Ganguli and Satyanarayana (1977), Bellew (1978), Ganguli (1980) and Linsker (1981)] arising mainly out of the shear kinematic drift of the particles in the sheared magnetic field.

b. Dispersion Relation

The general dispersion relation for CDICI in the absence of shear is given by

$$k^2 + \sum_{n,a} \frac{\Gamma_n(b_a)}{\lambda_a^2} \left[1 + \left(\frac{\omega - k_{\parallel} V_a}{|k_{\parallel}| v_a} \right) Z \left(\frac{\omega - n\Omega_a - k_{\parallel} V_a}{|k_{\parallel}| v_a} \right) \right] = 0, \quad (2)$$

where $b_a = k_{\perp}^2 \rho_a^2 / 2$, $\Gamma_n(b) = I_n(b) e^{-b}$ and $I_n(b)$ are modified Bessel's function.

As previously described we study the effects of the magnetic shear by replacing k_{\parallel} by $k_{\parallel} u$, where $u = sx (\equiv k_{\parallel}(x)/k_y)$ and ik_x by $\frac{\partial}{\partial x}$ in equation (2) (we have assumed $k_{\parallel}^0 = 0$). Transforming to the ion frame (i.e., setting $V_{di} = 0$), retaining the $n = 0$ term for the electrons and $n = 0, \pm 1, \pm 2$

terms for the ions (since we wish to study the first harmonic only) and expanding $\Gamma_n(b - (\rho_i^2/2)\partial^2/\partial x^2)$ to $O(\partial^2/\partial x^2)$ (here $b = k_y^2 \rho_i^2/2$), we obtain a second order differential equation for the electrostatic potential $\phi(x)$,

$$\{-A(x) \frac{\partial^2}{\partial x^2} + Q_1(x)\} \phi(x) = 0. \quad (3)$$

The equation can be reduced to (see Ganguli and Bakshi (1982)),

$$\{(\rho_i s)^2 \frac{\partial^2}{\partial u^2} + Q(u)\} \phi(u) = 0, \quad (4)$$

where,

$$Q(u) = - \frac{Q_1(u)}{\hat{A}(u)},$$

$$\begin{aligned} Q_1(u) = & 1 + \tau + \tau_1 \Gamma_0 Z(\zeta_1) + \tau_1 \Gamma_1 \{Z((1-p)\zeta_1) + Z((1+p)\zeta_1)\} \\ & + \tau_1 \Gamma_2 \{Z((1-2p)\zeta_1) + Z((1+2p)\zeta_1)\} \\ & - \tau \tau_e \left(1 - \frac{k_y v_d}{\omega}\right) Z(\zeta_e) \left(1 - \frac{k_y v_d}{\omega}\right), \end{aligned}$$

$$\begin{aligned} \hat{A}(u) = & \left(\frac{\tau_1}{\tau}\right) \{Z(\zeta_1) \Gamma'_0 + \{Z((1-p)\zeta_1) + Z((1+p)\zeta_1)\} \Gamma'_1 \\ & + \{Z((1-2p)\zeta_1) + Z((1+2p)\zeta_1)\} \Gamma'_2\}, \end{aligned}$$

and

$$\Gamma'_n = \frac{\partial \Gamma_n}{\partial b}.$$

We have assumed $k_x^2 \ll k_y^2$ in neglecting higher order derivatives in the expansion of Γ_n .

As shown in Ganguli and Bakshi (1982) we expand the "potential", $Q(u)$ of the differential equation (4) around $\xi = (u - u_0) = 0$ to $O(\xi^2)$. Here u_0 is the angle of propagation for the maximum growth rate in the absence of shear. We thus obtain,

$$\{(\rho_i s)^2 \frac{\partial^2}{\partial \eta^2} + a + \frac{Q_0''}{2} \eta^2\} \phi(\eta) = 0, \quad (5)$$

where,

$$\tau = \xi + Q_0'/Q_0'',$$

$$z = Q_0 - Q_0' 2/2Q_0'',$$

and

$$Q_0 = Q(u_0), \quad Q_0' = \frac{d}{du} Q(u)|_{u=u_0}, \quad Q_0'' = \frac{d^2}{du^2} Q(u)|_{u=u_0}.$$

The dispersion relation under the outgoing energy flux boundary condition similar to Pearlstein and Berk (1969), is

$$Q(\omega, u_0) = (2k+1)(\rho_1 s)(-Q_0''/2)^{1/2} + Q_0' 2/2Q_0''. \quad (6)$$

Note $Q(\omega, u_0) = 0$ yields the local dispersion relation maximized over k_{\perp} , while the right hand side of the equation (6) arises from of the non-local treatment. The first term in the right hand side is proportional to the magnetic shear and vanishes in the zero shear limit. The second term, is not explicitly shear dependent. This term can contribute significantly even for infinitesimal shear thereby making the non-local dispersion relation solutions much different from those of the local dispersion relation.

c. Finite Slab Effects.

We have given elsewhere (Bakshi, Ganguli and Palmadesso, 1983) the details of the modifications brought about by the finite slab size L_c . A finite width current is introduced by taking the electron distribution function to be a shifted Maxwellian with a drift velocity parallel to the magnetic field given by

$$V_d(x) = V_d^0 g(x_g/L_c),$$

$$g(\xi) = e^{-\xi^2}, \quad x_g = x + \frac{V_y}{\Omega_e}. \quad (7)$$

If we ignore the very small effects of order ρ_e^2/L_c^2 , where ρ_e is the electron gyro-radius, the current profile is found to be

$$j(x) = n_0 e V_d^0 g(\xi), \quad \xi \equiv \frac{x}{L_c}. \quad (8)$$

Such a current profile generates a self-consistent shear in the magnetic field, given by

$$\frac{B_y(x)}{B_z} = \frac{L_c}{L_s} \int_0^{\xi} g(\xi) d\xi, \quad (9)$$

where the shear length is defined by

$$\frac{1}{s} = L_s = \frac{c B_z}{4\pi n_0 e V_d^0}. \quad (10)$$

The corresponding variation in the parallel wavenumber,

$$k_{\parallel}(x) = k_{\parallel}^0 + k_y B_y(x)/B_z, \quad (11)$$

leads to the variation in the angle of propagation

$$u(x) = \frac{k_{\parallel}(x)}{k_y} = u_0 + \frac{L_c}{L_s} \int_0^{\xi} g(\xi) d\xi. \quad (12)$$

Thus the relation between the angle u and the physical distance x , or the scaled physical distance ξ is no longer linear. The non-local effects are again described by the differential equation obtained by letting $k_x \rightarrow (1/i)d/dx$, and $k_{\parallel} \rightarrow k_{\parallel}(x)$ as given by eq. (11) and $V_d \rightarrow V_d(x)$ as implied by eq. (8),

$$\left[\rho_1^2 \frac{d^2}{dx^2} + Q(u(x), V_d(x)) \right] \phi = 0 \quad (13a)$$

or

$$\left[\left(\frac{\rho_1}{L_c} \right)^2 \frac{d^2}{d\xi^2} + Q(u, V_d) \right] \phi = 0, \quad (13b)$$

with Q defined as in (4) apart from the x -dependence as stated above. Expanding Q around ξ_1 , where

$$Q'(\omega, \xi_1) = 0, \quad (14)$$

provides more accurate results as compared to expansion around ξ_0 or u_0 as in eq. (5), and the dispersion relation which generalizes eq. (6) is given by

$$Q(\omega, \xi_1) = (2\lambda + 1)(\rho_1/L_c) \left[-\frac{1}{2} Q''(\omega, \xi_1) \right]^{1/2}. \quad (15)$$

The eigenfrequency obtained from (15) depends on k_1^0 , which is as yet undetermined. The dominant mode, for a given k_y , is obtained by maximizing $\gamma = \text{Im}\omega(k_1^0)$ over k_1^0 .

III. RESULTS

We now discuss the implications of the non-local treatments of the preceding section. The results of the uniform shear model are contained in eq. (6), while the finite slab effects are given by eq. (15). Both these are generalizations of the local dispersion relation $Q(\omega, u_0) = 0$.

The non-local dispersion relation (6) is solved numerically by an iterative technique. We simplify the "potential" by expanding all the ion Z-functions except $n=1$ for large arguments, retain terms to $O(1/\xi_1^2)$ and treat $A(u)$ as a constant evaluated at u_0 . [For details see Ganguli and Bakshi (1982)].

Figure 2 shows a plot of γ/Ω_1 against b for various values of the shear and $\tau = 0.5$, $\mu = 1837$, $V_d/v_e = 0.25$. Note the difference between the local solution and the zero shear limit of the non-local solution. This large reduction in the growth rate is due to the second term in equation (6) arising from the non-local treatment. Figure 2 also shows that the value of b for which maximum growth occurs remains essentially unaltered from the local theory, even when shear is increased. In addition to the expected reduction of the maximum growth rate, the primary effect of increased shear is to narrow the band of unstable perpendicular wavelengths. The uneven spacing of the $\rho_1 s = 0$, 0.005 and 0.01 curves shows that non-linearity in the shear parameter (through the implicit dependence of ω on $(\rho_1 s)$) already sets in at $\rho_1 s = 0.01$.

In Figures 3 and 4 we provide additional γ/Ω_i versus b plots for typical space plasma parameters. In Figure 3 we consider a hydrogen plasma: $\mu = 1837$, $\tau = 0.75$, $V_d/V_e = 0.3$ and $\rho_i/s = 10^{-6}$. Note once again the big drop in the local growth rate as well as the significant reduction of the unstable perpendicular wavevector band. Figure 4 illustrates the same features for $\tau = 1$, $V_d/V_e = 0.35$ and the other parameters unchanged. The consequence of the non-local treatment is even more drastic in this case. The non-local treatment leads to a completely damped instability.

The drastic changes due to non-local effects stem from the implicit assumption that the driving current prevails over a sufficiently wide region in the x -direction so that k_{\parallel}/k_{\perp} can become arbitrarily large. This condition will not be met in many space plasma situations, and we need the results of the finite slab theory (Bakshi, Ganguli, and Palmadesso, 1983), which led to eq. (15).

Consideration of a finite width current sheet leads to two scale lengths, L_s and L_c , which govern the growth rate. Figure 5 shows the variation in (γ/Ω_i) vs. (L_c/ρ_i) for $\tau = 0.5$, $V_d^0/V_e = 0.28$, $\mu = 1837$ and $b = 0.6$, for three different shear parameters $(\rho_i/L_s) = 10^{-4}$, 10^{-5} and 10^{-6} . In each case the growth rate has the significantly reduced value, characteristic of the uniform shear model, if L_c is taken to be sufficiently large. As the slab width is decreased, the growth rate increases and climbs up to the local value when L_c is sufficiently small. Thus, there is a smooth transition from the pure shear reduced γ to the usual local γ .

The three curves in Figure 5 appear very similar, except for a relative displacement, and the essential universality of the transition curve (for small shears) can be brought out by plotting γ vs. (L_c/L_s) as in Figure 6. The shear reduced γ prevails for $L_c \gg L_s$, and the three curves continue to overlap for $L_c > (L_s/20)$. The curve describing the weakest shear $\rho_i/L_s = 10^{-6}$ almost attains the local value when $L_c = 10^{-2} L_s$. The physical reason for this transition to the local value is easily seen: the detuning or misalignment of the magnetic field lines across the length of the slab of order L_c here happens to be too small to have any impact on the instability. On the other hand, when $L_c \gg L_s$, enough misalignment occurs to produce local regions where the angle between the fixed wave direction

\bar{E} and the varying $\bar{E}(x)$ is sufficiently different from the optimal value (typically $k_1^0/k_{\perp} \sim 1/10$) to produce a much lower average growth rate.

An additional non-local effect, directly due to the variable current profile (and not the shear) is also evident in Figures 5 and 6. After attaining the local growth rate, if the slab size is further reduced, the growth rate again becomes smaller than the local value for $L_c/\rho_i < 10^2$. It is clear from Figure 5 that this effect is not sensitive to the value of the shear (at least in the range considered). The physical explanation for this reduction is also easily seen. The spatial variation of the current has a direct effect on the wave packet ϕ . The reduction of the current away from the center of the slab results in a reduced drive and a corresponding reduced γ . If L_c/ρ_i is further reduced to 10 or lower, a significant reduction γ occurs, with eventual quenching.

A typical potential function ϕ is displayed in Figure 7, with $V_{d2}/V_e = 0.28$, $\tau = 0.5$, $l = 1837$, $b = 0.6$, $L_s/\rho_i = 10^2$ and $L_c/\rho_i = \infty$. The independent variable u is the physical angle $u = x/L_s$, the origin of x is at the position where the field line is perpendicular to the given \bar{E} . As shown, $|\phi|$ is significant between 0.06 and 0.12 with a peak around $u_{mo} = 0.09$. This indicates that the wave propagates in the direction given by $k_1^0 \sim (0.09)k_{\perp}$.

Besides the changes in growth rate, the non-local theory also predicts a transition in the angular position of the peak of $|\phi|$, or in the effective angle u_{mo} between the direction normal to the local field line and the direction of the propagating wave. This is displayed in Figure 8, for the same parameters as in Figure 6, over a wide range of (L_c/L_s) . Note the transition from $u_{mo} = 0.13$ characteristic of local theory to the reduced $u_{mo} = 0.09$ of the pure shear dominated limit. The non-local effects thus reduce the effective angle k_1^0/k_{\perp} .

Figure 9 shows the variation of γ as a function of wavenumber. The local theory result prevails for weak shear and $L_c/L_s \lesssim 10^{-2}$, the pure shear dominated reduction occurs for $L_c \gtrsim L_s$ with a smooth transition in between. The $L_c = L_s$ curves, except for a slight change of parameters, correspond to the $\rho_{i1} = 0$ and $\rho_{i1} = 0.01$ curves of Figure 2.

We have also examined the CDICI in an oxygen plasma and note that the current thresholds are generally much lower compared with those of a

hydrogen plasma. The effect of the non-local treatment for a multispecies plasma is an interesting question which is now being investigated and will be reported elsewhere.

IV. DISCUSSION

There are several implications of the non-local effects discussed above. If the shear is small, we have shown that there are three different regimes depending on the scale size of the current channel, L_c :

(1) For $L_c > (L_s/10)$ there occurs, as compared to the results of the local theory, (a) a reduction in the growth rate, (b) a reduction in the bandwidth of k_{\perp} over which the instability prevails and (c) a reduction in the angle of propagation $u_{m0} = k_{\perp}^0/k_{\perp}$. This is the shear dominant regime.

(2) For $\rho_i \ll L_c \ll L_s$, one recovers the results of the local theory (except for one important aspect, which we discuss later in this section).

(3) For $L_c \gtrsim \rho_i$, again (a) there is a reduction in the growth rate, and (b) a reduction in the bandwidth of k_{\perp} over which the instability prevails, but (c) there is no reduction in u_{m0} , as compared to the results of the local theory. The instability is quenched for $L_c \lesssim 2\rho_i$.

Thus we have shown that local theory cannot be applied without reservations; one must first scrutinize the scale lengths for the given laboratory experiment, or the space plasma of interest, to ascertain which regime is relevant. In some situations, (e.g., the case $L_s = 10^3 \rho_i$ of Figure 6), the conditions for regime (2) cannot be strictly satisfied for any value of L_c , and the results of the local theory are not applicable. This aspect is accentuated as the shear increases.

In space plasmas, typical shear lengths are $L_s \sim$ few hundred km, and $\rho_i/L_s \sim 10^{-6}$. Thus the smaller sized (~ 1 km) auroral arcs would not qualify for regime (1). The quiet time, broader Birkeland current Region 1/Region 2 systems may be more appropriate for these effects. Also, since the current sheet width increases with altitude, the effects of regime (1) have a better chance of being significant at higher altitudes.

The transition from the shear-affected regime (1) to the local theory results of regime (2) was shown (Figure 6) to depend on L_c/L_s , essentially described by a universal curve independent of shear. The net change in the growth rate and the range of (L_c/L_s) over which the transition takes place will be governed by the physical parameters μ , τ and V_d/v_e , and the perpendicular wavenumber k_\perp . Under what conditions can we expect the effects of shear to be significant?

One can assess these trends by plotting the local growth rate as a function of the angle k_\perp/k_\parallel . As an illustration, we note that Figure 1 of Ganguli and Bakshi (1982) displays the effect of varying τ . It shows that the angular band over which the instability can occur becomes narrower as τ increases. The transition from regime (1) to regime (2) can be expected to occur when L_c/L_s , which represents the tilt produced by shear, becomes comparable to this angular bandwidth. Thus one can infer that for a given L_c , increasing τ will favor regime (1), making the shear more effective.

We can test this quantitatively by evaluating the growth rate as a function of L_c/L_s for two different values of τ . Figure 1 of Ganguli and Bakshi (1982) was for a fixed $b = 0.5$. Since the perpendicular wavenumber (or equivalently b) is a free parameter, one must maximize the growth rate over b as well. We have carried out these calculations for $V_d/v_e = 0.4$, $\mu = 1837$, $\tau = 0.5$ and 1 , and the results are displayed in Figures 10 and 11. The imaginary part of Q_1 ($\equiv Q_{1I}$), eq. (4), is plotted against $u = k_\perp/k_\parallel$ in Figure 10, with $b = 0.6$, $\omega_0 = 1.3037$ for $\tau = 0.5$ and $b = 0.9$, $\omega_0 = 1.2027$ for $\tau = 1$. The angular width of the domain where Q_{1I} is negative, indicative of instability, is clearly much smaller for $\tau = 1$.

The corresponding results for the growth rate as a function of (L_c/L_s) are displayed in Figure 11. The growth rate for each τ is normalized to the corresponding local growth rate γ_L . Noticeable departure from the local value begins at $(L_c/L_s) = 0.01$ for $\tau = 1$ and at 0.02 for $\tau = 0.5$, and proceeds much faster for the larger τ as L_c/L_s is increased. Thus the effects of shear are more significant for the larger τ , given a fixed current channel width.

Figure 1 of Ganguli and Bakshi (1982) also shows that the angular band width of the domain of instability increases with increasing V_d/v_e . But an increase in V_d also strengthens the shear, thereby increasing L_c/L_s . Near the threshold drift velocity, (where the system is marginally stable), the increase in angular band width proceeds faster than the increase in L_c/L_s ; thus an increase in V_d favors a move towards the local regime (2). On the other hand, if V_d is significantly larger than the threshold for marginal stability, the situation is reversed and an increase in V_d favors a move towards the shear dominated regime (1).

So far, we have only discussed the mode near the cyclotron frequency, $\omega \gtrsim \omega_{ci}$. What can we expect for the higher harmonic modes? The definition of Q_1 in eq. (4) must first be modified to include higher n terms from the full dispersion relation, eq. (2). We have evaluated Q_1 including terms up to $n = \pm 4$ and maximized over b to obtain optimal local growth rates. The results for Q_{1I} vs. u are displayed in Figure 12 for the first three cyclotron harmonics, with real frequencies $\omega_0 = 1.1897$, $b = 0.9$; $\omega_0 = 2.2237$, $b = 2.4$; $\omega_0 = 3.2499$, $b = 4.8$; and physical parameters $\tau = 1$, $\mu = 1837$, $V_d/v_e = 0.65$. The angular band width of the unstable zone ($Q_{1I} < 0$) becomes significantly smaller for higher harmonics. Thus the transition to the shear dominated regime (1) can be expected to occur for the higher harmonics for progressively smaller values of L_c/L_s .

These considerations show that the results of the local theory, regime (2), cannot be used without reservations, and a transition towards regime (1) is helped by increasing τ , considering higher harmonics, and increasing the drift velocities. It is also accentuated by increasing the current channel width, directly by considering wider channels or for the same current sheet, by scaling with altitude. A detailed numerical study of all of these effects over a wide range of parameters is beyond the scope of this work and will be given elsewhere. We anticipate that some of the situations of practical interest in space plasmas will fall in regime (2) while others will favor a move towards regime (1).

There is a subtler effect, implicit in the non-local treatment, which may be more widely relevant. Once any inhomogeneity is introduced in the x -direction, the symmetry in the x - y plane is broken, and one has to distinguish between the propagation along \hat{y} and the propagation (if any)

along \hat{x} . The same inhomogeneity precludes the use of Fourier transforms in the x-direction and the plane wave solutions $e^{ik_x x}$ are necessarily replaced by a wave packet, $\psi(x)$, which is localized (e.g., see Fig. 7) in the x-direction. Since the current systems have the structure of a sheet, the short direction becomes the slab direction and the waves propagate along \hat{y} and \hat{z} with wave vector components (k_y, k_z) , $k_y \gg k_z$.

Now let us consider the implications of this phenomenon concerning satellite measurements of ion cyclotron waves. A moving observer will see a Doppler shifted frequency

$$\omega' = \omega + \mathbf{k} \cdot \mathbf{v}_s$$

where \mathbf{v}_s is the velocity vector of the observer (satellite) and \mathbf{k} is the wave vector. Since \mathbf{k} has no component along x (the wave packet is localized), it follows that a satellite moving perpendicular to the current sheet (i.e., along our \hat{x} direction) will not see any Doppler-shift, irrespective of the size of k_y . Such a statement could not be made in the purely local theory, since there would be no essential difference between the two transverse directions \hat{x} and \hat{y} , and waves are as likely to be moving in any direction in the x - y plane. In a local theory, a wide range of Doppler shifts would be produced, from $-k_{\perp} v_s$ to $+k_{\perp} v_s$, since the maximum value of k_x is k_{\perp} . Some of the observations on S3-3 indicate no or little Doppler shift. While other explanations may be available, this inference from our non-local treatment must also be considered, since an inhomogeneous plasma mandates a non-local treatment. Thus, the extremely high degree of coherence of many of the observations can be understood in a very simple way. This idea can be further tested by analyzing satellite data from an orbit which crosses the current sheet at a significantly different angle.

Various phenomena described above would lead to an enhanced coherence for the observed ion cyclotron waves as seen by a moving observer. When conditions for regime (1) prevail, there is a significant reduction in the band of perpendicular wave numbers for which the instability can occur. This reduces the magnitude of the Doppler shift $\mathbf{k} \cdot \mathbf{v}_s$ as compared to the local theory for any direction of the satellite motion. On the other hand,

the directional preference for \vec{k}_\perp , required by the inhomogeneity for all regimes, shows that satellites moving perpendicular to the current sheet would see very coherent ion cyclotron waves, with no Doppler shift, irrespective of the size of \vec{k}_\perp . A study of all available observational information for various transit angles of the satellite motion could be very instructive.

V. OUTLOOK

In this paper, we have analyzed the implications of a non-local treatment of the CDICI, which is necessitated by the introduction of an inhomogeneous current profile. One cannot yet provide a detailed comparison between theory and observations; that would require additional work on the theoretical side and more detailed data from the observational side. New data from the Dynamic Explorer would be very helpful in this context.

But even without carrying out the additional theoretical studies, or awaiting the new observational data, a number of interesting questions have been raised in this paper, and it would be very helpful to look at all available data from a different angle, in terms of the framework of this paper.

The model of inhomogeneity of the current employed here was one-dimensional. Further generalizations of theory are needed if the current sheets are of limited extent in both transverse directions. Even within a one-dimensional model, there could be a sub-structure on a shorter distance scale, or even a random or stochastic current structure superposed on the underlying smooth current profile. These aspects also would require further generalizations. Thus it would be very valuable to learn from the present and future observations the detailed nature of the current distributions.

It is equally important to classify all the available observations on the ion cyclotron waves according to the satellite transit direction and study its correlations, if any, to the peak frequency and the width of the observed power spectrum.

Further improvements in understanding the CDIC can come in a number of other ways as well. Additional generalizations of theory should include variation (i.e., inhomogeneities) along the field lines. In terms of applications of the theory of the present level one should certainly consider multi-species plasmas, wider ranges of the ion to electron temperature ratio τ , wider ranges of the driving current V_d^0/v_e , and effects on higher harmonics. In terms of interpretation the results can be recast in terms of the convective growth rate approach (Ashour-Abdalla and Thorne, 1978), which takes into account the small group velocity of the ion cyclotron waves. These and other related topics are under further investigation.

We also note that Hwang, Fontheim and Ong (1983) have recently considered the effects on electrostatic waves of a cold electron current sheet of finite thickness, and concluded that the current sheet partially stabilizes the system and contributes to the coherence of the excited waves. Since they did not consider the effects of magnetic shear, the correspondence is with our regime (3), where the non-local effects stem directly from the finite width of the current channel. Even in this regime their approach is restricted to $\rho_i \ll L_c$. Also their assumption of a sharp change in the current at the boundaries is not pertinent to the space plasmas. We also note that they have concentrated more on the ion-acoustic wave, and have no thermal spreads, but some of their conclusions are similar to ours.

ACKNOWLEDGMENTS

We would like to thank Dr. Joel Fedder of the Naval Research Laboratory for numerous useful comments. We also wish to thank Dr. M. Temerin and Dr. D. Winningham for very helpful discussions regarding space plasma observational data and procedures, past and present. This work was supported by the Office of the Naval Research and the National Aeronautics and Space Administration.

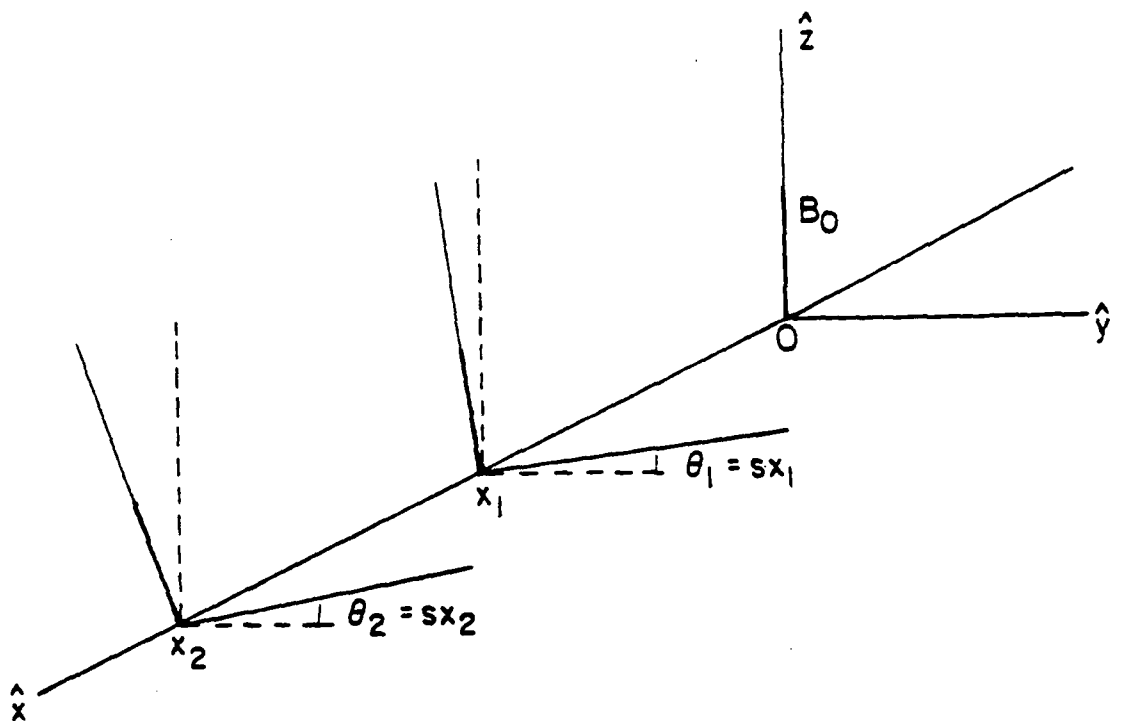


Figure 1. A sketch of a sheared magnetic field. At $x = 0$ the magnetic field B_0 is in the z -direction. At $x = x_1$ the magnetic field rotates by an angle $\theta_1 = s x_1$, where $s = 1/L_s$. A wave perpendicular to the magnetic field B_0 at $x = 0$ is no longer so at $x = x_1$.

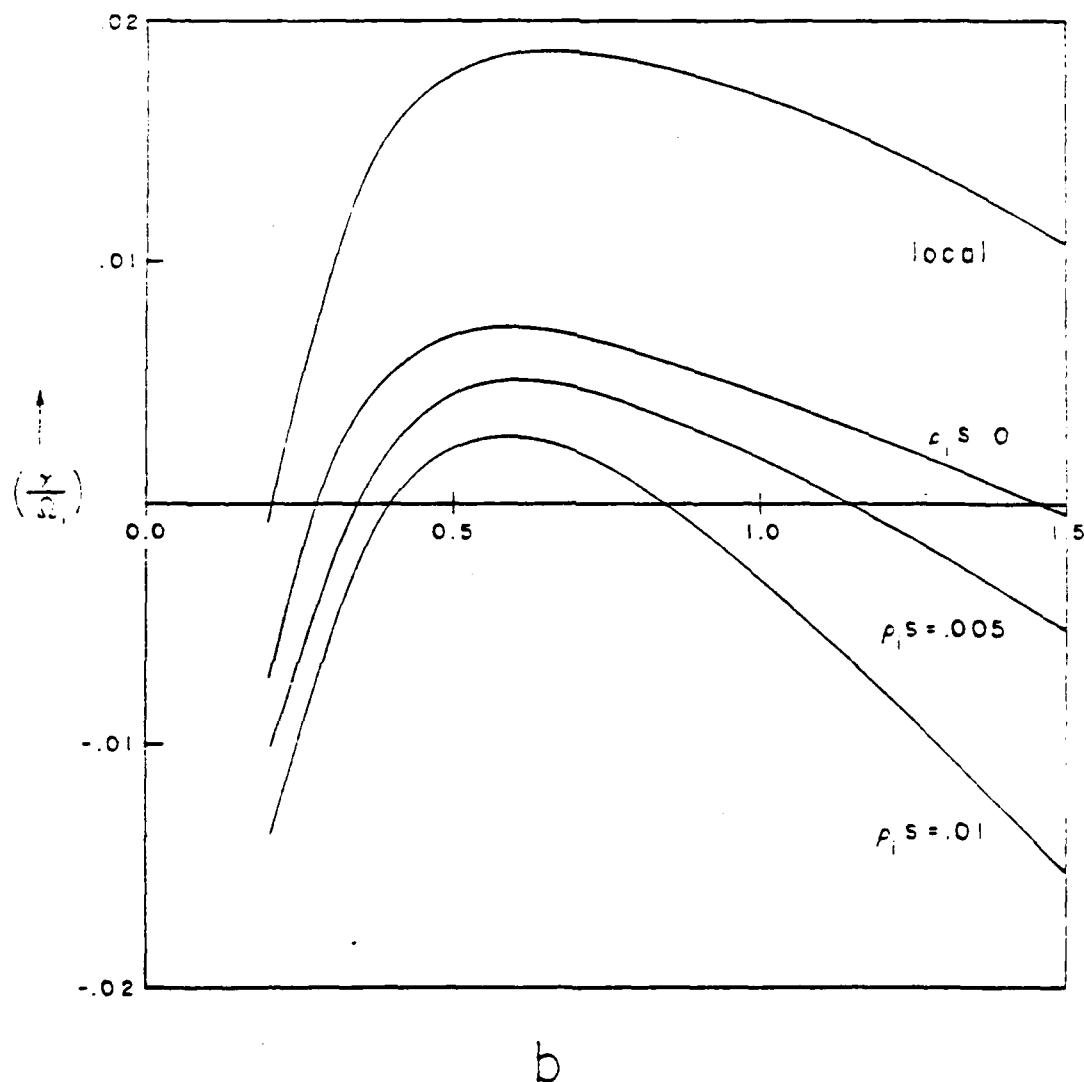


Figure 2. A plot of the growth rate (γ/ω_i) against b for various shear values. Here $\tau = 0.5$, $\mu = 1837$, and $V_2/V_e = 0.25$. The big difference between the local solution and the $(\rho_i s) = 0$ limit of the non-local solution is due to a shear independent term arising from the non-local treatment. The curves also indicate that the effect of the shear is more pronounced for larger b .

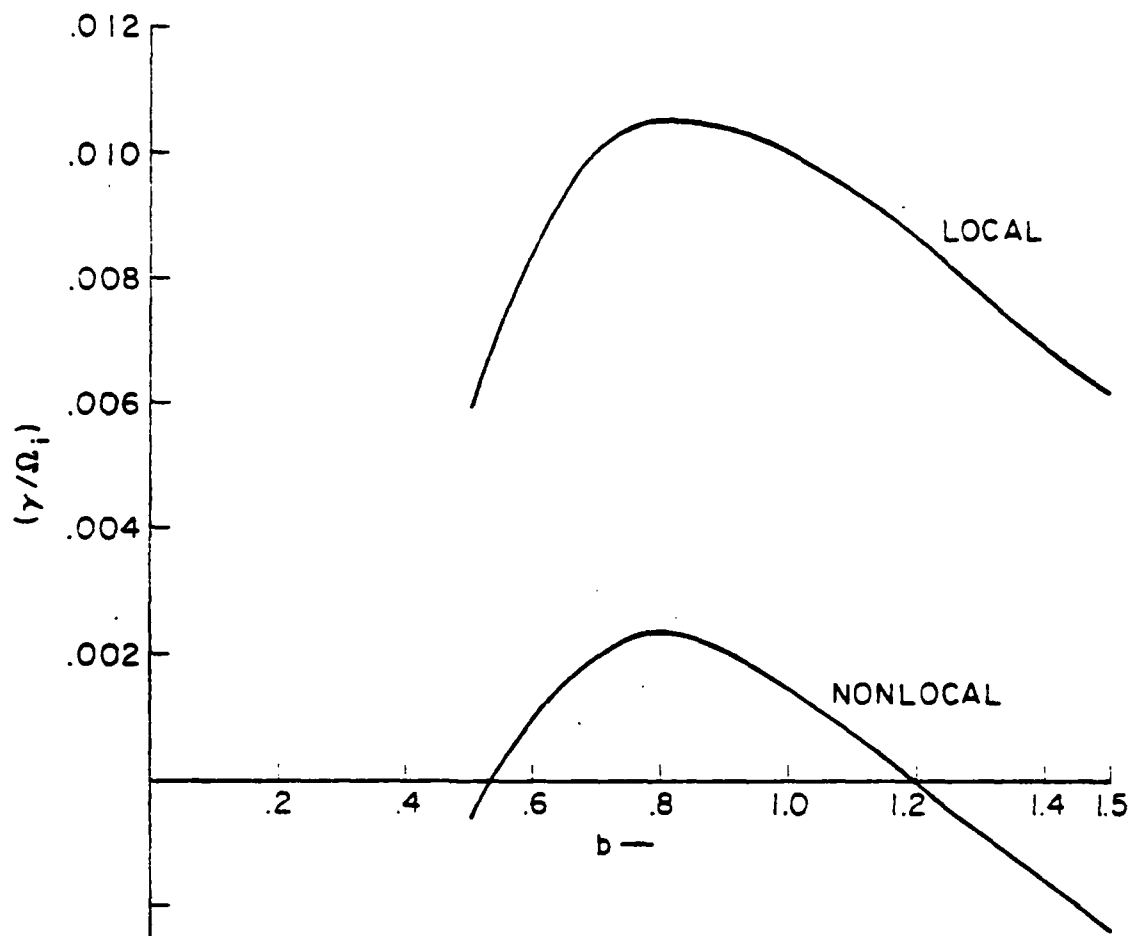


Figure 3. A plot similar to Figure 2. Here $\tau = 0.75$, $\mu = 1837$ and $V_d/v_e = 0.3$. We provide only the local and the non-local spectrum. The non-local curve has a very small shear, $(\rho_1 s) = 10^{-6}$. Note the significant reduction in the unstable perpendicular wavevector band.

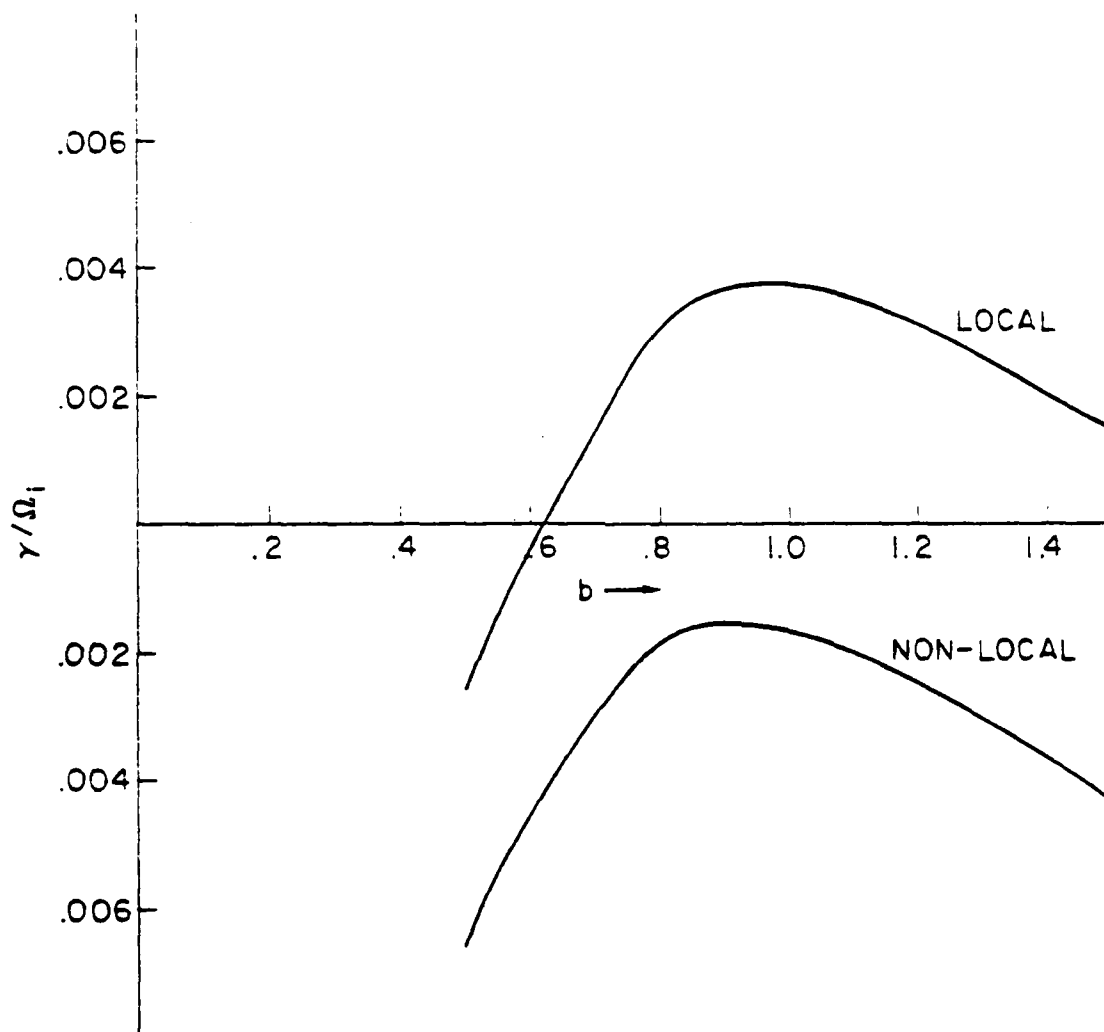


Figure 4. Growth rate versus b plot for $L = 1837$, and $V_0/v_e = 0.35$. The effect of the non-local treatment is very drastic in this case. The instability is totally suppressed.

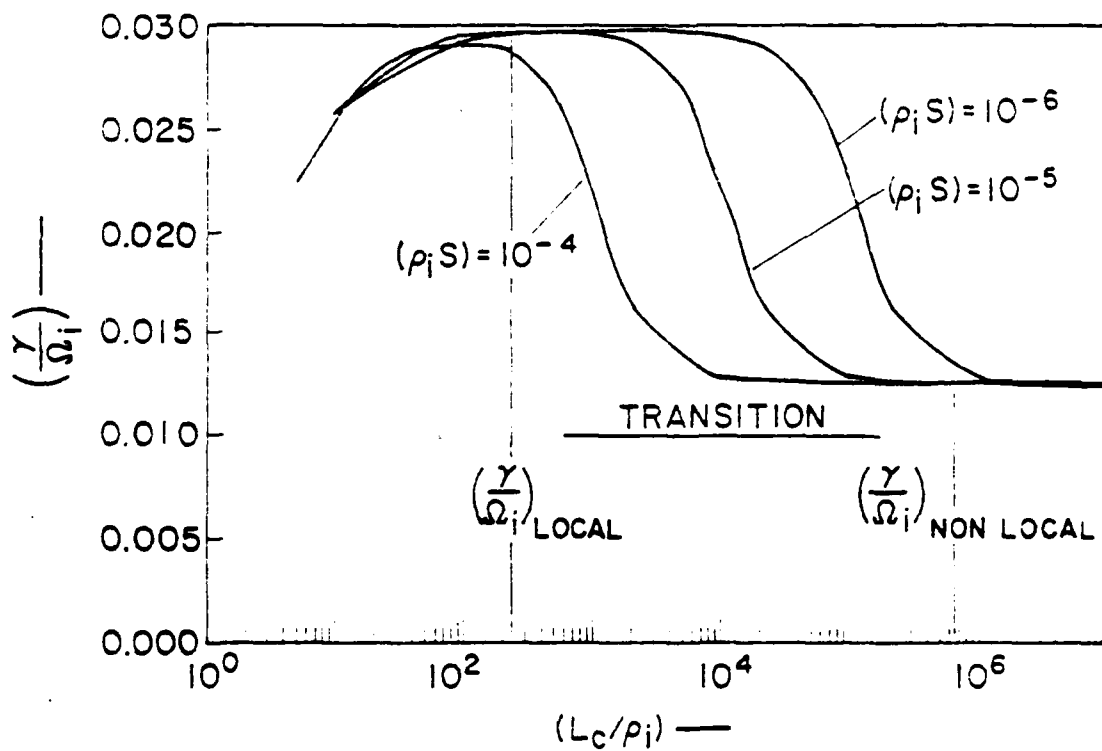


Figure 5. A plot of the growth rate $\left(\frac{\gamma}{\Omega_i}\right)$ against the current channel width (L_c/ρ_i) for three different magnetic shear lengths. Here $v_d^0 = 0.28 v_e$, $\nu = 1837$, $b = 0.6$, and $\tau = 0.5$.

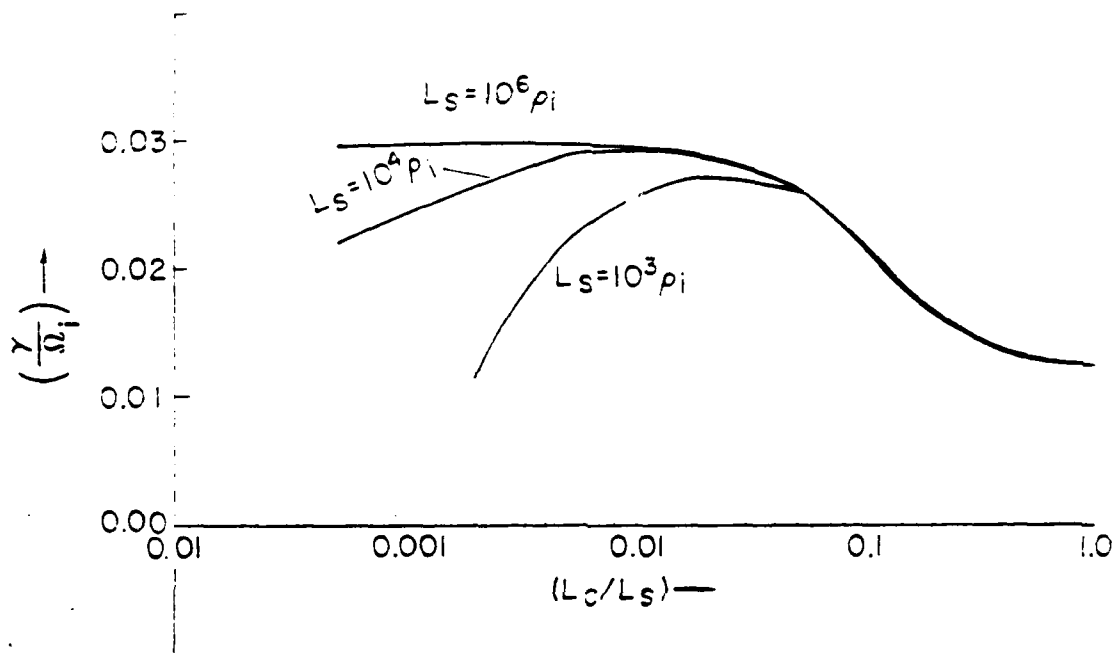


Figure 6. A plot of $\gamma(\frac{\tau}{\sigma_1})$ against L_c/L_s for three different L_s values. Here $b = 0.6$, $\nu = 1837$, $\tau = 0.5$, and $v_c^0 = 0.28 v_e$. The transition from local to the nonlocal results are universal, almost independent of the shear value.

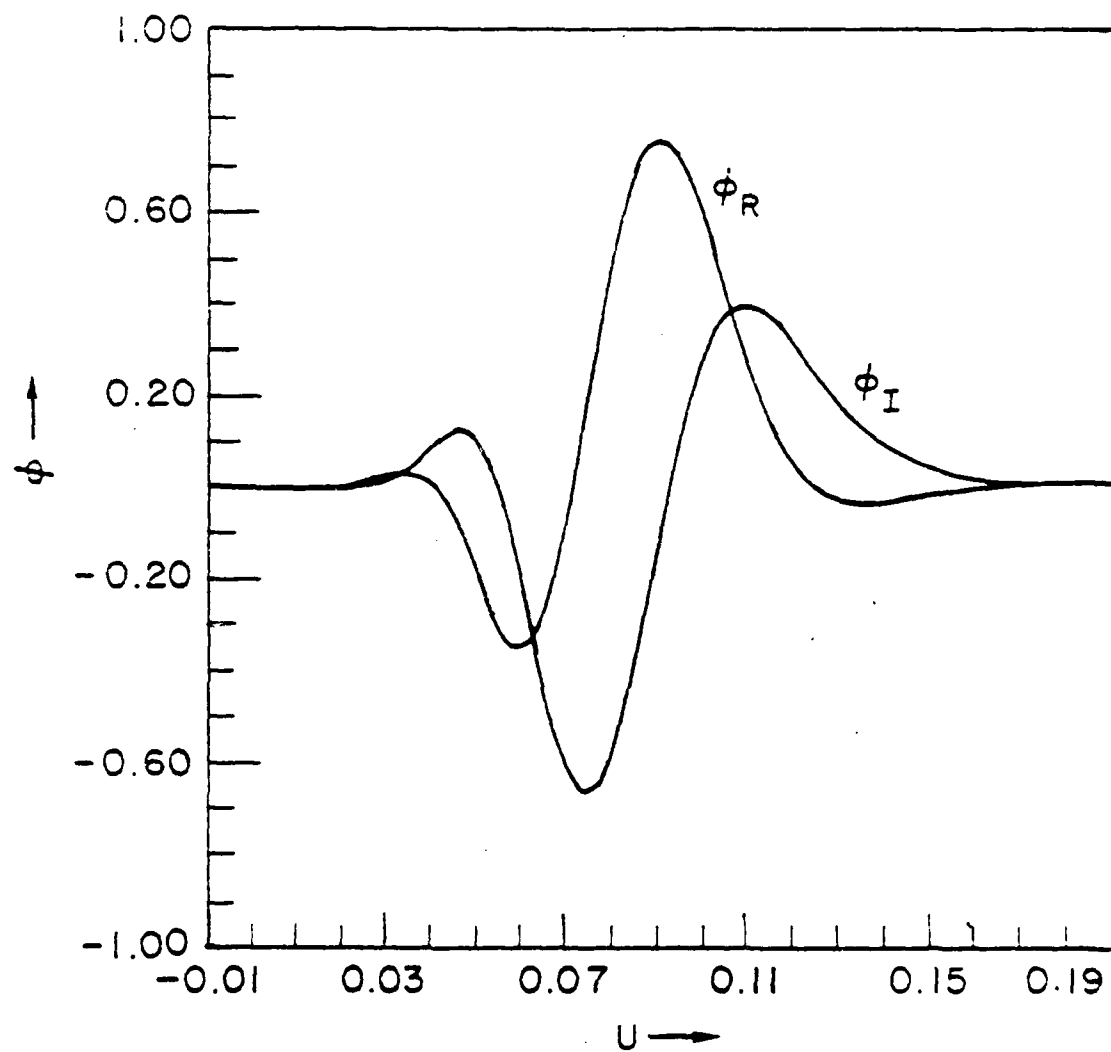


Figure 7. A plot of $\phi(u)$ against u for $L_c/\rho_1 = \infty$, and $(\rho_1 s) = 10^{-2}$, $b = 0.6$, $v_c^0 = 0.28 v_e$, and $\tau = 0.5$.

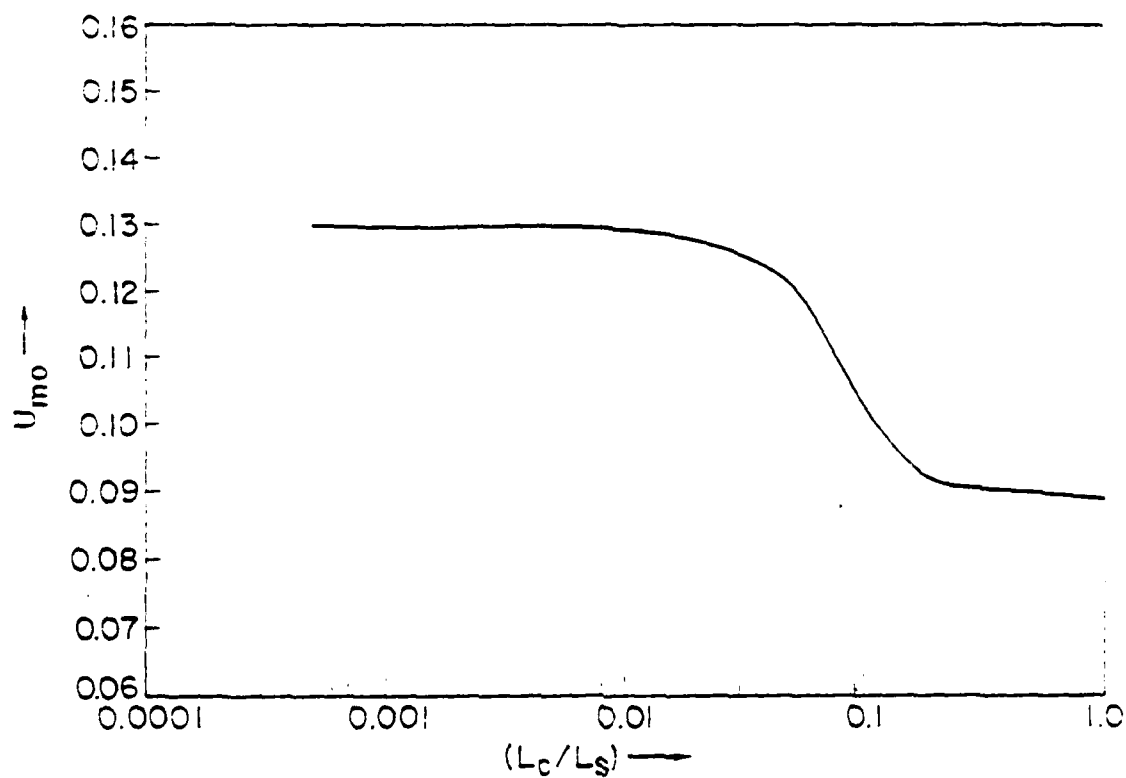


Figure 8. A plot for the real angle U_{m0} where $|\phi(u)|$ attains its maximum, against L_c/L_s . The physical parameters are same as in Figure 6.

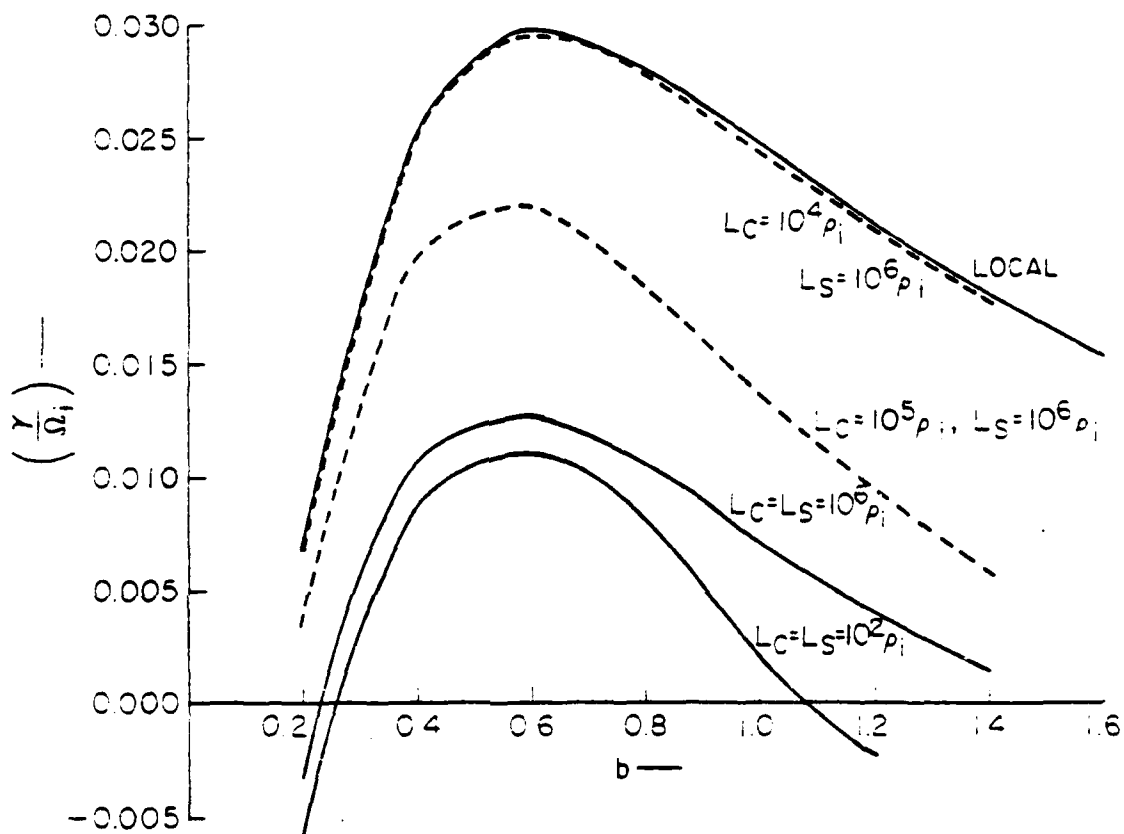


Figure 9. A plot of the growth rates against b . Here $\tau = 0.5$, $\mu = 1837$, $v_d^0 = 0.28 v_e$. The dotted lines show the transition from local to nonlocal values as L_C approaches L_S . The lowest solid line is for $L_C = L_S = 10^2 \rho_i$.

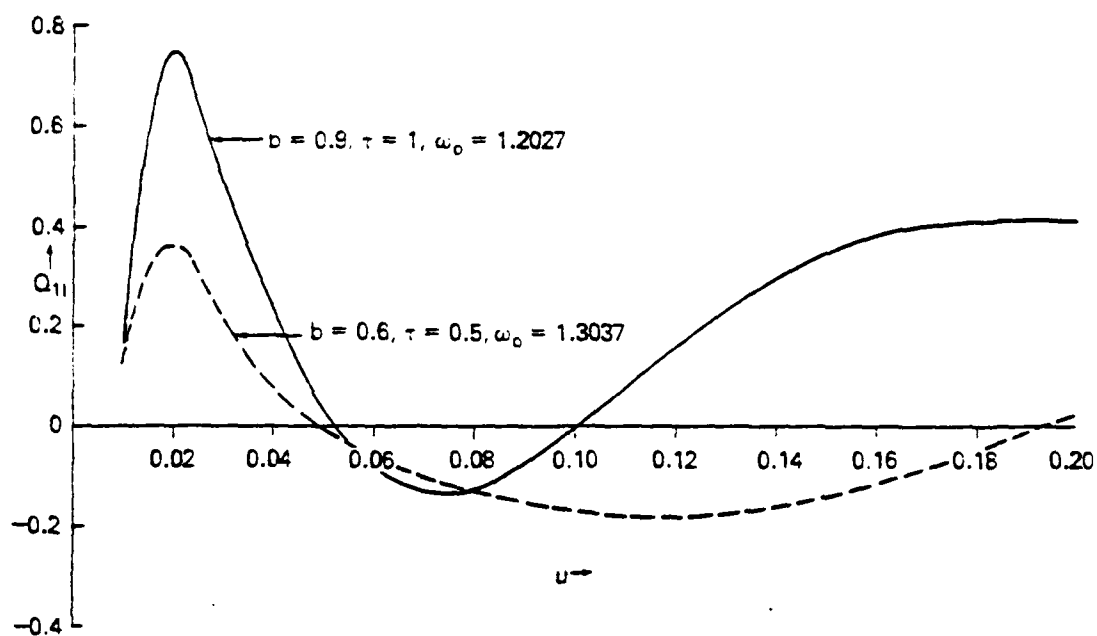


Figure 10. A plot of Q_{II} vs. u for $\tau = 0.5$ and 1, maximized over b to attain maximal growth rates.

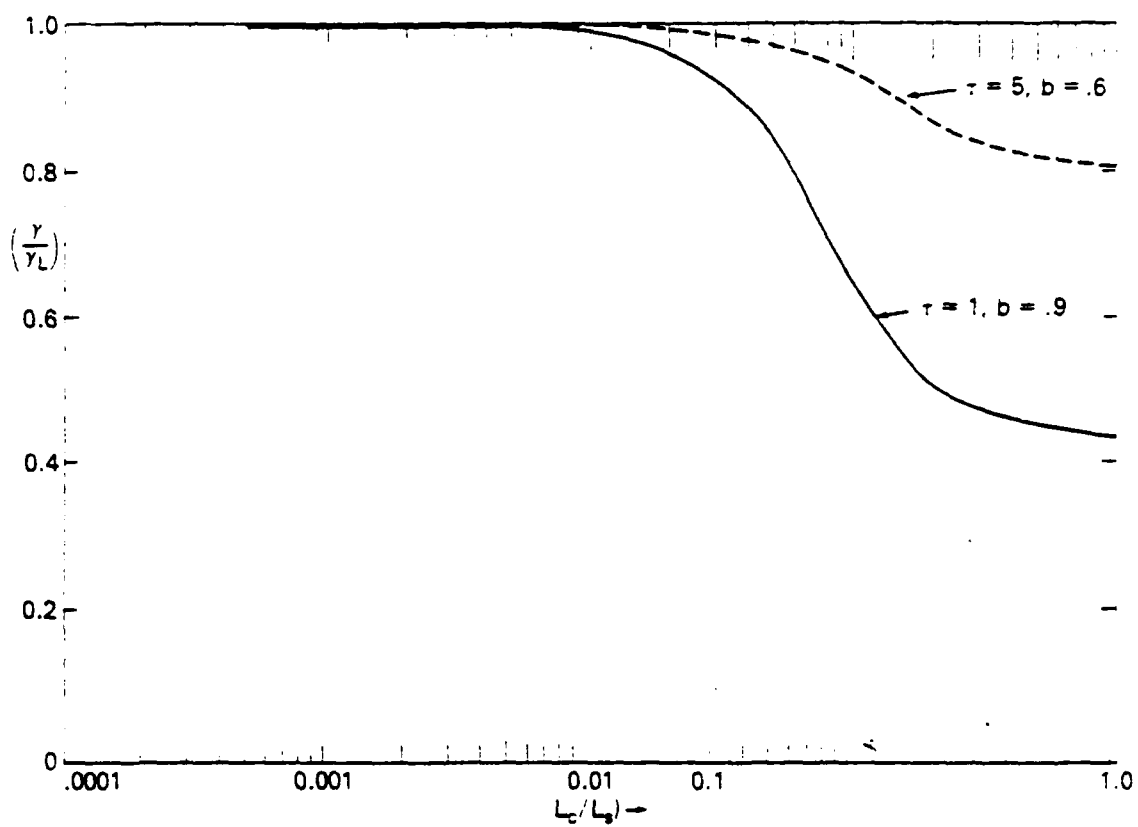


Figure 11. A plot of γ/γ_L vs. L_c/L_s for $\tau = 0.5$ and 1, for the parameters of Figure 10.

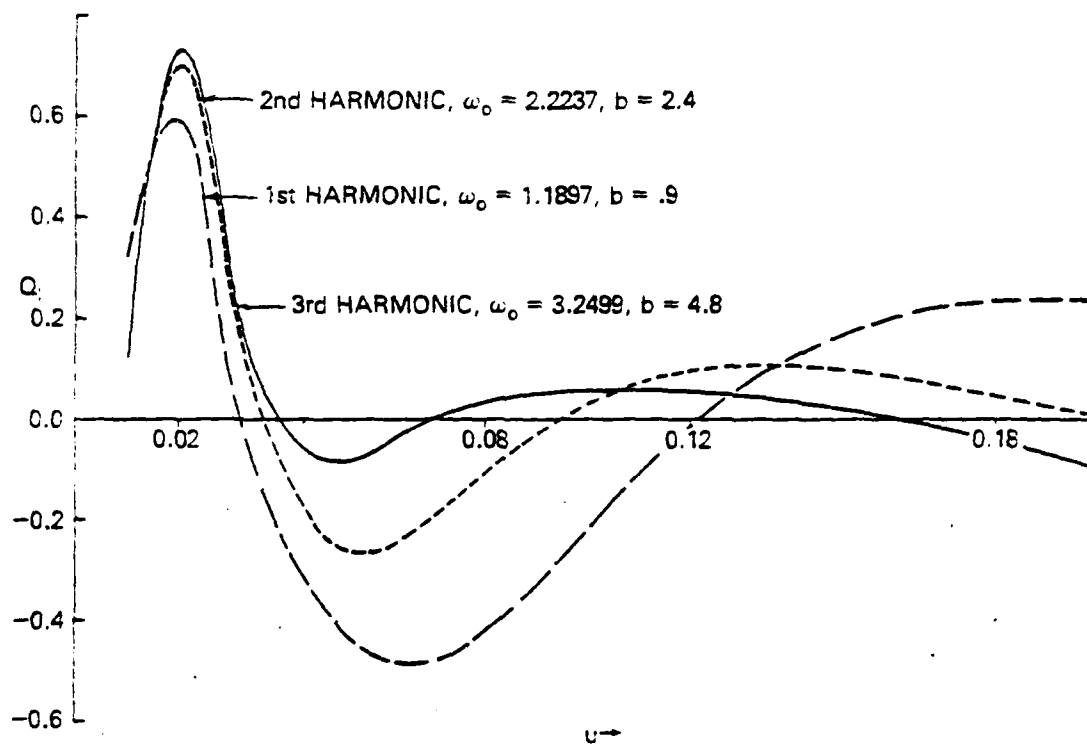


Figure 12. A plot of Q_{1I} vs. u for the first three cyclotron harmonics for $\tau = 1$, $V_d/V_e = 0.65$, maximized over b to attain maximal growth rates. The solid line is the third harmonic, the dashed line with small dashes is the second harmonic and the dashed line with the large dashes is the first harmonic.

REFERENCES

- Ashour-Abdalla, M. and R.M. Thorne, Toward a Unified View of Diffuse Auroral Precipitation, *J. Geophys. Res.*, 83, 4755, 1978.
- Bakshi, P., W. Bellew, G. Ganguli, and P. Satyanarayana, Particle Orbits in Sheared Magnetic Fields and Drift Wave Instabilities, Abstract G1, Annual Controlled Fusion Theory Meeting, San Diego, 1977.
- Bakshi, P., G. Ganguli, and P. Palmadesso, Finite Width Currents, Magnetic Shear and the Current Driven Ion Cyclotron Instability, *Phys. Fluids*, 26, 1808, 1983.
- Bellew, W., Application of Operator Methods to an Inhomogeneous Plasma in a Sheared Magnetic Field, Ph.D Thesis, Boston College, 1978.
- Drummond, W.E. and M.N. Rosenbluth, Anomalous Diffusion Arising from Microinstabilities in a Plasma, *Phys. Fluids*, 5, 1507, 1962.
- Ganguli, G., Effects of Magnetic Shear on Ion-Cyclotron Modes, Ph.D Thesis, Boston College, 1980.
- Ganguli, G. and P. Bakshi, Non-Local Aspects of Electrostatic Current Driven Ion Cyclotron Instability Due to Magnetic Shear, *Phys. Fluids* 25, 1830, 1982.
- Hwang, K.S., E.G. Fonthelm and R.S.B. Ong, Excitation of an Electrostatic Wave by a Cold Electron Current Sheet of Finite Thickness, *Planet. Space Sci.*, 31, 285, 1983.
- Kindel, J.M. and C.F. Kennel, Topside Current Instabilities, *J. Geophys. Res.*, 76, 3055, 1971.
- Kintner, P.M., M.C. Kelly and F.S. Mozer, Electrostatic Hydrogen Cyclotron Waves Near One Earth Radius Altitude in the Polar Magnetosphere, *Geophys. Res. Lett.*, 5, 139, 1978.
- Kintner, P.M., On the Distinction Between Electrostatic Ion Cyclotron Waves and Ion Cyclotron Harmonic Waves, *Geophys. Res. Lett.*, 7, 585, 1980.
- Linsker, R., Integral-Equation Formulation for Drift Eigen Modes in Cylindrically Symmetric Systems, *Phys. Fluids*, 24, 1485, 1981.
- Pearlstein, L.D. and H.L. Berk, Universal Eigen Mode in a Strongly Sheared Magnetic Field, *Phys. Rev. Lett.*, 23, 220, 1969.

- Ross, D. W. and S.M. Mahajan, Are Drift-Wave Eigen Modes Unstable?, Phys. Rev. Lett., 40, 324, 1978.
- TFR Group, Ion-Cyclotron Instability in the TFR Tokamak, Phys. Rev. Lett., 41, 113, 1978.
- Waltz, R.E. and R.R. Dominguez, Ion Cyclotron Modes in Tokamaks, Phys. Fluids, 24, 1575, 1981.

APPENDIX E
VELOCITY SHEAR STABILIZATION OF THE
CURRENT CONVECTIVE INSTABILITY

P. Satyanarayana
Science Applications, Inc.

and

S.L. Ossakow
Naval Research Laboratory

Velocity Shear Stabilization of the Current Convective Instability

P. Satyanarayana
Science Applications, Inc.
McLean, VA 22102

and

S.L. Ossakow
Plasma Physics Division
Naval Research Laboratory
Washington, D.C. 20375

December 1983

ABSTRACT

A nonlocal theory of the current convective instability in the presence of a transverse velocity shear is developed. It is found that the velocity shear stabilizes the short wavelength modes and preferentially excites a long wavelength mode. Application to east-west structure in the high latitude auroral F layer plasma enhancements is discussed.

I. INTRODUCTION

Large scale structure in plasma density enhancements in the auroral F layer ionosphere has been a topic of continued research over the past several years (Vickrey et al., 1980; Keskinen and Ossakow, 1982; 1983a,b; Tsunoda and Vickrey, 1983). Theoretically these so called F region plasma "blobs" have been shown to be susceptible to the $\underline{E} \times \underline{B}$ gradient drift instability (EBI) (Linson and Workman, 1970) and in an $\underline{E} \times \underline{B}$ stable geometry to the current convective instability (CCI) (Ossakow and Chaturvedi, 1979), or a combination of the two (Vickrey et al., 1980; Keskinen and Ossakow, 1982). The current convective instability was originally discussed in the context of the positive column of a laboratory gas discharge by Lehnert (1958), and Kadomtsev and Nedospasov, (1960). Ossakow and Chaturvedi (1979) suggested that the diffuse auroral precipitation, constituting a weak magnetic field aligned current (\hat{z}), could destabilize an inhomogeneous plasma having the density gradient pointing in the direction perpendicular (northward, \hat{x}) to the magnetic field. The unstable waves have wavevectors pointing in the direction perpendicular (eastward, \hat{y}) to both the ambient geomagnetic field and the density gradient. DNA Wideband satellite observations (Rino et al., 1978) indicated that a regularly occurring scintillation enhancement due to F region ionospheric irregularities can be identified in the nighttime auroral zone data. These data are characterized by diffuse auroral particle precipitation and total electron content (TEC) gradient pointing northward. Furthermore, the dominant modes appear to be in the north-south direction parallel to the density gradient in contrast to the predictions of the linear theory. Indeed, Chaturvedi and Ossakow (1979) have shown that waves parallel to the density gradient are generated by a nonlinear mode coupling mechanism.

There is increasing evidence that a strong velocity shear exists in the high latitude auroral region (Kelley et al., 1976; Fejer et al., 1983; S. Basu, private communication, 1983). The east-west plasma velocity is sheared as one moves in the north-south direction. Recent calculations have shown that velocity shear has a strong stabilizing influence on interchange instabilities, such as the Rayleigh-Taylor instability (Hamieri, 1979; Guzdar et al., 1982; 1983) and the $\underline{E} \times \underline{B}$ instability

(Perkins and Doles, 1975; Huba et al., 1983) leading one to anticipate similar effects in the case of the CCI also.

In this paper we investigate the effects of velocity shear on the CCI and its role in producing large scale east-west structure in ionospheric F layer plasma blobs (Tsunoda and Vickrey, 1983). We find that velocity shear stabilizes the short wavelength modes ($k_y L > 1$, where k_y is the east-west mode number, L is the density gradient scale length) and thus excites a long wavelength mode.

The organization of this paper is as follows. In the next section we present the general nonlocal theory and present its results in the third section. We discuss the results and apply them to the high latitude auroral ionosphere in the fourth section, and the fifth section contains the conclusions.

II. THEORY

The geometry we use is as follows. The background magnetic field and the field aligned currents are along the z-direction ($\underline{B} = B \hat{z}$; $\underline{V}_d = V_{dz} \hat{z}$). The density gradient and the inhomogeneous electric field [$E_{ox}(x)$] are along the x-direction (northward). The inhomogeneous electric field gives rise to an $\underline{E} \times \underline{B}$ sheared flow along the negative y direction (eastward).

The basic assumptions used in the analysis are as follows: (i) the perturbed quantities vary as $\delta f \sim \delta f(x) \exp[i(k_y y + k_z z - \omega t)]$, where k_y and k_z are the wavenumbers along the y and z directions and $\omega = \omega_r + i\gamma$, implying growth for $\gamma > 0$; (ii) the ordering in the frequencies is such that $\omega, v_{in}(v_{ei}) \ll \Omega_i (\Omega_e)$, where v_{in} and v_{ei} are the ion-neutral and electron-ion collision frequencies and Ω_e and Ω_i are the electron and ion cyclotron frequencies, respectively; (iii) we retain the ion inertia effects, thereby including the ion polarization drift, but ignore the electron inertia; and (iv) we ignore finite-Larmor radius effects by limiting the wavelength domain to $k\rho_i \ll 1$, where ρ_i is the mean ion Larmor radius.

A key feature of our analysis is that a nonlocal theory is developed. That is, the mode structure of the potential in the x direction, the direction in which the density and flow velocity are assumed to vary, is determined by a differential equation rather than an algebraic equation obtained by Fourier analysis. This technique allows one to study modes which have wavelengths comparable to the scale sizes of the inhomogeneities (i.e., $k_y L < 1$, where L represents the scale lengths of the boundary layer). In fact, nonlocal theory is essential to describe the Kelvin-Helmholtz instability driven by a transverse velocity shear (Mikhailovskii, 1974). We also note that since we are interested in the effects of transverse gradients in velocity and density and since the vertical gradient in the density is weaker than the northward density gradient we Fourier analyze in the z direction.

Based on the assumptions described above, the fundamental fluid equations used in the analysis are of continuity and momentum transfer in the neutral frame of reference

$$0 = -e(\underline{E} + (1/c)\underline{V}_e \times \underline{B}) - m v_{ei} \underline{V}_e \quad (1)$$

$$M \frac{d\underline{V}_i}{dt} = e(\underline{E} + (1/c)\underline{V}_i \times \underline{B}) - M v_{in} \underline{V}_i \quad (2)$$

$$\frac{\partial n_j}{\partial t} + \nabla \cdot (n_j \underline{V}_j) = 0 \quad (3)$$

where $m(M)$ is the electron (ion) mass, subscript j denotes species (e for electrons and i for ions), \underline{V} is velocity and \underline{E} is electric field, n is density, c is speed of light, and e is the absolute value of the electron charge. In this paper, we ignore the temperature effects and also neglect the electron-neutral collision frequency (ν_{en}) in comparison with the electron-ion Coulomb collision frequency (ν_{ei}). From eqs. (1) and (2) we obtain the zeroth order perpendicular electron and ion velocities as

$$\underline{V}_{e\perp} = (c/B)\underline{E} \times \underline{\hat{z}} + O(v_{ei}/\Omega_e), \quad (4)$$

$$\underline{V}_{i\perp} = (c/B) [\underline{E}_\perp \times \underline{\hat{z}} + (v_{in}/\Omega_i)\underline{E}_\perp + (1/\Omega_i) (\underline{V}_i \cdot \nabla) \underline{E}_\perp] . \quad (5)$$

where $\Omega_i \equiv eB/Mc$ is the ion cyclotron frequency.

Taking the dot product of eqs. (1) and (2) with $\underline{\hat{z}}$, we obtain the zeroth order parallel velocities as

$$V_{ez} = -e E_{oz} / m v_{ei}, \quad (6)$$

$$V_{iz} = e E_{oz} / M v_{in}. \quad (7)$$

We perturb equations (1)-(3) and linearize them in the electrostatic limit. We substitute $\underline{E} = -\nabla\phi = -\nabla(\phi_0(x) + \delta\phi)$, $\underline{V}_\alpha = \underline{V}_\alpha + \delta\underline{V}_\alpha$, and $n = n_0(x) + \delta n$ into eqs. (1)-(3). Since the equilibrium quantities vary in the x direction we do not Fourier analyze in the x direction. We Fourier analyze in the y and z directions. Here we assume the northward density gradient to be sharper than the vertical density gradient. Using eqs. (4) and (5) along with eqs. (1) and (2) we obtain the perturbed velocities in the perpendicular direction as

$$\delta\underline{V}_{e\perp} = (c/B) \delta\underline{E}_\perp \times \hat{z} + O(v_{ei}/\Omega_e), \quad (8)$$

$$\delta V_{ix} = \frac{(c/B)}{(1 + V_{oy}/\Omega_i)} \left[-ik_y \delta\phi + \frac{(i\omega - ik_y V_{oy} - v_{in})}{\Omega_i} \frac{\partial}{\partial x} \delta\phi \right], \quad (9)$$

$$\delta V_{iy} = (c/B) \left[\frac{\partial}{\partial x} \delta\phi - \frac{(\omega - k_y V_{oy} + iv_{in})}{\Omega_i} k_y \delta\phi \right]$$

where $V_{oy} = -(c/B) E_{ox}$. Here we have neglected the electron Pedersen drift compared with the ion Pedersen drift. From eqs. (1,2) and (6,7) the perturbed parallel velocities are given as

$$\delta V_{ez} = -e \delta E_z / m v_{ei}, \quad (10)$$

$$\delta V_{iz} = e \delta E_z / M v_{in}. \quad (11)$$

Since we study the effects of transverse velocity shear we can ignore the parallel ion inertia terms.

We substitute eqs. (4) thru (11) in eq. (3) and assume quasi-neutrality, $\delta n_e = \delta n_i = \delta n$, to obtain the mode structure equation for the

perturbed electrostatic potential as (where we have dropped δ from $\delta\phi$ and indicate the perturbed potential by ϕ)

$$\phi'' + p\phi' + q\phi = 0 \quad (12)$$

where

$$p = \varepsilon + (iv_{in}/\omega_2) \bar{k}^2 v_{oy}/\omega_1 \quad (13)$$

$$q = -k_y^2 - i k_z^2 (\Omega_e/\nu_{ei}) (\Omega_i/\omega_2) - \bar{k}^2 (k_z v_{oz}/\omega_1) (\Omega_i/\omega_2) \\ + k_y (V_{oy}' + V_{oy}\varepsilon)/\omega_2 \quad (14)$$

$$+ (iv_{in}/\omega_2) \{ \bar{k}^2 V_{oy}'\omega/\omega_1^2 - (k_y V_{oy}) [(n_o'/n_o)/\omega_1 \\ + ik_z^2 (\varepsilon V_{oy}/\omega_1) (\Omega_e/\nu_{ei})] \},$$

where we assumed $V_{oy}/\Omega_i \ll 1$ and ignored terms of $O(\nu_{ei}/\Omega_e)$ and

$$V_{oz} = (V_{ez} - V_{iz}), \quad \varepsilon = n_o'/n_o,$$

$$\bar{k}^2 = ik_z^2 (\Omega_e/\nu_{ei}) - k_y \varepsilon \quad (15)$$

$$\omega_1 = \omega - k_y V_{oy} - k_z V_{oz}, \quad \text{and } \omega_2 = \omega + iv_{in}.$$

The primes indicate derivatives with respect to x . Equation (12) is similar to the equations that have been derived in the context of the Rayleigh-Taylor (Guzdar et al., 1982; 1983) and $\underline{E} \times \underline{B}$ instabilities (Huba et al., 1983). In the absence of the velocity shear ($V_{oy} = V'_{oy} = 0$) the first three terms in $q(x)$ (eq. 14) yield the nonlocal current convective instability. Equation (12) is solved numerically in various parameter domains and the results are presented in the next section.

III. ANALYSIS

Before solving eq. (12) we consider some known limiting cases. First, in the absence of field aligned currents ($V_{oz} = 0$), for a homogeneous ($V_n = 0$) collisionless ($v_{in} = 0$) plasma eq. (12) yields the well known transverse ($k_z = 0$) Kelvin-Helmholtz instability (Mikhailovskii, 1974)

$$\phi'' + \left(-k_y^2 + \frac{k_y V_{oy}}{\omega - k_y V_{oy}} \right) \phi = 0 \quad (16)$$

The Kelvin-Helmholtz instability is shown in Fig. (1) curve A (Michalke, 1964). The velocity profile used is $V_{oy} = \bar{V}_{oy} \tanh(x/L)$. We see from the figure that the collisionless Kelvin-Helmholtz mode is unstable in the domain $0 < k_y L < 1$ with the growth rate maximizing at $k_y L \sim 1.5$ with a maximum value of $0.18 \bar{V}_{oy}/L$.

In the absence of the velocity shear we obtain

$$\phi'' + \epsilon \phi' + \left[-k_y^2 + ik_z^2 \frac{\Omega_e}{v_{ei}} \frac{\Omega_i}{\omega} + \frac{k_z V_{oz}}{\omega} \frac{\Omega_i}{\omega + iv_{in}} \left(ik_z^2 \frac{\Omega_e}{v_e} - k\epsilon \right) \right] \phi = 0 \quad (17)$$

Equation (17) describes the nonlocal current convective instability. In the local limit, $\partial/\partial x \ll k_y$, we obtain the local dispersion equation (Chaturvedi and Ossakow, 1981)

$$\omega^2 + \omega [iv_{in} + i(k_z^2/k_y^2)(\Omega_e \Omega_i / v_{ei})] - (k_z/k_y) \Omega_i V_{oz} \epsilon = 0. \quad (18)$$

The solution of eq. (18) yields the growth rate (Chaturvedi and Ossakow, 1981) with $\omega = \omega_r + i\gamma$ as

$$\gamma = \frac{(k_z/k_y) (v_{ei}/\Omega_e) V_{oz} \epsilon}{(k_z^2/k_y^2) + (v_{ei}\Omega_i/v_{in}\Omega_e)} \quad (19)$$

for $\bar{v}_{in}^2 > 4 (k_z/k_y) v_{oz} \epsilon \Omega_i$, where $\bar{v}_{in} = v_{in} + (k_z^2/k_y^2) (\Omega_e \Omega_i / v_{ei})$. Note that for instability k_z/k_y , v_{ei} , v_{oz} , and ϵ have to be nonzero. In fact, the optimum value of k_z/k_y can be calculated by maximizing eq. (19) with respect to k_z/k_y .

The growth rate maximizes at

$$k_z \approx k_y (v_{ei} v_{in} / \Omega_e \Omega_i)^{1/2}, \quad (20)$$

with a maximum value

$$\gamma_{max} \approx \frac{1}{2} v_{oz} \epsilon (v_{ei} \Omega_i / v_{in} \Omega_e)^{1/2}. \quad (21)$$

For $v_{ei} / \Omega_e = 10^{-4}$, $v_{in} / \Omega_i = 10^{-4}$,

$$(\gamma / v_{oz} \epsilon)_{max} \approx 0.5 \quad (22)$$

Now we solve eq. (17) numerically for various k_y 's using the density profile,

$$n_o(x) = \bar{n}_o (1 + \delta \tanh(x/L)) / (1 - \delta) \quad (23)$$

shown in figure 2 for $\delta = 0.8$.

Figure (1) curve B shows the growth rate normalized to v_{oz}/L as a function of $k_y L$ for $\delta = 0.8$ and k_z given by eq. (20). We note that the growth rate increases monotonically with $k_y L$ and asymptotes to the local growth rate (eq. 22).

We now introduce the velocity shear and solve eq. (12) numerically. We use the density profile given in eq. (23). The velocity profile is determined self-consistently from the zeroth order continuity equation

$$\frac{\partial}{\partial x} (n_o(x) \underline{v}_1(x)) = 0 \quad (24)$$

which becomes for constant ion-neutral collision frequency

$$n_o(x) v_{oy}(x) = \text{constant} .$$

Using these self-consistent profiles the eigenvalues are determined for various values of the parameter $\hat{s} (\equiv \bar{v}_{oy}/v_{oz})$, which serves as a measure of the velocity shear. In Fig. (3) we plot the growth rates normalized to the shear-free current convective growth rate, $\gamma/(v_{oz}/L)$, as a function of the normalized wavenumbers, $k_y L$. We choose $v_{ei}/\Omega_e = 10^{-4}$, $v_{in}/\Omega_i = 10^{-4}$, and $\delta = 0.8$. Curve A gives the case $\hat{s} = 0$ (same as curve B, Fig. (1)). Curves B, C and D are for $\hat{s} = 0.5, 1$, and 2 , respectively. We can draw several conclusions from this figure. First, velocity shear stabilizes the short wavelength modes (Perkins and Doles, 1975; Guzdar et al., 1982; 1983; Huba et al., 1983). Second, the growth rate maximizes at $k_y L \sim 1.5$ for $\hat{s} = 0.5$; and as \hat{s} is increased the peak growth rate decreases and the growth rate maximizes at longer wavelengths. For $\hat{s} = 2$, the growth rate maximizes at $k_y L \sim 0.55$ with $\gamma_{\max} \sim 0.083(v_{oz}/L)$. Third, when $\hat{s} = 1$, i.e., when the horizontal flow velocity is of the order of the vertical plasma drift velocity, modes with $\lambda \sim (2\pi/0.9)L$ are the fastest growing modes ($\gamma_{\max} \sim 0.142 v_{oz}/L \sim 0.142 v_{oy}/L$).

IV. DISCUSSION

Recent experiments conducted at Chatanika (Tsunoda and Vickrey, 1983) indicate that high latitude F-region plasma blobs have an east-west plasma density structure with scale sizes of 150 km and greater. Even though these experiments did not measure the velocity shear in this region, other evidence (Kelley and Carlson, 1977) indicates the presence of a strong east-west flow velocity shear of the order $1 - 20 \text{ sec}^{-1}$ in the high latitude auroral region. Assuming that the east-west flow is $\sim 250 \text{ m/s}$ and the shear scale length (of the order of the density gradient scale length; $L_N = L_V$) is 25 km, Fig. (3) shows that the generalized current convective instability has perpendicular scale sizes of order 150 km ($\hat{s} = 1$; $V_{oy} = V_{oz}$; $k_y L = 0.9$). The corresponding growth rate is given as $\gamma \sim 0.142 (V_{oz}/L) \sim 0.142 \cdot 10^{-2} \text{ s}^{-1}$ (around 10 minutes e-folding time). For larger shears, for example, with the east-west flow velocity, V_{oy} , twice that of the field aligned flow, V_{oz} , the instability generates irregularities of scale sizes around 300 km, but with a smaller growth rate, $0.08 (V_{oz}/L)$ (20 min e-folding time scale for V_{oz}/L around 10^{-2} s^{-1}).

Since velocity shear has similar effects on the $\underline{E} \times \underline{B}$ gradient drift instability (Perkins and Doles, 1975; Huba et al., 1983) it is important to compare our present results with the results of Huba et al. (1983). Referring to Fig. (5) of the paper by Huba et al., we see that east-west flow comparable to the equilibrium north-south flow (due to the horizontal electric fields generating the $\underline{E} \times \underline{B}$ instability) excites modes with wavelengths $\sim 60 \text{ km}$ ($k_y L = 2.6$, $L = 25 \text{ km}$). The growth rate of these modes is $\sim 0.5 (V_{ox}/L)$ with e-folding times of the order 3 minutes (for $V_{ox}/L \cdot 10^{-2}$). From this we can see that in the high latitude auroral region, the generalized CCI and EBI (CCI and EBI with velocity shear) can excite long wavelength modes with east-west scale sizes of 100 km or greater. However, we point out that in the absence of the $\underline{E} \times \underline{B}$ instability (zero westward electric field in the presence of say a poleward density gradient on a blob) the soft particle precipitation causing in turn currents of moderate strength $\sim 250 \text{ m/s}$ ($4 \text{ } \mu\text{A/m}^2$, $n = 10^{11} \text{ m}^{-3}$) can still excite the long wavelength modes.

V. CONCLUSIONS

We have studied the effects of velocity shear on the current convective instability. We have shown that velocity shear suppresses the short wavelength modes and preferentially excites a long wavelength mode with $k_y L < 1$. This suggests that a generalized current convective instability (CCI with east-west flow velocity shear) with currents $\sim 4 \mu\text{A}/\text{m}^2$ (~ 250 m/s parallel flow) can possibly excite modes with wavelengths of 150 km or more. Since the $\underline{E} \times \underline{B}$ instability can also excite long wavelength modes ($\lambda \sim 60$ km with a westward electric field $\sim 10 \text{ mV/m}$, and north-south flow \sim east-west flow), we conjecture that the soft particle precipitation alone can destabilize a stable $\underline{E} \times \underline{B}$ high latitude auroral F region geometry by the CCI (Ossakow and Chaturvedi, 1979). In turn, The CCI in the presence of velocity shear can generate irregularities in the long wavelength domain.

We note that a unified treatment of current convective and $\underline{E} \times \underline{B}$ instabilities, with velocity shear and magnetic shear and nonlinear effects included, is needed in order to come to a better understanding of the morphology of the irregularities evident in auroral F region plasma enhancements. This subject is presently under investigation and will be presented in a future paper.

ACKNOWLEDGEMENTS

We would like to thank P.K. Chaturvedi, J. Huba, and M.J. Keskinen for useful discussions. This work was supported by DNA and ONR.

REFERENCES

- Chaturvedi, P.K., and S.L. Ossakow, Nonlinear stabilization of the current convective instability in the diffuse aurora, Geophys. Res. Lett., 6, 957, 1979.
- Chaturvedi, P.K., and S.L. Ossakow, The current convective instability as applied to the auroral ionosphere, J. Geophys. Res., 86, 4811, 1981.
- Fejer, B.G., R.W. Reed, D.T. Farley, W.E. Swartz, and M.C. Kelley, A resonant peak observed in the spectra of auroral radar echoes and its possible association with ion-cyclotron waves, J. Geophys. Res., (to be published, 1983).
- Guzdar, P.N., P. Satyanarayana, J.D. Huba, and S.L. Ossakow, Influence of velocity shear on the Rayleigh-Taylor instability, Geophys. Res. Lett., 9, 547, 1982.
- Guzdar, P.N., P. Satyanarayana, J.D. Huba, and S.L. Ossakow, Correction to "Influence of velocity shear on the Rayleigh-Taylor instability", Geophys. Res. Lett., 10, 492, 1983.
- Hamieri, E., Shear stabilization of the Rayleigh-Taylor modes, Phys. Fluids, 22, 89, 1979.
- Huba, J.D., S.L. Ossakow, P. Satyanarayana, and P.N. Guzdar, Linear theory of the $E \times B$ instability with an inhomogeneous electric field, J. Geophys. Res., 88, 425, 1983.
- Kadomtsev, B.B. and A.V. Nedospasov, Instability of the positive column in a magnetic field and the "anomalous diffusion effect," J. Nucl. Energy, Part C, 1, 230, 1960.
- Kelley, M.C., and C.W. Carlson, Observations of intense velocity shear and associated electrostatic waves near an auroral arc, J. Geophys. Res., 82, 2343, 1977.
- Kelley, M.C., J.F. Vickrey, C.W. Carlson, and R. Torbert, On the origin and spatial extent of high-latitude F region irregularities, J. Geophys. Res., 87, 4469, 1982.
- Keskinen, M.J., and S.L. Ossakow, Nonlinear evolution of plasma enhancements in the auroral ionosphere I: long wavelength irregularities, J. Geophys. Res., 87, 144, 1982.

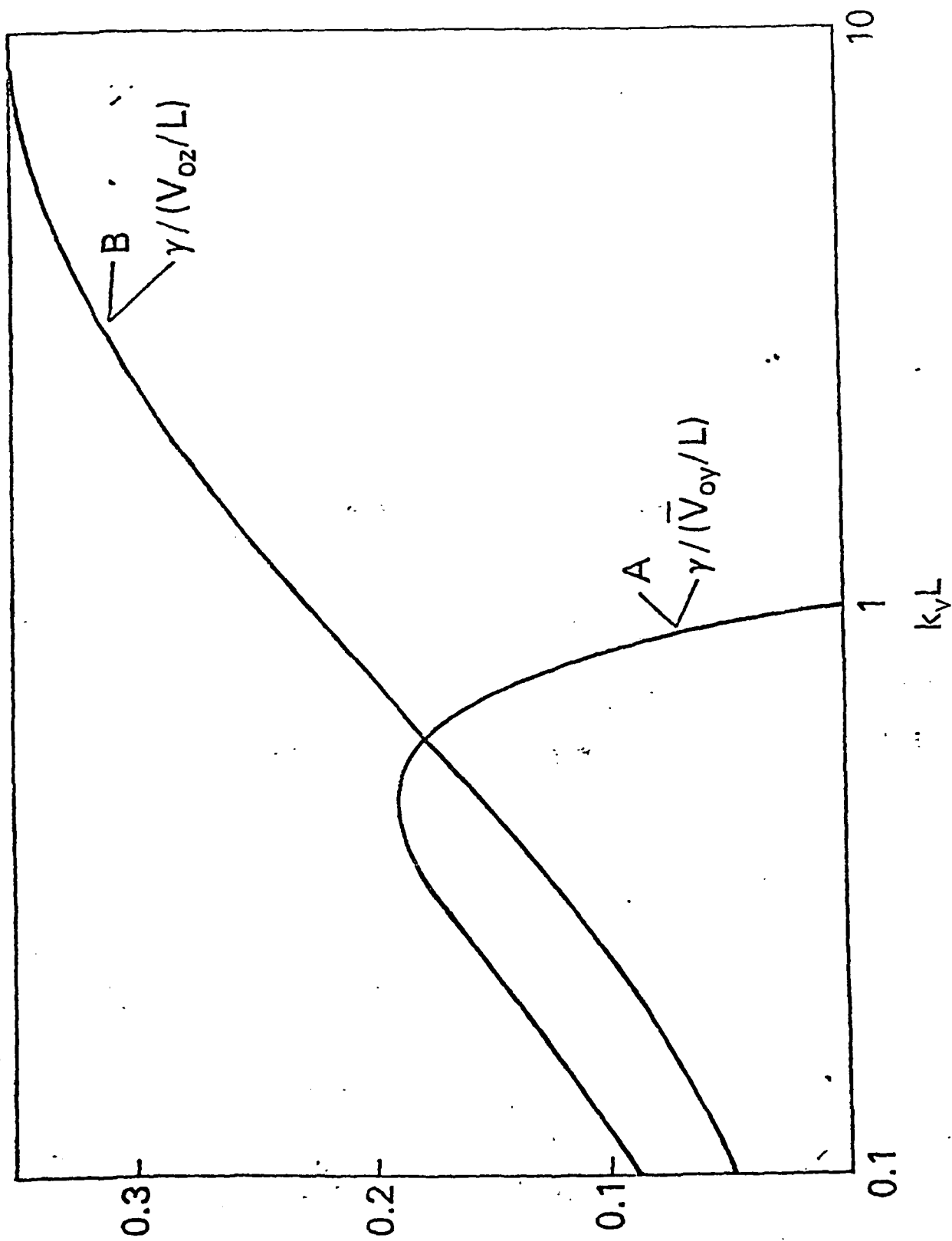
- Keskinen, M.J., and S.L. Ossakow, Nonlinear evolution of convecting plasma enhancements in the auroral ionosphere II: small scale irregularities, J. Geophys. Res., 88, 474, 1983a.
- Keskinen, M.J. and S.L. Ossakow, Theories of high latitude ionospheric irregularities: A review, Radio Sci., (to be published 1983b).
- Lehnert, B., Diffusion processes in the positive column in a longitudinal magnetic field, in Proceedings of the Second Geneva Conference on the Peaceful Uses of Atomic Energy, 32, 349, 1958.
- Linson, L.M., and J.B. Workman, Formation of striations in ionospheric plasma clouds, J. Geophys. Res., 75, 3211, 1970.
- Michalke, A., On the inviscid instability of the hyperbolic-tangent velocity profile, J. Fluid Mech., 19, 543, 1964.
- Mikhailovskii, A.B., Theory of Plasma Instabilities: Vol. II, Consultants Bureau, New York, p. 141, 1974.
- Ossakow, S.L. and P.K. Chaturvedi, Current convective instability in the diffuse aurora, Geophys. Res. Lett., 6, 332, 1979.
- Perkins, F.W., and J.H. Doles III, Velocity shear and the $E \times B$ instability, J. Geophys. Res., 80, 211, 1975.
- Tsunoda, R.T., and J.F. Vickrey, Evidence of east-west structure in large-scale F-region plasma enhancements in the auroral zone, J. Geophys. Res., (to be published, 1983).
- Vickrey, J.F., C.L. Rino, and T.A. Potemra, Chatanika/Triad observations of unstable ionization enhancements in the auroral F-region, Geophys. Res. Lett., 7, 789, 1980.

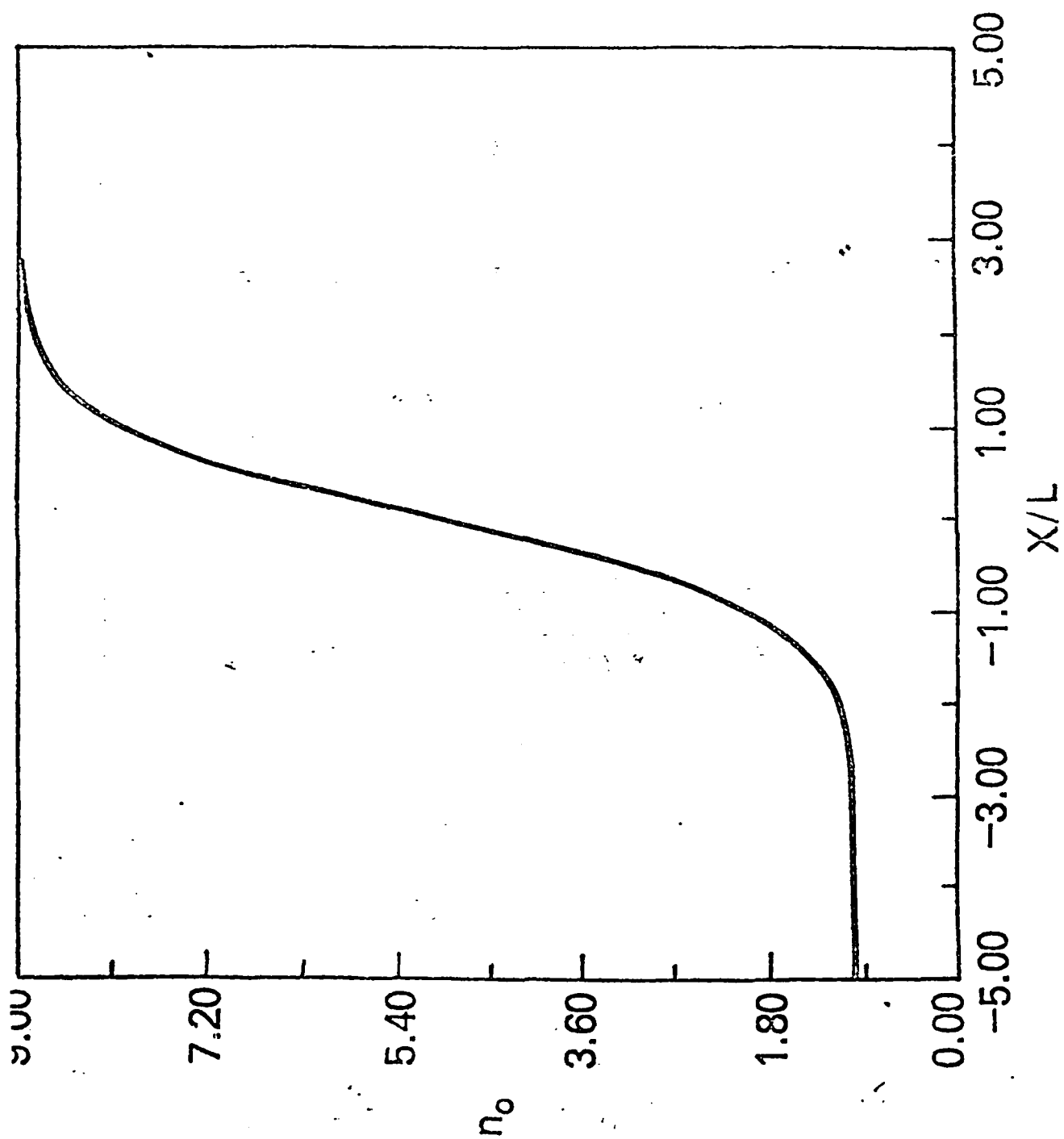
FIGURE CAPTIONS

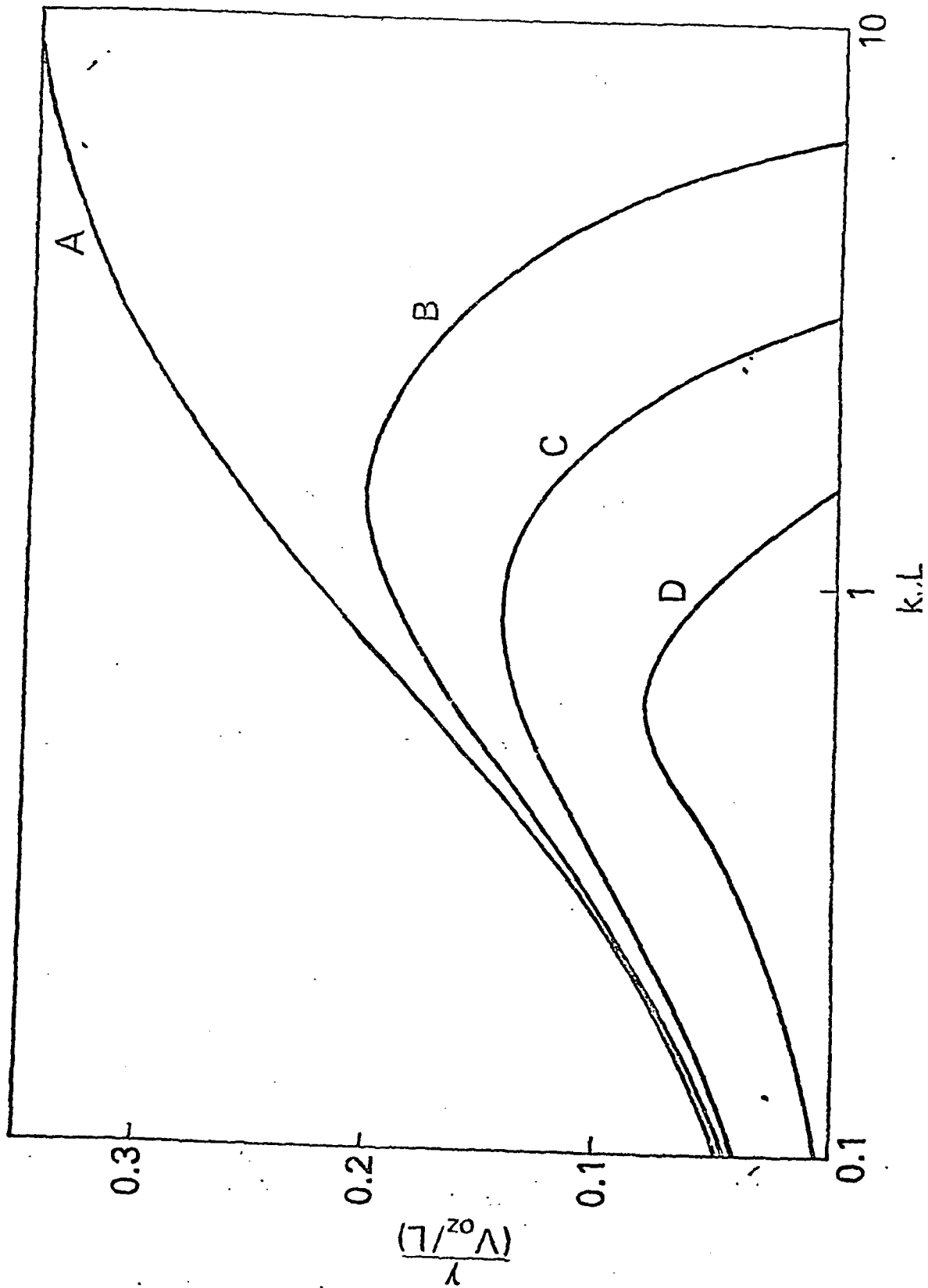
Figure 1. Normalized growth rate versus $k_y L$ curves for Kelvin-Helmholtz (curve A) and current convective (curve B) instabilities. Curve A refers to velocity profile $V_{oy} = \bar{V}_{oy} \tanh x/L$. Curve B refers to the density profile of eq. (23), with $\delta = 0.8$, and $v_{in}/\Omega_i = 10^{-4}$, $v_{ei}/\Omega_e = 10^{-4}$.

Figure 2. Density profile given in eq. (23) for $\delta = 0.8$.

Figure 3. Generalized current convective instability as a function of $\hat{s} (\equiv \bar{V}_{oy}/V_{oz})$ for $\delta = 0.8$, $v_{ei}/\Omega_e = 10^{-4}$, and $v_{in}/\Omega_i = 10^{-4}$. Curve A refers to $\hat{s} = 0$. Curves B, C, and D refer to $\hat{s} = 0.5$, 1, and 2, respectively.







APPENDIX F

INFLUENCE OF MAGNETIC SHEAR ON THE COLLISIONAL
CURRENT DRIVEN ION CYCLOTRON INSTABILITY

P. Satyanarayana and G. Ganguli
Science Applications, Inc.

and

S.L. Ossakow
Naval Research Laboratory

Influence of Magnetic Shear on the
Collisional Current Driven Ion Cyclotron Instability

P. Satyanarayana and G. Ganguli
Science Applications Inc., McLean, Virginia 22102.

and

S. L. Ossakow
Plasma Physics Division
Naval Research Laboratory, Washington, D. C. 20375

September 1983

F-3

PRECEDING PAGE BLANK-NOT FILMED

ABSTRACT

The effects of magnetic shear on the collisional current driven ion cyclotron instability are discussed by incorporating the self-consistent magnetic shear produced by the currents driving the instability itself. It is found that moderately large magnetic shear is required to significantly modify the properties of the local instability, and that the wave packet localizes around $k_z/k_y \ll 1$, thereby indicating that the mode is propagating almost perpendicular to the magnetic field and that the mode is confined to a region of a few hundred meters along the direction of the magnetic field under auroral conditions.

I. INTRODUCTION

Intense field aligned currents observed in the auroral E and F regions (Park and Cloutier, 1971, Cahill et al., 1974, Kelley et al., 1975) were conjectured to be responsible for the generation of electrostatic ion cyclotron waves. Since the ionosphere is collisional in the E and F regions the field aligned currents give rise to negative energy waves which grow due to the dissipation associated with electron-neutral collisions (Chaturvedi, 1976). These are electrostatic waves and lead to density irregularities in the medium. In fact, radar measurements in the E region detect irregularities collocated with auroral electrojets (Greenwald et al., 1975) and a.c. field measurements (Kelley et al., 1975) have been identified as being due to unstable ion cyclotron waves (Drummond and Rosenbluth, 1962 - collisionless domain; Kindel and Kennel, 1971 - weakly collisional domain). Sounding rockets launched from Syowa station, indeed, detected transversely propagating electrostatic plasma instabilities of scale sizes around 200 km in association with strong field aligned currents (Ogawa et al., 1981). Chaturvedi (1976), using a local fluid analysis, showed that, in a partially ionized plasma, field aligned currents can support almost transversely propagating ion cyclotron waves owing to resistivity experienced by electron parallel motion (electron-neutral collisions), while the ion-neutral collisions were found to have a mild stabilizing effect. The field aligned currents observed are around $1-10 \mu A/m^2$ (Kelley et al., 1975), and these currents along the magnetic field usually generate some magnetic shear which in turn changes the mode structure. This is especially so in the case of collisionless current driven ion cyclotron waves (Ganguli and Bakshi, 1982). Recently Burke et al. (1983) also reported observations of large currents $\sim 135 \mu A/m^2$.

In this brief report we investigate the effects of a self-consistent magnetic shear on the collisional current driven ion cyclotron instability (CIC). Since the self-consistent magnetic shear is small and the nonlocal effects are absent in this fluid example (as opposed to the kinetic collisionless case, where nonlocal effects strongly modify the mode structure even for small shears, Ganguli and Bakshi (1982)), we find that the magnetic shear has mild stabilizing effects on the current driven ion

cyclotron instability in the domains of interest pertaining to auroral conditions (drift velocities, $V_d \sim 0.5 - 5$ km/s electron-neutral collisions, $\nu_{en} \sim 10^4$ s⁻¹). However, we find that magnetic shear localizes the wave packet around $k_z/k_y \ll 1$, indicating that the mode is almost perpendicularly propagating. Also, we studied this problem for strong shears in various domains and found that strong magnetic shear stabilizes the instability. The paper is organized as follows: in the next section we give the theory and derive the nonlocal mode structure equation. In the third section we present the results, and in the last section we apply the results to the auroral ionosphere and discuss future work.

II. THEORY

Consider a partially ionized plasma such as the one encountered in the auroral E region. The relevant geometry for high latitude E region is as follows: The magnetic field is aligned with the z-direction along which also flow the currents that drive the CIC. Due to the self-consistent shear produced by the field aligned currents, as we go along the x-direction, the magnetic field picks up a component along the y-direction

$$\underline{B}(x) = B (\hat{z} + x/L_s \hat{y}) . \quad (1)$$

This implies that the parallel wave vector becomes a function of x,

$$k_z = k_z^0 + k_y x/L_s , \quad (2)$$

where L_s is the shear length. The self-consistent shear is calculated from the Maxwell's equation

$$\begin{aligned} \nabla \times \underline{B} &= \frac{4\pi}{c} \underline{J} \\ &= \frac{4\pi}{c} (ne \underline{v}_d) , \end{aligned} \quad (3)$$

where \underline{v}_d is the drift velocity parallel to the z-direction, and is given by

$$\rho_s/L_s = \alpha (V_d/c_s) , \quad (4)$$

where c_s is the sound speed, $(T_e/m_i)^{1/2}$, $\rho_s = c_s/\Omega_i$, Ω_i being the ion cyclotron frequency and

$$\alpha \equiv (c_s/c)^2 (M/m) (\omega_{pe}^2 / \Omega_e^2) \quad (5)$$

where ω_{pe} and Ω_e are the electron plasma and gyro frequencies respectively,

c is the speed of light, M and m are the ion (NO^+) and electron masses, respectively.

The basic equations describing the problem are, the electron and ion continuity equations

$$\frac{\partial n_\alpha}{\partial t} + \nabla \cdot (n_\alpha \underline{V}_\alpha) = 0 \quad (6)$$

where α indicates the species. The equation of motion for the ions is,

$$Mn \frac{d}{dt} \underline{V}_i = -\nabla p_i + en(-\nabla\phi + \frac{\underline{V}_i \times \underline{B}}{c}) - Mn\nu_{in} \underline{V}_i, \quad (7)$$

while the equation of motion for electrons is,

$$0 = -\nabla p_e - en(-\nabla\phi + \underline{V}_e \times \underline{B}) - mn\nu_e \underline{V}_e, \quad (8)$$

where ν_e and ν_{in} are electron-neutral and ion-neutral collision frequencies.

From Eq. (8) for electrons, we obtain the perpendicular and parallel (to \underline{B} \hat{z}) components of electron velocities

$$\underline{V}_{e\perp} = \frac{1}{\Omega_e} \frac{1}{(1+\nu_e^2/\Omega_e^2)} \left[\left(\frac{\nabla p_e}{mn} - \frac{e}{m} \nabla\phi \right) \times \hat{z} - \left(\frac{\nabla p_e}{mn} - \frac{e}{m} \nabla\phi \right) \frac{\nu_e}{\Omega_e} \right] \quad (9)$$

$$\underline{V}_{ez} = -\frac{1}{\nu_e} \left[-\frac{\nabla p_e}{mn} - \frac{e}{m} \nabla\phi \right]. \quad (10)$$

From Eq. (10) we define

$$\underline{V}_d \equiv \underline{V}_{e\parallel}^0 = \frac{\Omega_e}{\nu_e} \left(\frac{c}{B} \nabla\phi^0 \right). \quad (11)$$

From Eq. (7) we obtain for the ions

$$\underline{V}_{i\perp} = \frac{i\omega/\Omega_i}{[1+(i\omega+\nu_i)^2/\Omega_i^2]} \left[\left(\frac{c}{B} \nabla\phi + \frac{1}{\Omega_i} \frac{\nabla p_i}{Mn} \right) \times \hat{z} \right] \quad (12)$$

and

$$V_{iz} \approx \frac{1}{-i\omega} \left[\frac{\nabla p_e}{Mn} - \frac{e}{M} \nabla \phi \right] \quad (13)$$

where we have assumed $T_e \sim T_i$, $\phi = \phi^0 + \hat{\phi}$ and that the perturbed potential $\hat{\phi}$ varies as

$$\hat{\phi}(x) e^{-i(\omega t - k_y y - k_z z)}$$

We do not Fourier analyse in the x-direction since the magnetic field is assumed to vary in that direction. Substituting Eqs. (9) thru (13) in Eq. (6) we obtain, after subtracting the electron continuity equation from the ion continuity equation, the nonlocal mode structure equation

$$\frac{\partial^2 \hat{\phi}}{\partial x^2} + \frac{k_z^2 (\omega^2 - \Omega_i^2 - k_y^2 c_s^2) + i(m/M) k_y^2 v_e (\omega - k_z v_d) + i\omega v_{in} k_z^2}{k_z^2 c_s^2 - i(m/M) v_e (\omega - k_z v_d)} \hat{\phi} - k_y^2 \hat{\phi} = 0, \quad (14)$$

where $k_z = k_z^0 + k_y x/L_s$ and where quasi-neutrality has been assumed. The local limit of Eq. (14) ($L_s \rightarrow \infty$ and $\partial/\partial x \ll k_y$) yields $Q(x) = 0$, where $Q(x)$ is the second term in the above equation. This gives the results obtained previously by Chaturvedi (1976). The linear local growth rate is

$$\gamma = -\frac{m}{2M} \frac{k_y^2}{k_z^2} \left(1 - \frac{k \cdot v_d}{\omega_r} \right) v_e - \frac{v_{in}}{2} \quad (15)$$

where

$$\omega_r^2 \approx \Omega_i^2 + k_y^2 c_s^2.$$

$$\omega \equiv \omega_r + i\gamma$$

Eq. (15) leads to the threshold condition

$$\frac{k \cdot v_d}{\omega_r} > \omega_r \left(1 + \frac{M}{m} \frac{k_z^2}{k_y^2} \frac{v_i}{v_e} \right). \quad (16)$$

Note that the nonlocal treatment allows for the formation of a wave packet in the x-direction compared with the plane wave $[\exp(ik_x x)]$ solutions of Chaturvedi (1976).

We solve Eq. (14) analytically and numerically to determine the eigenvalues and eigenfunctions. We follow the techniques developed by Ganguli and Bakshi (1982) to solve Eq. (14) as

$$\frac{\partial^2 \hat{\phi}}{\partial x^2} + Q(x) \hat{\phi} = 0, \quad (17)$$

where

$$Q(x) = \frac{[(\omega^2 - \Omega_i^2 - k_y^2 c_s^2) + i \omega v_i] \frac{k_y^2 x^2}{L_s^2} + i \frac{m}{M} v_e (\omega - k_y v_d x/L_s) \frac{k_y^2}{y}}{k_y^2 c_s^2 x^2 / L_s^2 - (\frac{m}{M}) v_e (\omega - k_y v_d x/L_s)} - \frac{k_y^2}{y}. \quad (18)$$

We expand $Q(x)$ around $\xi \equiv x - x_0 = 0$ to $O(\xi^2)$ where x_0 is the value of x for which the local growth rate is a maximum,

$$\frac{x_0}{\rho_s} = \frac{2 \omega}{k_y v_d} \quad (19)$$

Now, we have

$$\frac{\partial^2 \hat{\phi}}{\partial \eta^2} + (a + \frac{Q_0''}{2} \eta^2) \hat{\phi}(\eta) = 0 \quad (20)$$

where $\eta = \xi + \frac{Q_0'}{Q_0''}$ and $a = Q_0 - \frac{Q_0'^2}{2Q_0''}$.

The primes indicate the derivatives evaluated at $x = x_0$. Equation (20), which is a Weber equation type, has the solution (for the $\ell = 0$ mode)

$$\hat{\phi}(x) = \phi \exp[-\frac{1}{2} (x - x_{m0})^2 / x_m^2] \exp[iq(x)] \quad (21)$$

where ℓ is the order of the mode and $q(x)$ is a real function. The wavepacket peaks at (Ganguli and Bakshi, 1982)

$$x_{m0} = x_0 - \frac{\text{Re} [Q_0' / Q_0'' (-Q_0''/2)^{1/2}]}{\text{Re} (-Q_0''/2)^{1/2}} \quad (22)$$

The dispersion relation is given by

$$(2\ell + 1) \left(-\frac{Q_0''}{2}\right)^{1/2} \rho_s / L_s + \frac{Q_0'^2}{2Q_0''} = Q(\omega, x_0). \quad (23)$$

Since $Q_0'(x_0) = 0$, Eq. (23) reduces, for the $\ell = 0$ mode, to

$$Q(\omega, k, x_0) = [-Q'_0/2]^{1/2} \rho_s/L_s. \quad (24)$$

We note that the term involving Q'_0 introduces the nonlocal effects and in the collisionless kinetic case significantly modifies the properties of the mode; whereas, in our case this term vanishes and thus does not yield any nonlocal effects. Eq. (24) is solved to obtain the eigenfrequencies and are compared with those obtained by solving Eq. (14) numerically. We find good agreement between the analytical and numerical results. The results are presented in the next section.

III. RESULTS

In Fig. (1) we plot the growth rate normalized to the ion cyclotron frequency (γ/Ω_i) versus the normalized wavenumber ($k_y \rho_s$) for $V_d/c_s = 50$, $v_e/\Omega_e = 0.01$, and $v_{in}/\Omega_i = 0.01$. In plotting these results we treated ρ_s/L_s as an external parameter. The solid line represents the shear-free case and the dotted line represents the case where $\rho_s/L_s = 0.01$. We see from the figure that for any significant reduction in the growth rate large magnetic shear, ρ_s/L_s of order 10^{-2} , is needed.

In order to throw some light on the magnetic shear required to significantly reduce the growth rate, we plot, in Fig.(2), the normalized growth rate against the normalized shear length (ρ_s/L_s), treating ρ_s/L_s as an external parameter. We choose $k_y \rho_s = 0.3$, and 0.5 and plot the growth rate for the parameters of Fig.(1). This figure shows that moderate to strong magnetic magnetic shears, $\rho_s/L_s \geq 0.01$, are required to reduce the growth rate significantly. For $\rho_s/L_s > .04$, the growth rate drops significantly and the instability is stabilized; however, the theory begins to break down for large shear value $\rho_s/L_s > 0.1$. We find that for large shears, the growth rate drops linearly as a function of inverse shear length. For very small shears, $\rho_s/L_s < 10^{-4}$ the growth rate remains essentially constant and begins to decrease significantly for $\rho_s/L_s \sim 0.01$.

In Fig. (3) we present the wave eigenfunctions for the following parameters: $V_d = 50 c_s$, $v_{ei}/\Omega_e = 10^{-2}$, $v_{in}/\Omega_i = 10^{-2}$ and for $k_y \rho_s = 0.3$, $\gamma/\Omega_i = 0.24$. The solid line represents the real part of the wave function (ϕ) and the dotted line $|\phi|$. Two important features are to be noted in this figure. One feature is that the wavepacket localizes around $x_0/\rho_s \ll 1$, i.e., for small shear lengths k_z/k_y is $\ll 1$, indicating that the mode is almost perpendicularly propagating. This can also be seen from Eq. (19) which yields

$$k_z/k_y \sim 2 (\omega/k_y V_d) (\rho_s/L_s) \ll 1 \text{ for } \rho_s/L_s \sim 10^{-7}.$$

The second feature is that the width of the wave packet is of the order $200 \rho_s$ suggesting a localization region of 500 meters for

$\rho_s \approx 2.5$ meters (corresponding to NO^+ ions in the ionosphere).

The effect of self-consistent magnetic shear is understood by plotting the normalized growth rate versus the normalized drift velocity. For this purpose, we use Eq. (4), to express the shear length in terms of the drift velocity. In figure 4, we plot the growth rate for $\alpha \sim 10^{-6}$, 10^{-5} , and 10^{-4} ($\omega_{pe}^2/\omega_{ce}^2 = 10^2, 10^3$, and 10^4 respectively; $c_s = 500$ m/s) and for $v_e/\Omega_e = 0.01$, $v_{in}/\Omega_i = 0.01$, and $k_y \rho_s = 0.3$. We also give the shear-free local growth rate (curve A) to compare with the growth rate with shear. Three points are to be noted in this figure: (1) $\alpha = 10^{-6}$ corresponds to ionospheric parameters. We find that the growth rate is not too different from the shear-free case. In fact, the growth rate curve overlaps curve A and eventually turns around for $V_d/c_s > 500$. (2) Curve B, which gives the growth rate for $\alpha \sim 10^{-5}$, shows that the growth rate drops significantly beyond drift velocities $> 150 c_s$; (3) curve C, which represents the growth rate for $\alpha \sim 10^{-4}$, shows that the optimum drift velocity (the drift velocity for which the growth rate is a maximum), $80 c_s$, is much smaller for this case. This leads to the conclusion that the optimum drift velocity decreases as the parameter α is increased. At large drift velocities, the self-consistent magnetic shear produced is large enough that the mode is stabilized and the growth rate tends to zero.

IV. DISCUSSION

We now apply the results to the high latitude ionospheric conditions. We choose $v_{in}/\Omega_i = 10^{-2}$, $v_e/\Omega_e = 10^{-2}$, and $V_d \sim 20 c_s$. For $V_d = 20 c_s$ the corresponding shear length is about 1000 km (NO^+ ions, $n \sim 10^5 \text{ cm}^{-3}$). We find that the growth rate is 0.9 s^{-1} , for modes with wavelengths of 50 meters ($k_y \rho_s = 0.3$, and $\rho_s = 2.5$ meters), which is comparable with the local growth rate. From the plots of the wave functions we see that the mode is localized in the north-south direction in a region of

$$\Delta x \sim 200 \rho_s = 500 \text{ m} \quad \text{Moreover, we find that } k_y \gg k_x \text{ (} k_x \sim 1/\Delta x \text{)}$$

which indicates the strong two dimensional structure of the mode in the plane perpendicular to the magnetic field during the linear phase of the instability.

We conclude that the magnetic shear corresponding to normal auroral conditions with field aligned currents of the order of $\mu\text{A/m}^2$ is small and thus does not appreciably alter the current driven collisional ion cyclotron mode discussed by Chaturvedi (1976). Even strong currents under some disturbed conditions, $\sim 135 \mu\text{A/m}^2$, reported by Burke et al. (1983) do not produce significant shear in the magnetic field to have any effect on the CIC. Currents of the order mA/m^2 or more possibly produce significant effects.

Finally, we discuss the limitations of the present theory. The theory is valid in the domain, $k_z/k_y < 1$, and $\rho_s/L_s < 0.1$. For higher shear values and for $k_y \rho_s \sim 1$ the theory breaks down, furthermore, the real frequency becomes large and the mode branches off into an ion-acoustic wave. A more complete treatment should also treat this domain to understand the effects of magnetic shear on the ion-acoustic waves. We have done an MHD analysis and arrived at the mode structure equation with a potential term, $Q(x)$ [Eq. (18)], whose real part is independent of the parallel wavenumber, k_z ; whereas, in the collisional case the real part of $Q(x)$ depends on k_z and drastically affects the collisionless kinetic ion cyclotron instability (Ganguli and Bakshi, 1982). We will present the kinetic analysis of the collisional ion cyclotron waves in the presense of magnetic shear in a future paper. For higher drift velocities (comparable to the $\underline{E} \times \underline{B}$ drift velocities) where the self-consistent magnetic shear plays a significant

role in determining the mode structure, a complete treatment is needed which includes an electric field along the y-direction and the related velocity shear.

In conclusion, we have examined the influence of magnetic shear on the collisional current driven ion cyclotron instability. Self consistent magnetic shear corresponding to moderate drift velocities near the threshold velocity for the instability does not have significant effects on the instability. We find that the mode is almost perpendicularly propagating and is localized in a region extending upto a few hundred kilometers in the direction of the magnetic field under auroral conditions. However, in domains where the plasma density is high such that the parameter $\omega_{pe}^2/\omega_{ce}^2$ is large, we find that the growth rate of a particular mode maximizes at an optimum drift velocity much larger than the sound speed. Finally, we find that strong shears ($\rho_s/L_s \geq 0.05$) significantly reduce the growth rate and stabilize the collisional current driven ion cyclotron instability. This strong shear corresponds to large parallel drift velocities ($V_d \gg c_s$), as seen in fig. 4.

ACKNOWLEDGEMENTS

We would like to thank P.K. Chaturvedi for helpful discussions. This work has been supported by DNA and ONR.

REFERENCES

- Burke, W., Silevitch, M., and Hardy, D.A. (1983) J. Geophys. Res., 88, 3127.
- Cahill, L.J., Potter, W.E., Kintner, P.M., Arnoldy, R.L., and Choy, L.W. (1974) J. Geophys. Res., 79, 3147.
- Chaturvedi, P.K., and KAW, P.K. (1975) Plasma Phys., 17, 447.
- Chaturvedi, P.K. (1976) J. Geophys. Res., 81, 6169.
- D'Angelo, N. (1973) J. Geophys. Res., 78, 3987.
- Drummond, W.E., and Rosenbluth, M.N. (1962) Phys. Fluids, 5, 1507.
- Ganguli, G., and Bakshi, P. (1982) Phys. Fluids, 25, 1830.
- Greenwald, R.A. (1974) J. Geophys. Res., 79, 4807.
- Greenwald, R.A., Ecklund, W.L., and Balsley, B. (1975) J. Geophys. Res., 80, 131.
- Kelley, M.C., Bering, E.A., and Mozer, F.S. (1975) Phys. Fluids, 18, 1950.
- Kindel, J.M., and Kennel, C.F. (1971) J. Geophys. Res., 76, 3055.
- Ogawa, T., Mori, H., Miyazaki, S., and Yamagishi, H. (1981) Proceedings of the Third Symposium on Co-ordinated Observations of the Ionosphere and Magnetosphere in the Polar Region, Tokyo.
- Park, R.J., and Cloutier, P.A. (1971) J. Geophys. Res., 76, 7714.

FIGURE CAPTIONS

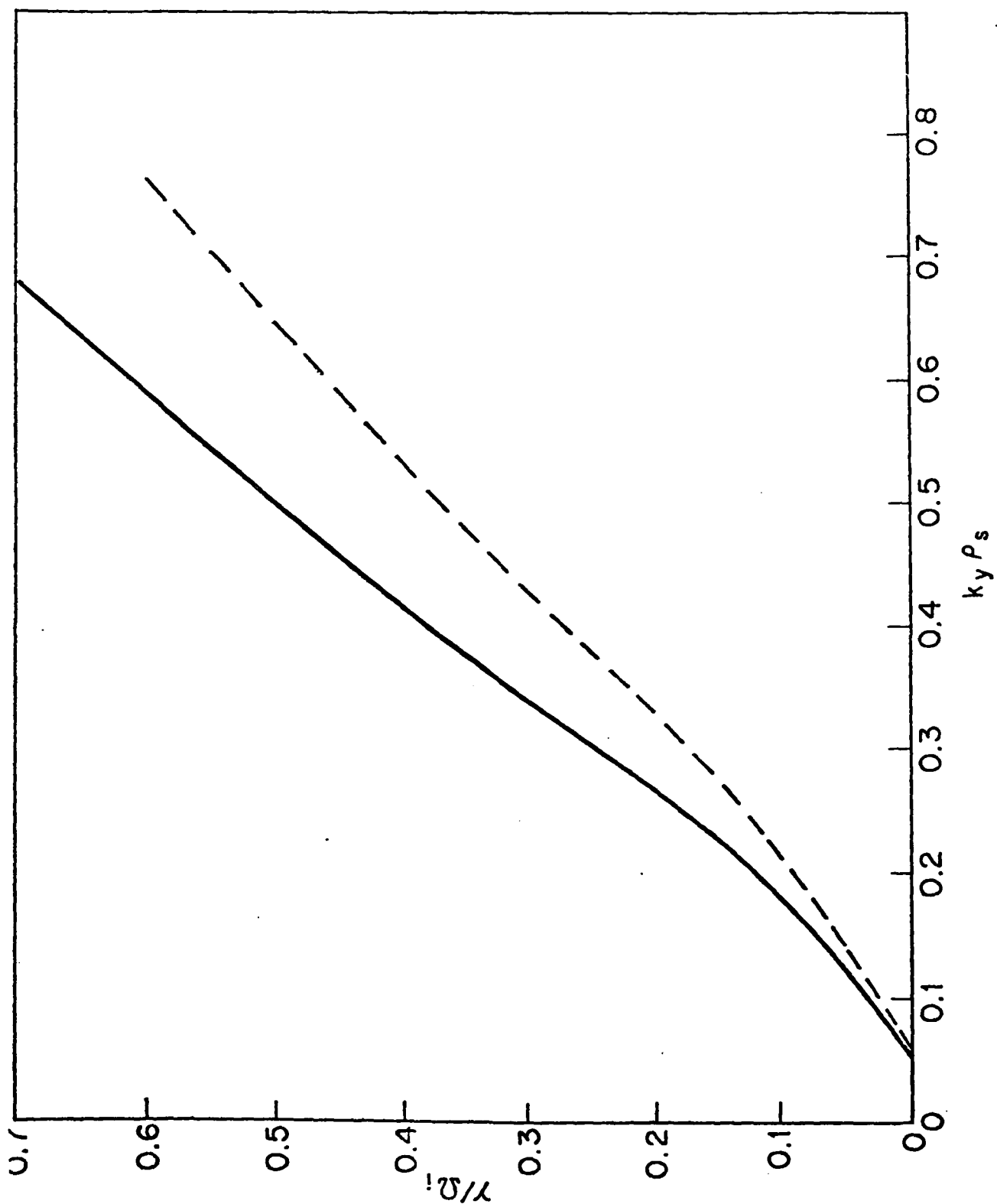
Figure 1. Plot of normalized growth rate (γ/Ω_i) versus the normalized wave number $(k_y \rho_s)$. The parameters used are $v_e/\Omega_e = 0.01$, $v_{in}/\Omega_i = 0.01$, $V_d/c_s = 50$. The solid line represents the shear free case, and the dotted line represents the case where $\rho_s/L_s = 0.01$.

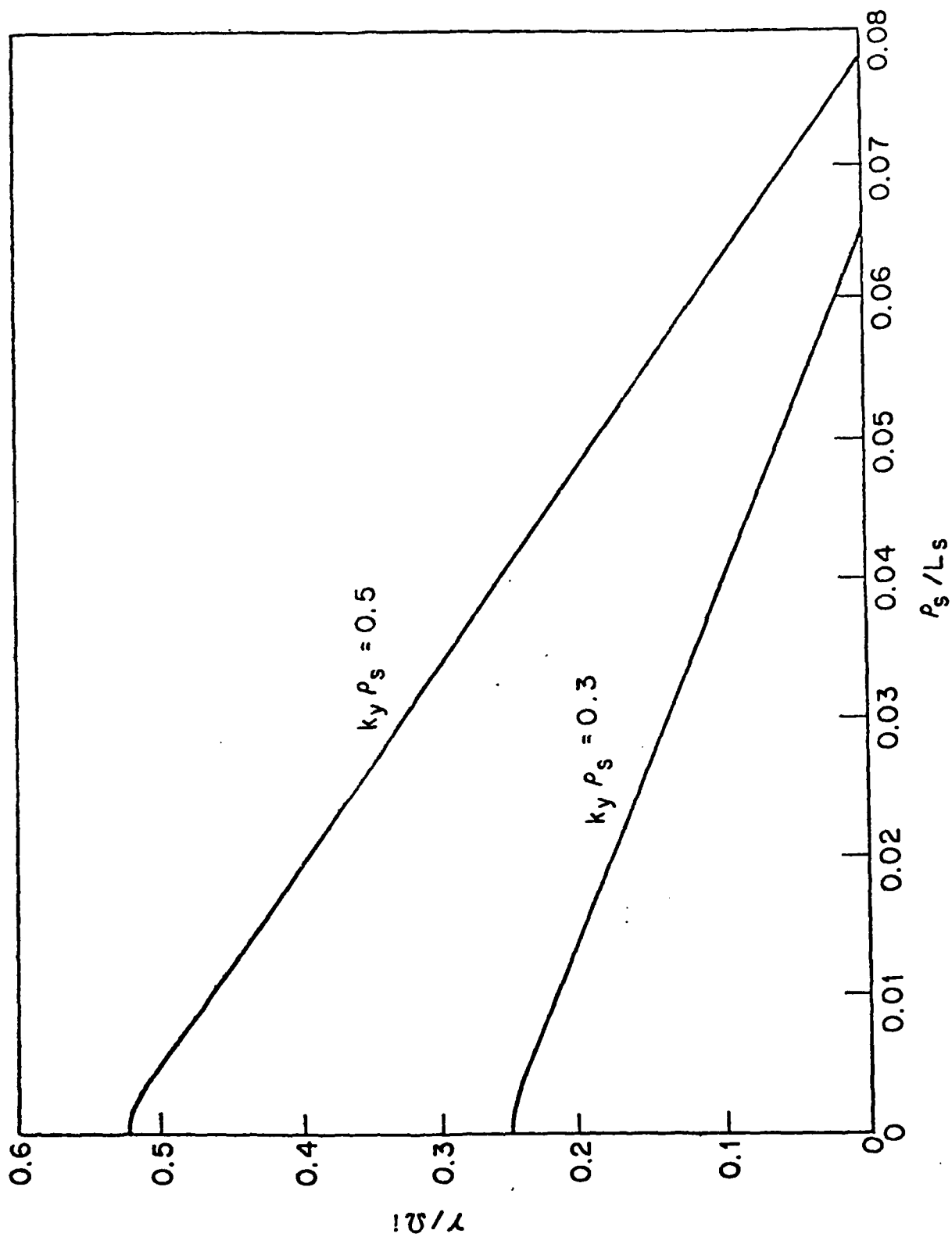
Figure 2. Normalized growth rate (γ/Ω_i) versus ρ_s/L_s treating ρ_s/L_s as an external parameter for $V_d/c_s = 50$, $k_y \rho_s = 0.3$, and 0.5 , and for $v_e/\Omega_e = 0.01$, $v_{in}/\Omega_i = 0.01$.

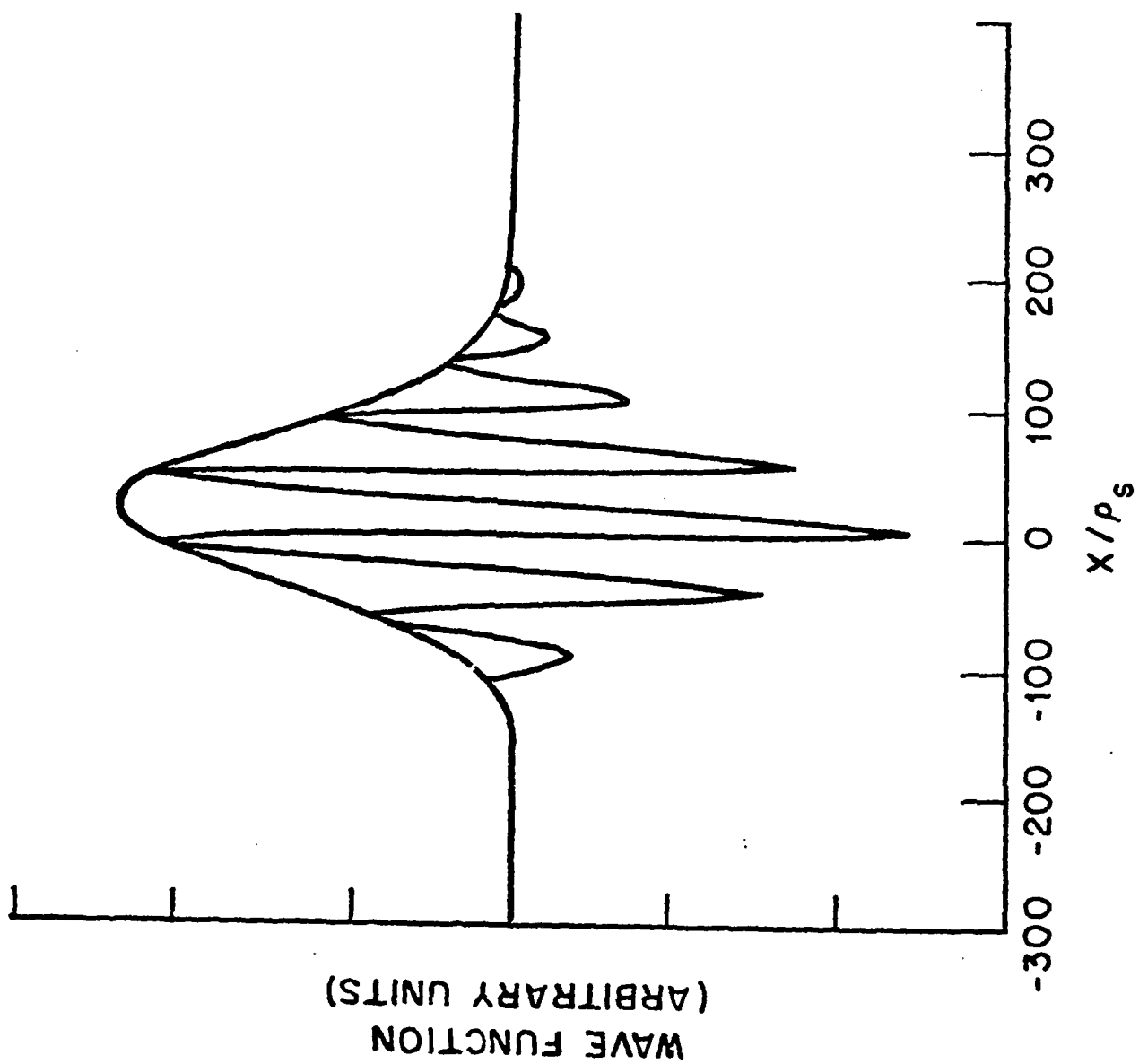
Figure 3. Plot of wave eigenfunctions for the same parameters as Fig. (1) and for $k_y \rho_s = 0.3$, $\gamma/\Omega_i = 0.25$, and $\rho_s/L_s = 0.001$.

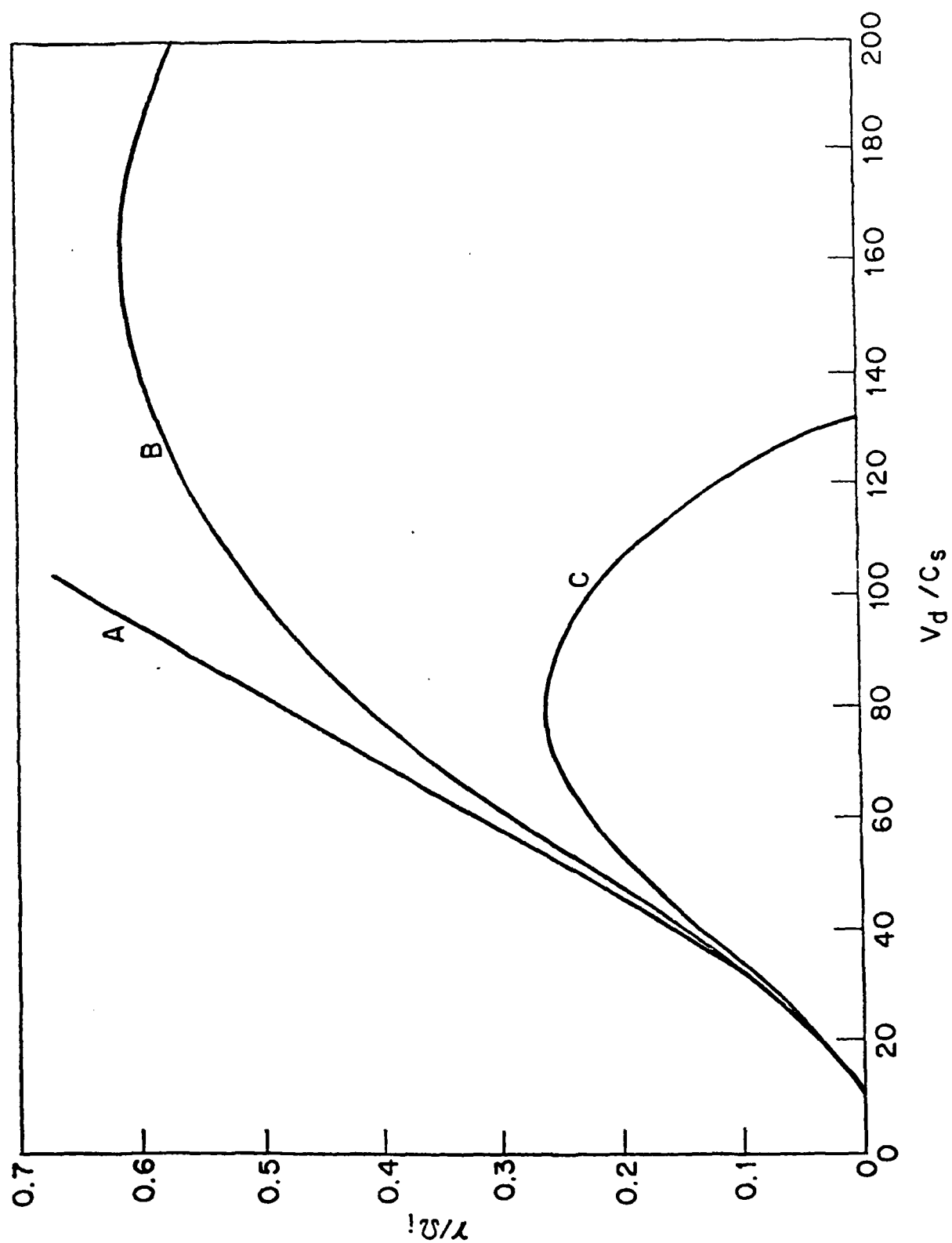
Figure 4. Growth rate versus the drift velocity curves with and without self-consistent magnetic shear for the following parameters:

$k_y \rho_s = 0.3$, $v_e/\Omega_e = 0.01$, and $v_{in}/\Omega_i = 0.01$. Curve A represents the shear-free case and $\alpha = 10^{-6}$. Curve B, and C are for $\alpha = 10^{-5}$, and 10^{-4} and these correspond to $\omega_{pe}^2/\omega_{ce}^2 = 10^3$, and 10^4 .









APPENDIX G
RAYLEIGH-TAYLOR INSTABILITY IN THE PRESENCE OF
A STRATIFIED SHEAR LAYER

P. Satyanarayana and P.N. Guzdar
Science Applications, Inc.

and

J.D. Huba and S.L. Ossakow
Naval Research Laboratory

Rayleigh-Taylor Instability in the Presence of
a Stratified Shear Layer

P. Satyanarayana and P.M. Guzdar*
Science Applications, Inc.
McLean, Virginia 22102

and

J.D. Huba and S.L. Ossakow
Plasma Physics Division
Naval Research Laboratory
Washington, D.C. 20375

September 1983

Abstract

A nonlocal theory of the Rayleigh-Taylor instability which includes the effect of a transverse velocity shear is presented. A two fluid model is used to describe an inhomogeneous plasma under the influence of gravity and sheared equilibrium flow velocity, and to derive a differential equation describing the generalized Rayleigh-Taylor instability. An extensive parametric study is made in the collisionless and collisional regimes, and the corresponding dispersion curves are presented. The results are applied to the equatorial F region and to barium releases in the ionosphere.

* Present address: University of Maryland, College Park, Md 20742

I. Introduction

The Rayleigh-Taylor instability (Rayleigh, 1894; Taylor, 1950) arises in a wide range of physical phenomena. This instability is primarily driven by a gravitational force acting on an inverted density gradient (e.g., a heavy fluid supported by a light fluid). In a magnetized plasma these modes can exist in both the collisionless and collisional domains. For example, theoretical models (Hudson and Kennel, 1975; Ossakow, 1979) and numerical simulations (Scannapieco and Ossakow, 1976; Ossakow et al., 1979; Zalesak and Ossakow, 1980; Zalesak et al., 1982) of the collisional Rayleigh-Taylor instability in the earth's ionosphere show that the mode evolves into plasma bubbles that extend upward from the bottomside to the topside of the F-layer. The collisionless interchange type instability (ballooning mode) can exist in the earth's plasmasphere (Vinas, 1980) as well as in laboratory plasmas (Coppi and Rosenbluth, 1966; Coppi et al., 1979). These collisionless modes arise due to an unfavorable curvature in the magnetic field (simulating an effective gravity) in the presence of a pressure gradient. This instability may also arise in the acceleration of a heavy fluid by one of lower density as in targets accelerated by laser ablation (Emery et al., 1982 and references therein) or the deceleration of barium clouds injected in the ionosphere (Phillip, 1971; Rosenberg, 1971; Davis et al., 1974; Fedder, 1980).

In some of the above situations, the equilibrium flow velocity is observed to be inhomogeneous. For example, in the ionosphere, the horizontal plasma velocity during equatorial spread F (ESF) reverses its direction as a function of altitude (Kudeki et al., 1981; Tsunoda, 1981a; Tsunoda and White, 1981; Kelley et al., 1981). In the plasmasphere, steep shear in the flow velocity can exist due to the dominating corotating electric field inside the plasmasphere and a convective magnetospheric electric field penetrating across

the plasmopause. This can lead to a Kelvin-Helmholtz type erosion of the outer edge of the plasmasphere (Viñas, 1980; Viñas and Madden, 1983). In targets accelerated by laser ablation, the Rayleigh-Taylor instability (Bodner, 1974) nonlinearly evolves into a bubble and spike structure (as during ESF) and develops a strong shear in the flow velocity (Harlow and Welsh, 1966; Daly, 1967; Emery et al., 1982). In the absence of any other driving mechanism, the velocity shear gives rise to a transverse Kelvin-Helmholtz instability in fluids (Kelvin, 1910; Chandrasekhar, 1961) and in magnetized plasmas (Mikhailovskii, 1974). All of the above examples suggest a need for a detailed study of configurations in which the two driving mechanisms co-exist, namely, inhomogeneous velocity flows and gravity (or similar forces).

The influence of velocity shear on interchange instabilities has been studied by Drazin (1958) and Chandrasekhar (1961) in the context of fluid models; by Hamieri (1979) in the context of laboratory plasmas; by Vinas (1980) in the context of the plasmasphere; and by Guzdar et al. (1982; 1983) in the context of equatorial spread F. In this paper we report on our detailed study of the influence of velocity shear on the collisionless and collisional Rayleigh-Taylor instability and apply the results to a variety of geophysical phenomena. We find that the velocity shear can have a dramatic effect on the Rayleigh-Taylor instability (Guzdar et al., 1982; 1983). A sufficiently strong velocity shear can stabilize the most unstable modes (i.e., those for which $kL > 1$ where L is the scale length of the inhomogeneity and k is the perpendicular wave number), which leads to maximum growth in the long wavelength regime (for which $kL < 1$). Thus velocity shear, in some domains, preferentially excites a long wavelength mode, in sharp contrast to the behavior of the mode in the absence of velocity shear.

This paper is divided into five sections. In the next section, we derive the general mode structure equation describing an inhomogeneous collisional plasma which contains a sheared velocity flow and which is under the action of gravity. In the third section we discuss the stability of this plasma in two limits, namely, the Rayleigh-Taylor limit (no velocity shear), and the Kelvin-Helmholtz limit (no gravity). In the fourth section we present the results of the analysis of the generalized Rayleigh-Taylor instability, i.e., when both velocity shear and gravity are present. In the final section, we discuss the results and apply them to geophysical phenomena.

II. Theory

We consider an infinite slab of magnetized plasma. The coordinate system is shown in Fig. 1. The magnetic field is uniform and is in the \hat{z} direction ($\underline{B} = B \hat{z}$), the acceleration due to gravity is in the x direction ($\underline{g} = -g \hat{x}$), the ambient electric field is inhomogeneous and is in the x direction ($\underline{E}_0 = E_0(x) \hat{x}$), and the density is inhomogeneous in the x direction ($n_0 = n_0(x)$). The inhomogeneity in the background electric field leads to a sheared equilibrium flow, $\underline{V}_0(x) = -c E_0(x)/B \hat{y}$.

The basic assumptions used in the analysis are as follows: (1) the perturbed quantities vary as $\delta p \sim \delta p(x) \exp [i(k_y y - \omega t)]$, where k_y is the wave number along y direction and $\omega = \omega_r + i\gamma$, implying growth for $\gamma > 0$; (2) the ordering in the frequencies is such that $\omega, \nu_{in} \ll \Omega_i$, where ν_{in} is the ion-neutral collision frequency and Ω_i is the ion-gyro-frequency; (3) we ignore finite-gyroradius effects by limiting the wavelength domain to $k\rho_i \ll 1$, where ρ_i is the mean ion-Larmor radius; (4) we neglect perturbations along the magnetic field ($k_{\parallel} = 0$) so that only two dimensional mode structure in the x - y plane is obtained; (5) we retain ion inertia effects, thereby including the ion polarization drift, but ignore electron inertia; and (6) we neglect ion and electron pressure.

A key feature of our analysis is that a nonlocal theory is developed. That is, the mode structure of the potential in the x direction, the direction in which density and the flow velocity are assumed to vary, is determined by a differential equation rather than an algebraic equation obtained by Fourier analysis. This technique allows one to study modes which have wavelengths comparable to the scale size of the inhomogeneities (i.e., $k_y L < 1$, where L represents scale lengths of the boundary layer). In fact, nonlocal theory is

crucial to describe the Kelvin-Helmholtz instability driven by transverse velocity shear (Mikhailovskii, 1974).

Based upon the assumptions discussed above, the fundamental fluid equations used in the analysis are continuity and momentum transfer in the neutral frame of reference:

$$\frac{\partial n_\alpha}{\partial t} + \nabla \cdot (n_\alpha \underline{V}_\alpha) = 0, \quad (1)$$

$$0 = \underline{E} + \frac{1}{c} \underline{V}_e \times \underline{B}, \quad (2)$$

$$m_i \left(\frac{\partial}{\partial t} + \underline{V}_i \cdot \nabla \right) \underline{V}_i = e \underline{E} + \frac{e}{c} (\underline{V}_i \times \underline{B}) - m_i v_{in} \underline{V}_i + m_i \underline{g}. \quad (3)$$

where α denotes species (e for electrons; i for ions).

The equilibrium velocities are, for electrons

$$\underline{V}_{e0}(x) \equiv \underline{V}_0(x) = (c/B) \underline{E}_0(x) \times \hat{z}, \quad (4)$$

and for ions (to order v_{in}/Ω_i)

$$\underline{V}_{i0}(x) = (c/B) \left\{ [\underline{E}_0 + (m_i/e)\underline{g}] \times \hat{z} + (v_{in}/\Omega_i) [\underline{E}_0 + (m_i/e)\underline{g}] + (1/\Omega_i) (\underline{V}_{i0} \cdot \nabla) \underline{E}_0 \right\} \quad (5)$$

where $\Omega_i = eB/m_i c$. The electrons simply $\underline{E} \times \underline{B}$ drift, while the ions drift with \underline{V}_{i0} , which incorporates the $\underline{E} \times \underline{B}$ drift, and the effects of gravity and the polarization electric field.

We substitute $\underline{E} = -\nabla\phi = -\nabla(\phi_0(x) + \delta\phi)$, $\underline{V}_\alpha = \underline{V}_{\alpha 0}(x) + \delta\underline{V}_\alpha$, $n = n_0(x) + \delta n$ into Eqs. (1) - (3). To obtain the perturbed velocities we do not Fourier analyze the perturbed quantities in the x direction since the

equilibrium quantities vary in that direction; we Fourier analyze only in the y direction. Linearizing Eqs. (2) and (3) and making use of Eqs. (4) and (5), we find the perturbed velocities to be

$$\delta \underline{v}_e = (c/B) [ik_y \delta \phi \hat{x} + \frac{\partial}{\partial x} \delta \phi \hat{y}], \quad (6)$$

$$\begin{aligned} \delta \underline{v}_i = & \frac{(c/B)}{(1 + V_0^2/\Omega_i^2)} [-ik_y \delta \phi + \frac{i\tilde{\omega} - v_{in}}{\Omega_i} \frac{\partial}{\partial x} \delta \phi] \hat{x} \\ & + (c/B) [\frac{\partial}{\partial x} \delta \phi - \frac{\tilde{\omega} + iv_{in}}{\Omega_i} k_y \delta \phi] \hat{y}, \end{aligned} \quad (7)$$

where $\tilde{\omega} = \omega - k_y V_0(x)$ and $V_0 = V_{0y} = -(c/B) E_{0x}$.

We substitute Eqs. (6) and (7) into Eq. (1), to obtain

$$\frac{\partial}{\partial t} \delta n_e + ik_y V_0 \delta n_e - i \frac{c}{B} k_y \delta \phi n_0' = 0 \quad (8)$$

and

$$\begin{aligned} \frac{\partial}{\partial t} \delta n_i - \frac{c}{B} \Omega_i n_0 [(-i\omega + v_{in} + k_y V_0) (\frac{\partial^2}{\partial x^2} - k_y^2) \delta \phi \\ + ik_y V_0' \delta \phi + v_{in}' \frac{\partial}{\partial x} \delta \phi] \\ - \frac{c}{B} ik_y (1 - V_0^2/\Omega_i^2) n_0' \delta \phi \\ - \frac{c}{B} \Omega_i (-i\omega + v_{in} + ik_y V_0) n_0' \frac{\partial}{\partial x} \delta \phi \\ + (g/\Omega_i - V_0) ik_y \delta n_i + (v_{in}/\Omega_i) (g/\Omega_i - V_0) \frac{\partial}{\partial x} \delta n_i \\ + \frac{\delta n_i}{\Omega_i} [(g/\Omega_i - V_0) v_{in}' + v_{in} V_0'] = 0 \end{aligned} \quad (9)$$

where we have ignored terms of order $O(\omega/\Omega_i)$ but have retained terms proportional to ω/v_{in} and the derivatives of the equilibrium quantities with respect to x (indicated by the primes). We now subtract the electron continuity equation, Eq. (9), from the ion continuity equation, Eq. (10), and impose quasineutrality ($\delta n_e = \delta n_i$). We use Eq. (8) to eliminate δn_i and obtain the mode structure equation

$$\frac{\partial^2}{\partial x^2} \delta\phi + p \frac{\partial}{\partial x} \delta\phi + q \delta\phi = 0, \quad (10)$$

where

$$p = \frac{n'_0}{n_0} + \frac{iv_{in}}{(\tilde{\omega} + iv_{in})} \left(\frac{v'_{in}}{v_{in}} - \frac{(n'_0/n_0)k_y v_0}{\tilde{\omega}} \right) \quad (11)$$

$$q = -k_y^2 + \frac{k_y(V'_0 (n'_0/n_0) + V''_0)}{(\tilde{\omega} + iv_{in})} + \frac{k_y^2 g (n'_0/n_0)}{\tilde{\omega} (\tilde{\omega} + iv_{in})} - \frac{iv_{in} k_y v_0}{\tilde{\omega} (\tilde{\omega} + iv_{in})} \left[\frac{\omega}{\tilde{\omega}} (n'_0/n_0)(V'_0/V_0) + (n'_0/n_0) + (v'_{in}/v_{in})(n'_0/n_0) \right] \quad (12)$$

Note that the solution of Eq. (10) allows for wavepacket formation instead of plane waves. The properties of the wavepacket are governed by the coefficients p and q . From the expression for q we see that the second term involves the free energy associated with the inhomogeneous plasma flow giving rise to Kelvin-Helmholtz instability. The third term has the gravity and the inverted density gradient leading to Rayleigh-Taylor instability. The last term becomes important in the moderately collisional domain.

Now we define the following dimensionless parameters in order to cast Eq. (10) into a dimensionless form

$$\hat{\omega} = \omega/(g/L)^{1/2}, \quad \hat{v} = v_{in}/(g/L)^{1/2}, \quad \hat{v}_0 = v_0/(gL)^{1/2}, \quad \text{and} \quad \hat{k} = k_y L \quad (13)$$

where L is the characteristic inhomogeneity scale length. We also normalize x with L and define a new independent variable $\chi \equiv x/L$. With these definitions, Eqs. (10)-(12) become

$$\frac{\partial^2}{\partial \chi^2} \delta\phi + p \frac{\partial}{\partial \chi} \delta\phi + q \delta\phi = 0, \quad (14)$$

$$p = (n_0/n'_0) + i \frac{\hat{v}}{\omega_2} \left[\frac{\hat{v}'}{\hat{v}} - \frac{(n'_0/n_0) \hat{k} \hat{v}_0}{\hat{\omega}_1} \right], \quad (15)$$

$$q = -\hat{k}^2 + \hat{k} \left\{ \frac{[\hat{v}'_0 (n'_0/n_0) + \hat{v}'_0]}{\hat{\omega}_2} + \frac{\hat{k}^2 (n'_0/n_0)}{\hat{\omega}_1 \hat{\omega}_2} \right\} - \frac{i \hat{v}}{\hat{\omega}_1 \hat{\omega}_2} \hat{k} \hat{v}_0 [(\hat{v}'_0/\hat{v}_0)(n'_0/n_0)(\hat{\omega}/\omega) + (n'_0/n_0) + (n'_0/n_0)(\hat{v}'/\hat{v})] \quad (16)$$

where $\hat{\omega}_1 = \hat{\omega} - \hat{k} \hat{v}_0(\chi)$ and $\hat{\omega}_2 = \hat{\omega}_1 + i \hat{v}$.

We use the transformation

$$\delta\phi(\chi) = \psi(\chi) e^{-\int^{\chi} p(\eta) d\eta} \quad (17)$$

to write the Eq. (14) as

$$\psi'' + Q(x) \psi = 0, \quad (18)$$

where

$$Q(x) = q(x) - p'(x)/2 - p(x)^{2/4}. \quad (19)$$

In solving the eigenvalue problem, we use WKB boundary conditions on ψ :

$$\psi \rightarrow (1/Q)^{1/4} \exp\left(-\int_0^x Q(\eta) d\eta\right) \quad \text{as } x \rightarrow \pm \infty. \quad (20)$$

We refer to $Q(x)$ as the potential function and we give the plots of $Q(x)$ and ψ when we solve Eq. (18) numerically in the next section.

Equations similar to Eq. (18) have been obtained by several authors studying the stability of stratified shear layers in neutral fluids (Drazin, 1958). However, usually a Rayleigh-Taylor stable density profile was chosen, mainly to examine the influence of inertia on the velocity shear induced mixing phenomenon. This situation differs slightly from the one considered in this paper, since we study a situation where inverted density gradients and velocity shear both are sources of free energy. The collisionless case can be compared with the neutral fluid case, and when we set $\hat{v} = 0$, in Eqs. (14)-(16) we regain the mode structure equation obtained by Drazin (1958). Drazin (1958) considers a weakly inhomogeneous plasma, i.e., by setting n'_0/n_0 to zero everywhere except in the driving term containing the gravity, and obtains a simple equation

$$\psi'' + \left[-\hat{k}^2 + \frac{R}{(\alpha - v_0)^2} + \frac{v_0''}{(\alpha - v_0)} \right] \psi = 0 \quad (21)$$

where

$$R \equiv \frac{(g/L)}{(\bar{v}_0/L)^2} \quad (22)$$

and $\alpha = \omega/k_y$. For this weakly inhomogeneous case, the analysis shows that a neutral stability boundary (where the real and the imaginary parts of c are zero) can be obtained as

$$R = \hat{k}^2(1 - \hat{k}^2). \quad (23)$$

This implies that for $R < 1/4$ the system is stable. Hamieri (1979) considered a more general case applicable to a Tormac machine and arrived at a less stringent condition. A theoretical analysis in the collisionless and collisional cases will be presented in a future paper.

III. Analysis and Results

The generalized mode structure equation [Eq. (14)] can be better understood by first considering two limiting cases: (A) the collisionless and collisional Rayleigh-Taylor instability without velocity shear, and (B) the Kelvin-Helmholtz instability with no collisions or gravity.

A. Rayleigh-Taylor Instability

Setting $V_0 = 0$ in Eq. (14) we obtain

$$\psi'' + (n'_0/n_0) \psi' - \hat{k}^2 \left[1 - \frac{n'_0/n_0}{\hat{\omega}(\hat{\omega} + i\nu)} \right] \psi = 0 \quad (24)$$

Eq. (24) can be solved in the local approximation,

$$\psi(x) \propto \exp(ik_x x); \quad k_y^2 L^2 \gg k_x^2 L^2 \gg 1 \quad (25)$$

and we obtain the well known dispersion relation (Haerendel, 1974; Hudson and Kennel, 1975)

$$\omega^2 + i\nu_{in} \omega + g/L_n = 0 \quad (26)$$

which has the solution

$$\omega = -\frac{i\nu_{in}}{2} \left[1 \pm (1 - 4g/L_n \nu_{in}^2)^{1/2} \right], \quad (27)$$

where $L_n^{-1} = \frac{1}{n_0} \frac{\partial n_0}{\partial x}$. Instability can occur when $g/L_n < 0$. The collisionless and collisional solutions are, respectively,

$$\omega = \pm (g/L_n)^{1/2} \quad v_{in} \ll |2(g/L_n)^{1/2}|, \quad (28)$$

$$\omega = -i (g/L_n)/v_{in} \quad v_{in} \gg |2(g/L_n)^{1/2}|. \quad (29)$$

We now solve Eq. (24) numerically for a density profile

$$n_0 = \bar{n}_0 \exp(-\frac{\chi^2}{2}) + \Delta n. \quad (30)$$

The results are shown in Fig. 2, which is a plot of normalized growth rate, $\hat{\gamma} = \gamma/(g/L)^{1/2}$, vs normalized wave numbers, $\hat{k} = k_y L$. Curve A is for the collisionless Rayleigh-Taylor instability and curve B is for the collisional Rayleigh-Taylor instability with $\hat{v} = 0.5$. We use $\Delta n/n_0 = 0.01$ for both cases. As expected, the growth rate maximizes in the regime $\hat{k} \gg 1$ and the maximum growth rate agrees well with the growth rate predicted by local theory [Eq. (27)] with the growth rate evaluated at the maximum density gradient. The potential function ($Q(\chi)$ given by Eq. (19)) and the wave function ($\psi(\chi)$), corresponding to $\hat{k} = 1.0$ are shown in Figs. 3 and 4, respectively. We note that for $\Delta = 0.01$, n'_0/n_0 has a maximum at $\chi = -2.4$ and a potential well [$-Q(x)$ is a minimum] is formed around this point as can be seen from Fig. 3. We see from Fig. 4 that the wave function also localizes at $\chi = -2.4$. The negative sign implies that the Rayleigh-Taylor instability is active where the density gradient opposes the gravity. We note that the wave function spreads out into the positive region of the x -axis, where the Rayleigh-Taylor instability is locally stable (gravity acts in the same direction as the density gradient).

B. Kelvin-Helmholtz Instability

We retain the flow velocity $V_0 = V_0(x)$ but consider a collisionless, uniform fluid with no gravity. Eq. (14) becomes

$$\psi'' + \left[-k_y^2 + \frac{k_y V_0'}{(\omega - k_y V_0)} \right] \psi = 0, \quad (31)$$

which is well known (Mikhailovskii, 1974). Rayleigh's theorem (Mikhailovskii, 1974) predicts an instability if the velocity profile has a vanishing second derivative between the boundaries, i.e., $[\partial^2 V_0 / \partial x^2]_{x_0} = 0$, where $x_1 < x_0 < x_2$ and x_1 and x_2 are the boundaries.

Equation (31) is solved for an equilibrium velocity profile

$$V_0 = \bar{V}_0 \tanh(x/L) \hat{y} \quad (32)$$

and the results are shown in Fig. 5 (curve A) in which we plot $\gamma/(V_0/L)$ versus $k_y L$. The instability is purely growing and is bounded between $k_y L = 0$ and 1 with a maximum growth rate of $\gamma \sim 0.18 (V_0/L)$ at $k_y L \approx 0.45$ (Michalke, 1964).

When a density gradient is included, we arrive at the following equation

$$\psi'' + (n_0'/n_0) \psi + \left[-k_y^2 + \frac{[V_0'' + V_0' (n_0'/n_0)]}{(\omega - k_y V_0)} \right] \psi = 0. \quad (33)$$

Using the same procedure as outlined following Eq. (31), we can show that for instability the density and velocity profiles should be such that

$\left[\frac{1}{n_0} \frac{\partial}{\partial x} (n_0 V_0') \right]_{x_0} = 0$ where x_0 is any point within the boundaries. It is interesting to note from Eq. (33) that no instability exists if the density and velocity profiles are such that $V_0''/V_0' = -n_0'/n_0$. Equation (33) is

solved numerically for the velocity profile given in Eq. (32) (in this example we have set the density and shear scale lengths to be equal). The properties of this mode are shown in curve B of Fig. 5 for an exponentially decreasing density profile. Two features are to be noted here: (1) that the density gradient has a stabilizing influence which reduces the maximum growth rate from $\gamma = 0.18 (V_0/L)$ to $\gamma = 0.074 (V_0/L)$, and (2) that the instability exists in the region $0.1 < k_y L < 0.9$ shifting the wave number at which the growth rate maximizes from $k_y L = 0.45$ to $k_y L = 0.55$.

1V. Generalized Rayleigh-Taylor Instability

In the previous section we considered the limiting cases where an inverted density gradient in the presence of gravity and a velocity shear individually give rise to different instabilities. We now consider the general problem where both free energy sources jointly give rise to a generalized Rayleigh-Taylor instability (Hamieri, 1979; Vinas, 1980).

We consider two different cases: (A) a self-consistent equilibrium, and (B) a general equilibrium based on the experimental observations.

A. Self-consistent Equilibrium

We choose the following density profile

$$n_0(x) = \bar{n}_0 (1 + \epsilon \tanh(x/L)) / (1 - \epsilon), \quad (34)$$

and the following velocity profile

$$V_0(x) = \bar{V}_0 (\bar{n}_0 / n_0(x)) \quad (35)$$

such that

$$\hat{V}_0 = \frac{\bar{V}_0}{(gL)^{1/2}} \frac{\bar{n}_0}{n_0(x)} \equiv \hat{s} \frac{\bar{n}_0}{n_0(x)},$$

where we have defined a dimensionless parameter $\hat{s} \equiv \bar{V}_0 / (gL)^{1/2}$. Note that the zeroth order continuity equation is satisfied by these profiles for v_{in} constant, i.e.,

$$\frac{\partial}{\partial x} [(n_0(x) V_{10x}(x))] = 0. \quad (36)$$

which implies

$$n_0(x) E_0(x) = \text{constant}$$

or using the definition of V_0 from Eq. (4),

$$n_0(x) V_0(x) = \text{constant}.$$

We solve Eq. (14) numerically using these profiles and present the results below.

In Fig. 6 we plot the normalized growth rate $\hat{\gamma}$ versus \hat{k} for the collisionless and collisional cases. The solid lines represent the collisionless case ($\hat{\nu} = 0$) and the dashed lines represent the collisional case ($\hat{\nu} = 0.5$). We set $\epsilon = 0.8$ in the density profile. Several points are to be noted in this figure. First, we note that in a shear-free, collisionless Rayleigh-Taylor plasma the growth rate asymptotes to the local growth rate evaluated at the peak density gradient, (solid line), i.e.,

$$\gamma(\hat{k} \gg 1) = \left[g(n'_0 / n_0) \right]_{\chi = \bar{\chi}}^{1/2}. \quad (37)$$

For the density profile given in Eq. (36) n'_0/n_0 maximizes at $\bar{\chi}$ obtained from

$$\tanh \chi = [-1 \pm (1 - \epsilon^2)^{1/2}] / \epsilon. \quad (38)$$

For $\epsilon = 0.8$ Eq. (38) yields $\bar{\chi} = -0.55$ and using this in Eq. (37) we find the local growth rate to be $\hat{\gamma} = 1.0$. This agrees with the growth rate for large \hat{k} (see Fig. 6, solid line). Second, we find that ion-neutral collisions have a stabilizing influence as seen from the dashed line, which represents the growth rate curve for $\hat{v} = 0.5$ and $\hat{s} = 0$. Third, in a collisionless Rayleigh-Taylor unstable plasma, for $\hat{s} = 1.0$ (shear frequency, \bar{V}_0/L , equal to $\sqrt{g/L}$) velocity shear stabilizes the short wavelength modes (solid line; $\hat{s} = 1.0$); the cut-off mode number, where the growth rate becomes zero, is $\hat{k}_c \sim 11.0$. As a result the growth rate maximizes at $\hat{k} \sim 1.5$ and has a maximum value $\hat{\gamma}_m = 0.675$. Fourth, in a collisional plasma also, with $\hat{v} \sim 0.5$ the short wavelength modes are completely stabilized (dashed line; $\hat{s} = 1.0$). The cut-off mode number in this case is, $\hat{k}_c \sim 10.0$, which is less than that of the collisionless case. The peak growth rate is also smaller with $\hat{\gamma}_m = 0.45$ occurring at $\hat{k} = 1.5$. We see that the ion-neutral collisions not only reduce the growth rate but also reduce the cut-off mode number.

In Fig. 7 we give the plots of the wavefunction for $\hat{s} = 0$, $\hat{k} = 0.5$, $\hat{v} = 0.5$, and $\epsilon = 0.8$. We note that the wavefunction localizes at $x_0 = -0.55$ which is the point where the density gradient (n'_0/n_0) has an extremum. The wavefunction localizes at this point because $Q(\chi)$ has a local minimum. We refer to this point (for $\hat{s} = 0$) as the Rayleigh-Taylor localization point. The negative sign indicates that the density gradient has to oppose the gravity for instability.

In Fig. 8 we give the wavefunction for the case $\hat{s} = 1$ with the same v_{in} and ϵ as in Fig. 7. The solid and the dotted lines represent the real and imaginary parts of the wavefunction, respectively. We note that when

the velocity shear is introduced into the problem, the wavefunction picks up an imaginary part. Furthermore, we find that for $\hat{k} \geq 1$, the wavefunction localizes at a point closer to the origin in the velocity shear layer.

In comparing our results with Drazin (1958) we note that since we use a density profile whose density gradient is not a constant, and since we have a Raleigh-Taylor unstable plasma, our threshold condition on R is quite different. This aspect will be dealt with in a future paper.

B. General Equilibrium

Recent experimental observations, made during equatorial spread F (ESF) (Kudeki et al., 1981) and in the high latitude ionospheric F region (Kelley et al., 1978), indicate that ionospheric plasmas usually support inhomogeneous equilibrium plasma flows. In the case of ESF it was found that the flow velocity reverses its direction as a function of altitude (\hat{x} , the direction of the density gradient). Furthermore, the velocity reversal point moves up as the spread F develops. This equilibrium situation, where the flow velocity profile is not related to the density profile in a simple manner, is generated by the coupling of the plasma to the neutral atmosphere, for example, by the neutral winds and the inherent shear in the neutral wind velocity or in the case of ESF due to an incomplete coupling caused by background ionospheric Pedersen conductivity away from the equatorial plane (Zalesak et al., 1982). Our earlier numerical results indicate that the inhomogeneity in $\omega - k_y V_0(x)$, and not necessarily the V_0' and V_0'' , is primarily responsible for stabilizing the short wavelength interchanger modes (Huba et al., 1983). Therefore, based on the experimental observations (Kudeki et al., 1981; Tsunoda et al., 1981) and our numerical results (Huba et al., 1983), we choose the following density and velocity profiles for a general equilibrium study:

$$n_0(x) = \bar{n}_0 (1 + \varepsilon \tanh x)/(1 - \varepsilon) \quad (39)$$

$$V_0(x) = \bar{V}_0 \tanh (x - x_0) \quad (40)$$

where x_0 is the velocity reversal point (in the ionospheric case, x_0 is the point where the westward flow becomes eastward). Using these profiles we solve Eq. (14) numerically. Also, for simplicity, we choose the density gradient scale length and velocity shear scale length to be equal. The numerical results are given below.

First we study the role of x_0 on stability and determine the optimum x_0 to be used in later calculations. We set $\hat{v} = 0.5$ and $\varepsilon = 0.8$. In Fig. 9 we plot the normalized growth rate $\hat{\gamma}$ versus \hat{k} . Curve A shows the nonlocal collisionless Rayleigh-Taylor instability ($\hat{s} = 0$). Curves B, C, and D correspond to $\hat{s} = 1$ for different values of x_0 . Curve B gives the growth rates for $\hat{s} = 1$ and $x_0 = -2.0$ which shows a significant reduction in the growth rate. The growth rate maximizes with $\hat{\gamma} = 0.52$ at $\hat{k} \sim 3.0$. However, when x_0 is set to -0.55 (the Rayleigh-Taylor localization point) the growth rate is sharply reduced, maximizing at $\hat{k} \sim 0.5$ with $\hat{\gamma} = 0.256$ (curve C). For $x_0 = 0$ (curve D) there is a significant reduction in the growth rate and a severe reduction of the \hat{k} domain for instability. The instability is bounded between $\hat{k} = 0.5$ and 3.6 . Here, the growth rate peaks around $\hat{k} \sim 1.7$.

For $x_0 = 2.0$ (not shown) the growth rate curve is similar to that of $x_0 = -2.0$ (curve C). From this we conclude that the effects of velocity shear are strongest when the velocity reversal point falls in the Rayleigh-Taylor localization region.

AD-A142 573

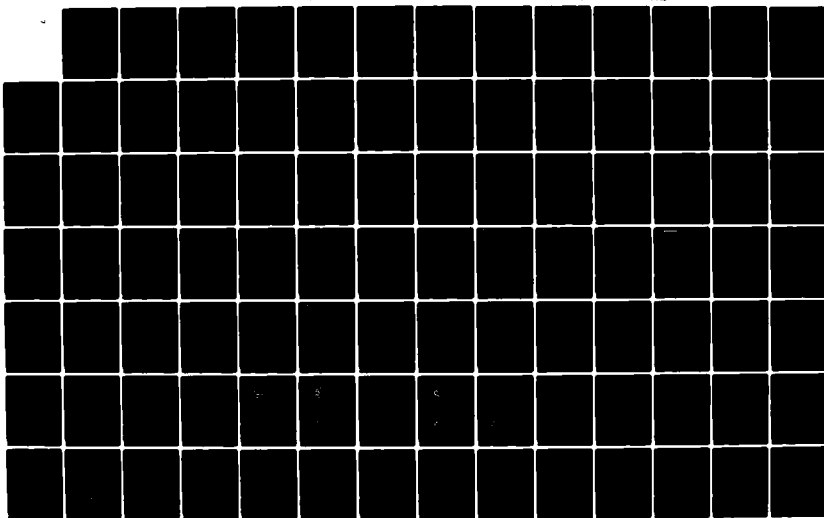
GEOPHYSICAL PLASMAS AND ATMOSPHERIC MODELING(U) SCIENCE
APPLICATIONS INC MCLEAN VA E HYMAN ET AL. MAR 84
SAI-84/1554 SBI-AD-E001 718 N00014-83-C-2034

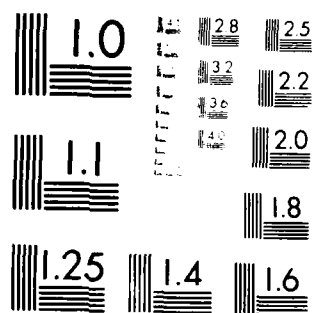
36

UNCLASSIFIED

F/G 4/1

NL





MICROCOPY RESOLUTION TEST CHART
 NATIONAL BUREAU OF STANDARDS-1963-A

In order to throw some light on the variation of the dispersion curves as a function of the velocity shear we plot $\hat{\gamma}$ versus \hat{k} for various values of \hat{s} keeping \hat{v} , ϵ , and χ_0 fixed at 0.5, 0.8, and -0.55, respectively, in Fig. 10. This figure shows that the general (non self-consistent) profiles yield results similar to those of the self-consistent profiles (sec. IV.A; see fig. 6). As \hat{s} is increased, \hat{k}_m the mode number at which the growth rate maximizes, moves towards smaller \hat{k} and the growth rate is substantially reduced. For very large shear, $\hat{s} \gg 1$, the mode becomes purely Kelvin-Helmholtz like, preferentially exciting a long wavelength mode ($\hat{k} \sim 0.45$) with the cut-off \hat{k} less than 1.0 (to be compared with Fig. 5). This aspect is further illustrated in Fig. 11 where we plot $\hat{\gamma}$ versus \hat{s} for several values of \hat{k} . The figure shows that for $\hat{v} = 0.5$, modes with $\hat{k} < 0.8$ are always unstable. No amount of shear (measured in units of \hat{s}) stabilizes these modes due to the onset of the Kelvin-Helmholtz instability for these large \hat{s} and small \hat{k} . Furthermore, for the parameters used in the figure, moderate to strong velocity shear stabilizes modes with $\hat{k} > 0.8$. An empirical estimate of the shear that stabilizes the smallest \hat{k} mode can be obtained from the $\hat{k} = 0.8$ curve in Fig. 11, i.e., $\hat{s} = 2.5$ or $\bar{V}_0/L \sim 2.5 \sqrt{g/L}$; the figure also shows that the critical shear depends on the wavenumber.

From Fig. 10 we see that for $\hat{v} = 0.5$, the mode with $\hat{k} = 0.45$ is the fastest growing mode for large \hat{s} . It is interesting to study the behavior of this mode as a function of \hat{s} . In Fig. 12 we plot $\hat{\gamma}$ (for $\hat{k} = 0.45$) versus \hat{s} . Curves A and B represent the collisionless ($\hat{v} = 0$) and collisional ($\hat{v} = 0.5$) cases respectively. Note that for $\hat{s} = 0$, $\hat{\gamma}$ is purely Rayleigh-Taylor-like; but as \hat{s} increases, $\hat{\gamma}$ initially decreases, which shows that velocity shear is reducing the growth rate of the Rayleigh-Taylor instability. Beyond $\hat{s} > 1$ the velocity shear dominates and the Kelvin-

Helmholtz mode sets in. We note that $\hat{\gamma}$ increases linearly with \hat{s} for large \hat{s} since it is normalized to $\sqrt{g/L}$ and not \bar{V}_0/L . For the collisional case we see that the velocity shear has a stronger influence over a broader domain in \hat{s} and the Kelvin-helmholtz type instability sets in for larger ($\hat{s} > 2.5$).

We see from Fig. 10 that the cut-off mode numbers and the mode numbers where the growth rate maximizes vary significantly as a function of velocity shear. In order to show the values they asymptote to for large velocity shear, we plot the cut off mode numbers \hat{k}_c (curves A), and the mode numbers of the fastest growing modes, \hat{k}_m (curves B) as a function of \hat{s} in Fig. 13. We use $\chi_0 = -0.55$, $\epsilon = 0.8$, and $\hat{v} = 0$ and 0.5 . Solid lines represent the collisionless case ($\hat{v} = 0$) and dashed lines represent the collisional case ($\hat{v} = 0.5$). From the figure, we see that \hat{k}_m , and \hat{k}_c fall sharply as \hat{s} is increased and asymptote to smaller \hat{k} values. For $\hat{v} = 0$, (solid lines) \hat{k}_m asymptotes to 0.5 and \hat{k}_c asymptotes to 1.0 . Because for large \hat{s} the mode is Kelvin-Helmholtz-like, \hat{k}_m and \hat{k}_c , as expected, attain the values shown in Fig. 5. For $\hat{v} = 0.5$ (dashed lines) both \hat{k}_m and \hat{k}_c are initially smaller than those for the collisionless case. However, as \hat{s} is increased these maximum and cut-off wavenumbers achieve a minimum value, then rise and again asymptote to similar values as those corresponding to the collisionless case, namely 0.5 and 1.0 , respectively.

Finally, in Fig. 14 we show the effects of introducing a spatially dependent collision frequency. In the ionosphere the ion-neutral collision frequency decreases exponentially as a function of the altitude. We use the profile $\hat{v} = 0.5\exp(-x/L)$, choosing the scale length to be the same as the density gradient scale length for simplicity. Curve A shows the growth rate curve for constant collision frequency, $\hat{v} = 0.5$, and for $\hat{s} = 1.0$, and $\epsilon = 0.8$. The growth rate maximizes at $\hat{\gamma}_m = 0.256$ around $\hat{k} = 0.55$. Curve B,

with $\hat{v} = \hat{v}(x)$, shows a drastic reduction in the growth rate. The maximum growth rate ($\hat{\gamma}_m = 0.09$) occurs at $\hat{k} \sim 0.7$. Interestingly, in this case the lowerbound of the instability is shifted. The domain of unstable wave numbers is $0.15 < \hat{k} < 1.2$; whereas, for the constant collision frequency case the domain was $0 < \hat{k} < 1.2$ (the lower bound for curve A is not shown in the figure). Curve C for a weaker shear, namely $\hat{s} = 0.5$, shows that the maximum growth rate is comparable to that of curve A. However, in this case modes with wave numbers $\hat{k} > 3.0$ are completely stabilized.

V. Discussion and Conclusions

We have investigated the influence of velocity shear on the Rayleigh-Taylor instability. The Rayleigh-Taylor instability is driven by gravity and an inverted density gradient. In general this instability is most unstable in the short wavelength domain, $k_y L > 1$, where L is the density inhomogeneity scale length and k_y is perpendicular to the density gradient and the magnetic field. We obtain the well known results that the maximum growth rate is given by $\sqrt{g/L}$ ($g/v_{in} L$) in the collisionless (collisional) domain. On the other hand, a sheared transverse velocity drives the Kelvin-Helmholtz instability in the long wavelength domain, $k_y L < 1$. In the presense of transverse velocity shear, the short wavelength spectrum ($k_y L > 1$) of the Rayleigh-Taylor instability is strongly suppressed or stabilized and the growth rate maximizes in the long wavelength domain ($k_y L < 1$). Thus, velocity shear causes a long wavelength mode to be preferentially excited; whereas in the absense of velocity shear the dominant wave mode usually has a shorter wavelength determined by initial conditions or non-linear processes. This prominent conclusion had been stated in an earlier paper (Guzdar et. al., 1982, 1983). We note that the wavepacket generally localizes in the region where the density gradient opposes the gravity, which in our case also happens to be the shear layer. The wave function falls off rapidly away from the localization region of the Rayleigh-Taylor instability, but still has some finite amplitude in the stable region (where $g \cdot \nabla n$ is positive). This is due to the global sampling of the entire density profile.

Another interesting feature of the generalized (including velocity shear) Rayleigh-Taylor instability is its crucial dependence on the velocity reversal-point. In the absense of velocity shear, the wave function localizes at a point, say x_w , determined primarily by the background density profile. In the

case of the hyperbolic tangent density profile (Eq. 34), the wave function localizes in the region where the density gradient opposes the gravity. If the velocity reversal point, χ_0 (where the y-component of the equilibrium velocity changes sign), is in the region where the density gradient is parallel to the gravity, the velocity shear has a generally stabilizing influence without the characteristic peak in the growth rate vs wave number curve in the long wavelength domain (Fig. 9). However, when $\chi_w = \chi_0$, velocity shear reduces the growth rate significantly and moves the peak toward longer wavelengths, preferentially exciting longer wavelength modes.

Two possible applications of this theory to ionospheric phenomena have been discussed in a previous paper (Guzdar et al., 1982, 1983). Briefly, the major feature of this theory, viz., preferential excitation of a long wavelength mode, may explain (1) the structuring (1-3 km) of barium releases which are injected across the magnetic field (Linson et al., 1980; Wescott et al., 1980), and (2) the long wavelength (few hundred kms) oscillations of the bottomside F layer during equatorial spread F (Tsunoda and White, 1981; Kelley et al., 1981).

The shaped barium release experiment (Wescott et al., 1980) was conducted at high latitudes in the presence of a pulsating aurora at an altitude of 571 km. Numerical simulations showed that a charge separation induced radial polarization electric field results in an $\underline{E} \times \underline{B}$ velocity shear. This shear layer seems to be located in the region where the density gradient is steepest (Wescott et al., 1980). Our analysis does not strictly apply in the auroral environment. However, the basic instability leading to structuring of the barium cloud is possibly a Rayleigh-Taylor type instability (Phillip, 1971; Fedder, 1980) due to the deceleration of the cloud (Scholer, 1970). So our results in the collisionless domain could be applied to this case. For

example, gradient scale sizes of 500 m - 1 km can lead to irregularity scale sizes of 1.5 - 3 kms with growth rates $\sim 10^{-2} \text{ sec}^{-1}$.

Kudeki et al. (1981) have shown, from the observations at Jicamarca using a Radar interferometer technique, that the velocity reversal point moves upward as the spread-F structures evolve. The position of the F-peak was not available at the time of these measurements. However, we conjecture that since the velocity reversal point is at a different location with respect to the F-peak at different times, the velocity shear induced long wavelength modulations of the bottom side F-layer may not be apparent at all times, but may be seen when the velocity reversal point is in the Rayleigh-Taylor localization region (namely, in the bottom side of the F region).

Tsunoda (1983) recently has shown that the background density gradient has a scale length of 25 km when long wavelength fluctuations were observed in the bottom side of the F-layer. No velocity shear measurements, such as the strength of the shear or velocity reversal point, were available. We point out that the measured absence of the velocity shear prior to or immediately after the onset of the wave-like structure is expected because ALTAIR needs the formation of the bubble and spike structures to measure the plasma velocities. Despite the lack of shear data in his paper there is reasonable agreement between the data and the theoretical results. However, data on velocity shear, for example by alternate techniques, are crucial to confirm or disprove the theory. The question of short circuiting effects by the E-layer, raised by Tsunoda (1983), needs a closer examination and is not addressed here.

Similar results were obtained by Vinas (1980) in connection with the investigations of the erosion of the plasmopause. He conjectured that strong velocity shear could exist in the plasmopause region and lead to long

wavelength irregularities in competition with the ballooning mode type interchange phenomenon. However, an important difference exists in comparing Vinas' theory with ours, namely, that g/L is positive in his case, meaning that the heavy fluid supports the lighter fluid. We also find similar results in the topside of the equatorial ionosphere, where gravity acts in the same direction as that of the density gradient (a situation similar to Vinas' case) and the collision frequency is very small. These results indicate that in a Rayleigh-Taylor stable plasma the velocity shear could excite Kelvin-Helmholtz type modes. Thus we can conclude that in the absence of equatorial spread F if the flow velocity in the topside ionosphere is sufficiently strongly inhomogeneous, it can induce some large scale irregularities. Figure 5 (curve B) shows that if sufficient velocity shear exists, irregularities of scale sizes of ~ 300 km with weak growth rates (10^{-3} s^{-1}) could possibly exist in the weakly collisional topside of the ionosphere.

In conclusion, we have shown that:

- (i) Sheared plasma velocity flows can have pronounced effects on the collisional and collisionless Rayleigh-Taylor instabilities. Sufficiently strong velocity shear preferentially excites a long wavelength mode. This result may explain the long wavelength oscillations of the bottomside F layer during equatorial spread F and the prompt structuring of injected barium clouds (Guzdar et al., 1982; 1983).
- (ii) Since the wavefunction localizes in the Rayleigh-Taylor unstable region we expect these long wavelength fluctuations to be seen at the bottomside of the F-layer.

- (iii) This phenomenon is most likely to occur when the velocity reversal point is within the Rayleigh-Taylor localization region (where gravity opposes the density gradient).
- (iv) The generalized Rayleigh-Taylor instability is qualitatively similar but has quantitatively different properties in the collisional and collisionless domains (see fig. 12). The cut-off mode numbers and maximally growing mode numbers are different in these two cases (see fig. 13).
- (v) The properties of the Rayleigh-Taylor instability are similar for self-consistent as well as for general equilibrium density and velocity profiles.
- (vi) As the velocity shear is increased, the cut-off mode numbers and the maximally growing mode numbers asymptote to values similar to those of the collisionless Kelvin-Helmholtz instability (see fig. 12).
- (vii) A spatially dependent collision frequency alters the results drastically by reducing the growth rate, and by restricting the band of unstable wave numbers to a smaller region (see fig. 14).

ACKNOWLEDGMENTS

This work has been supported by Defence Nuclear Agency and Office of Naval Research. We thank P. Chaturvedi for helpful discussions.

REFERENCES

- Bodner, S.E., Rayleigh-Taylor instability and laser-pellet fusion, Phys. Rev. Lett., 83, 761, 1974.
- Chandrasekhar, S., Hydrodynamic and Hydromagnetic Stability, Int. Ser. Monographs on Physics, Clarendon Press, Oxford, 1961, p. 494.
- Coppi, B., and M.N. Rosenbluth, Collisional interchange instabilities in shear and Jdl/B stabilized systems, in Proceedings of the 1965 International Conference on Plasma Physics and controlled Nuclear Fusion Research, Paper CN-21/106, International Atomic Energy Agency, Vienna, 1966.
- Coppi, B., J. Filreis, and F. Pegoraro, Analytical representation and physics of ballooning modes, Ann. Phys. (N.Y.) 121, 1, 1979.
- Daly, B.J., Numerical study of the fluid Rayleigh-Taylor instability, Phys. Fluids., 10, 297, 1967
- Davis, T.N., G.J. Romick, E.M. Wescott, R.A. Jeffries, D.M. Kerr, and K.M. Peek, Observations of the development of striations in large barium clouds, Planet. Space Sci., 22, 67, 1974.
- Drazin, P.G., The stability of a shear layer in an unbounded heterogeneous inviscid fluid, J. Fluid Mech., 4, 214, 1958.
- Emery, M.H., J.H. Gardner, and J.P. Boris, The Rayleigh-Taylor and Kelvin-Helmholtz instabilities in targets accelerated by laser ablation, Phys. Rev. Lett., 48, 677, 1982.
- Fedder, J.A., Structuring of collisionless, high velocity ion clouds, Memo Rept. 4307, Nav. Res. Lab., Washington, D.C., September, 1980.
- Fejer, B.G., and M.C. Kelley, Ionospheric irregularities, Rev. Geophys. Space Phys., 18, 401, 1980.

- Guzdar, P.N., P. Satyanarayana, J.D. Huba, and S.L. Ossakow, Influence of velocity shear on Rayleigh-Taylor instability, Geophys. Res. Lett., 9, 547, 1982.
- Guzdar, P.N., P. Satyanarayana, J.D. Huba, and S.L. Ossakow, Correction to "Influence of velocity shear on Rayleigh-Taylor instability", Geophys. Res. Lett., 10, 492, 1983.
- Haerendel, G. Theory of equatorial spread F, Preprint, Max-Planck Institute for Physik und Astrophysik, Garching, West Germany, 1974.
- Hamieri, E., Shear stabilization of the Rayleigh-Taylor modes, Phys. Fluids., 22, 89, 1979.
- Harlow, F.H. and J.E. Welch, Numerical study of large amplitude free-surface motions, Phys. Fluids., 9, 842, 1966.
- Huba, J.D., S.L. Ossakow, P. Satyanarayana, and P.N. Guzdar, Linear theory of the $E \times B$ instability with an inhomogeneous electric field, J. Geophys. Res., 88, 425, 1983.
- Hudson, M.K., and C.F. Kennel, Linear theory of equatorial spread F, J. Geophys. Res., 80, 4581, 1975.
- Kelley, M.C., M.F. Larsen, C. La Hoz, and J.P. McClure, Gravity wave initiation of equatorial spread F: A case study, J. Geophys. Res., 86, 9087, 1981.
- Kelvin, Lord, Hydrodynamics and General Dynamics, Cambridge University Press, Cambridge, 1910, p. 69
- Kudeki, E., B.G. Fejer, D.R. Farley, and H.M. Ierick, Interferometer studies of equatorial F region irregularities and drifts, Geophys. Res. Lett., 8, 377, 1981.
- Linson, L.M., and J.B. Workman, Formation of striations in ionospheric plasma clouds, J. Geophys. Res., 75, 3211, 1970.

- Michalke, A., On the inviscid instability of the hyperbolic-tangent velocity profile, J. Fluid Mech., 19, 543, 1964.
- Mikhailovskii, A.B., Theory of Plasma Instabilities: Vol. II, Consultants Bureau, New York, 1974, p. 141.
- Ossakow, S.L. Ionospheric irregularities, Rev. Geophys. Space Phys., 17, 521, 1979.
- Perkins, F.W. and J.H. Doles III, Velocity shear and the $E \times B$ instability, J. Geophys. Res., 80, 211, 1975.
- Pillip, W., Expansion of an ion cloud in the earth's magnetic field, Planet. Space Sci., 19, 1095, 1971.
- Rayleigh, Lord, Theory of Sound, Dover Publications, Inc., New York, 1894.
- Rosenberg, N.W., Observations of striation formation in a barium ion cloud, J. Geophys. Res., 76, 6856, 1971.
- Scannapieco, A.J. and S.L. Ossakow, Nonlinear equatorial spread F, Geophys. Res. Lett., 3, 451, 1976.
- Scannapieco, A.J., S.L. Ossakow, S.R. Goldman, and J.M. Pierre, Plasma cloud late time striation spectra, J. Geophys. Res., 81, 6037, 1976.
- Scholer, M., On the motion of artificial ion clouds in the magnetosphere, Planet. Space Sci., 18, 977, 1970.
- Simons, D.J., M.B. Pongratz, and S.P. Gary, Prompt striations in ionospheric barium clouds due to a velocity space instability, J. Geophys. Res., 85, 671, 1980.
- Taylor, G. I., The instability of liquid surfaces when accelerated in a direction perpendicular to their planes. I, Pro. of Roy. Soc., (London) Ser. A201, 192, 1950.
- Tsunoda, R.T., Time evolution and dynamics of equatorial backscatter plumes, 1. Growth phase, J. Geophys. Res., 86, 139, 1981a.

- Tsunoda, R.T., ALTAIR radar study of equatorial spread F, SRI International Final Report, DNA 5689F, February, 1981b.
- Tsunoda, R.T., R.C. Livingston, and C.L. Rino, Evidence of a velocity shear in bulk plasma motion associated with the post-sunset rise of the equatorial F-layer, Geophys. Res. Lett., 8, 807, 1981.
- Tsunoda, R.T., and B.R. White, On the generation and growth of equatorial backscatter plumes-1. Wave structure in the bottomside F layer, J. Geophys. Res., 86, 3610, 1981.
- Tsunoda, R.T., On the generation and growth of equatorial backscatter plumes-2. Structuring of the west wall of the upwellings, J. Geophys. Res., 88, 4869, 1983.
- Viñas, A.F., Magnetohydrodynamic analysis of the stability of the plasma pause, Ph.D. thesis, MIT, 1980.
- Viñas, A.F. and T. Madden, Shear flow ballooning instability as a possible mechanism for micropulsations at the plasma pause, J. Geophys. Res., (submitted, 1983).
- Wescott, E.M., H.C. Stenback-Nielsen, T.J. Hallinan, C.S. Deehr, G.J. Romick, J.V. Olsen, J.G. Roederer, and R. Sydora, A high-altitude barium radial injection experiment, Geophys. Res. Lett., 7, 1037, 1980.
- Zabusky, N.J., J.H. Doles III, and F.W. Perkins, Deformation and striation of plasma clouds in the ionosphere, 2. Numerical simulation of a non-linear two-dimensional model, J. Geophys. Res., 78, 711, 1973.

Zalesak, S.T., and S.L. Ossakow, Nonlinear equatorial spread F: Spatially large bubbles resulting from large horizontal scale initial perturbations, J. Geophys. Res., 85, 2131, 1980.

Zalesak, S.T., S.L. Ossakow, and P.K. Chaturvedi, Nonlinear equatorial spread F: The effect of neutral winds and background Pedersen conductivity, J. Geophys. Res., 87, 151, 1982.

FIGURE CAPTIONS

- Figure 1. Plasma configuration and slab geometry used in the analysis.
- Figure 2. Normalized growth rate $\hat{\gamma} \equiv \gamma/\sqrt{g/L}$ vs $\hat{k} \equiv k_y L$ for the Rayleigh-Taylor instability. Curve A represents the collisionless mode ($\hat{v} = 0$); curve B represents the collisional mode ($\hat{v} = 0.5$), where $\hat{v} = v/\sqrt{g/L}$. The density profile used is a Gaussian-like profile $n_0 e^{-x^2/2L^2} + \Delta n$, with $\Delta n/n_0 = 0.01$.
- Figure 3. Plot of potential term, $Q(x)$, as a function of x for the collisional case and density profile used in Fig. 2.
- Figure 4. Plot of the wavefunction for $\hat{\omega}_r = 0$, $\hat{\gamma} = .693$, $\hat{k} = 1.0$, and for the collisional case and density profile used in Fig. 2.
- Figure 5. Growth rate $\gamma/(\bar{v}_0/L)$ vs $\hat{k} \equiv k_y L$ for the Kelvin-Helmholtz mode. Curve A represents the case $\hat{v} = 0$, $\nabla n = 0$; Curve B represents the case $\hat{v} = 0$, and $n_0 = \bar{n}_0 \exp(-x/L)$.
- Figure 6. Growth rate $\hat{\gamma}$ vs \hat{k} for the generalized Rayleigh-Taylor instability. Solid lines represent the collisionless case ($\hat{v} = 0.0$, $\hat{s} = 0.0$, and 1.0); dashed lines represent the collisional case ($\hat{v} = 0.5$, $\hat{s} = 0.0$, and 1.0). The profiles used are the self-consistent profiles, Eqs. (34) and (35).

Figure 7. The wave function corresponding to Fig. 6 (solid line; $\hat{s} = 0$) and $\hat{k} = 0.5$.

Figure 8. Real and imaginary parts of the wavefunction, corresponding to Fig. 6 (dotted line, $\hat{s} = 1.0$) and $\hat{k} = 0.5$.

Figure 9. Variation of the dispersion curve, $\hat{\gamma}$ vs \hat{k} , for different transition points (χ_0), of the flow velocity profile given by $V = \bar{V}_0 \tanh(\chi - \chi_0)$ for $\chi_0 = -0.5, -2.0$, and 0.0 . Parameters used are $\hat{s} = 1$, $\hat{v} = 0.5$, $\epsilon = 0.8$, and for the profiles given in Eqs. (39) and (40). Curve A corresponds to shear-free case ($\hat{s} = 0$) where as curves B, C, and D correspond to $\hat{s} = 1.0$ and $\chi_0 = -2.0, -0.55$, and 0.0 respectively.

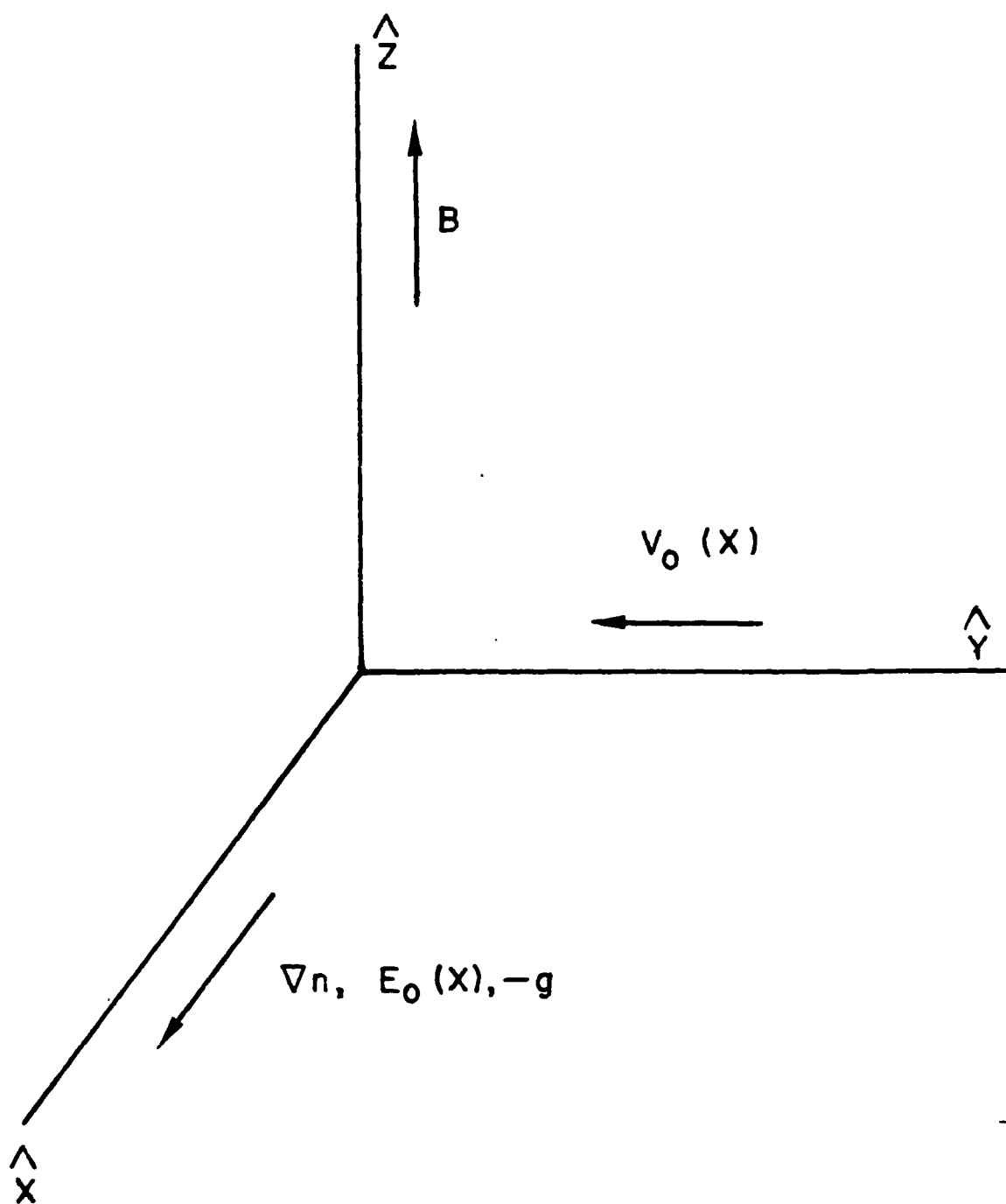
Figure 10. Study of the growth rate as a function of the mode number in the collisional domain $\hat{\gamma}$ vs \hat{k} and for $\hat{s} = 0, 0.25, 1.0, 2.0$, and 4.0 . We have used $\chi_0 = -0.55$, $\hat{v} = 0.5$, and $\epsilon = 0.8$.

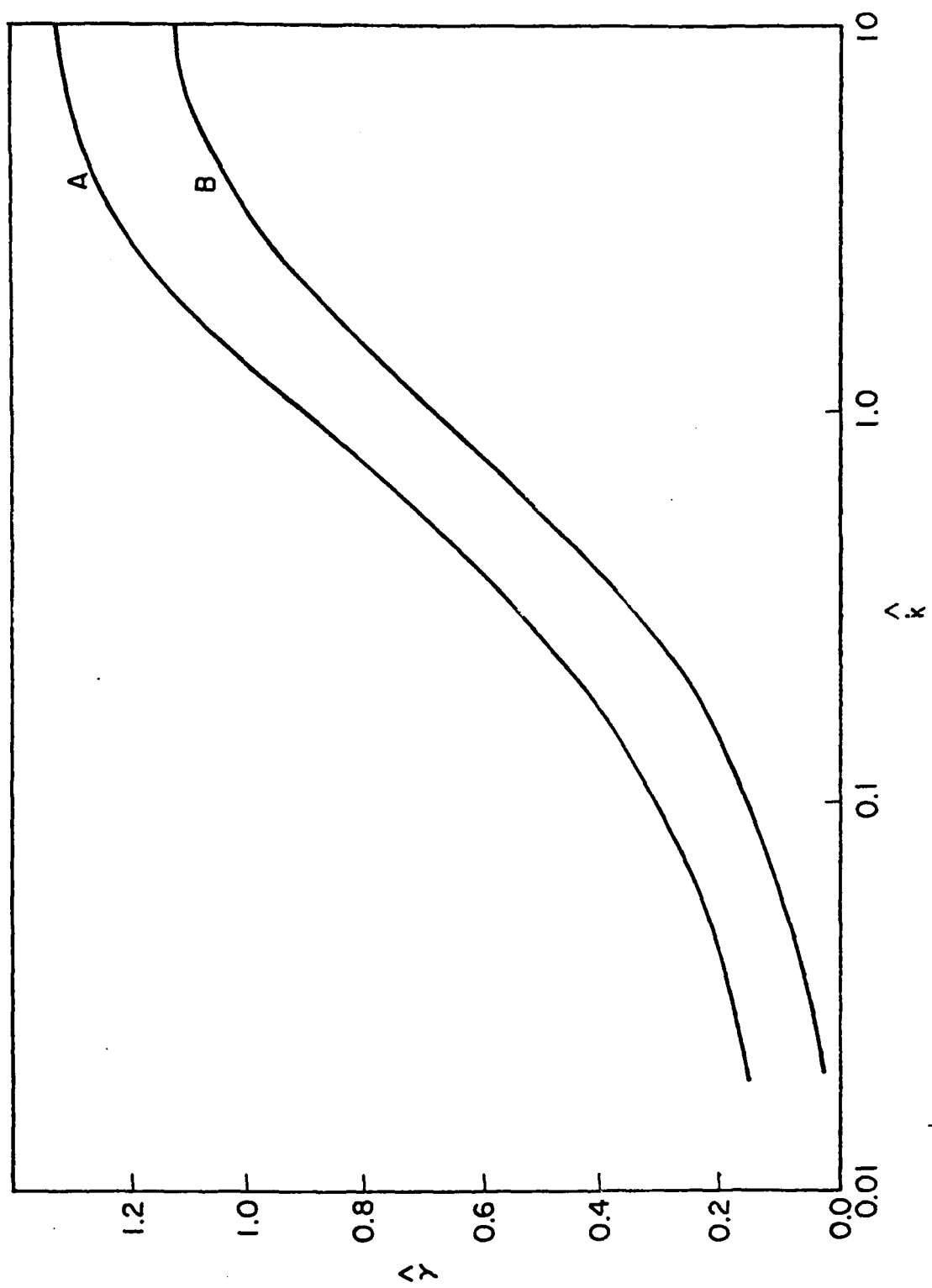
Figure 11. Study of growth rate $\hat{\gamma}$ as a function of \hat{s} for $\hat{k} = 0.4$ thru 2.0 . The parameters used are $\epsilon = 0.8$, $\hat{v} = 0.5$, and $\chi_0 = -0.55$.

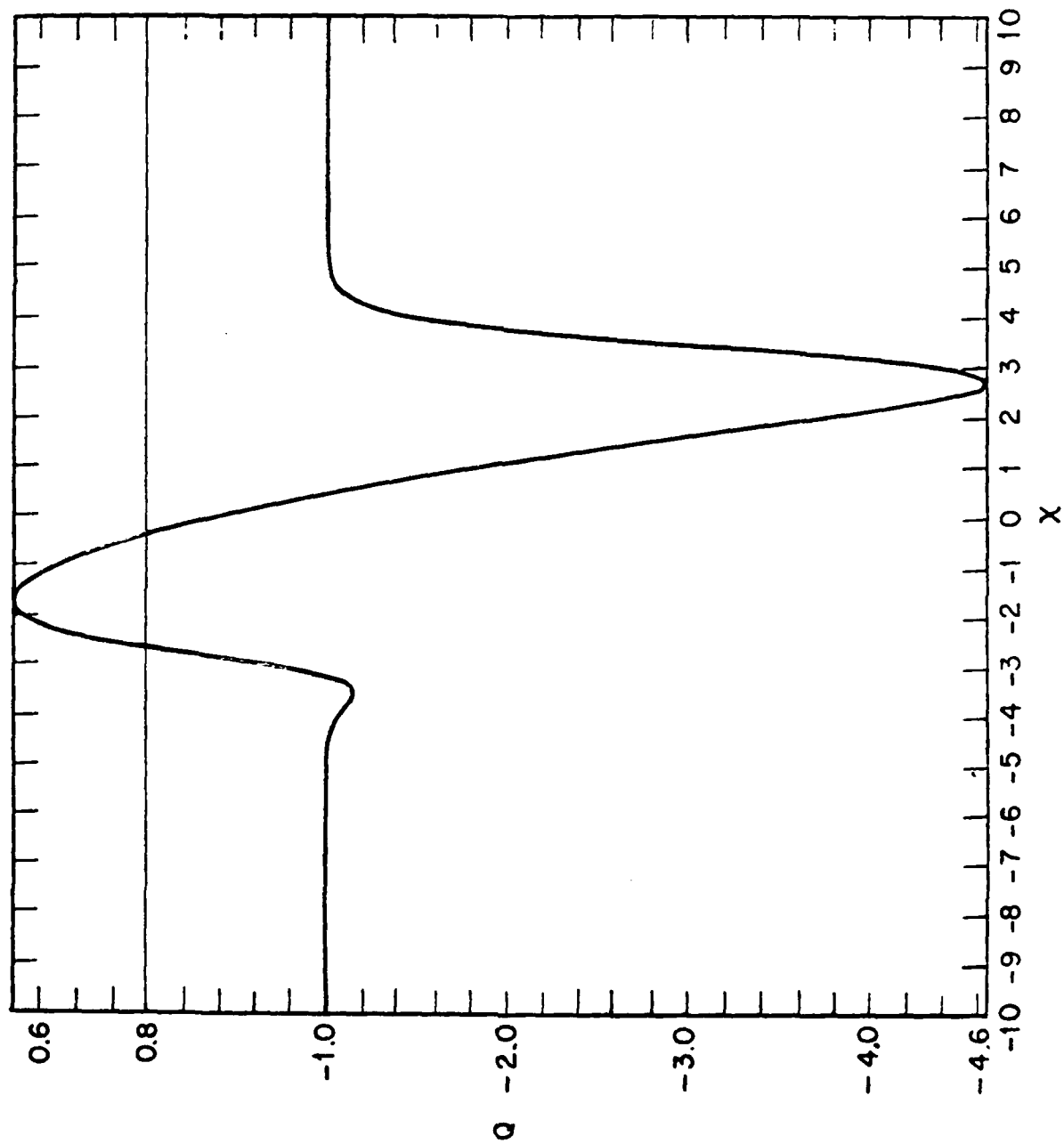
Figure 12. Study of $\hat{\gamma}$ versus \hat{s} , for $\hat{k} = 0.45$ where the Kelvin-Helmholtz instability has maximum growth rate. Curves A and B refer to $\hat{v} = 0.0$ and 0.5 respectively.

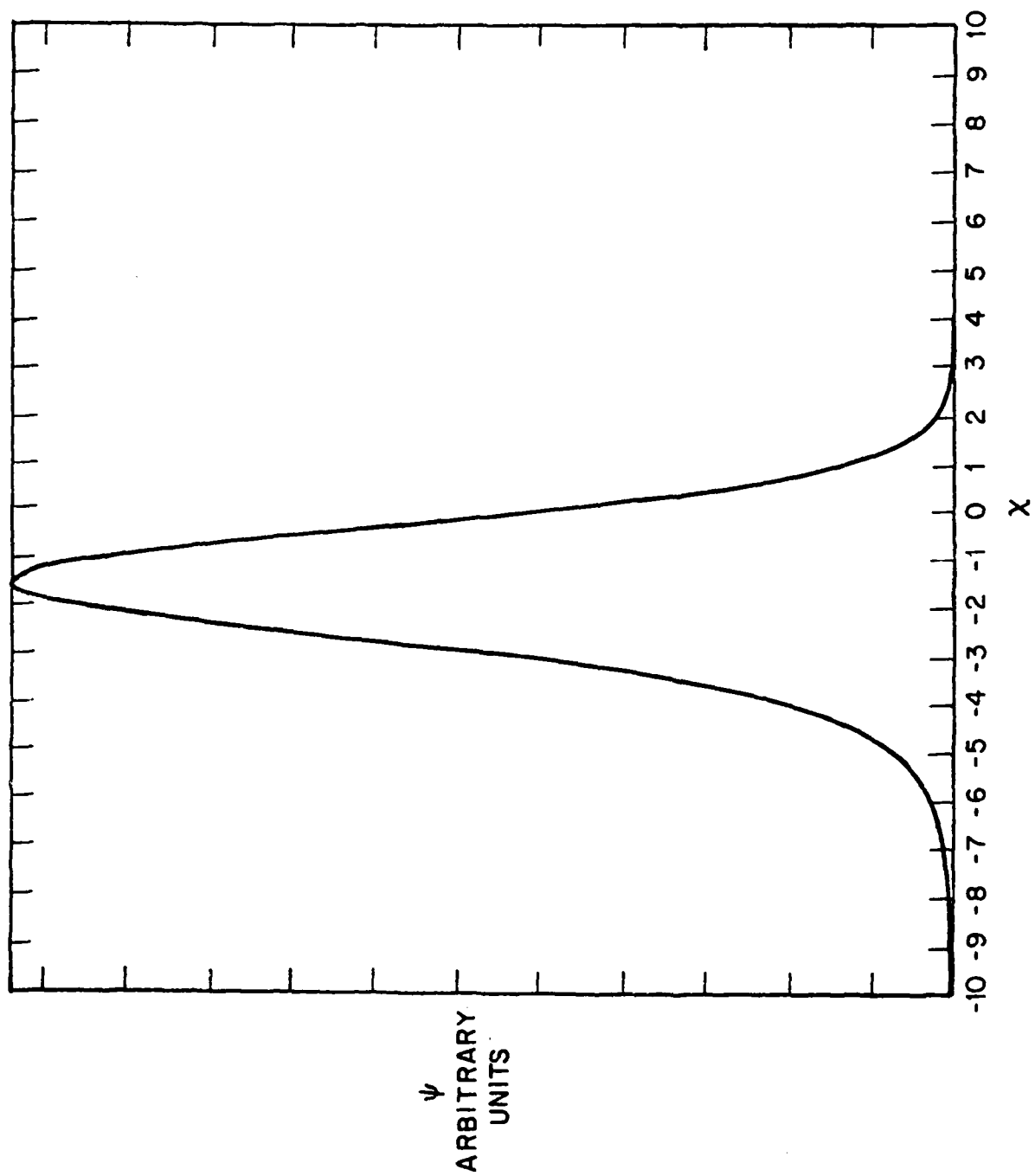
Figure 13. Plots of \hat{k}_c (cut-off mode numbers) and \hat{k}_m (mode numbers where the growth rate maximizes) as a function of \hat{s} . The solid and dashed lines correspond to the collisionless and collisional ($\hat{\nu} = 0.5$) cases respectively. Curves A and B refer to \hat{k}_c and \hat{k}_m , respectively.

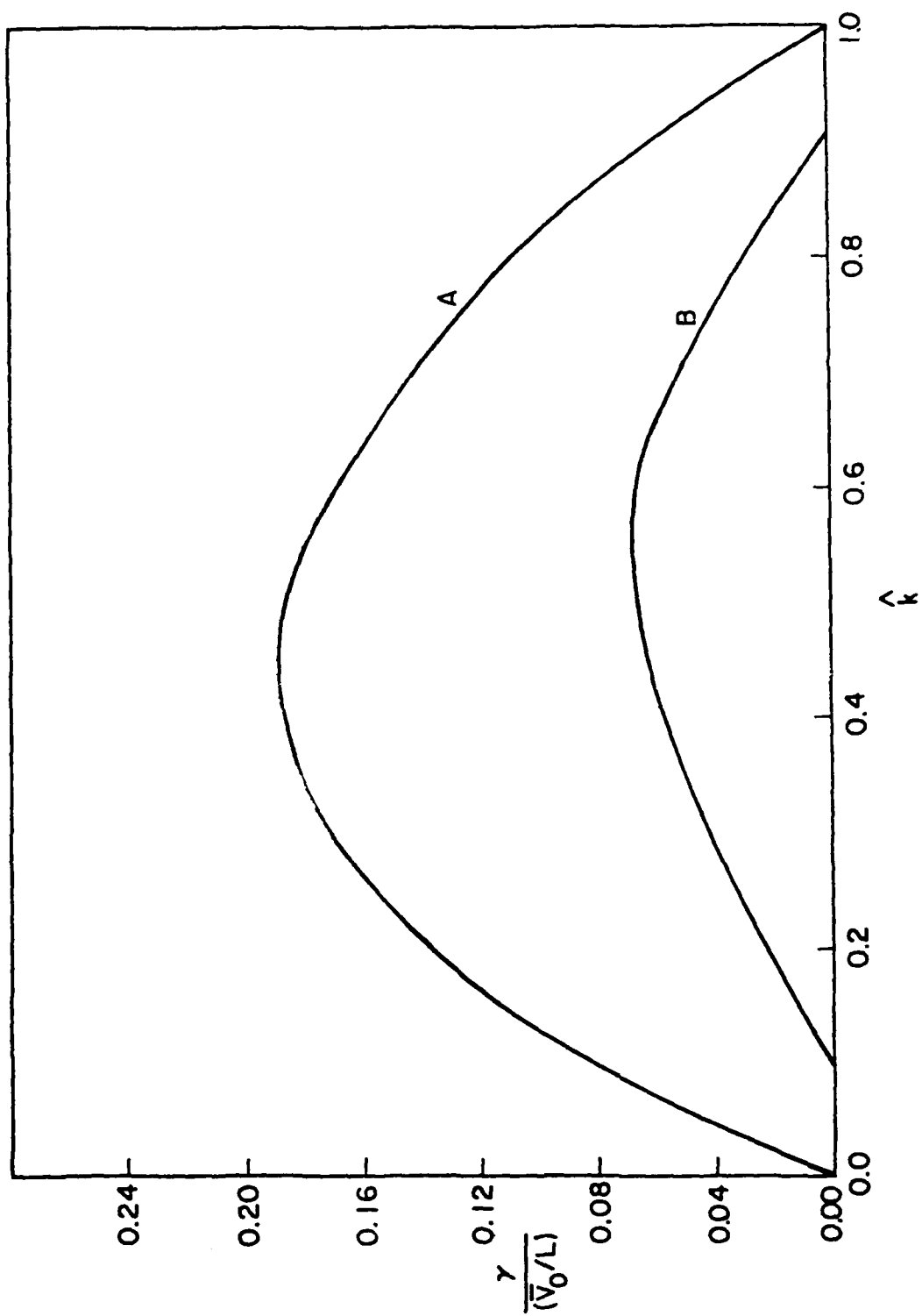
Figure 14. Normalized growth rate versus the normalized wavenumbers for the case of a spatially dependent collision frequency. The density and velocity profiles are given in Eqs. (39) and (40). The parameters used are $\epsilon = 0.8$, $\chi_0 = -0.55$, and $\hat{\nu} = 0.5$. Curve A refers to constant collision frequency, $\hat{\nu} = 0.5$, and $\hat{s} = 1.0$. Curves B and C refer to $\hat{\nu} = 0.5 \exp(-\chi)$ and for $\hat{s} = 1.0$ and 0.5 respectively.

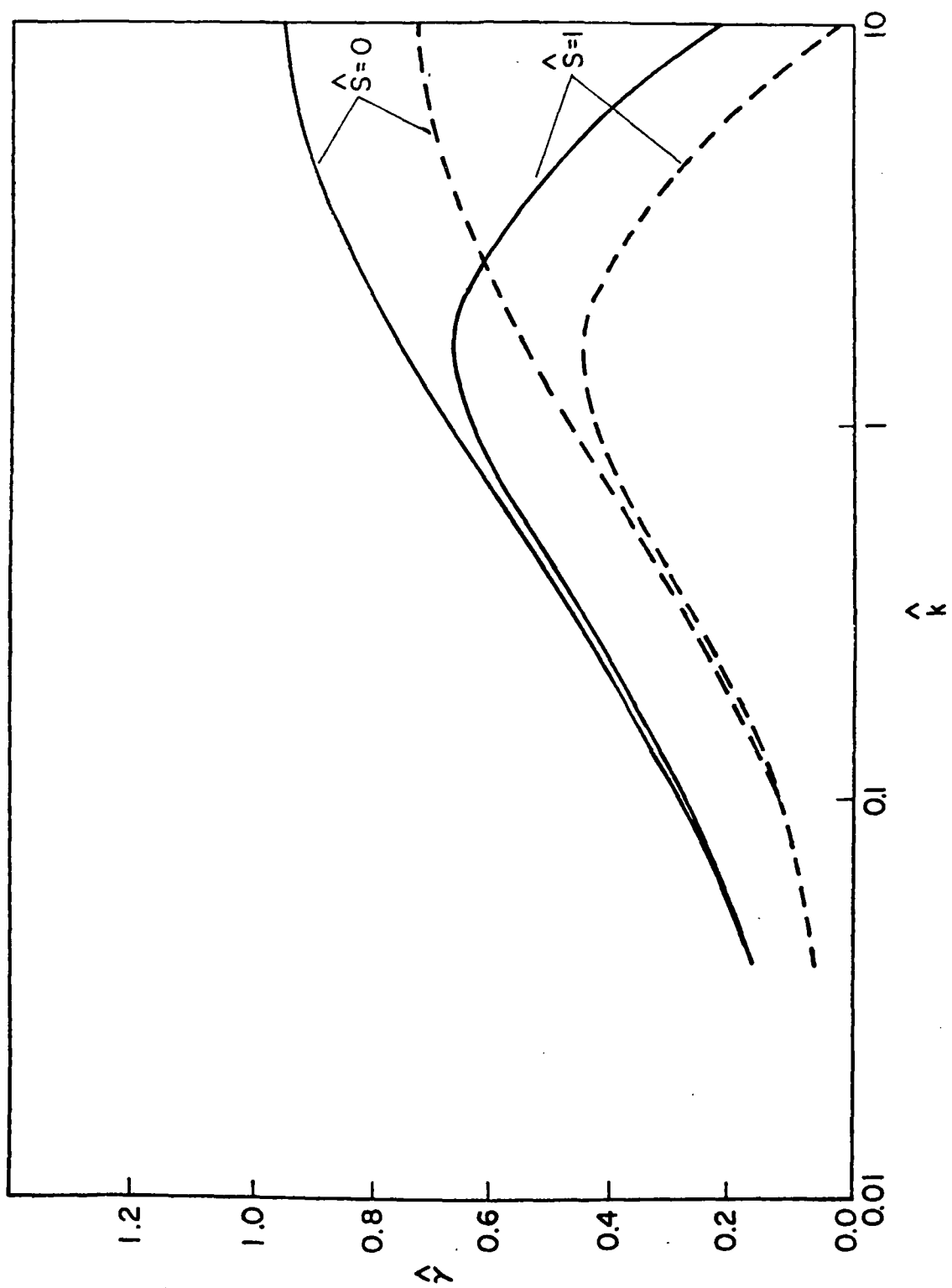


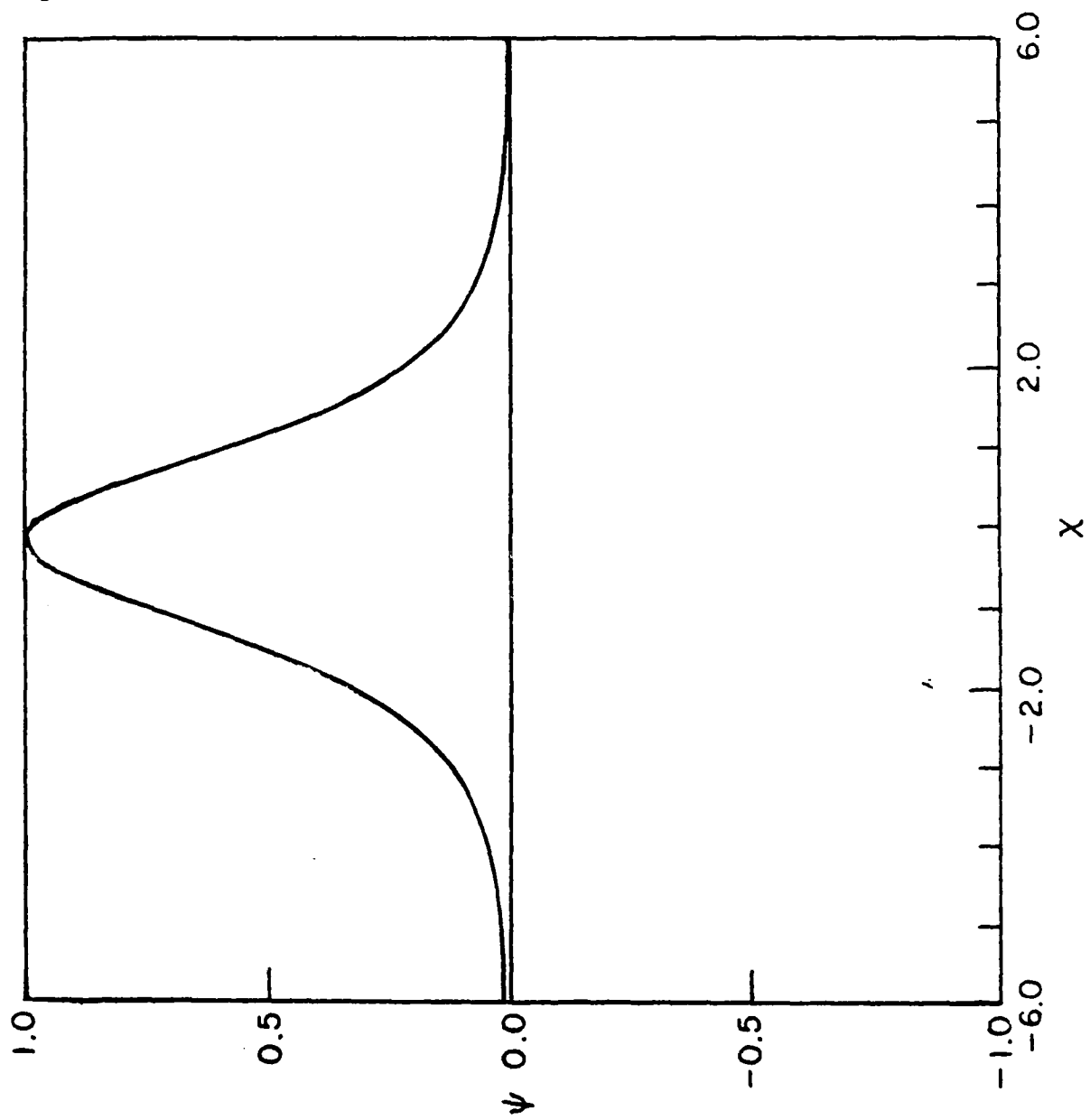


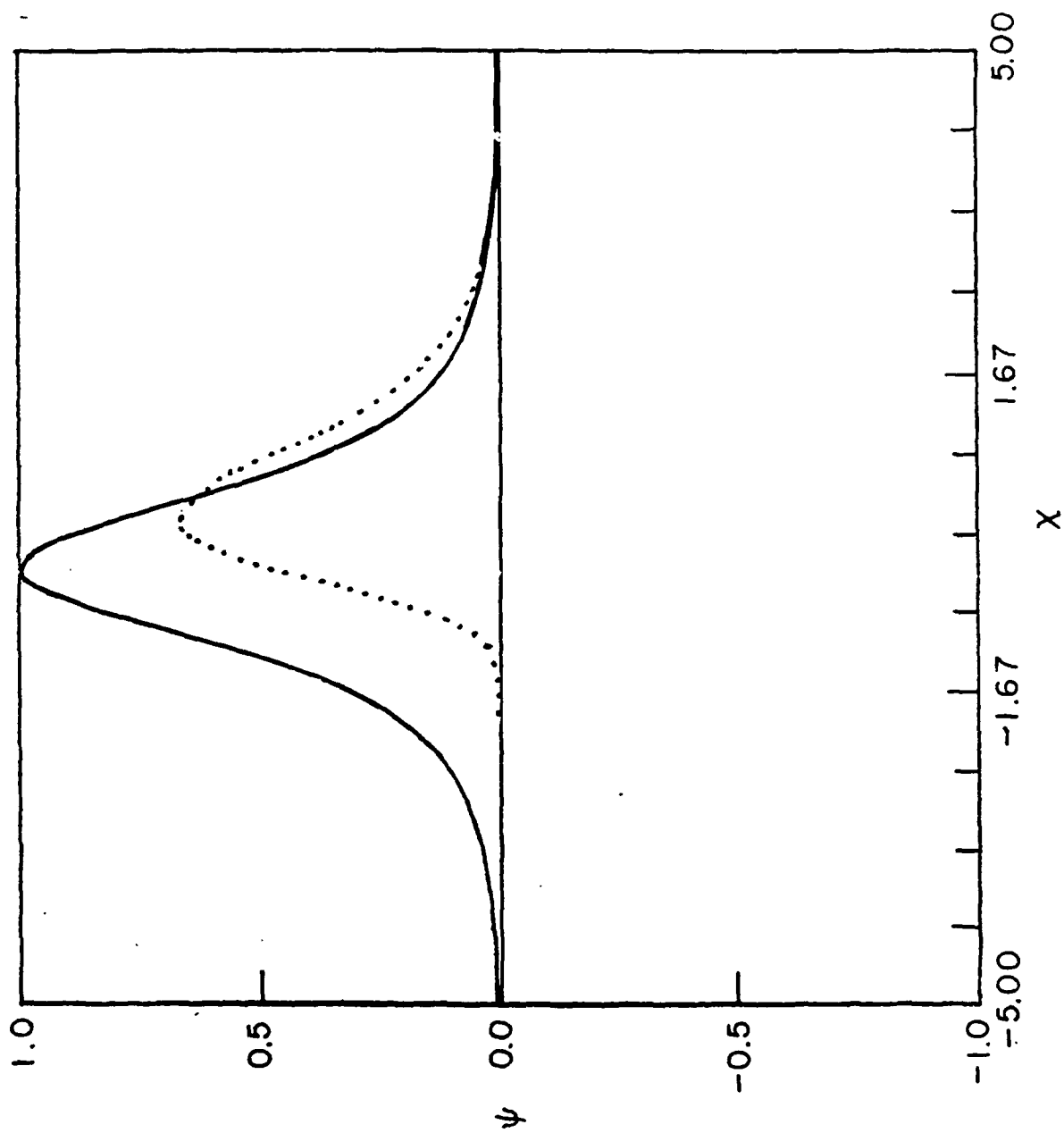


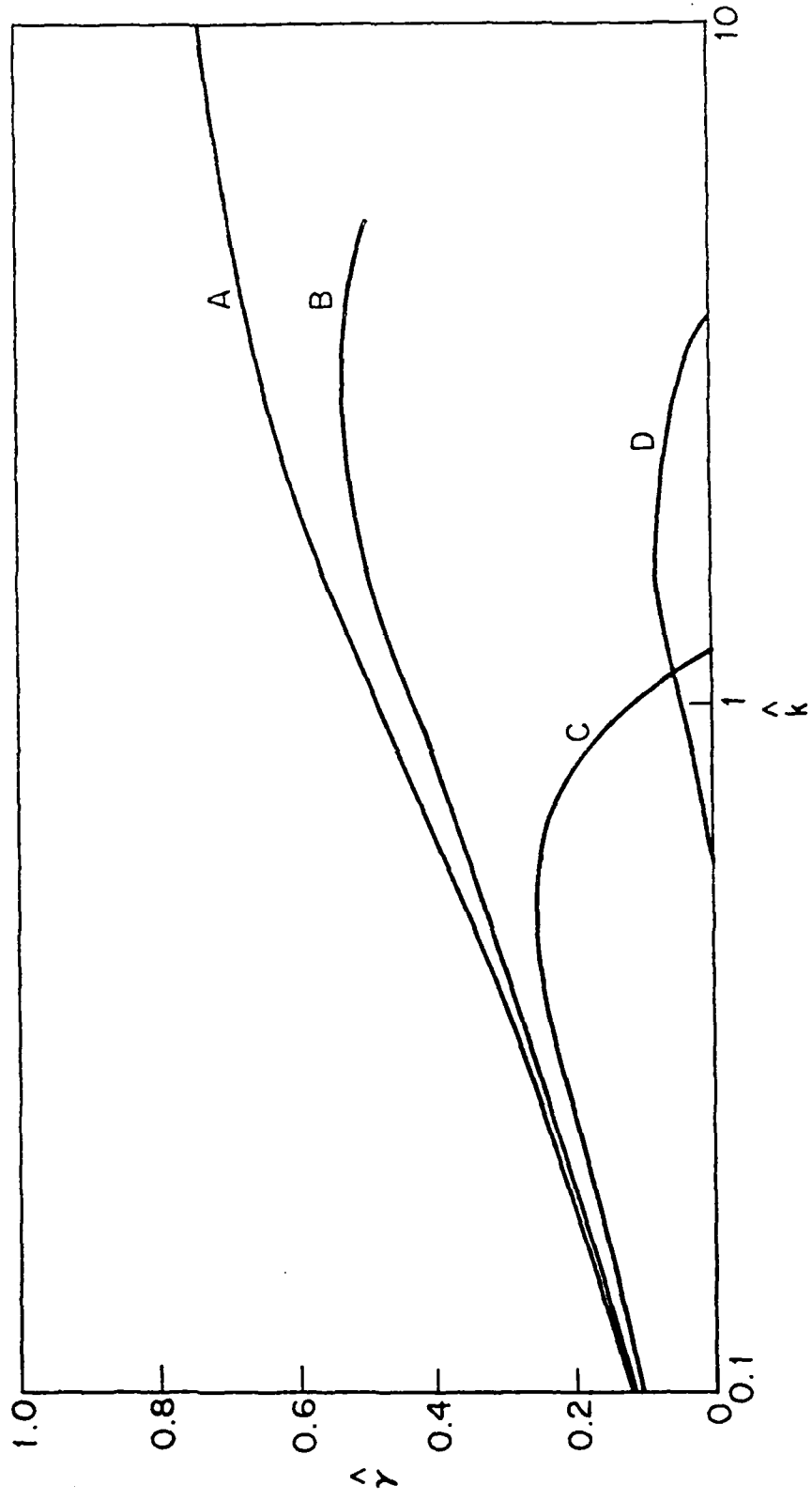


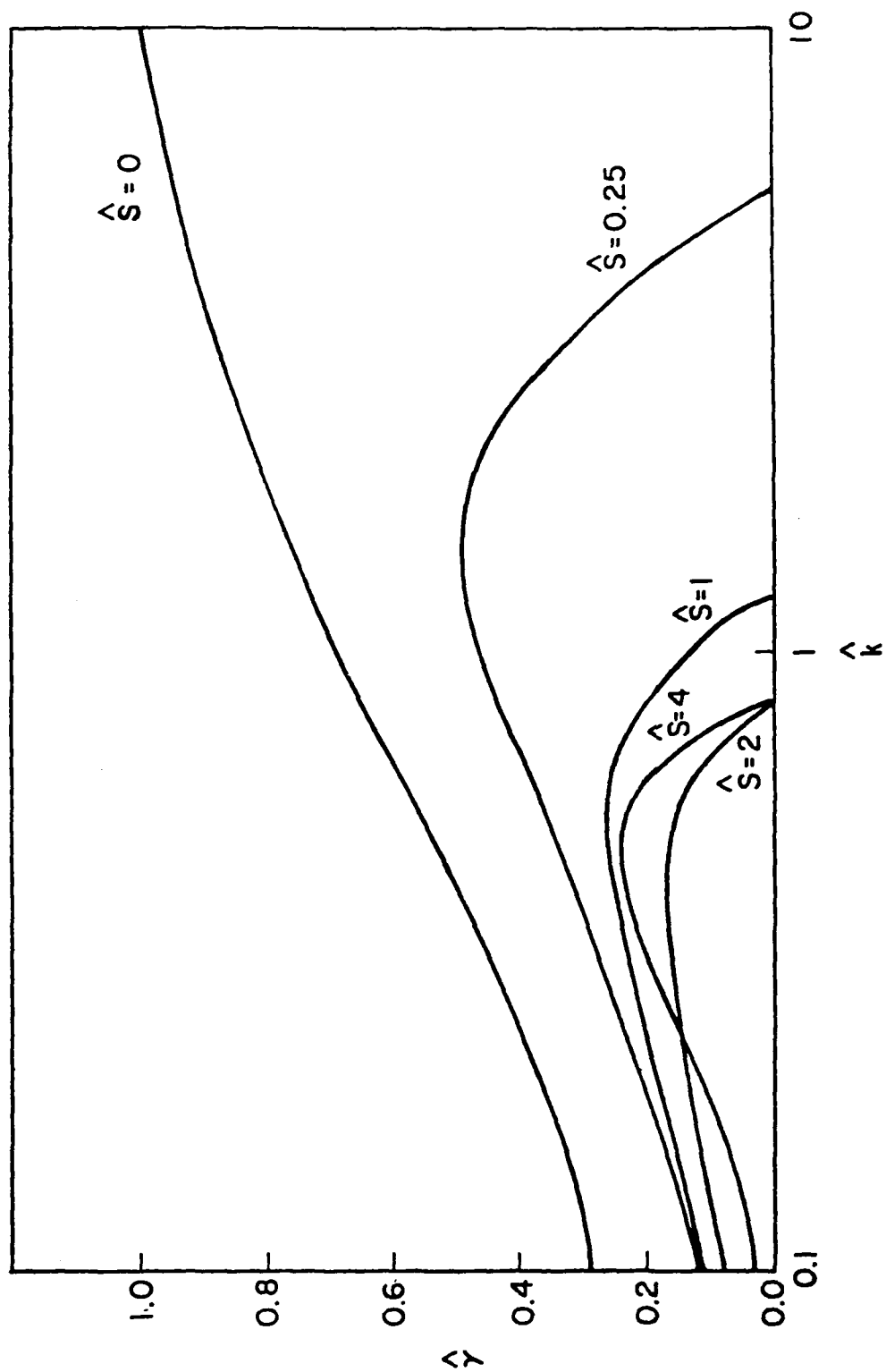


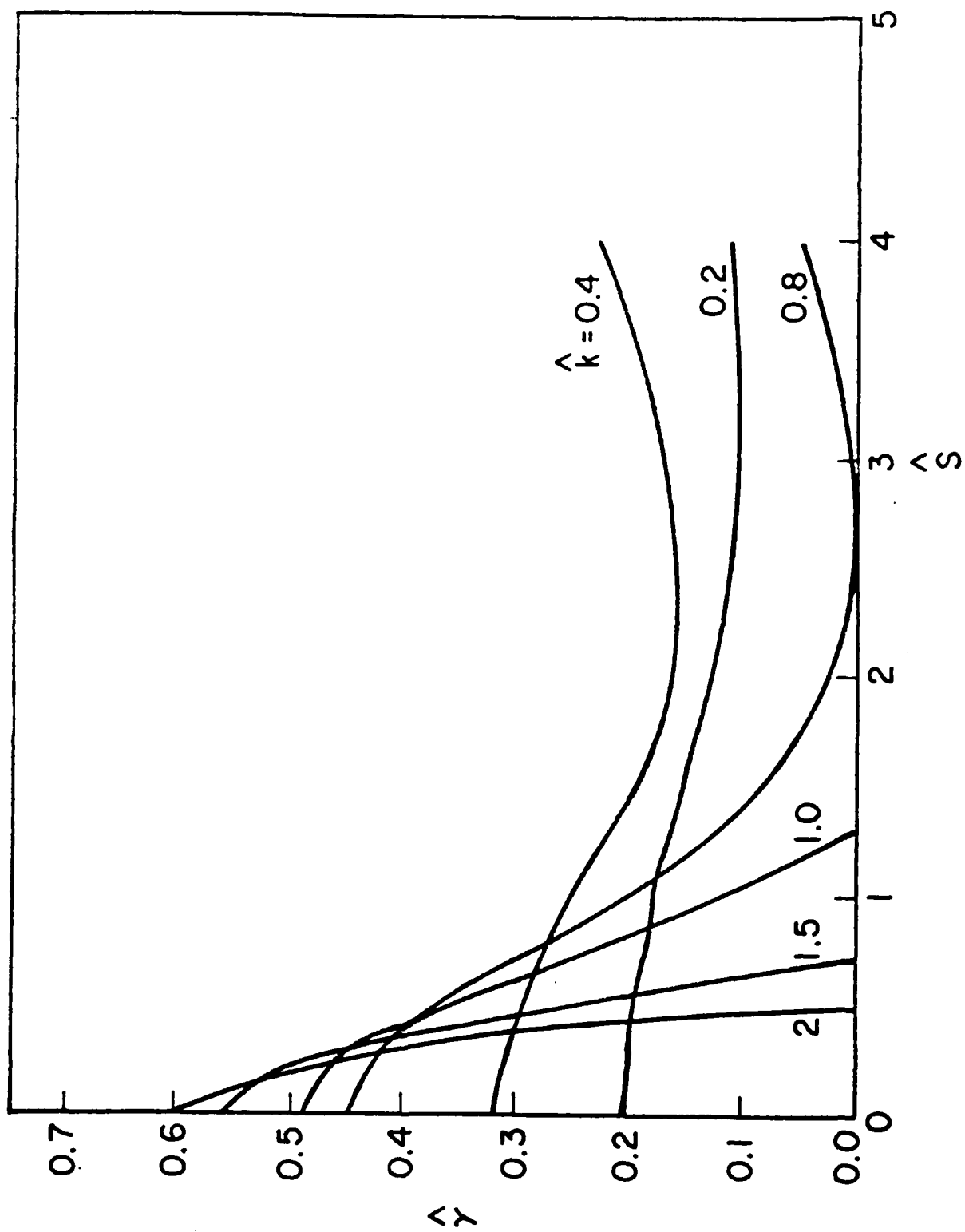


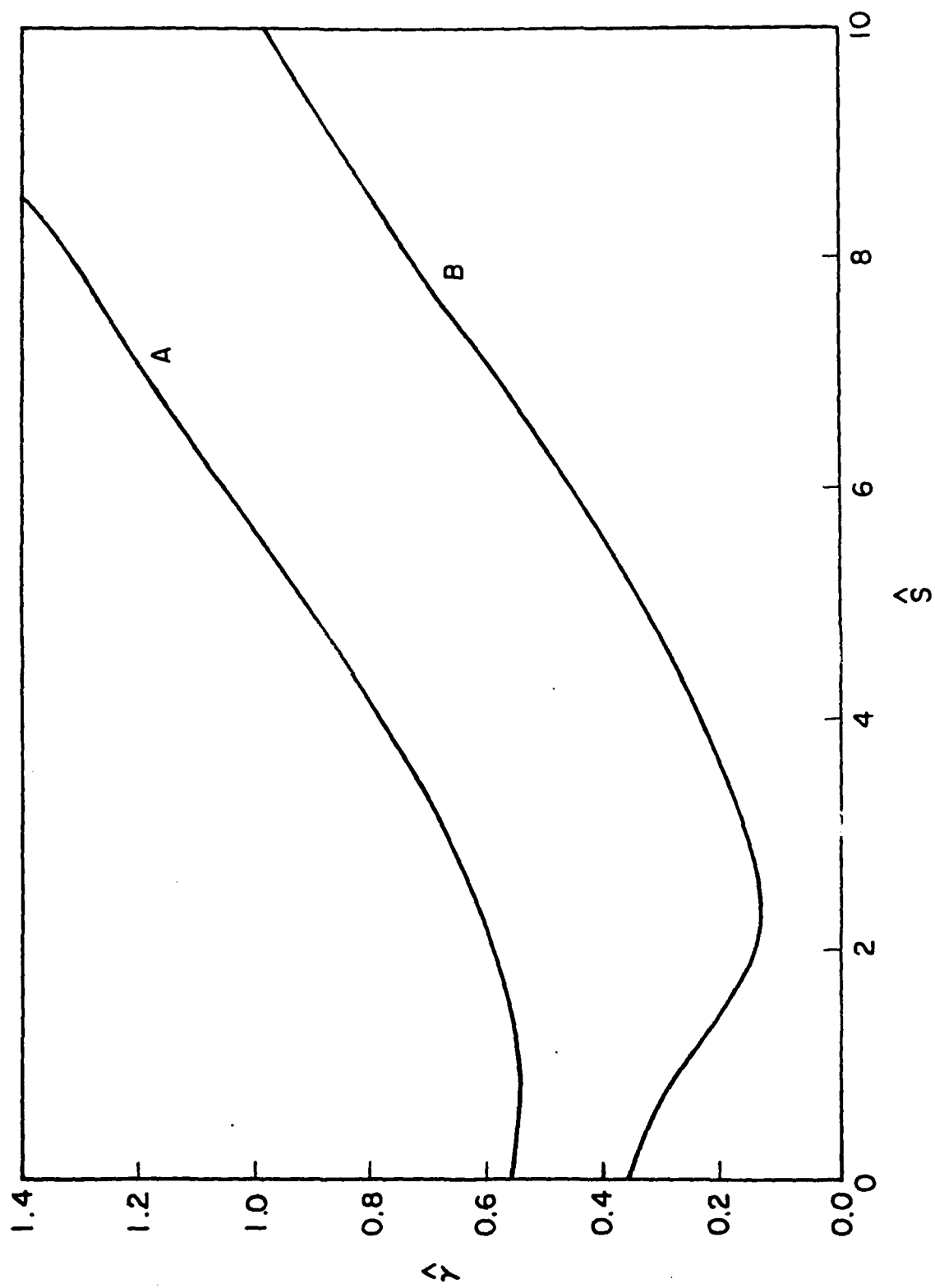


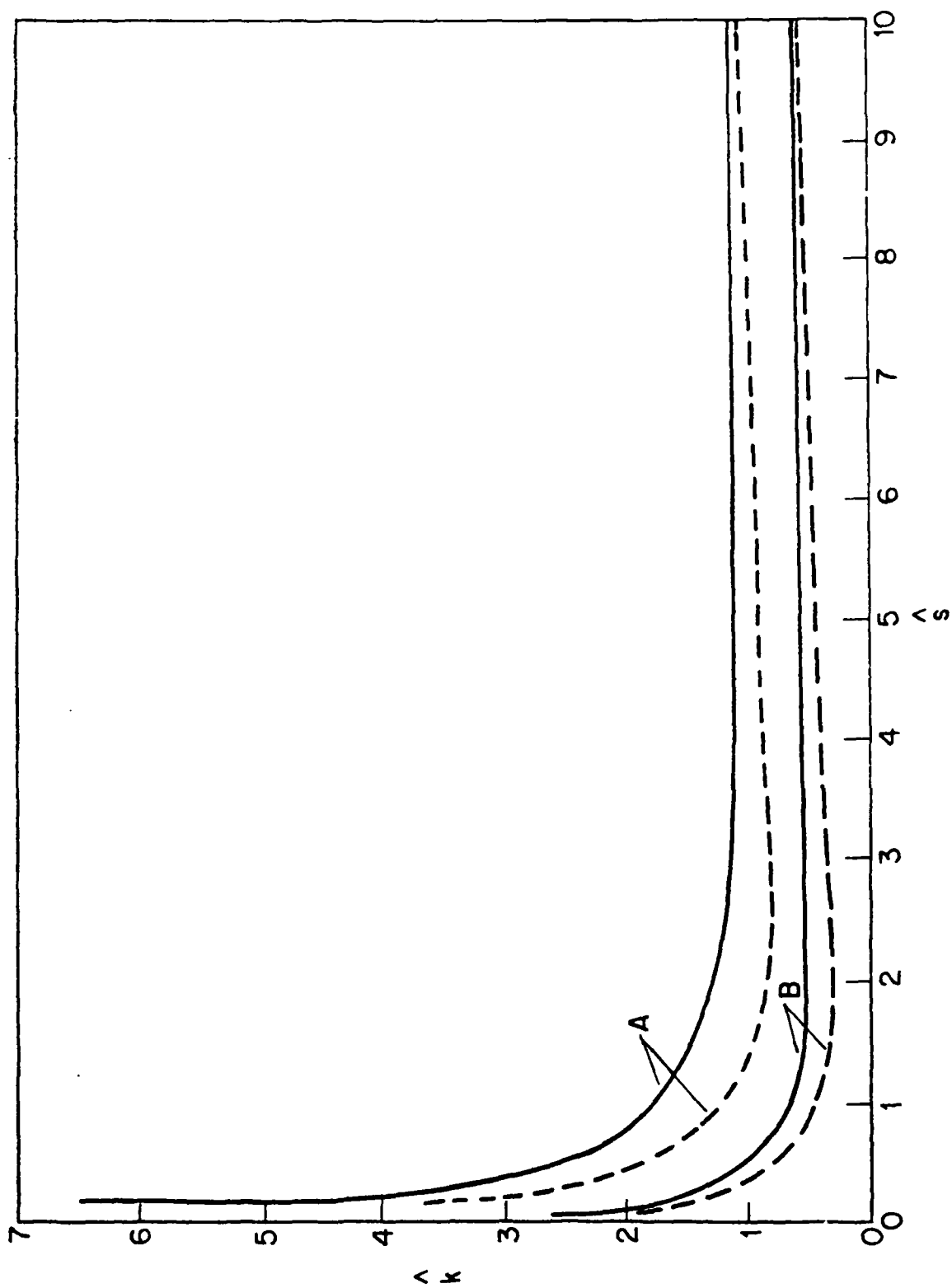


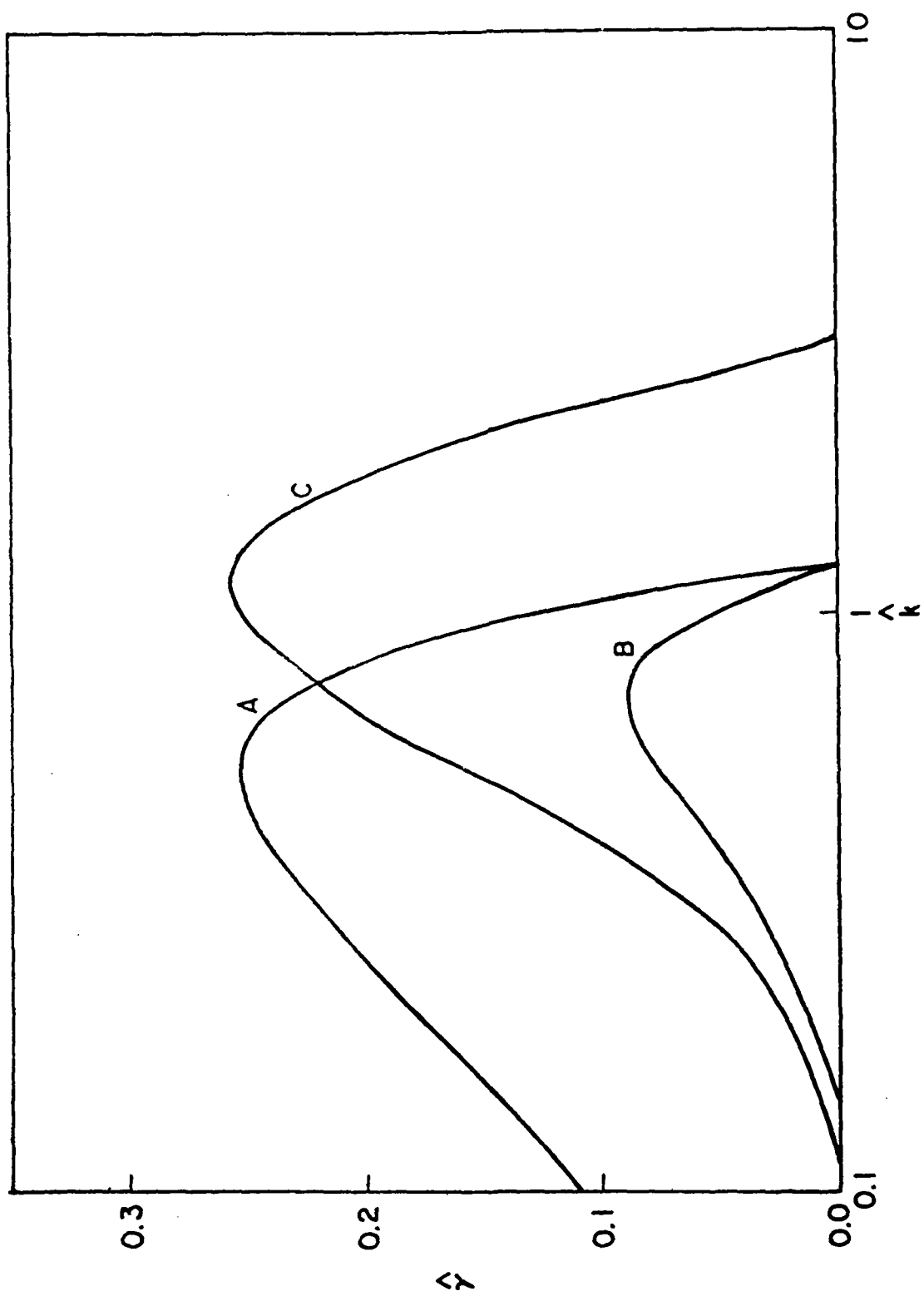












APPENDIX H

FINITE TEMPERATURE EFFECTS ON THE EVOLUTION OF
IONOSPHERIC BARIUM CLOUDS IN THE PRESENCE OF A
CONDUCTING BACKGROUND IONOSPHERE

S.T. Zalesak, S.L. Ossakow and J.A. Fedder
Naval Research Laboratory

and

P.K. Chaturvedi
Science Applications, Inc.

Finite Temperature Effects on the Evolution
of Ionospheric Barium Clouds in the Presence
of a Conducting Background Ionosphere.

S.T. Zalesak
P.K. Chaturvedi*
S.L. Ossakow
J.A. Fedder

Geophysical and Plasma Dynamics Branch
Plasma Physics Division
Naval Research Laboratory
Washington, D.C. 20375

November 1983

* Science Applications, Inc., McLean, VA 22102

H-3

PRECEDING PAGE BLANK-NOT FILMED

Abstract

It is shown that a consideration both of the finite ion temperature of the plasma comprising ionospheric barium clouds and of the shorting effects of the presence of a background conducting ionosphere will give rise to 1) effective perpendicular (to the magnetic field) diffusion rates for barium which are much higher than those given by electron ambipolar rates; and 2) a shear in ion motion at the edge of the barium cloud. Here we shall focus our attention primarily on the first effect. Both of these effects are at first glance stabilizing. It has been noted, however, that electrons may only diffuse perpendicularly at the much lower ambipolar rate and hence the "electron cloud", as defined by regions of elevated magnetic-field-line electron density N_e , is not affected by the apparently high diffusion rates for barium. Here we show that the question of whether this enhanced diffusion can affect the tendency of the barium cloud to bifurcate depends upon neither the barium diffusion rates, nor upon N_e per se, but rather upon the effect the barium diffusion has on the profile of magnetic-field-line-integrated Pedersen conductivity, Σ_p . We find that the determining factor is the relative ion compressibility of the barium and background plasma. Our findings are in agreement with the linear analysis of Francis and Perkins [1975]: relatively incompressible backgrounds (e.g., F regions) are stabilizing while relatively compressible backgrounds (e.g. E regions) are destabilizing. Of course in the latter case of an E region, important recombination chemistry effects and the aforementioned shear effects may alter this conclusion.

1. Introduction

The nonlinear evolution of an artificial plasma cloud (e.g., a barium ion cloud) released in the earth's ionosphere is characterized by an overall bulk $\underline{E} \times \underline{B}$ motion, a one-sided steepening of plasma gradients, and by bifurcation, a process which we define here to mean the splitting of the cloud into two or more pieces. These pieces are sometimes referred to as "striations". All of the above motion and the resultant plasma structures are observed to be magnetic-field-aligned. That is, the plasma motion parallel to magnetic field lines consists primarily of diffusion and falling, while the perpendicular plasma motion is virtually identical for all plasma along a given field line. Hence one's best view of the structuring of the cloud is from a vantage point looking parallel to the magnetic field \underline{B} . This simplified description of barium cloud dynamics, seen along a line of sight parallel to \underline{B} , is depicted in Fig. 1. The sequence of drifting, steepening and bifurcating is, for sufficiently large striations, recursive: each striation becomes a new cloud which in turn forms its own striations. In the absence of some dissipative mechanism, it is believed that this process would continue indefinitely. In reality, the striation size becomes small enough to be comparable to the characteristic scale lengths of physical dissipation mechanisms, and further bifurcation ceases. A previous study by McDonald et al. [1981] attempted to quantify this concept within the context of a "one-level model", a mathematical model in which all conducting plasma was constrained to lie in a single two-dimensional plane perpendicular to the magnetic field. Implicit in this model is the assignment of a single Pedersen mobility and hence compressibility to both the barium and background ionospheric plasma. In this model, the leading candidate for a dissipative mechanism is the

ambipolar diffusion of electrons caused by electron-ion collisions. Using this mechanism, McDonald et al. [1981] calculated final unbifurcating striation sizes for barium clouds of ~ 20 m (perpendicular to E). However, there is experimental evidence for the existence of long-lived "blobs" of plasma several hundred meters in diameter. The apparent stability of such large plasma structures has yet to find a satisfactory explanation within the one-level model. Here we postulate that the existence of a conducting background plasma with ion Pedersen mobility different from that of the barium plasma, combined with the finite temperature of the barium plasma, may allow the existence of stable striations with scale sizes of hundreds of meters. The essence of the mechanism is a phenomenon commonly referred to as "end shorting" first investigated in the context of barium clouds by Shiau and Simon [1974], who considered a completely incompressible background ionosphere, and showed that the normal electron ambipolar diffusion rates would be replaced by some fraction of the much higher ion diffusion rates caused by collisions of ions with neutrals. Francis and Perkins [1975] generalized the work of Shiau and Simon [1974] by considering the cases of both incompressible and compressible background ionospheres. They concurred with Shiau and Simon [1974] that incompressible backgrounds exert a stabilizing influence, but noted that compressible backgrounds are destabilizing. In contrast, Vickrey and Kelley [1982] concluded that a background (compressible) E region should exert a stabilizing influence on high latitude irregularities. We shall address the question of the correctness of the above two analyses in a later paper. For the moment we note that: 1) Francis and Perkins [1975] performed a rigorous stability analysis of the problem; Vickrey and Kelley [1982] did not; 2) Francis and Perkins [1975] self-consistently included

image formation (compressibility) in both the cloud and the background;
Vickrey and Kelley [1982] did not; 3) Vickrey and Kelley [1982] included
recombination chemistry; Francis and Perkins [1975] did not.

Our own conclusions are based on our view of barium cloud dynamics as
consisting of a two-stage feed-back loop:

1) At any given time, the distribution of plasma density will,
through the effect of these distributions on magnetic-field-line integrated
Pedersen and Hall conductivities, bring about the creation of polarization
electric fields whose purpose it is to maintain quasi-neutrality;

2) these electric fields, through Hall and Pedersen mobilities,
affect the velocity of the plasma, which in turn affects the distribution
of plasma density at the next instant of time.

We emphasize that it is only through its influence on magnetic-field-
line integrated Pedersen and Hall conductivities that a change in plasma
distribution [e.g., diffusion] will affect the polarization fields, which
are the engine of plasma structure.

2. The Motion of Ionospheric Plasma

We shall be concerned here with the motion of plasma consisting of ions and electrons in the presence of a neutral gas and magnetic field \underline{B} , subject to an external force. We shall also be interested in the electric current \underline{J} arising from the differential motion of the various species comprising the plasma. In the course of deriving the equations we make the following assumptions:

1) We assume the plasma can be adequately described by the fluid approximation. This assumes that the effective collision rate of each plasma species with itself is sufficiently high to maintain near Maxwellian distribution functions on time scales short compared to the times of interest, and is well satisfied for the plasmas we treat here.

2) We assume that the electric fields \underline{E} are electrostatic (i.e., $\nabla \times \underline{E} = 0$) and hence can be described using a scalar potential ϕ such that $\underline{E} = -\nabla\phi$. Note that this implies $\partial \underline{B} / \partial t = 0$. The validity of this assumption can be related to the fact that the Alfvén velocity is much larger than any other propagation speed of interest for the plasmas we treat here. The assumption is also checked a posteriori by verifying that the calculated currents and displacement currents produce negligible time variations in \underline{B} which in turn produce negligible $\nabla \times \underline{E}$.

3) We assume plasma quasi-neutrality; that is,

$$\sum n_i q_i = n_e e \quad (2.1)$$

where n is the number density, q is ion species charge, e is the electron charge, the subscripts i and e refer to ions and electrons respectively, and the sum is taken over all ion species. This assumption is a statement

that the Debye length is small compared to all length scales of interest, and again can be verified a posteriori by evaluating $\nabla \cdot \underline{E}$. Note that this assumption implies that $\nabla \cdot \underline{J} = 0$, where \underline{J} is the electric current.

In addition to the above there are some other assumptions which, while they are not essential to the basic model, are nonetheless valid for many of the physical situations which we shall treat and impart a simplicity which we shall find convenient here:

4) We assume the electrostatic potential ϕ to be constant along magnetic field lines. As we shall see later, the electrical conductivity along magnetic field lines is much greater than that perpendicular to magnetic field lines, meaning that appreciable differences in potential along a field line will quickly be reduced by the resultant current. This assumption will break down for sufficiently small scale lengths perpendicular to the magnetic field, and for sufficiently large distances along the magnetic field.

5) We assume that the inertial terms in the plasma species momentum equations, i.e., the left hand side of Equation (2.3), are negligible with respect to the other terms in the equation. This assumption is justified whenever the time scales of interest are longer than the mean time between collisions for ions.

6) We neglect collisions between ions and electrons and between ions of different species. Later we shall also neglect collisions of electrons with neutrals. There are two reasons for this. First, the ion-neutral collision term v_{in} can be shown to be the dominant term in the diffusion physics we consider here. (One must be careful, however, since these same assumptions will yield zero diffusion when the background conductivity is set to zero. To obtain the correct electron ambipolar rate in this limit,

the electron-ion and electron-neutral collision terms must be retained. We are not interested in this limit in this paper). Second, although exact closed form expressions for the ion and electron velocities in terms of the applied forces is possible when ion-electron collisions are retained [Fedder, 1980], the expressions are considerably more complex than those given below.

The continuity and momentum equations describing a single ion species and its associated electrons are:

$$\frac{\partial n_{\alpha}}{\partial t} + \nabla \cdot (n_{\alpha} \underline{v}_{\alpha}) = 0 \quad (2.2)$$

$$\begin{aligned} \left(\frac{\partial}{\partial t} + \underline{v}_{\alpha} \cdot \nabla \right) \underline{v}_{\alpha} = & \frac{q_{\alpha}}{m_{\alpha}} \left(\underline{E} + \frac{\underline{v}_{\alpha} \times \underline{B}}{c} \right) - \nu_{\alpha n} (\underline{v}_{\alpha} - \underline{U}_n) \\ & - \frac{\nabla P_{\alpha}}{n_{\alpha} m_{\alpha}} + \underline{g} \end{aligned} \quad (2.3)$$

where the subscript α takes on values i and e (denoting ions and electrons, respectively), n is the number density, \underline{v} is the fluid velocity, P is pressure, \underline{E} is the electric field, \underline{g} is the gravitational acceleration, q is the charge, $\nu_{\alpha n}$ is the collision frequency with the neutral gas, \underline{U}_n is the neutral wind velocity, c is the speed of light, and m is the particle mass. We can rewrite this equation as

$$\underline{F}_{\alpha} / m_{\alpha} + \frac{q_{\alpha}}{m_{\alpha} c} (\underline{v}_{\alpha} \times \underline{B}) - \nu_{\alpha n} \underline{v}_{\alpha} = 0 \quad (2.4)$$

where

$$\begin{aligned} \underline{F}_a \equiv & q_a \underline{E} + m_a g + v_{an} m_a \underline{U} - \nabla P_a / n_a \\ & - \left(\frac{\partial}{\partial t} + \underline{v}_a \cdot \nabla \right) \underline{v}_a m_a \end{aligned} \quad (2.5)$$

If we place ourselves in a Cartesian coordinate system in which \underline{B} is aligned along the z axis, and if we treat \underline{F}_a as a given quantity then a componentwise evaluation of Equation (2.4) yields a set of three equations in three unknowns, the three components of \underline{v}_a . The formal solution is

$$\underline{v}_{a1} = k_{1a} \underline{F}_{a1} + k_{2a} \underline{F}_{a1} \times \hat{z} \quad (2.6)$$

$$\underline{v}_{a1} = k_{oa} \underline{F}_1 \quad (2.7)$$

where

$$k_{1a} = \frac{v_{an}}{\Omega_a} \frac{c}{|q_a B|} \left[1 - \frac{(v_{an}/\Omega_a)^2}{1 + (v_{an}/\Omega_a)^2} \right] \quad (2.8)$$

$$k_{2a} = \frac{c}{q_a B} \left[1 - \frac{(v_{an}/\Omega_a)^2}{1 + (v_{an}/\Omega_a)^2} \right] \quad (2.9)$$

$$k_{oa} = (m_a v_{an})^{-1} \quad (2.10)$$

$$\hat{z} \equiv \underline{B}/|B| \quad (2.11)$$

$$\Omega_a \equiv \left| \frac{q_a B}{m_a c} \right| \quad (2.12)$$

The vector subscripts \perp and \parallel refer to the components of the vector which are perpendicular and parallel respectively to \hat{z} . The quantities k_1 , k_2 , and k_0 above are referred to as the Pedersen, Hall, and direct mobilities respectively. It should be pointed out that Equations (2.6) and (2.7) are only truly closed form expressions when the inertial terms (the last term on the right hand side of Equation (7)) are neglected, an assumption we have made previously. Typical ranges for collision frequencies are: $\nu_{in} \sim 30 \text{ sec}^{-1}$, $\nu_{en} \sim 800 \text{ sec}^{-1}$ at 150 km altitude; and $\nu_{in} \sim 10^{-1} \text{ sec}^{-1}$, $\nu_{en} \sim 1 \text{ sec}^{-1}$ at 500 km altitude.

As we will see later, we will use the concept of "layers" to distinguish the various ion species, so for the moment we can consider only a single ion species, denoted by subscript i , and the associated electrons, denoted by subscript e . We will also consider only singly charged ions so that $q_i = e$ and $q_e = -e$. Noting that $\nu_{en}/\Omega_e \approx 0$ we obtain

$$k_{1i} = \frac{\nu_{in}}{\Omega_i} R_i \frac{c}{e|B|} \quad (2.13)$$

$$k_{1e} = 0 \quad (2.14)$$

$$k_{2i} = R_i \frac{c}{eB} \quad (2.15)$$

$$k_{2e} = -\frac{c}{eB} \quad (2.16)$$

where

$$R_i \equiv (1 + \nu_{in}^2/\Omega_i^2)^{-1} \quad (2.17)$$

We now define the perpendicular current

$$\underline{J}_\perp \equiv \sum_{\alpha} n_{\alpha} q_{\alpha} \underline{v}_{\alpha\perp} \quad (2.18)$$

Substituting Equations (2.13) through (2.16) and (2.6) into Equation (2.18), and using the quasi-neutrality approximation

$$n_i \approx n_e \equiv n \quad (2.19)$$

we obtain

$$\begin{aligned} \underline{J}_\perp &= \frac{v_{in}}{\Omega_i} R_i \frac{nc}{|B|} \underline{F}_{i\perp} \\ &+ \frac{nc}{B} (R_i \underline{F}_{i\perp} + \underline{F}_{e\perp}) \times \hat{z} \end{aligned} \quad (2.20)$$

For the barium cloud problem we shall treat here, we shall only consider neutral winds, electric fields, gravity, and pressure gradients as external forces. Hence

$$\underline{F}_{i\perp} = e \underline{E}_\perp + m_i \underline{g}_\perp + v_{in} m_i \underline{u}_{n\perp} - \nabla P_i / n \quad (2.21)$$

$$\underline{F}_{e\perp} = -e \underline{E}_\perp + m_e \underline{g}_\perp - \nabla P_e / n \quad (2.22)$$

Note that we have neglected the small term $v_{en} m_e$ in Equation (2.22).

We obtain

$$\begin{aligned} \underline{J}_\perp = & \frac{v_{in}}{\Omega_i} R_i \frac{nc}{|B|} (e \underline{E}_\perp + m_i \underline{g}_\perp + v_{in} m_i \underline{U}_{n\perp} - \nabla P_i / n) \\ & + R_i \frac{nc}{B} [e \underline{E}_\perp (1 - R_i^{-1}) + m_i + \frac{m_e}{R_i}] \underline{g}_\perp + v_{in} m_i \underline{U}_{n\perp} \\ & - \nabla P_i / n - \nabla P_e R_i^{-1} / n] \times \hat{z} \end{aligned} \quad (2.23)$$

Since $0.01 < R_i < 1.0$ we may neglect m_e/R_i with respect to m_i .

Defining the Pedersen conductivity

$$\sigma_p \equiv R_i \frac{v_{in}}{\Omega_i} \frac{n c e}{|B|} \quad (2.24)$$

and noting that $1 - R_i^{-1} = -v_{in}^2 / \Omega_i^2$ we obtain

$$\begin{aligned} \underline{J}_\perp = & \sigma_p \left[\underline{E}_\perp + \frac{m_i}{e} \underline{g}_\perp + v_{in} \frac{m_i}{e} \underline{U}_{n\perp} - \frac{\nabla P_i}{ne} \right. \\ & + \frac{B}{|B|} \left(-\frac{v_{in}}{\Omega_i} \underline{E}_\perp + \frac{\Omega_i m_i}{v_{in} e} \underline{g}_\perp + \Omega_i \frac{m_i}{e} \underline{U}_{n\perp} \right. \\ & \left. \left. - \frac{\Omega_i}{v_{in} ne} (\nabla P_i + R_i^{-1} \nabla P_e) \right) \right] \times \hat{z} \end{aligned} \quad (2.25)$$

Our need for an expression for \underline{J}_\perp stems from our need for its divergence to evaluate $\nabla \cdot \underline{J}$ ($= 0$ by quasi-neutrality), as we shall see in the next section.

3. Mathematical Model

We shall model our physical system using a simplified model as depicted in Figure 2. The magnetic field lines are assumed to be straight, to be aligned along the z axis of our cartesian coordinate system, and to terminate in insulators at $z = \pm \infty$. The plasma of interest is threaded by these magnetic field lines, and is divided into thin planes or "layers" of plasma perpendicular to the magnetic field. Since we have neglected collisions between different plasma species, we may use the device of layers to treat multiple ion species at a single point in space simply by allowing multiple layers to occupy the same plane in space, one for each ion species. In this way a "layer" consists only of a single ion species and its associated electrons.

Our quasi-neutrality assumption demands that

$$\nabla \cdot \underline{J} = \frac{\partial}{\partial x} J_x + \frac{\partial}{\partial y} J_y + \frac{\partial}{\partial z} J_z = 0 \quad (3.1)$$

Integrating Equation (3.1) along z and noting from Figure 2 that J_z vanishes at $z = \pm \infty$ we obtain

$$\int_{-\infty}^{+\infty} \nabla_{\perp} \cdot \underline{J}_{\perp} dz = 0 \quad (3.2)$$

where

$$\nabla_{\perp} \equiv \hat{x} \frac{\partial}{\partial x} + \hat{y} \frac{\partial}{\partial y} \quad (3.3)$$

From our model as depicted in Figure 2 we may approximate the integral in Equation (3.2) by a discrete sum

$$\sum_{k=1}^K \nabla_{\perp} \cdot \underline{J}_{\perp k} \Delta z_k = 0 \quad (3.4)$$

where the subscript k refers to the layer number, K is the total number of layers in the system, and Δz_k is the thickness of layer k measured along the magnetic field line. Within a layer, both the ion density n and the ion-neutral collision frequency ν_{in} are assumed to be constant along a magnetic field line. This enables us to introduce the three magnetic-field-line integrated quantities:

$$N_k \equiv n_k \Delta z_k \quad (3.5)$$

$$\Sigma_{pk} \equiv \sigma_{pk} \Delta z_k = N_k \left(\frac{\nu_{in}}{\Omega_i} R_i \right)_k \frac{ce}{|B|} \quad (3.6)$$

$$\Sigma_{hk} \equiv \left(\frac{\nu_{in}}{\Omega_i} \right)_k \Sigma_{pk} \quad (3.7)$$

By our assumption of equipotential magnetic field lines and electrostatic electric fields

$$\underline{E}_{\perp k}(x,y) = \underline{E}_0 - \nabla_{\perp} \phi(x,y) \text{ for all } k \quad (3.8)$$

where $\underline{E}_0 \equiv E_{0x} \hat{x} + E_{0y} \hat{y}$ is a constant, externally imposed electric field.

Then Equation (3.4) becomes

$$\nabla_{\perp} \cdot \left[\sum_{k=1}^K (\Sigma_{pk}) \nabla_{\perp} \phi \right] + \sum_{k=1}^K H_k = \sum_{k=1}^K \nabla_{\perp} \cdot \underline{J}_{\perp k}^{\text{ext}} \quad (3.9)$$

where

$$\begin{aligned} H_k &\equiv - \frac{\partial}{\partial x} \left(\Sigma_{hk} \frac{\partial \phi}{\partial y} \right) + \frac{\partial}{\partial y} \left(\Sigma_{hk} \frac{\partial \phi}{\partial x} \right) \\ &= - \frac{\partial \phi}{\partial y} \frac{\partial \Sigma_{hk}}{\partial x} + \frac{\partial \phi}{\partial x} \frac{\partial \Sigma_{hk}}{\partial y} \end{aligned} \quad (3.10)$$

$$\begin{aligned} \underline{J}_{\perp k}^{\text{ext}} &\equiv \Sigma_{pk} \left[\frac{m_i}{e} \underline{E}_{\perp} + v_{in} \frac{m_i}{e} \underline{U}_{\perp} - \frac{\nabla P_i}{ne} + \underline{E}_0 \right. \\ &\quad + \frac{B}{|B|} \left(\frac{\Omega_i m_i}{v_{in} e} \underline{E}_{\perp} + \Omega_i \frac{m_i}{e} \underline{U}_{\perp} - \frac{\Omega_i}{ne v_{in}} (\nabla P_i + R_i^{-1} \nabla P_e) \right. \\ &\quad \left. \left. - \frac{v_{in}}{\Omega_i} \underline{E}_0 \right) \times \hat{z} \right]_k \end{aligned} \quad (3.11)$$

and the subscript k denoting layer number on terms within parenthesis operates on all terms within those parentheses.

The system of equations we must solve consists of (3.9)-(3.11) and an equation of continuity for each layer:

$$\frac{\partial N_k}{\partial t} + \nabla \cdot (N_k \underline{v}_{\perp k}) = 0 \quad k=1, \dots, K \quad (3.12)$$

where \underline{v}_i is given by Eq. (2.6)-(2.12).

4. Simplified Two-Level Model

We make the following further simplifications in our model:

a) We find that for ionospheric barium clouds the currents parallel to \underline{B} are carried primarily by electrons, and the motion of ions parallel to \underline{B} consists primarily of a slow diffusion plus a bulk falling of the cloud to lower altitudes (since $\underline{g} \cdot \underline{B} \neq 0$). It is therefore sufficient to represent the ions as an array of two-dimensional planes or layers of plasma perpendicular to \underline{B} , each moving with the bulk "falling" velocity along \underline{B} , and hence to treat numerically only the transport of ions perpendicular to \underline{B} within each layer.

b) We limit our discussion to a model consisting of only two layers or species of ions.

c) We assume that the ion neutral collision frequency ν_{in} is constant within a layer.

d) We assume that the only forces acting on the plasma are an external electric field \underline{E}_0 and pressure gradients.

With the above assumptions we have

$$\begin{aligned} \underline{j}_{lk}^{ext} = & \sum_{pk} \left(\underline{E}_0 - \frac{\nabla P_i}{ne} \right)_k \\ & + \frac{B}{|B|} \left[\frac{\nu_{in}}{\Omega_i E_0} - \frac{\Omega_i}{ne \nu_{in}} (\nabla P_i + R_i^{-1} \nabla P_e) \right]_k \times \hat{z} \end{aligned} \quad (4.1)$$

If we assume \underline{B} is along the positive z axis then $B/|B| = 1$ and we get

$$\begin{aligned} \nabla_1 \cdot \underline{j}_{lk}^{ext} = & \nabla_1 \cdot \left(\sum_{pk} \left(\underline{E}_0 - \frac{\nabla P_i}{ne} \right)_k \right) \\ & + \nabla_1 \cdot \left(\sum_p \frac{\nu_{in}}{\Omega_i} \underline{E}_0 \times \hat{z} \right)_k + H_{pk} \end{aligned} \quad (4.2)$$

where

$$H_{pk} = - \nabla_{\perp} \cdot \left[\sum_p \frac{\Omega_i}{n e v_{in}} (\nabla P_i + R_i^{-1} \nabla P_e) \times \hat{z} \right]_k \quad (4.3)$$

Now

$$\begin{aligned} \left[\sum_p \frac{\Omega_i}{n e v_{in}} \right]_k &= \left[R_i \frac{v_{in}}{\Omega_i} \frac{n c e}{|B|} \Delta z \frac{\Omega_i}{v_i n e} \right]_k \\ &= \left[R_i \frac{c}{|B|} \Delta z \right]_k \end{aligned} \quad (4.4)$$

which is a constant within a layer if v_{in} is constant within a layer (one of our assumptions). Then

$$H_{pk} = - \nabla_{\perp} \cdot (\text{constant } \nabla (P_i + R_i^{-1} P_e) \times \hat{z}) = 0 \quad (4.5)$$

(since $\nabla_{\perp} \cdot (\nabla C \times \hat{z}) = 0$ for any scalar field C).

Our final equations to be solved are then

$$\frac{\partial N_k}{\partial t} + \nabla_{\perp} \cdot (N_k \mathbf{v}_{k\perp}) = 0 \quad k=1,2 \quad (4.6)$$

$$\begin{aligned} \nabla_{\perp} \cdot [(\sum_{p1} + \sum_{p2}) \nabla_{\perp} \phi] + H &= E_0 \cdot \nabla_{\perp} (\sum_{p1} + \sum_{p2}) \\ &- \nabla_{\perp} \cdot \left(\sum_{p1} \frac{\nabla P_{i1}}{n_1 e} + \sum_{p2} \frac{\nabla P_{i2}}{n_2 e} \right) \end{aligned} \quad (4.7)$$

where

$$H \equiv - \frac{\partial}{\partial x} [(\Sigma_{h1} + \Sigma_{h2})(\frac{\partial \phi}{\partial y} - E_{oy})] + \frac{\partial}{\partial y} [(\Sigma_{h1} + \Sigma_{h2})(\frac{\partial \phi}{\partial x} - E_{ox})] \quad (4.8)$$

Looking at Eq. (4.7) we notice that ϕ may be separated into two parts:

$$\phi = \phi_E + \phi_P \quad (4.9)$$

$$\nabla_1 \cdot [(\Sigma_{p1} + \Sigma_{p2})\nabla_1 \phi_E] + H = E_o \cdot \nabla_1 (\Sigma_{p1} + \Sigma_{p2}) \quad (4.10)$$

$$\nabla_1 \cdot [(\Sigma_{p1} + \Sigma_{p2})\nabla_1 \phi_P] = - \nabla_1 (\Sigma_{p1} \frac{\nabla P_{11}}{n_1 e} + \Sigma_{p2} \frac{\nabla P_{12}}{n_2 e}) \quad (4.11)$$

For reasons which shall become clear as we progress, we shall regard ϕ_E as that part of the potential field which tends to drive the cloud toward bifurcation. In fact, Eq. (4.10) coupled with (4.6) just form the basic inviscid two-level equations [Scannapieco et al., 1976]. We shall regard ϕ_P as that part of the potential field which tends to diffuse or anti-diffuse the edges of the cloud. First let us look at solutions to (4.11). If ∇P_{11} and ∇P_{12} vanish at our boundaries, the unique solution consistent with zero Neumann boundary conditions (vanishing of the normal derivative of ϕ_P at the boundary) is:

$$- (\Sigma_{p1} + \Sigma_{p2})\nabla_1 \phi_P = \Sigma_{p1} \frac{\nabla P_{11}}{n_1 e} + \Sigma_{p2} \frac{\nabla P_{12}}{n_2 e} \quad (4.12)$$

In general, the motion resulting from the forces proportional to $\nabla \phi_P$, ∇P_{11} and ∇P_{12} will be quite complex, not describable as the simple

superposition of a shear and a diffusion; but in the special case of one of the layers being uniform, e.g., N_2 and T_{i2} (T_i = ion temperature) hence Σ_{p2} and P_{i2} uniform, then

$$\nabla \phi_P = \frac{-\Sigma_{p1}}{\Sigma_{p1} + \Sigma_{p2}} \frac{\nabla P_{i1}}{n_1 e} \quad (4.13)$$

We shall now treat this special case. One may conveniently think of level 1 as representing the barium cloud and level 2 the uniform background ionosphere.

We now use the equation of state

$$P_i = n T_i$$

where T_i is in energy units (T_i is the product of Boltzmann's constant and the temperature in degrees Kelvin), and assume thermal conductivities high enough such that T_i is constant and hence

$$\nabla P_i = T_i \nabla n \quad (4.14)$$

Then

$$\nabla \phi_P = \frac{-\Sigma_{p1}}{\Sigma_{p1} + \Sigma_{p2}} \frac{T_{i1} \nabla n_1}{n_1 e}$$

The velocity in level 1 resulting from the combined action of ∇P_1 and ϕ_P is

$$\begin{aligned} \underline{v}_{11P} = & \left[\frac{v_{1n}}{\Omega_1} R_i \frac{c}{e|B|} (-e\nabla\phi_P - T_i \frac{\nabla n}{n}) \right]_1 \\ & + \left[R_i \frac{c}{eB} (-e\nabla\phi_P - T_i \frac{\nabla n}{n}) \right]_1 \times \hat{z} \end{aligned} \quad (4.15)$$

Now

$$\begin{aligned} & (-e\nabla\phi_P - T_i \frac{\nabla n}{n})_1 \\ & = T_{i1} \frac{v_{n1}}{n_1} \left(\frac{\Sigma_{p1}}{\Sigma_{p1} + \Sigma_{p2}} - 1 \right) \\ & = -T_{i1} \frac{v_{n1}}{n_1} \left(\frac{\Sigma_{p2}}{\Sigma_{p1} + \Sigma_{p2}} \right) \end{aligned} \quad (4.16)$$

$$\begin{aligned} \underline{v}_{11P} = & \frac{-\Sigma_{p2}}{\Sigma_{p1} + \Sigma_{p2}} \left[\left(\frac{v_{1n}}{\Omega_1} R_i \frac{c}{e|B|} T_i \frac{\nabla n}{n} \right)_1 \right. \\ & \left. + \left(R_i \frac{c}{eB} T_i \frac{\nabla n}{n} \right)_1 \times \hat{z} \right] \end{aligned} \quad (4.17)$$

Note we have used $\frac{\nabla n}{n} = \frac{\nabla N}{N}$.

It is convenient to divide \underline{v}_{11P} into two parts:

$$\underline{v}_{11P} = \underline{v}_{D1} + \underline{v}_{S1}$$

with the subscripts i and P suppressed but understood.

$$\underline{v}_{D1} = - \frac{\Sigma_{p2}}{\Sigma_{p1} + \Sigma_{p2}} \left(\frac{v_{1n}}{\Omega_1} R_i \frac{c}{e|B|} T_i \frac{\nabla N}{N} \right)_1 \quad (4.18)$$

$$\underline{v}_{S1} = - \frac{\Sigma_{p2}}{\Sigma_{p1} + \Sigma_{p2}} \left(R_1 \frac{c}{eB} T_1 \frac{\nabla N}{N} \right)_1 \times \hat{z} \quad (4.19)$$

That \underline{v}_{S1} represents shear flow at plasma gradients can be seen by noting that the velocity is always perpendicular to ∇N , and is largest where $\frac{\Sigma_{p2}}{\Sigma_{p1} + \Sigma_{p2}} \frac{\nabla N}{N}$ is a maximum, decaying in magnitude away from the region. \underline{v}_S is of interest because it is a shear flow and hence may be stabilizing in certain cases (see Perkins and Doles [1975], Huba et al. [1982]). We do not consider the effects of \underline{v}_S further in this paper except to note that for the special case of a uniform layer 2 being considered here, $\nabla \cdot \underline{v}_{S1} = 0$ and $\nabla N_1 \cdot \underline{v}_{S1} = 0$ which together imply $\nabla \cdot (N_1 \underline{v}_{S1}) = 0$, which is to say that \underline{v}_{S1} has no effect on the time evolution of N_1 . Since this breaks the feedback loop, it is difficult to see how a shear stabilization mechanism could be active in this case.

A consideration of \underline{v}_D is really the heart of this paper. \underline{v}_D is the source for ion diffusion in level 1. More importantly, it is the source for the diffusion of the total integrated Pedersen and Hall conductivities if level 2 is sufficiently incompressible (i.e., if v_{in}/Ω_1 in level 2 is sufficiently small), as we will show. Let us look at the effect of \underline{v}_D on the ion continuity equation for level 1:

$$\begin{aligned} \frac{\partial N_1}{\partial t} &= - \nabla \cdot (N_1 \underline{v}_{D1}) \\ &= + \nabla \cdot \left[\frac{\Sigma_{p2}}{\Sigma_{p1} + \Sigma_{p2}} \left(\frac{v_{in}}{\Omega_1} R_1 \frac{c}{e|B|} T_1 \nabla N \right)_1 \right] \end{aligned} \quad (4.20)$$

This is just a diffusion equation for N_1 with diffusion coefficient

$$D_o = \frac{\Sigma_{p2}}{\Sigma_{p1} + \Sigma_{p2}} \left(\frac{v_{in}}{\Omega_1} R_1 \frac{c}{e|B|} T_1 \right)_1 \quad (4.21)$$

For a barium cloud (level 1) at 180 km altitude we take $T_1 \sim 1000^\circ \text{ K}$, $\frac{v_{in}}{\Omega_1} \sim 0.06$, $B = 0.5 \text{ g}$, and get

$$D_o = \frac{\Sigma_{p2}}{\Sigma_{p1} + \Sigma_{p2}} (100 \text{ m}^2/\text{sec}) \quad (4.22)$$

In the less dense regions of the barium cloud where Σ_{p1} is small compared to Σ_{p2} , the ion diffusion coefficient is quite large indeed. By contrast ambipolar diffusion rates induced by electron-ion and electron-neutral collisions yield diffusion coefficients on the order of $1 \text{ m}^2/\text{sec}$. Thus our neglect of these collision terms seems justified. Unfortunately, N_1 is not the relevant quantity if one is interested in the effect of $\underline{v_D}$ on barium cloud dynamics. A look at Eq. (4.10) will convince the reader that if one wants to affect the time evolution of ϕ_E , the quantity which determines the bifurcation process, it is necessary to change the quantities

$\Sigma_p \equiv \Sigma_{p1} + \Sigma_{p2}$ and $\Sigma_h \equiv \Sigma_{h1} + \Sigma_{h2}$, the total field line integrated Pedersen and Hall conductivities. Again we assume an initially uniform distribution of Σ_{p2} and N_2 . We can only show the effects of $\underline{v_D}$ in the first instant of time here. Once images form in level 2, the problem yields only to numerical techniques. We need the velocity $\underline{v_{D2}}$ in level 2.

$$\underline{v_{D2}} = \left(\frac{v_{in}}{\Omega_1} R_1 \right)_2 \frac{c}{e|B|} \frac{\Sigma_{p1}}{\Sigma_{p1} + \Sigma_{p2}} \left(T_{11} \frac{v N_1}{N_1} \right) \quad (4.23)$$

As a check, let us see the effect on $(N_1 + N_2)$

$$\begin{aligned}
\frac{\partial N_2}{\partial t} &= -\nabla \cdot (N_2 \underline{v}_{D2}) \\
&= -\nabla \cdot (\Sigma_{p2} e^{-2} \frac{\Sigma_{p1}}{\Sigma_{p1} + \Sigma_{p2}} (T_{i1} \frac{\nabla N_1}{N_1}))
\end{aligned} \tag{4.24}$$

$$\begin{aligned}
\frac{\partial N_1}{\partial t} &= -\nabla_1 (N_1 \underline{v}_{D1}) \\
&= +\nabla \cdot (\frac{\Sigma_{p2}}{\Sigma_{p1} + \Sigma_{p2}} \Sigma_{p1} e^{-2} T_{i1} \frac{\nabla N_1}{N_1}) \\
&= -\frac{\partial N_2}{\partial t}
\end{aligned} \tag{4.25}$$

so we see that

$$\frac{\partial (N_1 + N_2)}{\partial t} = 0 \tag{4.26}$$

which when combined with quasi-neutrality, is simply a statement that electrons can't diffuse. This is consistent with our neglect of electron-ion and electron-neutral collisions.

Now let us look at the effect of \underline{v}_D on $\Sigma_p = \Sigma_{p1} + \Sigma_{p2}$. A similar analysis can be performed for Σ_h with similar results. However the bifurcation effects of Σ_h are small compared to those of Σ_p , and we shall not consider them here.

$$\frac{\partial \Sigma_{p1}}{\partial t} = (\frac{v_{in}}{\Omega_1} R_1)_1 \frac{ce}{|B|} \frac{\partial N_1}{\partial t} = \nabla \cdot (\underline{v}_{D1} \Sigma_{p1}) \tag{4.27}$$

$$\frac{\partial \Sigma_{p2}}{\partial t} = (\frac{v_{in}}{\Omega_1} R_1)_2 \frac{ce}{|B|} \frac{\partial N_2}{\partial t} = \nabla \cdot (\underline{v}_{D2} \Sigma_{p2}) \tag{4.28}$$

but

$$\frac{\partial N_1}{\partial \tau} = - \frac{\partial N_2}{\partial \tau} = - \frac{|B|}{ce} \left(\frac{v_{in}}{\Omega_i} R_i \right)_1^{-1} \frac{\partial \Sigma_{p2}}{\partial \tau} \quad (4.29)$$

$$\frac{\partial \Sigma_{p1}}{\partial \tau} = - \frac{\left(\frac{v_{in}}{\Omega_i} R_i \right)_1 \frac{\partial \Sigma_{p2}}{\partial \tau}}{\left(\frac{v_{in}}{\Omega_i} R_i \right)_2} \quad (4.30)$$

$$\frac{\partial (\Sigma_{p1} + \Sigma_{p2})}{\partial \tau} = \frac{\partial \Sigma_{p1}}{\partial \tau} \left[1 - \left(\frac{v_{in}}{\Omega_i} R_i \right)_2 / \left(\frac{v_{in}}{\Omega_i} R_i \right)_1 \right] \quad (4.31)$$

Now

$$\frac{\partial \Sigma_{p1}}{\partial \tau} = - \nabla_1 \cdot (\underline{v}_{D1} \Sigma_{p1}) \quad (4.32)$$

We note that in Eq. (4.18) we may set $\nabla N_1 / N_1 = \nabla \Sigma_{p1} / \Sigma_{p1}$ so that

$$\frac{\partial \Sigma_{p1}}{\partial \tau} = \nabla \cdot \left[\frac{\Sigma_{p2}}{\Sigma_{p1} + \Sigma_{p2}} \left(\frac{v_{in}}{\Omega_i} R_i \frac{c}{e|B|} T_i \right)_1 \nabla \Sigma_{p1} \right] \quad (4.33)$$

Now since

$$\nabla \Sigma_{p2} = 0 \quad (4.34)$$

we have

$$\nabla (\Sigma_{p1} + \Sigma_{p2}) = \nabla \Sigma_{p1} \quad (4.35)$$

and

$$\frac{\partial(\Sigma_{p1} + \Sigma_{p2})}{\partial t} = v_{\perp} \cdot \left[\left(1 - (v_{in R_i / \Omega_i})_2 / (v_{in R_i / \Omega_i})_1 \right) \left(\frac{\Sigma_{p2}}{\Sigma_{p1} + \Sigma_{p2}} \right) \right. \\ \left. \left(\frac{v_{in}}{\Omega_i} R_i \frac{c}{eB} T_i \right)_1 \nabla(\Sigma_{p1} + \Sigma_{p2}) \right] \quad (4.36)$$

so we see that for Σ_p we again have a diffusion equation, but this time our nominal $100 \text{ m}^2/\text{sec}$ diffusion coefficient is not only multiplied by $\Sigma_{p2}/(\Sigma_{p1} + \Sigma_{p2})$, reducing its effectiveness in the dense portions of the cloud, but it is further multiplied by the factor F where

$$F = 1 - \frac{(v_{in R_i / \Omega_i})_2}{(v_{in R_i / \Omega_i})_1} \quad (4.37)$$

Note that if $v_{in R_i / \Omega_i}$ is the same for both layers, the diffusion is reduced to zero. Furthermore, if $(v_{in R_i / \Omega_i})_2 > (v_{in R_i / \Omega_i})_1$ (a compressible background plasma, e.g., an E region) the diffusion coefficient is negative. That is, gradients in Σ_p will actually be steepened, rather than smoothed. For this reason we conclude that unless some rather fast recombination chemistry is taking place in the E region, the presence of a background E region is destabilizing, in accord with the findings of Francis and Perkins [1975].

The opposite extreme of $(v_{in R_i / \Omega_i})_2 \ll (v_{in R_i / \Omega_i})_1$ (background F region ionosphere) is more interesting since it closely approximates the conditions of most barium releases. It also yields the full nominal $100 \text{ m}^2/\text{sec}$ diffusion coefficient, since $F = 1.0$, giving us some hope of stopping the bifurcation process at space scales of hundreds of meters.

Note that in this case the diffusion rate for Σ_p is the same as that for N_1 . Also note that the case of $(v_{in1} R_1 / \Omega_1)_2$ small is the case where the Pedersen mobility and hence compressibility of the background is extremely low, meaning that only minimal images will be formed. It is a good approximation to take Σ_{p2} to be uniform for all time. One might well ask how this is possible given that the electrons can't diffuse, and that the barium ions are being allowed to diffuse in level 1. The answer is that there are (small) images: the electrons lost to a field line in level 1 are "soaked up" on the same field line in level 2. But the number of electrons N_2 in level 2 is extremely large. (N_2 must be large in order to contribute a significant Pedersen conductivity and yet have small $v_{in1} R_1 / \Omega_1$ (see Eq. 2.24)). Thus the electrons that are soaked up in level 2 induce only an extremely small percentage change in Σ_{p2} .

5. Diffusion Characteristics for a Simplified Two-level Model with a Nearly Incompressible Background Layer

In the last section we demonstrated that when the background ionosphere (layer 2) is nearly incompressible ($(v_{in} R_1 / \Omega_1)_2$ is small) then the primary effect of a finite barium ion temperature is to introduce into the continuity equation for both N_1 and for Σ_p a diffusion term with diffusion coefficient D_0 given by Eq. (4.21). For parameters appropriate to a barium cloud at 180 km altitude we get Eq. (4.22):

$$D_0 = \frac{\Sigma_{p2}}{\Sigma_{p1} + \Sigma_{p2}} (100 \text{ m}^2/\text{sec}) \quad (4.22)$$

Since level 2 is nearly incompressible, we may regard Σ_{p2} as a constant. Since it is proportional to N_1 , the integrated barium cloud density, Σ_{p1} is larger in the center of the cloud and decays toward zero at the cloud edges. This means that the diffusion coefficient approaches $100 \text{ m}^2/\text{sec}$ near the cloud edges, but may be considerably less than that value near the cloud center if $\Sigma_{p1} \gg \Sigma_{p2}$.

Previous attempts to explain the persistence of scale sizes of hundreds of meters for long periods of time after barium releases have inevitably encountered the following problems: 1) The diffusion coefficients required to stop the bifurcation of plasma clouds several hundred meters in diameter were higher than one could explain theoretically; 2) assuming the existence of such large (ordinary) diffusion coefficients, their effect would not only be to stop the bifurcation of the cloud, but also to diffuse the cloud away entirely in several minutes. The form of the diffusion coefficient given by Eq. (4.22) would seem to offer us some hope of overcoming both of these problems. Its success depends on

the accuracy of the following qualitative picture of barium cloud bifurcation: We postulate a barium cloud such that $\Sigma_{p1} \geq 5 \Sigma_{p2}$ so that the diffusion well inside the cloud is considerably reduced over that at its edges. We further postulate that bifurcation is a process which, in the absence of diffusion, starts at the edges of barium clouds and works its way inward. Our diffusion then satisfies the needed criteria perfectly: 1) It is very effective at the edges of the cloud, stopping bifurcation before it starts; 2) it is very ineffective at the central core of the cloud, giving it a long lifetime. Note that if this picture is correct then the barium clouds commonly known as large M clouds where

$$M \equiv \frac{\Sigma_{p1} + \Sigma_{p2}}{\Sigma_{p2}} \quad (5.1)$$

will have extremely long lifetimes. In fact for $M \geq 100$, the decay of the core is probably determined by ambipolar diffusion rates. The accuracy of this picture is best determined by numerical simulation techniques, to which we turn in the next section.

6. Preliminary Numerical Simulations Using a Simplified Two-level Model with a Nearly Incompressible Background Layer

In this section we attempt to answer numerically the question posed in the last section: if we consider a barium cloud whose background conductivity is due primarily to high F region plasma (nearly incompressible plasma), is the diffusion coefficient given by Eq. (4.22) sufficient to stop the bifurcation of that cloud at a diameter of several hundred meters? In order to isolate the effects of this diffusion coefficient, we will make some further simplifications in our two-level model: 1) We assume that N_2 and hence Σ_{p2} remain uniform during all times of interest. This is completely consistent with our assumption of a nearly incompressible background plasma, as discussed at the end of Section 4; 2) We neglect the shear component v_s of the pressure-induced ion velocity as defined in Eq. (4.19). Again this is consistent with our assumption of a nearly incompressible background plasma which in turn implies a uniform Σ_{p2} , as shown in the discussion following Eq. (4.19); 3) We neglect the "Hall term" H in Eq. (4.4) and hence in Eq. (4.10). This is a good approximation as long as $v_{in}/\Omega_i < 0.1$; 4) We neglect Pedersen convection. That is, for all terms except those causing ion diffusion, we approximate the ion velocity with the electron velocity (see Eq. (6.4) below). We know from our previous [Zalesak et. al., 1983] that the Pedersen mobility of the ions in response to $(\underline{E}_0 - \nabla\phi_E)$ can have an effect on the "freezing" phenomenon, and it is our desire to isolate the effects of the pressure-induced diffusion. Hence we neglect ion Pedersen mobility except in the diffusion term.

The final equations to be solved numerically are then

$$\frac{\partial N_1}{\partial \tau} + \nabla_1 \cdot (N_1 \underline{v}_1) - \nabla_1 \cdot (D \nabla N_1) \quad (6.1)$$

$$\frac{\partial N_2}{\partial \tau} = 0 \quad (6.2)$$

$$\nabla_1 ((\Sigma_{p1} + \Sigma_{p2}) \nabla_1 \phi_E) = \underline{E}_0 \cdot \nabla_1 (\Sigma_{p1} + \Sigma_{p2}) \quad (6.3)$$

$$\underline{v}_1 = \frac{C}{B^2} (\underline{E}_0 - \nabla \phi_E) \times \underline{B} \quad (6.4)$$

$$D = \frac{\Sigma_{p2}}{\Sigma_{p1} + \Sigma_{p2}} D_{i0} \quad (6.5)$$

$$\Sigma_{pk} \equiv N_k \left(\frac{v_{in}/\Omega_i}{1 + (v_{in}/\Omega_i)^2} \right)_k \frac{ce}{|B|} \quad (6.6)$$

The initial conditions for the simulations were as follows

$$\Sigma_{p2} = 1.0 \quad (6.7)$$

$$\Sigma_{p1} = 4.0 \exp (r^4/r_0^4) \quad (6.8)$$

$$r^2 = (x - x_0)^2 + (y - y_0)^2 \quad (6.9)$$

$$r_0 = (250 \text{ m}) (1 + 0.001 \sin 8\theta) \quad (6.10)$$

$$\theta = \arctan ((y - y_0)/(x - x_0)) \quad (6.11)$$

$$B = 0.5 \text{ gauss} \quad (6.12)$$

$$cE_0/B = 100 \text{ m/sec} \quad (6.13)$$

where x_0 and y_0 are the coordinates of the cloud center.

The above equations are solved numerically on a finite difference grid in an x-y cartesian geometry perpendicular to the magnetic field, which is assumed to be aligned along the z-axis. The 83 x 60 grid is stretched in all four directions, with the central 56 x 32 portion of the grid, which is centered on the steepening backside of the cloud, having a grid spacing of 10 m in both directions. The grid stretching allows the boundaries to be placed 4 km away from the edges of the central uniform mesh in all directions. The potential equation (6.3) is solved using a vectorized incomplete Cholesky conjugate gradient algorithm due to Hain (1980), which is an extension of the algorithm of Kershaw (1978). The continuity equation (6.1) is integrated forward in time using the fully multidimensional flux-corrected transport algorithms of Zalesak [1979].

In Figure 3 we show isodensity contours of Σ_{p1} for the initial conditions for all of the calculations we shall show. We have performed three calculations, varying the value of D_{10} from zero up to the physically realistic value of 100 m²/sec. The purpose of this sequence is to show first that the diffusion does have an effect on the evolution of the cloud, and second to show that this effect is much larger than that due to any numerical diffusion which may be present in the calculations. In Figure 4 we show the results for $D_{10} = 0$. Note that even at the very early time of 14 seconds, bifurcation has already started. By 24 seconds, the main portion of the cloud has completely sheared in two. In Figure 5, we show the results for $D_{10} = 25 \text{ m}^2/\text{sec}$, one fourth of the physically realistic

value. The development of the cloud has slowed considerably, showing that even at one fourth its physically realistic value, the physical diffusion is dominating the effects of whatever numerical diffusion may be present. At 14 seconds the cloud has not clearly begun to bifurcate. At 25 seconds, bifurcation has occurred, but is qualitatively and quantitatively different from that which took place when $D_{10} = 0$. In Figure 6 we show the evolution of the cloud with the full, physically realistic value for D_{10} of $100 \text{ m}^2/\text{sec}$. Bifurcation has now been halted. Rather, the cloud evolves into a streamlined "bullet" or "tadpole" shape in time, and then undergoes a slow diffusive decay. Even at the latest time calculated, 75 sec, there is no hint whatsoever of imminent bifurcation. Noting that for this cloud $M = (\Sigma_{p1} + \Sigma_{p2})/\Sigma_{p2}$ is 5 in the center of the cloud, which yields an effective diffusion coefficient of $20 \text{ m}^2/\text{sec}$ there. This is still enough to result in substantial decay of the central core on time scales of minutes. Clouds with larger values of M in their centers would of course be longer-lived.

7. Conclusions and Future Work

The primary conclusion of this paper can be stated simply: Under realistic ionospheric conditions, barium striations hundreds of meters in diameter can be long-lived, quasi-stable, non-bifurcating structures. These structures may resemble "tadpoles", with a dense head, steep density gradients at the front, and a long, less dense tail. If what one means by the term "freezing" is the above phenomenon, then we have shown that freezing does indeed exist.

The next obvious step is to test some of the approximations we have made in our preliminary numerical simulation model. Pedersen convection should be put back into the model, as well as the "Hall terms" in the potential equation. Finite images should be accounted for. Also we would like to test the combined effect of the presence of both a relatively incompressible F region background and a compressible E region on the dynamics of the cloud. Recombination chemistry must be included in this E region if it is to be modeled accurately (see Vickery and Kelley, 1982).

It is also clear that we must address the validity of the perfect mapping of the electrostatic potential along B. Given that we are now dealing with structures only a few hundred meters in diameter, with gradient scale lengths of a few tens of meters, it seems likely that we will have to deal with the question of how far the polarization field produced by the barium cloud maps along the magnetic field (Goldman et. al, 1976, Glassman and Sperling, 1983). One possible effect might be that the effective value of M would be increased, since the barium cloud could no longer "see" background plasma that was far from the cloud position along B.

References

- Fedder, J.A., Conductivity formulas for the disturbed ionosphere, NRL Memo Report 4329, Nav. Res. Lab., Washington, D.C., Sept., 1980.
- Francis, S.H., and F.W. Perkins, Determination of striation scale sizes for plasma clouds in the ionosphere, J. Geophys. Res., 80, 3111, 1975.
- Glassman, A.J. and J.L. Sperling, Electromagnetic theory of collisional interchange instabilities, J. Geophys. Res., in press, 1983.
- Goldman, S.R., L. Baker, S.L. Ossakow, and A.J. Scannapieco, Striation formation associated with barium clouds in an inhomogeneous ionosphere, J. Geophys. Res., 81, 5097, 1976.
- Hain, K., A non-recursive incomplete Cholesky decomposition method for the solution of linear equations with a sparse matrix, NRL Memo Report 4264, Nav. Res. Lab., Washington, D.C., June 1980.
- Huba, J.D., S.L. Ossakow, P. Satyanarayana, and P.N. Guzdar, Linear theory of the $\underline{E} \times \underline{B}$ instability with an inhomogeneous electric field, J. Geophys. Res., 88, 425, 1983.
- Kershaw, D.S., The incomplete Cholesky-conjugate gradient method for the iterative solution of systems of linear equations, J. Comput. Phys., 26, 43, 1978.
- McDonald, B.E., Ossakow, S.L., Zalesak, S.T., and Zubusky, N.J., "Scale sizes and lifetimes of F region striations as determined by the condition of marginal stability," J. Geophys. Res., 86, 5775, 1981.
- Perkins, F.W., and J.H. Doles III, Velocity shear and the $\underline{E} \times \underline{B}$ instability, J. Geophys. Res., 80, 211, 1975.
- Scannapieco, A.J., S.L. Ossakow, S.R. Goldman, and J.M. Pierre, Plasma cloud late time striation spectra, J. Geophys. Res., 81, 6037, 1976.

Shiau, J.N., and A. Simon, Barium cloud growth and striation in a conducting background, J. Geophys. Res., 79, 1895, 1974.

Vickrey, J.F., and M.C. Kelley, The effects of a conducting E layer on classical F region cross-field plasma diffusion, J. Geophys. Res., 87 4461, 1982.

Zalesak, S.T., "Fully multidimensional flux-corrected transport algorithms for fluids," J. Comp. Phys., 31, 335, 1979.

Zalesak, S.T., J.A. Fedder, and S.L. Ossakow, Analysis and numerical simulation of the effect of ion Pedersen mobility on ionospheric barium clouds, J. Geophys. Res., 88, 8003, 1983.

Figure Captions

Figure 1. Sketch of the time evolution of a typical barium cloud in a plane perpendicular to the magnetic field, subject to an upward directed neutral wind or equivalently to a rightward directed external electric field. Lines demarking the cloud denote plasma density contours, with the highest plasma density in the center of cloud.

Figure 2. Model of plasma and magnetic field geometry used in this paper. Field lines terminate on insulators at $z = \pm \infty$. Plasma is divided into "layers" along z for mathematical and numerical treatment. Each layer consists of a single ion species and its associated electrons. Multiple collocated ion species are treated by having multiple collocated "layers".

Figure 3. Isodensity contours, with areas between alternate contours shown cross-hatched, for the barium cloud used for the three numerical simulations shown in this paper. The center of the cloud is located at the point (0,0). The boundaries in x are located at ± 4.9 km. The boundaries in y are located at -4.0 km and $+5.3$ km respectively. The cross-hatching is done at every other grid line, so that one rectangle of cross hatching represents a 2×2 array of computational cells. Contours for this and all other plots in this paper are drawn at values for Σ_{pl} of 0.31, 0.71, 1.24, 1.92, and 2.82 (logarithmic spacing for total Pedersen conductivity).

Figure 4. Time evolution of the cloud depicted in Figure 3 for the case $D_{10} = 0$. Shown are isodensity contours at a) 14 sec, b) 24 sec. Contour values are as given in Figure 3.

Figure 5. Time evolution of the cloud depicted in Figure 3 for the case $D_{10} = 25 \text{ m}^2/\text{sec}$. Shown are isodensity contours at a) 14 sec, b) 24 sec. Contour values are as given in Figure 3.

Figure 6. Time evolution of the cloud depicted in Figure 3 for the case $D_{10} = 100 \text{ m}^2/\text{sec}$ (the physically realistic case). Shown are isodensity contours at a) 14 sec, b) 25 sec, c) 39 sec, d) 50 sec, e) 64 sec, f) 75 sec.

NEW CLOUDS

CLOUD SPLITS

STRIATIONS
BEGIN

INSTABILITY

STEEPENING
ON ONE SIDE

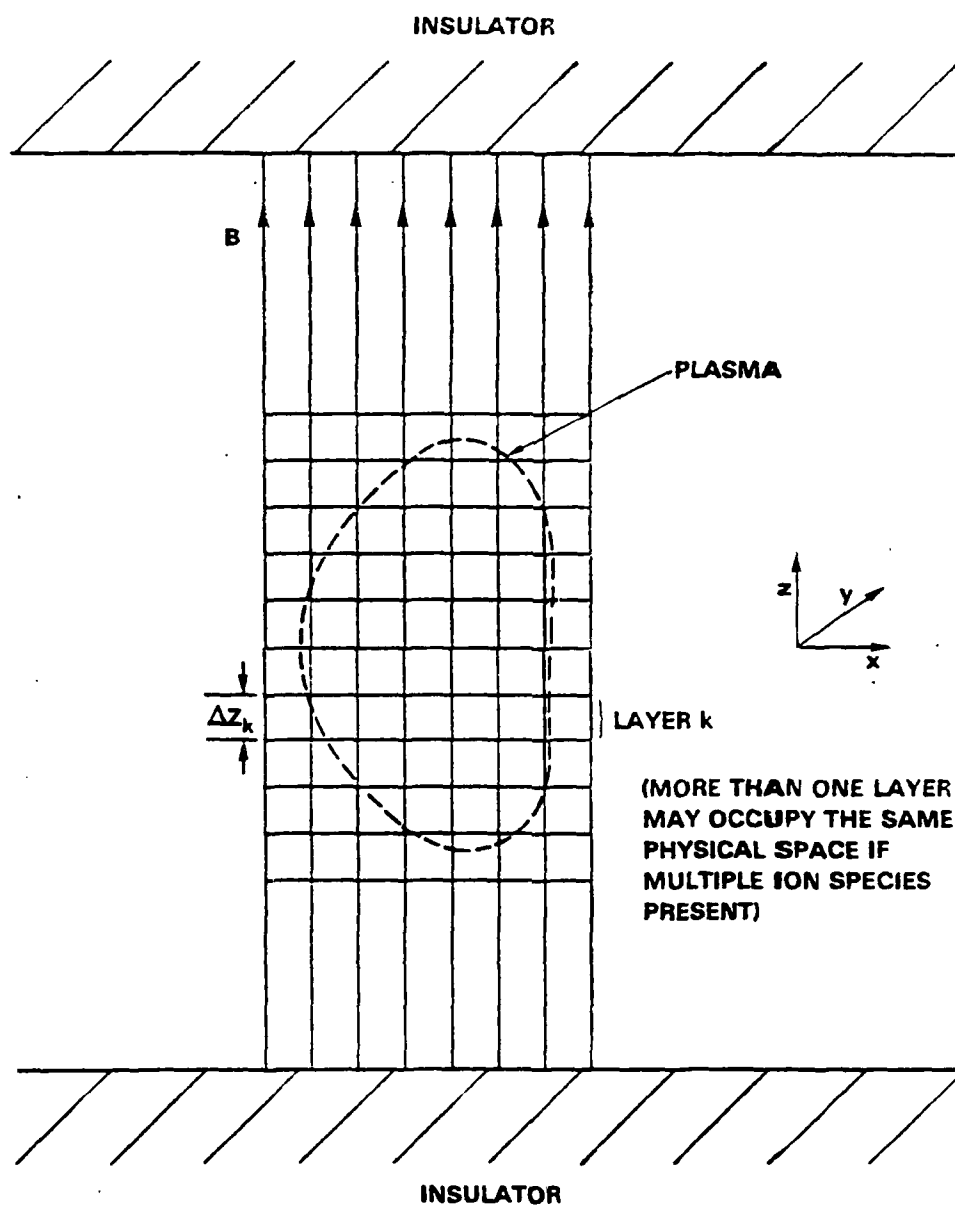
INITIAL CLOUD

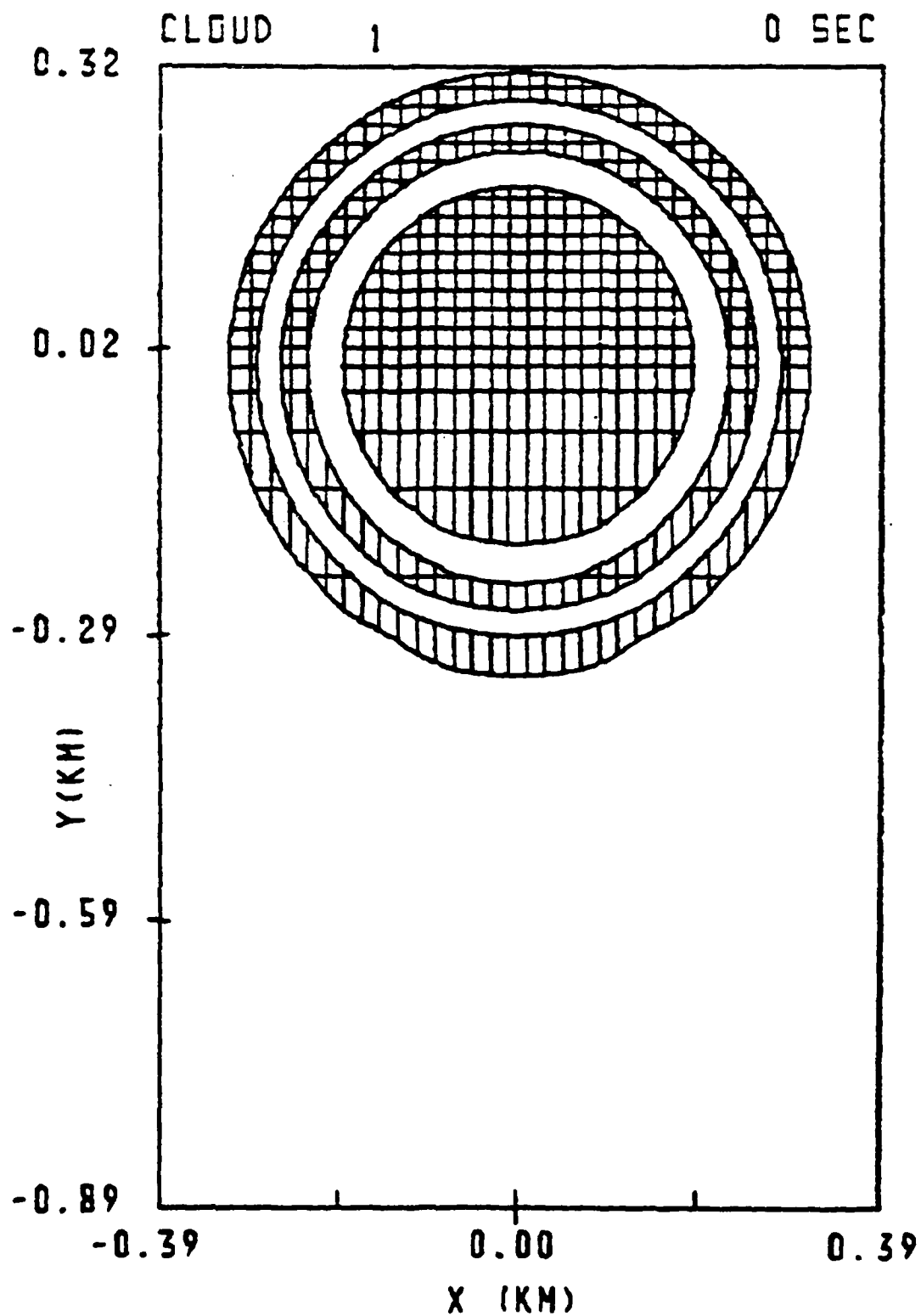
NEUTRAL WIND

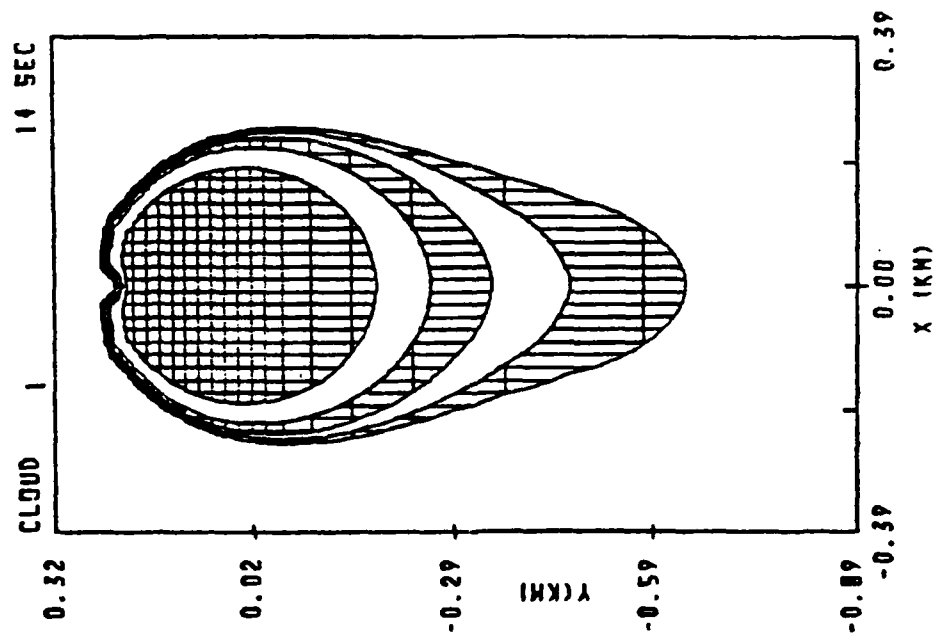
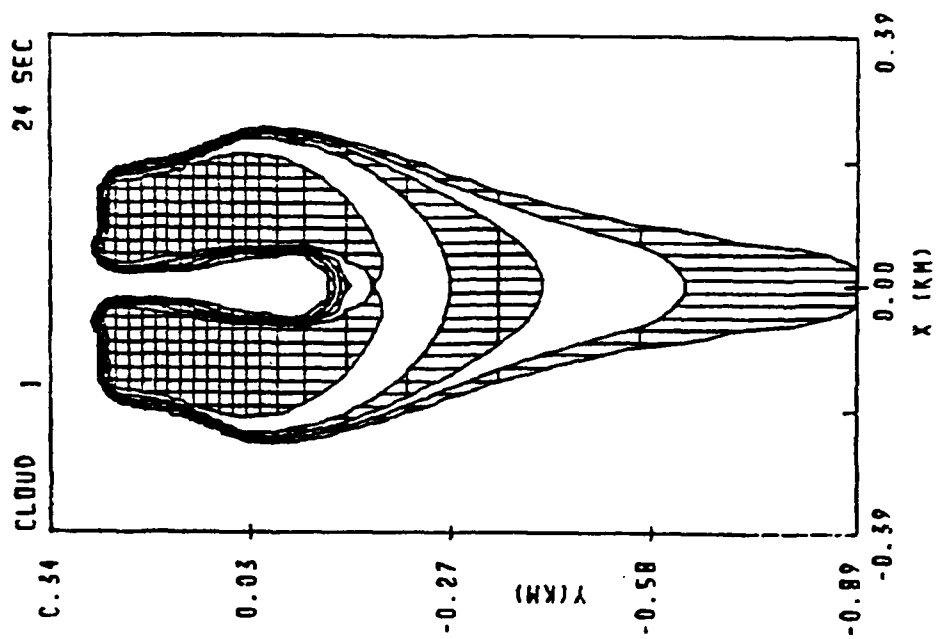
• \bar{B}

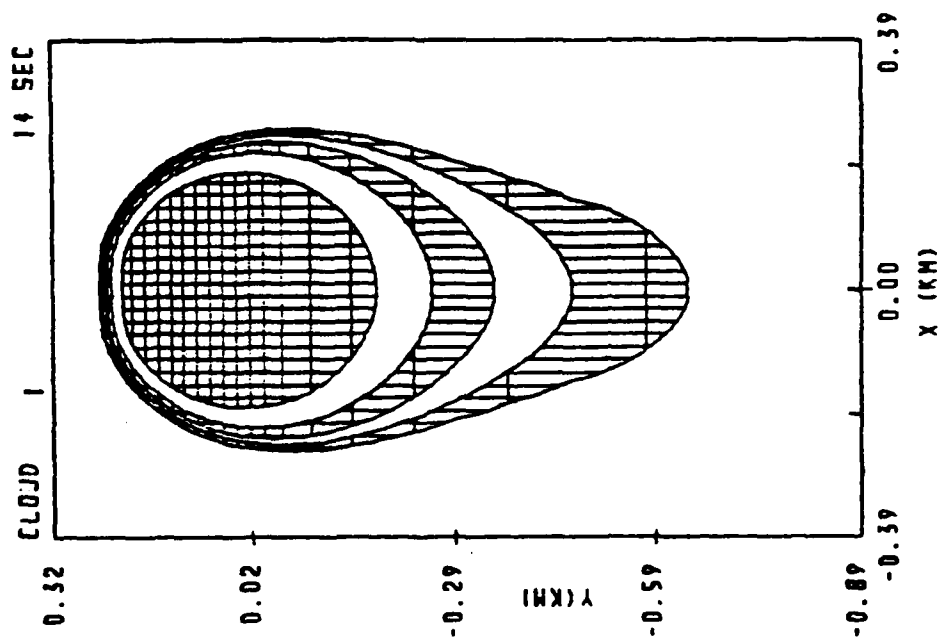
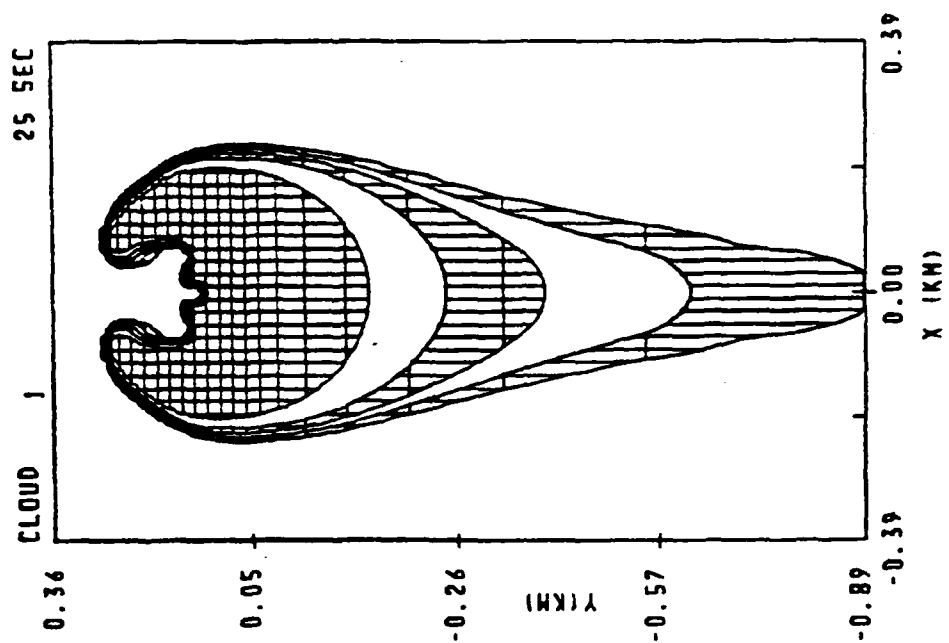
(ARROWS DENOTE E_p)

$t = 0$ $t > 0$



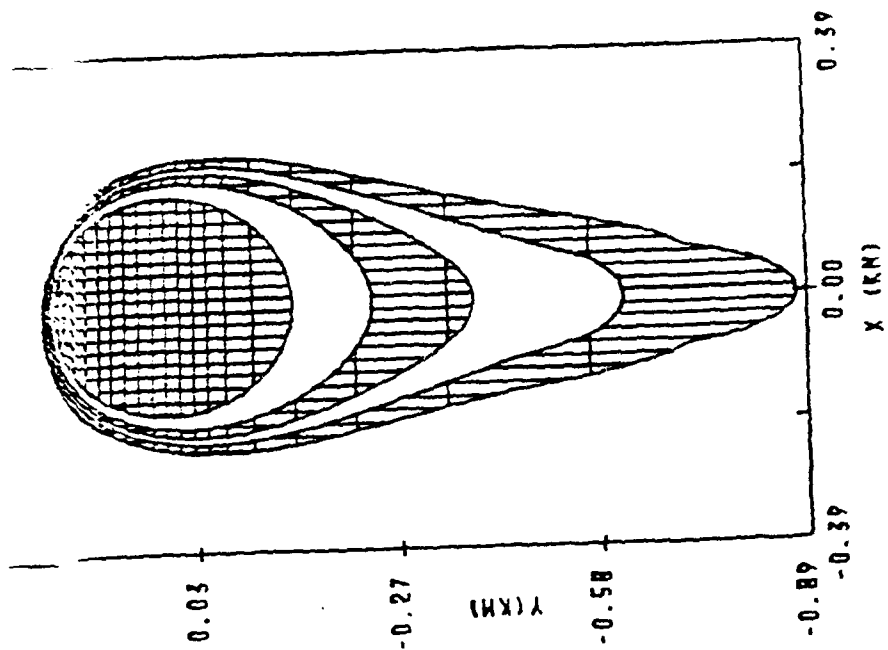






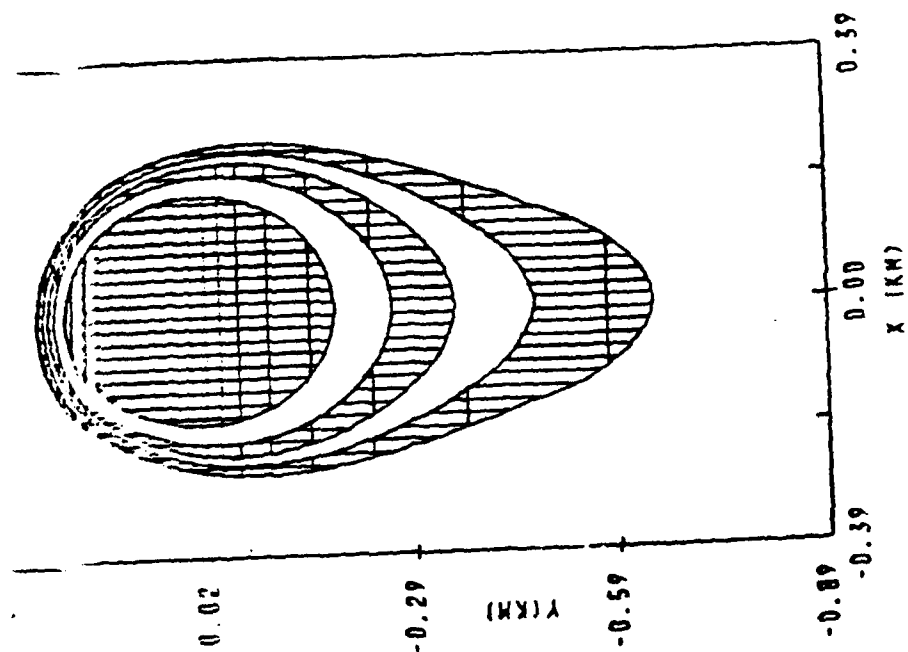
25 SEC

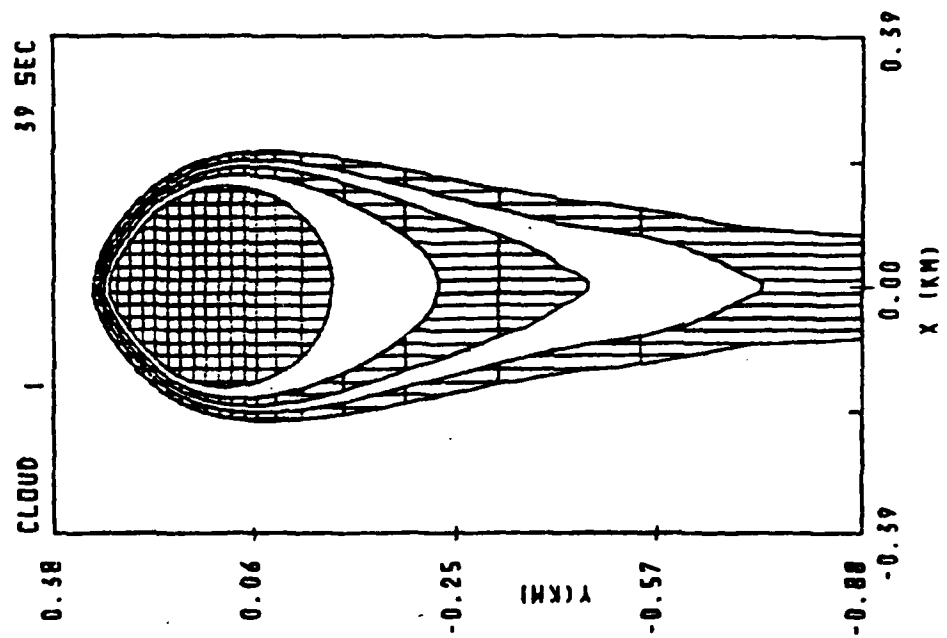
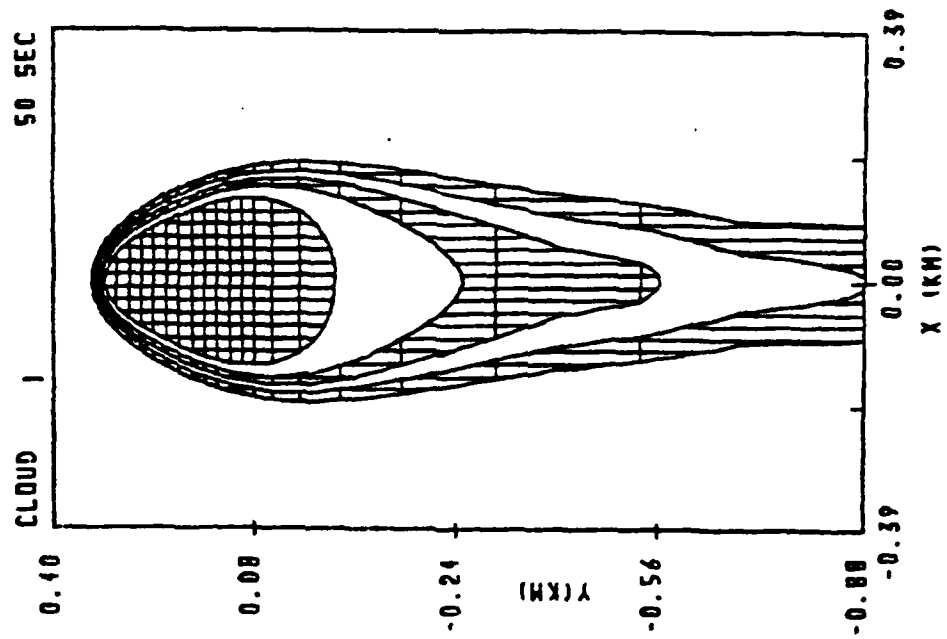
CLOUD



14 SEC

CLOUD





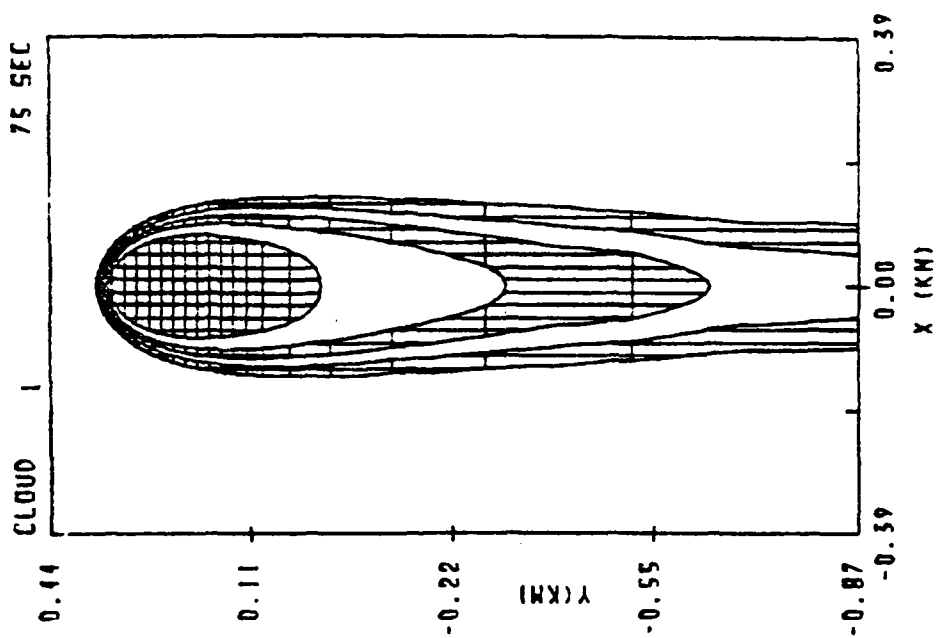


Fig. 6(a)

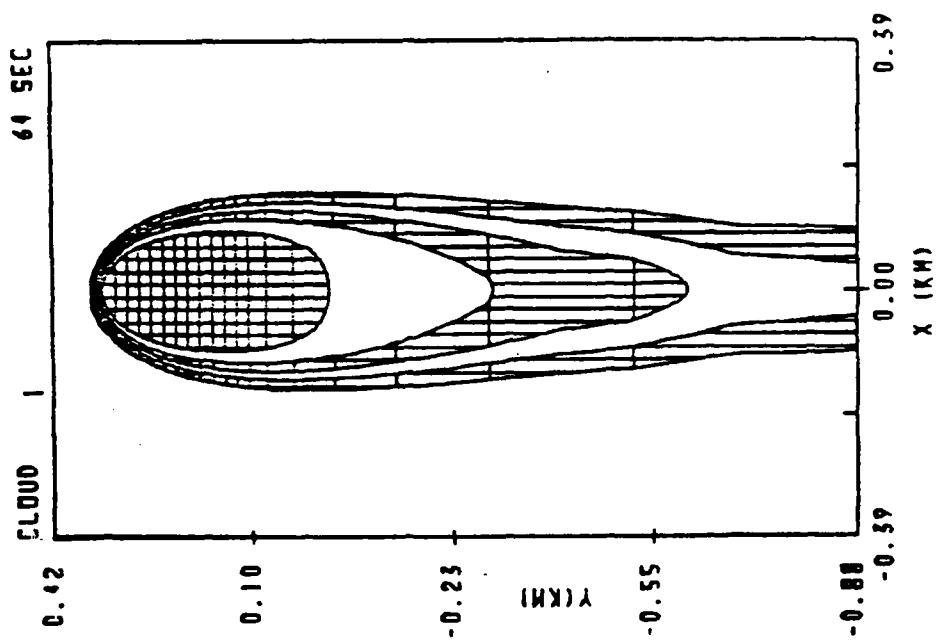


Fig. 6(b)

APPENDIX I
SATURATION OF THE LOWER-HYBRID-DRIFT
INSTABILITY BY MODE COUPLING

J.F. Drake
University of Maryland & Science Applications, Inc.

P.N. Guzdar
Science Applications, Inc.

and

J.D. Huba
Naval Research Laboratory

Saturation of the lower-hybrid-drift instability by mode coupling

J. F. Drake

University of Maryland, College Park, Maryland 20742

P. N. Guzdar

Science Applications, Inc., McLean, Virginia 22102

J. D. Huba

Geophysical and Plasma Dynamics Branch, Plasma Physics Division, Naval Research Laboratory, Washington, D.C. 20375

(Received 27 October 1982; accepted 4 January 1983)

A nonlinear mode-coupling theory of the lower-hybrid-drift instability is presented. It is found that the instability saturates by transferring energy from the growing, long wavelength modes to the damped, short wavelength modes. The saturation energy, mean square of the potential fluctuations, and diffusion coefficient are calculated self-consistently.

A first principles theory of the nonlinear saturation of the lower-hybrid-drift instability and associated particle transport is presented. A nonlinear equation describing 2-D lower-hybrid-drift turbulence is derived which includes the nonlinear $\mathbf{E} \times \mathbf{B}$ and polarization drifts of the electrons, adiabatic ions, and realistic sources and sinks of energy. The equation is solved numerically to obtain the evolution and saturation of the wave spectrum, as well as the self-consistent particle flux which yields the diffusion coefficient.

The lower-hybrid-drift instability is a flute mode ($\mathbf{k} \cdot \mathbf{B} = 0$) which is driven unstable in a plasma with strong inhomogeneities, $\rho_e/L_n > (m_e/m_i)^{1/2}$, where ρ_e and L_n are the ion Larmor radius and density scale length, respectively. The linear behavior of the instability is well understood.^{1,2} In the weak drift regime ($V_{di} < v_{ti}$, where $V_{di} = v_{ti}^2/2\Omega_e L_n$ is the ion diamagnetic drift velocity and v_{ti} is the ion thermal velocity) the mode is driven unstable by the resonant interaction of the wave with the drifting ions when $\omega/k_y < V_{di}$. The growth rate maximizes at $k_y \sim \rho_e^{-1} \equiv \rho_e^{-1} (m_e/m_i)^{1/2}$. In a finite β plasma, the mode is stable for $k_y \rho_e > 1$, and approaches marginal stability as $k_y \rho_e \rightarrow 0$ (see Ref. 3). The wave frequency is such that $\Omega_e \ll \omega \ll \Omega_i$, so that the electrons are strongly magnetized while the ions can be treated as unmagnetized. In a finite β plasma the resonant interaction of ∇B drifting electrons with the wave is stabilizing.

The nonlinear behavior of the instability is much less well understood. Ion trapping has been observed to quench the growth of the instability in particle simulations.⁴ The onset of stochastic electron heating has also been proposed to explain saturation in these simulations.⁵ On the other hand, ion trapping is not a viable saturation mechanism when a broad 2-D spectrum of waves is excited, and it has not been observed in recent simulations using realistic mass ratios where such spectra develop.⁶ In this letter we focus on the nonlinear coupling of stable and unstable waves to satu-

rate the instability.

We consider a slab equilibrium of cold electrons and warm ions with a density profile $n_0(x)$ supported by a magnetic field $B_0(x)$. The equilibrium ion velocity distribution is taken to be a Maxwellian with an average drift velocity $\mathbf{V}_i = V_{di} \hat{e}_y$. Because of the flute nature of the instability ($\mathbf{k} \cdot \mathbf{B} = 0$), we self-consistently limit the spatial variations to the xy plane (as contrasted with universal drift-wave turbulence which is inherently 3-D). In the weak drift regime the ions respond to the perturbed potential $\phi(x, y, t)$ adiabatically to lowest order since $\omega \ll kv_{ti}$. Thus,

$$n_i = n_0 \left[1 + \sqrt{\pi} v_{ti}^{-1} |\nabla^{-1}| \left(\frac{\partial}{\partial t} + V_{di} \frac{\partial}{\partial y} \right) \right] \exp \left(\frac{-e\phi}{T_i} \right), \quad (1)$$

where the term proportional to $\sqrt{\pi}$ in (1) is a small correction describing the resonant ion interaction. The perturbed electron motion is simply given by the $\mathbf{E} \times \mathbf{B}$ and polarization drifts,

$$\mathbf{V}_e = \frac{c}{B} \nabla \phi \times \hat{e}_z - \frac{c}{B\Omega_e} \frac{d}{dt} \nabla \phi, \quad (2)$$

where $d/dt = \partial/\partial t + \mathbf{V}_e \cdot \nabla$. Using (2), the electron continuity equation can be written as

$$\frac{d}{dt} \ln n_e = -\rho_e^2 \frac{d}{dt} \nabla^2 \left(\frac{e\phi}{T_e} \right), \quad (3)$$

Finally, invoking charge neutrality ($n_e = n_i$) and combining (1) and (3), we obtain the nonlinear equation

$$\begin{aligned} (1 - \hat{\nabla}^2) \hat{\phi}_+ + \hat{\phi}_- - \gamma_0 |\nabla^{-1}| (\hat{\phi}_+ + \hat{\phi}_-) + \gamma_e \hat{\phi} \\ + (\nabla \hat{\phi} \times \hat{e}_z \cdot \nabla) \nabla^2 \hat{\phi} + \gamma_0 \nabla \hat{\phi} \\ \times \hat{e}_z \cdot \nabla |\nabla^{-1}| (\hat{\phi}_+ + \hat{\phi}_-) = 0, \end{aligned} \quad (4)$$

where $\hat{\nabla}^2 = \rho_e \nabla^2$, $\tau = (\rho_e/L_n) \Omega_e t$, $\hat{\phi} = (e\phi/T_e)(L_n/\rho_e)$ and the subscripts on $\hat{\phi}$ denote a derivative with respect to that variable. The quantity γ_e represents the wave damping due

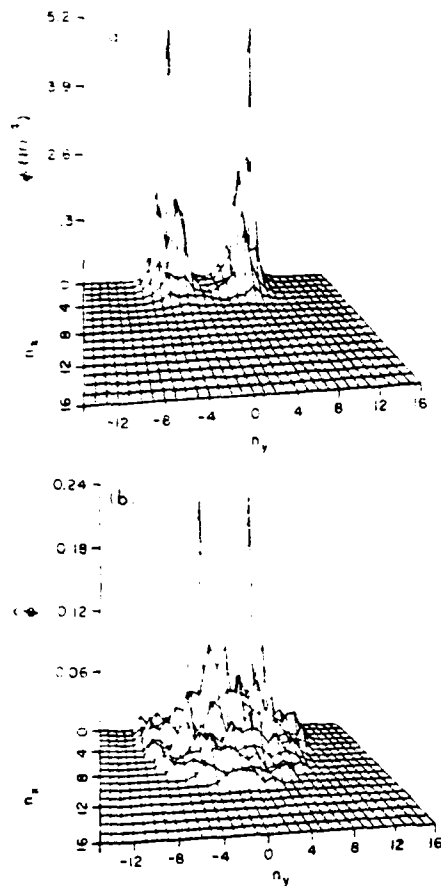


FIG. 1. Instantaneous 2-D wave spectra of lower-hybrid-drift wave turbulence. (a) Linear stage. The dominant linear modes are $(n_x, n_y) = (0, \pm 5)$. (b) Nonlinear stage. The dominant modes are $(n_x, n_y) = (0, \pm 3)$. Note the shift to longer wavelength in the nonlinear saturated state.

to ∇B resonant electrons in a finite β plasma. Equation (4) is only valid for $\gamma_0 = \pi^{1/2} V_{di}/v_i \ll 1$ since the adiabatic ion response can only be justified in this limit. Linearizing this equation, we obtain the complex eigenvalue (in our normalized units),

$$\hat{\omega} = \hat{\omega}_k = \frac{\hat{k}_y}{1 + \hat{k}^2} + i\gamma_0 \frac{\hat{k}^2 |\hat{k}|}{(1 + \hat{k}^2)^3} - i\gamma_e \frac{1}{1 + \hat{k}^2}. \quad (5)$$

In the limit $\gamma_e, \gamma_0 \rightarrow 0$, (4) reduces to the Hasegawa-Mima equation in which the nonlinearity arises from the nonlinear polarization drift.⁷ This equation has two invariants, energy and enstrophy, neither of which is preserved in the more general (4). When γ_0 is finite, the $\mathbf{E} \times \mathbf{B}$ nonlinearity also appears in (4). This nonlinearity has been considered, by Horton⁸ and more recently by Waltz,⁹ in studying universal mode turbulence. However, our equation differs from their work in that we do not assume that $\phi_- + \phi_+$ is replaced by its linear counterpart $-i\hat{\omega}_k - \hat{k}_y \phi_-$. Thus, our equation is second order in time rather than first order.

The direction of energy flow described by (4) can be understood by calculating the stability of a single large-amplitude wave ϕ_0 with \mathbf{k}_0 and $\hat{\omega}_0$ satisfying (5). A perturbation of wave vector \mathbf{k} is coupled through the pump to modes with

$\mathbf{k} \pm p\mathbf{k}_0$, $p = 1, 2, \dots$. For simplicity, we consider only the coupling of $\phi_0(\mathbf{k})$ with its nearest neighbors $\phi_{\pm}(\mathbf{k}_{\pm})$ where $\hat{\omega}_{\pm} = \hat{\omega}_0 \pm \hat{\omega}_k$, and $\mathbf{k}_{\pm} = \mathbf{k} \pm \mathbf{k}_0$, i.e., $p = 1$. The dispersion relation for this $(\mathbf{k}, \mathbf{k}_{\pm})$ coupled system is

$$\epsilon(\mathbf{k}, \hat{\omega}) + \phi_0^2 \left(\frac{M(\mathbf{k}_0, \mathbf{k}_{\pm})}{\epsilon(\mathbf{k}_{\pm}, \hat{\omega}_{\pm})} - (\mathbf{k} - \mathbf{k}_{\pm}) \right) = 0, \quad (6)$$

where $\epsilon(\mathbf{k}, \hat{\omega}) = \omega[1 - \hat{k}^2(1 - i\delta_k)] - \hat{k}_y - i\gamma_e \hat{\omega}$, $\delta_k = \gamma_0 \hat{k}_y / (\omega - \omega_0/k^2)$ and $M(\mathbf{k}_0, \mathbf{k}_{\pm}) = \mathbf{k}_0 \times \mathbf{k}_{\pm} \hat{e}_z / [\hat{k}^2(1 - i\delta_k) - \hat{k}_{\pm}^2(1 - i\delta_{k_{\pm}})]$. When γ_0 and γ_e are neglected in (6) and we take the limit $\hat{\omega} \gg \hat{\omega}_k$, the decay modes are purely growing with a growth rate which peaks around $\mathbf{k} \cdot \mathbf{k}_0 \approx 0$ with $|\mathbf{k}| \approx |\mathbf{k}_0|$. A necessary requirement for instability is that one of the decay waves $(\mathbf{k}, \mathbf{k}_{\pm})$ has a longer wavelength than the pump. For this situation, in which (4) reduces to the Hasegawa-Mima equation, the wave energy inevitably cascades to longer and longer wavelengths so that no stationary wave spectrum can result.¹⁰ When γ_0 is included, this conclusion no longer remains valid. Taking the limit $|\mathbf{k}| \ll |\mathbf{k}_0|$ and again assuming $\hat{\omega} \gg \hat{\omega}_k$, the dispersion relation is given by

$$\hat{\omega}^2 = \frac{2\phi_0^2 (\mathbf{k} \times \mathbf{k}_0 \hat{e}_z)^2 \hat{k}^4}{1 + \hat{k}^2} \left(1 - i \frac{\gamma_0 \hat{\omega} (2 - \hat{k}^2)}{\hat{k}^2 (1 + \hat{k}^2)} \right). \quad (7)$$

Equation (7) yields a dissipative instability which is driven unstable by the $\mathbf{E} \times \mathbf{B}$ nonlinearity. This instability produces a flow of energy from long to short wavelengths and, as will be demonstrated, enables the wave spectrum to reach a steady state.

We solve (4) numerically by decomposing it into two coupled, first-order (in time) differential equations which are advanced in time. These equations are solved by a spectral method developed by Fyfe *et al.*,¹¹ based on the work of Orszag.¹² The potential ϕ is Fourier-decomposed, i.e., $\phi \sim \exp(i\mathbf{k} \cdot \mathbf{x})$, where $\mathbf{k} = \mathbf{n}/\lambda$ and $\mathbf{n} = n_x \hat{e}_x + n_y \hat{e}_y$ with n_x and n_y integers, and $\lambda = 5$ (which fixes the \mathbf{n} for which $|\mathbf{k}| = 1$). The numerical results presented in this letter are nominally computed on a 32×32 mesh.

The electron damping γ_e controls the region of instability in \mathbf{k} space by stabilizing short wavelength modes. We have chosen

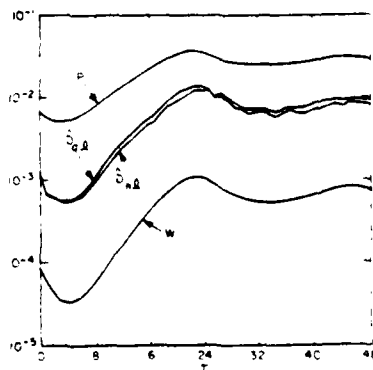


FIG. 2. Time evolution of the wave energy (W), mean square of the potential fluctuations (P), and diffusion coefficients (D)—quasilinear: D_{qu} —nonlinear for $\gamma_0 = 0.5$.

$$\gamma_{\pm} = \gamma_0 \hat{k}^{\pm 1/2} (1 - \hat{k}^2 - 2\hat{k}^2 \gamma_0^{-2})^{1/2}, \quad (18)$$

with $\hat{k}_m = 1.6$, which yields an unstable wave spectrum which is realistic for the lower-hybrid-drift instability in finite- β plasmas. The growth rate peaks at $(\hat{k}_x, \hat{k}_y) = (0, \pm 1)$ and is stable for $\hat{k}_x > 1.6$ and $\hat{k}_y > 1$.

The ϕ spectrum is initialized with random noise with $\phi \sim 10^{-2} - 10^{-1}$, and the system is allowed to evolve until the wave energy, given by

$$\frac{W}{nT} = \left(\frac{m_e}{\pi m_i} \right) \gamma_0^2 \sum_{\mathbf{k}} (1 - \hat{k}^2) |\hat{\phi}_{\mathbf{k}}|^2 \quad (9)$$

reaches a steady-state value. The mean square of the potential fluctuations,

$$P = \left\langle \left(\frac{e\phi}{T} \right)^2 \right\rangle = \left[\left(\frac{2m_e}{\pi m_i} \right) \gamma_0^2 \sum_{\mathbf{k}} |\hat{\phi}_{\mathbf{k}}|^2 \right]^{1/2}, \quad (10)$$

as well as the nonlinear and quasilinear diffusion coefficients

$$\begin{aligned} \hat{D}_{nl} &= \frac{D_{nl}}{v_{ex} \rho_{ex}} \\ &= \left(\frac{2m_e}{\pi m_i} \right)^{1/2} \gamma_0^2 \sum_{\mathbf{k}} \left(\frac{\hat{k}_x}{\hat{k}} \right) \hat{\phi}^* \left(\hat{k}_x \hat{\phi}_{\mathbf{k}} - i \frac{\partial \hat{\phi}_{\mathbf{k}}}{\partial \tau} \right), \end{aligned} \quad (11)$$

$$\begin{aligned} \hat{D}_q &= \frac{D_q}{v_{ex} \rho_{ex}} \\ &= \left(\frac{2m_e}{\pi m_i} \right)^{1/2} \gamma_0^2 \sum_{\mathbf{k}} |\hat{k}_x \hat{k}_y| |\hat{\phi}_{\mathbf{k}}|^2 (1 - \hat{k}^2)^{-1}, \end{aligned} \quad (12)$$

respectively, are also computed. The nonlinear diffusion coefficient \hat{D}_{nl} is derived by averaging the particle flux in the x direction over y , i.e., $\hat{D}_{nl} \propto \langle n V_x \rangle_y$. The quasilinear expression is then obtained by approximating $\partial/\partial\tau = -i\hat{\omega}_{\mathbf{k}}$ and using (5) in (11).

In Fig. 1 we show instantaneous 2-D wave spectra in n space for $\gamma_0 = 0.5$. Figure 1(a) shows the spectrum during the linear phase of the instability, and Fig. 1(b) shows the spectrum after saturation. In the linear regime, the wave spectrum is strongly peaked around the most unstable modes, $(n_x, n_y) = (0, \pm 5)$. The spectrum begins to saturate as these modes couple through an $n_x = 0$ mode (typically with $n_y \sim 4$) to damped modes with $n_x \gtrsim n_y$. A peak in the wave spectrum appears around (4,0) at this time. This transient phase is completed as the total wave energy saturates and spreads through most of the unstable, weakly damped volume of n space as shown in Fig. 1(b). The spectrum typically remains peaked around $n_x \sim 0$ with n_y typically somewhat smaller than that of the linearly most unstable mode [see Fig. 1(b) for which the dominant modes are $(n_x, n_y) = (0, \pm 3)$]. The 2-D wave spectrum exhibits substantial variability in time, even after saturation, as the unstable and stable modes continue to exchange energy in a dynamic manner.

The time evolution of the total wave energy (W), mean square of the potential fluctuations (P), and the nonlinear (\hat{D}_{nl}) and quasilinear diffusion (\hat{D}_q) coefficients are shown in Fig. 2. All of these quantities exhibit a similar temporal behavior. The initial decay ($\tau < 4$) is associated with the rapid dissipation of energy initialized in the damped modes, and is followed by a linear growth phase ($4 < \tau < 20$). Subsequently, mode coupling occurs which leads to saturation of the insta-

bility, albeit with some initial overshoot ($\tau \sim 24$). The level of the total wave energy and other parameters of Fig. 2 are quite stationary in time after saturation. Also, the stationary values of all four quantities are relatively insensitive to the initialization of ϕ .

We note that in Fig. 2, the quasilinear diffusion coefficient (\hat{D}_q) tracks the actual, nonlinear diffusion coefficient (\hat{D}_{nl}) quite well during the entire time evolution of the instability. An important point which must be emphasized with regard to \hat{D}_{nl} is that both species, electrons and ions, continue to exchange both energy and momentum even after a steady state is reached; the electrons through the ∇B resonance and the ions by direct resonant interaction. If the instability had saturated by ion trapping and the electrons had no resonant interaction with the wave, there would be no diffusion in the steady state since the electrons could not exchange momentum with the ions. Both species must have a dissipative interaction with the waves to have diffusion.

A number of runs have been made for different values of γ_0 , the drift parameter. The saturation level of ϕ is found to be nearly independent of γ_0 . Thus, from Eqs. (11) and (12), it is found that $(\hat{D}_{nl}) \propto \gamma_0^2 \propto V_{di}^2/v_{ex}^2$.

Next, we compare our stationary values of P and \hat{D}_{nl} with those obtained from "wave energy bound" calculations.¹³ The "energy bound" results from equating the wave energy with the kinetic energy associated with the relative drift of the electrons and ions, $m_e n (V_{di} - V_{ae})^2/2$. This free energy bound is actually an extreme underestimate of the free energy in a finite- β plasma, since the instability can also feed off the magnetic free energy, which typically greatly exceeds the drift energy.¹⁴ Nevertheless, this bound has been widely invoked and seems to yield reasonable transport rates when compared with experimental observations. The "drift energy bound" yields a potential $P_{er} \simeq (m_e/\pi m_i)^{1/2} \gamma_0$, where we have assumed $T_e \ll T_i$. The scaling of P_{er} is identical with that given in (10) since ϕ is independent of γ_0 . For the case $\gamma_0 = 0.5$, $P/P_{er} \simeq 3$ (from Fig. 2) so that the actual fluctuation level obtained from our code is slightly larger than calculated from the "energy bound." Finally we compare \hat{D}_{nl} with that obtained from the simple formula $\hat{D} = (\gamma/k^2)_m / V_{ex} \rho_{ex}$, where γ and k are evaluated where γ peaks. We find $\hat{D} \simeq (m_e/\pi m_i)^{1/2} \gamma_0^2$, which again has the same scaling as \hat{D}_{nl} but is a factor of 2.4 smaller for $\gamma_0 = 0.5$ (from Fig. 2).

Measurements of lower-hybrid-drift turbulence in a θ pinch by CO₂ laser scattering have been reported recently.¹⁵ The observed wave spectra were flute-like ($\mathbf{k} \cdot \mathbf{B} \simeq 0$) with clear peaks around $\hat{k}_y \simeq 0.7$ (a factor of two smaller than the most unstable linear mode), and $\hat{k}_x < \hat{k}_y$. Data were taken for three different filling pressures, corresponding to three values of V_{di}/v_{ex} . Electron-ion collisions were apparently significant [$\nu_{ei} \sim (\Omega_e \Omega_i)^{1/2}$] for the two highest filling pressures so we can only compare our results with the data from the lowest filling pressure, which corresponds to $V_{di}/v_{ex} = 0.52$ ($\gamma_0 \simeq 0.9$). The measured density fluctuation, $\tilde{n}/n_0 \sim 0.014$, is quite close (smaller by a factor of 2) to our theoretical prediction of $\tilde{n}/n_0 \simeq 0.25$. In addition, the shift to long wavelength is consistent with our calculated spectra [compare Figs. 1(a) and 1(b)].

Computer simulations of the lower-hybrid-drift instability with realistic mass ratios have also been performed recently using a fluid-kinetic numerical scheme.⁹ Unfortunately, these computations have been carried out for $V_{th}/v_i > 1$, which is outside the range of validity of our present theory. Nevertheless, a broad spectrum of modes is observed in k space in the simulations which is consistent with our calculations.

In conclusion, the lower-hybrid-drift instability can saturate via a mode coupling process. The basic saturation mechanism involves a transfer of energy from the growing, long wavelength modes to the damped, short wavelength modes. The nonlinear $\mathbf{E} \times \mathbf{B}$ drift plays a crucial role in this saturation mechanism by preventing the polarization drift nonlinearity from driving the wave energy towards the undamped, long-wavelength modes. The saturation energy and diffusion coefficient associated with the wave turbulence scales as $(V_{th}/v_i)^2$.

ACKNOWLEDGMENTS

We are very grateful to Dave Fyfe and Glenn Joyce for providing us with their spectral method code. We also thank

Dave Montgomery for several helpful discussions.

This research has been supported by ONR and NASA. One of us (J. F. D.) was partially supported by DOE.

- ⁹N. A. Krall and P. C. Liewer, *Phys. Rev. A* **4**, 2094 (1971).
- ¹⁰R. C. Davidson, N. T. Gladd, C. S. Wu, and J. D. Huba, *Phys. Fluids* **20**, 301 (1977).
- ¹¹J. F. Drake, J. D. Huba, and N. T. Gladd (submitted to *Phys. Fluids* 1982).
- ¹²D. Winske and P. C. Liewer, *Phys. Fluids* **21**, 1017 (1978).
- ¹³J. F. Drake and T. T. Lee, *Phys. Fluids* **24**, 1115 (1981).
- ¹⁴J. U. Brackbill, D. W. Forslund, K. Quest, and D. Winske (private communication).
- ¹⁵A. Hasegawa and K. Mima, *Phys. Fluids* **21**, 87 (1978).
- ¹⁶W. Horton, *Phys. Rev. Lett.* **37**, 1269 (1976).
- ¹⁷R. E. Waltz, *Phys. Fluids* **26**, 169 (1983).
- ¹⁸D. Fyfe and D. Montgomery, *Phys. Fluids* **22**, 246 (1974).
- ¹⁹D. Fyfe, G. Joyce, and D. Montgomery, *J. Plasma Phys.* **17**, 317 (1977).
- ²⁰S. A. Orszag, *Stud. Appl. Math.* **50**, 293 (1971).
- ²¹R. C. Davidson, *Phys. Fluids* **21**, 1017 (1978).
- ²²J. F. Drake, N. T. Gladd, and J. D. Huba, *Phys. Fluids* **24**, 301 (1981).
- ²³H. U. Fahrbach, W. Koppendorfer, M. Munich, J. Neuhauser, H. Rohr, G. Schramm, J. Sommer, and E. Holzhauser, *Nucl. Fusion* **21**, 257 (1981).

APPENDIX J

NONLINEAR MODE COUPLING THEORY OF THE
LOWER-HYBRID-DRIFT INSTABILITY

J.F. Drake
University of Maryland & Science Applications, Inc.

P.N. Guzdar and A.B. Hassam
Science Applications, Inc.

and

J.D. Huba
Naval Research Laboratory

Nonlinear Mode Coupling Theory of the Lower-Hybrid-Drift Instability

J. F. DRAKE,* P. N. GUZDAR,** A. B. HASSAM** AND J. D. HUBA

*Geophysical and Plasma Dynamics Branch
Plasma Physics Division*

**University of Maryland
College Park, MD 20742*

***Science Applications, Inc.
McLean, VA 22102*

November 25, 1983

This research was supported by the Office of Naval Research and the National Aeronautics and Space Administration.



NAVAL RESEARCH LABORATORY
Washington, D.C.

Approved for public release; distribution unlimited.

REPORT DOCUMENTATION PAGE		READ INSTRUCTIONS BEFORE COMPLETING FORM
1. REPORT NUMBER	2. GOVT ACCESSION NO.	3. RECIPIENT'S CATALOG NUMBER
NRL Memorandum Report 5209		
4. TITLE (and Subtitle)		5. TYPE OF REPORT & PERIOD COVERED
NONLINEAR MODE COUPLING THEORY OF THE LOWER-HYBRID-DRIFT INSTABILITY		Interim report on a continuing NRL problem.
		6. PERFORMING ORG. REPORT NUMBER
7. AUTHOR(s)		8. CONTRACT OR GRANT NUMBER(s)
J.F. Drake,* P.N. Guzdar,** A.B. Hassam** and J.D. Huba		
9. PERFORMING ORGANIZATION NAME AND ADDRESS		10. PROGRAM ELEMENT, PROJECT, TASK AREA & WORK UNIT NUMBERS
Naval Research Laboratory Washington, DC 20375		W-15494; 61153N; RR033-02-44; 47-1982-0-3; 47-0884-0-3
11. CONTROLLING OFFICE NAME AND ADDRESS		12. REPORT DATE
Office of Naval Research National Aeronautics & Space Admin. Arlington, VA 22203 Washington, DC 20546		November 25, 1983
		13. NUMBER OF PAGES
		46
14. MONITORING AGENCY NAME & ADDRESS (if different from Controlling Office)		15. SECURITY CLASS. (of this report)
		UNCLASSIFIED
		15a. DECLASSIFICATION/DOWNGRADING SCHEDULE
16. DISTRIBUTION STATEMENT (of this Report)		
Approved for public release; distribution unlimited.		
17. DISTRIBUTION STATEMENT (of the abstract entered in Block 20, if different from Report)		
18. SUPPLEMENTARY NOTES		
*Present address: University of Maryland, College Park, MD 20742		
**Present address: Science Applications, Inc., McLean, VA 22102		
This research was supported by the Office of Naval Research and the National Aeronautics and Space Administration.		
19. KEY WORDS (Continue on reverse side if necessary and identify by block number)		
Lower-hybrid-drift instability Nonlinear plasma theory Magnetospheric physics Ionospheric physics		
20. ABSTRACT (Continue on reverse side if necessary and identify by block number)		
A nonlinear mode coupling theory of the lower-hybrid-drift instability is presented. A two-dimensional nonlinear wave equation is derived which describes lower-hybrid-drift wave turbulence in the plane transverse to \mathbf{B} ($\mathbf{k} \cdot \mathbf{B} = 0$), and which is valid for finite β , collisional and collisionless plasmas. The instability saturates by transferring energy from growing, long wavelength modes to damped, short wavelength modes. Detailed numerical results are presented which compare favorably to both recent computer simulations and experimental observations. Applications of this theory to space plasmas, the earth's magnetotail and the equatorial F region ionosphere, are discussed.		

DD FORM 1473

1 JAN 73

EDITION OF 1 NOV 65 IS OBSOLETE
5/N 0102-014-6601

SECURITY CLASSIFICATION OF THIS PAGE (When Data Entered)

CONTENTS

I. INTRODUCTION	1
II. DERIVATION OF THE MODE COUPLING EQUATION	3
III. NUMERICAL COMPUTATIONS	12
IV. NUMERICAL RESULTS: COLLISIONLESS DAMPING	16
V. NUMERICAL RESULTS: COLLISIONAL DAMPING	24
VI. SUMMARY AND APPLICATIONS	28
ACKNOWLEDGMENTS	34
REFERENCES	36
APPENDIX	38

NONLINEAR MODE COUPLING THEORY OF THE LOWER-HYBRID-DRIFT INSTABILITY

1. Introduction

The lower-hybrid-drift instability has been of considerable interest to plasma physicists for more than a decade as a driving mechanism for the anomalous transport of particles, momentum and energy in both laboratory and space plasmas. In laboratory applications, this instability was initially studied to explain anomalous sheath broadening in theta pinch implosions, but has recently been applied to other laboratory confinement devices such as toroidal reversed field pinches² and compact torii.³ In space plasma, it has been proposed as a mechanism to provide anomalous resistivity for reconnection events in the magnetosphere.⁴ Experimentally, the lower-hybrid-drift instability has been observed in a recent theta pinch experiment,⁵ and satellite data indicate that it exists in the earth's magnetotail and magnetopause.⁶

The linear theory of the lower-hybrid-drift instability is well understood.⁷⁻⁹ The mode can be excited in inhomogeneous plasmas when $\rho_i/L_n > (m_e/m_i)^{1/4}$ where ρ_i is the mean ion Larmor radius and L_n is the scale length of the density gradient. At maximum growth it is characterized by $\omega_r \lesssim \omega_{lh}$, $\gamma \lesssim \omega_r$, $k \cdot B = 0$, and $k\rho_{es} \sim 1$ where $\omega = \omega_r + i\gamma$, ω_{lh} is the lower hybrid frequency and $\rho_{es} = \rho_i (m_e/2m_i)^{1/2}$. Since the instability is high frequency ($\omega \gg \Omega_i$) and short wavelength ($k\rho_i \gg 1$) the ions are treated as unmagnetized while the electrons are treated as strongly magnetized. In the weak drift regime $V_{di}/v_i < 1$ (where V_{di} is the ion diamagnetic drift velocity and v_i is the ion thermal velocity), $\omega \lesssim kV_{di}$ and the mode is driven unstable by the resonant interaction of the drift wave with the ions. In finite β plasmas, electrons also resonate with the wave via their ∇B drift. The resultant electron damping is stabilizing for $k\rho_{es} > 1$. In the high drift regime ($V_{di}/v_i > 1$), the mode is driven unstable via the interaction of a positive energy lower hybrid wave and a negative energy drift wave. In this paper we focus on the weak drift regime.

The nonlinear development of the lower-hybrid-drift instability is complex and not as well understood as the linear theory. A variety of nonlinear saturation mechanisms have been proposed to date. Ion trapping¹⁰ and stochastic electron heating¹¹ have been proposed to quench the growth of the instability in particle simulations. However, ion trapping is not a

Manuscript approved September 7, 1983.

viable saturation mechanism when a broad 2D spectrum of waves is excited,¹² and it has not been observed in recent simulations using realistic mass ratios where such spectra develop.¹³ Stochastic electron heating does not onset until a rather large threshold, $\tilde{n}/n \gtrsim 0.25$, is exceeded where \tilde{n} is the density fluctuation of the wave. A wave energy bound based on the available free-energy in the relative electron-ion flow (current) has also been invoked to calculate a maximum wave amplitude.¹⁴ In a finite β plasma, however, the current and self-consistent magnetic field are coupled and the magnetic field energy can also be tapped.¹⁵ The free energy then becomes extremely large and does not realistically act as a bound. Finally, electron resonance broadening has been proposed as a saturation mechanism.¹⁶ It has been recently shown in more refined calculations that "resonance broadening" does not cause a net dissipation of energy but merely leads to an exchange of energy between modes in k space unless wave-particle resonances are included.^{17,18} This mechanism can therefore only stabilize the wave spectrum in finite β plasmas.¹⁹

In this paper we present a nonlinear mode coupling theory of the lower-hybrid-drift instability. Our preliminary calculations have been presented previously.²⁰ The basic result is that the instability can saturate by transferring energy from growing, long-wavelength modes to damped, short-wavelength modes. This saturation mechanism is consistent with recent computer simulations¹³ and with experimental observations.⁵ In this paper, we extend the earlier theory to self-consistently incorporate finite β effects, and to include electron collisions in order to compare our results with experimental observations.

The organization of the paper is as follows. In the next section we derive the nonlinear wave equation and the wave energy transfer with the two basic nonlinearities: the nonlinear electron $\mathbf{E} \times \mathbf{B}$ and polarization drifts. In Section III we discuss the numerical methods used to study the mode coupling process. In Section IV we present results based upon ∇B electron damping of the short wavelength modes, while in Section V we present results based upon collisional damping of the modes. In Section VI we summarize our theory, compare our theoretical results with experimental observations, and discuss some applications of our results to space plasmas.

II. Derivation of the Mode Coupling Equation

We consider a slab equilibrium of cold electron and warm ions with a density profile $n_0(x)$ supported by a magnetic field $\underline{B} = B_0(x)\hat{e}_z$ as shown in Fig. 1. Equilibrium pressure balance requires

$$\frac{\partial}{\partial x} [P_0(x) + B_0^2(x)/8\pi] = 0. \quad (1)$$

The ratio of thermal to magnetic pressure, $\beta = 8\pi n T_i / B_0^2$, is assumed to be of order unity so that electromagnetic corrections to the lower-hybrid-drift instability must be retained. The equilibrium ion velocity distribution is taken to be a Maxwellian with an average drift velocity $\underline{V}_i = V_{di} \hat{e}_y$ where $V_{di} = (v_i^2/2\Omega_i) \partial \ln n / \partial x$, $v_i^2 = 2T_i/m_i$ and $\Omega_i = eB_0/m_i c$.

Because of the flute nature of the instability ($\underline{k} \cdot \underline{B} = 0$), we self-consistently limit the spatial variations to the xy plane. In this limit the electric and magnetic fields can be represented by the scalar potential ϕ and the vector potentials A_x and A_y as⁸

$$\underline{B} = B_z \hat{e}_z = (\partial A_y / \partial x - \partial A_x / \partial y) \hat{e}_z \quad (2)$$

$$\underline{E} = -\nabla\phi - c^{-1} \partial A / \partial t \quad (3)$$

with $\nabla \cdot \underline{A} = 0$. Even when $\beta \sim 1$, the induction component of \underline{E} is small so that it can generally be discarded except when the $\nabla\phi$ component of \underline{E} does not contribute.

We are interested in time scales of order $\partial/\partial t \gg \Omega_i$ so that the ion response to both the equilibrium and perturbed magnetic fields can be neglected. Furthermore, in the weak drift regime the ions respond to the perturbed potential ϕ adiabatically to lowest order since $\partial/\partial t \ll v_i |\nabla|$.⁸ Thus,

$$n_i = n_0 [1 + \sqrt{\pi} v_i^{-1} |\nabla|^{-1} (\frac{\partial}{\partial t} + V_{di} \frac{\partial}{\partial y})] \exp(-e\phi/T_i), \quad (4)$$

where the term proportional to $\sqrt{\pi}$ in (4) is a small correction describing the resonant ion interaction.

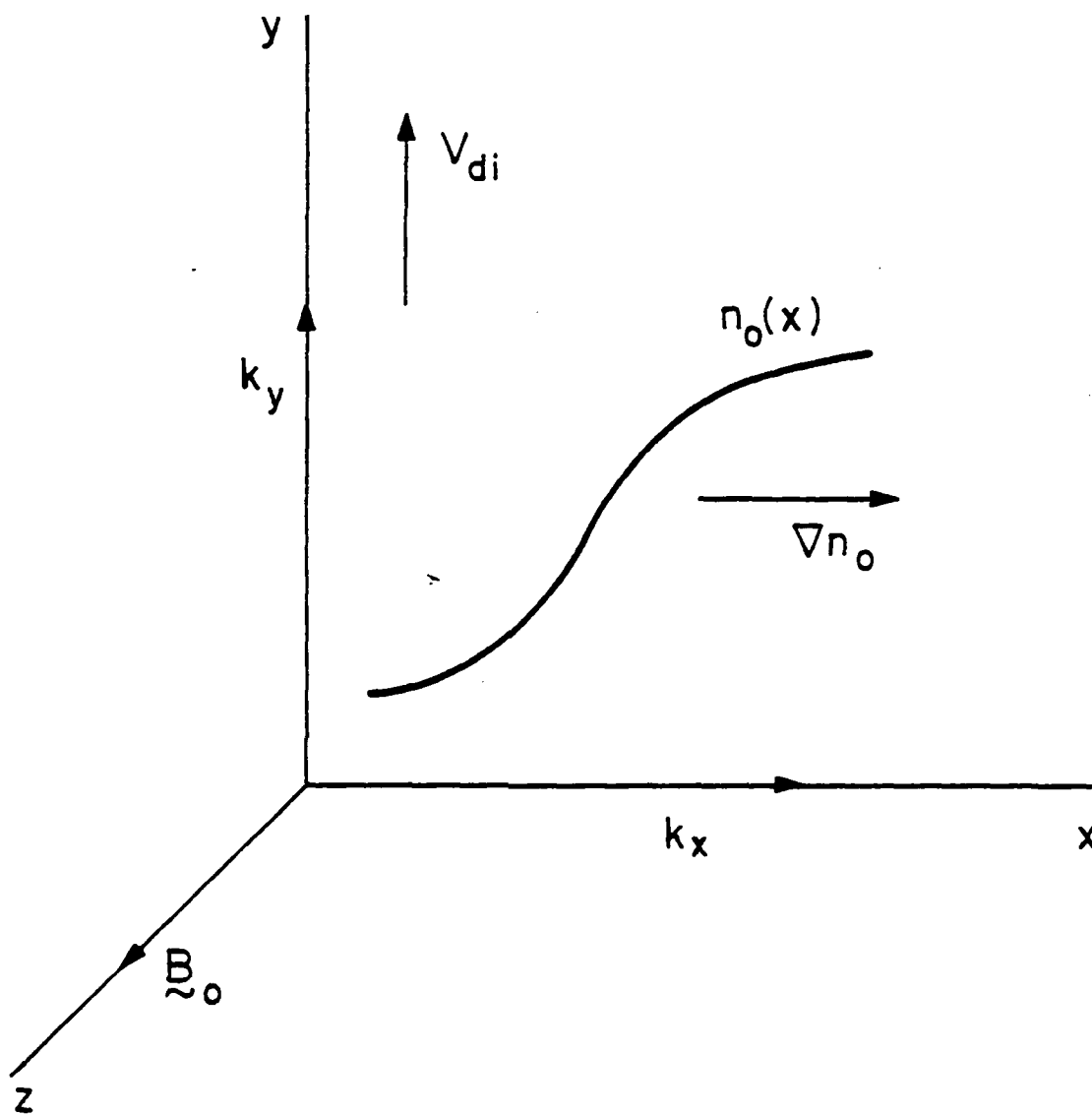


Fig. 1: The basic equilibrium configuration is shown. The unstable wave spectrum is taken to be two-dimensional with $\vec{k} \cdot \vec{B}_0 = 0$.

In contrast to the ions, the electrons are strongly magnetized since $\partial/\partial t \ll \Omega_e$. The electron motion is simply given by the $\underline{E} \times \underline{B}$ and polarization drifts,

$$\underline{V}_e = \frac{c}{B_z} \underline{E} \times \hat{e}_z - \frac{c}{\Omega_e} \frac{d}{dt} \frac{\underline{E}}{B_z} \quad (5)$$

where $d/dt = \partial/\partial t + \underline{V}_E \cdot \nabla$ and $\underline{V}_E = c \underline{E} \times \hat{e}_z / B_z$. The electron density can be calculated from the continuity equation,

$$d \ln n_e / dt + \nabla \cdot \underline{V}_e = 0. \quad (6)$$

The electron compression $\nabla \cdot \underline{V}_e$ is obtained from Eq. (5). To lowest order,

$$\nabla \cdot \underline{V}_e = \frac{c}{B_z \Omega_e} \frac{d}{dt} \nabla^2 \phi - \frac{d}{dt} \ln B_z. \quad (7)$$

The first term in Eq. (7) arises from the polarization drift and the second from the compression of the flux tube in a finite β plasma. The continuity equation can now be written as

$$\frac{d}{dt} \ln(n_e / B_z) + \frac{c}{B_z \Omega_e} \frac{d}{dt} \nabla^2 \phi = 0 \quad (8)$$

so that the rate of change of the number of electrons in a flux tube (n_e / B_z) is given by the polarization drift. The time variation of B_z in Eq. (8) is calculated from Ampere's Law

$$\nabla^2 A_x = - (4\pi/c) J_x = - (4\pi n_e / B_z) \partial \phi / \partial y, \quad (9)$$

where J_x is dominated by the $\underline{E} \times \underline{B}$ drift of the electrons. Using $\nabla \cdot \underline{A} = 0$, we find that $\nabla^2 A_x = - \partial B_z / \partial y$ so that

$$\frac{\partial}{\partial y} \left[\frac{B_z^2}{8\pi} - n_0 e \phi \right] = 0, \quad (10)$$

which can be integrated to evaluate

$$\frac{\partial}{\partial t} \ln B_z = \frac{e}{2} \frac{\partial}{\partial t} \left(\frac{e \phi}{T_i} \right) \quad (11)$$

in Eq. (7). The convective derivative of B_z can similarly be evaluated using Eq. (10) in conjunction with the equilibrium pressure balance relation,

$$\mathbf{v}_E \cdot \nabla \ln B_z = \frac{\beta}{2} \frac{c}{B_z} \frac{\partial \ln n}{\partial x} \frac{\partial \phi}{\partial y}. \quad (12)$$

Finally, invoking charge neutrality ($n_e = n_i$) and combining (8), (11) and (12), we obtain the nonlinear equation

$$\begin{aligned} (1 - \hat{v}^2) \hat{\phi}_T + \hat{\phi}_y - \gamma_0 |\hat{v}|^{-1} (\hat{\phi}_{TT} + \hat{\phi}_{Ty}) + \gamma_e \hat{\phi} \\ + (\hat{\nabla} \hat{\phi} \times \hat{e}_z \cdot \hat{\nabla}) \hat{v}^2 \hat{\phi} + \gamma_0 \hat{\nabla} \hat{\phi} \times \hat{e}_z \cdot \hat{\nabla} |\hat{v}|^{-1} (\hat{\phi}_T + \hat{\phi}_y) = 0 \end{aligned} \quad (13)$$

where

$$\begin{aligned} \hat{v} &= \frac{\rho_{es}}{(1 + \beta/2)^{1/2}} \nabla \\ \tau &= \frac{\rho_{es}}{L_n} \Omega_e (1 + \beta/2)^{1/2} t \\ \hat{\phi} &= \frac{L_n}{\rho_{es}} (1 + \beta/2)^{1/2} \frac{e\phi}{T_i} \\ \gamma_0 &= \pi^{1/2} (v_{di}/v_i) / (1 + \beta/2) \end{aligned}$$

and the subscripts on $\hat{\phi}$ denote a derivative with respect to that variable. The quantity γ_e represents the wave damping due to electrons, which can result either from \mathbf{v} resonant particles in a finite β plasma⁸ or collisional viscosity.²¹ Equation (13) is only valid for $\gamma_0 < 1$ since the adiabatic ion response can only be justified in this limit. Linearizing this equation, we obtain the complex eigenvalue (in our normalized units),

$$\hat{\omega} = \hat{\omega}_k = \frac{\hat{k}_y}{1 + \hat{k}^2} + i\gamma_0 \frac{|\hat{k}| \hat{k}_y^2}{(1 + \hat{k}^2)^3} - i \frac{\gamma_e}{1 + \hat{k}^2}. \quad (14)$$

Since Eq. (13) is second order in time, there is an additional root,

$$\hat{\omega} = i(k_y)(1 + \hat{k}^2/\gamma_0), \quad (15)$$

which is spurious since it violates the assumption that $\hat{\omega} \ll kv_z$. This root is growing and therefore must be eliminated before carrying out our numerical computations (see Sec. III).

In the flute limit considered here, the magnetic perturbations and equilibrium VB_z do not structurally alter the equation for $\hat{\phi}$. They enter the equations through the factors $(1 + \beta/2)$ which appear in the normalized variables defined in Eq. (13). We ignore this trivial finite β modification to the equations in the remainder of this paper.

In the limit $\gamma_e, \gamma_0 \rightarrow 0$, Eq. (13) reduces to the Hasegawa-Mima equation in which the nonlinearity arises from the nonlinear polarization drift.²² This equation has two invariants, energy and enstrophy, neither of which is preserved in the more general Eq. (13). When γ_0 is finite, the $\hat{E} \times \hat{B}$ nonlinearity also appears in Eq. (13). This nonlinearity has been considered previously in studies of universal mode turbulence.^{23,24}

Our calculation differs from previous work in that we do not make the quasi-linear hypothesis that

$$\hat{\phi}_z + \hat{\phi}_y = -i(\hat{\omega}_k - \hat{k}_y)\hat{\phi} \quad (16)$$

in the terms proportional to γ_0 in Eq. (13). Thus, our equation is second order in time rather than first order. In Sec. III it is shown that the spectrum always saturates when $\hat{\phi} \sim 1$ so that the linear and nonlinear terms in Eq. (13) are comparable. The quasi-linear hypothesis can therefore not be justified in drift-wave turbulence. A similar second order equation has been derived for dissipative drift waves.²⁶

It is recognized that both universal and dissipative drift wave turbulence are inherently three-dimensional since $k_{\parallel} = k \cdot \hat{B}/B$ is required for the mode to exist and the spatial variations in the two directions perpendicular to \hat{B} are required to calculate the mode coupling. In 2-D models of this turbulence the coupling of modes with differing k_{\parallel} 's is ignored.²³⁻²⁶ There is no theoretical justification for this procedure so that care must be taken in applying the results of model calculations to experimental observations. By contrast, the lower-hybrid-drift instability

is a flute mode so that the neglect of the coupling along \hat{z} can be justified and the results of the 2-D model can be directly compared with experimental observations.

A qualitative understanding of the direction of the flow of energy described by Eq. (13) can be obtained by calculating the stability of a single, large-amplitude wave $\hat{\phi}_0$ with \hat{k}_0 and $\hat{\omega}_0$ satisfying the linear dispersion relation in Eq. (14). A perturbation of wavevector \hat{k} is coupled through the pump to modes with $\hat{k} \pm p \hat{k}_0$ ($p = 1, 2, \dots$). For simplicity, we consider only the coupling of $(\hat{\omega}, \hat{k})$ with its nearest neighbors $(\hat{\omega}_\pm, \hat{k}_\pm)$ where $\hat{\omega}_\pm = \hat{\omega} \pm \hat{\omega}_0$ and $\hat{k}_\pm = \hat{k} \pm \hat{k}_0$, i.e., $p = 1$. The dispersion relation for this (\hat{k}, \hat{k}_\pm) coupled system is (see Appendix)

$$\varepsilon(\hat{\omega}, \hat{k}) + |\hat{\phi}_0|^2 \left[\frac{M(-\hat{k}_0, \hat{k}_\pm) M(\hat{k}, \hat{k}_0)}{\varepsilon(\hat{\omega}_\pm, \hat{k}_\pm)} + \hat{k}_0 + -\hat{k}_0 \right] = 0 \quad (17)$$

where

$$\varepsilon(\hat{\omega}, \hat{k}) = \hat{\omega} [1 + \hat{k}^2 (1 - i\delta_k)] - \hat{k}_y + i\gamma_e$$

$$\delta_k = \gamma_0 (\hat{k}_y - \hat{\omega}) / \hat{k}^3$$

$$M(\hat{k}_1, \hat{k}_2) = \hat{k}_1 \times \hat{k}_2 \cdot \hat{e}_z [\hat{k}_1^2 (1 - i\delta_{k1}) - \hat{k}_2^2 (1 - i\delta_{k2})]$$

When γ_0 and γ_e are neglected in Eq. (17) and we take the limit $\hat{\omega} \gg \hat{\omega}_k$, the dispersion relation simplifies to

$$\hat{\omega}^2 = |\hat{\phi}_0|^2 (\hat{k}_0 \times \hat{k} \cdot \hat{e}_z)^2 \frac{\hat{k}_0^2 - \hat{k}^2}{1 + \hat{k}^2} \left(\frac{\hat{k}_0^2 - \hat{k}_+^2}{1 + \hat{k}_+^2} + \frac{\hat{k}_0^2 - \hat{k}_-^2}{1 + \hat{k}_-^2} \right). \quad (18)$$

The decay modes are purely growing with a growth rate which peaks around $\hat{k} \cdot \hat{k}_0 = 0$ with $\hat{k}/\hat{k}_0 = 0.6 - 0.8$, depending on the magnitude of \hat{k}_0 . A necessary requirement for instability is that one of the three decay modes (\hat{k}, \hat{k}_\pm) has a longer wavelength than the pump.²⁷ This decay process with $\hat{k} \cdot \hat{k}_0 = 0$ and $\hat{k}/\hat{k}_0 \leq 1$ is clearly seen in our numerical simulation during the initial phase of saturation (Sec. III) of the instability. For this situation, in which Eq. (13) reduces to the Hasegawa-Mima equation, the wave energy inevitably cascades to longer and longer wavelengths so that no stationary wave spectrum can result.²⁸

When γ_0 is included, this conclusion no longer remains valid. Taking the limit $k_0 \ll k$ and again assuming $\hat{\omega} \gg \hat{\omega}_k$, the dispersion relation is given by

$$\hat{\omega}^2 = \frac{2|\hat{\phi}_0|^2 |\hat{k} \times \hat{k}_0 \cdot \hat{e}_z|^2 \hat{k}^4}{1 + \hat{k}^2} \left[1 + i \frac{\gamma_0 \hat{\omega} (2 + \hat{k}^2)}{\hat{k}^3 (1 + \hat{k}^2)} \right]. \quad (19)$$

Equation (19) yields a dissipative instability when γ_0 is finite. The destabilizing term can be traced back to the $\mathbf{E} \times \mathbf{B}$ nonlinearity. This dissipative instability produces a flow of energy from long to short wavelength and, as will be demonstrated, prevents the condensation of wave energy at long wavelengths, enabling the wave spectrum to reach a steady state.

The dispersion relation in Eq. (19) contains no amplitude threshold for instability as long as k is in the proper direction. In the more general dispersion relation in Eq. (17), where the linear frequencies are retained, $\hat{\phi}_0$ must exceed a threshold before the instability onsets unless the frequency matching condition

$$\Delta\omega \equiv \hat{\omega}_k - \hat{\omega}_{k\pm} \pm \hat{\omega}_0 = 0 \quad (20)$$

is satisfied. For $\hat{k}_0 = \hat{k}_0 \hat{e}_y$ and $\hat{k}_0, \hat{k} \ll 1$, this matching condition becomes

$$\hat{k}_x^2 = -3(\hat{k}_y^2 + \hat{k}_y \hat{k}_0). \quad (21)$$

The locus of modes which satisfies Eq. (20), those with $\hat{k}_y < 0$ and $|\hat{k}_y| < \hat{k}_0$, are shown in Fig. 2. There is no threshold for instability of these modes (neglecting dissipation). Nevertheless, for the lower hybrid drift instability both of the decay modes k and $k + k_0$ shown in Fig. 2 are individually unstable so that the mode coupling process can not saturate the instability.

Interacting modes with $\Delta\omega \neq 0$ can be driven unstable when $\hat{\phi}_0$ exceeds a threshold. For the case $\hat{k}_0 = \hat{k}_0 \hat{e}_y$, this threshold can be easily calculated. The dispersion relation in Eq. (17) simplifies to

$$\hat{\omega}^2 = (\hat{\omega}_0 - \hat{\omega}_{k\pm})^2 - 2 \frac{|\hat{\phi}_0|^2 \hat{k}^4 \hat{k}_0^2 (\hat{k}_0^2 - \hat{k}^2)}{(1 + \hat{k}^2)(1 + \hat{k}_0^2 + \hat{k}^2)}, \quad (22)$$

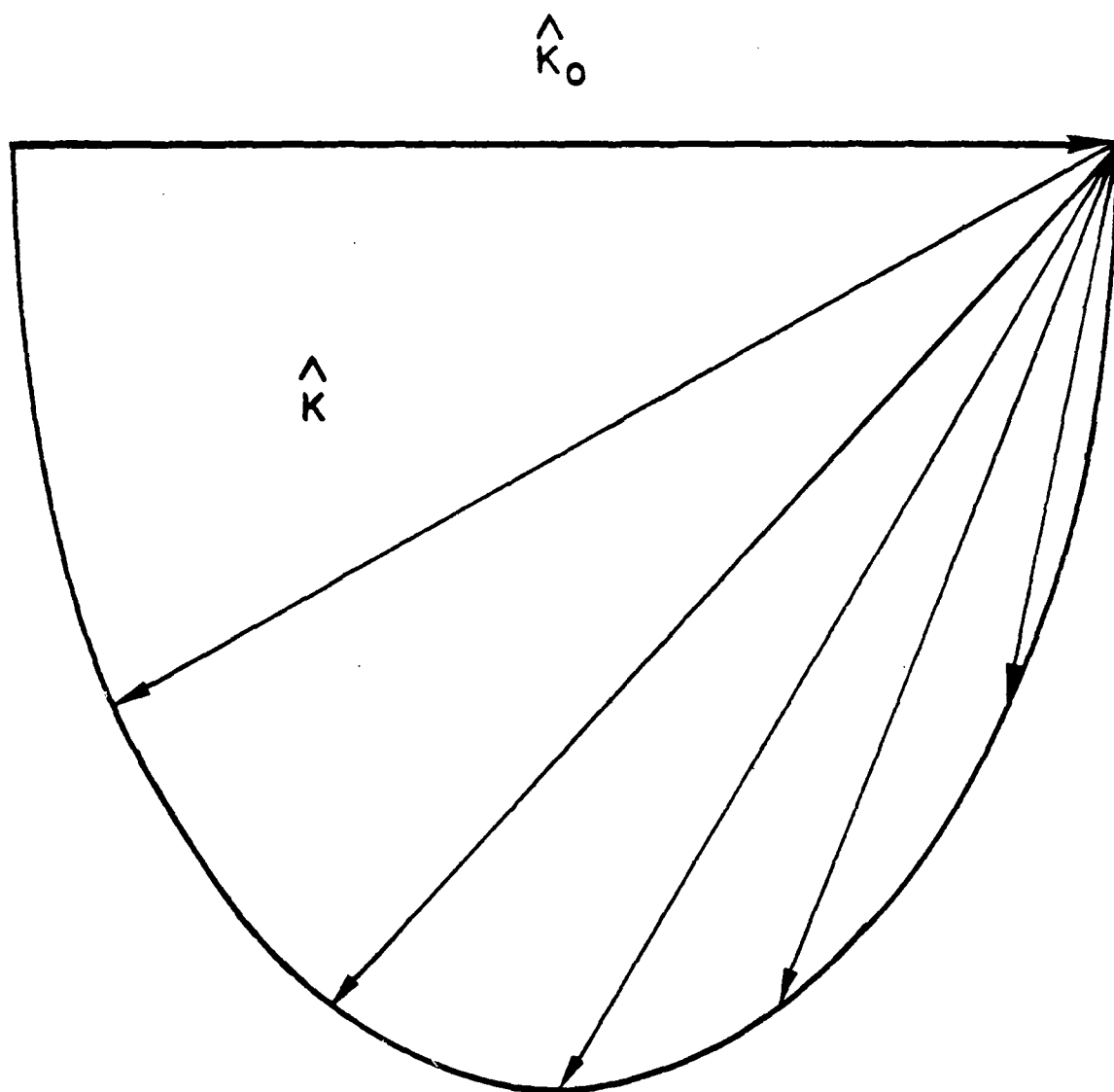


Fig. 2: The locus of modes $\hat{k}_x = k_{0es}$ which satisfy the frequency matching condition $\Delta\omega = \hat{\omega}_k - \omega_{k\pm} \pm \omega_0 = 0$, with $k_{\pm} = k \pm k_0$ and $\hat{\omega}_k = k_y / (1 + k^2)$, is shown.

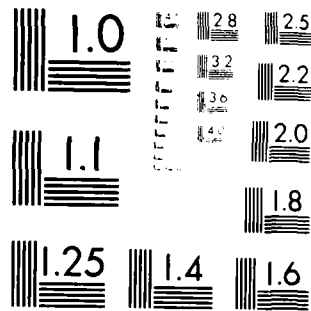
GEOPHYSICAL PLASMAS AND ATMOSPHERIC MODELING(U) SCIENCE
APPLICATIONS INC MCLEAN VA E HYMAN ET AL. MAR 84
SA1-84/1554 SBI-AD-E001 718 N00014-83-C-2034

4/6

F/G 4/1

NL

A 10x10 grid of squares. The top 8 rows are entirely black. The bottom 2 rows (rows 9 and 10) are mostly black, but contain a few white squares. Specifically, in row 9, the 7th and 8th squares from the left are white. In row 10, the 7th and 8th squares from the left are white, and the 9th square is also white. All other squares in the grid are black.



MICROCOPY RESOLUTION TEST CHART
 NATIONAL BUREAU OF STANDARDS-1963-A

where the dissipative sources and sinks have been neglected. In this limit $\hat{\omega}_k = \hat{k}_y = 0$ and $\omega_{k+} = -\omega_{k-}$ so that $\Delta\omega = \hat{\omega}_0 - \hat{\omega}_{k+}$ is the frequency mismatch. To have instability,

$$|\hat{\phi}|_c > |\hat{\phi}_0|_c^2 \equiv \frac{1 + \hat{k}^2}{2(1 + \hat{k}^2 + \hat{k}_0^2)(1 + \hat{k}_0^2)(\hat{k}_0^2 - \hat{k}^2)}. \quad (23)$$

For cases of interest $\hat{k}_0 \sim 1$ and $|\hat{\phi}_0|_c = .25$. At this amplitude the nonlinearity overcomes the linear frequency mismatch of the modes and a broad range of modes is driven unstable. As a consequence, we would expect the wave spectrum to saturate at around this level even when $\gamma_0 \ll 1$, i.e., the driving rate is small. This conclusion is verified in our numerical computations.

The particle flux can be calculated self-consistently with the wave spectrum. The rate of change of the density $\bar{n}(x) \equiv \langle n_e(x, y) \rangle_y$, where $\langle \rangle_y$ is a spatial average over y , is obtained by averaging the electron continuity equation,

$$\frac{\partial \bar{n}}{\partial t} + \frac{\partial}{\partial x} \langle n_e v_{ex} \rangle_y = 0. \quad (24)$$

To lowest order, $v_{ex} = -(c/B)\partial\phi/\partial y$, the polarization drift being small. The electron density can not be calculated directly since Eq. (24) for n_e can not be inverted analytically. However, since $n_e = n_i$, we can use the expression for n_i in Eq. (4) to obtain an explicit expression for the diffusion coefficient $D = -\langle n_e v_{ex} \rangle_y / (\partial \bar{n} / \partial x)$,

$$\hat{D} = D/D_0 = \left(\frac{2}{\pi}\right)^{1/2} \gamma_0^2 \sum_k \frac{\hat{k}_y}{|k|} \hat{\phi}_k (\hat{k}_y \hat{\phi}_k - i \frac{\partial \hat{\phi}_k}{\partial \tau}). \quad (25)$$

$$D_0 = c_{es}^2 \omega_{lh}^{-2}$$

Note that the normalization factor D_0 of the diffusion coefficient corresponds to a step size ρ_{es} with a correlation time ω_{lh}^{-1} . In the quasilinear limit $\partial/\partial\tau = -i\hat{\omega}_k$ and \hat{D} is given by

$$\hat{D}_{q1} = \left(\frac{2}{\pi}\right)^{1/2} \gamma_0^2 \sum_k \hat{k} \hat{k}_y^2 |\hat{\phi}_k|^2 (1 + \hat{k}^2)^{-1}. \quad (26)$$

The time evolution of both \hat{D} and \hat{D}_{q1} will be computed along with the wave spectrum in Sec. III.

III. Numerical Computations

The nonlinear equation for $\hat{\phi}$ in Eq. (13) is too complex to solve analytically and we have therefore adopted a computational approach. It is convenient to separate the second order Eq. (13) into two complex first order equations by defining a new function

$$\psi \equiv \hat{\nabla}^2 \hat{\phi} + \gamma_0 |\hat{\nabla}|^{-1} [(\hat{\phi}_x + \hat{\phi}_y)]. \quad (27)$$

Equation (13) for $\hat{\phi}$ can then be written as

$$\hat{\phi}_x - \psi_x + \hat{\phi}_y + \gamma_e \hat{\phi} + \hat{\nabla} \hat{\phi} \times \hat{e}_z \cdot \hat{\nabla} \psi = 0. \quad (28)$$

Since $\gamma_0 \ll 1$, we find from Eq. (27) that to lowest order

$$\hat{\phi} \approx \hat{\nabla}^{-2} \psi. \quad (29)$$

The second term on the right side of Eq. (27) is already small since it is proportional to γ_0 so that $\hat{\phi}$ in this term can be approximated to lowest order. Equation (27) then becomes an evolution equation for ψ ,

$$\psi_x = -\psi_y + |\hat{\nabla}| \hat{\nabla}^2 (\psi - \hat{\nabla}^2 \hat{\phi}) / \gamma_0. \quad (30)$$

Finally, eliminating ψ_x in Eq. (28) using Eq. (30), we obtain a similar evolution equation for $\hat{\phi}$,

$$\hat{\phi}_x = -\hat{\phi}_y + \gamma_e \hat{\phi} - \psi_y + |\hat{\nabla}| \hat{\nabla}^2 (\psi - \hat{\nabla}^2 \hat{\phi}) / \gamma_0 - \hat{\nabla} \hat{\phi} \times \hat{e}_z \cdot \hat{\nabla} \psi. \quad (31)$$

Note that the iteration procedure which was carried out on Eq. (27) eliminated the spurious unstable root. The dispersion relation which results from linearizing Eqs. (30) and (31) yields the correct eigenvalue of the lower hybrid drift instability given in Eq. (14) plus a spurious damped root,

$$\hat{\omega} = -\frac{1}{2}|\hat{k}|^3(1 + \hat{k}^2)/\gamma_0, \quad (32)$$

which does not cause any numerical difficulties. All of our numerical computations are based on the two coupled equations for \hat{e} and \hat{u} in (30) and (31).

The inclusion of the electron damping $\hat{\gamma}_e$ in Eq. (31) is essential in order to obtain a saturated spectrum since in the absence of this term all modes in k space are unstable [see the growth rate in Eq. (14)]. We have used two forms of electron dissipation in our calculations. The first arises from the VB resonant electrons in a finite β plasma. Explicit expressions for this damping rate have been derived in Ref. 9. In the long wavelength limit

$$\gamma_e = \gamma_{e0} |\hat{k}_y| \hat{k}^4 \quad (33)$$

with

$$\gamma_{e0} = \pi \frac{(1 + 2\beta_i)^2}{\beta_i \beta_e^2 (2 + \beta_i)} \exp(-2/\beta_e) \quad (34)$$

where β_e and β_i are the individual electron and ion values of beta. In the short wavelength limit, $\hat{\gamma}_e$ scales as $\hat{k}_y \hat{k}^2$ so we take as a model

$$\gamma_e = \gamma_{e0} \hat{k}_y \hat{k}^4 / (1 + \hat{k}^2). \quad (35)$$

An important feature of the VB resonant damping is that it scales as \hat{k}^5 as $\hat{k} \rightarrow 0$. Since the growth term in Eq. (14) scales as \hat{k}^3 in the long wavelength limit, modes with $\hat{k}_x = 0$ remain unstable even as $\hat{k}_y \rightarrow 0$. For large \hat{k} all modes are stable. The boundary between stable and unstable regions of k space is shown in Fig. 3a for $\gamma_{e0}/\gamma_0 = 0.1$ and 1.0. The area below the bounding curves is unstable. As γ_{e0}/γ_0 increases the unstable spectrum collapses toward long wavelength but unstable modes always remain.

Electron collisional viscosity is important in laboratory experiments where measurements of lower-hybrid-drift wave turbulence have been made. The electron damping rate for this case is given by²¹

$$\gamma_e = \nu_0 \hat{k}^2 \quad (36)$$

where

$$\nu_0 = \nu_e L_n / \Omega_e \rho_{es}, \quad (37)$$

ν_e is the electron-ion collision frequency

$$\nu_e = 2.9 \times 10^{-6} (\lambda n_e / T_e^{3/2}) s^{-1},$$

λ is the Coulomb logarithm, n_e is the electron density in cm^{-3} and T_e is the electron temperature in ev. In this case the collisional damping dominates the growth at both large and small \hat{k} so that the unstable region of \hat{k} space is localized around $\hat{k} \sim 1$ as shown in Fig. 3b for several values of ν_0/γ_0 . There is no instability when $\nu_0/\gamma_0 > \sqrt{3}/16$.

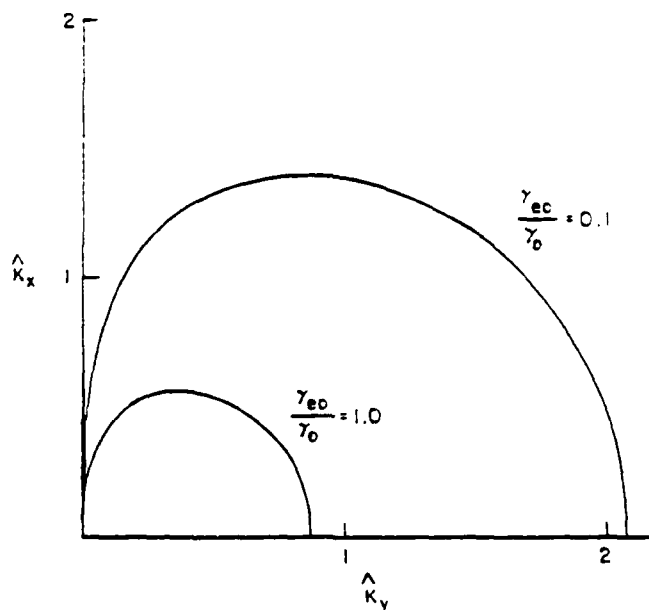
The coupled equations for $\hat{\phi}$ and ψ in (30) and (31) are solved using a pseudo-spectral method code developed by Fyfe et al.,²⁹ based on the work of Orszag.³⁰ The dependent variables $\hat{\phi}$ and ψ are Fourier-decomposed,

$$\hat{\phi}(\hat{x}, \tau) = \sum_{\hat{k}} \hat{\phi}(\hat{k}, \tau) \exp(i\hat{k} \cdot \hat{x}), \quad (38)$$

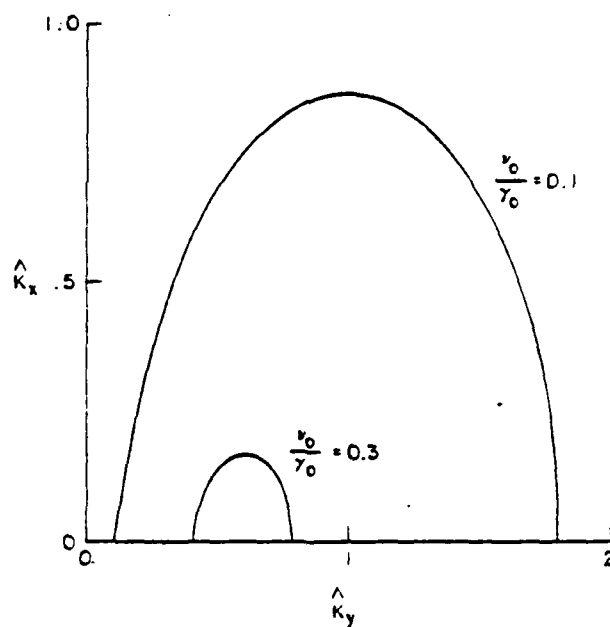
where $\hat{k} = \hat{n}/\lambda$ and $\hat{n} = n_x \hat{e}_x + n_y \hat{e}_y$ with n_x and n_y integers. The parameter λ fixes the value of $|\hat{n}|$ for which $|\hat{k}| = 1$. The nonlinear term in Eq. (31) is computed by fast Fourier transforming $\hat{\nabla}\hat{\phi}$ and $\hat{\nabla}\psi$ from \hat{k} to configuration space, calculating the product $\hat{\nabla}\hat{\phi} \times \hat{e}_z \cdot \hat{\nabla}\psi$ in configuration space and then fast Fourier transforming the result back to \hat{k} space. The equations are then stepped forward in time in \hat{k} space and the cycle is repeated.

The numerical results presented in this paper are nominally computed on a 32 x 32 mesh. However, to prevent aliasing of the wave energy during the fast Fourier transformation, it is necessary to zero all modes with $n > 32/3$ so that the useful volume of \hat{k} space is actually much less than one would expect.

A number of tests have been made to ensure that the code is correctly advancing the equations in time. The growth rates of the modes as obtained from the code during the linear growth phase have been checked with the



(a)



(b)

Fig. 3: The region of instability in \hat{k} space (below bounding curves) is shown for (a) collisionless plasma and (b) collisional plasma, where γ_0 , γ_{e0} and ν_0 are the normalized ion growth rate, electron VB damping rate and electron collisional damping rate. Collisional damping stabilizes the spectrum for $\gamma_{e0}/\gamma_0 > \sqrt{3}/16$.

solution of the linear dispersion relation. We have zeroed all but three interacting modes in the full code and cross-checked their nonlinear behavior with an independent code written to specifically study the interaction of only three waves. The sensitivity of our results to the step size of the time integration, as well as to the number of modes (some runs have been carried out on a 64×64 mesh), have also been checked.

IV. Numerical Results: Collisionless Damping

In collisionless, finite- β plasmas the VB resonant electron damping limits the range of unstable modes as shown in Fig. 3a. In this section we present the results of our numerical computations for this case. Preliminary results were previously presented for this collisionless case although the structure of our electron damping is now more realistic than that which was used in past computations.²⁰

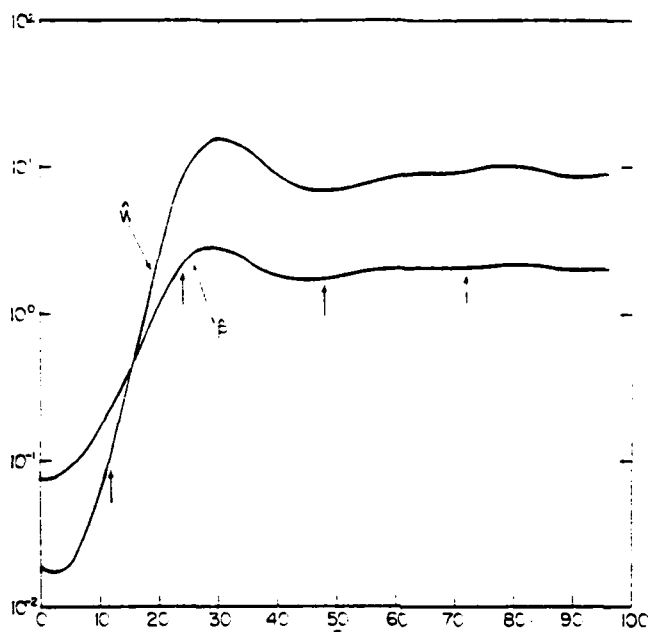
In Figs. 4-6 we present in some detail the results of our computations for the case $\gamma_0 = 0.5$, $\gamma_{e0} = 0.01$ and $\lambda = 5$ ($k_y \rho_{es} = 1$ for $n_y = 5$). The $\hat{\phi}$ spectrum is initialized with random noise with $\phi \sim 10^{-3}$ and Eqs. (30) and (31) are evolved until the wave energy (in our normalized units),

$$\hat{W} = \frac{1}{2} \sum_k (1 + k^2) |\hat{\phi}_k|^2, \quad (39)$$

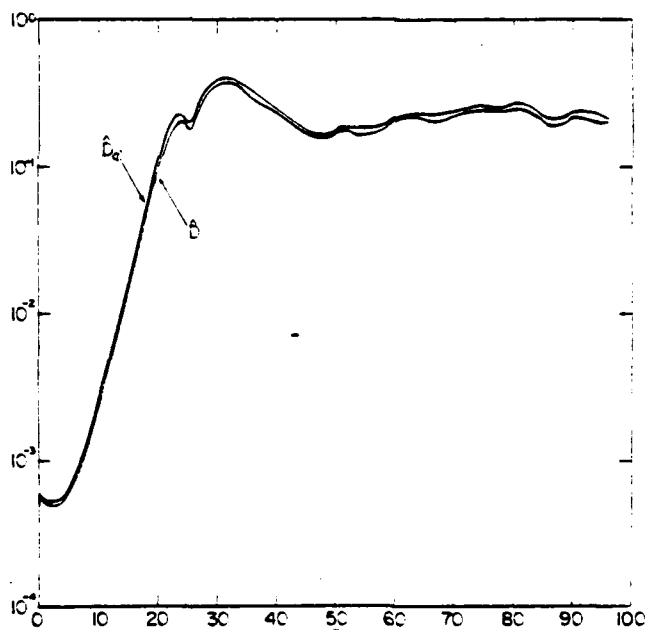
approaches a steady state value. The time history of \hat{W} , the root-mean-square potential,

$$\hat{P} = \langle \hat{\phi}^2 \rangle^{1/2} = \left(\sum_k |\hat{\phi}_k|^2 \right)^{1/2} \quad (40)$$

and the diffusion coefficients \hat{D} and \hat{D}_{q1} [Eqs. (25) and (26), respectively] are shown in Fig. 4. All of these quantities exhibit a similar temporal behavior. The initial decay ($\tau < 4$) is associated with the rapid dissipation of energy initialized in the damped modes, and is followed by a linear growth phase ($4 < \tau < 30$). Subsequently, mode coupling occurs which leads to saturation of the instability, albeit with some initial overshoot ($\tau \sim 30$). The levels of the total wave energy and other parameters of Fig. 4 are quite stationary in time after saturation. Also, the stationary values of all four quantities are relatively insensitive to the initialization of $\hat{\phi}$.



(a)



(b)

Fig. 4: The time history of the normalized wave energy \hat{W} , root-mean-square potential \hat{P} , diffusion coefficient \hat{D} and quasilinear diffusion coefficient \hat{D}_{ql} are shown for $\gamma_0 = 0.5$, $\gamma_{e0} = 0.01$ and $v_e = 0$.

In Fig. 4 the potential \hat{P} asymptotes to 2.0 after saturation so that $\hat{\phi} \sim 1$, which is consistent with the discussion in Sec. II. The quasilinear diffusion coefficient (\hat{D}_{q1}) tracks the actual diffusion coefficient (\hat{D}) quite well during the entire time evolution of the instability. An important point which must be emphasized with regard to \hat{D} is that both species, electrons and ions, continue to exchange both energy and momentum even after a steady state is reached; the electrons through the \sqrt{B} resonance and the ions by direct resonant interaction. If the instability had saturated by ion trapping and the electrons had no resonant interaction with the wave, there would be no diffusion in the steady state since the electrons could not exchange momentum with the ions. Both species must have a dissipative interaction with the waves to have diffusion.

In Fig. 5 we show a sequence of snapshots of the 2-D wave spectrum in \underline{n} space as the instability grows and saturates. The times at which the snapshots are taken are indicated by the arrows in Fig. 4a. Only $n_x > 0$ is shown since the spectrum for $n_x < 0$ can be obtained from $n_x > 0$ by the reality condition $\hat{\phi}(-\underline{n}) = \hat{\phi}(\underline{n})$. Figure 5a shows the spectrum during the linear phase of the instability. The spectrum is strongly peaked around the most unstable modes, $(n_x, n_y) = (0, \pm 5)$. Figure 5b shows the spectrum just prior to saturation. Note the development of the prominent peak at $(4, 0)$, which is a marginally stable mode since $n_y = 0$, and the broadening of the main peaks of the spectrum in the n_x direction. These results are entirely consistent with the discussion of the parametric excitation of daughter waves by a pump in Sec. II. The pump wave $(0, \pm 5)$ couples and destabilizes the $(4, 0)$ and $(4, \pm 5)$ modes. These secondary peaks quickly grow to large amplitude and excite other modes in turn. This mode coupling process culminates as the total wave energy saturates and spreads through most of the unstable or weakly damped volume of \underline{n} space as shown in Fig. 5c. Two significant features of Fig. 5c are: the shift in the peaks of the wave spectrum toward long wavelength $(0, \pm 2)$; and the nearly isotropic spectrum of waves surrounding these peaks. The detailed wave spectrum exhibits substantial variability in time, even after saturation when the total wave energy is nearly constant. This can be clearly seen by comparing the spectrum in Fig. 5c with that at a later time in Fig. 5d. The unstable and stable modes clearly continue to exchange energy in a dynamic manner even after saturation. Nevertheless, the wave spectra at

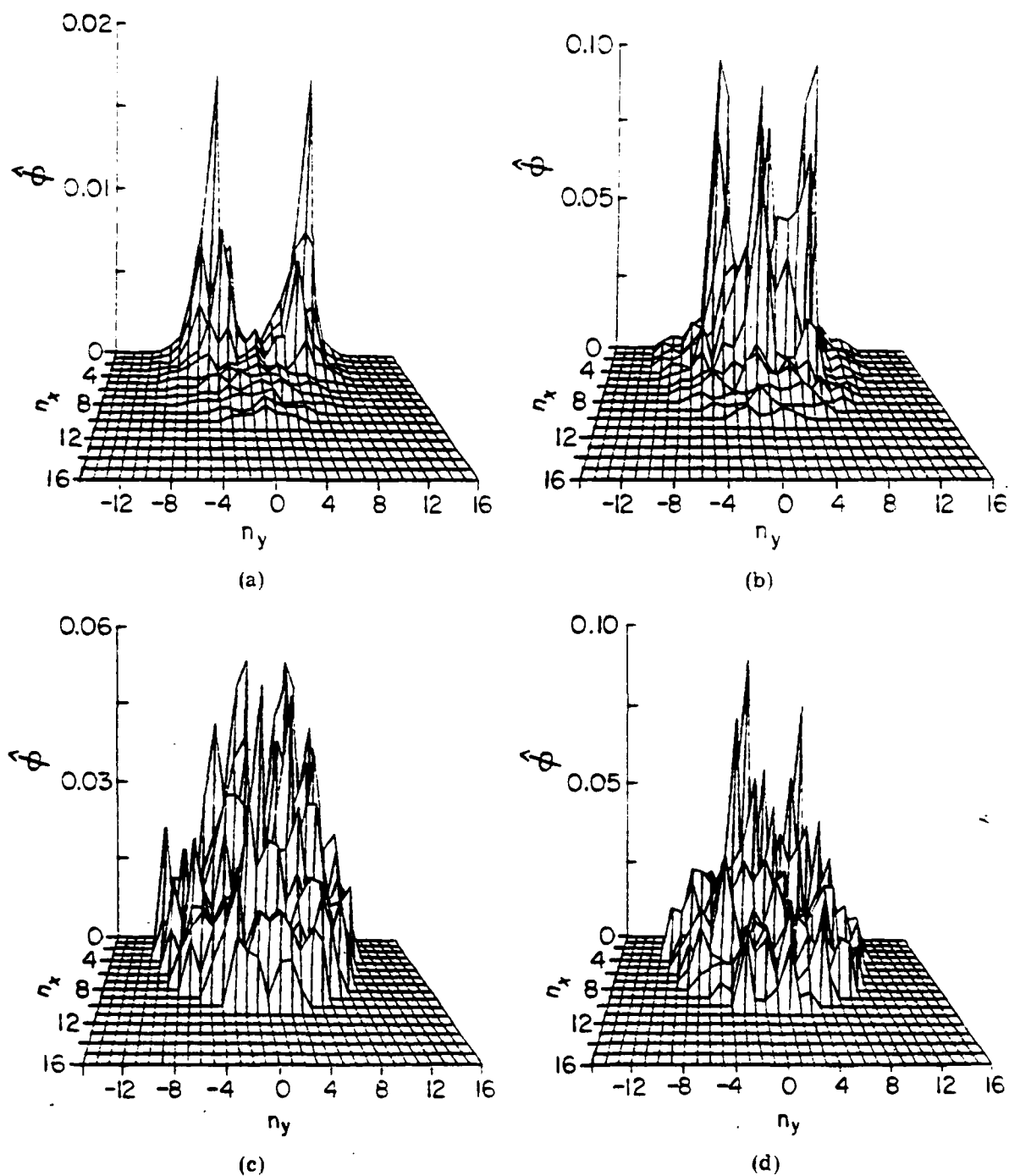


Fig. 5: Snapshots of the two-dimensional wave spectra are shown (a) during the linear phase, (b) during saturation, (c) just after saturation and (d) well after saturation for the run shown in Fig. 4, where $\hat{n} = 5 \hat{k}$. The times of the snapshots are marked with arrows in Fig. 4a.

late time are always characterized by peaks which are shifted towards long wavelength from the most unstable mode and by a broad spectrum of noise. Finally, in Fig. 6a we show the wave spectrum averaged over the time interval $112 < \tau < 192$. Much of the irregularity which was evident in the instantaneous spectra has now disappeared. The averaged spectrum is strongly peaked around $(0, \pm 3)$ with much smaller secondary peaks at $(\pm 2, 0)$. A contour plot of this average spectrum is shown in Fig. 6b. Note the cleft in the spectrum along $k_y = 0$.

A number of runs have been made with different values of the drift parameter γ_0 and the coefficient of the electron damping γ_{e0} . In Fig. 7 we show the diffusion coefficient \hat{D} and potential \hat{P} at saturation as functions of the drift parameter γ_0 . The electron damping γ_{e0} was varied with γ_0 so that the spectrum of unstable waves in \hat{k} space did not change, i.e., $\gamma_{e0} = 0.1 \gamma_0$. The potential \hat{P} is quite insensitive to γ_0 while the diffusion coefficient scales approximately as γ_0^2 (the reference curve $\hat{D} = 0.76 \gamma_0^2$ is shown for comparison). The insensitivity of \hat{P} , and consequently $\hat{\phi}$, to γ_0 is consistent with the idea, expressed previously in Sec. II, that the non-linear polarization drift in Eq. (13) must exceed the linear frequency mismatch of the interacting waves in order for effective energy exchange (and therefore saturation of the instability) to take place.

In Fig. 8 we show \hat{P} and \hat{D} as a function of γ_0 with $\gamma_{e0} = 0.11$. In this case the linearly unstable spectrum collapses towards longer wavelengths as γ_0 decreases as previously shown in Fig. 3a. The dependence of \hat{P} and \hat{D} on γ_0 in this case is basically similar to that in Fig. 7. The normalized potential \hat{P} has a weak dependence on γ_0 , increasing slightly as γ_0 decreases. The diffusion coefficient again scales as γ_0^2 (the reference curve $\hat{D} = 0.76 \gamma_0^2$ is shown).

The somewhat surprising conclusion which can be drawn from Figs. 7 and 8 is that the diffusion coefficient \hat{D} is very insensitive to the dissipation rate γ_{e0} ; much less sensitive, for example, than \hat{P} . For $\gamma_0 = 0.25$, the diffusion coefficient $\hat{D} = 0.06$ in both Figs. 7 and 8 even though $\gamma_{e0} = 0.03$ and 0.11 , respectively. By contrast, \hat{P} is 50% higher in Fig. 8 than in Fig. 7 for $\gamma_0 = .25$. As γ_{e0} is increased for a fixed value of γ_0 , $\hat{\phi}$ increases while the spectrum shifts towards longer wavelength so that \hat{D} does not change [see Eq. (26) for \hat{D}_{q1}]. The shift towards long wavelength

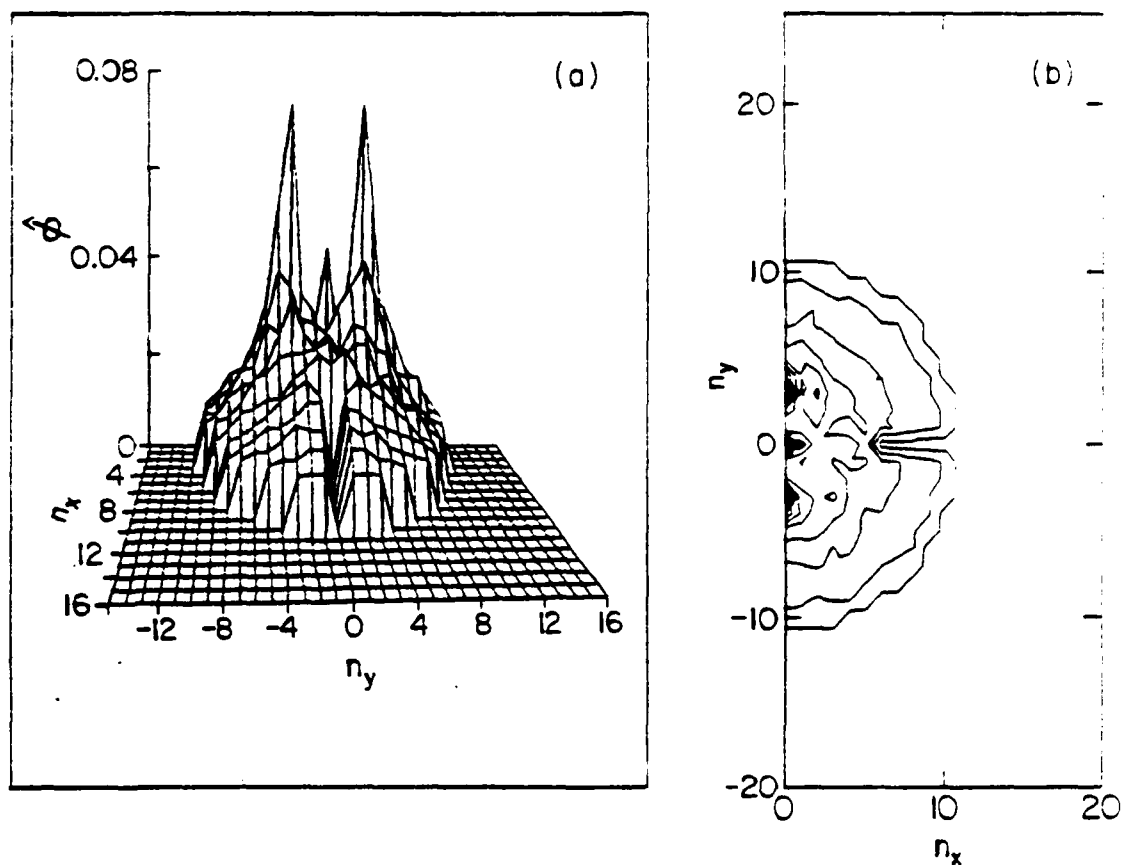


Fig. 6. The time averaged wave spectrum (a) and associated constant c contours (b) are shown for the run presented in Fig. 4. The spectrum was averaged over the interval $112 < \tau < 192$.

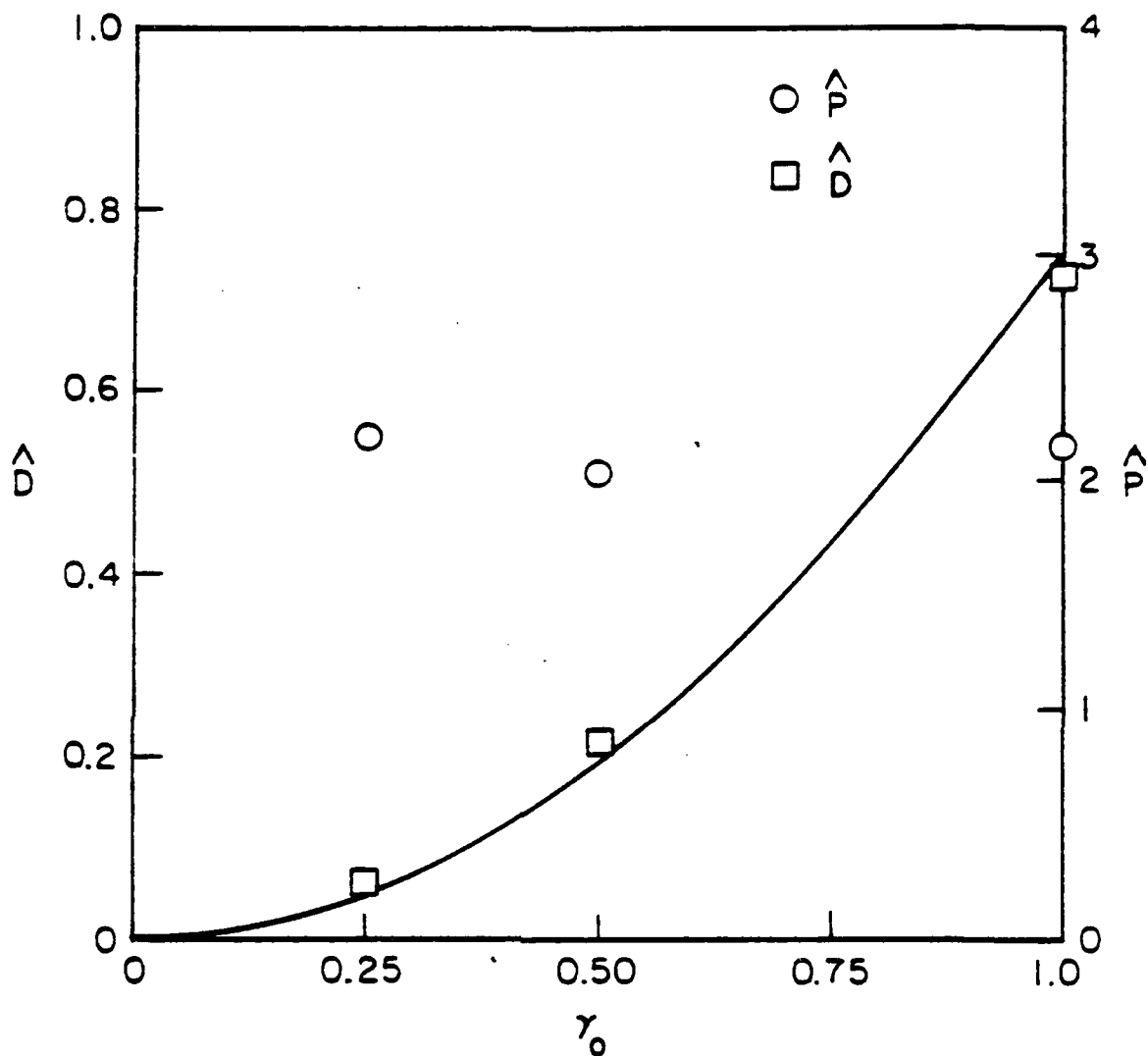


Fig. 7: The dependence of the diffusion coefficient \hat{D} and the root-mean-square potential \hat{P} on the ion driving term $\gamma_0 = \sqrt{\pi} V_{di}/v_i$ is shown for a fixed linearly unstable spectrum of waves ($\gamma_{eq}/\gamma_0 = 0.1$ and $v_0 = 0$). The reference curve is given by $D = 0.76 \gamma_0^2$.

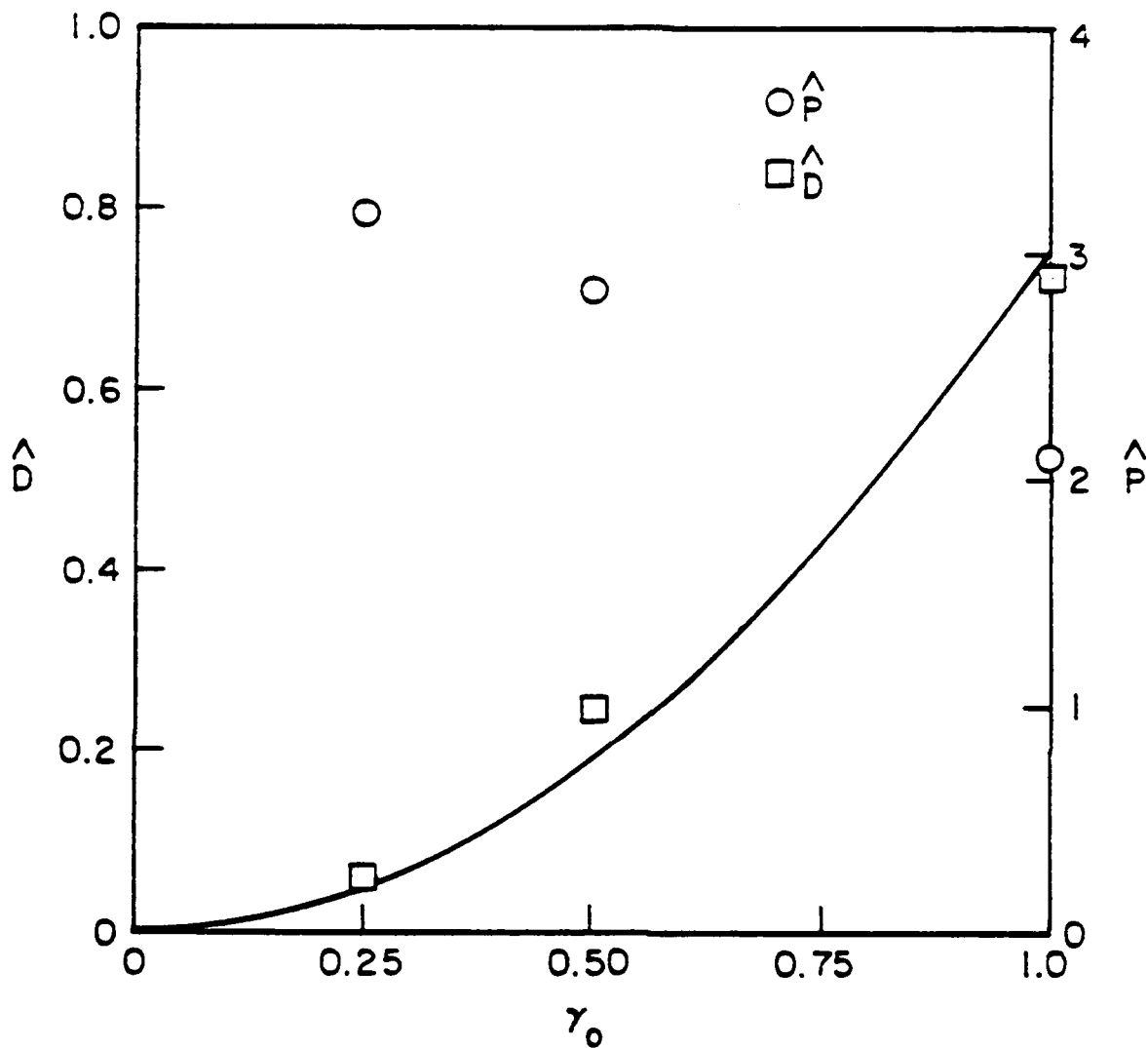


Fig. 8: The dependence of \hat{D} and \hat{P} on γ_0 is shown for a fixed electron ∇E damping rate $\gamma_{e0} = 0.11$ with $v_0 = 0$. The reference curve is again given by $\hat{D} = 0.76 \gamma_0^2$.

as ν_{e0} increases can be clearly seen in plots of the 2-D wave spectrum. By comparing the quasilinear diffusion coefficient in Eq. (26) with the portion of the linear growth rate in Eq. (14) which comes from the resonant ion interaction and the expression for the wave energy in Eq. (39), we find that roughly

$$\hat{D} \sim \partial W_i / \partial t,$$

where $\partial W_i / \partial t$ is the rate at which energy is extracted from the ions. Thus, our numerical results indicate that the rate at which the instability is taking energy from the ions is nearly independent of the electron damping. Of course, damped modes must always be included in the simulation or the wave energy does not saturate. The damping rate γ_{e0} must therefore remain finite.

V. Numerical Results: Collisional Damping

In laboratory and ionospheric plasmas classical damping can dominate the collisionless VB electron damping. As noted previously in Fig. 3b, collisional damping stabilizes both long and short wavelength modes and, unlike the VB resonant electron damping, can stabilize the entire spectrum. The results of our numerical computations for this case are summarized in Fig. 9 where we show the dependence of the saturated values of \hat{D} and \hat{P} on the collisional damping coefficient ν_0 for $\gamma_0 = 1.0$. The diffusion coefficient \hat{D} and potential \hat{P} are virtually independent of ν_0 . This result is rather surprising because as ν_0 increases the range of unstable modes in k space decreases dramatically (Fig. 3b) and, as a consequence, the characteristic wave spectra after saturation in the three cases presented in Fig. 9 are rather different. The spectra in the cases $\nu_0 = 0.05$ and 0.10 are similar to those presented in Sec. IV, the spectrum being somewhat broader for $\nu_0 = 0.05$ because the range of linearly unstable modes extends to larger values of $|k|$. For $\nu_0 = 0.15$ the linearly unstable region of k space has become rather localized and, as shown in Fig. 10, the saturated wave spectrum is much more peaked. The two dominant peaks at $n = (0, \pm 4)$ correspond to the most unstable modes while the secondary peak at $n = (2, 0)$ is the parametrically generated daughter wave. In this case the damping of the modes with finite n_x is so large

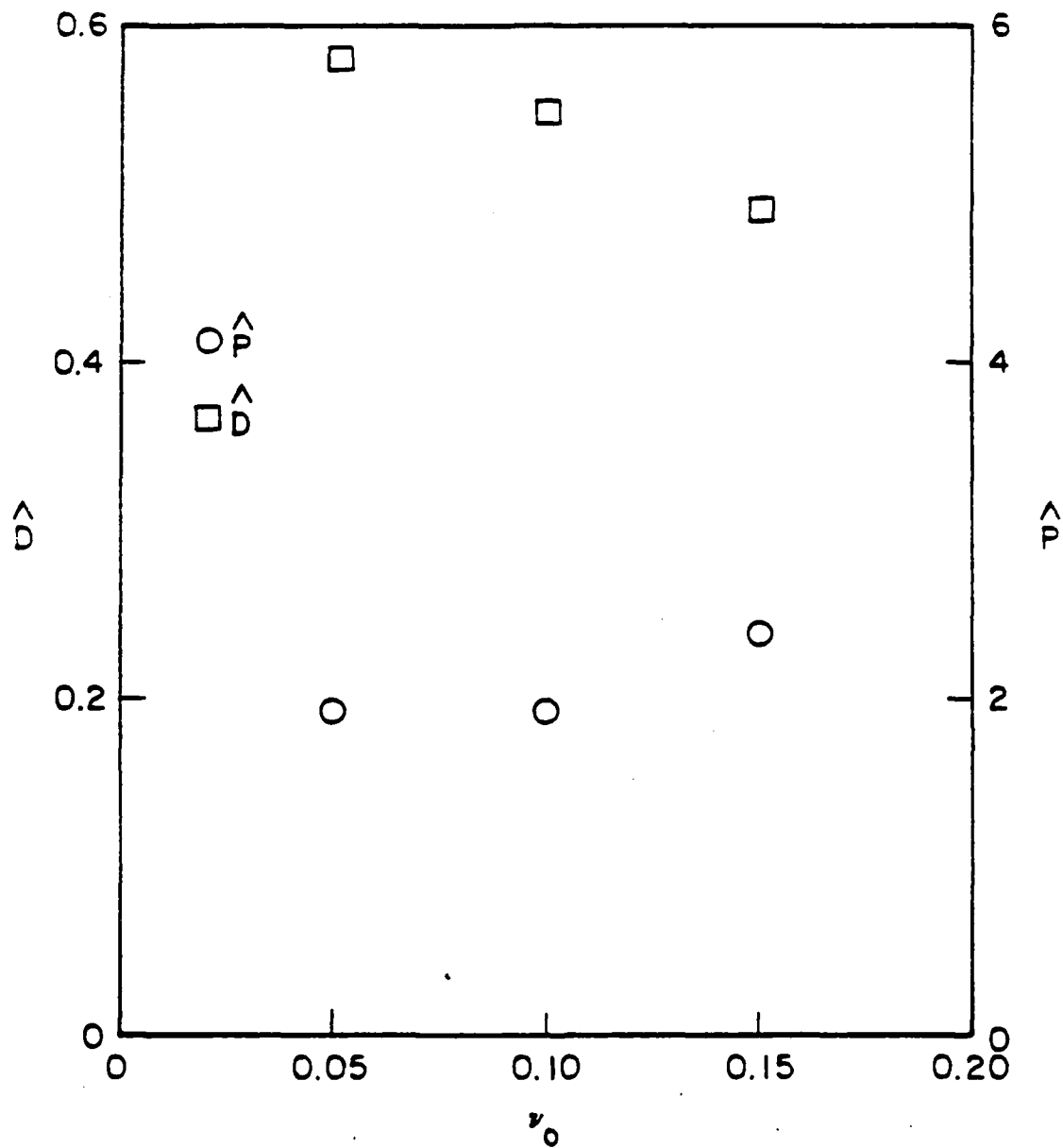


Fig. 9: The dependence of \hat{D} and \hat{P} on the electron collisional damping rate is shown with $\gamma_0 = 1.0$ and $\gamma_{e0} = 0$.

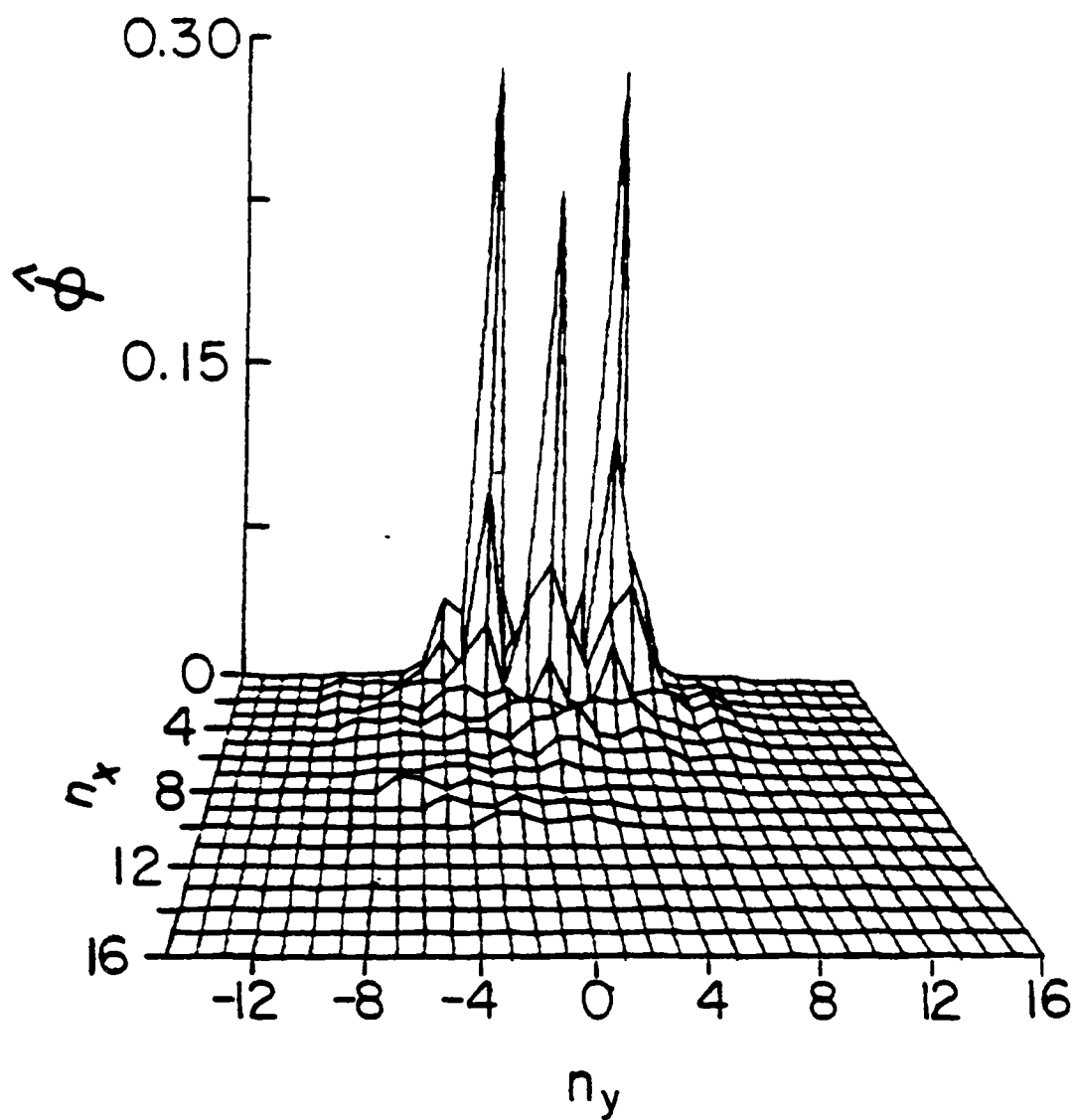


Fig. 10: The two-dimensional wave spectrum is shown for $\gamma_0 = 1.0$ and $\nu_0 = 0.15$, which is close to marginal stability.

(except for $n_y = 0$) that the energy which is pumped into them is rapidly dissipated and the wave spectrum remains quite narrow. Nevertheless, the saturated values of both \hat{P} and \hat{D} are virtually the same as those computed for smaller values of v_0 . This result is a consequence of the structure of the nonlinearity in Eq. (13) which only couples modes k' , k with $k' \times k = 0$. For the case of a narrow wave spectrum such as that shown in Fig. 10 the coupling of the modes is quite weak. Therefore, even though the growth rates of the unstable waves are small, the coupling of wave energy to the stable modes is correspondingly very weak and the saturation amplitude remains large.

From our numerical results we conclude that the saturation of the lower-hybrid-drift instability remains large even as collisions force the mode towards marginal stability. At marginal stability, of course, $\hat{\phi} \rightarrow 0$. This rather discontinuous behavior as collisionality increases seems rather unphysical and compels us to re-evaluate our assumptions. In the Introduction we argued that ion trapping was not a viable saturation mechanism when a broad, two-dimensional wave spectrum is excited. As we approach marginal stability by increasing the collisionality, the spectrum becomes quite narrow so that ion trapping should, at some point, become effective and saturate the instability at a lower amplitude than that which we have calculated from our mode coupling theory. Ion trapping occurs when the bounce time ω_{bi}^{-1} of an ion in the wave potential becomes comparable to the growth time γ^{-1} of the instability or

$$\omega_{bi}^2 \approx k^2 e\phi / m_i = \gamma^2. \quad (41)$$

In our normalized units,

$$\hat{\phi} \approx \gamma^2 (m_i / m_e)^{1/2} v_{di} / v_i \quad (42)$$

for $\hat{k} \sim 1$ so that $\hat{\phi} \rightarrow 0$ as the mode approaches marginal stability. Saturation by ion trapping occurs at a lower amplitude than that resulting from mode coupling when

$$\gamma < (m_e / m_i)^{1/4} (v_i / v_{di})^{1/2}. \quad (43)$$

VI. Summary and Applications

A nonlinear wave equation [see Eq. (13)] has been derived which describes two-dimensional ($\mathbf{k} \cdot \mathbf{B} = 0$) lower-hybrid-drift wave turbulence in a finite β plasma. As in the linear theory of this instability in the weak drift regime, the ions are treated as unmagnetized and to lowest order respond adiabatically to the potential fluctuations. The resonant ion contribution is included as a correction to provide the driving energy for the instability. The nonlinear portion of the wave equation arises from the electrons through their $\mathbf{E} \times \mathbf{B}$ and polarization drifts. In addition, electron dissipation is included either through the collisionless ∇B resonance or through collisional viscosity.

The nonlinear wave equation has been solved numerically using a pseudo-spectral method code to obtain the evolution and saturation of the wave spectrum as well as the self-consistent particle flux. The wave energy typically saturates as the peaked unstable spectrum spreads throughout the unstable and weakly damped regions of \mathbf{k} space. The saturated wave spectrum is characterized by two main components: a broad, nearly isotropic spectrum with $|\mathbf{k}| \gtrsim \rho_{es}^{-1}$; and a jagged spectrum consisting of narrow peaks in the range $|\mathbf{k}| \sim 0.5 \rho_{es}^{-1}$. These peaks are typically displaced towards long wavelength from the linearly most unstable waves by almost a factor of two. The peaks move around in \mathbf{k} space as the waves exchange energy in a dynamic fashion.

Our numerical computations demonstrate that the wave energy saturates when the nonlinearity becomes comparable to the linear frequency of the modes,

$$\frac{\partial}{\partial t} \sim \omega_k \sim \mathbf{V}_e \cdot \nabla \sim k V_e, \quad (44)$$

where \mathbf{V}_e is the $\mathbf{E} \times \mathbf{B}$ velocity of the electrons and $\omega_k = k_y v_{di} / (1 + k^2 \rho_{es}^2)$. For the most unstable modes, $k \rho_{es} \sim 1$, $\omega_k \sim v_{di} / \rho_{es} \sim \omega_{lh} v_{di} / v_i$ and (44) can be written as

$$e_c/T_i \approx 2-3 (2\pi_e/\pi_i)^{1/2} v_{di}/v_i, \quad (45)$$

where the numerical factor comes from the detailed computations. We have also found that the saturation level is relatively insensitive to both the magnitude of the electron dissipation, as long as the damping is sufficient to stabilize the shortest wavelengths in the computational grid, and the damping (growth) rate of the long wavelength modes.

Our interpretation of the saturation amplitude in Eq. (45) is that effective energy exchange between the linearly growing and damped modes can only take place when the nonlinearity becomes sufficiently large to overcome the linear frequency mismatch

$$\Delta\omega = \omega_{k1} + \omega_{k2} + \omega_{k3} \quad (46)$$

between interacting waves, k_1 , k_2 and k_3 . Below the threshold given in Eq. (45), only a few modes which satisfy $\Delta\omega \approx 0$ can exchange energy. Above this threshold all modes can exchange energy. The saturation amplitude in Eq. (45) also corresponds to the threshold for electron $\mathbf{E} \times \mathbf{B}$ trapping³¹ so that strong mode coupling is really a consequence of the strong nonlinear behavior of the electrons during this trapping process.

The particle flux has been computed self-consistently in parallel with the nonlinear evolution of the wave spectrum. Both the exact and quasilinear expressions for the particle diffusion coefficient D are then calculated from the flux. The quasilinear expression (D_{ql}) tracks the exact expression (D) within a factor of two. To lowest order

$$D \sim \Delta x^2 / \Delta t \sim \rho_{es}^2 \gamma_i \quad (47)$$

where the step size is given by $\Delta x \sim \rho_{es}$ and correlation time by $\Delta t \sim \gamma_i^{-1}$ where $\gamma_i \sim \omega_{lh} (v_{di}/v_i)^2$ is the growth rate of the most unstable mode in the absence of electron dissipation. The diffusion coefficient then becomes

$$D = 2.4 \rho_{es}^2 (v_{di}/v_i)^2 \omega_{lh}, \quad (48)$$

where the numerical factor comes from the detailed computations. The diffusion coefficient in (48) is very insensitive to the electron dissipation, less sensitive than the saturation amplitude e_0/T_e given in Eq. (45). At first glance Eq. (47) seems to imply that the usual estimate $\gamma \sim k^2 D$ or $D \sim \rho_{es}^2 \gamma$, where γ is the maximum growth rate of the instability, is quite accurate. However, the insensitivity of D to the electron dissipation implies that this estimate is not valid. The growth rate γ decreases rather sharply as the electron dissipation is increased so that $D \sim \rho_{es}^2 \gamma$ should also decrease. It does not so that this estimate fails to reproduce the computational results.

We now compare the results of our mode coupling calculation with laboratory observations of lower-hybrid-drift wave turbulence and with the results of recent computer simulations of this instability. A CO_2 laser scattering experiment was recently carried out on the Garching, 10m θ -pinch.⁵ The measured density fluctuations were flute-like ($k_z B = 0$) with clear peaks around $k_y \sim 0.5 \rho_{es}^{-1}$. The lower-hybrid-drift instability was therefore identified as the source of these fluctuations. Our computational results are in good agreement with several prominent features of the observed wave spectra. They measure a broad angular spectrum with $k_x \lesssim k_y$. They also observe that the peak in the wave spectrum is shifted towards long wavelength by about a factor of two from the linearly most unstable mode. In the experiment data were taken for three different filling pressures, corresponding to three values of V_{di}/v_i . We have found that classical electron-ion collisions have a significant influence on the growth rate of the lower-hybrid-drift instability in this experiment especially for the two highest filling pressures. In Table I we summarize some of the parameters of their experiment including the ratio of the electron-ion collision frequency ν_{ei} to the critical collision frequency,

$$\nu_c = .814 (V_{di}/v_i)^2 \omega_{lh}$$

required to completely stabilize the lower-hybrid-drift wave. In calculating ν_{ei} we have ignored impurities by taking $Z_{eff} = 1$. The highest pressure case (8m Torr) is very close to marginal stability and, given the uncertainty in experimental parameters, could even be stable. We have completed numerical computations for the three cases given in Table I. For

Table I

Parameters of Garching Experiment

P_0 (m Torr)	$n_e(10^{14}/\text{cm}^3)$	$T_e(\text{ev})$	$B(\text{T})$	v_{di}/v_i	$v_e(10^6/\text{sec})$	v_e/v_c
3	1	115	.79	.52	3.3	.0067
5	2.3	74	.77	.25	13.7	.12
8	5.2	77	.73	.17	28.5	.56

the two lowest filling pressures, 3 and 5 m Torr, the instability saturates with $\tilde{n}/n = 3.4 \times 10^{-2}$ and 1.4×10^{-2} , respectively, compared with the measured values of 1.4×10^{-2} and 2.3×10^{-3} . Our calculated saturation levels are 2-3 times larger than measured experimentally. In the case of 8 m Torr the spectrum is close to marginal stability and as a consequence the saturated wave spectrum is strongly peaked around the narrow band of unstable modes at $k_y \rho_{es} \sim 0.58$. Because the spectrum is quite narrow, ion trapping cannot be neglected so that the supposition made in Ref. 5 that ion trapping saturates the instability is probably valid for this case.

A number of computer simulations of the lower-hybrid-drift instability have been carried out over the past several years.^{10,13,32-34} Before comparing our results with these simulations, we would like to point out several difficulties which must be overcome in simulating this instability which are not widely recognized. The large disparity between the electron gyro time scale, Ω_e^{-1} , and the growth time of the instability, $(v_i/v_{di})^2 (m_i/m_e)^{1/2} \Omega_e^{-1}$, have forced the theorists to use artificially small mass ratios, $(m_i/m_e)^{1/2}$, and high drift velocities, v_{di}/v_i , in their codes. As a consequence, the parameter

$$\rho_{es}/L_n \sim (m_e/m_i)^{1/2} (v_{di}/v_i),$$

which should be a small number, is of order unity. Cases with larger mass ratios had to be run with larger drift velocities so ρ_{es}/L_n has not been varied significantly. The parameter ρ_{es}/L_n is significant for our computations for two reasons. First, the ratio of the rate of change of the magnetic free energy to particle drift energy in a finite β plasma scales as L_n^2/ρ_{es}^2 .¹⁵ For realistic parameters the magnetic free energy therefore greatly exceeds the drift free energy and the lower-hybrid-drift instability has no free energy bound. In the simulations this has not been the case. Second, in calculations of the nonlocal structure of the lower hybrid drift instability, it has been shown that the number of unstable harmonics in the x direction scales as L_n/ρ_{es} so that for realistic parameters a broad spectrum of unstable modes should be excited.³⁵ This is again not the case in many simulations. Recently, fluid-particle hybrid codes have been developed and simulations of the lower hybrid drift instability have been carried out with $\rho_{es}/L_n \ll 1$.¹³ In these simulations

a broad spectrum of modes in k space is excited with $k_x \ll k_y$. The cleft in the wave spectrum along $k_y = 0$, as shown in Fig. 6, is also seen in the wave spectra from these simulations. Finally, the amplitude of the potential fluctuations at saturation as obtained from these simulations is given by

$$e_0/T_i = 2.4(2m_e/m_i)^{1/2}(V_{di}/v_i)^2$$

which is in excellent agreement with our results [see Eq. (45)]. One caveat to this comparison is that most of their simulations were carried out for $V_{di}/v_i \geq 1$ while our theory strictly applies only for $V_{di}/v_i < 1$.

Finally, we now consider two physical systems, the earth's magnetosphere and ionosphere, where lower-hybrid-drift turbulence is expected to be important. The plasma in the neutral sheet of magnetotail is essentially collisionless. The lower-hybrid-drift instability has previously been proposed as a mechanism for dissipating magnetic energy in this reversed field configuration.⁴ In the most simple 1-D model of magnetic field annihilation the flux merging velocity V_B is simply given by¹⁵

$$V_B = \rho_{es}^2 v / \lambda$$

where v is the collision frequency (anomalous or classical) and λ is the scale length of the magnetic field. The anomalous collision frequency due to lower-hybrid-drift turbulence is given by $v = D/\rho_{es}^2$ so that from Eq. (48), we find

$$V_B/V_A = 2.4(m_e/m_i)^{1/2}(V_{di}/v_i)^3,$$

where $V_A^2 = B^2/4\pi m_i n$ is the Alfvén velocity. The rate of dissipation of magnetic flux is quite small during typical quiet conditions when $V_{di}/v_i \sim 0.1$ while during substorm activity when substantial thinning of the sheet has been reported ($V_{di}/v_i \ll 1$), the dissipation rate can be quite large.

The lower-hybrid-drift instability has also been suggested as a mechanism to generate small-scale irregularities ($\lambda \lesssim 1$ m) in the ionosphere during equatorial spread F (ESF),^{21,36} and observational evidence supports this mechanism.^{37,38} An important quantity to experimentalists is the power spectrum of density fluctuations during ESF.^{38,39} Recently, Singh and Szuszczyewicz³⁸ have presented a composite of ESF wave spectra from medium to short wavelengths. They find that (1) the spectra in the medium and intermediate wavelength domain ($\lambda \sim 50$ m \rightarrow 200 m) scale as $k^{-1.5 \pm 0.4}$ and $k^{-2.4 \pm 0.2}$, respectively; (2) the transitional wavelengths ($\lambda \sim 200$ m \rightarrow 20 m) have a $k^{-4.8 \pm 0.2}$ dependence, presumably due to drift waves; (3) the power spectrum breaks at $ko_i \gtrsim 1$ ($\lambda \lesssim 20$ m) to a shallower k dependence; and (4) the shortest wavelength observations (1 m $\lesssim \lambda \lesssim 20$ m) are consistent with a wave-particle interaction such as the lower-hybrid-drift instability. In order to apply the results of our nonlinear theory to the ionosphere we show in Fig. 11 a plot of $|\hat{c}_k|^2 = (e\phi/T_i)^2 (v_i/V_{di})^2 (m_i/2m_e)$ versus $n^2 = 9k^2 = 9k^2 \rho_{es}^2$ after saturation for $V_{di}/v_i = 0.56$ and $v_e/\omega_{ce} = 0.04$. Since we assume quasi-neutrality and the ions are basically adiabatic ($\delta n_i/n \sim e\phi/T_i$), Fig. 11 can be interpreted as an instantaneous power spectrum of density fluctuations associated with the lower-hybrid-drift instability. The arrow at $n^2 \sim 9$ denotes the fastest growing linear mode (for typical ionospheric parameters $B \sim 0.3$ G, and $T_i \sim 0.1$ eV this corresponds to $\lambda \sim 15$ cm). Two important aspects of this figure bear comment. First, there is substantial power in the long wavelength regime ($n^2 \lesssim 9$) and the spectrum is relatively flat, consistent with observational results. And second, the short wavelength spectrum ($n^2 > 9$) corresponds to a k^{-6} dependence, somewhat steeper than the transitional regime which has a $k^{-4.8}$ dependence. Thus, we predict that the very short wavelength power spectrum ($\lambda \lesssim 15$ cm) has a k^{-6} behavior. Experimentalists are unable to resolve the power spectrum of these very short wavelength modes so that our results cannot be verified at this time but await further improvements in experimental techniques.

Acknowledgments

This research has been supported by ONR and NASA. One of us (J.F.D.) was partially supported by DOE.

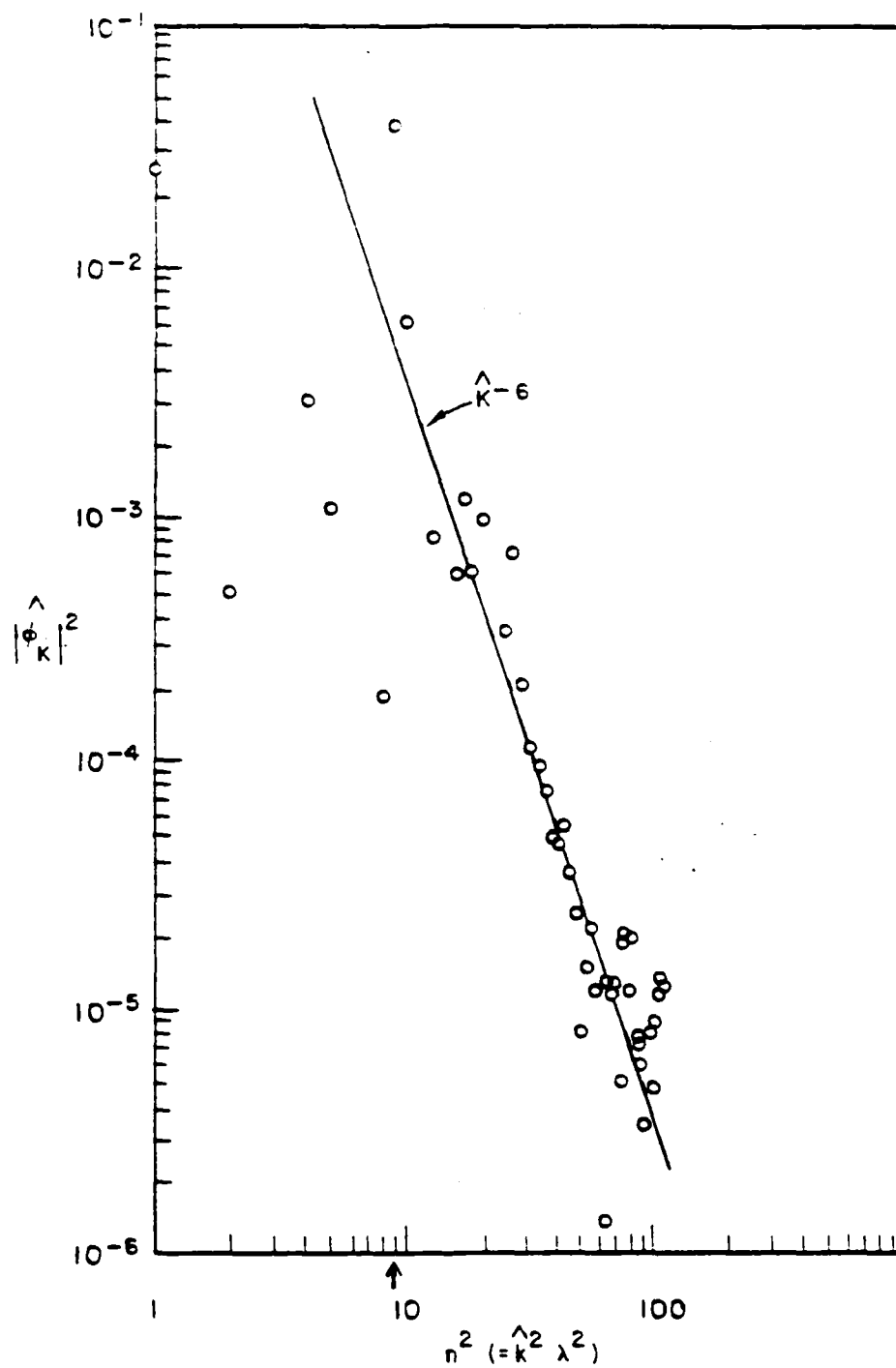


Fig. 11: The instantaneous power spectrum is shown after saturation for $v_{di}/v_i = 0.56$ ($\gamma_0 = 1.0$) and $v_e/\omega_{lh} = 0.04$ ($v_0 = 0.05$).

References

1. W.D. Davis, A.W. DeSilva, W. Dove, H.R. Griem, N.A. Krall and P.C. Liewer, in Plasma Physics and Controlled Nuclear Fusion Research (International Atomic Energy Agency, Vienna, 1971), Vol. III, p. 289.
2. R.C. Davidson, N.T. Gladd and Y. Goren, Phys. Fluids 21, 992 (1978).
3. M. Tuszewski and R.K. Linford, Phys. Fluids 25, 765 (1982).
4. J.D. Huba, N.T. Gladd and K. Papadopoulos, J. Geophys. Res., 83, 5217 (1978).
5. H.U. Fahrbach, W. Koppendorfer, M. Munich, J. Neuhauser, H. Rohr, G. Schramm, J. Sommer and E. Holzhauer, Nucl. Fusion, 21, 257 (1981).
6. R.L. McPherron, Rev. Geophys. Space Phys., 17, 657 (1979).
7. N.A. Krall and P.C. Liewer, Phys. Rev. A, 4, 2094 (1971).
8. R.C. Davidson, N.T. Gladd, C.S. Wu and J.D. Huba, Phys. Fluids 20, 301 (1977).
9. J.F. Drake, J.D. Huba and N.T. Gladd, Phys. Fluids 26, 2247 (1983).
10. D. Winske and P.C. Liewer, Phys. Fluids 21, 1017 (1978).
11. J.F. Drake and T.T. Lee, Phys. Fluids 24, 1115 (1981).
12. R.Z. Sagdeev and A.A. Galeev, Nonlinear Plasma Theory (W.A. Benjamin, Inc., New York, 1969), Ch. II, p. 37.
13. J.U. Brackbill, D.W. Forslund, K. Quest and D. Winske (private communication).
14. R.C. Davidson, Phys. Fluids 21, 1017 (1978).
15. J.F. Drake, N.T. Gladd and J.D. Huba, Phys. Fluids 24, 78 (1981).
16. S.P. Gary, Phys. Fluids 23, 1193 (1980).
17. T.H. Dupree and D.J. Tetreault, Phys. Fluids 21, 425 (1978).
18. P.H. Diamond and J.R. Myra, Phys. Fluids 26, 1481 (1983).
19. J.D. Huba and K. Papadopoulos, Phys. Fluids 21, 121 (1978).
20. J.F. Drake, P.N. Guzdar and J.D. Huba, Phys. Fluids 26, 601 (1983).
21. J.D. Huba and S.L. Ossakow, J. Geophys. Res., 86, 829 (1981).
22. A. Hasegawa and K. Mima, Phys. Fluids 21, 87 (1978).
23. W. Horton, Phys. Rev. Lett. 37, 1269 (1976).
24. R.E. Waltz, Phys. Fluids 26, 169 (1983).
25. P.W. Terry and W. Horton, Phys. Fluids 26, 106 (1983).

26. H. Hasegawa and D.G. Pettifor, Phys. Rev. Lett. 50, 130 (1983).
27. A. Hasegawa, C.G. Maciennan and Y. Kodama, Phys. Fluids 22, 2122 (1979).
28. D. Fyfe and D. Montgomery, Phys. Fluids 22, 246 (1974).
29. D. Fyfe, G. Joyce and D. Montgomery, J. Plasma Phys. 17, 317 (1977).
30. S.A. Orszag, Stud. Appl. Math. 50, 293 (1971).
31. H. Ching, Phys. Fluids 16, 130 (1973); R.E. Aamodt, Phys. Fluids 20, 960 (1977).
32. D. Winske, Phys. Fluids 24, 1069 (1981).
33. M. Tanaka and T. Sato, J. Geophys. Res. 86, 5541 (1981); Phys. Rev. Lett. 47, 714 (1981).
34. Y.-J. Chen and C.K. Birdsall, Phys. Fluids 26, 180 (1983).
35. J.D. Huba, J.F. Drake and N.T. Gladd, Phys. Fluids 23, 552 (1980); J.R. Myra, P.J. Catto and R.E. Aamodt, Phys. Fluids 24, 651 (1981).
36. J.D. Huba, P.K. Chaturvedi, S.L. Ossakow, and D.M. Towle, Geophys. Res. Lett. 5, 695 (1978).
37. W.R. Hoegy, S.A. Curtis, L.H. Brace, N.C. Maynard, and R.A. Heelis, Geophys. Res. Lett. 9, 993 (1982).
38. M. Singh and E.P. Szuszczewicz, to be published in J. Geophys. Res. (1983).
39. M.C. Kelley, R. Pfaff, K.D. Baker, J.C. Ulwick, R. Livingston, C. Rino, and R. Tsunoda, J. Geophys. Res. 87, 1575 (1982).

Appendix

One caveat needs to be added to the discussion of the mode coupling in lower-hybrid-drift turbulence presented in Sec. II. The dispersion relation in Eq. (17) was derived by keeping only the interaction of $(\hat{\omega}, \hat{k})$ with its nearest neighbors $(\hat{\omega}_{\pm}, \hat{k}_{\pm})$. Unfortunately, the coupling to higher order modes $\hat{k} \pm p\hat{k}_0$ with $p > 1$ cannot be neglected in general. This can be most easily understood in the limit $\hat{\omega} \gg \hat{\omega}_k, \hat{\omega}_{\pm}$ [see Eq. (18)]. Since we have made no a priori assumption on \hat{k} , the dispersion relation should remain invariant under the operation $\hat{k} \rightarrow \hat{k} \pm p\hat{k}_0$. The dispersion relation in Eq. (17) does not have this property and therefore cannot be correct. In this limit there is no small parameter which allows the coupling to higher order modes to be neglected. The coupling can be cut off, however, by adding dissipation to the system. When the modes $\hat{k} \pm p\hat{k}_0$ (with $p > 1$) are heavily damped, the coupling to these modes can be neglected and the dispersion relation in Eq. (17) is correct. For the parameters considered in this paper, these modes are indeed heavily damped so that the dispersion relation in (17) can be justified.

APPENDIX K
PARAMETER SURVEY FOR COLLISIONLESS COUPLING IN A
LASER SIMULATION OF HANE

R.A. Smith
Science Applications, Inc.

and

J.D. Huba
Naval Research Laboratory

Parameter Survey for Collisionless Coupling in a Laser Simulation of HANE

R. A. SMITH* AND J. D. HUBA

*Geophysical and Plasma Dynamics Branch
Plasma Physics Division*

**Science Applications, Inc.
McLean, VA 22102*

June 1, 1983

This research was sponsored by the Defense Nuclear Agency under Subtask S99QMXBC,
work unit 00067 and work unit title "Plasma Structure Evolution."



NAVAL RESEARCH LABORATORY
Washington, D.C.

Approved for public release; distribution unlimited.

K-3

PRECEDING PAGE BLANK-NOT FILMED

REPORT DOCUMENTATION PAGE		READ INSTRUCTIONS BEFORE COMPLETING FORM
1. REPORT NUMBER	2. GOVT ACCESSION NO.	3. REPORT CATALOG NUMBER
NRL Memorandum Report 5082		
4. TITLE (and Subtitle)		5. AUTHOR (Last, First, Middle Initial)
PARAMETER SURVEY FOR COLLISIONLESS COUPLING IN A LASER SIMULATION OF		Internal report on a continuing NRL problem.
6. PERFORMING ORG. REPORT NUMBER		
7. CONTRACT OR GRANT NUMBER(s)		
8. PERFORMING ORGANIZATION NAME AND ADDRESS		9. PROGRAM ELEMENT, PROJECT, TASK AREA & WORK UNIT NUMBERS
Naval Research Laboratory Washington, D.C. 20375		62715H: 47-0889-0-3
10. CONTROLLING OFFICE NAME AND ADDRESS		11. REPORT DATE
Defense Nuclear Agency Washington, D.C. 20305		June 1, 1983
12. NUMBER OF PAGES		13. SECURITY CLASS. of this report
36		UNCLASSIFIED
14. MONITORING AGENCY NAME & ADDRESS (if different from Controlling Office)		15. SECURITY CLASSIFICATION DOWNGRADING SCHEDULE
16. DISTRIBUTION STATEMENT (of this Report)		
Approved for public release; distribution unlimited.		
17. DISTRIBUTION STATEMENT (of the abstract entered in Block 20, if different from Report)		
18. SUPPLEMENTARY NOTES		
*Present address: Science Applications, Inc., McLean, VA 22102. This research was sponsored by the Defense Nuclear Agency under Subtask S99QMXBC, work unit 00067 and work unit title "Plasma Structure Evolution."		
19. KEY WORDS (Continue on reverse side if necessary and identify by block number)		
HANE coupling Turbulent coupling Laser simulation of HANE		
20. ABSTRACT (Continue on reverse side if necessary and identify by block number)		
<p>We present a set of criteria for collisionless coupling of debris-air plasmas via the magnetized ion-ion instability (MII) for conditions relevant to the NRL DNA laser experiment. The criteria are based upon (1) a transit time of ions across the coupling shell sufficiently long to allow significant momentum exchange between the debris and air ions; (2) non-stabilization of the MII by electromagnetic effects; (3) a system size</p> <p style="text-align: right;">(Continues)</p>		

DD FORM 1473 JAN 73

EDITION OF 1 NOV 65 IS OBSOLETE
S/N 0102-014-6601

SECURITY CLASSIFICATION OF THIS PAGE (When Data Entered)

K-5

PRECEDING PAGE BLANK-NOT FILMED

20 ABSTRACT (Continued)

sufficiently large to contain at least a target mass of background gas; and (4) allowance for a high β expansion (i.e., super-Alfvenic expansion). A series of figures are presented which display these criteria graphically and indicate the coupling regime for parameters pertinent to the NRL experiment. We conclude that the proposed NRL upgraded facility (e.g., stronger magnetic field and larger target chamber) should be adequate to test the collisionless coupling criteria set forth in Lampe et al. (1975).

CONTENTS

I. INTRODUCTION.....	1
II. COUPLING INSTABILITIES.....	3
A. Unmagnetized ion-ion instability.....	4
B. Magnetized ion-ion instability.....	6
C. Modified two stream instability.....	7
III. COUPLING CRITERIA.....	8
A. Definition of the coupling criteria.....	9
B. Quantitative evaluation of the criteria.....	10
C. Graphical presentation of coupling criteria.....	14
IV. DISCUSSION.....	15
ACKNOWLEDGMENTS.....	25
REFERENCES.....	25

PARAMETER SURVEY FOR COLLISIONLESS COUPLING IN A LASER SIMULATION OF HANE

1. INTRODUCTION

It is well known that a high altitude nuclear explosion (HANE) can significantly disturb the natural ionosphere by producing large-scale, long-lasting ionization irregularities. These irregularities can have an adverse effect on radar and communication systems (e.g., scintillations). Thus, in order to understand and aid the operation of such systems in a nuclear environment, it is crucial to determine the behavior of the ionosphere following a HANE. To this end, DNA has supported an extensive research effort, both experimental and theoretical, to investigate the dynamics of the debris-air interaction and the subsequent evolution of the plasmas. The experimental research has involved laboratory experiments in the early 1970's (NRL, AVCO) and plasma cloud releases in the ionosphere; the theoretical research has been directed at developing advanced computer codes to model a HANE, and using naturally occurring and man-made ionospheric phenomena as a test bed for the HANE theories and codes.

Recently renewed interest in the laboratory simulation of a HANE has been stimulated in the DNA community (Vesecky et al., 1980; Cornwall et al., 1981). Longmire et al. (1981) have examined the scaling of a HANE to a laboratory experiment in which a target is "exploded" using a laser. One of the purposes of such an experiment would be to simulate the early-time phase of a HANE, and to determine whether or not collisionless coupling between the debris and air, via plasma microturbulence, is an important process. Longmire et al. (1981) concluded that such an experiment is feasible although non-trivial. Tsai et al. (1982) have re-examined the scaling laws involved between a HANE and a laser simulation. They have found that a "faithful" simulation of early-time phenomena is not possible in the laboratory as it would require extremely large magnetic fields ($B \sim \text{few} \times 10^6 \text{ G}$) and densities ($n \sim \text{solid state}$). However, they derive a set of "approximate" scaling laws which are amenable to laboratory conditions, and which should allow insight into the physics of the debris-air interaction. They conclude that the experimental facilities at NRL are adequate to perform such a simulation.

The purpose of this report is to examine the plasma conditions necessary (and hopefully achievable) for collisionless debris-air coupling to occur in the NRL experiment. The primary use of this work will be for

Manuscript approved March 28, 1983.

the experimentalists to use as a rough guide in choosing the appropriate parameters for the experiment (e.g., density, magnetic field, laser energy, targets and background gas). Thus, we present a series of graphs which indicate expected coupling regimes, based upon the magnetized ion-ion instability, as a function of laser energy, background gas density and atomic mass, and magnetic field strength. The important coupling physics issues used in this analysis are the following.

1. Magnetized ion-ion instability: We believe that the dominant instability that will lead to debris-air coupling is the magnetized ion-ion instability. The requirement for instability that may pose a problem in the simulation is $V_{da} < \alpha V_{Aa}$ where α is a parameter of order unity and is a function of the plasma conditions, V_{da} is the relative debris-air velocity in the radial direction and V_{Aa} is the Alfvén velocity.

2. System size: We require that the size of the experiment be greater than a mass radius, i.e., $L_s > R_w$ where L_s is the size of the experiment and R_w is the mass radius defined by $(4\pi/3)\rho_a R_w^3 = M_d$. Here, ρ_a is the background gas density and M_d is the debris mass.

3. Coupling time: We require that the instability occurs on a sufficiently fast time scale so that coupling can occur, i.e., $v_c \tau_{tr} > 1$ where v_c is the effective collision frequency, $\tau_{tr} = \Delta/V_{da}$ is the transit time of an air ion in the debris, and Δ is the width of the coupling shell.

4. Magnetic field compression: We incorporate magnetic field compression in the criteria which depend upon the field. The relationship used is $B_c/B_0 = R/2\Delta$ where B_c is the compressed field, B_0 is the ambient field, R is the expansion radius of the debris shell, and Δ is the width of the debris shell (Wright, 1972).

The organization of the paper is as follows. In the next section, we discuss in greater detail the important physics issues upon which we base our analysis and which we believe are relevant to the NRL laser simulation. In Section III we discuss our results as they apply to the simulation and present figures indicating "coupling regimes." In the final section we discuss the implications of this work, as well as the limitations of the theory. Throughout the paper we use the expressions target and debris interchangeably, as well as background gas and air. We

conclude that there exist parameter regimes, which will be accessible to the NRL laser facility, in which collisionless coupling should occur.

II. COUPLING INSTABILITIES

In the mid-1970s, the NRL theory group studied a variety of plasma microinstabilities within the context of HANE (Lampe et al., 1975). The purpose of this research was to describe physical processes which could couple the debris-air plasmas, and provide a mechanism to heat the plasmas. The basic physical process involved is the "scattering" of particles from collective, fluctuating fields, associated with the instabilities, which can provide "anomalous transport coefficients" substantially larger than classical transport coefficients. We now give a brief overview of the instabilities considered by Lampe et al. (1975) which can lead to debris-air coupling and discuss their potential importance in regard to the laser simulation.

Prior to discussing the various instabilities, we first present Figs. 1 and 2 in order to indicate the geometry and the sources of free energy necessary to drive the plasma instabilities. In Fig. 1a we show the debris-air shell in the electron frame of reference. The debris is streaming in the radial (or x) direction; relative to the debris, the air plasma is streaming opposite to the debris (the -r or -x direction). Thus, in the radial (or x) direction there are three relative streaming velocities which can provide energy for an instability. They are (1) the relative debris-air velocity ($V_{da} = V_d - V_a$); (2) the relative debris-electron velocity ($V_{de} = V_d$); and (3) the relative air-electron velocity ($V_{ae} = V_a$). There are also azimuthal currents (in the ϕ or y direction) which are set up to support the magnetic field gradients shown in Fig. 1b. These currents are driven by electron flow so that only a relative electron-ion drift exists in this direction $\mathbf{J} = -n_e \mathbf{v}_e \hat{e}_{\phi,y}$.

The slab geometry and plasma configuration appropriate to early-time is shown in Fig. 2. The ambient magnetic field and plasma parameters (density (n) and temperature (T)) are functions of r or x. The flows for the ions and electrons are, respectively,

$$\mathbf{v}_i = (V_d - V_a) \hat{e}_{r,x} \quad (1)$$

and

$$\underline{V}_e = V_e \hat{e}_{\theta,y} \quad (2)$$

Strictly speaking, both \underline{V}_i and \underline{V}_e are also functions of x in the coupling shell; these inhomogeneities were ignored in Lampe et al. (1975) and will also be neglected in the present analysis. However, we note that such velocity inhomogeneities may affect the plasma instabilities under consideration. We defer such an analysis to a future report.

It is clear that two generic types of instabilities may exist in the early-time debris-air interaction: ion-ion streaming instabilities and electron-ion streaming instabilities. The ion-ion instabilities (i.e., magnetized ion-ion and unmagnetized ion-ion) occur only in the radial (or x) direction and can provide momentum transfer between the debris and air (i.e., coupling) and can heat the ions (Papadopoulos et al., 1971). The electron-ion instabilities (i.e., modified two stream, beam cyclotron, ion acoustic) can occur in both the radial (or x) and azimuthal (or y) directions. These instabilities primarily heat electrons, although the radial modified two stream instability can provide debris-air coupling (McBride et al., 1972). The azimuthal electron-ion instabilities limit the size of the magnetic field gradients and can cause radial diffusion of the magnetic field, density and temperature. Since the main emphasis of the laser simulation is on debris-air coupling, we restrict our attention to those instabilities which occur in the radial (or x) direction and can provide debris-air coupling: the unmagnetized and magnetized ion-ion instabilities, and the modified two stream instability.

A. Unmagnetized ion-ion instability

The turn-on conditions for the unmagnetized ion-ion instability (UII) is given by (Lampe et al., 1975)

$$\frac{V_{ji}}{V_j} \gtrsim 4 \alpha_{ji}^{-1/3} \quad (3)$$

and

$$\frac{V_{ji}}{V_i} \gtrsim 2 \quad (4)$$

where

$$\alpha_{ji} = \frac{n_j z_j^2 m_i}{n_i z_i^2 m_j} < 1, \quad (5)$$

$v_{ji} = |v_{ji}| = |v_j - v_i|$ is the relative streaming velocity between the ion species (i.e., debris and air), v is the thermal velocity, n is the density, z is the charge, and m is the mass of each species accordingly. In the laser simulations to date, it appears that these conditions are easily satisfied since $v_{da}/v_d \sim 8$ and $v_{da}/v_a \sim 10$ (B. Ripin, private communication).

However, in order to prevent the instability from being stabilized by electron shielding it is necessary that

$$v_{ji} < 1.5 c_i (1 + \alpha_{ji})^{1/3, 3/2} \quad (6)$$

where

$$c_i = \left(\frac{n_i z_i^2 T_e}{n_e m_i} \right)^{1/2}. \quad (7)$$

Assuming $a = i$, $d = j$, $n_a/n_e \sim 1/2$, $\alpha_{da} \sim 1/2$, and $v_{da} \sim 6 \times 10^7$ cm/sec, we find that

$$T_e > 550 \frac{A_a}{Z_a} \text{ eV} \quad (7)$$

where A_a and Z_a are the atomic mass and charge state of the background gas. It is believed that the electron temperature in the laser simulation is $T_e \sim 100$ eV in the debris shell shortly after the laser pulse has been terminated (B. Ripin, private communication), so that it is unlikely that the unmagnetized ion-ion instability will occur (this is especially true for an air background).

B. Magnetized ion-ion instability

The turn-on conditions for the magnetized ion-ion instability (MII) are the same as in the case of the unmagnetized ion-ion instability (Eqs. (3) and (4)) and these criteria should be satisfied in the laser experiment. On the other hand, in order to avoid electromagnetic stabilization of the instability, it is required that

$$V_{ji} < \alpha_0 V_{Ai} \quad (9)$$

where $\alpha_0 \sim 0(1)$ and is

$$\alpha_0 = 1.2 \left(\frac{n_i}{n_e} \right) Z_i (1 + \alpha_{ji}^{1/3})^{3/2} (1 + s_e)^{1/2}. \quad (10)$$

Here, $s_e = 8\pi n_e T_e / B^2$ and $V_{Ai} = B / (4\pi n_i m_i)^{1/2}$.

Another criterion for instability discussed in Lampe et al. (1975) is

$$L_s > \alpha_1 \frac{V_{di}}{\Omega_p} \quad (11)$$

where L_s is the system size and $\alpha_1 \sim 0(1)$ and is

$$\alpha_1 = 4.4 \left(\frac{n_e^2 A_i A_j}{n_i n_j Z_i Z_j} \right)^{1/2} (1 + \alpha_{ji}^{1/3})^{3/2} \quad (12)$$

Also, $\Omega_p = e B / m_p c$ and m_p is the proton mass. Equation (11) is a statement that the parallel wavelength associated with the instability is small enough to fit into the system. As a rough estimate of L_s for the simulation, we assume $V_{da} \sim 6 \times 10^7$ cm/sec and $B \sim 2 \times 10^3$ so that $L_s > 3$ cm is required. We note that this system size will be achievable in the NRL experiment. We also comment that Eq. (11) may not be required since the magnetized ion-ion instability is insensitive to the particle dynamics parallel to the field. A careful treatment of the influence of parallel wave effects on the instability in a magnetic field profile appropriate to a HANE and the experiment is needed. Thus, we do not consider this criterion as a major obstacle to the experiment.

C. Modified two stream instability

The turn-on condition for the modified two stream is

$$V_{ie} > 2v_i \quad (13)$$

where $V_{ie} = V_d$ or V_a , depending upon which ion species is being considered and v_i is the corresponding thermal velocity of the ions. This condition is likely to be met in the NRL simulation. In order to avoid electromagnetic stabilization of this instability, it is required that

$$V_{ie} < \alpha_2 V_{Ai} \quad (14)$$

where $\alpha_2 \sim 0(1)$ and is

$$\alpha_2 = \frac{n_i}{n_e} Z_i (1 + f_e)^{1/2} g \quad (15)$$

where g is a function of order unity (Lampe et al., 1975 - see p. 10 and 11).

Finally, there is also a condition on the size of the system given roughly by

$$L_s > 2\pi\alpha_3 \frac{V_{ie}}{\omega_{Hi}} \frac{m_i}{m_e}^{1/2} \quad (16)$$

where $\alpha_3 = 1/0(1 + \theta)$, $\theta \sim 0(1)$ and $\omega_{Hi} = \omega_{pi}/(1 + \omega_{pe}^2/\Omega_e^2)^{1/2}$. We note that Eq. (16) is an important consideration for the modified two stream instability since the instability relies upon the electron dynamics parallel to the magnetic field. Assuming $V_{ie} \sim 3 \times 10^7$ cm/sec and $B \sim 2 \times 10^3$ G, we find $L_s > 6$ cm which is somewhat more restrictive than the magnetized ion-ion condition.

Based upon the criteria outlined for the various ion-ion coupling instabilities, and the expected operating conditions of the NRL laser experiment, we believe the most likely and the most important coupling instability to be excited is the magnetized ion-ion instability. The unmagnetized ion-ion instability will only be excited if the electrons can be heated to high temperatures ($T_e \gtrsim 1$ keV)-which is not expected to occur

in the experiment after the laser beam is terminated. The modified two stream instability is more restricted by the system size is than the magnetized ion-ion instability. The modified two stream instability may be excited in the experiment, but the coupling criteria are similar to those of the magnetized ion-ion instability. Thus, in estimating the appropriate parameters to be used in laser experiment, we base our analysis on the criteria associated with the magnetized ion-ion instability. Aside from the turn-on conditions associated with the MII instability, the remaining crucial parameter to be stated is the effective collision frequency (or anomalous collision frequency) produced by the this instability. This collision frequency is (Lampe et al., 1975)

$$\nu_{ij} = 0.15 \omega_{Hi} \frac{\rho_i}{\rho} f(\alpha_{ji}) \quad (17)$$

where $\omega_{Hi} = \omega_{pi} / (1 + \omega_{pe}^2 / \Omega_e^2)^{1/2}$, ρ is the mass density, and

$$f(\alpha_{ji}) = \alpha_{ji}^{2/3} + (3^{1/2} / 2^{1/3}) (\alpha_{ji}^{1/3} - \alpha_{ji}^{2/3}). \quad (18)$$

III. COUPLING CRITERIA

The theory of the various instabilities of interest, even in the simplified local form presented by Lampe et al. (1975), involves many parameters that vary in a complicated manner, both in time and space, during the early-time expansion. Thus, detailed theoretical predictions of the coupling are difficult, and so our approach is to attempt to relate the local description of the instability condition of Lampe et al. (1975), through some simplifying heuristic criteria, to initial conditions and parameters which are controllable in the experiment. Examples of such parameters are the ambient magnetic field strength B_0 , the expansion velocity V_d , the ambient background density n_a , the kinetic yield of the target W , and so forth. We may then hope to provide, as initial guidance for the experiment design, parameter envelopes within which short-scale-length coupling might be expected to occur.

We stress that such estimates are approximate. Moreover, we have not yet attempted to relate the resulting parameter spaces to the scaling criteria developed by other authors, e.g., Longmire et al. (1981) or Tsai et al. (1982), for several reasons. First, we expect that the experimental phenomenology will still be of interest to HANE so long as qualitative scaling is preserved, i.e., most dimensionless ratios which are small, of order unity, or large in HANE are, respectively, small, of order unity, or large in the experiment, without necessarily translating the exact scaling (Tsai et al., 1982). Second, it may be desirable or even necessary to suppress certain effects in the experiment in order to provide an unambiguous test of short-scale-length coupling theory by isolating the parameter regime in which it is expected to dominate. For example, collisions and charge exchange can only provide complicating effects which may mask the conclusions regarding short-scale-length coupling, especially insofar as some of the chemical reactions which may enter at higher density (such as ternary reactions) do not scale correctly.

A. Definition of the coupling criteria

The basic criteria we adopt are the following:

1. Transit-time criterion

We require that a parcel of air (or background gas) spend at least one momentum-transfer time constant in traversing the coupling shell. The coupling shell thickness is denoted by $\Delta(R)$ at some expansion radius R and has a nominal expansion velocity $V_d(R)$ through a stationary background gas (i.e., $V_a = 0$). Denoting the anomalous collision frequency for momentum transfer from the debris to the ambient gas by ν_{ad} , we then have

$$\nu_{ad} \tau_{tr} = \frac{\nu_{ad} L}{V_d} > 1. \quad (19)$$

We adopt (19) as a physically reasonable estimate since the wave turbulence to produce coupling primarily occurs in the coupling shell. Also, we evaluate Eq. (19) at $R = R_w$ since collisionless coupling is strongest at roughly R_w (R. Clark, private communication).

2. Non-stabilization by electromagnetic effects

The magnetized ion-ion instability is stabilized by electromagnetic effects unless Eq. (9) is satisfied.

3. System-size criterion

Assuming that coupling occurs near the radius at a target mass R_w , we require

$$R_w \ll L, \quad (20)$$

where L is the characteristic system dimension, i.e., the size of the laser target chamber.

4. High-beta expansion criterion

In order that the debris not expend a major fraction of its energy in field compression (which may then be mistaken for short-scale-length coupling) we require

$$R_w \ll R_B \quad (21)$$

where R_B is the radius of a volume containing magnetic energy equal to the kinetic yield:

$$R_B = \left(\frac{6W}{B_0^2} \right)^{1/3} \quad (22)$$

Note that because of the R^3 dependence of a spherical expansion, inequality (22) is already strong for $R_w \leq R_B/2$.

B. Quantitative evaluation of the criteria

The initial parameters that may be easily controlled experimentally, i.e., those which may be varied over the widest range, are the ambient background gas density n_a and the kinetic yield W . We shall cast the coupling criteria outlined above into inequalities relating these two quantities. Eventually, the experimentalists will have control over the ambient magnetic field and we will also present results with this quantity as a control variable.

In order to evaluate the coupling criteria, several quantities need to be calculated: (1) $\Delta(R_w)$ - the coupling shell width at a mass radius; (2) n_d/n_2 - the ratio of the debris density to the background gas density; and (3) B_c/B_0 - the ratio of the compressed magnetic field to the ambient magnetic field. We now discuss each of these quantities.

We approximate the shell thickness Δ by

$$\Delta(R) \approx V_d \tau_\ell + \frac{\Delta V_d}{V_d} R \quad (22)$$

where τ_ℓ is the length of the laser pulse, ΔV_d is the thermal spread in the velocity of the debris, V_d is the expansion velocity, and R is the position of the coupling shell. Taking typical values for the NRL experiment, we assume $\tau_\ell \sim 4 \times 10^{-9}$ sec, $\eta_d \equiv \Delta V_d/V_d \sim .25$, $V_d \sim 4 \times 10^7$ cm/sec (B. Ripin, private communication), and $R = R_w$ so that

$$\Delta(R_w) \approx .16 + .25 R_w \text{ cm.} \quad (23)$$

Again, for typical experimental conditions we note that

$$R_w \gg V_d \tau_\ell / \eta_d, \quad (24)$$

so Eq. (23) becomes

$$\Delta(R_w) \approx \eta_d R_w \approx R_w / 4. \quad (25)$$

The ratio of the debris density to the background gas density is a function of position in the coupling shell. Rather than consider a variety of values, we use the average debris density in the coupling shell. This is a simplifying assumption and our results are not overly sensitive to this parameter. The average debris density in the coupling shell is given by

$$\bar{n}_d \sim \frac{M_d}{4\pi R_w^2 m_d \Delta} \sim \frac{M_d}{4\pi \eta_d R_w^3 m_d} \quad (26)$$

where M_d is the target mass and m_d is the mass of a debris ion. Making use of the definition of R_w (i.e., $(4\pi/3)\rho_a R_w^3 = M_d$) we find that

$$\frac{\bar{n}_d}{n_a} \approx \frac{A_a}{3n_d A_d} \quad (27)$$

Based on Eq. (27), we note that

$$\alpha_{da} \approx \frac{Z_d^2 A_a^2}{Z_a^2 A_d^2} \frac{1}{3n_d} \quad (28)$$

where $m_{a,d} = A_{a,d} m_p$ and m_p is the proton mass. Similarly, α_{ad} is defined

$$\alpha_{ad} = 3n_d \frac{Z_a^2 A_d^2}{Z_d^2 A_a^2}$$

Finally, we also need an estimate of the magnetic field compression in the coupling shell. A simple estimate based on the conservation of flux, as in the Longmire coupling shell model, gives the compressed field B_c (in the equatorial plane of the expansion) in terms of the ambient field B_0 as

$$\frac{B_c}{B_0} \sim \frac{R_w}{2\Delta} \sim \frac{1}{2n_d} \quad (29)$$

We note that for $n_d \lesssim 1/4$ the field compression in the NRL experiment is expected to be modest, i.e., $B_c/B_0 \sim 2$, which is consistent with experimental results thus far (S. Kacenjar, private communication).

Based on the coupling criteria outlined in Section III.A and the quantities defined above, we now present a set of quantitative conditions required for collisionless coupling via the magnetized ion-ion instability in the NRL DNA laser experiment. We first define the following quantities to be used in our results:

$$f(\alpha_{ji}) = \alpha_{ji}^{2/3} + (3^{1/2}/2^{1/3}) (\alpha_{ji}^{1/3} - \alpha_{ji}^{2/3}) \quad (30)$$

$$K_{ji} = f^{-1}(\alpha_{ji}) \left[1 + \frac{n_j A_j}{n_i A_i} \right] (A_i/Z_i)^{1/2} \left[1 + \frac{n_j Z_j}{n_i Z_i} \right]^{1/2} \quad (31)$$

$$H_{da} = \frac{1}{n_d^2 A_a} \left[1 + \frac{A_a Z_d}{3n_d A_d Z_a} \right]^{-2} \left[1 + \left(\frac{1}{3n_d} \frac{A_a^2 Z_d^2}{A_d^2 Z_a^2} \right)^{1/3} \right]^3 \quad (32)$$

$$H_{ad} = \frac{3}{n_d^2 A_a} \left[1 + 3n_d \frac{Z_a A_d}{Z_d A_a} \right]^{-2} \left[1 + \left(3n_d \frac{A_d^2 Z_a^2}{A_a^2 Z_d^2} \right)^{1/3} \right]^3 \quad (33)$$

$$v_{d7} = v_d / 10^7 \text{ cm/sec} \quad (34)$$

$$B_{03} = B_0 / 10^3 \text{ G} \quad (35)$$

$$n_{a14} = n_a / 10^{14} \text{ cm}^{-3} \quad (36)$$

Equations (34) - (36) are the debris velocity, ambient magnetic field, and background gas density, respectively, normalized to numerical values relevant to the experiment.

The coupling criteria are as follows.

1. Transit time criterion (τ_{tr})

$$W \geq 1.17 \times 10^{-4} A_a v_{d7}^5 \frac{n_{a14}}{B_{03}^3} \begin{cases} K_{da}^3 & ; \alpha_{da} < 1 \\ K_{ad}^3 & ; \alpha_{ad} < 1 \end{cases} \quad (37)$$

where W is the kinetic yield of the debris measured in joules.

2. Non-stabilization by electromagnetic effects (em)

$$n_{a14} \leq 1.50 \frac{B_{03}^2}{v_{d7}^2} \begin{cases} H_{da} & ; \alpha_{da} < 1 \\ H_{ad} & ; \alpha_{ad} < 1 \end{cases} \quad (38)$$

3. System size criterion (L)

$$W \leq 0.90 A_a v_{d7}^2 n_{a14} L^3 \quad (39)$$

Note that Eqs. (37) and (39) combine to give a minimum system length

$$L \geq 0.71 \frac{K_{ji}}{(A_a n_{a14})^{1/2}} ; \alpha_{ji} < 1 \quad (40)$$

4. High beta expansion (β)

$$n_{a14} \geq 4.80 \frac{B_{03}^2}{A_a v_{d7}^2} \quad (41)$$

C. Graphical presentation of coupling criteria

We now present a series of figures for various experimental parameters, such as target materials, background gases, debris velocities, and system sizes, as a function of kinetic yield, background gas density, and ambient magnetic field. These figures should serve as a guide to the experimentalists and be useful in designing experiments to test collisionless coupling of the debris-air plasmas via the magnetized ion-ion instability.

Schematically, the figures presented will correspond to those shown in Fig. 3 and are obtained as follows. First, the quantities A_a , A_d , Z_a , and Z_d are fixed at some specified values. A_a and A_d are the atomic masses (in proton units) of the background gas and the target material, respectively, and are known for each run. Z_a and Z_d are the charge states of the background and target plasmas, respectively, and are not well-known. We anticipate that many charge states will coexist and vary in time within the coupling shell. For the purpose of obtaining approximate coupling regimes we make the simplifying assumption of an average charge state for each ion species. The values chosen are based upon previous theoretical work (R. Clark, private communication) and experimental work (J. Grun, private communication). Second, the parameters B_0 and V_d (Fig. 3a) or n_a and V_d (Fig. 3b) are fixed at some relevant values, and conditions (37) - (41) are plotted as functions of kinetic yield W (in joules) versus the density n_a (Fig. 3a) or the ambient magnetic field B_0 (Fig. 3b). The boundary lines for each condition are denoted by τ_{tr} [Eq. (37)], em [Eq. (38)], L [Eq. (40)], and β [Eq. (41)], and are based upon solving these conditions as equalities. The shading indicates the side of the line for which the inequalities hold and indicate the parameters (W and n_a or W and B_0) needed for coupling. In both Figs. 3a and 3b, it is found that there is a coupling regime defined by a "box" or "window" in the parameter space (W , n_a) or (W , B_0). Figures 4 - 7 show some examples for parameters accessible (or eventually accessible) to the NRL laser facility.

Figures 4 and 5 are for an aluminum target ($A_d = 29$) with an average charge state of 10 ($Z_d = 10$), and a nitrogen background gas ($A_a = 14$) with an average charge state of 3 ($Z_a = 3$). Figure 4 displays kinetic yield W versus background density n_a for two sets of debris velocity and ambient

magnetic field values: (a) $V_d = 2 \times 10^7$ cm/sec and $B_0 = 800$ G and (b) $V_d = 4 \times 10^7$ cm/sec and $B_0 = 4000$ G. The first set of parameters is achievable with the present NRL laser facility. For this set, very low densities are required for coupling, 6×10^{12} cm $^{-3} < n_a < 4 \times 10^{13}$ cm $^{-3}$, and a larger system size ($L > 5$ cm) than is presently available ($L \sim 3$ cm). The second set of parameters uses a significantly larger ambient magnetic field $B_0 = 4000$ G (which should be obtainable in the experiment in the near future). It is found that coupling can occur for higher density plasmas 5×10^{13} cm $^{-3} < n_a < 4 \times 10^{14}$ cm $^{-3}$ and smaller system sizes ($L > 2$ cm) than the previous case. Figure 5 is a plot of kinetic yield W versus the ambient magnetic field B_0 . The species and charge states are the same as in Fig. 4 but a higher debris velocity is used ($V_d = 6 \times 10^7$ cm/sec) and the system size is taken, for illustration, to be 10 cm. The coupling regimes are shown for three sets of densities: $n_a = 10^{14}$, 10^{15} , and 10^{16} cm $^{-3}$. We note that as the density increases, the range of W and the magnitude of the ambient magnetic field required for coupling both increase. Since the ambient magnetic field in the NRL experiment will be such that $B_0 < 10$ kG, the experiment will require low density background plasmas ($n_a < 10^{15}$ cm $^{-3}$) to obtain coupling for an Al-N system. Thus, from Figs. 4 and 5 we find that the NRL DNA laser experiment should be able to achieve collisionless coupling via the MII instability using an aluminum target and a nitrogen background gas in future experiments using an upgraded magnetic field and target chamber. The present facility ($B_0 = 800$ G and $L < 3$ cm) is inadequate to obtain coupling based upon our criteria.

In Figs. 6 and 7 we present the coupling regimes analogous to Figs. 4 and 5 but using a carbon target ($A_d = 12$) with an average charge state of 4 ($Z_d = 4$) and a hydrogen background ($A_a = 1$) with a charge state of 1 ($Z_a = 1$). In Fig. 6 we plot W versus n_a for $V_d = 3 \times 10^7$ cm/sec, and $B_0 = 800$ G and 4000 G. It should be noted that for $B_0 = 800$ G, the required densities 3.5×10^{13} cm $^{-3} < n_a < 2.8 \times 10^{14}$ cm $^{-3}$ are somewhat higher than those of the Al-N system (Fig. 4). However, larger kinetic yields are also required so that the coupling regime is somewhat smaller than the Al-N system. Also, a large system size ($L > 5.5$ cm) is needed, greater than what is presently available. On the other hand, for $B_0 = 4000$ G, the densities required are in the range 8×10^{14} cm $^{-3} < n_a < 6 \times 10^{15}$ cm $^{-3}$, and the system size is $L > 1.1$ cm. In Fig. 7 we show W versus B_0 for $V_d = 6 \times 10^7$ cm/sec and $L = 10$

cm for three values of density: $n_a = 10^{14}$, 10^{15} , and 10^{16} cm^{-3} . The qualitative behavior of these curves are similar to Fig. 5. However, the quantitative behavior is more favorable to coupling in the upgraded NRL laser facility in that a larger range of densities is accessible for coupling in the regime $B_0 < 10 \text{ kG}$, i.e., $n_a < 10^{16} \text{ cm}^{-3}$ rather than $n_a < 10^{15} \text{ cm}^{-3}$ for the Al-N system (Fig. 5).

IV. DISCUSSION

We have presented a set of criteria for collisionless coupling of debris-air plasmas via the magnetized ion-ion instability (Lampe et al., 1975) for conditions relevant to the NRL DNA laser experiment. The criteria are defined by Eqs. (37) - (41) and are based upon (1) a transit time of ions across the coupling shell sufficiently long to allow significant momentum exchange between the debris and air ions; (2) non-stabilization of the MII because of electromagnetic effects; (3) a system size (i.e., target chamber) sufficiently large to contain at least a target mass of background gas; and (4) allowance for a high β expansion, i.e., super-Alfvénic expansion. A series of figures (Figs. 4 -7) are presented which display these criteria graphically and which indicate coupling regimes for parameters pertinent to the NRL experiment. We have specifically considered experiments using both an aluminum target with a nitrogen background, and a carbon target with a hydrogen background. In general, lighter target and background gases provide a broader (more easily accessible) range of experimental parameters for which collisionless coupling can occur. We conclude that the present NRL laser facility ($B_0 = 800 \text{ G}$ and $L < 4 \text{ cm}$) is inadequate to allow collisionless coupling to occur, but that the proposed, upgraded facility ($B_0 < 10 \text{ kG}$ and $L < 10 \text{ cm}$) is adequate to test the collisionless coupling criteria set forth in this analysis (Lampe et al., 1975).

Finally, we emphasize that this report has considered an idealized situation: several simplifying assumptions have been made in the analysis. First, we consider constant, average charge states of each ion species although it is clear that multiple charge states may exist that vary in time in the experiment (J. Grun, private communication). Second,

we consider fully ionized plasmas and ignore any collisional effects. Again, this assumption is an over-simplification and collisional effects need to be carefully addressed for interpretation of experimental results. For example, the pre-ionization of the background gas due to the initial radiation "flash" appears to be small ($<$ a few percent at a mass radius) (Hyman et al., 1983), so that the expanding debris shell may collisionally ionize the background gas. And finally, we note that the chemistry and radiation physics associated with the experiment is critically dependent upon the types of targets and background gases used. It may be worthwhile in running experiments to use materials which have relatively simple chemistry and radiation physics (e.g., use a helium background gas instead of hydrogen). Nonetheless, we believe our results are a useful guide to the experimentalists as a first step in designing experiments to study collisionless coupling.

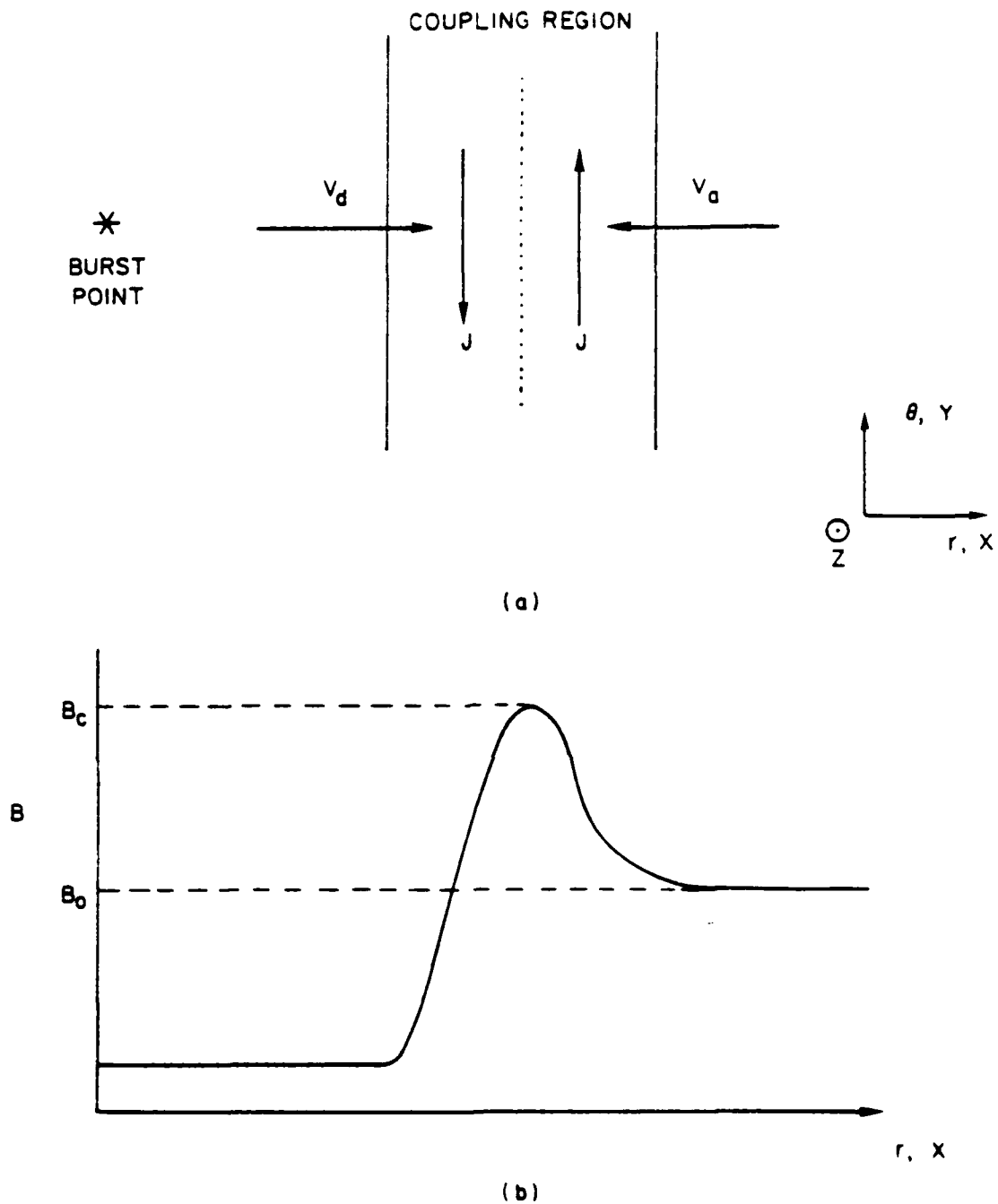


Figure 1

Schematic of relative drift velocities and magnetic field strength in the coupling shell following a HANE.

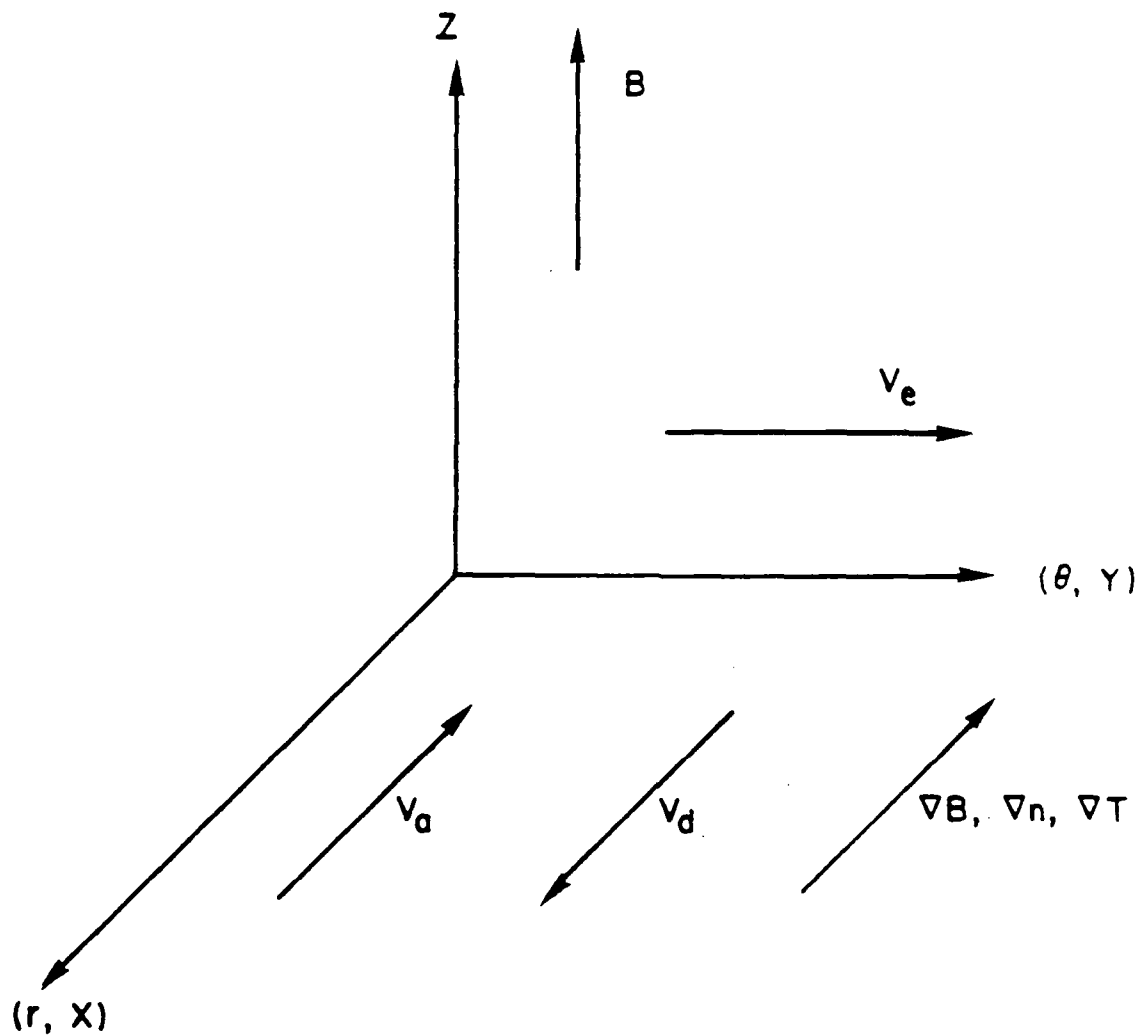
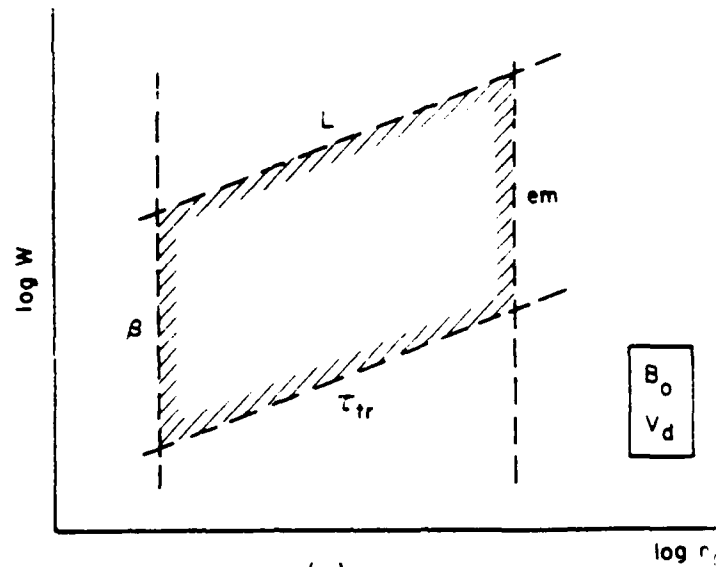
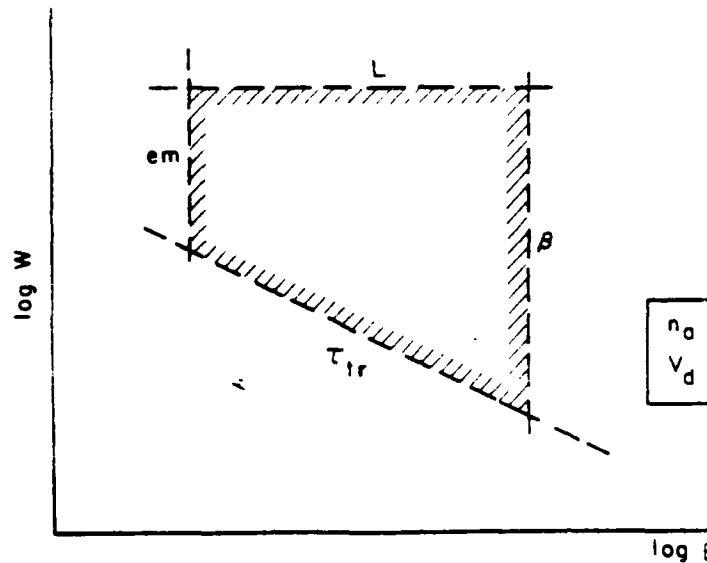


Figure 2

Slab geometry of the coupling shell region.



(a)



(b)

Figure 3

Schematic of coupling regime figures. The interior of the shaded side indicate the parameters necessary for coupling. Here, τ_{tr} , em , L , and β denote the criteria defined by (37) - (40), respectively. (a) Schematic of kinetic yield W versus background density n_a ; B_0 and V_d must be specified. (b) Schematic of kinetic yield W versus ambient magnetic field B_0 ; n_a and V_d must be specified. In both (a) and (b), A_a , A_d , Z_a , and Z_d must be specified.

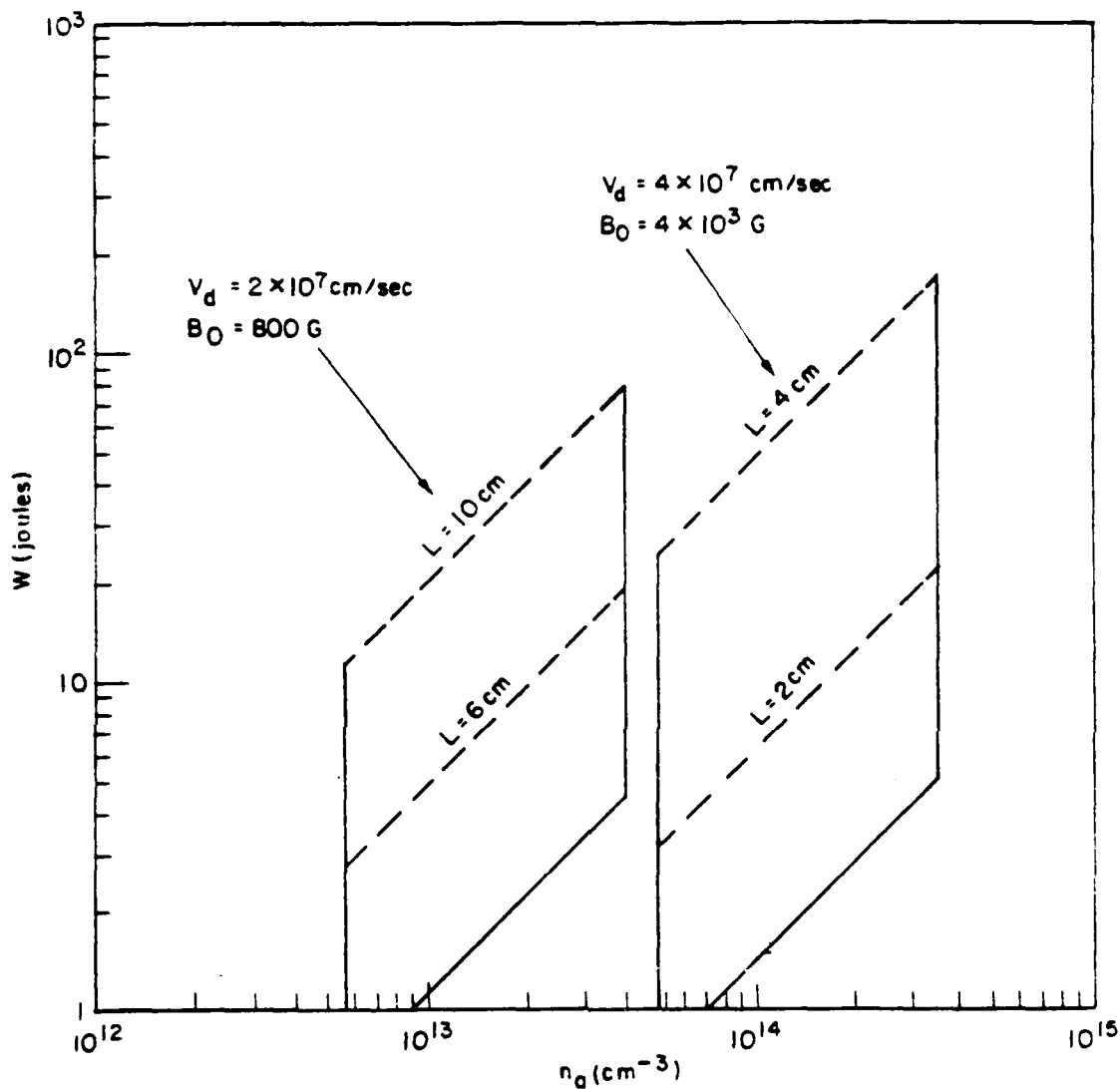


Figure 4

Plot of kinetic yield W (joules) versus background density n_a (cm^{-3}) for an aluminum target ($A_d = 29$) with an average charge state of 10 ($Z_d = 10$), and a nitrogen background gas ($A_a = 14$) with an average charge state of 3 ($Z_a = 3$). Two cases are considered: (1) $V_d = 2 \times 10^7$ cm/sec and $B_0 = 800$ G with $L = 6$ and 10 cm, and (2) $V_d = 4 \times 10^7$ cm/sec and $B_0 = 4000$ G with $L = 2$ and 4 cm.

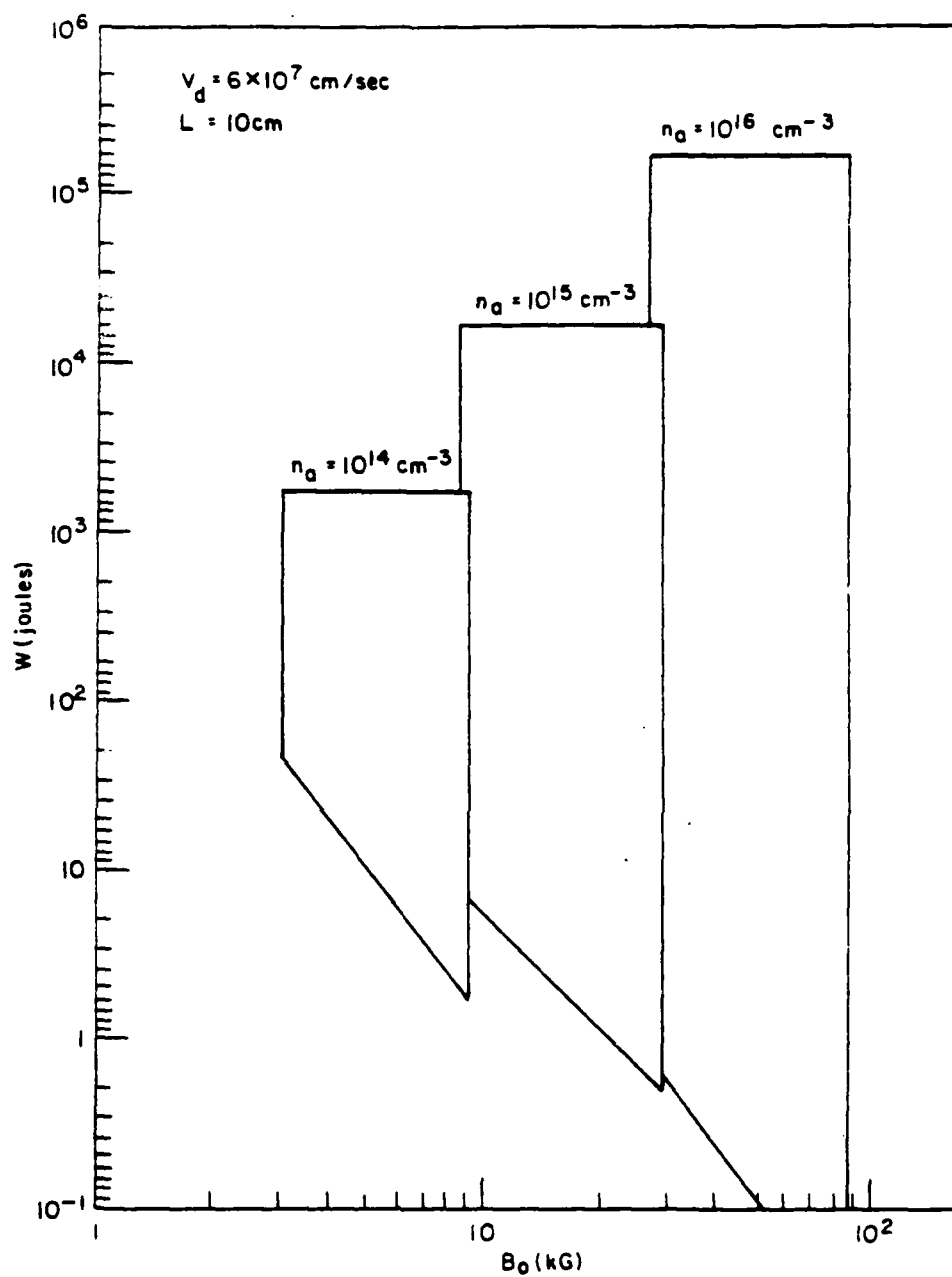


Figure 5

Plot of kinetic yield W (joules) versus ambient magnetic field B_0 (G) for the same target/gas as Fig. 4. We take $V_d = 6 \times 10^7 \text{ cm/sec}$, $L = 10 \text{ cm}$, and $n_a = 10^{14}$, 10^{15} , and 10^{16} cm^{-3} .

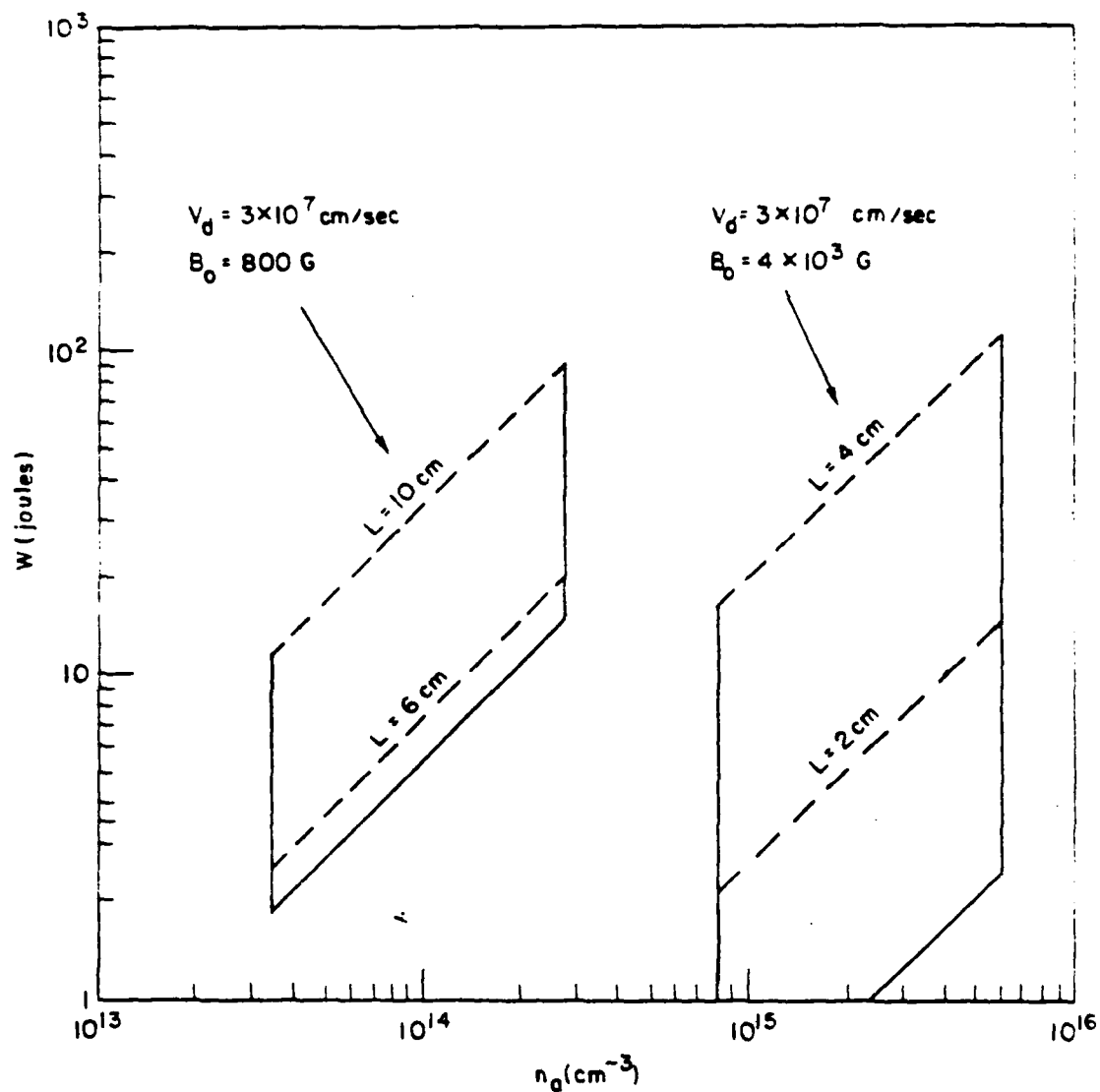


Figure 6

Plot of kinetic yield W (joules) versus background density n_a (cm^{-3}) for a carbon target ($A_d = 12$) with an average charge state of 4 ($Z_d = 4$), and a hydrogen background gas ($A_a = 1$) with a charge state of 1 ($Z_a = 1$). Two cases are considered: (1) $V_d = 3 \times 10^7 \text{ cm/sec}$ and $B_0 = 800 \text{ G}$ with $L = 6$ and 10 cm , and (2) $V_d = 3 \times 10^7 \text{ cm/sec}$ and $B_0 = 4000 \text{ G}$ with $L = 2$ and 4 cm .

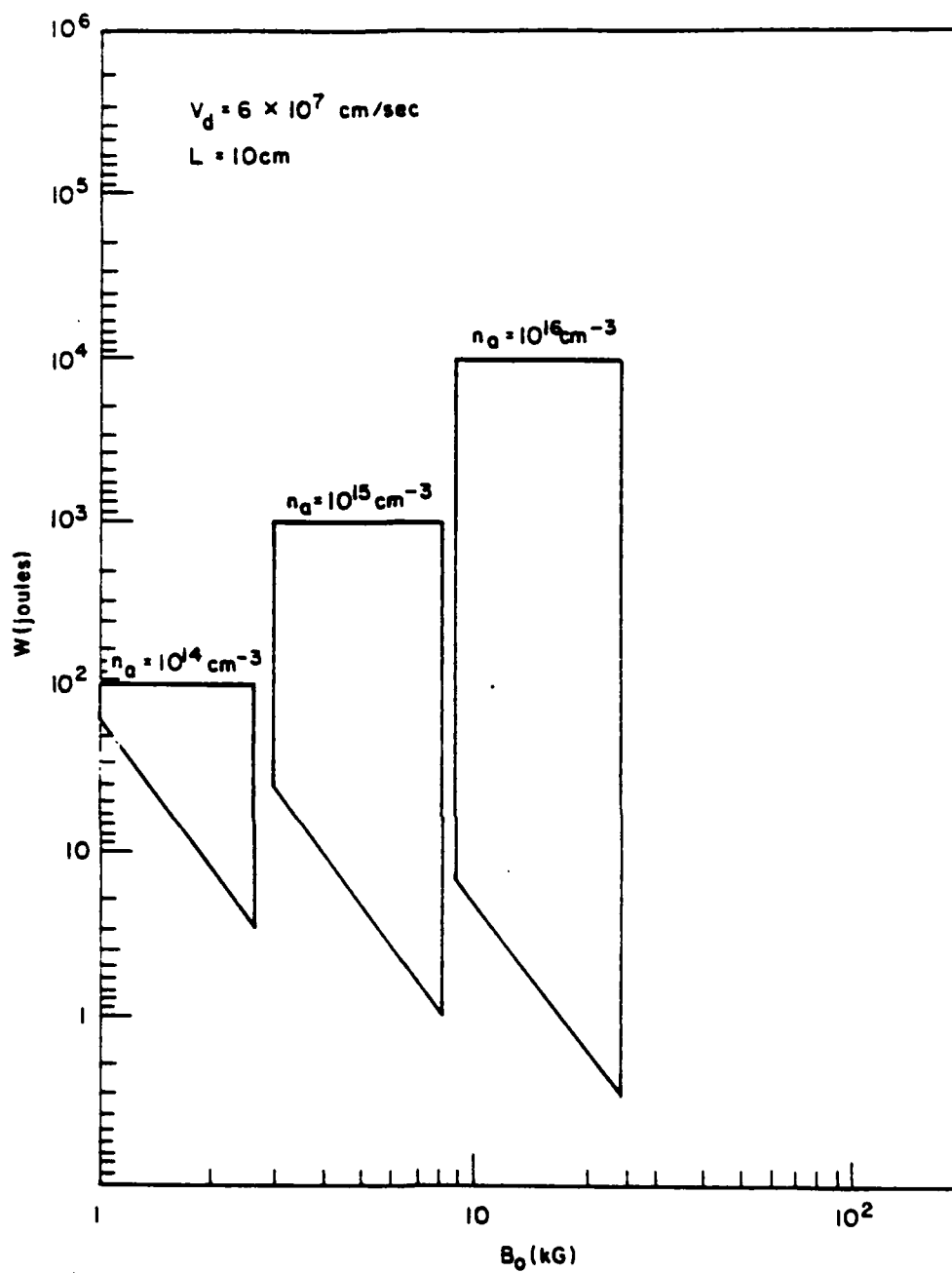


Figure 7

Plot of kinetic yield W (joules) versus ambient magnetic field B_0 (G) for the same target/gas as Fig. 6. We take $V_d = 6 \times 10^7 \text{ cm/sec}$, $L=10 \text{ cm}$, and $n_a = 10^{14}$, 10^{15} , and 10^{16} cm^{-3} .

ACKNOWLEDGMENTS

We thank Barry Ripin, Steve Kacenjar, and Jacob Grun for discussions of current experimental results and future plans, and Bob Clark and Dennis Papadopoulos for discussions regarding the coupling instabilities. We also thank Barry Ripin for a critical reading of the manuscript.

This research has been supported by the Defense Nuclear Agency.

REFERENCES

- Cornwall, M. S. Flatté, D. Hammer, and J. Vesecky, "Studies of the effect of striations on radio communications," JASON report JSR-81-31, 1981.
- Hyman, E., M. Mulbrandon, and J.D. Huba, "Preliminary report of UVDEP and PRODEP results for the NRL laser/HANE experiment," in preparation, 1983.
- Lampe, M., W.L. Manheimer, and K. Papadopoulos, "Anomalous transport coefficients for HANE applications due to plasma microinstabilities," NRL Memo 3076, 1975.
- Longmire, C., M. Alme, R. Kilb, and L. Wright, "Scaling of debris-air coupling," MRC Report AMRC-R-338, 1981.
- McBride, J.B., E. Ott, J.B. Boris, and J.H. Orens, "Theory and simulation of turbulent heating by the modified two stream instability," Phys. Fluids, 15, 2367, 1972.
- Papadopoulos, K., R.C. Davidson, J.M. Dawson, I. Haber, D.A. Hammer, N.A. Krall, and R. Shanny, "Heating of counterstreaming ion beams in an external magnetic field," Phys. Fluids, 14, 849, 1971.
- Tsai, W., L.L. DeRaad, Jr., and R. LeLevier, "Scaling laws for simulating early-time high-altitude nuclear explosion phenomena," R & D Associates Report, 1982.
- Vesecky, J.F., J.W. Chamberlain, J.M. Cornwall, D.A. Hammer, and F.W. Perkins, "Irregularities in ionospheric plasma clouds: Their evolution and effect on radio communication," JASON report JSR-80-15, 1980.
- Wright, L., "Early-time model of laser plasma expansion," Phys. Fluids, 14, 1905, 1971.

APPENDIX L
PRELIMINARY REPORT ON UVDEP AND PRODEP
RESULTS FOR THE NRL LASER/HANE EXPERIMENT

E. Hyman
Science Applications, Inc.

and

M. Mulbrandon and J.D. Huba
Naval Research Laboratory

Preliminary Report on UVDEP and PRODEP Results for the NRL Laser/HANE Experiment

E. HYMAN,* M. MULBRANDON AND J. D. HUBA

*Geophysical and Plasma Dynamics Branch
Plasma Physics Division*

**Science Applications, Inc.
McLean, VA 22102*

August 16, 1983

This research was sponsored by the Defense Nuclear Agency under Subtask S99QMXBC,
work unit 00067, and work unit title "Plasma Structure Evolution."



NAVAL RESEARCH LABORATORY
Washington, D.C.

Approved for public release; distribution unlimited.

L-3

PRECEDING PAGE BLANK-NOT FILMED

REPORT DOCUMENTATION PAGE		READ INSTRUCTIONS BEFORE COMPLETING FORM
1. REPORT NUMBER	2. GOVT ACCESSION NO.	3. RECIPIENT'S CATALOG NUMBER
RI. Memorandum Report 5146		
4. TITLE and Subtitle	5. TYPE OF REPORT & PERIOD COVERED	
PRELIMINARY REPORT ON UVDEP AND PRODEP RESULTS FOR THE NRL LASER HANE EXPERIMENT	Interim report on a continuing NRL problem.	
6. AUTHOR	8. CONTRACT OR GRANT NUMBER(s)	
E. Hyman,* M. Mulbrandon and J.D. Huba		
9. PERFORMING ORGANIZATION NAME AND ADDRESS	10. PROGRAM ELEMENT PROJECT TASK AREA & WORK UNIT NUMBERS	
Naval Research Laboratory Washington, DC 20375	62715H; 47-0889-0-3	
11. CONTROLLING OFFICE NAME AND ADDRESS	12. REPORT DATE	
Defense Nuclear Agency Washington, DC 20305	August 16, 1983	
14. MONITORING AGENCY NAME & ADDRESS (if different from Controlling Office)	13. NUMBER OF PAGES	
	45	
	15. SECURITY CLASS (of this report)	
	UNCLASSIFIED	
	15a. DECLASSIFICATION DOWNGRADING SCHEDULE	
16. DISTRIBUTION STATEMENT (of this Report)		
Approved for public release; distribution unlimited.		
17. DISTRIBUTION STATEMENT (of the abstract entered in Block 20, if different from Report)		
18. SUPPLEMENTARY NOTES		
*Present address: Science Applications, Inc., McLean, VA 22102 This research was sponsored by the Defense Nuclear Agency under Subtask S99QMXBC, work unit 00067, and work unit title "Plasma Structure Evolution."		
19. KEY WORDS (Continue on reverse side if necessary and identify by block number)		
Laser HANE simulation Collisional effects (coupling) Radiation effects (ionization)		
20. ABSTRACT (Continue on reverse side if necessary and identify by block number)		
We present predictions for the NRL laser/HANE experiment of the effects on an N ₂ background gas of (1) x-rays emitted following laser irradiation of an aluminum target, (2) debris ions moving out from the target, and (3) deposition of uv radiation resulting from interaction between the debris ions and the background gas. We calculate both primary ionization and time dependent chemistry changes. Results are based on two NRL codes, UVDEP and PRODEP, developed for HANE studies. Certain assumptions (Continues)		

DD FORM 1473

1 JAN 73

EDITION OF 1 NOV 65 IS OBSOLETE

S/N 0102-014-6601

SECURITY CLASSIFICATION OF THIS PAGE (When Data Entered)

20 ABSTRACT (Continued)

made in the codes are uncertain and/or violated to some extent within the context of the NRL experiment. Hence, the results must be considered preliminary and first order.

CONTENTS

I. Introduction.....	1
II. Prompt X-Ray Emission and Deposition.....	2
A. Discussion.....	2
B. Results.....	4
III. Ion Energy Degradation and Background Ionization...	8
A. Discussion.....	8
B. Results.....	10
IV. Uv Emission Effects.....	13
V. Concluding Remarks.....	14
Acknowledgments	31
References.....	32

PRELIMINARY REPORT ON UVDEP AND PRODEP
RESULTS FOR THE NRL LASER/HANE EXPERIMENT

I. Introduction

Recently, there has been renewed interest in the laboratory simulation of HANE phenomena (Vesecky et al., 1980; Cornwall et al., 1981). DNA is presently sponsoring a major experiment at NRL in which a laser beam is used to "explode" a target. The subsequent interaction between the target plasma and the ambient gas in the target chamber is believed to be similar to the interaction between a weapon's debris and the atmosphere in certain parameter domains (Longmire et al., 1981; Tsai et al., 1982; Smith and Huba, 1983; Sperling, 1983). Thus, an understanding of the phenomena occurring in the laser experiment may provide insight into the physical processes and consequences of HANE.

One of the purposes of the experiment is to study the collisionless coupling of the debris and air plasma via plasma turbulence (Lampe et al., 1975). This coupling mechanism relies upon the excitation of one or more plasma instabilities in the debris shell. The fluctuating electric and magnetic fields that are generated provide a means by which momentum and energy can be exchanged between the debris and air plasmas. However, in order to study this process it is important to first determine (1) the initial state of the target plasma and background gas (e.g., the state of ionization after the laser beam has been terminated) and (2) the influence of collisional processes on the interaction between the target and background species (e.g., charge exchange, ionization processes, electron stripping). The purpose of this report is to address several of these problems using existing NRL codes (i.e., UVDEP and PRODEP). Specifically, we study (1) the preionization of the background gas due to the initial radiation flash (UVDEP); (2) the energy degradation of the ions due to several collisional processes (e.g., elastic scattering, ionization, charge exchange) (PRODEP). (3) the ionization of the background gas due to the target ions (PRODEP); (4) and the ionization produced by uv from the interaction of debris ions with the background (UVDEP).

For all studies we use an aluminum target and a background N_2 gas. The laser energy is taken to be 100 joules, with 25 joules in prompt x-rays and a kinetic yield of the debris ions of 60 joules. We assume that there are 6.8×10^{10} aluminum ions released with average velocity of 6.7×10^7

Manuscript approved May 24, 1983.

cm/sec. The mass distribution of debris is assumed to obey a cosine law around the forward direction (Grun et al., 1983). All radiation is assumed to come from a point source.

The organization of the paper is as follows. In Section II we discuss the influence of prompt x-ray emission and deposition into the background nitrogen gas using the code UVDEP. In Section III we make use of the code PRODEP to study the energy degradation of the target ions due to several collisional processes, and the amount of background ionization produced by these ions. In Section IV we present a discussion of uv emission effects and in the final section offer some concluding remarks.

II. Prompt X-Ray Emission and Deposition

A. Discussion

In a HANE event x-rays are emitted during the disassembly process. The energy released from nuclear processes heats the materials of the structure to kilovolt temperatures. This results in the emission of blackbody thermal radiation from the core of the device which diffuses outward through the outer layers of the device and the surrounding rocket, reentry vehicle, etc., and radiates into the atmosphere. These prompt x-rays have long mean free paths in the upper atmosphere and deposit their energy out to distances of thousands of kilometers, or down to an altitude of ~ 70 km. They ionize the atmosphere, altering it from its ambient state. It is this altered medium through which the bomb debris, the blast wave, the uv radiation, etc. subsequently must pass.

At NRL, a code has been developed, UVDEP, (Hyman, et al., 1971; Hyman, et al., 1977) which models the deposition both of prompt x-ray emission and the later uv emission, out to large distances from the burst. It tracks the resulting atmospheric chemistry in a time dependent way to times ~ 1 sec, which in the HANE case is the time scale up to which hydrodynamic processes are not too important, the uv emission is essentially complete, and the 'fast' chemistry is completed. The chemistry includes a modeling of both molecular and atomic atoms and ions.

In the laser experiment it is necessary first to calculate the x-ray emission spectrum. The spectrum is not black body. The laser pulse causes ablation of the aluminum target forming an aluminum plasma. The pulse has a duration of several nanoseconds and the x-ray emission occurs over a time scale not much longer than this. Thus, as in the HANE case, the x-radiation is prompt compared to time scales for other phenomenology of interest. A detailed radiation-hydrodynamic model to simulate the x-ray emission induced by a laser pulse on an aluminum target has been constructed at NRL (Duston et al., 1983). Figure 1 illustrates schematically the various regions modeled in this simulation. The model determines the electron plasma temperature and the distribution of Al charge states in each of the regions as a function of time. The x-ray emission is a result of bound-bound, bound-free, and free-free electron transitions of the various aluminum charge states present in the plasma at a given time. Thus, the spectrum calculated not only is not black body, but is also time dependent.

Different segments of the x-ray energy spectrum originate from different spatial regions. For example, more than three quarters of the energy for x-ray energies above ~ 1.5 keV is due to bound-bound transitions resulting from excitation of K-shell electrons of Al XII and Al XIII. These species occur in the hot blowoff region (Figure 1) where the electron plasma temperature is ~ 1 keV. Between ~ 0.5 keV and ~ 1.5 keV the x-ray spectrum is almost totally due to bound-free transitions, since this energy range corresponds to energies too small for K-shell transitions but too large for L-shell transitions. Below ~ 0.5 keV L-shell transitions from ions less ionized than Al XII contribute substantially. These ions occur in the cooler transition region (Figure 1). In this energy region bound-free transitions represent the major contributor down to ~ 0.04 keV, with bound-bound still important down to ~ 0.1 keV. Below 40 eV free-free transitions predominate. Figure 2 shows the spectrum of the total x-ray energy emitted per square centimeter indicating separately the bound-free and free-free contributions as well as the bound-bound lines as predicted by the model. Figure 3 gives the energy spectrum of the intensity at a particular time, near the time of peak emission. The two are, not surprisingly, similar in overall shape but exhibit differences of detail. At other times, away from the time of peak emission, the differences may be

more pronounced. To approximate the x-ray spectrum for use in UVDEP we divided it into segments each of which is fit by a power law (straight line on a log-log plot). In performing this fit we were careful to maintain the model predictions of the fraction of photon energy in various photon bins (Table III, Duston et al., 1983).

We have considered the following cases: (1) N_2 density = 10^{14} cm^{-3} , scaled to a STARFISH density (400 km), (2) N_2 density = 10^{16} cm^{-3} , scaled to a standard SPARTAN density (200 km), and (3) N_2 density = 10^{17} cm^{-3} , scaled to CHECKMATE density (150 km). The scaling assumes that binary collisions in the HANE event and in the experiment play an equivalent role. However, when referring to these scaled HANE events one needs to keep in mind differences: the existence of an exponential atmosphere in the real event but not in the laser experiment; the fact that N_2 is not the only species in the real event, and not even an important one in the STARFISH case; and the fact that magnetic fields are not scaled properly in the experiment. Still, for the early time phenomenology, which is a primary goal for the experiment to simulate, these differences are either not crucial or can be accounted for, hopefully, by theory. Finally, in calculating the deposition of x-ray energy we have not accounted for the possible dependence of emission with angle in the forward direction. This is probably not a serious error, since the dependence should be weak except at very large angles.

B. Results

We first consider the case N_2 density = 10^{14} cm^{-3} , which corresponds to a scaled STARFISH altitude. Figure 4 is a plot of electron density as a function of distance from the target at three times subsequent to the passage of the x-rays. The first time, (1) $t = 0$ is the time just after the x-rays have been deposited but before any chemistry has occurred. The other two times are (2) $t = 1 \times 10^{-7} \text{ sec}$ and (3) $t = 5 \times 10^{-6} \text{ sec}$ after time $t = 0$. The upper scale gives an expanded picture of the first 10 cm and the lower shows the electron density dependence out to 70 cm.

Before continuing with a discussion of these results one important caveat needs to be stated. The following results concern only the effect of the x-rays. As the debris moves out, this is the environment it moves

into. Once the debris reaches a particular distance from the target, however, it will significantly change the electron density. Assuming the debris moves with a velocity of 6.7×10^7 cm/sec it will have reached out to 6.7 cm by 10^{-7} sec and, therefore, have altered the electron densities on this curve in Figure 4 closer in than 6.7 cm. By 5×10^{-6} sec, debris moving with 6.7×10^7 cm/sec will more than cover the entire region plotted in Figure 4. Generally speaking, where the debris has reached it will have caused much more ionization than the x-rays (see Section III). Because the debris mass tends to be peaked in the forward direction with a dependence $\sim \cos \theta$, θ the angle away from forward, off-angle its effect is likely to be less dominant over the x-ray effect than is the case in the forward direction.

More important is the question of whether the debris will continue moving out with this velocity indefinitely or will couple with the background and lose its kinetic energy. If it couples, its directed energy will likely be significantly altered once it interacts with a weapon mass of background. If the background were fully ionized, this corresponds to a weapon radius of a few centimeters for this density (see section III). However, the average ionization in this region due to x-rays is only $\sim 10\%$, so that a true weapon mass corresponds to a much larger dimension, unless there is a mechanism for coupling with the neutral atmosphere or via an anomalous ionization process. If coupling does occur the beam will be slowed or stopped and the results in Figure 4 will be valid beyond that radius. When the debris interacts with the N_2 it will generate hot electrons with a temperature and for a duration that depends on the nature of the coupling, collisional or non-collisional. The hot electrons will excite electronic levels in the debris-air mixture resulting in uv emission. The uv will be deposited mostly outside the debris-coupling region, but on the average at closer distances than the x-rays and will, in general, greatly alter the electron densities outside the coupling region. In the example being discussed here, N_2 density = 10^{14} cm $^{-3}$, we do not expect uv emission to be important, whether coupling occurs or not, just as it was not important in STARFISH. Uv effects will be described in Section IV.

With the above profiles, let us take a more careful look at the early results. After the initial ionization of N_2 by the x-rays we are left with hot electrons throughout the mesh (20-30 ev). These electrons further ionize N_2 , at first, and also begin dissociatively recombining the N_2^+ . The resulting N and N^+ can also be ionized by the still hot electrons. Thus, the initial effect of the chemistry is to increase the electron density. Because of the high N_2 density, the electrons cool predominantly by ionizing N_2 , so that the electron temperature at a given time is nearly independent of distance from the target, except very near the target where N_2 has been depleted. Figure 5 shows the time dependence of the electron density and temperature at three distances from the target: (1) 0.5 cm, (2) 5.0 cm, and (3) 50. cm. The temperature curves are nearly identical at 0.5 cm and 50. cm. At 5.0 cm, where the N_2 has been depleted, the temperature is essentially constant by 2×10^{-6} sec. The electron density here has already begun to drop by a few times 10^{-7} sec because of the depletion of neutrals even though the electron temperature is still high. At greater distances, where depletion of neutrals has not occurred and when the electron temperature has cooled to ~ 2 ev, ionization is no longer important and the electron density begins to decrease. Figure 6 shows the densities of N_2 , N_2^+ , N^+ , N , and $N(^2D)$ and the electron temperature (T_e) as a function of distance from the target at 10^{-7} sec. The near constancy of electron temperature with distance from the target, discussed above, can be seen here. We see that N_2^+ is everywhere the major ion constituent. As electron temperatures drop or neutral species are depleted, electron densities stop increasing. But the time scales to deplete electrons are longer than the time scales exhibited here. N_2^+ dissociatively recombines with a rate coefficient between 10^{-7} cm³/sec - 10^{-8} cm³/sec at these temperatures, which gives a time scale for depletion of electrons, even where $N_2^+ \sim 10^{13}$ cm⁻³, of 10^{-7} - 10^{-5} sec. This is also, of course, the time scale for the buildup of N and $N(^2D)$. N^+ recombines radiatively on a much slower time scale. Thus, except for the electron temperature, which drops fairly rapidly (Figure 5), the profiles shown in Figure 6 will not change in time significantly until (and unless) the debris or uv alters the state of affairs.

We next consider the case N_2 density = 10^{16} cm^{-3} which scales to a "standard altitude" SPARTAN. Here uv emission is likely to be important, but we will postpone the analysis of uv effects to Section IV and consider only the effects of x-rays. For the laser experiment at this density, if the background is totally ionized, a weapon radius is $\leq 1 \text{ cm}$. Figure 7 shows electron densities as a function of distance from the target, due to x-ray deposition, for several times after deposition. These curves suggest that the debris probably does intercept a weapon mass within a few centimeters of the target. The times plotted are (1) $t = 0.0$, (2) 1×10^{-8} , (3) 1×10^{-7} , and (4) $5 \times 10^{-7} \text{ sec}$ after deposition. If coupling does not occur, only the nearest 0.67 cm would be altered for the $t = 10^{-8} \text{ sec}$ curve. At 10^{-7} sec , 6.7 cm would be changed by the debris, and at $5 \times 10^{-7} \text{ sec}$ the entire plotted curve would be altered. If coupling does occur, the beam would probably be stopped in the first few centimeters, but uv emission and deposition would then alter the x-ray results. Neglecting these effects, for the moment, we now consider the x-ray only results in more detail.

In contrast to the N_2 density = 10^{14} cm^{-3} case, processes with the N_2 density = 10^{16} cm^{-3} occur much faster. At 1.0 cm the electron density appears in Figure 7 to drop monotonically from the time zero value to its value at $t = 5 \times 10^{-7} \text{ sec}$. What, in fact, has happened is the electron density has peaked by $t \sim 3 \times 10^{-9} \text{ sec}$. The major ion at this time is N_2^+ , which from then on decreases at a faster rate than new ions are produced, since the electron temperature is dropping very rapidly. By $t = 1 \times 10^{-7} \text{ sec}$, at 1.0 cm, the N_2^+ has been substantially depleted (Figure 8), N^+ is the major ion and the major neutral constituents are N and $N(^2D)$. At later times the N_2^+ continues to deplete, building up N and $N(^2D)$ somewhat more, but N^+ remains virtually unchanged because of the long time constant for radiative recombination of N^+ and the low electron temperature, which excludes substantial ionization.

At larger distances, the time scales are, of course, somewhat slower. At 10 cm, at time $t = 10^{-7} \text{ sec}$, N_2^+ is still the major constituent at $\sim 2.5 \times 10^{13} \text{ cm}^{-3}$. The temperature is very low, cutting off ionization. The N_2^+ will continue to drop until by several times 10^{-6} sec it will be

below the N^+ value. From then on the electron density will remain essentially constant at a value $n_e \sim 1.5 \times 10^{12} \text{ cm}^{-3}$ for a long time.

Finally, we plot the N_2 density = 10^{17} cm^{-3} case, scaled to a CHECKMATE altitude. A weapon mass of ionized background N_2 will be intercepted within about 0.5 cm of the target. Assuming coupling occurs, uv emission and deposition will be very important in altering the electron densities derived from x-ray deposition. Figure 9 is a plot of the x-ray induced electron densities at times (1) $t = 0.0$, (2) 5×10^{-9} , (3) 1×10^{-8} , and (4) 2×10^{-7} sec. The general characteristics are similar to the N_2 density = 10^{16} cm^{-3} case. Very close in (less than 0.4 cm) the temperature is high enough, and the N_2^+ has been recombined, so that electron densities are increasing. Slightly further out, (say, 0.4-0.7 cm) the temperature is too low for ionization to increase the electron density, but the N_2^+ density is small compared to N^+ so that the electron density is not changing, and the different curves in Figure 9 are merged. Beyond this region, N_2^+ is important, and its recombination governs the decrease in electron density and increase in N and $N(^2D)$. Ionization is not important because of the low electron temperature. Figure 10 shows the individual species and the electron temperature at $t = 1 \times 10^{-8}$ sec.

III. Ion Energy Degradation and Background Ionization

A. Discussion

We study the energy degradation of the ion beam due to several collisional processes, and the amount of background ionization produced by the beam using the code PRODEP. PRODEP is a code which was developed at NRL to study proton deposition in the atmosphere (Rogerson and Davis, 1974; Rogerson and Davis, 1975). The code is one-dimensional and is based upon the continuous slowing down approximation (CSDA). The collisional effects included in PRODEP are collisional ionization, electron stripping, charge exchange, and elastic collisions. PRODEP does not account for any interactions between the debris and background ions. We have modified PRODEP to study the case of a beam of aluminum ions (Al^+) propagating through a nitrogen gas (N_2). We consider a set of parameters relevant to

the NRL laser experiment and present results pertaining to (1) the energy degradation of the aluminum ion beam due to collisional effects, and (2) the ionization of the nitrogen gas due to the ion beam.

The fundamental equation used in the CSDA is

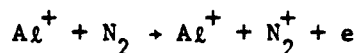
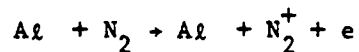
$$dE = - F(x) L(E) dx \quad (1)$$

where dE is the incremental energy change in the ion beam in kev as it traverses a distance dx through a background gas of $F(x)$ atoms per cm^2 . In Eq. (1), $L(E)$ is the ion energy loss function in $kev\ cm^2/atom$ and is comprised of four parts in our model. Specifically,

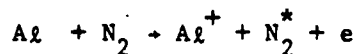
$$L(E) = \text{ionization} + \text{electron stripping} + \text{charge exchange} \quad (2) \\ + \text{elastic collisions}$$

The reactions considered are

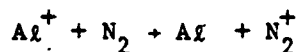
1. Ionization



2. Electron stripping



3. Charge exchange



The cross sections for these reactions were provided by Rogerson (private communication). Further details of the code can be found in Rogerson and Davis (1974) and Rogerson and Davis (1975).

Prior to discussing the results from PRODEP for the NRL laser experiment it is important to note the assumptions used in the code. First, it is assumed that the fractional energy loss per process is small. Second, the code is one-dimensional so that the scattering process is assumed to be symmetric. Third, only singly ionized states are considered. And fourth, it is assumed that the ions interact only with a neutral background gas. We point out that not all of these assumptions are well-justified in the NRL experiment. In particular, (1) the debris ions do not come off the target in a spherically symmetric manner; (2) there are indications that the debris ions are in multiple charge states that vary in time (J. Grun, private communication); and (3) close to the target the assumption of a predominately neutral gas clearly breaks down. Thus, the results from PRODEP must be interpreted with care in attempting to relate them to the NRL experiment. Nonetheless, several of the results are pertinent to the experiment and provide a good, first-order understanding of some of the collisional processes occurring in the experiment.

B. Results

We now present PRODEP results for conditions relevant to the NRL experiment. It is implicitly assumed that coupling has not occurred. An important quantity used in the analysis is F which is the number of molecules encountered per cm^2 . In order to make contact with experimental results, the following relationship is used

$$F = n\ell \quad (2)$$

where n is the density of the background gas (cm^{-3}) and ℓ is the distance the ions have travelled in the background gas (cm). Thus, for a given F used in the code, different values of n and ℓ can be applied to the experiment through Eq. (2).

The initial energy distribution for the ion beam (Al^+) is given by

$$\Gamma(E) = \frac{\Delta E^2}{(E-E_0)^2 + \Delta E^2} \quad (3)$$

where $E_0 = 60 \text{ keV}$, $\Delta E = 0.23E_0$. The total energy in the ion beam is 60 joules. The average initial ion velocity of the beam is $v_0 = 6.7 \times 10^7 \text{ cm/sec}$ with an energy flux of $4.8 \times 10^{15} \text{ keV/cm}^2$. This value of the flux

corresponds to an average flux at 3.5 cm from the target, or to the flux at 4.2 cm in the forward direction in the laser experiment.

We first present "time of flight" curves (Figure 11) and the energy distribution (Figure 12) corresponding to each curve. The "time of flight" curves are shown since they correspond to the type of measurements made in the NRL experiment (J. Grun, private communication). To facilitate comparison with the experiment, and to make the results depend only on F , the time is normalized so that an ion of average energy E_0 in vacuum will impact the detector at $t_{\text{norm}} = 70$ on a scale 0 to 256 (i.e., $t_{\text{norm}} = 70 V_0 t_{\text{real}}/l$). In Figure 11 we show "time of flight" curves for the initial conditions described above and taking $F = 10^{15}, 10^{16}, 10^{17}, 5 \times 10^{17}$ and 10^{18} cm^{-2} . The plot is number of particles on an arbitrary scale versus normalized time. The curves for $F = 10^{15}$ and 10^{16} cm^{-2} are indistinguishable and are effectively the same as would arise if $F = 0$ (i.e., an ion beam propagating through a vacuum). The ions to the left of the peak (at $t \sim 70$) are the "fast" particles ($E > 60 \text{ kev}$) while those to the right of the peak are the "slow" particles ($E < 60 \text{ kev}$). Note that the "time of flight" curves are not symmetrical about the peak, while the energy distributions (Figure 12) are symmetrical. Thus, for $F < 10^{16} \text{ cm}^{-2}$ we see that there is no energy degradation of the ion beam because of collisional interactions with the background gas. For $F = 10^{17} \text{ cm}^{-2}$ (or $n = 10^{16} \text{ cm}^{-3}$ for $l = 10 \text{ cm}$) the "time of flight" curve is slightly displaced from the $F = 10^{16} \text{ cm}^{-2}$ curve (Figure 11), while there is a more noticeable change in the energy distribution (Figure 12). As F increases further, $F = 5 \times 10^{17}$ and 10^{18} cm^{-2} (or $n = 5 \times 10^{16}$ or 10^{17} cm^{-3} for $l = 10 \text{ cm}$), a significant change in the "time of flight" curves (Figure 11) occurs, along with a marked change in the energy distribution. The peak of the "time of flight" curves shift to the right, indicating a slowing down of the "average" velocity of the beam, and the curves become broader. However, the broadening of the "time of flight" curves does not correspond to a broadening of the energy distribution. Note that the energy distributions for $F = 5 \times 10^{17}$ and 10^{18} cm^{-2} (Figure 12) maintain approximately the same width ΔE but the peak energy E_0 decreases significantly. We expect that in the experiment the ion beam (i.e., debris ions) will broaden its energy distribution if energy degradation occurs.

PRODEP does not entirely account for this effect because in each energy channel all ions are slowed by the same amount, with no allowance for statistical variations.

The results shown in Figs. 11 and 12 are consistent with measurements made to date in the NRL laser experiment, although a detailed comparison cannot be made at this time. The reason for this is that the existing PRODEP code can only treat an aluminum target and nitrogen background, while the relevant existing data from the experiment is for a carbon target with nitrogen and hydrogen backgrounds. Nonetheless the experimental results presented by J. Grun at the DNA NRL meeting in January, 1983 indicated that for $F < 4 \times 10^{16} \text{ cm}^{-2}$ the debris "time of flight" curves were essentially unchanged from the vacuum case. This agrees with our results shown in Fig. 11 which indicate that for $F < 10^{17} \text{ cm}^{-2}$ the "time of flight" curves are virtually the same. Clearly, a more detailed comparison is needed to assess the predictions made by PRODEP in regard to the NRL laser experiment.

In Figure 13 we show a plot of percent of background primary ionized gas (N_2^+/N_2) as a function of distance for the average flux. Three curves are shown, $n = 10^{14}$, 10^{16} and 10^{17} cm^{-3} . For the most part $N_2^+/N_2 \propto 1/r^2$ in each case but, as expected, there is more absorption of the beam at the higher n values. These curves are only correct for $x \geq 3.5 \text{ cm}$ at which $N_2^+/N_2 \approx 9\%$. If we extrapolate these curves to the regime $x \leq 3.5 \text{ cm}$ as denoted by the dotted line, they will intersect 100% ionization near 1. cm. The dashed curves show the percent of primary ionization produced by x-rays for these same densities. For both the x-rays and the beam the $F = 10^{14}$ curves fall off as $1/r^2$ but at the larger densities absorption causes the curves to fall off faster. For all densities the ionization produced by the ions is about an order of magnitude greater than that produced by the x-rays. Directly in front of the target the 9% ionization distance occurs at 4.2 cm so the difference is even greater. The results presented here are primary ionization with no effects of chemistry. The electron density and ion composition will change in time due to chemistry effects in a manner similar to that described in Section II.

IV. Uv Emission Effects

Until we have completed development of our early time codes which specify when coupling occurs, the nature of the coupling, and the resulting uv emission, we cannot predict with certainty whether the debris will be slowed, and if so, how far from the target, and what portion of the beam kinetic yield will be converted to uv. Consider, first, the N_2 density = 10^{16} cm^{-3} case. In the laser experiment approximately 60% of the yield is kinetic so that uv effects are potentially more important than would be the case in a typical HANE event. To bracket the likely effects of uv we have considered two possible cases: (1) uv yield 30% of kinetic and (2) uv yield 60% of kinetic. In discussing these results one must understand that they are based upon debris-background coupling. The debris loses its energy so that it does not continue moving out from the target much past a few cm, and has a substantial portion of its directed energy converted to uv radiation. The code UVDEP assumes the uv originates from a point source at the target, an assumption that is not terribly good near the target. We have used a uv spectrum obtained from CHECKMATE calculations, which is a relatively low energy uv spectrum. The hardness of the spectrum, which can only be determined from full early time calculations may also affect the results given here.

Figure 14 shows the electron density as a function of distance from the target at $t = 5 \times 10^{-7}$ sec with no uv and at $t = 5.5 \times 10^{-7}$ sec for the two cases, 30% and 60% of the kinetic yield in uv. Clearly, the uv very significantly alters the ionization. The time dependence of the electron density for two points distant 2 cm and 10 cm, respectively, from the target is exhibited in Figure 15. The uv is emitted in time with 57% emitted by $t = 2 \times 10^{-7}$ sec and 98% by $t = 5.5 \times 10^{-7}$ sec. Consequently, at each point the electron density for the different cases initially begins falling in the same way. As the uv deposition builds up, the curves diverge with the electron density increasing. Only after the bulk of the uv has been emitted does the electron density begin to fall again. The effect of uv is clearly significant under the assumptions we have made.

Consider, now the N_2 density = 10^{17} cm^{-3} case. At this higher density we expect a higher uv yield than in the previous example. We consider two cases here: (1) 62% of the kinetic yield is converted to uv radiation and

(2) 90% of the kinetic yield is converted to uv radiation. If coupling occurs the debris should be stopped within ~ 1 cm. Figure 16 shows the electron density profile for no uv at $t = 1 \times 10^{-7}$ sec and for 62% and 90% of the kinetic yield converted to uv at $t = 1.1 \times 10^{-7}$ sec. The interesting point here is that at a density of 10^{17} cm^{-3} the uv is essentially totally absorbed within a distance of ~ 5 cm. from the target. At closer in distances the uv is clearly important. At 2 cm from the target the uv has increased the electron density by more than an order of magnitude at 10^{-7} sec.

V. Concluding Remarks

We have made a preliminary investigation of the role of radiation and collisional effects in the NRL laser/HANE experiment. The issues we have addressed are (1) the preionization of the background gas due to the initial radiation flash; (2) the energy degradation of the ions due to the several collisional processes (see Eq. (2)); (3) the ionization of the background gas due to the target ions; and (4) the ionization produced by uv radiation from the interaction of debris ions with the background gas. Our study has been based upon existing NRL codes (UVDEP and PRODEP) and considers an aluminum target and a background nitrogen gas. We have also considered parameter regimes accessible to the NRL experiment which scale (via binary collisions) to STARFISH, SPARTAN and CHECKMATE events. We emphasize that certain assumptions made in the codes are uncertain and/or violated to some extent within the context of the experiment since they were developed for actual HANE phenomena. Hence, the results must be considered preliminary and first order. More viable results depend upon further developments in early-time modeling currently underway at NRL.

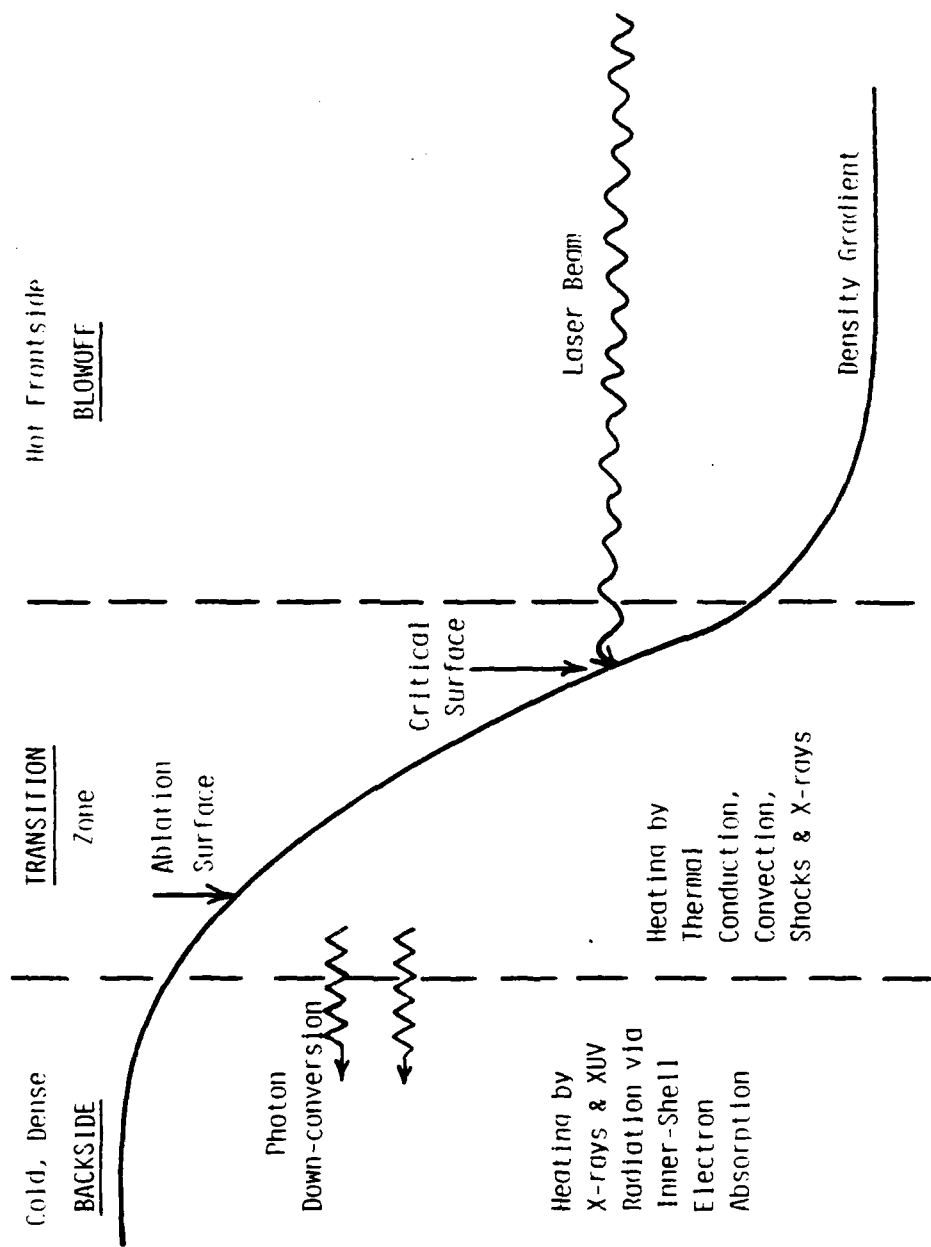


Figure 1 Laser-target simulation regions.

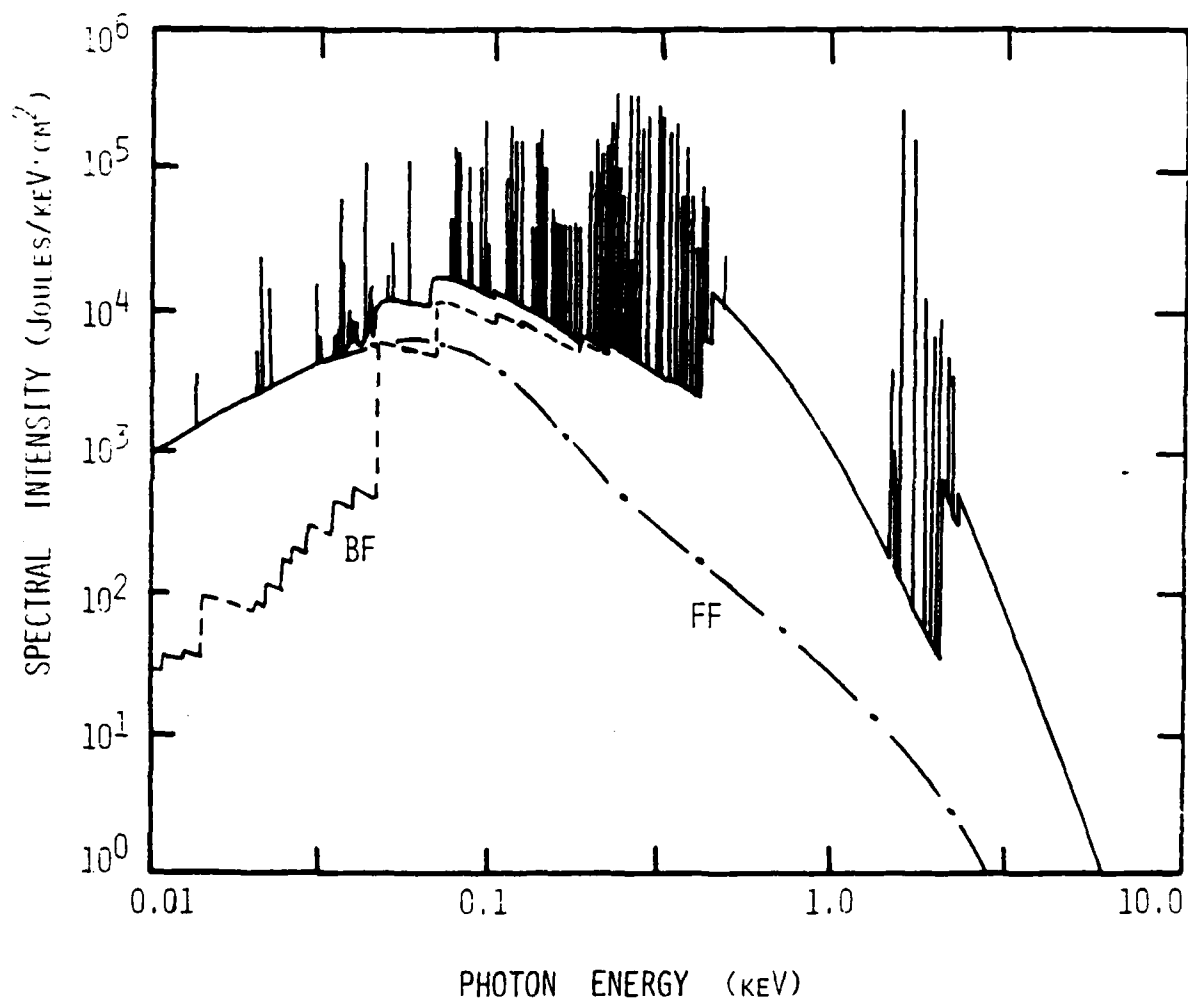


Figure 2 X-ray spectrum of total energy emitted by laser irradiated aluminum target per square centimeter of target.

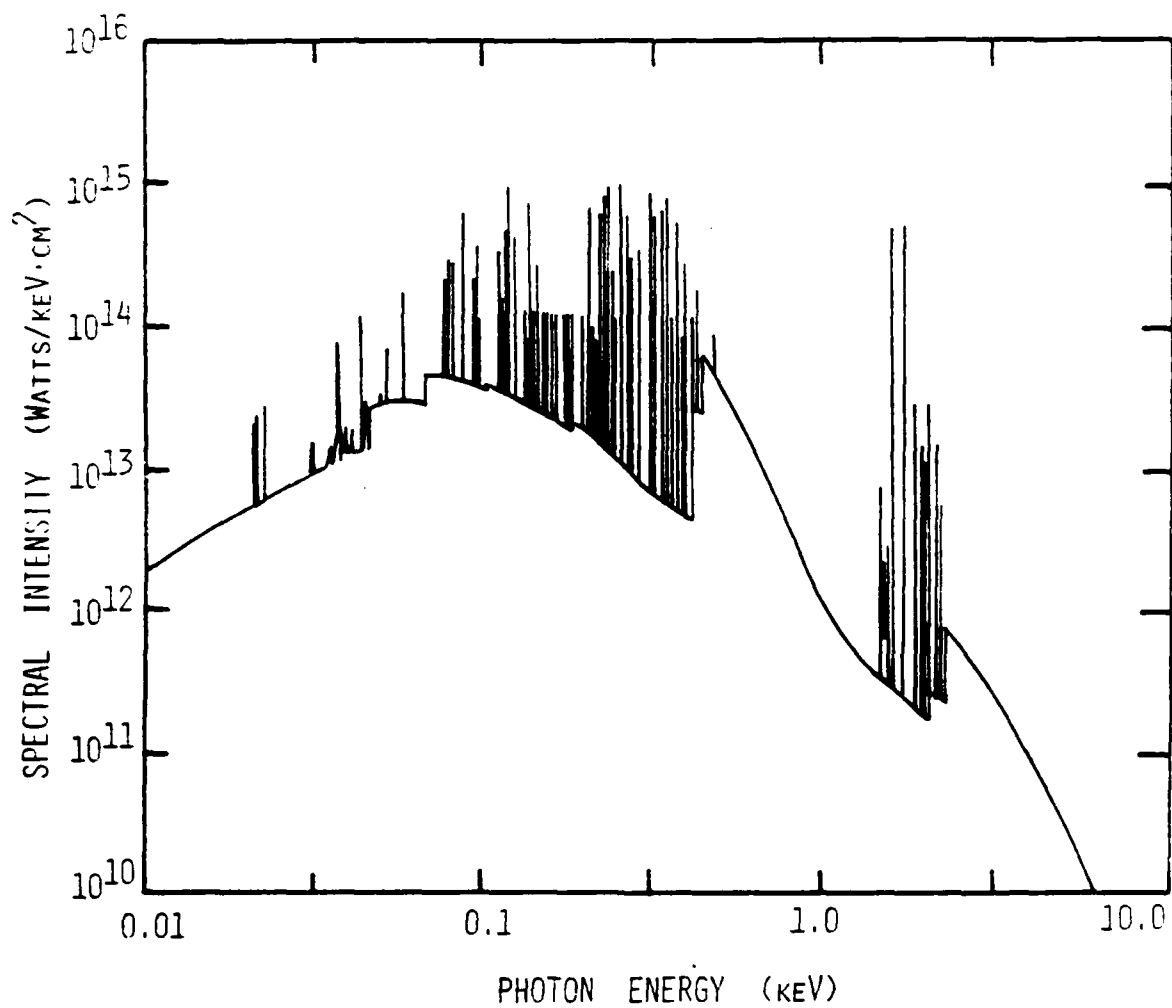


Figure 3 X-ray spectral intensity near time of peak emission of laser irradiated aluminum target.

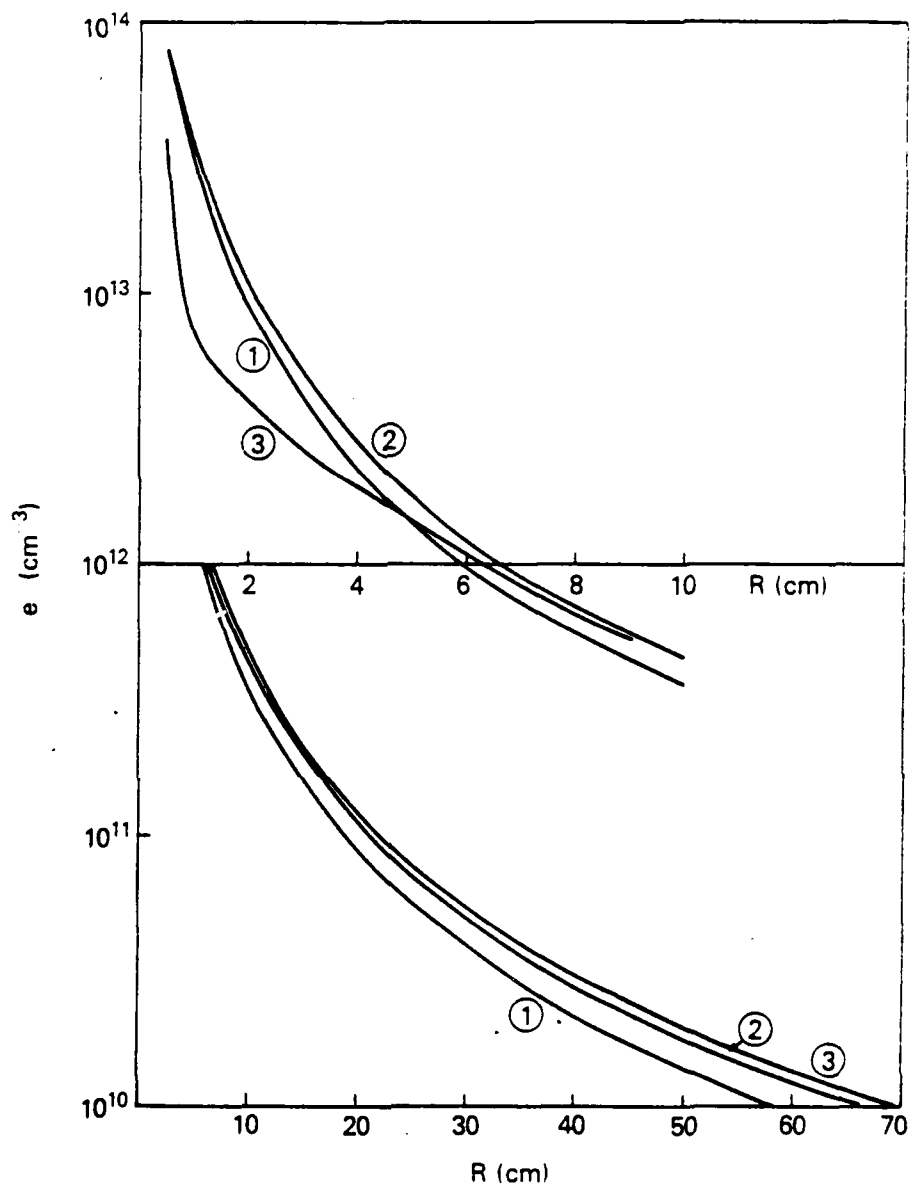


Figure 4 Electron density as a function of distance from target: (a) Upper scale = first 10 cm, (b) Lower scale = to 70 cm. Ambient $N_2 = 10^{14} \text{ cm}^{-3}$. Curve labels give time after x-ray deposition: (1) = 0.0 sec, (2) = 1×10^{-7} sec, (3) = 5×10^{-6} sec.

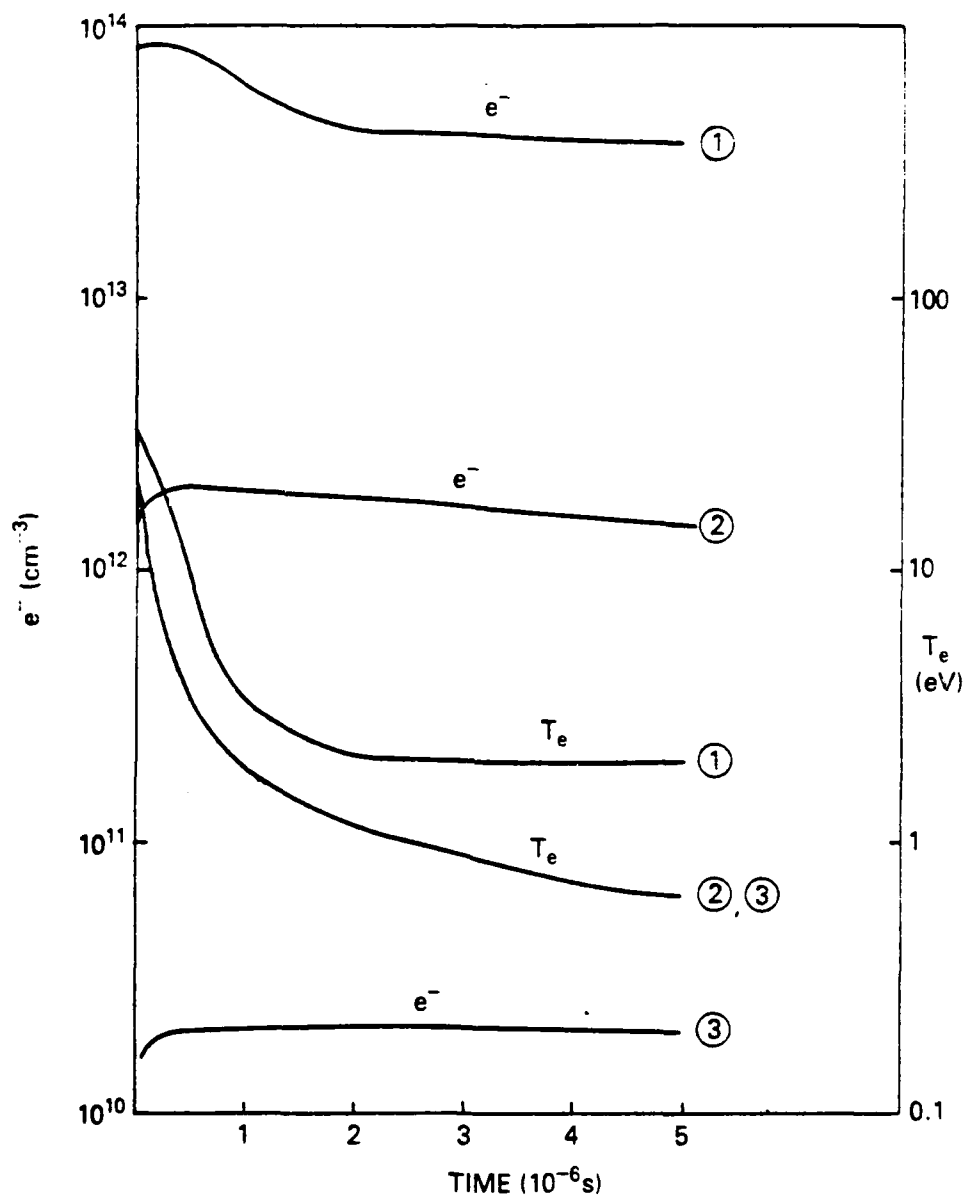


Figure 5 Electron density and temperature as a function of time after x-ray deposition at three distances from target: (1) 0.5 cm, (2) 5.0 cm, and (3) 50. cm. Ambient $N_2 = 10^{14} \text{ cm}^{-3}$.

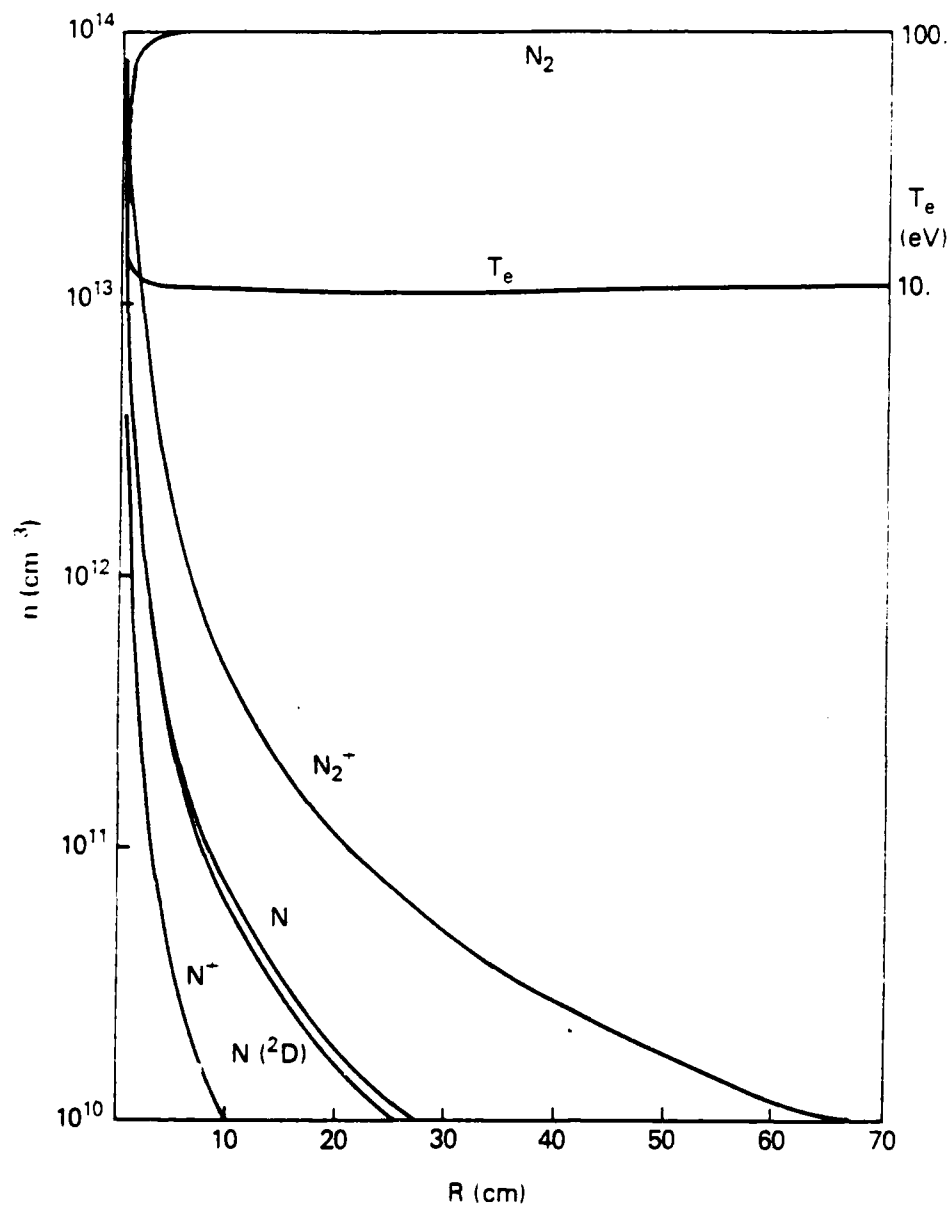


Figure 6 Specie densities and electron temperature at 1×10^{-7} sec after x-ray deposition as a function of distance from the target. Ambient $N_2 = 10^{14} \text{ cm}^{-3}$.

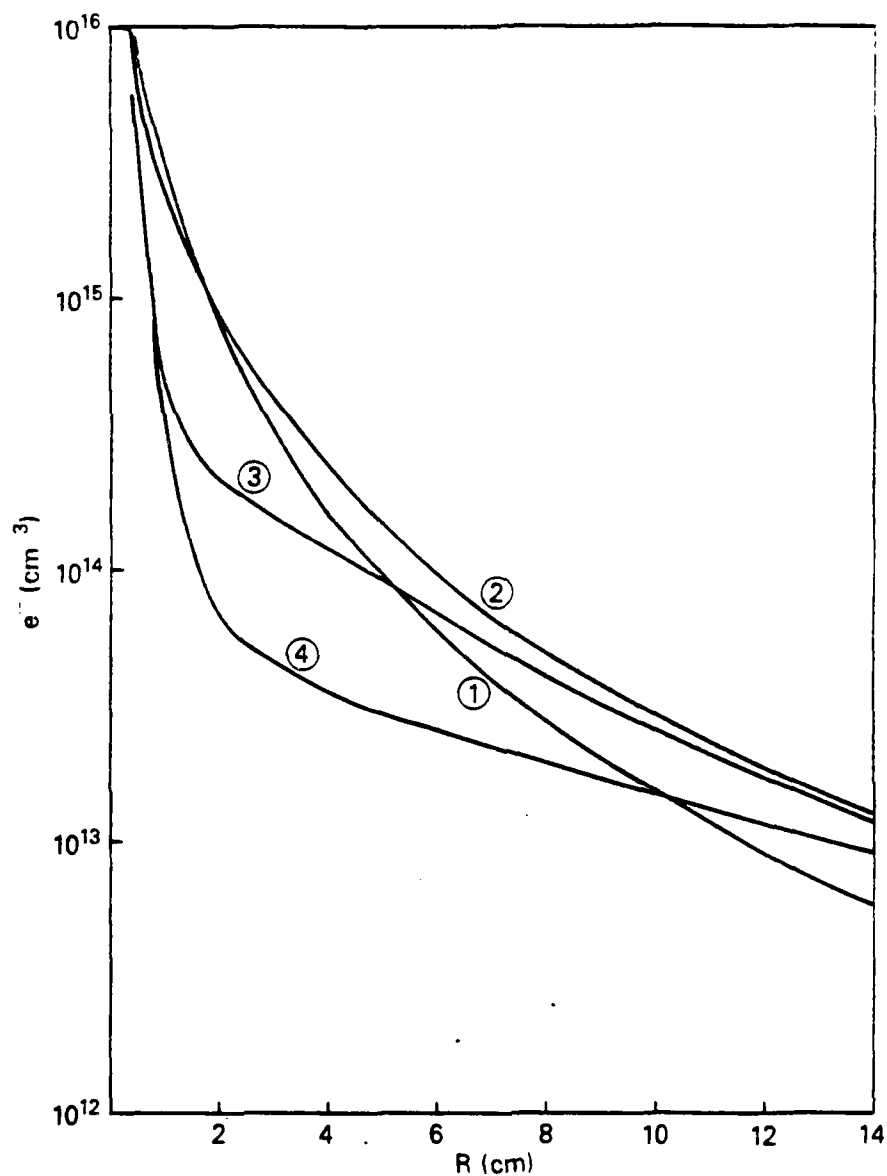


Figure 7 Electron density as a function of distance from target. Ambient $N_2 = 10^{16} \text{ cm}^{-3}$. Curve labels give time after x-ray deposition: (1) = 0.0 sec, (2) 1×10^{-8} sec, (3) = 1×10^{-7} sec, (4) = 5×10^{-7} sec.

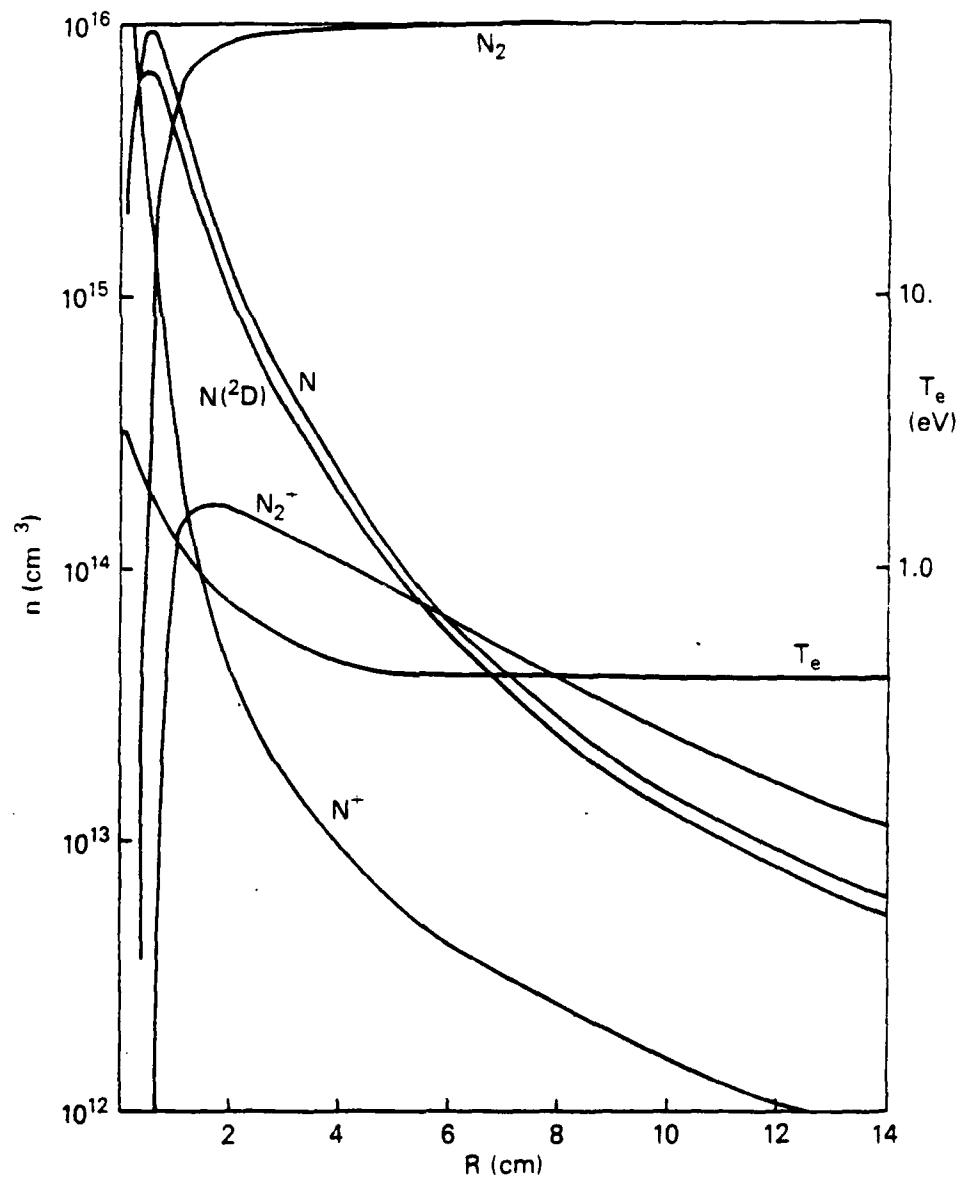


Figure 8 Specie densities and electron temperature at 1×10^{-7} sec after x-ray deposition as a function of distance from the target. Ambient $N_2 = 10^{16} \text{ cm}^{-3}$.

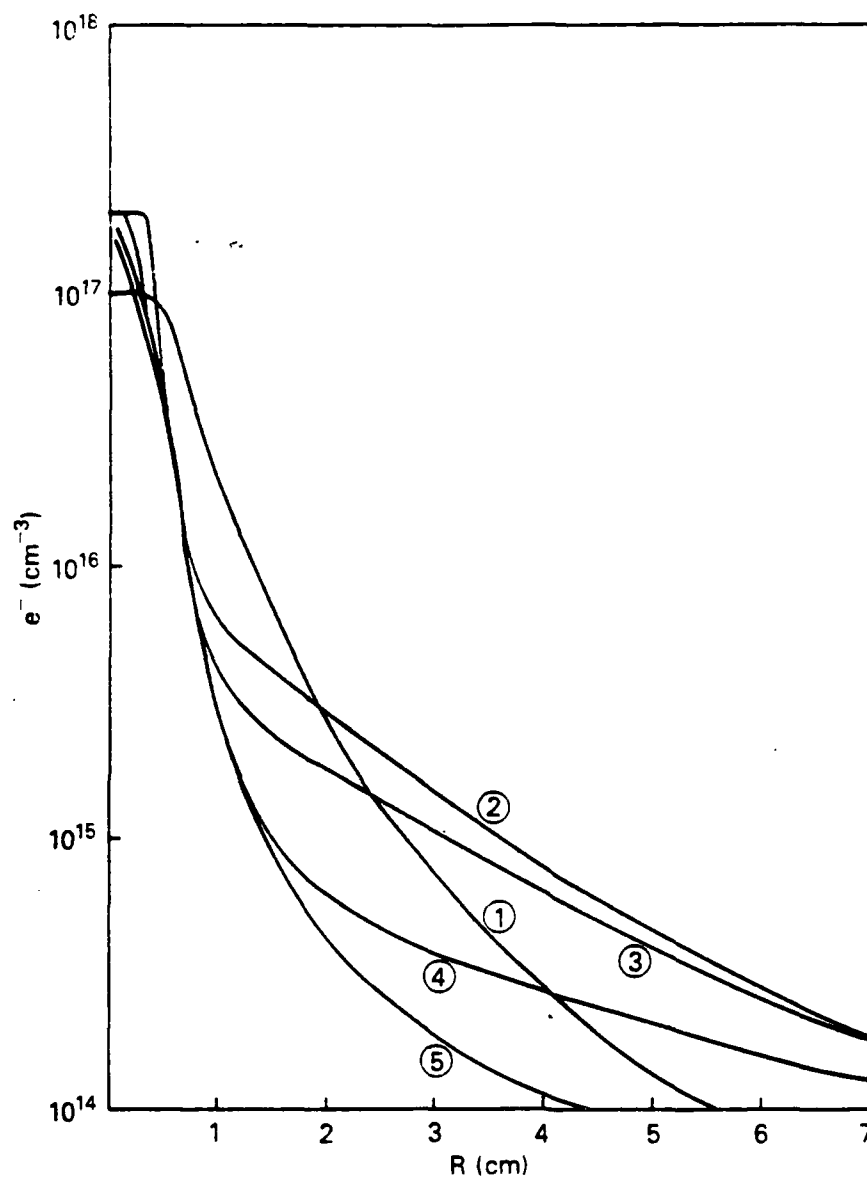


Figure 9 Electron density as a function of distance from target. Ambient $N_2 = 10^{17} \text{ cm}^{-3}$. Curve labels give time after x-ray deposition: (1) = 0.0 sec, (2) = 5×10^{-9} sec, (3) 1×10^{-8} sec, (4) 5×10^{-8} sec, (5) = 2×10^{-7} sec.

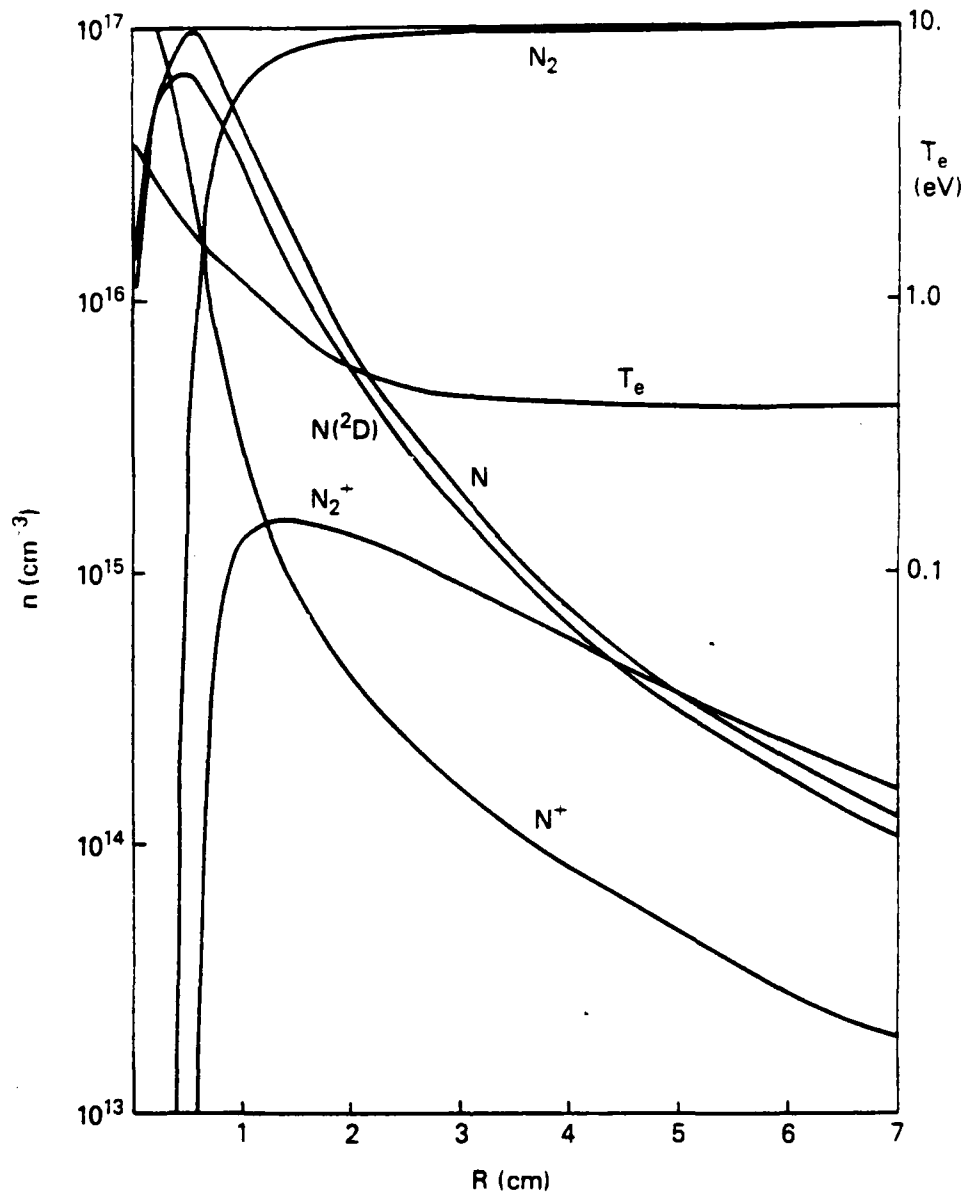


Figure 10 Species densities and electron temperature at 1×10^{-8} sec after x-ray deposition as a function of distance from the target. Ambient $N_2 = 10^{17} \text{ cm}^{-3}$.

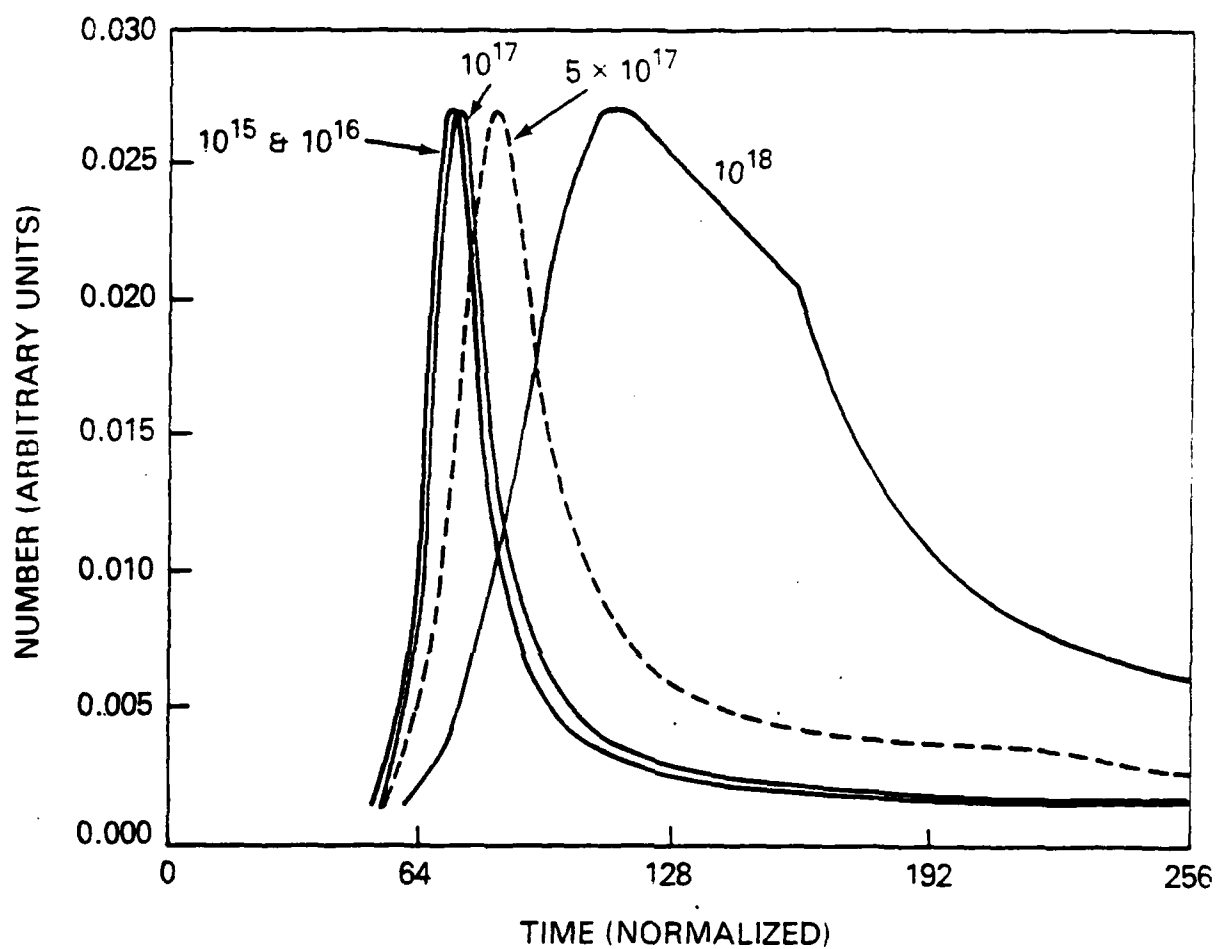


Figure 11 Distribution function of debris ions as a function of normalized time of flight (see text) for different values of F = number of molecules/cm² encountered by beam.

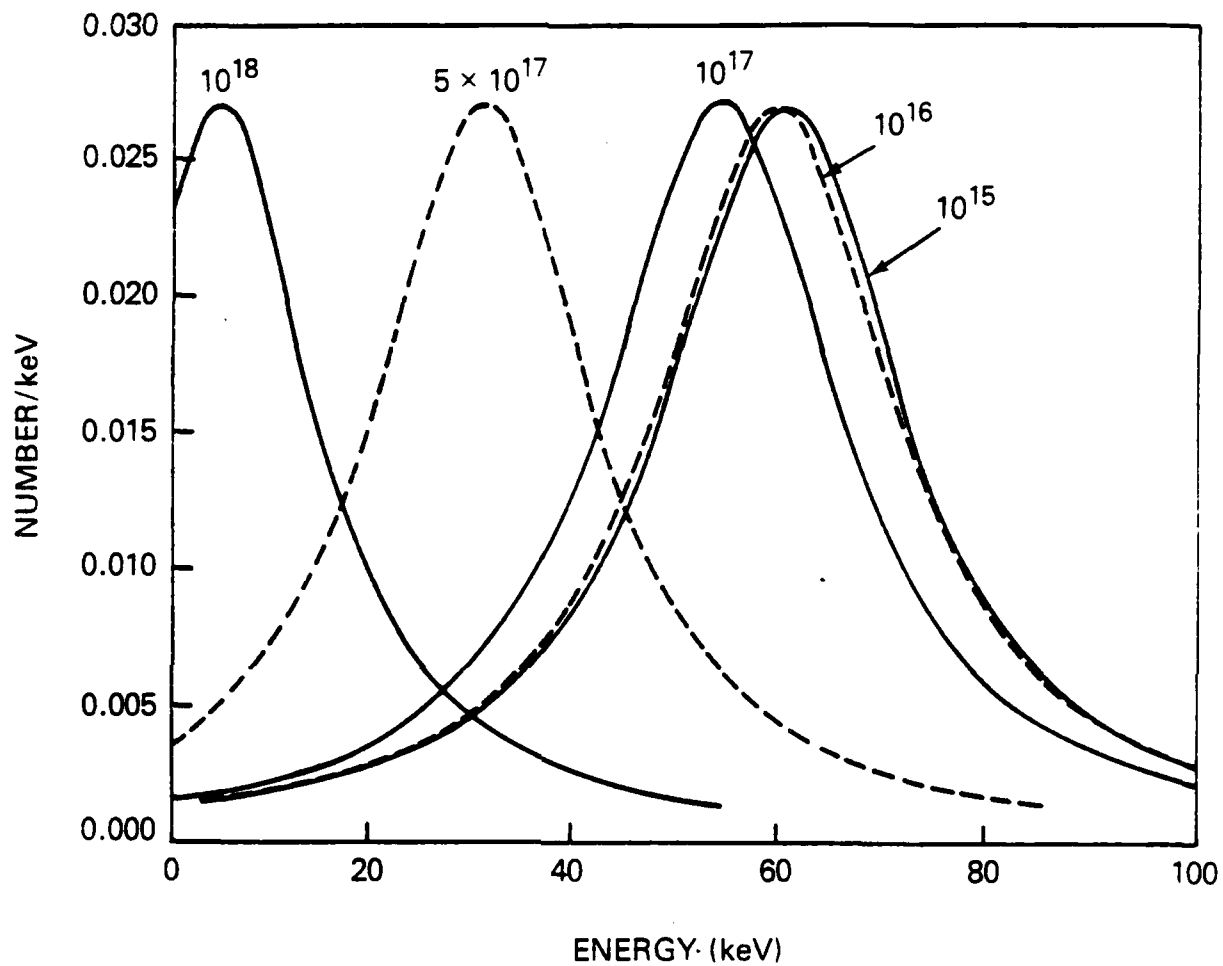


Figure 12 Energy distribution function (number/kev) of debris ions for different values of F = number of molecules/cm² encountered by beam.

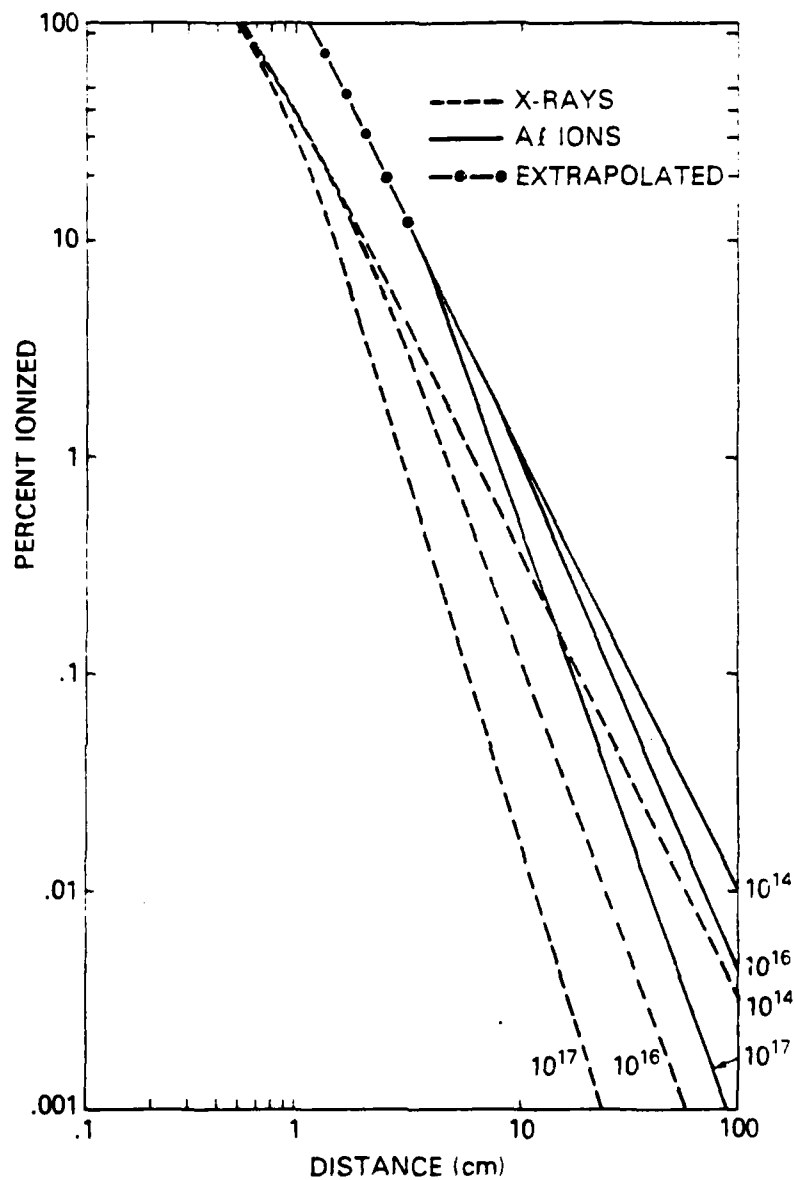


Figure 13 Percent primary ionization due to debris ions (solid curves) and x-rays (dashed curves) as a function of distance from target for various ambient N_2 densities.

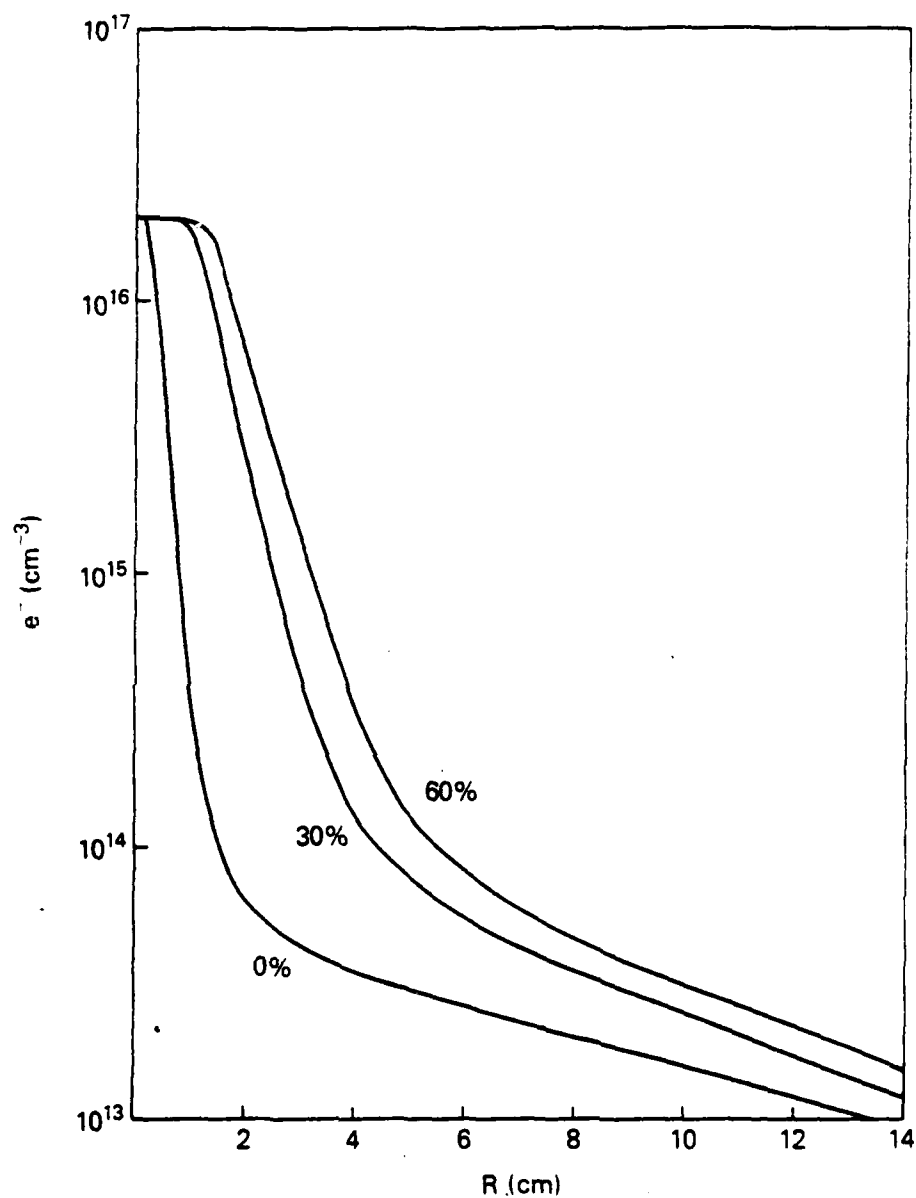


Figure 14 Electron density as a function of distance from target at approximately 5×10^{-7} sec after x-ray deposition. Ambient $N_2 = 10^{16} \text{ cm}^{-3}$. Curve labels give percent of kinetic yield of debris ions converted to uv.

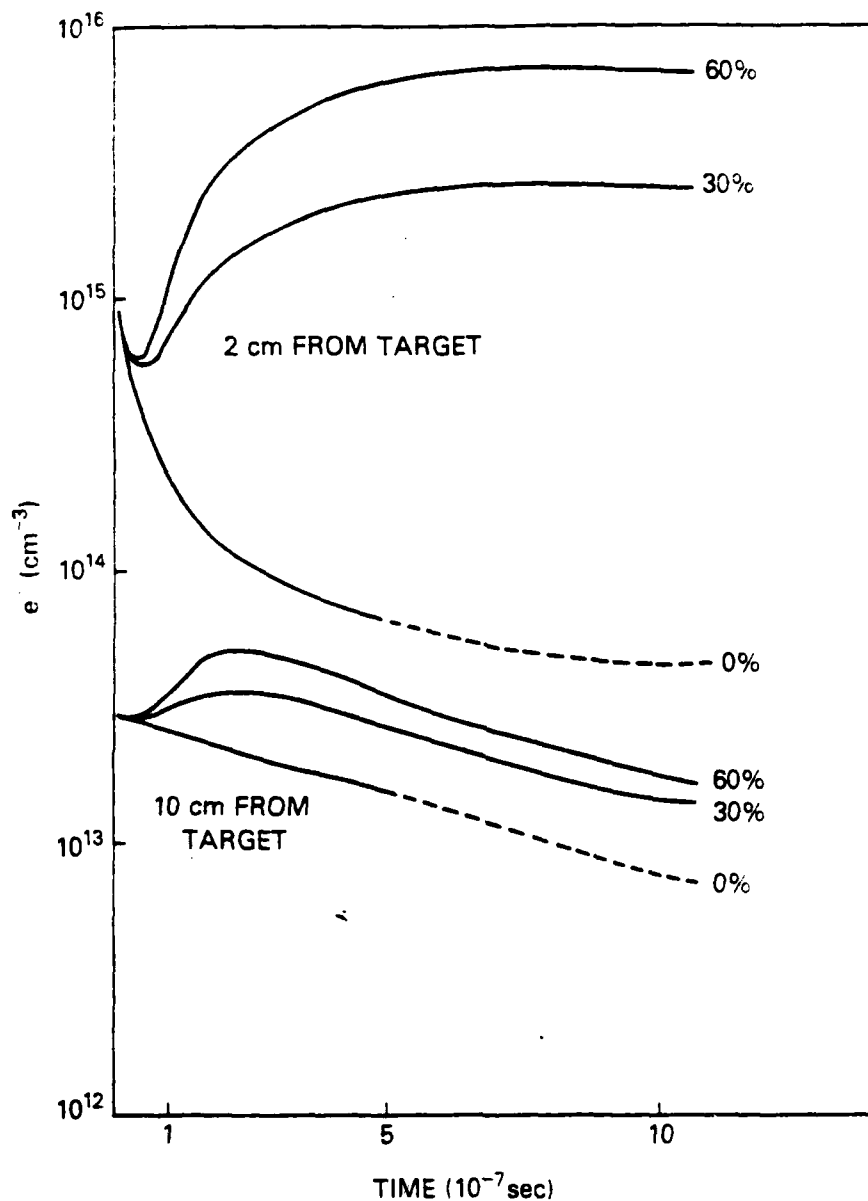


Figure 15 Electron density as a function of time after x-ray deposition at distances of 2.0 cm and 10.0 cm from target. Ambient $N_2 = 10^{16} \text{ cm}^{-3}$. Curve labels give percent of kinetic yield of debris ions converted to uv. Dashed lines are extrapolations beyond calculation.

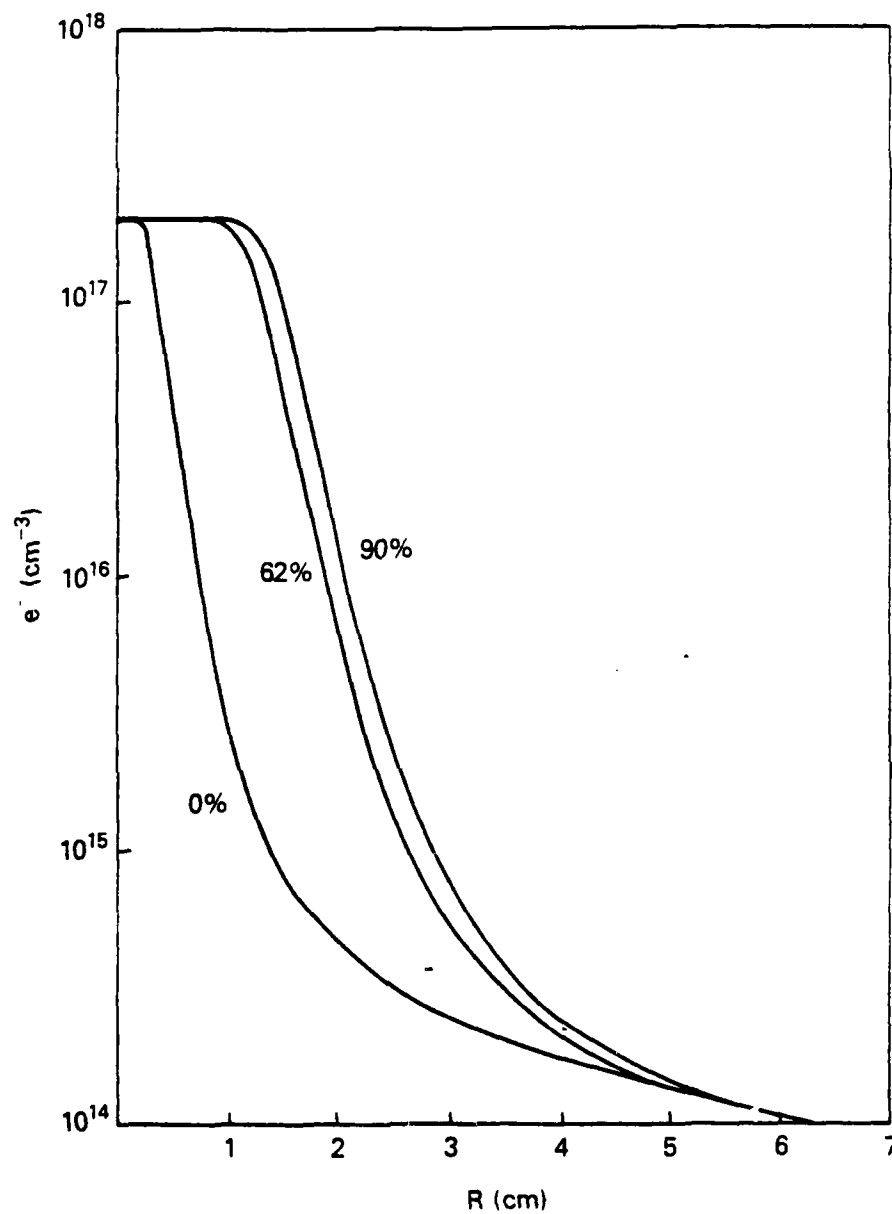


Figure 16 Electron density as a function of distance from target at approximately 1×10^{-7} sec after x-ray deposition. Ambient $\text{N}_2 = 10^{17} \text{ cm}^{-3}$. Curve labels give percent of kinetic yield of debris ions converted to uv.

Acknowledgments

The authors would like to thank J. Davis, R. Clark, D. Duston, and J. Rogerson of NRL's Plasma Radiation Branch for many fruitful discussions concerning the appropriate x-ray spectrum for this experiment and aid in establishing reasonable ion-neutral cross sections. We also wish to thank B. Ripin of NRL's Laser Plasma Branch and J. Grun of Mission Research Corporation for many helpful discussions concerning the laser experiment. This work was funded by the Defense Nuclear Agency.

References

- Cornwall, J.M., S. Flatté, D. Hammer, and J. Vesecky, "Studies of the effect of striations on radio communications," JASON Report JSR-81-31, 1981.
- Duston, D., R.W. Clark, J. Davis, and J.P. Apruzese, "Radiation energetics of a laser-produced plasma," Phys. Rev. A, 27, 1441, 1983.
- Grun, J., S.P. Obenschain, B.H. Ripin, R.R. Whitlock, E.A. McLean, J. Gardner, M.J. Herbst, and J.A. Stamper, "Ablative acceleration of planar targets to high velocities," Phys. Fluids, 26, 588, 1983.
- Hyman, E., T. Young, and T. Coffey (see authors for reference), 1971.
- Hyman, E., M. Mulbrandon, S.L. Ossakow, and J. Pierre, (see authors for reference), 1977.
- Lampe, M., W.L. Manheimer, and K. Papadopoulos, "Anomalous transport coefficients for HANE applications due to plasma microinstabilities," NRL Memo Rept. 3076, 1975.
- Longmire, C., M. Alme, R. Kilb, and L. Wright, "Scaling of debris-air coupling," MRC Report AMRC-R-338, 1981.
- Rogerson, J.E. and J. Davis, "Preliminary report on a program to study proton deposition in the atmosphere," NRL Memo Rept. 2967, 1974.
- Rogerson, J.E. and J. Davis, "Improved model to study proton deposition in the atmosphere," NRL Memo Report 3042, 1975.
- Smith, R.A. and J.D. Huba, "Parameter survey for collisionless coupling in a laser simulation of HANE," NRL Memo Report 5092, 1983.
- Sperling, J.L., "The scaling of some processes affecting structure in the high-altitude nuclear environment," JAYCOR Report J530-83-102, 1983.
- Tsai, W., L.L. DeRood, Jr., and R. LeLevier, "Scaling laws for simulating early-time high-altitude nuclear explosion phenomena," R & D Associates Report RDA-TR-125003-001, 1982.
- Vesecky, J.F., J.W. Chamberlain, J.M. Cornwall, D.A. Hammer, and F.W. Perkins, "Irregularities in ionospheric plasma clouds: Their evolution and effect on radio communications," JASON Report JSR-80-15, 1980.

APPENDIX M
ELECTRON ACCELERATION VS BULK HEATING BY THE
MODIFIED TWO STREAM INSTABILITY

K. Papadopoulos
Science Applications, Inc.

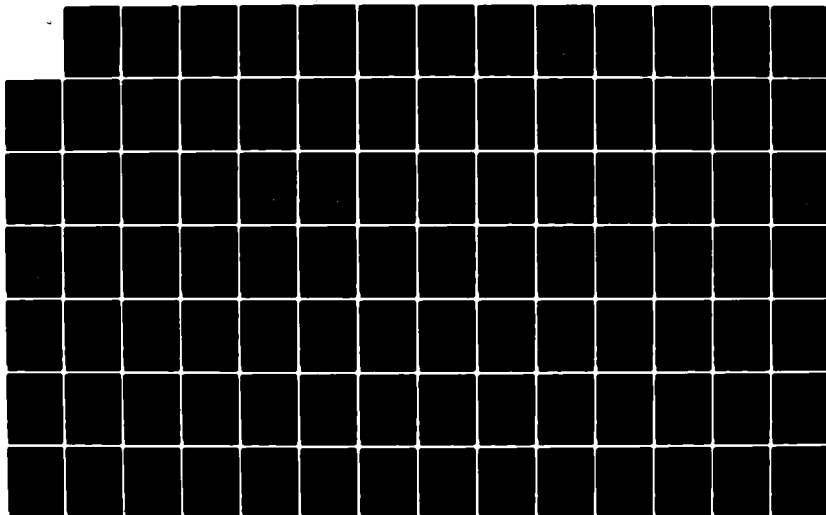
AD-A142 573 GEOPHYSICAL PLASMAS AND ATMOSPHERIC MODELING(U) SCIENCE
APPLICATIONS INC MCLEAN VA E HYMAN ET AL. MAR 84
SAI-84/1554 SBI-AD-E001 718 N00014-83-C-2034

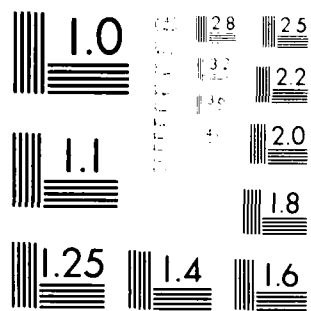
5/6

UNCLASSIFIED

F/G 4/1

NL





MICROCOPY RESOLUTION TEST CHART
 NATIONAL BUREAU OF STANDARDS-1963-A

ELECTRON ACCELERATION VS BULK HEATING BY THE
MODIFIED TWO STREAM INSTABILITY

K. Papadopoulos

Science Applications, Inc.
1710 Goodridge Drive
McLean, Virginia 22102
(703) 734-5804

The modified two stream instability (MTSI) is an important anomalous transport process in the early time development of HANE. A summary of the conditions for its development and the appropriate energy transport coefficients can be found in Lampe et. al.¹ The coefficients derived in this memorandum¹ were used in multifluid codes such as KLYSMA which determined the early time coupling phenomenology. Since in KLYSMA the electrons are treated as a single one temperature fluid, the energy transfer to electrons was in the form of bulk heating. As first discussed in Lampe and Papadopoulos² the energy transfer to electrons from the MTSI is often dominated by energetic tail formation rather than bulk electron heating. Recent simulations by Tanaka and Papadopoulos³ have confirmed these results and clarified the physics underlying the electron energization process. Whether it is necessary to incorporate the energy transfer to suprathermal tails rather than bulk electron heating in the HANE codes depends critically on the phenomenology aspect under consideration. If ionization processes play an important role the presence of non Maxwellian tails is usually important. The same is true if one is interested in line radiation signatures for diagnostic purposes. Both of the above considerations are relevant to the NRL experiment. In nuclear test cases such as STARFISH or SPARTAN in the 150-300 km, the location and properties of the energetic electron patches depends quite critically in the partition of the energy transfer to electrons during coupling between bulk heating and tail formation. The purpose of this note is to present some simple prescriptions in the spirit of Lampe et. al.,¹ which allow incorporation of the effects of tail formation in multifluid codes, such as KLYSMA, and examine some of the HANE aspects affected by such considerations.

Before discussing the modifications of the Lampe et. al.,¹ prescriptions to include energetic electron tail formation, we present a simplified physical picture of the non linear physics involved in the energy transfer. The standard situation for the occurrence of MTSI is shown in Figure 1 (for details see Ref. 1). Assuming for simplicity a single ion species with $Z=1$ and mass M , MTSI can occur between the ion beam 1 and the electrons if $U_1 < V_A \sqrt{1+\beta_e}$ and between the ion beam 2 and the electrons if $U_2 < V_A \sqrt{1+\beta_e}$. The free energy source in each case is $\frac{1}{2} n_1 M U_1^2$ and $\frac{1}{2} n_2 M U_2^2$, with the exception of the single ion species case in which the instability is driven by a diamagnetic current associated with $\nabla \times B$, in which case the free energy is small (i.e.,

$\frac{1}{2} n U_1^2$, where m is the electron mass). Let us first assume $n_2 \ll n_1$ and consider the interaction between beam 1 and electrons. The role of beam 2, is simply to maintain U_1 constant. In this case $n_1 \approx n_e$ and we have the MTSI case studied by McBride et. al.⁴ The hydrodynamic instability of interest here saturates by ion trapping. If electron trapping in the direction parallel to the magnetic field occurs before ion trapping the energy transfer to electrons is in the form of bulk heating. In this case the results given in Lampe et. al.,¹ can be safely used. The ratio of the ion trapping potential Φ_i to the electron trapping potential Φ_e , is given by

$$\frac{\Phi_i}{\Phi_e} = \frac{M (U_1 - V_{ph})^2}{m V_{ph}^2 \left(\frac{K}{K_z}\right)^2} \theta^2 \quad (1)$$

where K , K_z are the instability wave number and its projection along the magnetic field and $\hat{\theta} \equiv \theta \left(\frac{M}{m}\right)^{1/2}$ with θ being the angle to the magnetic field of the linearly most unstable wave. For $\frac{U_1}{V_i} > 4$, where V_i is the ion thermal speed, $\hat{\theta}^2 > 1$

and the electrons are trapped before the ions, resulting in bulk electron heating. The electron to ion heating ratio is as given in Ref. 1 Equations (A.1.7) as

$$\frac{\dot{T}_e}{\dot{T}_i} = \frac{V_{ph}}{U_1} \approx O(1) \quad (2)$$

i.e., the usual equal electron and ion heating. For $\frac{U_1}{V_i} < 4$, in which case $\hat{\theta}^2 < 1$, however, $\Phi_e > \Phi_i$ and the instability saturates by ion trapping while there is substantial free energy in the direction parallel to the field. This, as graphically shown in Ref. 2 and theoretically explained in Ref. 5 in terms of adiabatic mode conversion, is absorbed by a small fraction of electrons leading to the formation of suprathermal electron tails. The tail temperature can be approximated by

$$T_T = 16 \left(\frac{1}{2} M V_{ph}^2 \right) \quad (3)$$

while the electron tail density n_T can be found by noting that Equation (A.1.7) are valid for the total energy transfer i.e.,

$$\frac{\frac{d}{dt} (n_i T_i)}{\frac{d}{dt} (n_T T_T)} = \frac{V_{ph}}{V_1} \quad (4)$$

The interaction between the beam 2 and the electrons can be analyzed in a similar fashion. However, since $\frac{n_2}{n_e} \ll 1$, the ratio $\frac{\phi_i}{\phi_e} < 1$ in all circumstances⁶. We therefore have in this case always suprathermal tail formation. As discussed in Ref. 6, in this case

$$T_T = 4 \frac{1}{2} M U_2^2 \quad (5)$$

while

$$\frac{n_T}{n_2} = \frac{1}{4} \left(\frac{n_2}{2n_e} \right)^{1/3} \quad (6)$$

The importance of suprathermal electrons to various situations of interest to HANE can be seen from Eqs. (3-6). Namely while the present version will give electron temperatures $T_e \approx T_i$ when MTSI operates, for conditions where $\epsilon^2 < 1$, in reality we will have $T_T \approx 16 T_i$ but with suprathermal tail density $n_T \approx \frac{1}{16} n$ (i.e., the total energy transfer to electrons does not change but is differently apportioned). These could be important to the data interpretation and physics involved in

- (i) Starfish with respect to the energetic electron patch. Namely, the present prescription will give $T_e \approx T_i \approx 1-4$ keV. If, however, the energy is deposited in tails their temperature will be $T_T \approx 16-40$ keV.
- (ii) For Checkmate and HANE in the 150-250 km range, since the presence of non Maxwellian tails could dominate the chemistry and atomic physics calculations.
- (iii) For the NRL laser experiment, where since the ablation mode at low laser irradiance ($I < 10^{14} \frac{W}{cm^2}$) yields an ion velocity distribution with $\frac{\Delta V}{V} \approx \frac{1}{4} - \frac{1}{5}$ we expect to be at all times in the

region of MTSI where production of suprathermal tails prevails. For expansion velocities $U \approx 5 \times 10^7 \frac{\text{cm}}{\text{sec}}$ and assuming that at early times the ratio of the laser target expanding density to ambient plasma density is of the order of 5 ($\frac{n_L}{n_0} \approx 5$), the electron and ion temperatures due to the MTSI will be in the range of $T_e \approx T_i \approx 3-4$ eV. A proper calculation including suprathermal tails will give $T_e \ll T_i \approx 3-4$ eV and $T_T \approx 50-70$ eV with density $\frac{n_T}{n_0} \approx .07$. For such energetic tails ionization processes can be quite important in the physics of the coupling region.

These are of course rather simplified considerations, and should be taken in this spirit. They are, however, indicative of the size of the effect under various conditions and should be used as guidelines as to when a more detailed investigation is justified.

The effects of suprathermal tails can be incorporated in multifluid codes by carrying an additional electron fluid with density n_T and temperature T_T . It is sufficient to modify the prescription for electron energy transfer due to MTSI so that for $\Theta^2 < 1$, (with Θ defined in Lampe et. al.,¹) the energy is transferred to the suprathermal electrons rather than bulk heating. The tail number density n_T will then be determined by using Eqs. (A.1.7) of Lampe et. al.,¹ which indicate that the ratio of energy transfer between electrons and ions depends only on the phase velocity of the wave.

References

1. M. Lampe, W. Manheimer and K. Papadopoulos NRL memo report 3076, (1975).
2. M. Lampe, and K. Papadopoulos Astrophys. J. 212, 886 (1977).
3. M. Tamaka and K. Papadopoulos Phys. Fl. (in press) (1983).
4. J. McBride, E. OH, J. P. Boris and J. Orens Phys. Fluids 15, 2367 (1972).
5. H. Rowland, M. Tamaka and K. Papadopoulos comm. in Plasma Physics (in press) (1983).
6. K. Papadopoulos, Comm. in Plasma Physics (in press) (1983).

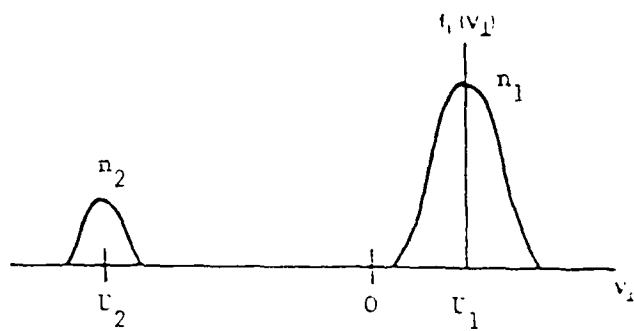


Figure 1. Ion distributions for MTSI as seen from the plasma (i.e., electron) reference frame.

APPENDIX N
SIMULATION OF A URANIUM VAPOR RELEASE
IN THE HIGH ALTITUDE ATMOSPHERE

J. Fedder and K. Hain
Naval Research Laboratory

and

E. Hyman
Science Applications, Inc.

Simulation of a Uranium Vapor Release in the High Altitude Atmosphere

J. FEDDER AND K. HAIN

*Geophysical and Plasma Dynamics Branch
Plasma Physics Division*

E. HYMAN

*Science Applications, Inc.
McLean, VA 22102*

November 22, 1983

This research was sponsored by the Defense Nuclear Agency under Subtask S125AMX10,
work unit 00079 and work unit title "Uranium Release Modeling."



**NAVAL RESEARCH LABORATORY
Washington, D.C.**

Approved for public release; distribution unlimited.

N-3

PRECEDING PAGE BLANK-NOT FILMED

REPORT DOCUMENTATION PAGE		READ INSTRUCTIONS BEFORE COMPLETING FORM
1. REPORT NUMBER	2. GPOV ACCESSION NO.	3. RECIPIENT'S CATALOG NUMBER
NRL Memorandum Report 5193		
4. TITLE and Subtitle	5. TYPE OF REPORT & PERIOD COVERED	
SIMULATION OF A URANIUM VAPOR RELEASE IN THE HIGH ALTITUDE ATMOSPHERE	Interim report on a continuing NRL problem.	
6. AUTHOR	7. PERFORMING ORG. REPORT NUMBER	
J. Fedder, K. Ham, and E. Hymian		
8. PERFORMING ORGANIZATION NAME AND ADDRESS	9. CONTRACT OR GRANT NUMBER	
Naval Research Laboratory Washington, DC 20375		
10. CONTROLLING OFFICE NAME AND ADDRESS	11. PROGRAM ELEMENT PROJECT TASK AREA & WORK UNIT NUMBERS	
Defense Nuclear Agency Washington, DC 20305	67215H: 47-1944-0-3	
12. MONITORING AGENCY NAME & ADDRESS (if different from Controlling Office)	13. REPORT DATE	
	November 22, 1983	
	14. NUMBER OF PAGES	
	48	
	15. SECURITY CLASS. of this report	
	UNCLASSIFIED	
	16. DECLASSIFICATION/DOWNGRADING SCHEDULE	
17. DISTRIBUTION STATEMENT (for this Report):		
Approved for public release; distribution unlimited.		
18. DISTRIBUTION STATEMENT (for the abstract entered in Block 20, if different from Report):		
19. SUPPLEMENTARY NOTES		
*Present address: Science Applications, Inc., McLean, VA 22102 This research was sponsored by the Defense Nuclear Agency under Subtask S125AMX10, work unit 00079 and work unit title "Uranium Release Modeling."		
20. KEY WORDS (Continue on reverse side if necessary and identify by block number)		
Uranium release Ionospheric infrared emission Ionospheric uranium chemistry Ionospheric striation formation		
21. ABSTRACT (Continue on reverse side if necessary and identify by block number)		
We present simulation results for a large uranium gas release in the ionosphere at an altitude of 200 km. The purpose of such an experimental release would be to study infrared emission line strengths and spectra of uranium oxides after a nuclear explosion. The simulation shows that the release would have high ion densities $\sim 10^8 \text{ cm}^{-3}$, that it would have a radius of about half a kilometer perpendicular to the geomagnetic field, and that it would spread to a few kilometers along the field. We also demonstrate the complete oxidation of U to UO_2^+ would require tens of seconds.		

DD FORM 1473
1 JAN 73EDITION OF 1 NOV 65 IS OBSOLETE
S/N 0102-014-6601

SECURITY CLASSIFICATION OF THIS PAGE (When Data Entered)

CONTENTS

I.	Introduction.....	1
II.	Simulation Model.....	2
III.	Results.....	5
IV.	Conclusions.....	7
	Acknowledgments	8
	References.....	37

SIMULATION OF A URANIUM VAPOR RELEASE IN THE HIGH ALTITUDE ATMOSPHERE

1. Introduction:

High altitude nuclear explosions can lead to greatly enhanced infrared radiation in the earth's atmosphere and can thereby have a deleterious effect on defensive infrared systems. This enhanced infrared radiation has a number of sources: direct plasma radiation from the nuclear burst; created plasma; creation of increased densities and/or increased temperatures of natural atmospheric infrared radiators such as hydroxyl, nitrogen oxides and carbon oxides; and also infrared radiation of weapon and vehicle debris species which are vaporized in the explosion. Recently it has been recognized that uranium and its oxides are likely to be the dominant infrared active species at 10 minutes and later following a high altitude nuclear detonation (Armstrong, 1981).

The Defense Nuclear Agency has an interest in developing methods to predict the infrared radiation after a high altitude nuclear event. Armstrong points out those areas where there is a severe lack of knowledge required to make accurate predictions. In order to measure the spectral fluxes and the strength of long wavelength infrared emission it is expected that fairly large releases of uranium vapor will be necessary in the earth's high atmosphere. Only after such measurements are made will accurate predictions become possible. With this requirement in mind, we have considered the scenario originally described by Reidy (1980) involving the prompt deposition of 2 kg of uranium vapor at an altitude of 200 km. Current experimental release techniques are short of being capable of this rapid deposition by orders of magnitude.

In this memorandum, we present results for the temporal evolution of a uranium vapor release at approximately 200 kilometer altitude in the earth's atmosphere. The results are obtained by numerical simulations using a simple model and can be used to plan such an experimental release. The results describe both the chemical and hydrodynamic evolution for one experimental scenario for time periods of a few tens of seconds. We predict a uranium ion cloud extended along the field but narrow perpendicular to the earth's magnetic field. The ion densities are high for minutes after release with the

Manuscript approved August 18, 1983.

ions, UO_2^+ and UO_2^- , formed in shells around the release point. The time scale for complete oxidation of U to UO_2^+ is demonstrated to be a few tens of seconds.

II. Simulation Model:

We consider a simple one-dimensional model of the uranium release. The temporal evolution of each species, denoted α , is described by equation 1.

$$\frac{\partial n_\alpha}{\partial t} = \frac{\partial n_\alpha}{\partial t} \text{ hydro} + \frac{\partial n_\alpha}{\partial t} \text{ diff} + \frac{\partial n_\alpha}{\partial t} \text{ chem} \quad (1)$$

The first term on the right is the change in the concentration from hydrodynamic transport. The second term describes diffusion of ions through ions and neutrals through neutrals. The third term treats chemical transformation of the individual species.

The hydrodynamic transport of ions and neutrals is done separately. The transport equations are:

continuity

$$\frac{\partial \rho_s}{\partial t} = - \nabla \cdot (\rho_s \underline{v}_s), \quad (2)$$

momentum

$$\frac{\partial \underline{v}_s}{\partial t} = - (\underline{v}_s \cdot \nabla) \underline{v}_s - \frac{1}{\rho_s} \nabla (p_s + q_s) - \sigma p_t (\underline{v}_s - \underline{v}_t) \quad (3)$$

and energy

$$\begin{aligned} \frac{\partial p_s}{\partial t} = & - \nabla \cdot (\rho_s \underline{v}_s) - (\gamma - 1) (p_s + q_s) \nabla \cdot \underline{v}_s \\ & - \sigma \rho_s \rho_t (T_t - T_s) + (\gamma - 1) \frac{\sigma \rho_s \rho_t}{(\rho_s + \rho_t)^2} \rho_s (\underline{v}_s - \underline{v}_t)^2 \end{aligned} \quad (4)$$

Here s denotes either the ions or the neutrals and t denotes the other. The symbols ρ , \underline{v} , p, T, and q are density, flow velocity, pressure, temperature,

and artificial viscosity respectively. λ is the ratio of thermal conductivity to the collisional coefficient of friction.

In this simple one dimensional model of transport we treat two specific cases: transport perpendicular and transport parallel to the ambient geomagnetic field. Perpendicular to B the neutrals are transported spherically and the ions are frozen to the unmoving field. Parallel to B , the neutrals are transported spherically and the ions are transported along a cartesian axis parallel to the field. The two cases of the simple one-dimensional model should give reasonable estimates for the size of a release cloud in the atmosphere. Since the transport model allows for diffusion between ions and neutrals our diffusion model only needs to consider neutrals and ions diffusing through themselves.

The diffusion equation in a multi constituent gas can be expressed (Burgers 1969)

$$\sum_{\alpha} \rho_{\alpha} \rho_{\alpha f} \sigma_{\alpha f} \left(\frac{v_{\alpha}}{\rho} - \frac{v_f}{\rho} \right) = T \left(\nabla_{\alpha} - \frac{\rho_{\alpha}}{\rho} \nabla \right). \quad (5)$$

where ρ is the total density. An exact solution for diffusion can be obtained by inversion of (5) and substitution of the species velocities into a set of coupled continuity equations for each specie. For our model here however we approximate (5) and obtain a decoupled set of continuity equations. We assume $\sigma_{\alpha f} = \sigma$, a constant, which allows us to express the effects of diffusion as

$$\frac{\partial \rho_{\alpha}}{\partial t} = -\nabla \cdot (\kappa \nabla \rho_{\alpha} / \rho), \quad (6)$$

where κ is a diffusion coefficient depending on σ . We have tested this simplified diffusion model and have obtained reasonable results. The simplification of diffusion, while not totally accurate, yields results which are within a factor of two.

The effects of chemistry on the species are computed in a series of rate equations

$$\frac{\partial n_{\alpha}}{\partial t} = k_{st} n_s n_t. \quad (7)$$

The reactions of concern and their rate coefficients, k_{st} , are shown in Table 1 which are taken from Armstrong (1981) and Archer (1982).

The final part of the model is the specification of the neutral atmosphere. We have taken species concentrations and a temperature appropriate to moderate solar activity, daytime, 200 km altitude conditions; they are $[O] = 4.4 \times 10^9 \text{ cm}^{-3}$, $[N_2] = 4.2 \times 10^9 \text{ cm}^{-3}$, and $[O_2] = 2.0 \times 10^8 \text{ cm}^{-3}$. The neutral atmospheric temperature is 0.1 ev.

III. Results:

We have solved the model equations 1,2,3,4,6, and 7 for a uranium vapor release at 200 km altitude in the atmosphere. We have assumed a prompt release of 2 kg of atomic uranium, approximately $5. \times 10^{22}$ atoms. The temperature of the uranium vapor is taken as 0.276 ev. Three sets of solutions were obtained with the diffusion coefficient, κ , as a parameter to study the effects of diffusion on the release evolution. In the first, or nominal, case κ was taken as $0.1 \text{ km}^2/\text{sec}$, a nominal diffusion coefficient at 200 km altitude. For an appropriate gradient scale length of 100 m the diffusion velocity is 100 m/sec. This value is about 17% of the sound speed at that altitude. We have also obtained results for diffusion coefficients 1/3 and 3 times the nominal value. The slower diffusion rates lead to very slow oxidation of the uranium vapor and are therefore uninteresting. In the following sections we show results for nominal diffusion and faster diffusion.

Figures 1 through 14 show results for the simulation perpendicular to the geomagnetic field with nominal diffusion. Figure 1 shows the initial conditions of the release. The vertical axis plots the logarithm to the base 10 of the gas concentration while the horizontal axis measures radius of the release in km. The uranium vapor has a radius of 200 m and has displaced the ambient atmospheric species. We have tested a number of initializations and find that the results after a few seconds are insensitive to details of the initial conditions.

Figures 2, 3, and 4 show the neutral gas concentration at 2, 5, and 10 seconds respectively. Initially both atomic and molecular oxygen are burned out of the release cloud in oxidizing the uranium gas. The atomic oxygen is able to diffuse into the cloud by about 5 seconds but the molecular oxygen continues to be consumed as it diffuses in for times longer than 10 seconds.

Table 1

Chemical Reaction Rate Coefficients

(1)	$U + O \rightarrow UO^+ + e^-$	$5 \times 10^{-10} \text{ cm}^3/\text{sec}$
(2)	$U + O_2 \rightarrow UO_2^+ + e^-$	$3.8 \times 10^{-12} \text{ cm}^3/\text{sec}$
(3)	$U + O_2 \rightarrow UO + O$	$1.8 \times 10^{-10} \text{ cm}^3/\text{sec}$
(4)	$UO + O \rightarrow UO_2^+ + e^-$	$4 \times 10^{-10} \text{ cm}^3/\text{sec}$
(5)	$UO + O_2 \rightarrow UO_2 + O$	$2 \times 10^{-9} \text{ cm}^3/\text{sec}$
(6)	$UO^+ + O_2 \rightarrow UO_2^+ + O$	$4 \times 10^{-9} \text{ cm}^3/\text{sec}$

The different behaviour of atomic and molecular oxygen is due primarily to their different concentrations in the ambient atmosphere; there just is not enough molecular oxygen around to rapidly fully oxidize the cloud.

The resulting ion cloud concentrations are presented in Figures 5 through 11 for post release times of 2 to 50 seconds. The UO^+ component forms in a shell like structure at a radius of about 200 meters from the release point. The shell is formed at a burning front between outward diffusing uranium vapor and inward diffusing atomic oxygen, and the ions are frozen in the geomagnetic field at their point of oxidation. The initial oxidation of uranium gas to UO^+ is complete by 5 seconds. Further burning of UO^+ to UO_2^+ by molecular oxygen then takes place in an outer shell which slowly moves inward as unconsumed molecular oxygen is able to diffuse inward. The complete oxidation of uranium vapor to UO_2^+ takes between 40 and 50 seconds. The final ion densities of 10^{11} cm^{-3} in the shell are higher than would occur in an actual release because this one-dimensional model does not allow for diffusion parallel to the magnetic field. From studying our one dimensional parallel release results we would expect the maximum ion cloud densities to be about 10^9 cm^{-3} for this release.

Figures 12, 13, and 14 show the results for UO^+ , UO_2^+ , and O_2 concentrations respectively in a different graphical format. We have plotted contours of concentration versus radius and time after release. Here the shell structure of the ion cloud is clearly seen. The UO^+ forms a shell at 200 meters radius immediately after release. The UO_2^+ shell initially forms at about 400 meters and gradually builds inward as oxidation takes place. We are also able to see the cavity formed in the ambient O_2 which is only slowly filled by diffusion from the outside.

A similar set of results for the evolution of the uranium release parallel to the geomagnetic field is shown in Figures 15 through 24. The initial conditions, which are identical to the previous case are shown in Figure 15; note the change in scale on the horizontal axis. The neutral concentrations for 2, 5, and 10 seconds after release are shown in Figures 16, 17, and 18 respectively. The ion concentrations for the same time intervals after release are shown in Figures 19, 20, and 21. The qualitative nature of the temporal and spatial evolution is like that discussed previously for the perpendicular release. The primary difference in the results is that here the

ion cloud is able to readily diffuse outward. This parallel diffusion allows the UO_2^+ to become very extended along the geomagnetic field. The UO^+ is however still confined to the release region as it is consumed by oxidation by molecular oxygen as it attempts to diffuse parallel to the magnetic field.

Figures 22, 23 and 24 show contours of UO^+ , UO_2^+ , and O_2 concentration respectively for the parallel simulation. Again the results are similar to those for the perpendicular simulation. The formation of an ion cloud shell about the release point is again clearly seen. The shell is broader in this case, and for UO_2^+ diffusion outward is very noticeable. The molecular oxygen is depleted in the release location, and for this case the burned out region is very much larger as the ions diffuse outward.

The results for the uranium release simulations with 3 times faster diffusion are shown in Figures 25 through 28. The initial conditions are the same as used for normal diffusion. Figures 25 and 26 present results of the perpendicular simulation 10 seconds after release for the neutrals and ions respectively. Figures 27 and 28 show results for the parallel simulation. The results in both instances are qualitatively similar to those represented previously. The major quantitative differences are a more rapid oxidation of UO^+ to UO_2^+ allowed by faster diffusion of O_2 into the ion cloud, and for the parallel case, a more rapid diffusion of UO_2^+ along the geomagnetic field. Nevertheless the time scale for the complete oxidation of U to UO_2^+ is still greater than 10 secs.

IV. Conclusions

The results of the numerical simulation of a uranium vapor release at about 200 km altitude have demonstrated a very consistent and understandable morphology. For the 2 kg prompt release considered here, it is clearly demonstrated that the uranium vapor will completely burn out the molecular oxygen of the ambient neutral atmosphere. Moreover diffusion of molecular oxygen from outside into the release cloud is not sufficient to rapidly oxidize the cloud to its final state, UO_2^+ . We have shown that the time scale for complete oxidation is a few tens of seconds.

It might be thought that increasing the altitude of release would alleviate the slow oxidation of the cloud owing to faster diffusion rates. Unfortunately this is probably not the case since the atmospheric molecular

oxygen density decreases rapidly with altitude and the burn out would be more severe. It would appear that the only solution to the slow oxidation problem would be to release the uranium vapor gradually. However, in this case one would not have a compact cloud for measurement but would have a long thin trail of oxidized uranium ions across the sky.

The morphology of the release simulated here has a clearly defined shell structure. The ion cloud is also greatly extended along the geomagnetic field. At early times after release the ions form a double shell with UO_2^+ ions forming outside the UO^+ shell. At later times there is a single shell of UO_2^+ ions with a diameter of about 1 km perpendicular to the magnetic field and a length along the field of more than 10 km. The simulation indicates that the ion density in the shell can be expected to be 10^8 to 10^9 cm^{-3} . This is a very high density when compared to the well studied barium vapor releases where the ion densities are normally 2 orders of magnitude lower.

These very high ion densities can have important implication for gradient drift structuring for the uranium release ion cloud. For barium releases, it has been demonstrated that ion clouds which have a large conductivity ratio compared to the background ionosphere form striations very slowly (Linson, 1975). Therefore, we would expect that a uranium vapor release would create a slowly structuring ion cloud. This situation may be somewhat alleviated by conducting the uranium release during daytime with higher ambient ionospheric conductivities. However, on balance the uranium ion cloud should only slowly form striations.

In summary, we conclude that a prompt uranium vapor release would result in a UO_2^+ ion cloud in a few tens of seconds. The ion cloud would have a shell like structure and be compact perpendicular to the magnetic field and very elongated along the field. The ion concentrations would range from 10^8 to 10^9 cm^{-3} and would develop striated structure very slowly.

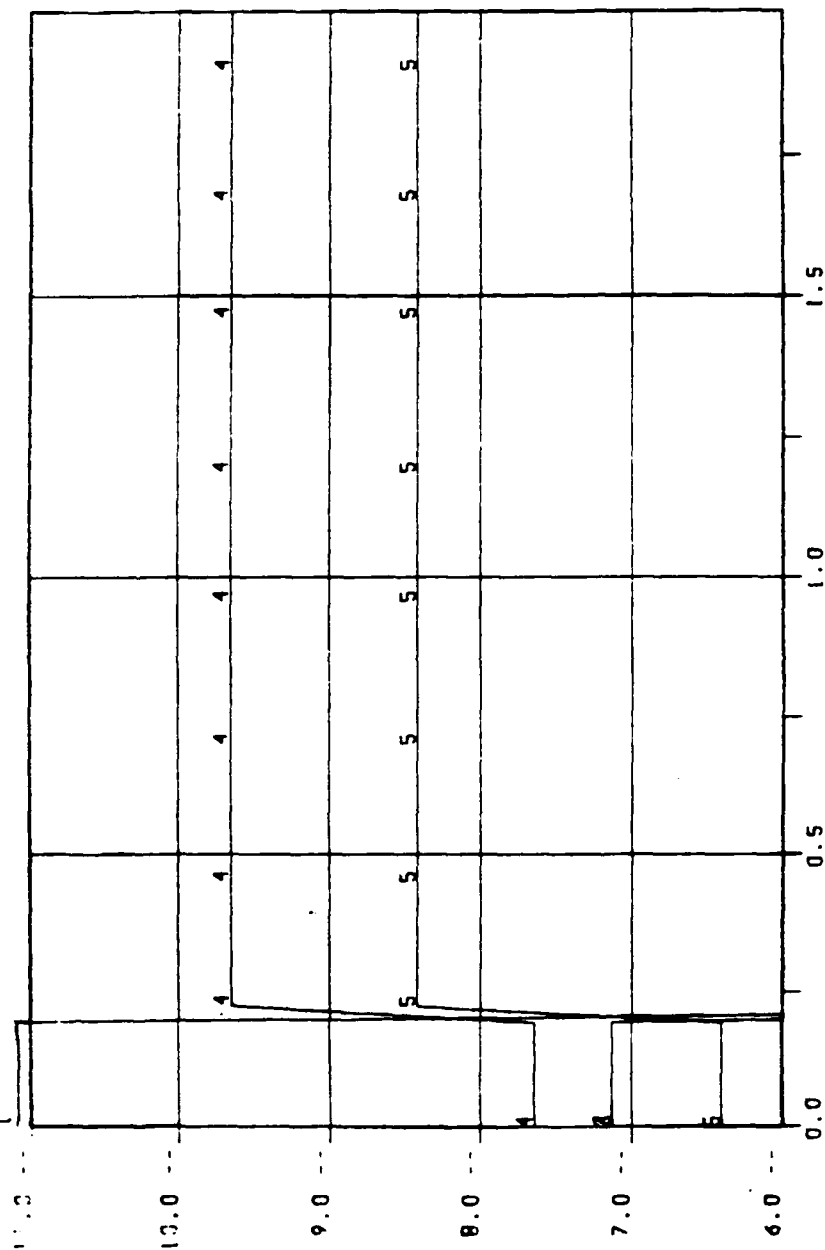
Acknowledgments

This work was supported by the Defense Nuclear Agency.

01/04/R3

TIME C.00E 00

NUM. DENS. LOG10



Distance
(km)

U-1, UD-2, UD2-3, 0-4, 02-5

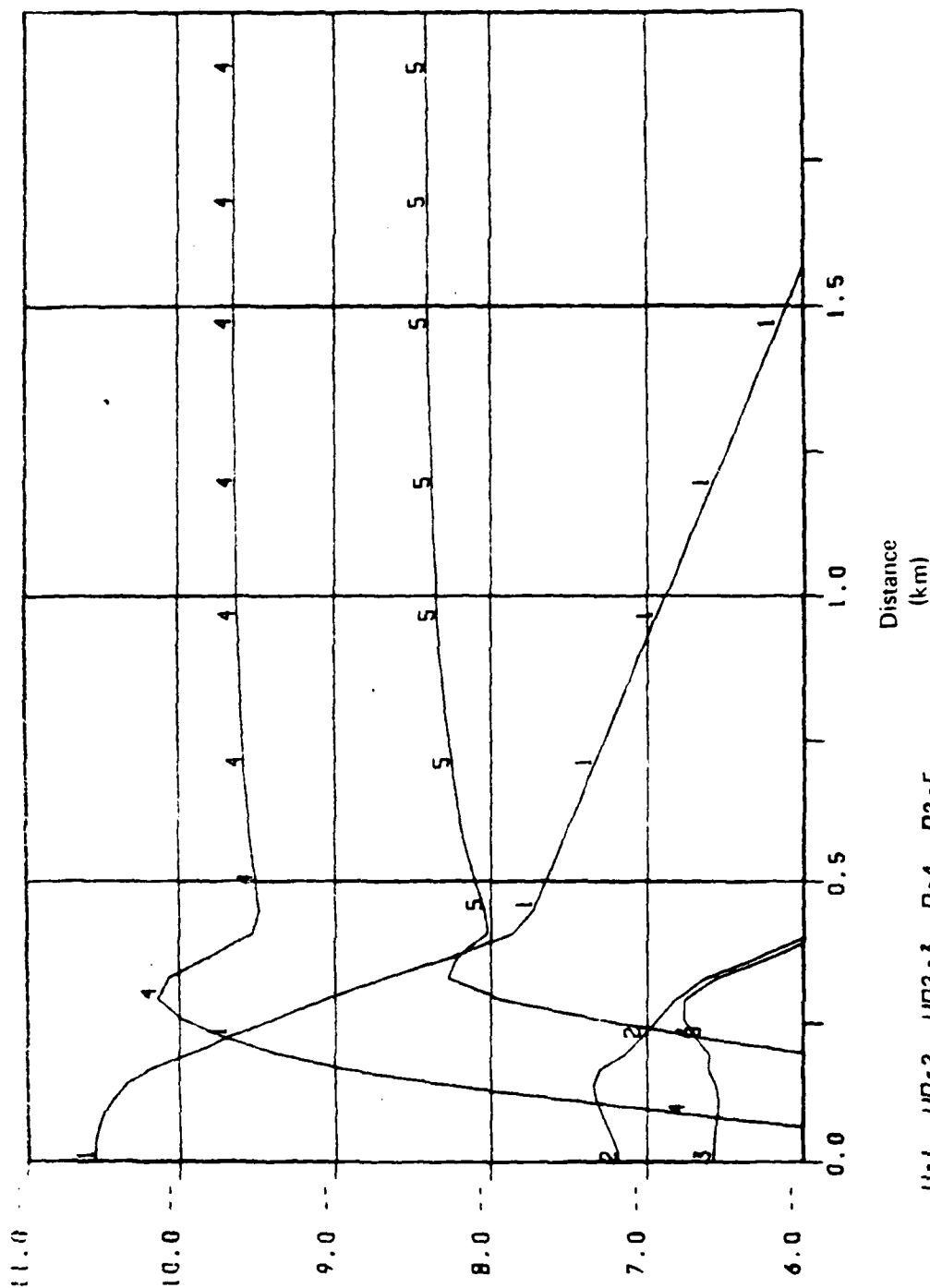
URR0

Figure 1. Initial conditions for simulation perpendicular to the geomagnetic field and nominal diffusion. Logarithm to base 10 of gas concentration in cm^{-3} are shown for U, UD, UD₂, 0, and 0₂ versus radius from burst point.

01/04/83

TIME 2.01E 00

NUM. DENS. LDR.10



U-1. U0-2. U02-3. 0-4. 02-5

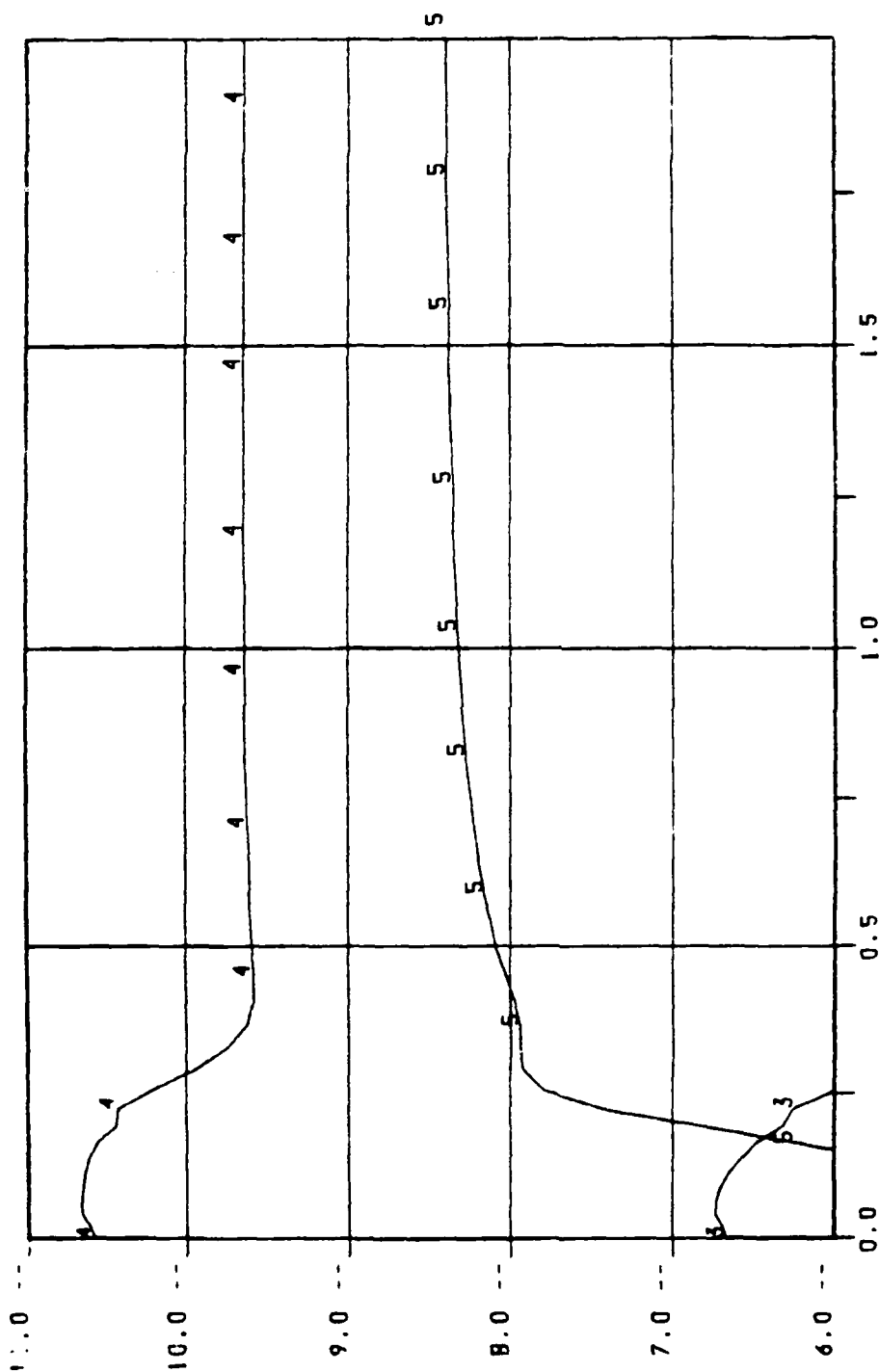
URRO

Figure 2. Neutral gas concentration at 2 seconds after release.

01/04/83

TIME 5.02E 00

NUT. NUM. DENS.LOG10



Distance
(km)

U-1, U0-2, U02-3, 0-4, 02-5

URR0

Figure 3. Neutral gas concentrations at 5 seconds after.

01/06/83

TIME 1.00E 01

NUT. NUM. DENS.LOG10

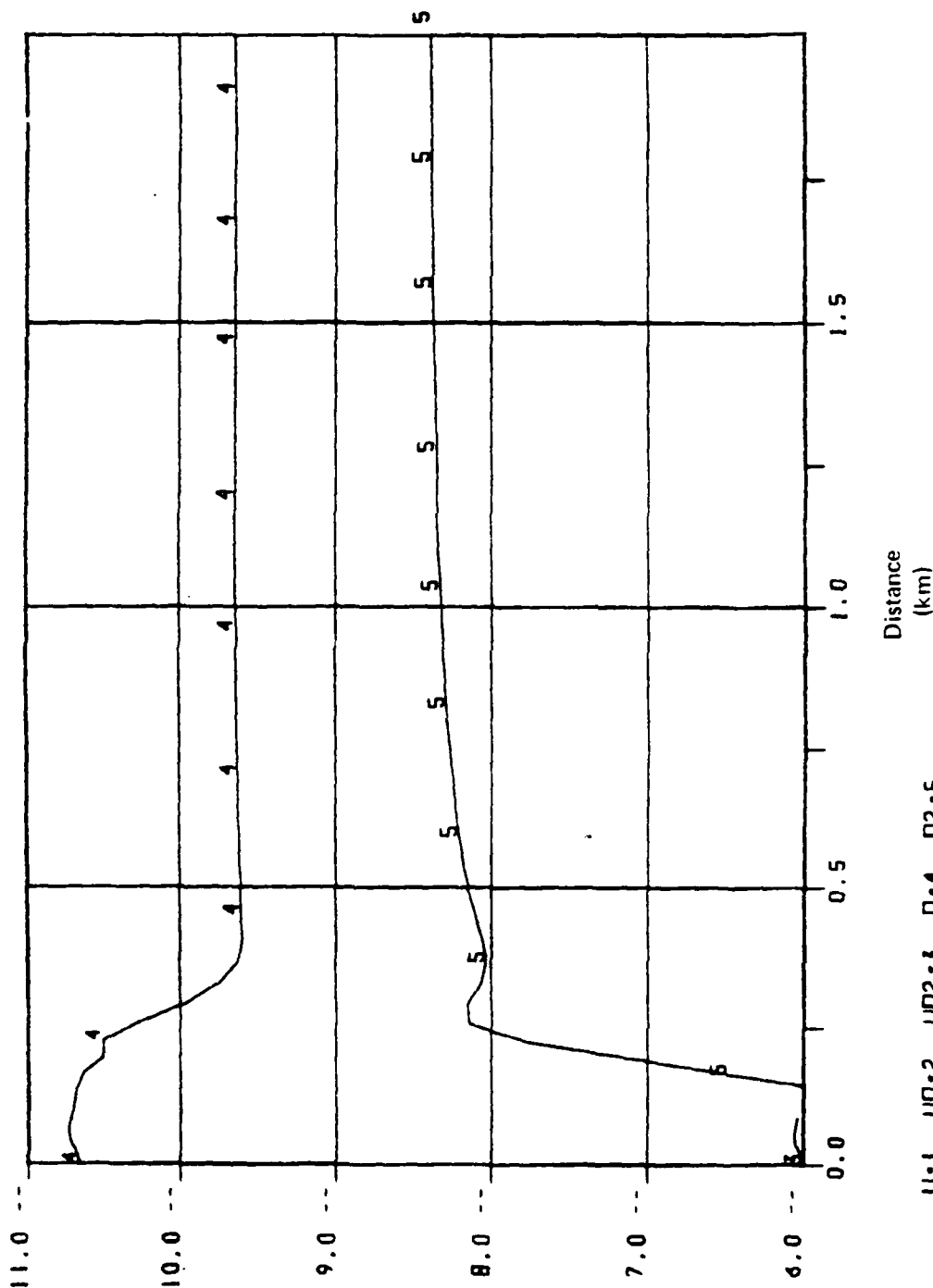
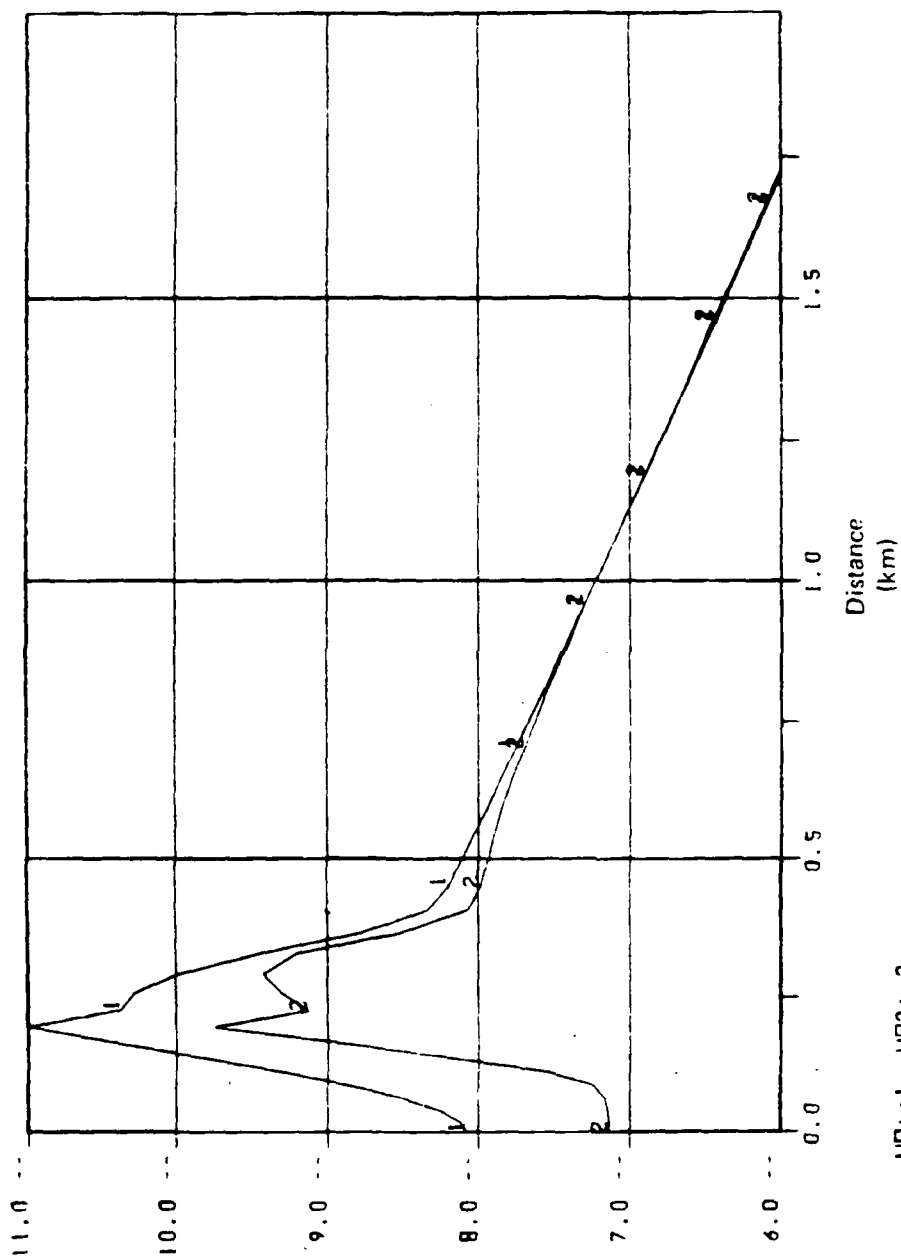


Figure 4. Neutral gas concentrations at 10 seconds after release.

01/04/83

TIME 2.01E 00

ION. NUM. DENS. LOG10



UD001. UD002

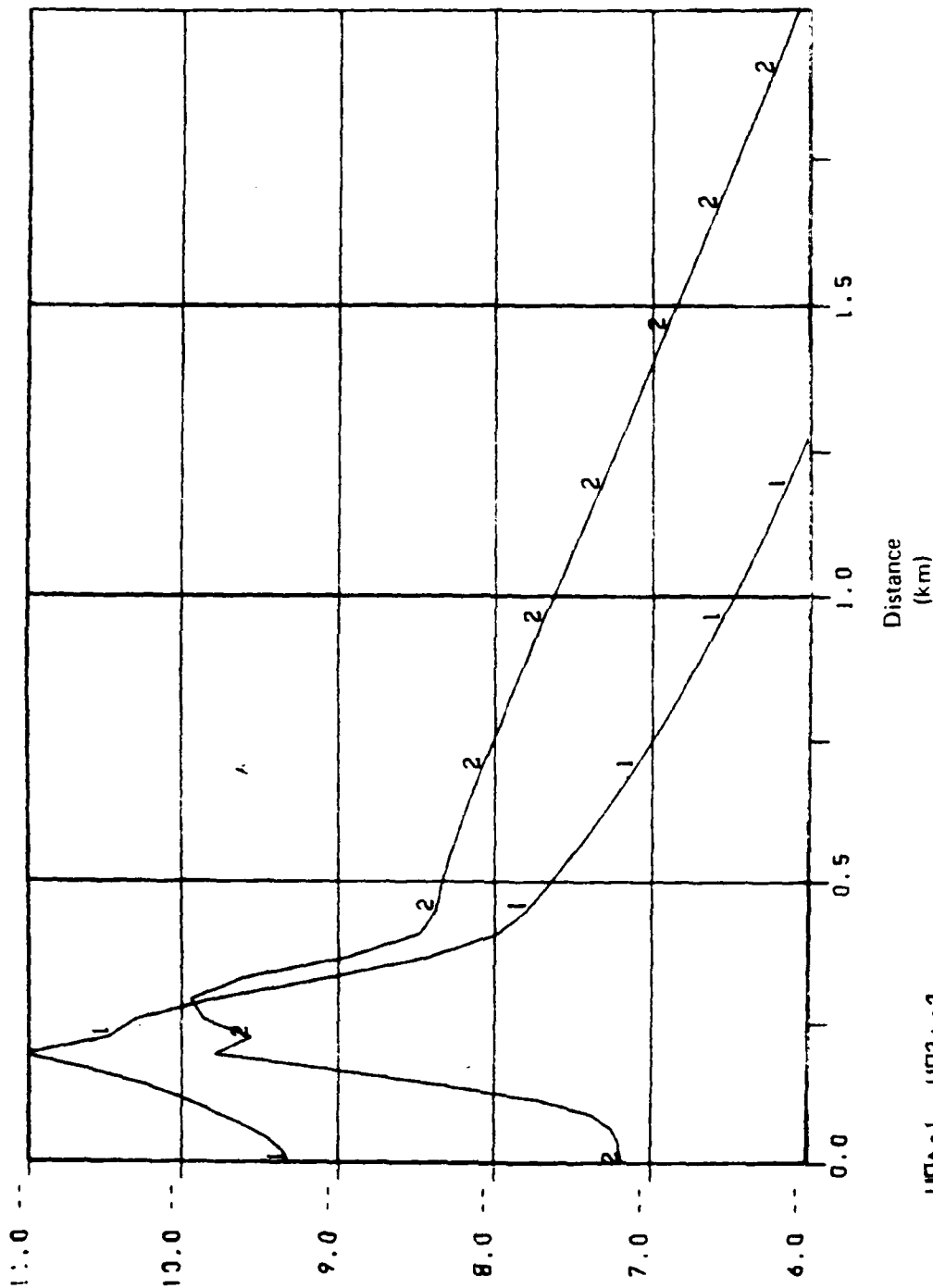
URR0

Figure 5. Ion gas concentrations at 2 seconds after release. Logarithm to base 10 of ion concentrations in cm⁻³ are shown for 10^4 and 10^5 versus distance from burst point perpendicular to geomagnetic field.

01/04/83

TIME 5.02E 00

ION. NUM. DENS. LOG10



URR0

Figure 6. Ion gas concentrations at 5 seconds after release.

01/06/R3

TIME 1.00E 01

ION. NUM. DENS. LOG10

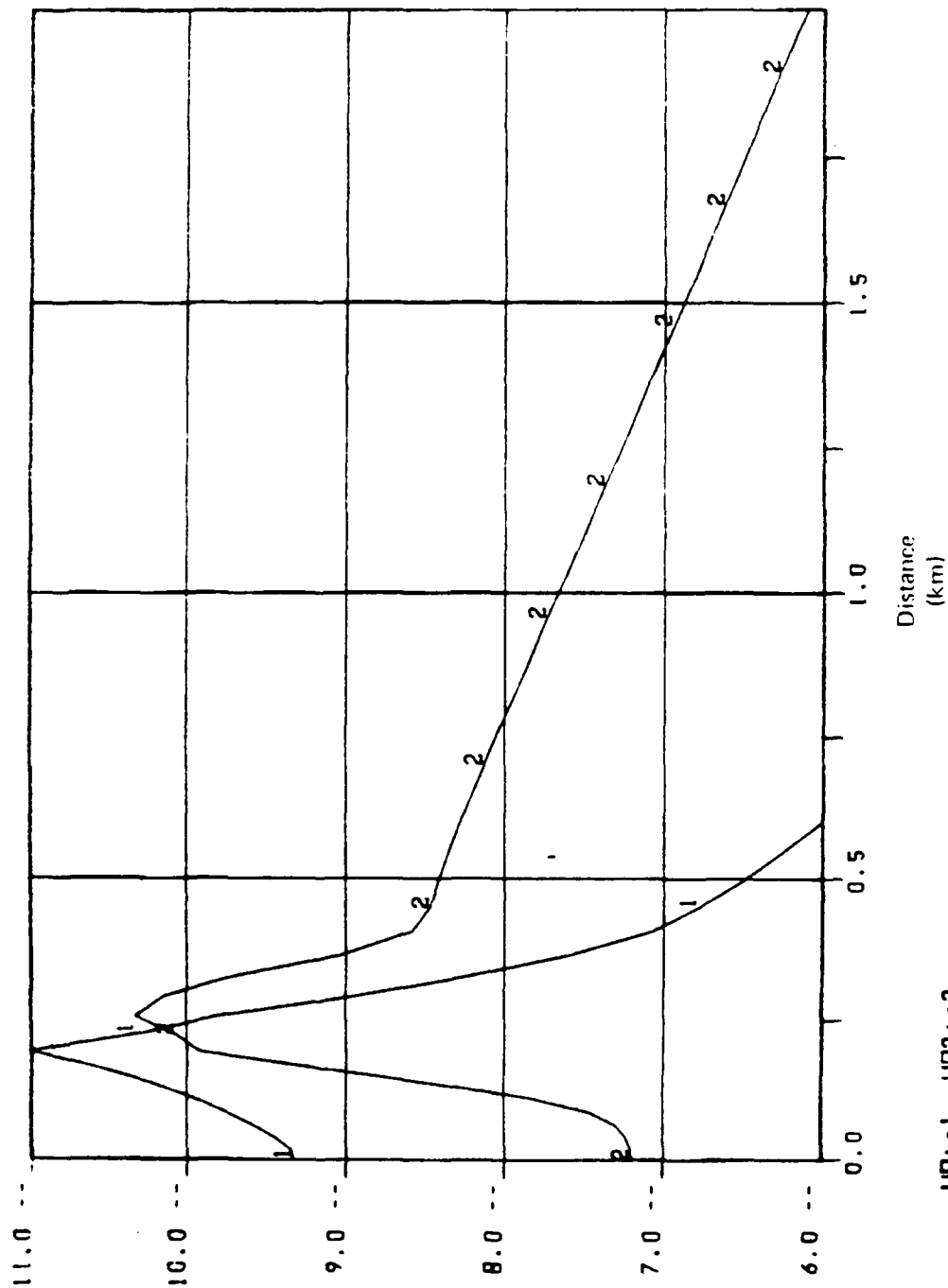
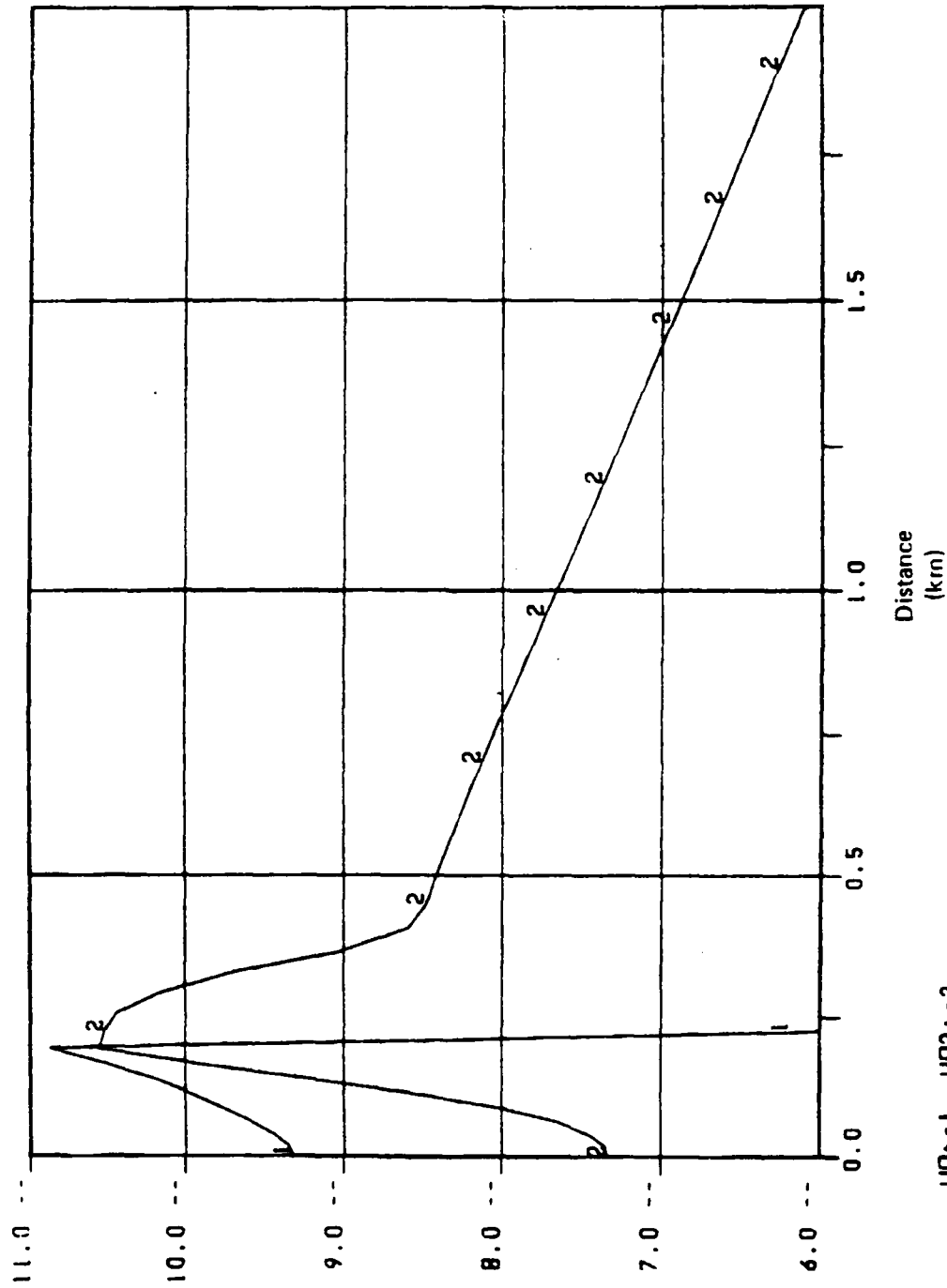


Figure 7. Ion gas concentrations at 10 seconds after release.

01/06/83

TIME 2.00E 01

ION. NUM. DENS.LOG10



U0+-1, U02+-2

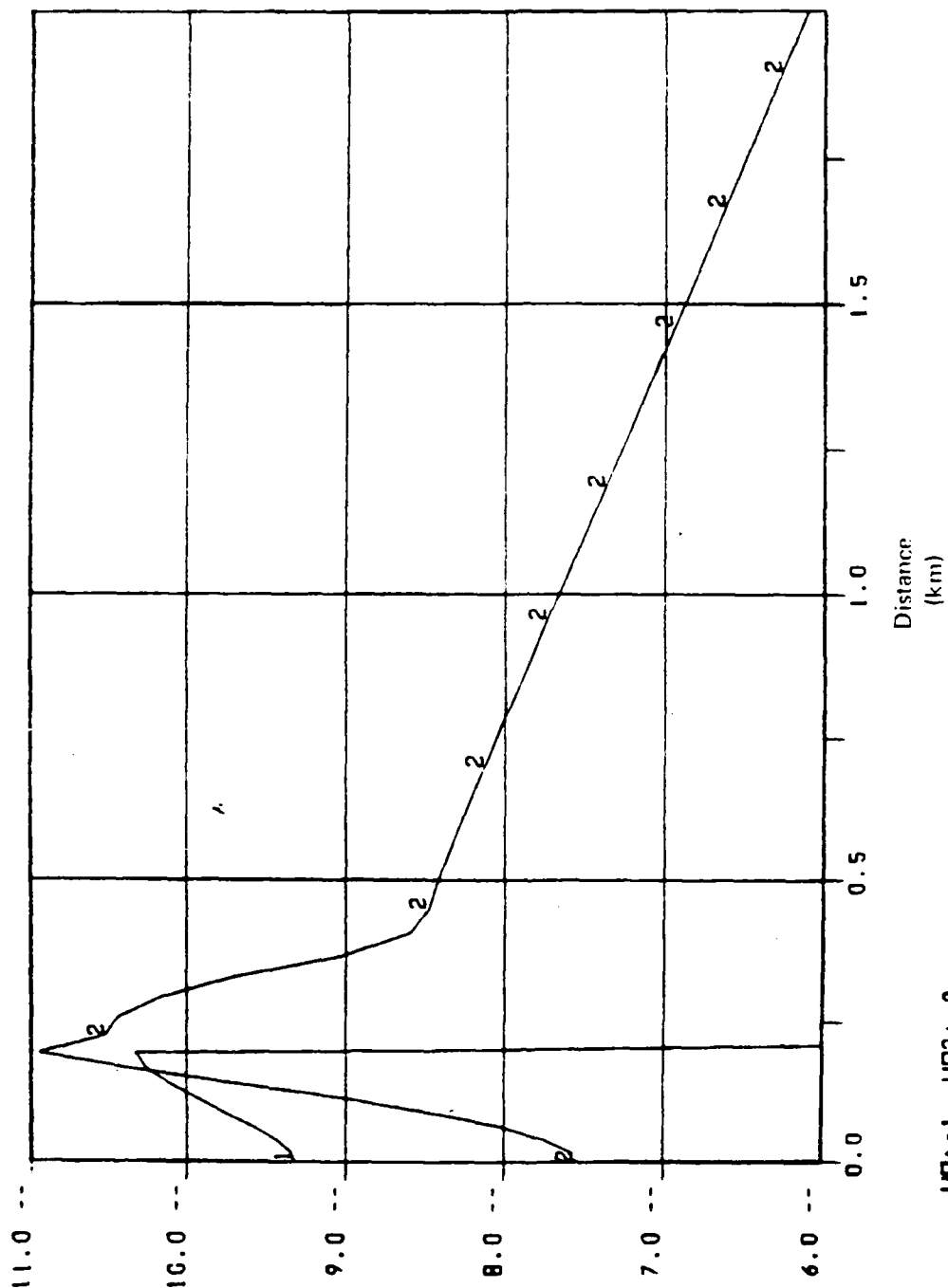
UR00

Figure 8. Ion gas concentrations at 20 seconds after release.

01/06/83

TIME 3.00E 01

ION. NUM. DENS. LOG10



UD1+1, UD2+2

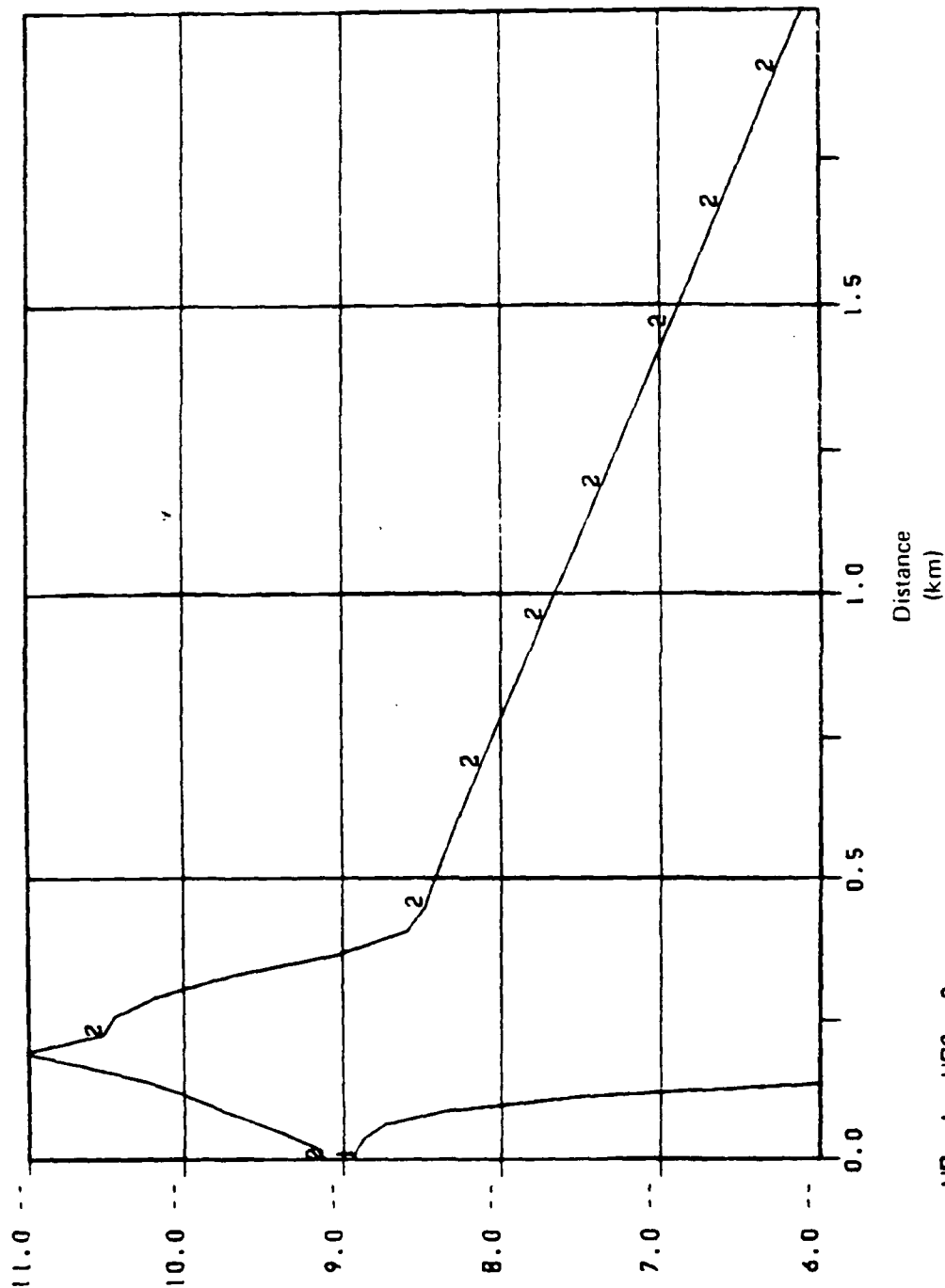
UR00

Figure 9. Ion gas concentrations at 30 seconds after release.

01/06/83

TIME 4.00E 01

IDN. NUM. DENS.LOG10



UD0+1, UD2+-2

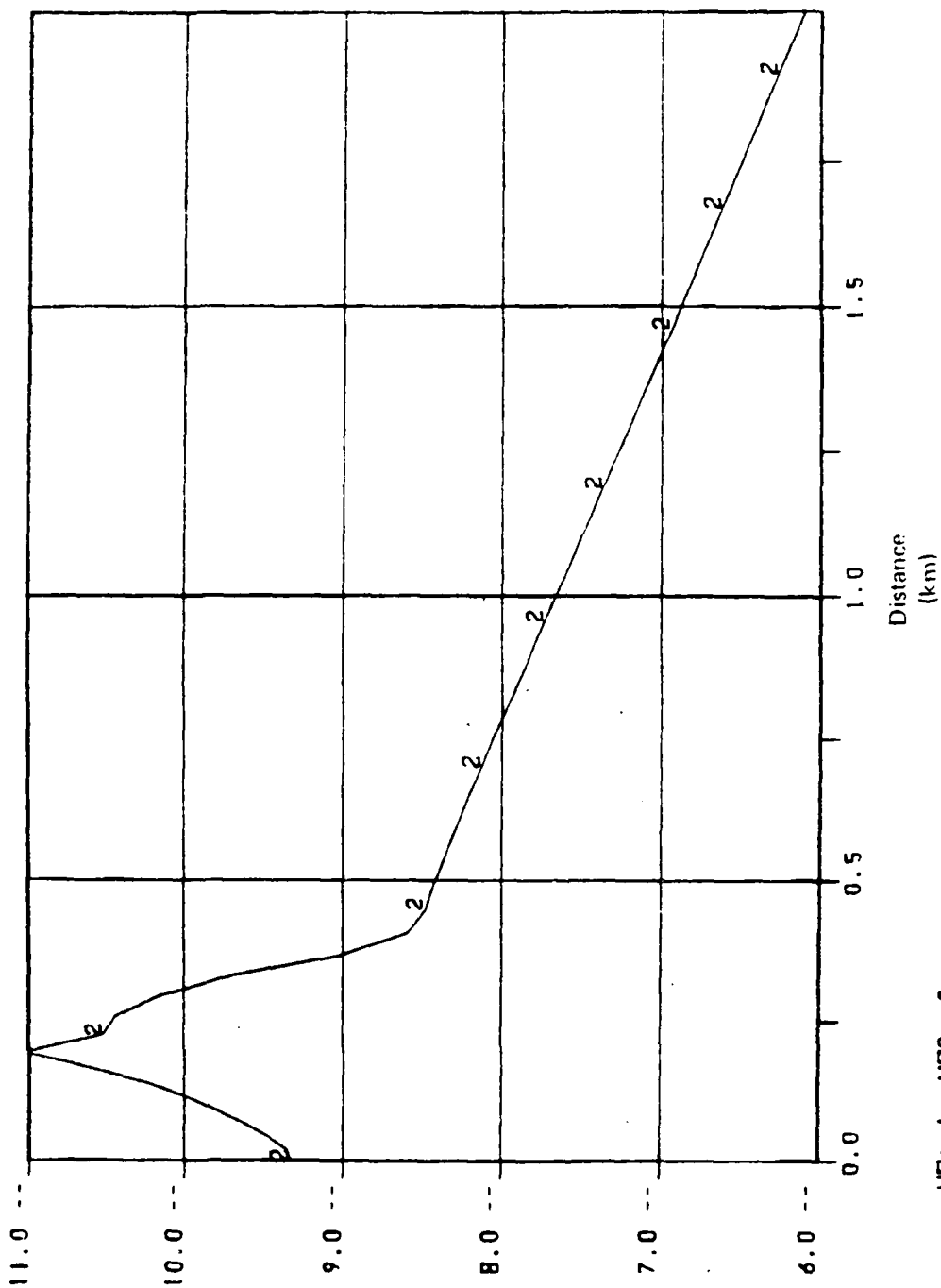
UR00

Figure 10. Ion gas concentrations at 40 seconds after release.

01/06/83

TIME 5.00E 01

ION. NUM. DENS. LOG10



UR00

Figure 11. Ion gas concentrations at 50 seconds after release.

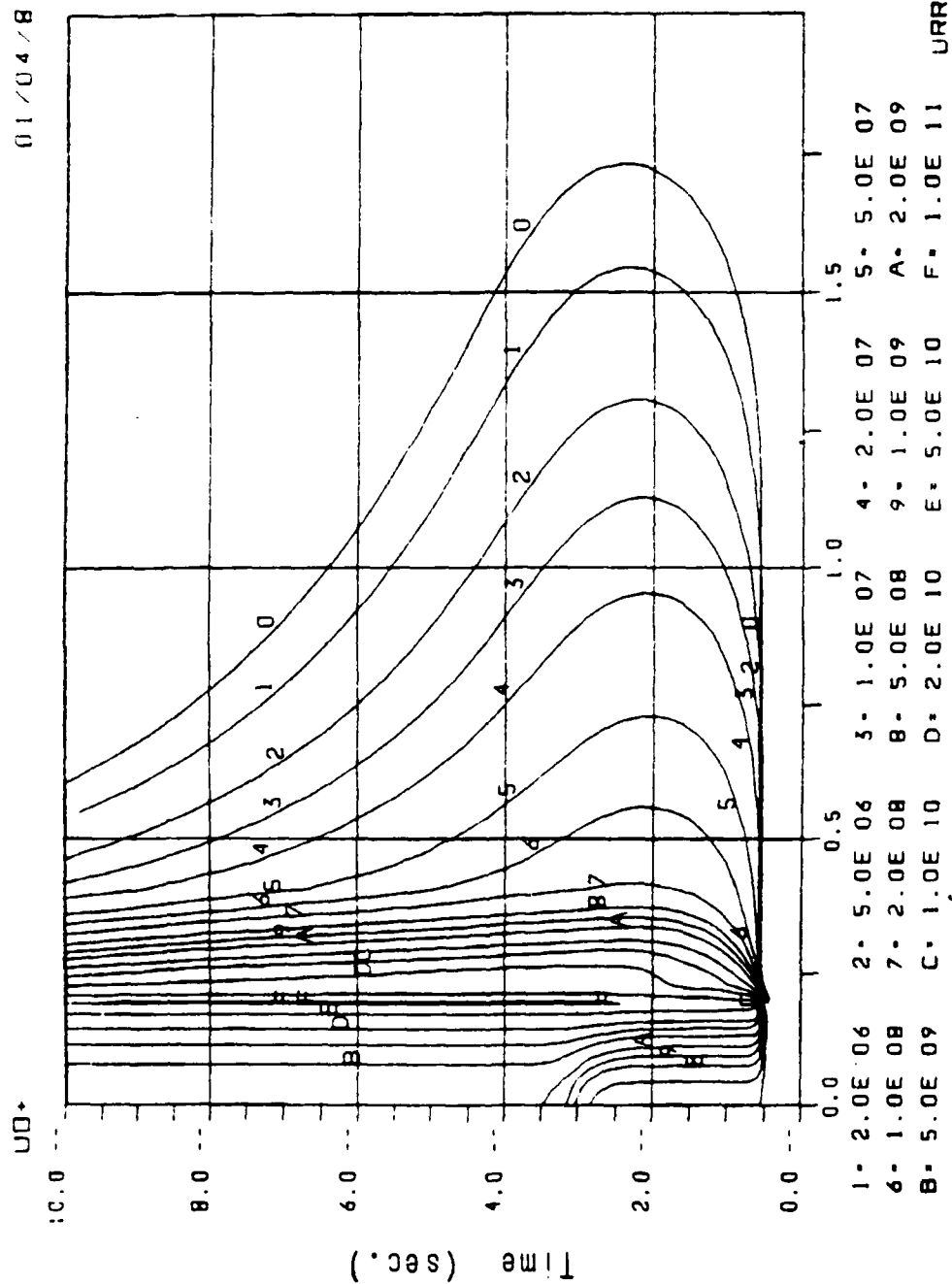


Figure 12. UO^+ ion concentration contours versus time and distance from release point. Contours are in cm^{-3} . Notice shell formation at 0.2 km which only gradually decays in time.

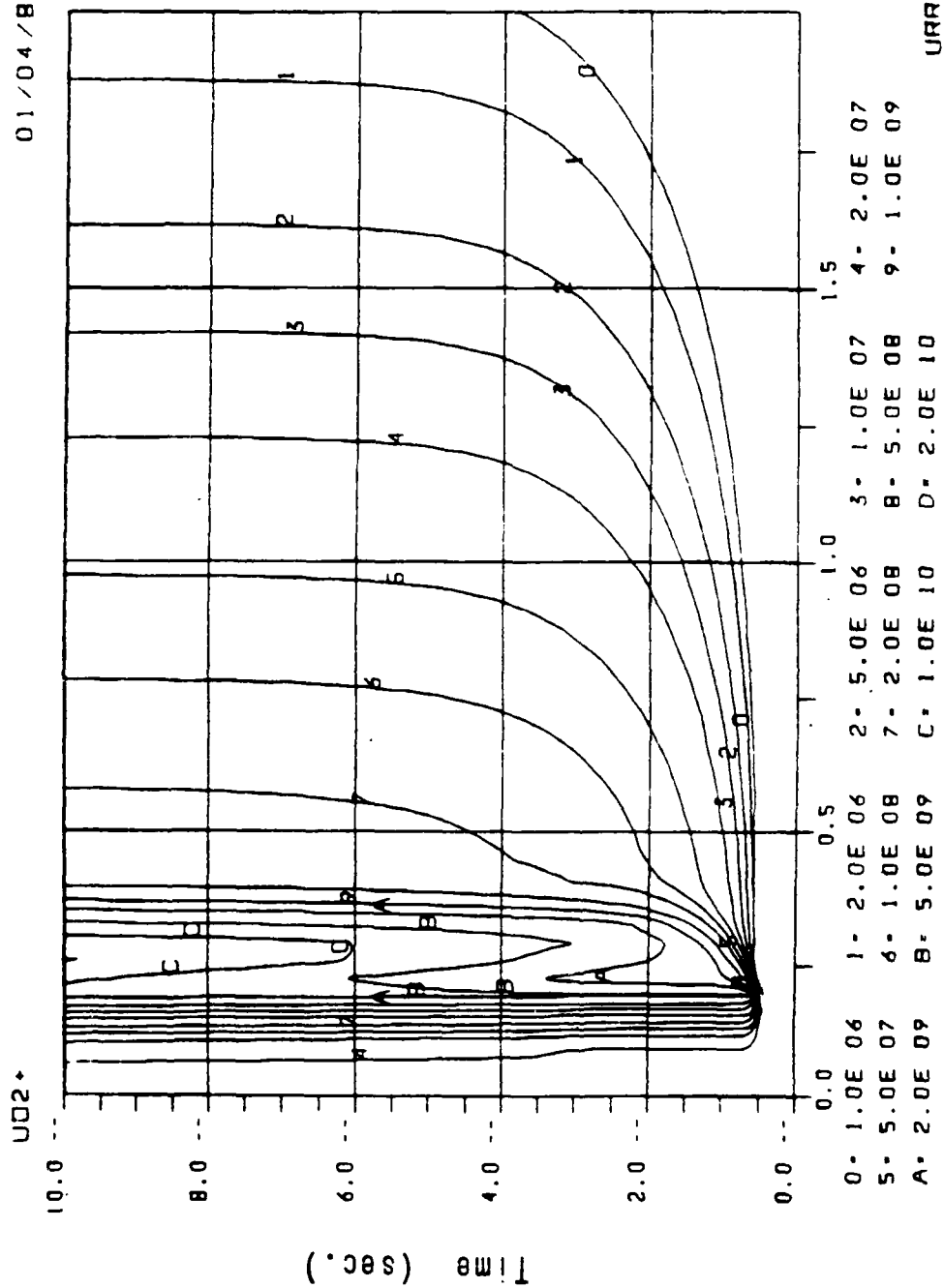


Figure 13. UO_2^+ concentration contours. Notice shell which forms gradually in time as UO_2^+ is oxidized by O_2 at about 0.25 km from release point.

01/04/B3

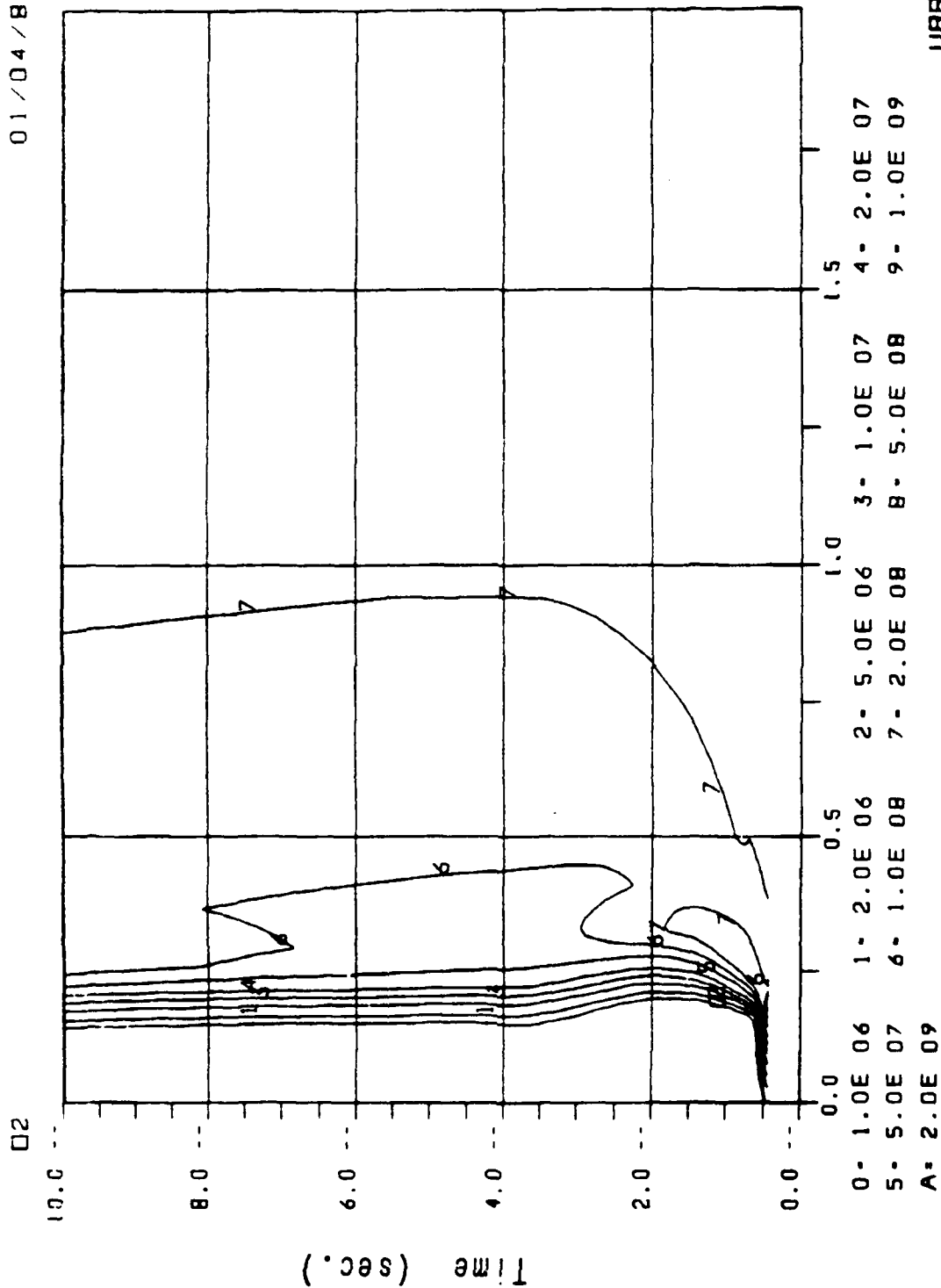
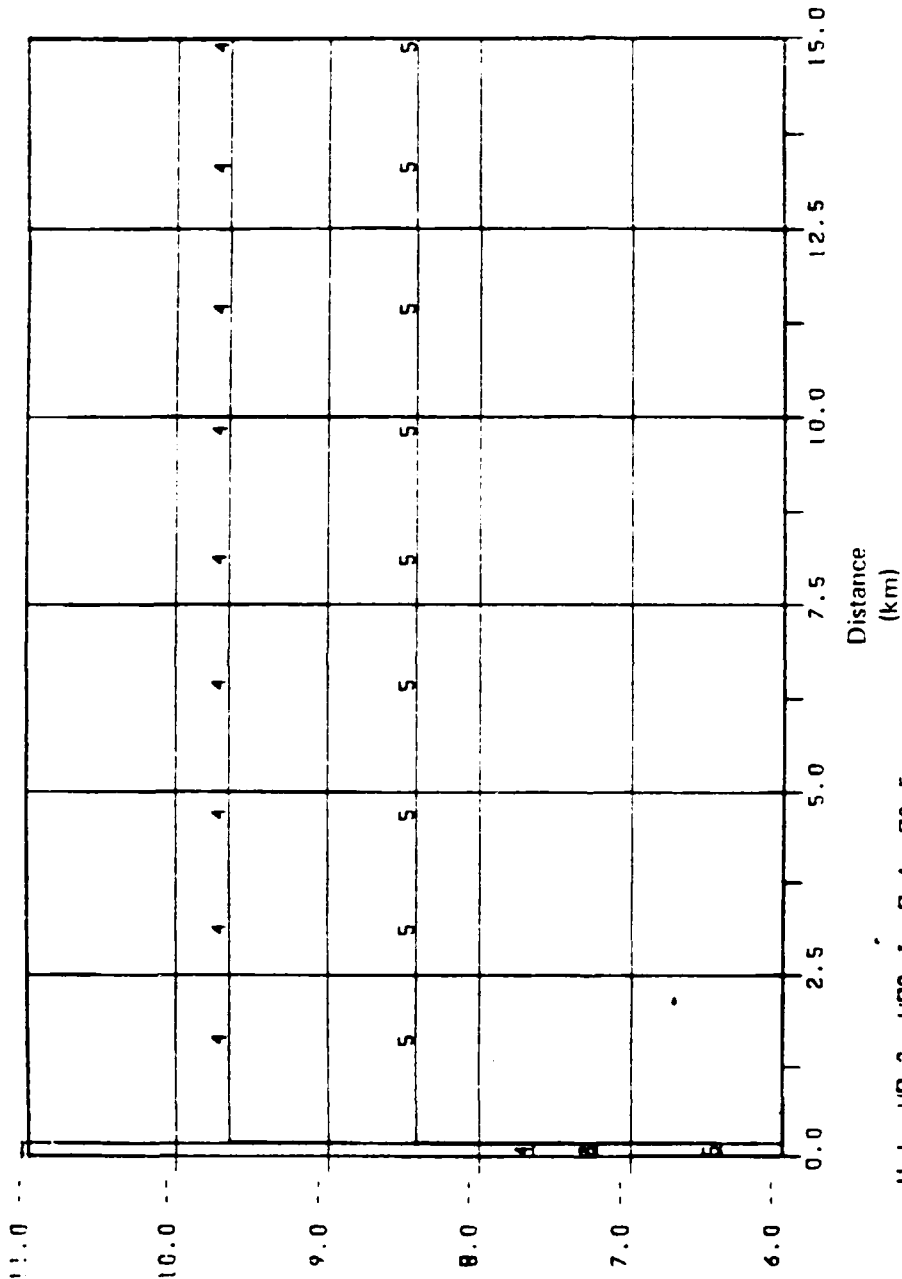


Figure 14. O_2 gas concentration contours. Notice deep hole created in O_2 near the release point which is only able to refill very slowly.

01/04/83

TIME 0.00E 00

NUM. DENS. LOG10



URRI

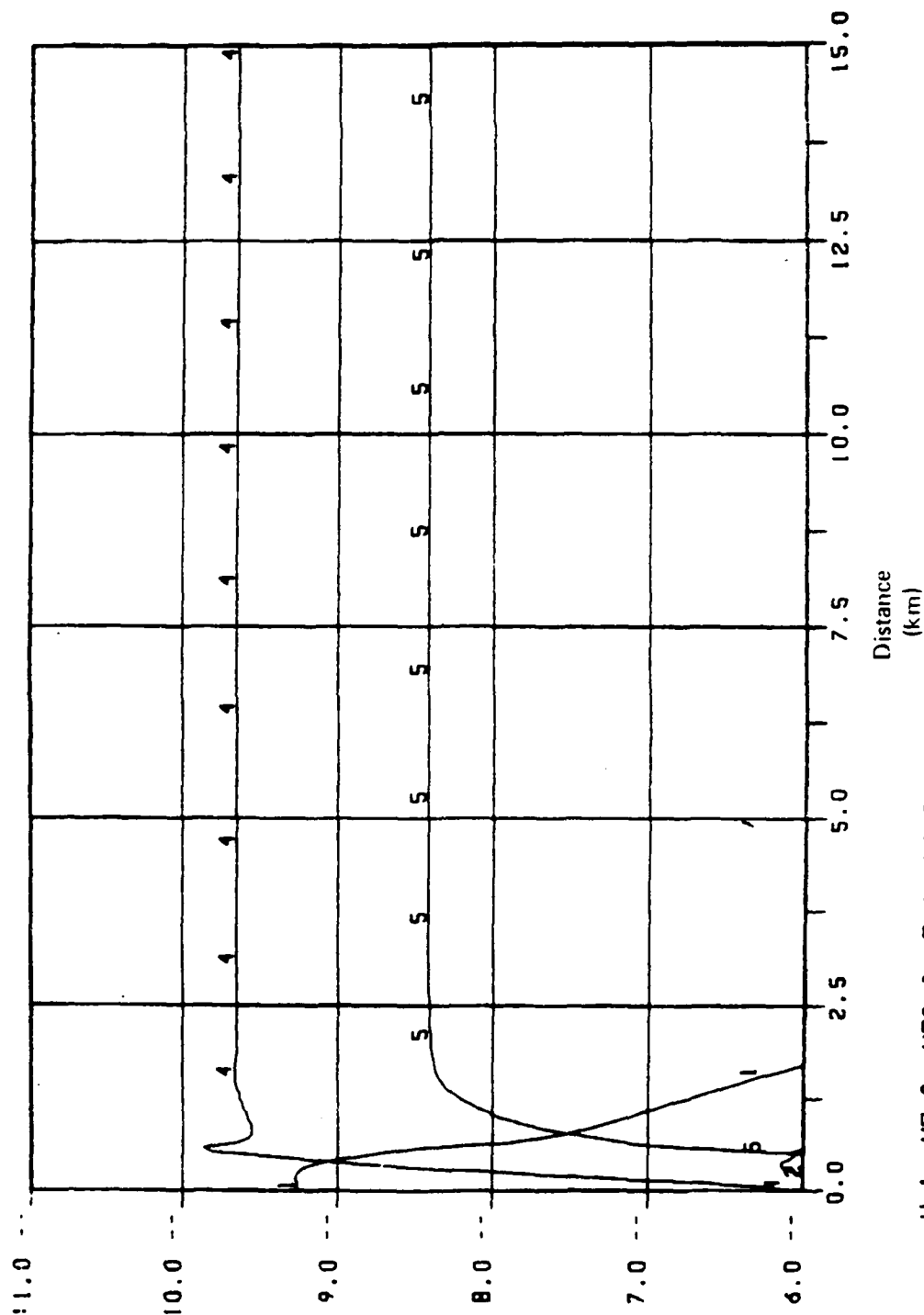
U-1, U0-2, U02-3, 0-4, 02-5

Figure 15. Initial conditions for simulation parallel to geomagnetic field and normal diffusion. Same species are shown as in Fig. 1. Note the greatly expanded horizontal scale from Fig. 1.

01/04/83

TIME 2.00E 00

NUM. DENS. LOG10



URRI

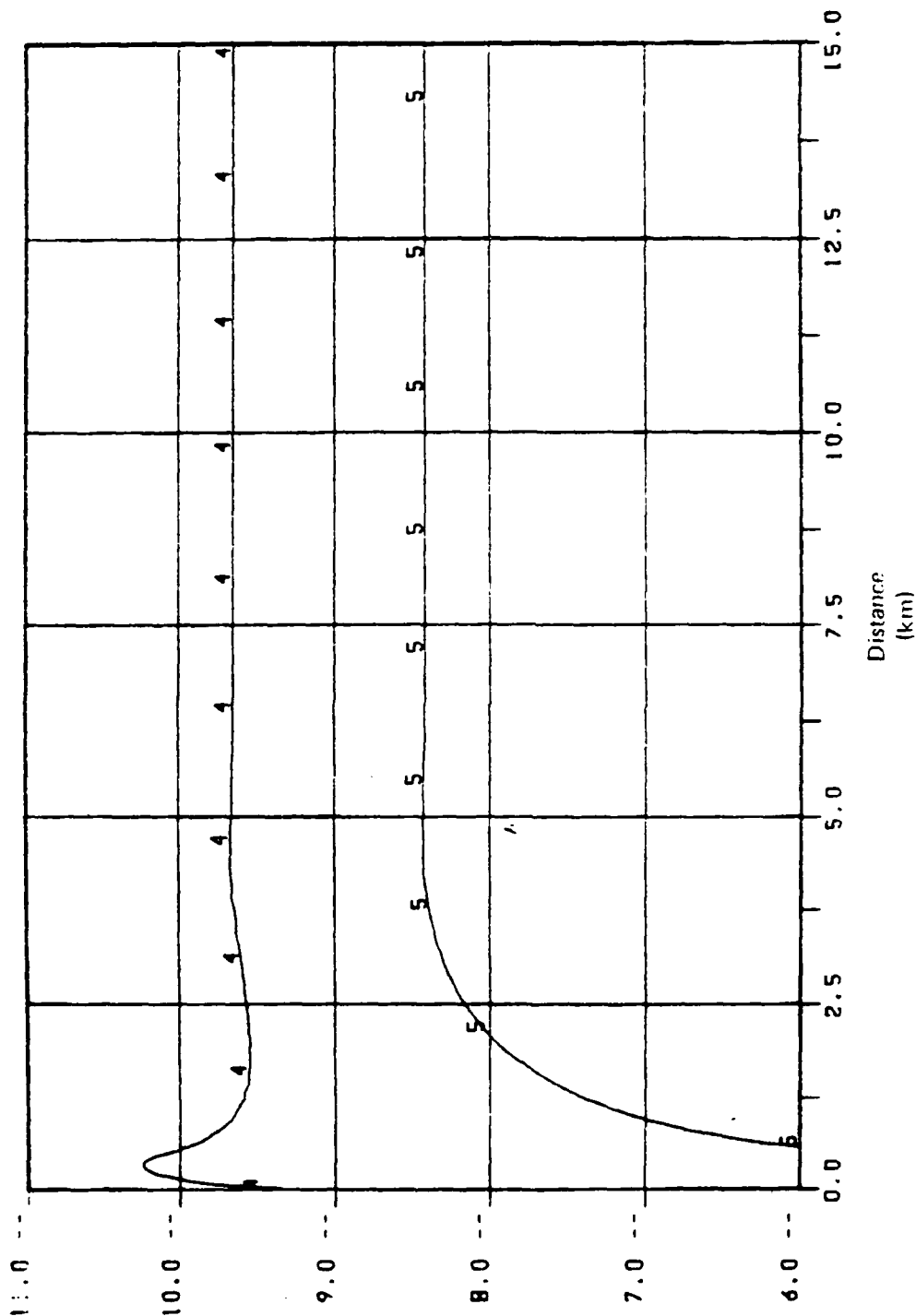
U-1. U0-2. U02-3. 0-4. 02-5

Figure 16. Neutral gas concentrations at 2 seconds after release.

01/04/B3

TIME 5.01E 00

NUT. NUM. DENS. LOG10



U-1, UD-2, UD2-3, D-4, D2-5

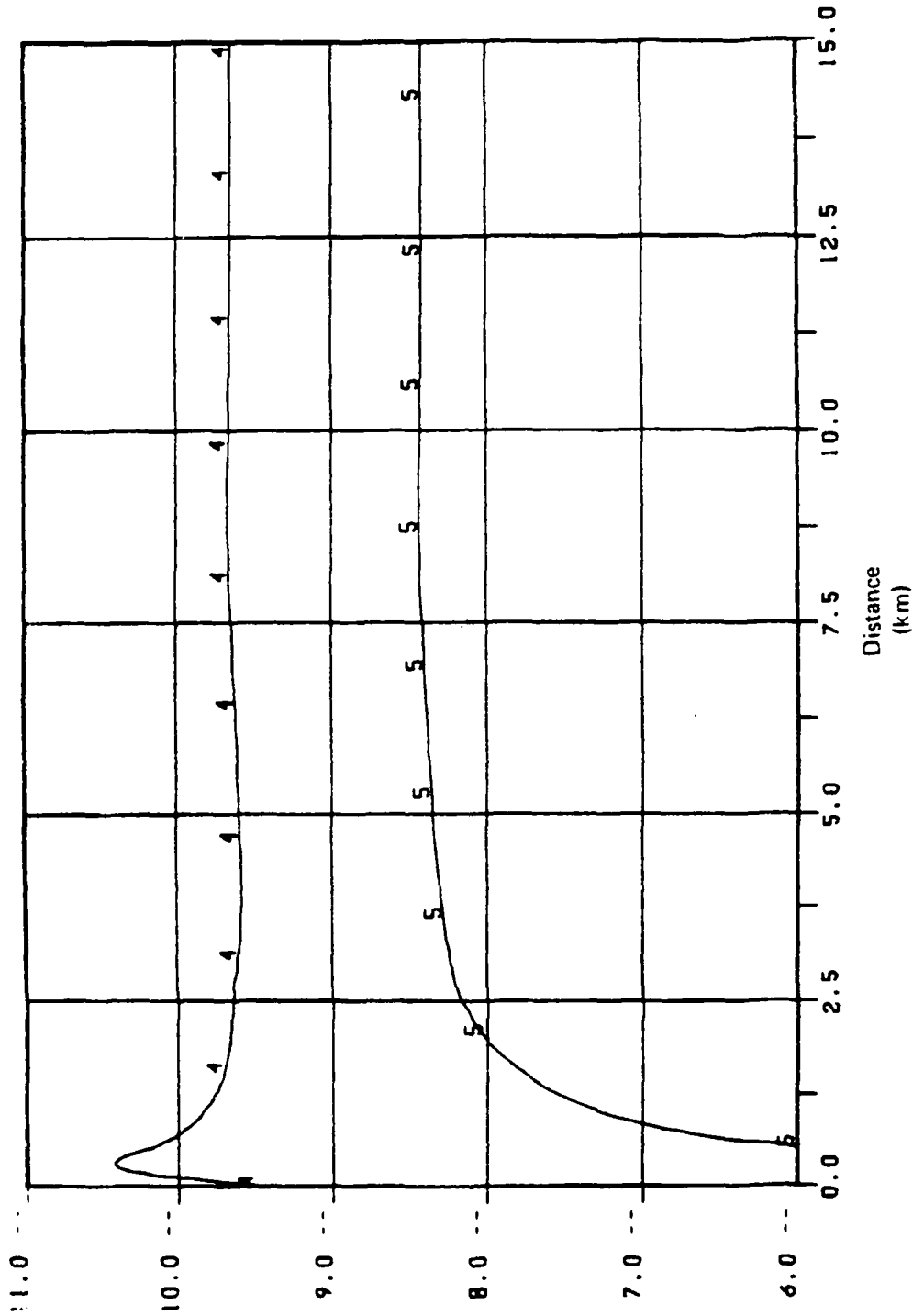
URRI

Figure 17. Neutral gas concentrations at 5 seconds after release.

01/04/83

TIME 1.00E 01

NUT. NUM. DENS. LOG10



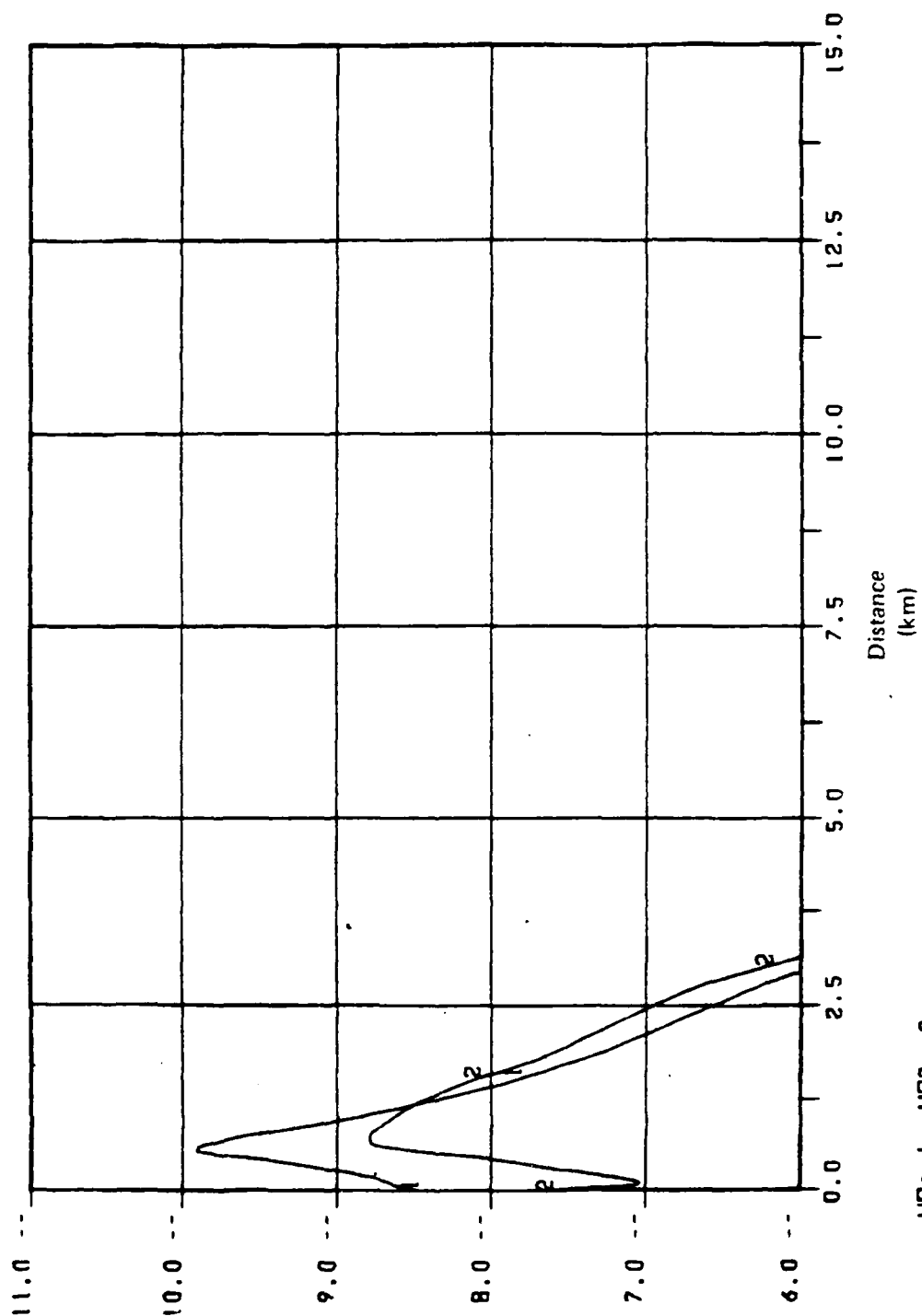
URRI

Figure 18. Neutral gas concentrations at 10 seconds after release.

01/04/B3

TIME 2.00E 00

ION. NUM. DENS. LOG10



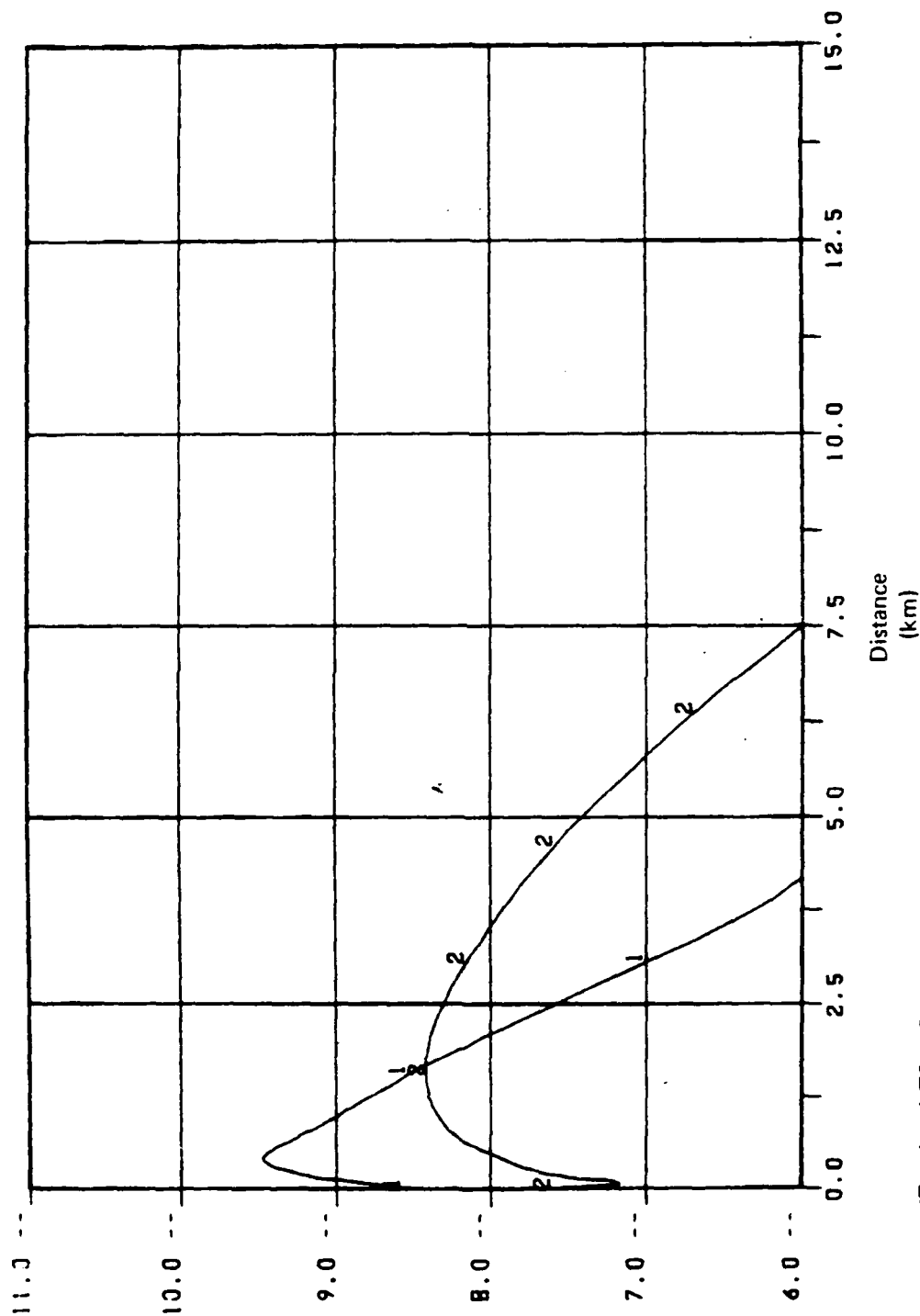
URRI

Figure 19. Ion concentrations for parallel simulation at 2 seconds, after release. Same species are shown as in Fig. 5.

01/04/83

TIME 5.01E 00

ION. NUM. DENS. LOG10



URRI

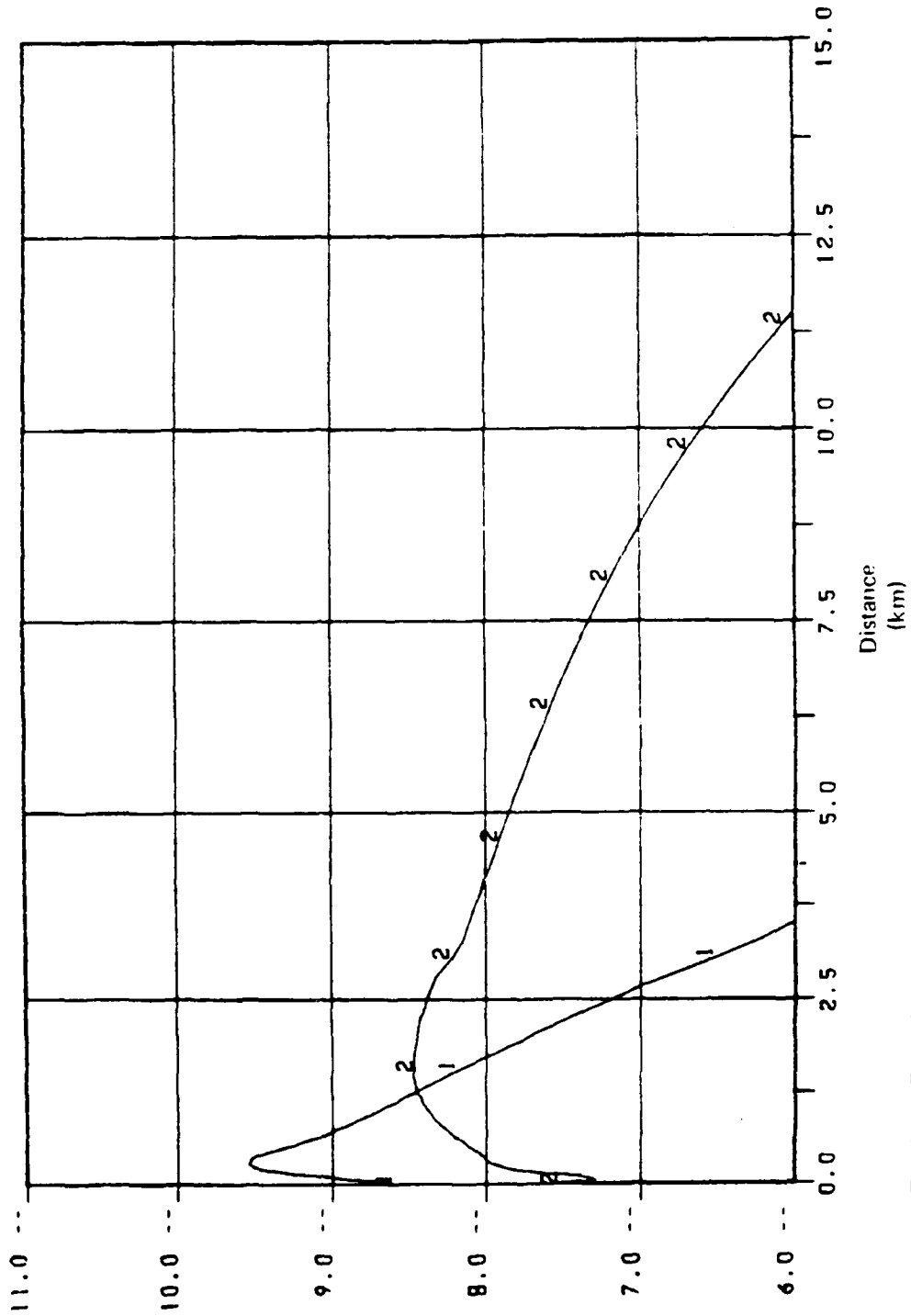
UO2+ 1. UO2++ 2

Figure 20. Ion concentrations at 5 seconds after release.

01/04/83

TIME 1.00E 01

ION. NUM. DENS. LOG10



UD*-1, UD2*-2

URR1

Figure 21. Ion concentration at 10 seconds after release.



Figure 22. U_0^+ concentration contours versus time and distance from release

point for simulation parallel to geomagnetic field. Contours are

in cm^{-3} . Notice shell formation at about 0.5 km from release

point which is slowly consumed by oxidation to UO_2^+ .

01/04/B3

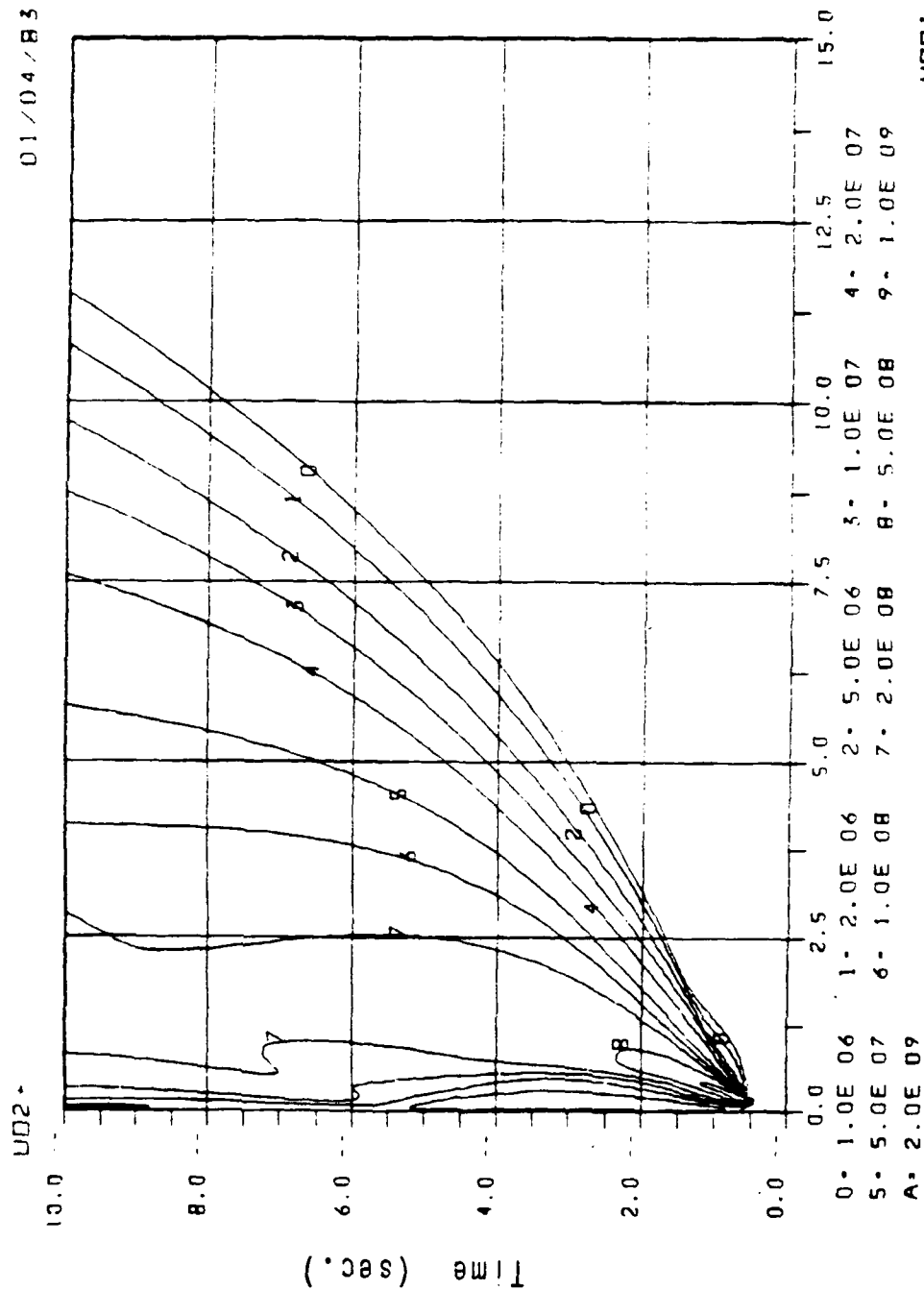


Figure 23. UD_2 concentration contours. Shell formation again takes place near release point, but in this case it spreads outwards owing to the action of nominal diffusion.

01/04/B3

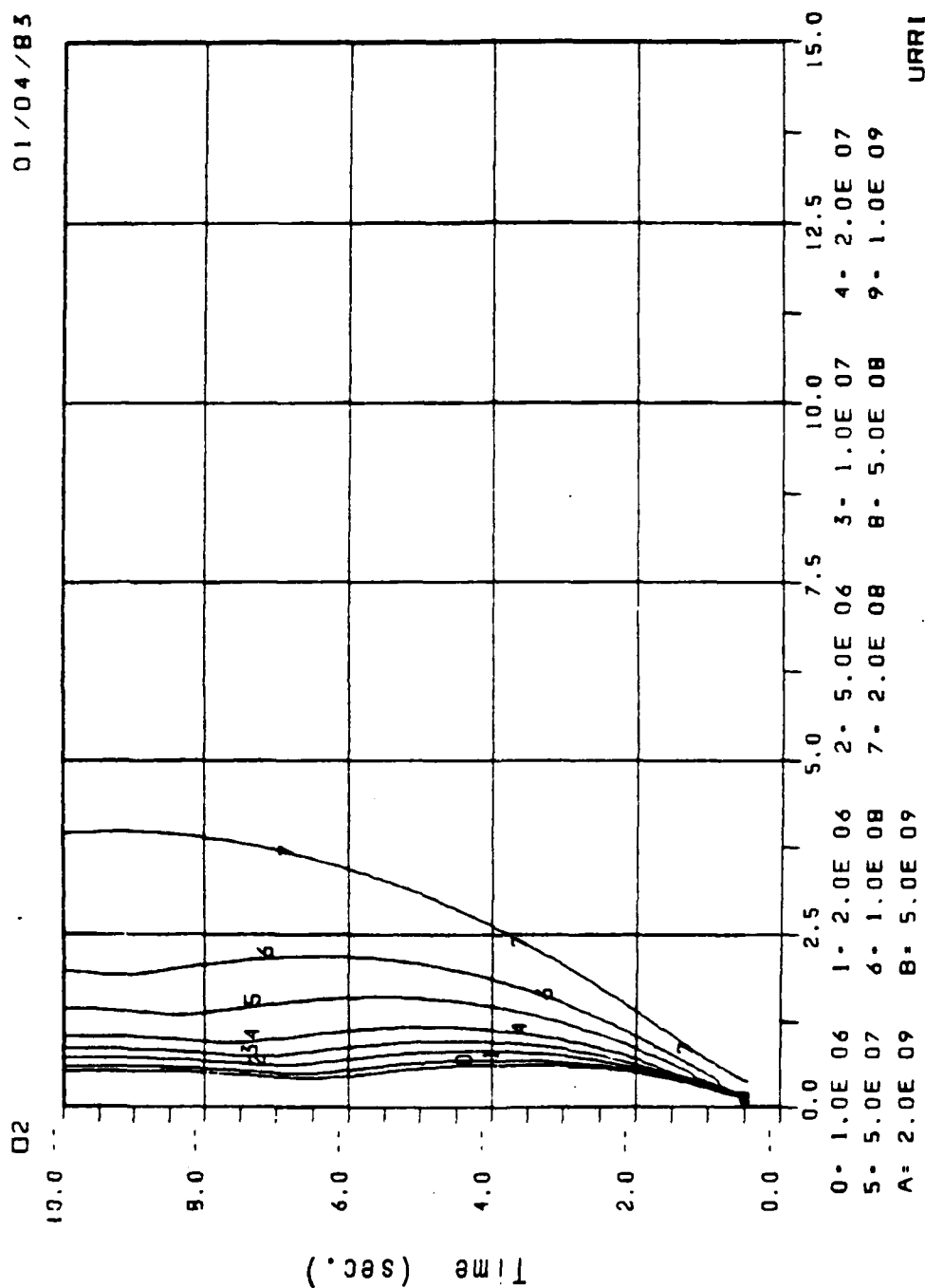


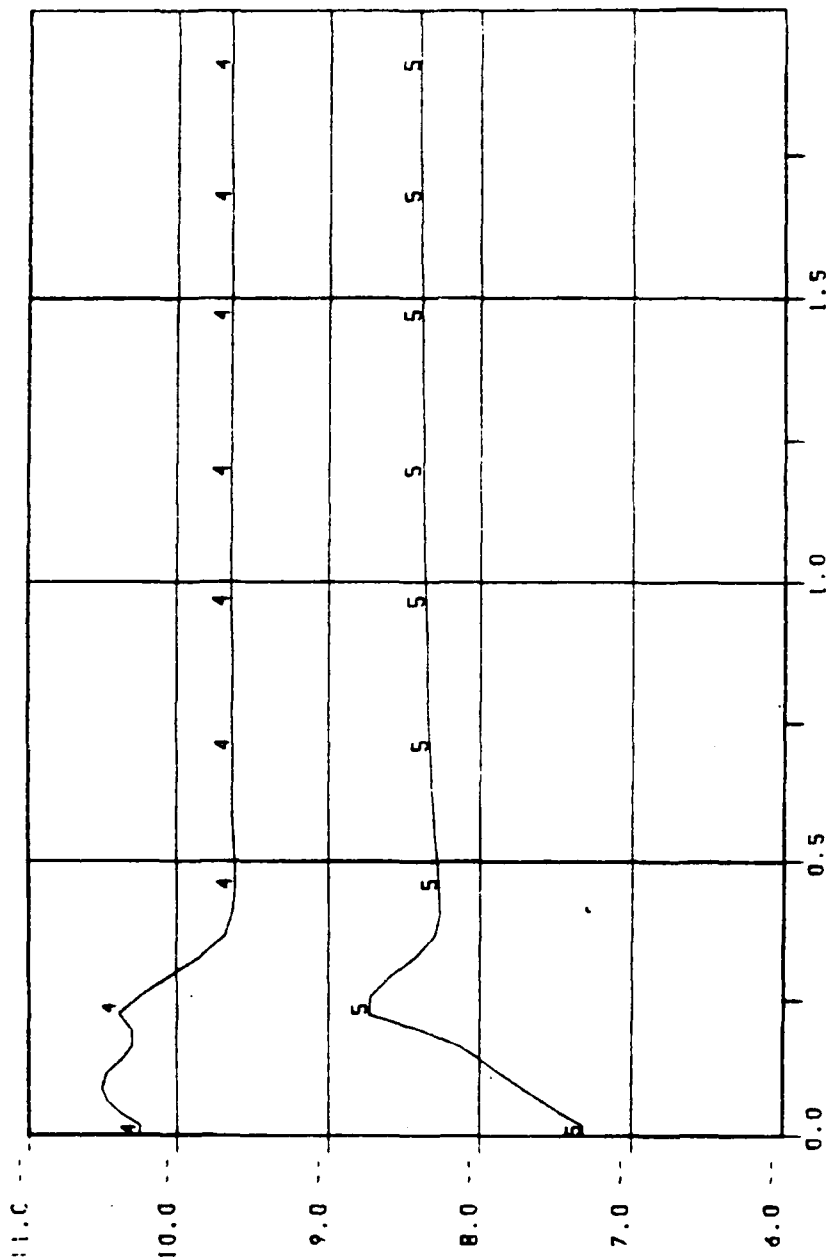
Figure 24. O₂ concentration contours. Note again the deep hole in O₂ formed

In vicinity of release which only gradually refills after oxidation of U and UO₂ ceases.

01/05/83

TIME 1.00E 01

NUT. NUM. DENS. LOG10



Distance (km)

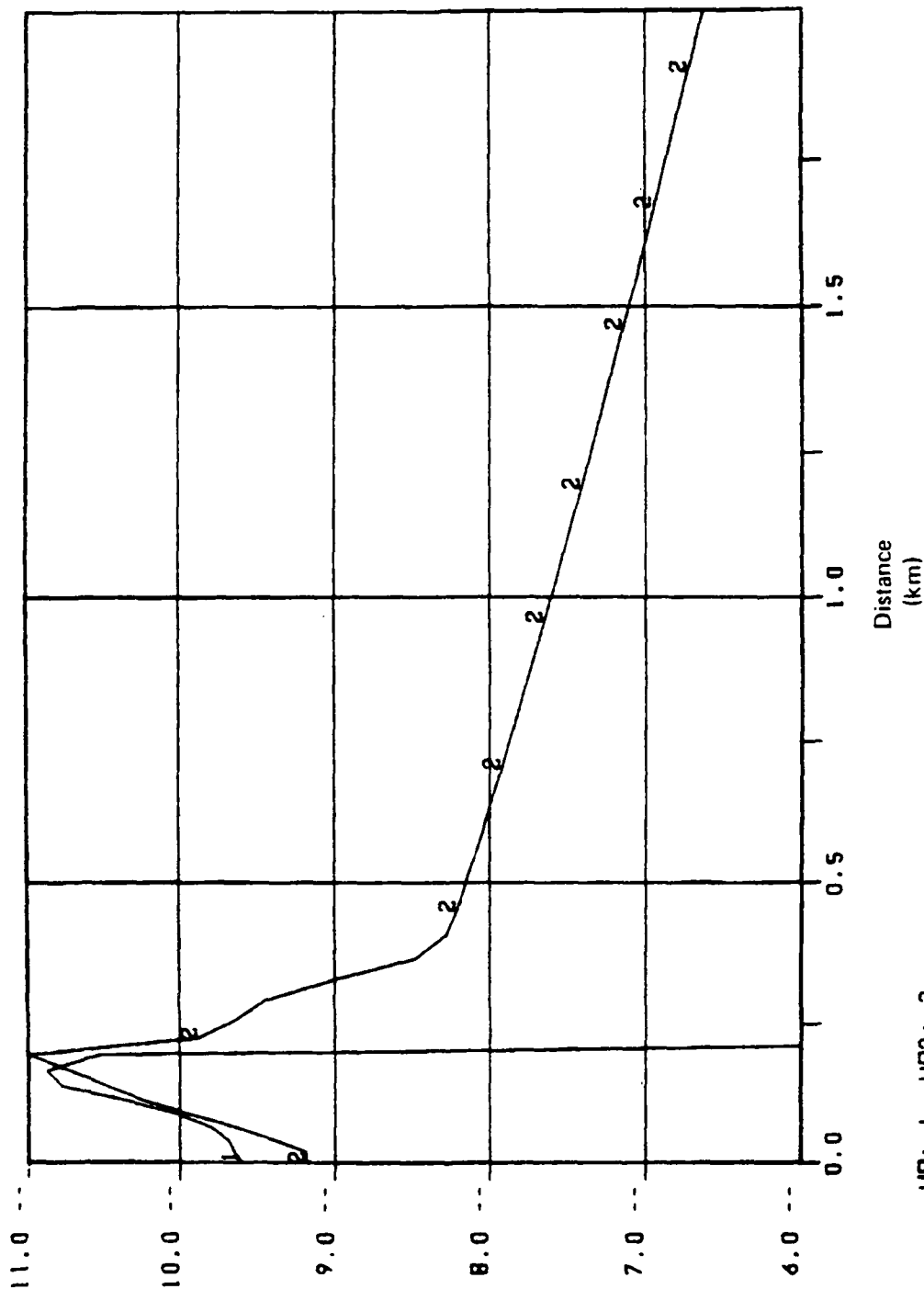
U-1. U0-2. U02-3. 0-4. 02-5

UR03

Figure 25. Neutral gas concentrations at 10 seconds for simulation perpendicular to geomagnetic field and faster than nominal diffusion.

01/05/83

ION. NUM. DENS.LOG10 TIME 1.00E 01



UD+1. UD2+2

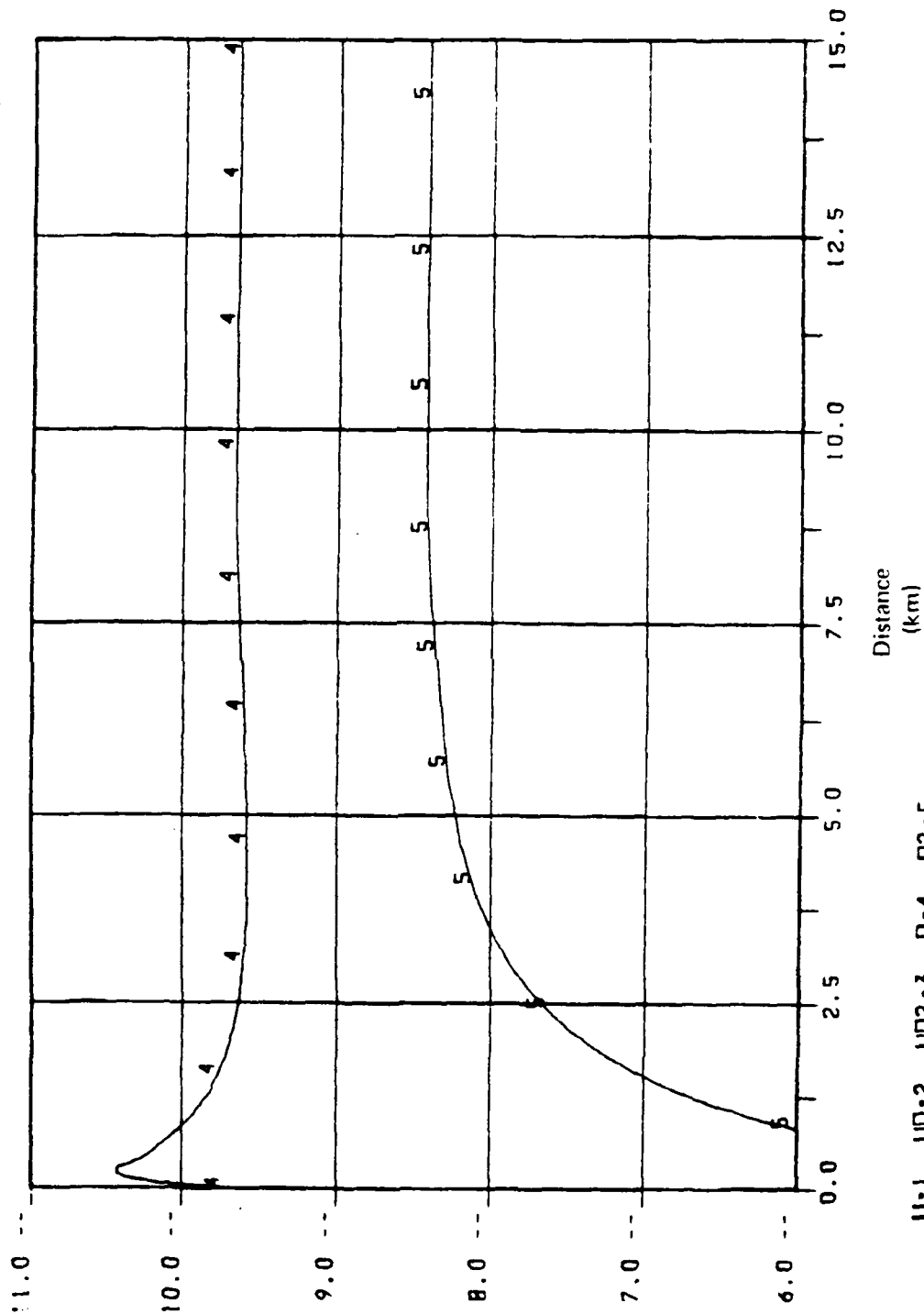
UR03

Figure 26. Ion gas concentrations at 10 seconds for simulation perpendicular to geomagnetic field and faster diffusion.

01/05/83

TIME 1.00E 01

NUT. NUM. DENS. LOG10



U-1, U0-2, U02-3, 0-4, 02-5

UR13

Figure 27. Neutral gas concentrations at 10 seconds for simulation parallel

ION. NUM. DENS. LOG10

TIME 1.00E 01

01/05/83

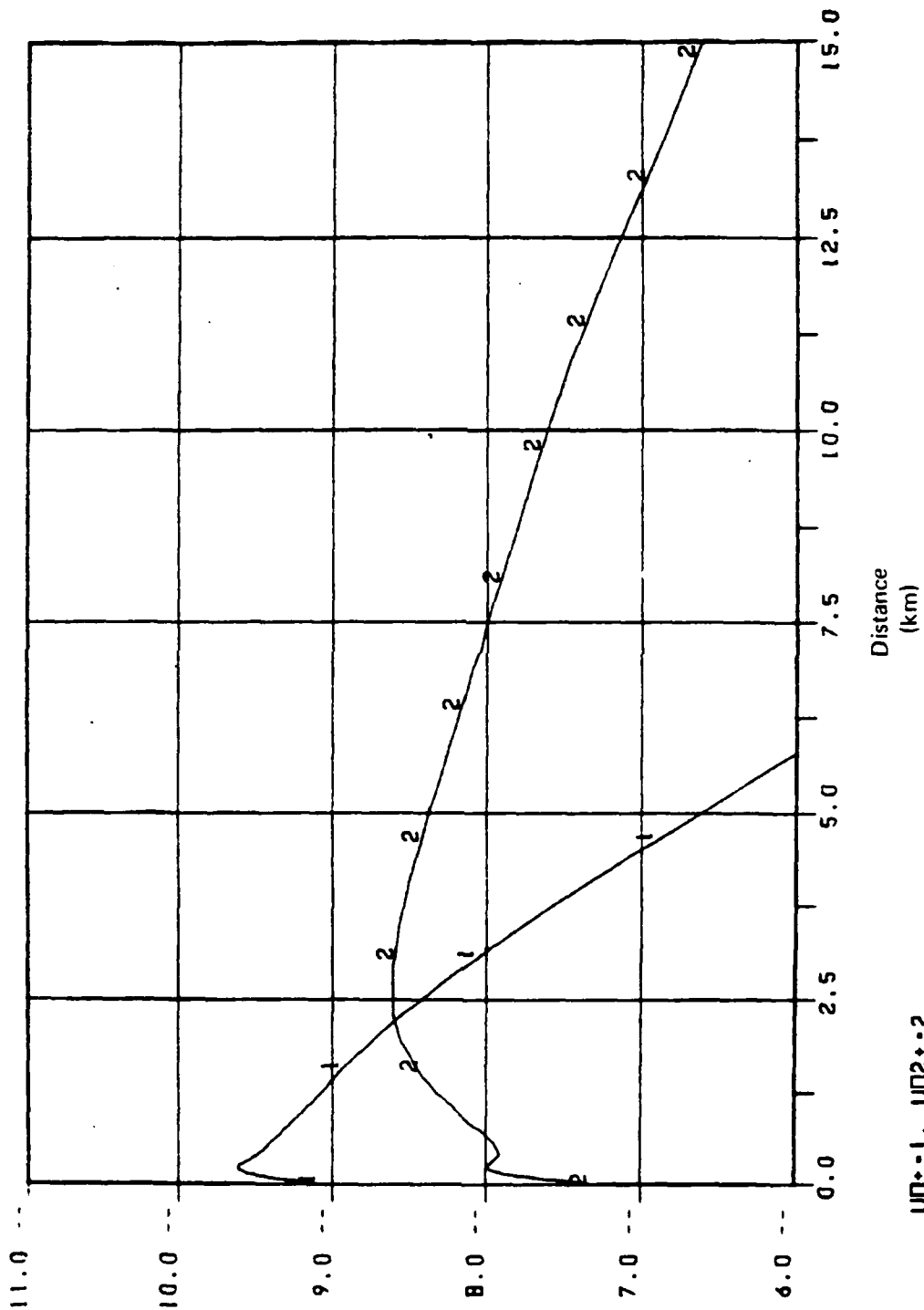


Figure 28. Ion gas concentrations at 10 seconds for simulation parallel to geomagnetic field and faster diffusion.

References

- Archer, D.H., letter from Archer to Lt. Col. McKechney DNA-RAEE, 27 August, 1982.
- Armstrong, R.A., "An Analysis of the Potential for LWIR Emission From Uranium and Aluminum Oxide After a Nuclear Airburst", Air Force Geophysics Lab., AFGL-TR-82-0064, 26 October, 1981.
- Burgers, J.M., Flow Equations for Composite Gases, Academic Press, New York, Chap. 3, 1969.
- Linson, L.M., "Slab Release and Onset Time of Striations in Multiple Barium Release Studies, KMR Ionospheric Monitoring Program, Spring 1975, HAPREX Final Report V.3 Stanford Res. Inst. Int., Menlo Park, CA., October, 1978.
- Reidy, W.P., "LWIR/Structural Release Characteristics," Proceedings of the DNA Infrared Program Meeting, 23-24 January, 1980.

APPENDIX O
HANE STRUCTURE AND EMISSION MODELS

E. Hyman
Science Applications, Inc.

M. Mulbrandon
Naval Research Laboratory

and

N. Zabusky
Fluid Sciences, Inc.

HANE STRUCTURE AND EMISSION MODELS

E. HYMAN*
M. MULBRANDON
N. ZABUSKY**

NAVAL RESEARCH LABORATORY

*SCIENCE APPLICATIONS, INC.

**FLUID SCIENCES

HANE STRUCTURE & EMISSION MODELS

In this presentation I am going to discuss a model for a HANE striation and the PSD that results when you make a 1D optical scan of the striation, assuming emission is optically thin. I am going to investigate how the PSD varies as you change parameters of the model or as you change the direction from which you view the striation. I will also present some initial multi-striation effects. As a preliminary to that, I will exhibit three idealized scan emission profiles and indicate the corresponding spectral index. (Viewgraph 1). The first profile is the top hat. It is the emission profile that you might observe if you scan directly down the magnetic field direction and scan alternately through a striation and through a place where there is no striation, or, more generally, if you scan through a striation in a direction that corresponds to an edge of the striation.

An example of what you get is shown in Viewgraph 2. This PSD comes from embedding a box consisting of 464 mesh points in an overall grid of 4096 mesh points. The ordinate gives the log of the square of the Fourier component. The abscissa gives the mode number which goes from 1 to 2048. The figure shows the k^{-2} dependence with mode number.

A second example is what you get when you scan across circular luminous rods and this was done by Rick Hake and Jeff Casper of SRI ("Structure Mode Definition and Comparison," SRI Technical Memo Report #1, January 1982). Viewgraphs 3, 4, and 5 show respectively, the distribution in position and intensity of an array of these rods that Hake and Casper devised (Viewgraph 3), the intensity profile resulting from a scan across this array (Viewgraph 4), and the resulting PSD which goes like k^{-3} (Viewgraph 5).

Finally, in Viewgraph 6 we look at a slightly more complex emission profile. Here we have a trapezoid with 480 mesh points embedded in an overall grid of 4096 points. Of the trapezoid's 480 mesh points, 448 are in the flat region and 32 are in the linear falloff region. What you get is two distinct regions: one in which there is a k^{-2} falloff, and then, at larger k , a region with a

falloff. That you get two distinct regions results from the fact that the trapezoid's linear falloff region is much smaller than its flat region so that there is a separation of scales. If the flat and linear falloff regions were comparable in size, there would be no distinct separation into a k^{-2} and a k^{-4} region.

We now present a tentative analytic model of a HANE striation based on parameters suggested by Zalesak and Fedder of NRL, Viewgraph 7. As shown by the expression for $F(\theta)$ there is an inner region where the density of electrons is assumed constant. Outside this region the density falls off radially with a gaussian dependence that varies with angle but falls to zero at the outer edge. The inner border is composed of two ellipses designed so that the minor axis of one is the major axis of the other. Where they meet the slopes, therefore, match. The same is true at the outer border. The particular analytic form we have chosen is based on an attempt to match parameters suggested by the NRL theory, while keeping the analytic expressions simple. The parameter A, used to insure that we go to zero on the outer ellipses, was chosen to be 3 for these studies. There is no unique reason why this analytic form is necessarily correct and we will want to look at other possibilities in the future. By varying parameters of the ellipses we can change the sharpness of the edges and vary the ratio of the edge dimension in front to that on the sides. The viewgraph indicates what is meant by a 0° scan and a 90° scan. In general, we will scan through a variety of angles from 0° to 90° .

Viewgraph 8 shows the symmetric radiance profile, with arbitrary units, that we would measure scanning this striation from 0° and assuming that the volume emission is proportional to the electron density everywhere. Viewgraph 9 shows the skewed profile observed from 90° .

In Viewgraph 10 we show the PSD for a model in which the gaussian edge at the front is 0.1 km and at the sides is 0.3 km. The view is from 10° . The line drawn on the plot has a slope of k^{-3} and shows that there is no well defined k^{-3} region. This is because the gaussian edge of 0.3 km is so large compared to the radius of the "flat" region = 0.5 km that the gaussian behavior dominates

and there is not sufficient separation of scales to give a k^{-3} region. Nor lower scale on the abscissa where we indicate scale sizes in km.

Viewgraph 11 has the same parameters as in Viewgraph 10 but, here view from 90° . The lack of symmetry from this direction damps out the oscillations that are seen in the view near 0° and results in a nearly monotonic line indicates a k^{-3} slope, and, here, we see a good fit down to below for a k^{-3} dependence. Here we have a much better separation of scales because edge at the front ~ 0.1 km is small compared to the 1.0 km extent of the fit.

Viewgraph 12 gives a table showing variation in the 'apparent' spectral index determined from a least squares fit as a function of the angle of scan. The column on the right gives the approximate wavelength below which deviation is significant.

In Viewgraph 13 we see the result of assuming thinner edges. Here we have assumed 0.05 km both on the front and at the sides. This is a plot for scan at 0° but I have drawn in the results for 90° . Note the excellent match of the oscillating region of the 0° case to that for 90° . That is, at small scale sizes the slope and amplitude are determined just by the edge size, which is the same for both views.

Viewgraph 14 shows the 0° view for the case where the edges are 0.1 km. Viewgraph 15 shows this same model and view where, now, we assume the emission is proportional to the square of the electron density. By over these various cases one can see how the PSD drops under various assumptions in the ~ 0.1 km wavelength domain.

Viewgraph 16 is a photograph of Checkmate striations from Chesnut ("Spatial-Frequency Analysis of Striated Nuclear Phenomena, Part 2. A Model of the Striated Checkmate Cloud" (U), DNA 27577, April 1972, CONFIDENTIAL). A semilog plot of the scan 650 in this viewgraph is exhibited in Viewgraph 17, also from Chesnut. By matching parameters with a detailed measurement by Chesnut of an individual striation we conclude that for that striation our model gives a good fit if in viewgraph 7 we take the core size to be 1.4 km, the tail region 7 km, and assume that we view the striation from an angle of 10° . We have used the square of the density to get the emission profile under the assumption that the emission is due to the recombining plasma.

A plot of the power spectrum of a striation with the above parameters (plotted semilog to match the scale in viewgraph 17) is shown in Viewgraph 18. By overlaying viewgraphs 17 and 18 we see that there is a good fit except for the minima exhibited in Viewgraph 18 (only the first of which is above the noise limit due to the photographic grain size). Also the very low k dependences of the viewgraphs do not match.

If we go to multiple, but identical, striations and place them randomly, subject to the two hump distribution resulting from the large scale horseshoe structure of Checkmate, we get the radiance profile shown in Viewgraph 19 and the power spectrum of Viewgraph 20. This again is a fairly close fit to the data but has the same minima as in Viewgraph 18.

One way to get rid of the minima is to assume there is a size distribution since then each different size striation will exhibit a minimum at a different location and the minima will be smeared out. There is another possibility, however, which does not require a range of striation sizes. While the individual striation profile that Chesnut studied appeared to be viewed from 10° (in terms of our model) the entire scan spans a range of viewing angle of $\sim 30^\circ$. If one averages power spectra from striations viewed at various angles from 0° to 30° the minima again get smeared out because of the noncylindrical symmetry of our model. Thus, a substantial range of striation sizes does not appear to be necessary to fit the data.

Viewgraph 21 is the power spectrum of Viewgraph 20 plotted on the more standard log-log scale. The k^{-4} line is plotted and shows a good fit of the data to a k^{-4} spectral dependence. This dependence has been found in the Che mate data before, although because of limitations of film noise, the dependence was seen over only a small range of k values. Our model predicts that the dependence should be valid to much smaller scale sizes than the data can give.

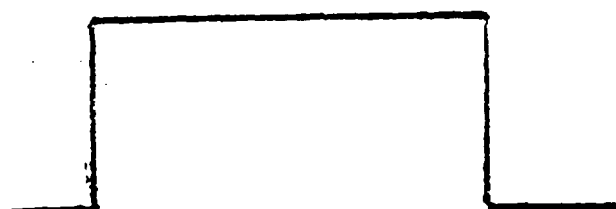
What is the significance of the k^{-4} dependence? If, in viewgraph 7, the striation consisted merely of the core region, with sharp edges, we would expect a k^{-3} falloff. Because of the long tail that is postulated in our model viewing the striation from 0° or near 0° , the emission profile changes from rounded elliptical arc to a triangular-like shape. But a triangular emission profile results in a k^{-4} dependence. Thus, the observation in the data of a k^{-4} spectral dependence is evidence for the long tail we have postulated.

Finally, it is possible to get a good fit, at low k values, to the data in viewgraph 17 if it is assumed that the striations are not randomly placed under the double gaussian of viewgraph 19, but instead tend to clump in bunches with ~ 20 km dimensions. There appears to us to be some justification in the data for this. Whether this is just a chance grouping of the striations for this particular data or represents something more fundamental must be the subject of further study.

POWER SPECTRAL INDICES FOR SIMPLE EMISSION PROFILES

Profile

$$|\hat{F}(k)|^2$$



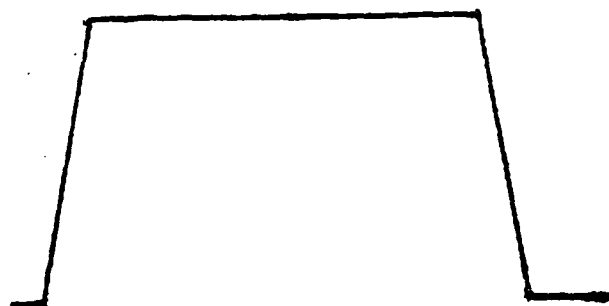
Top Hat

$$\sim k^{-2}$$



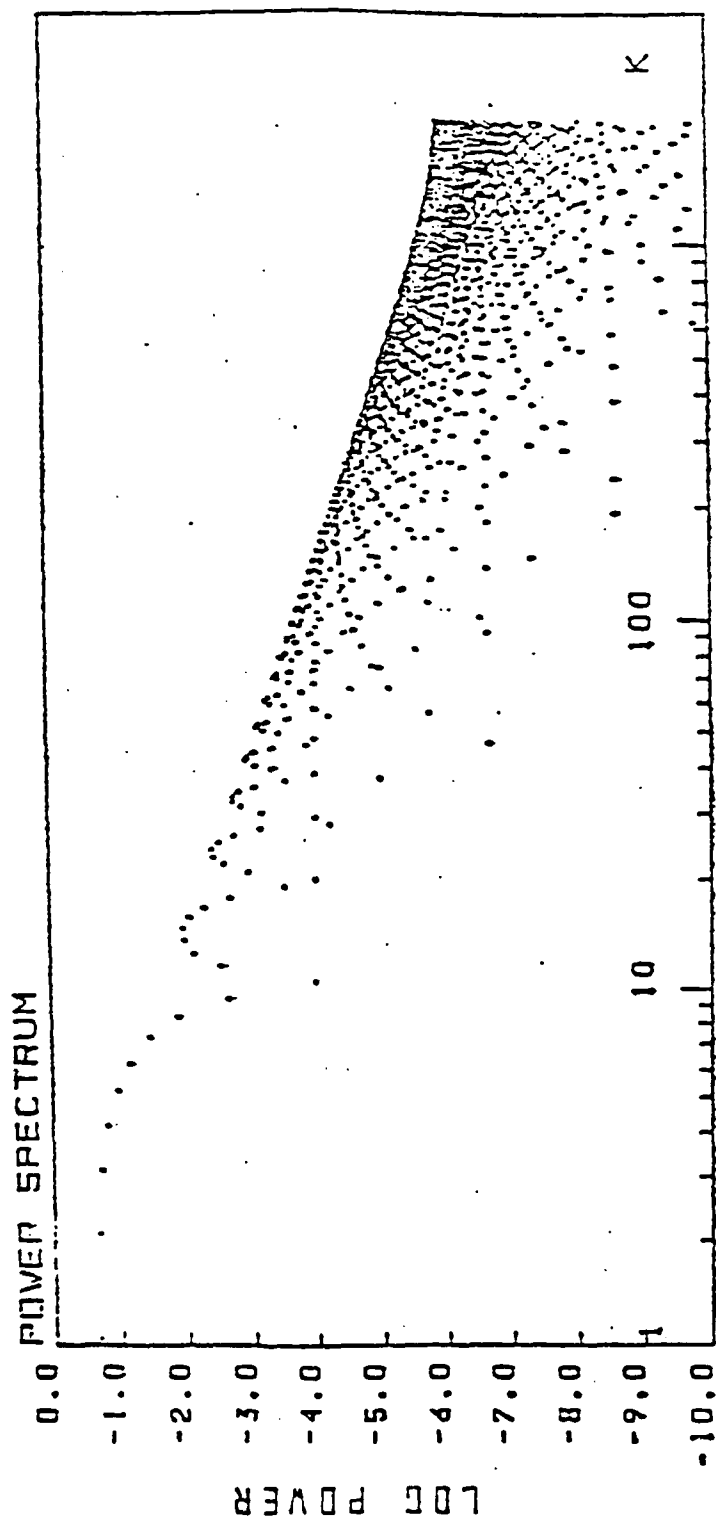
Circle

$$\sim k^{-3}$$



Trapezoid

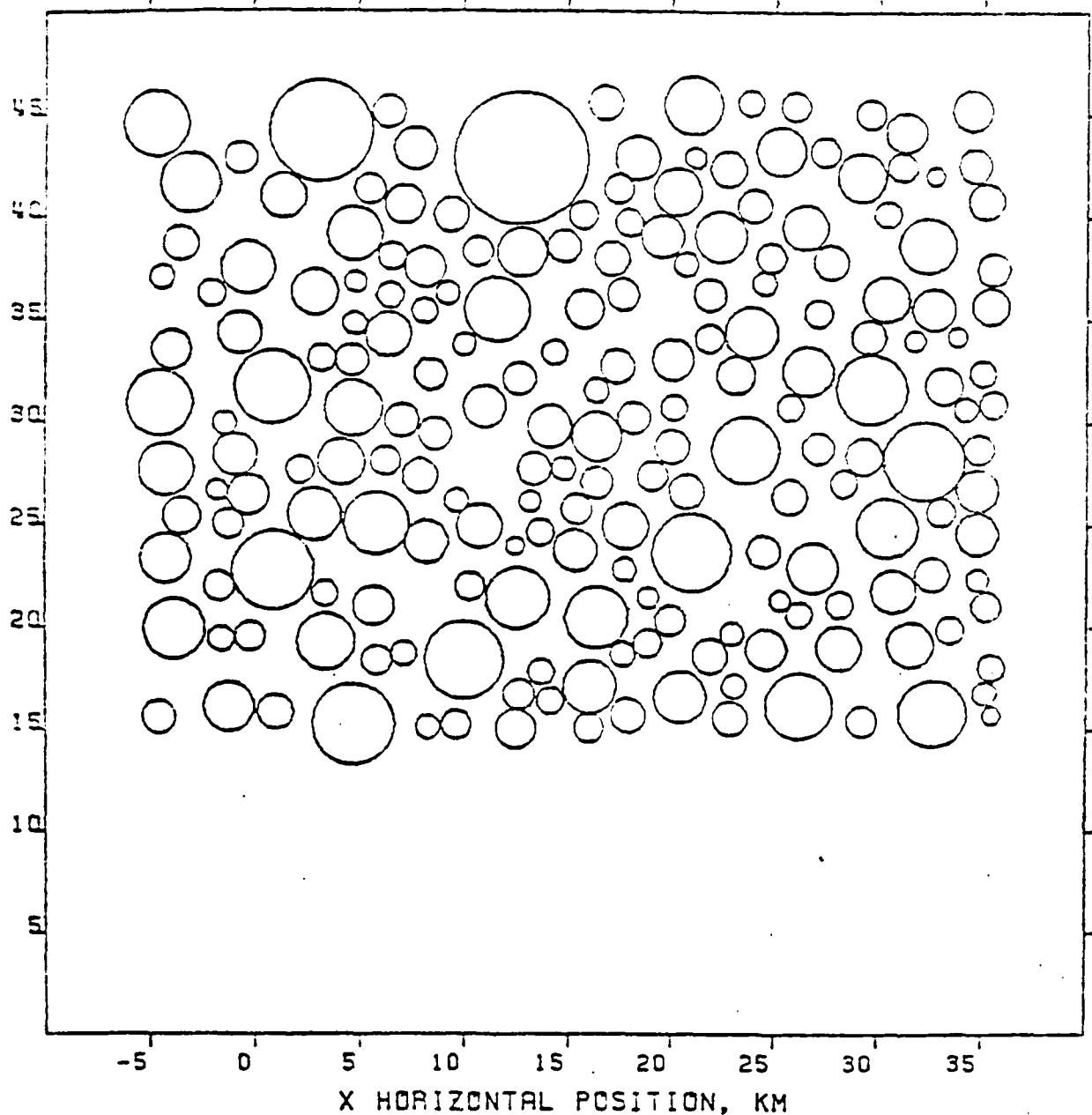
$$\sim k^{-2} \rightarrow k^{-4}$$



KM

MODEI 9200000

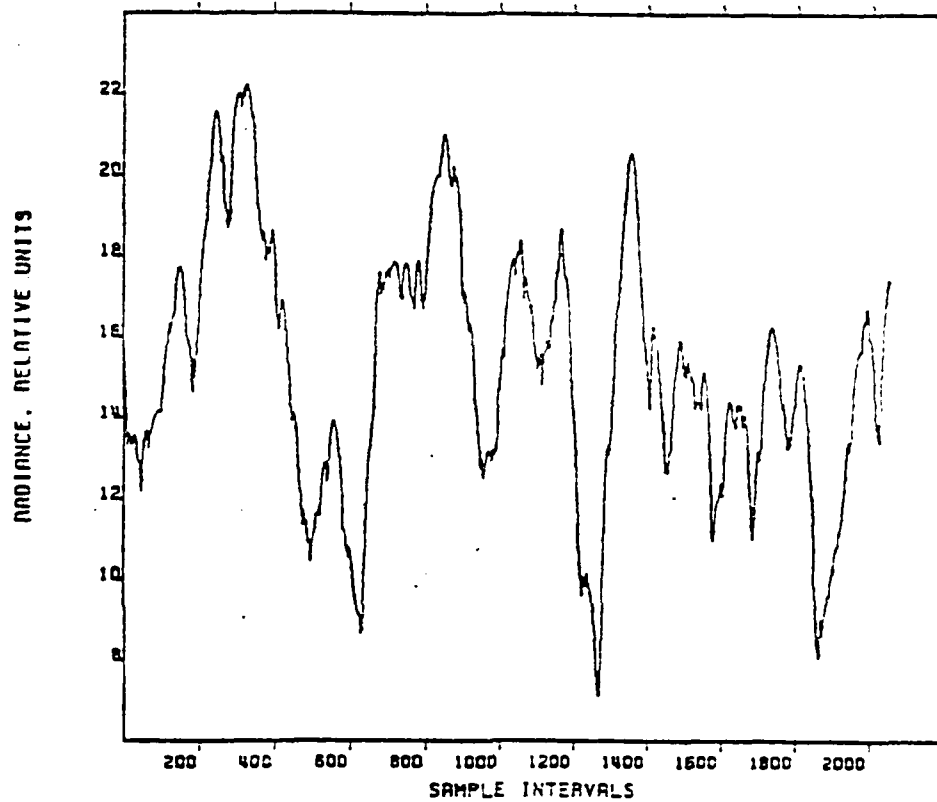
STRIATION SIZE AND LOCATION



D= 17 200 STRIATIONS ACROSS 41X 31 KM
 CLE SHOWS LUCITE ROD STRIATION FILL FACTOR= .5027
 C 21, 1981, 14:23:23.250

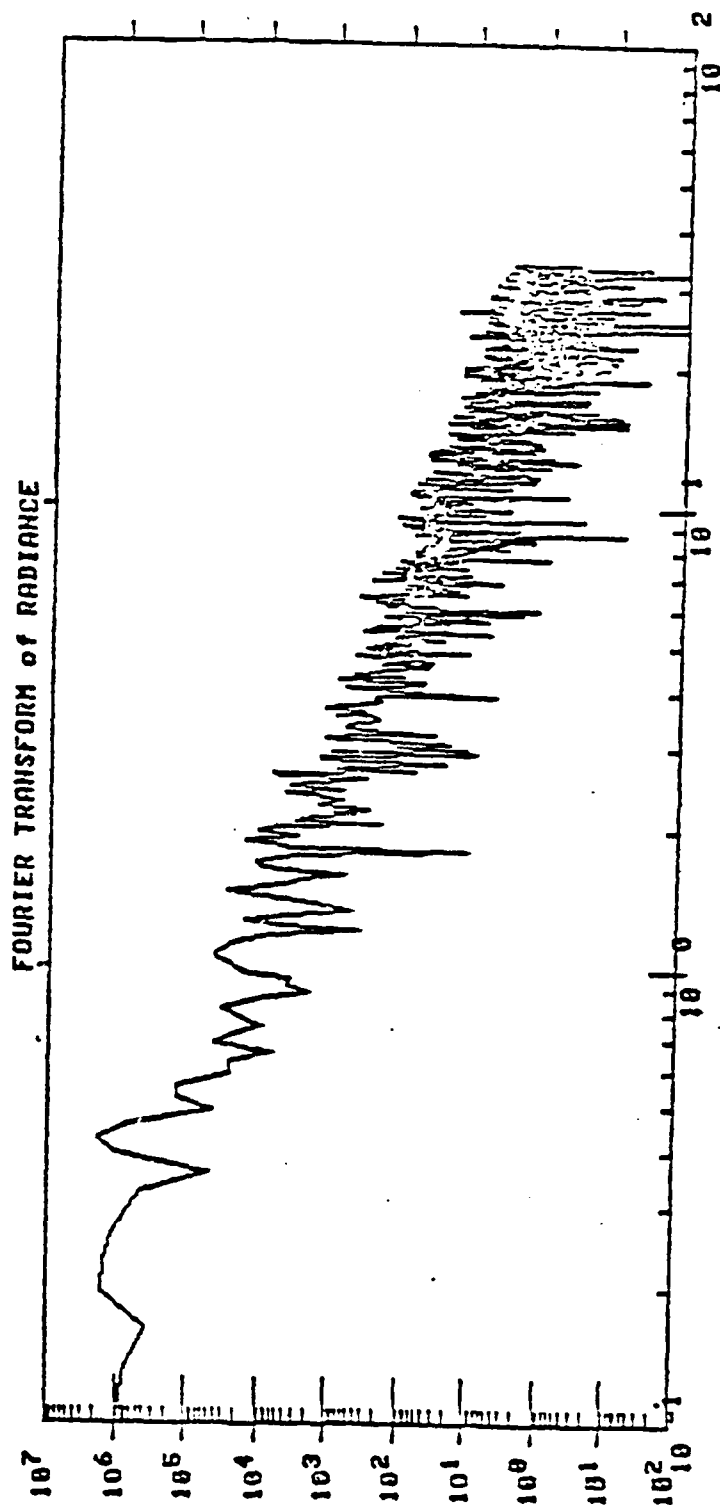
Figure 4

LUCITE ROD STRIATION RADIANCE



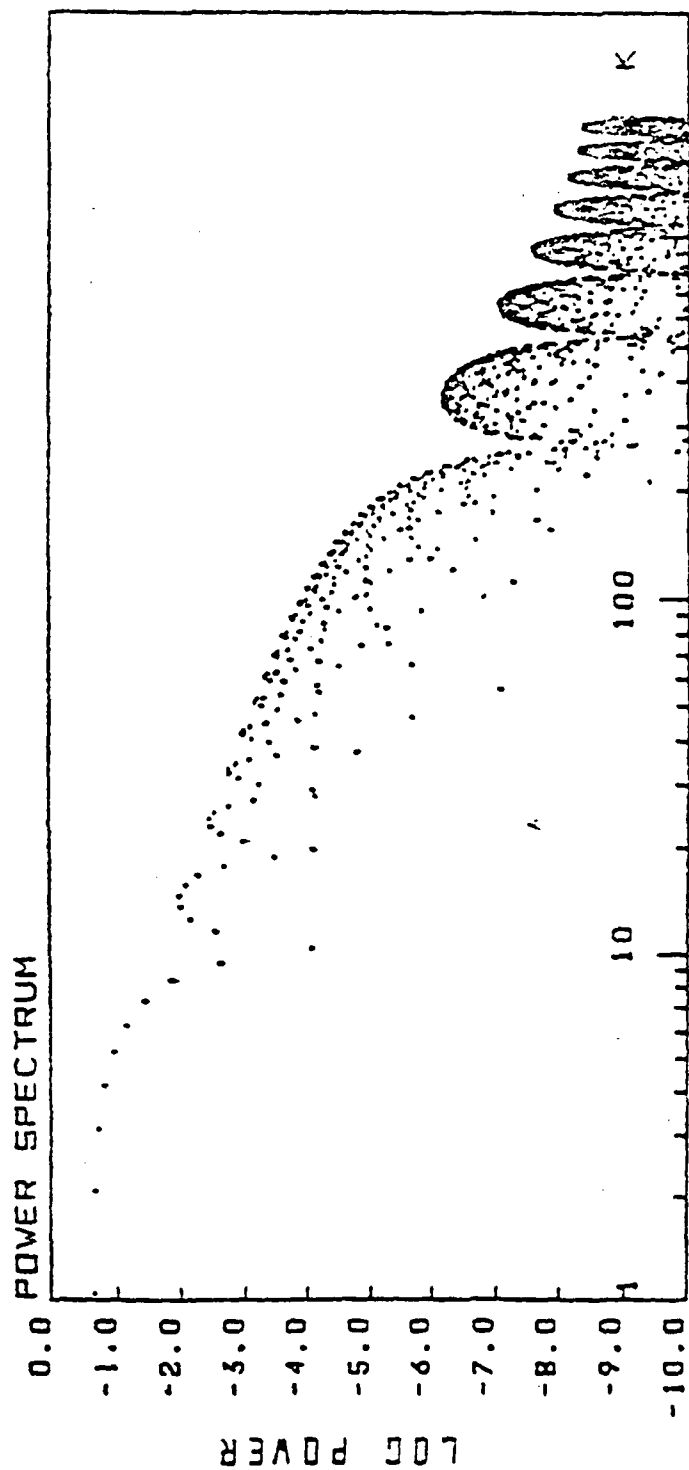
LUCITE ROD STRIATIONS
MEAN=15.2365 STANDARD DEVIATION= 3.132771
DEC 21, 1981, 14:23:23.250

Figure 5



SEED= 17 200 STRIATIONS ACROSS 41 km
 2040 SAMPLES ACROSS CENTER 31 km
 DEC 21, 1981, 14123123.250

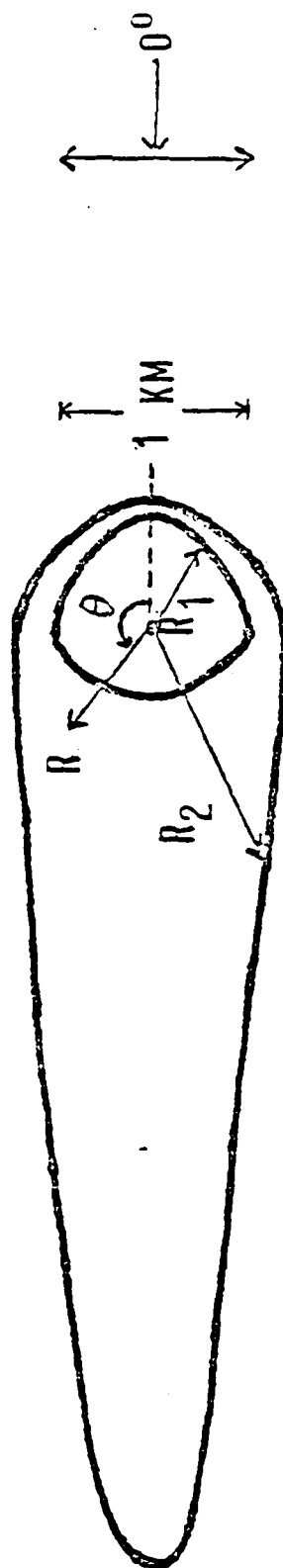
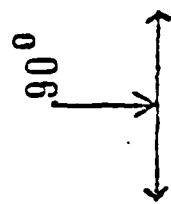
Figure 6



0-14

MODEL 2242402

ANALYTIC MODEL FOR HAIR STRIATION



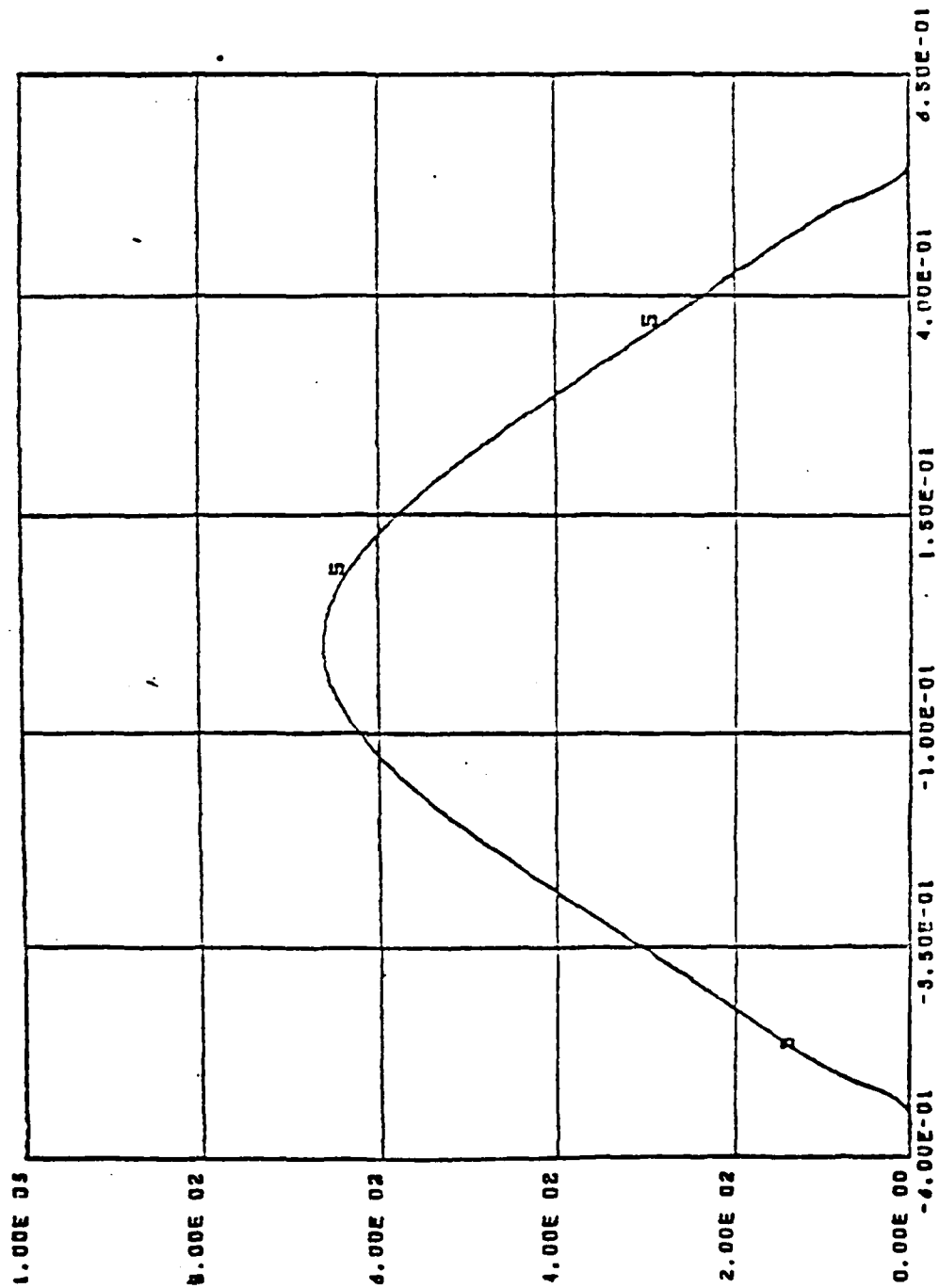
← 5 KM →

$$F(\theta) = 10. (1. - \exp(-A)) \quad R(\theta) < R_1(\theta)$$

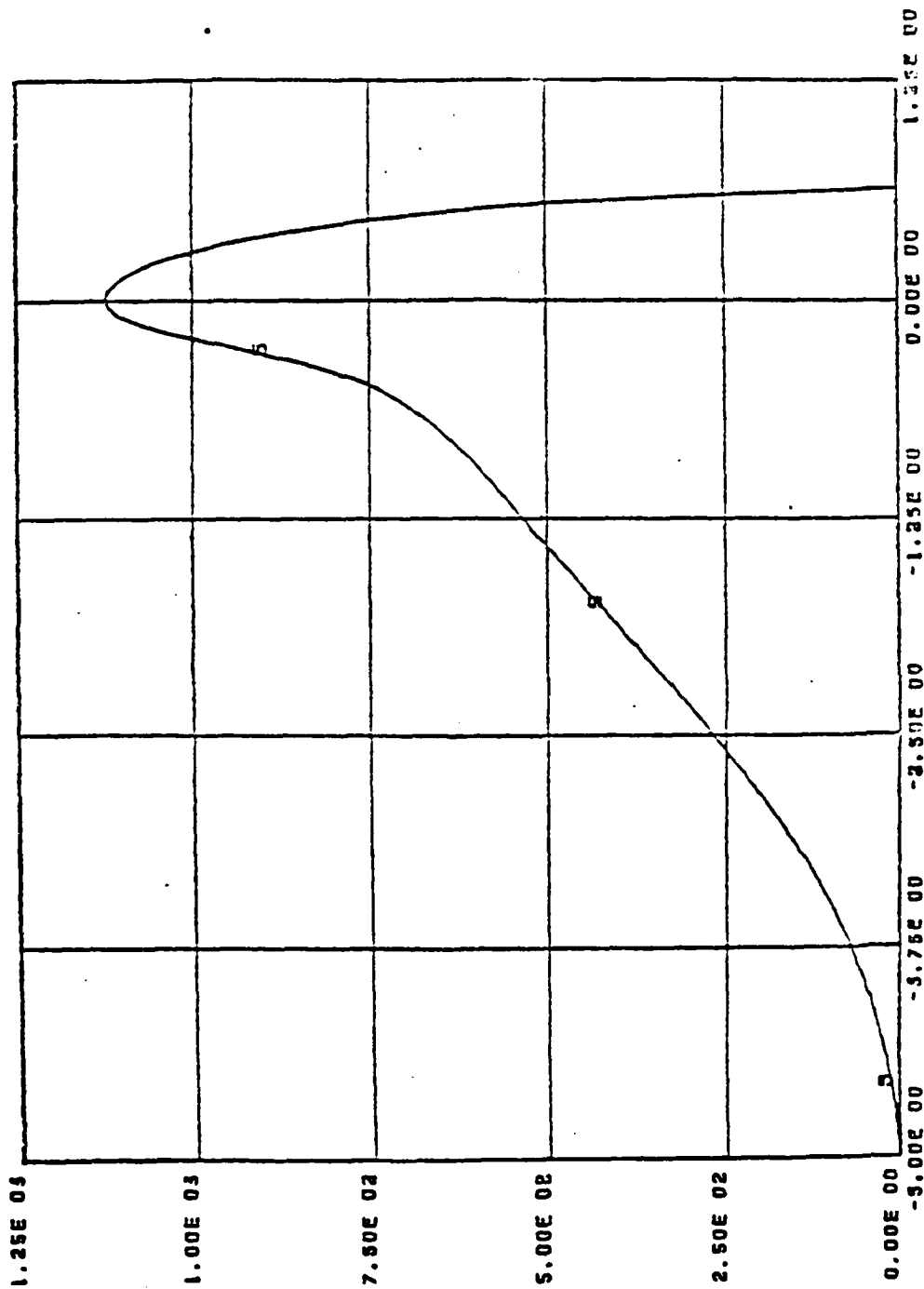
$$= 10. \left(\exp \left\{ -A \left[\frac{R(\theta) - R_1(\theta)}{R_2(\theta) - R_1(\theta)} \right]^2 \right\} - \exp(-A) \right) \quad R_1(\theta) < R(\theta) < R_2(\theta)$$

$$= 0 \quad R(\theta) > R_2(\theta)$$

PMT = 0.0000E 00



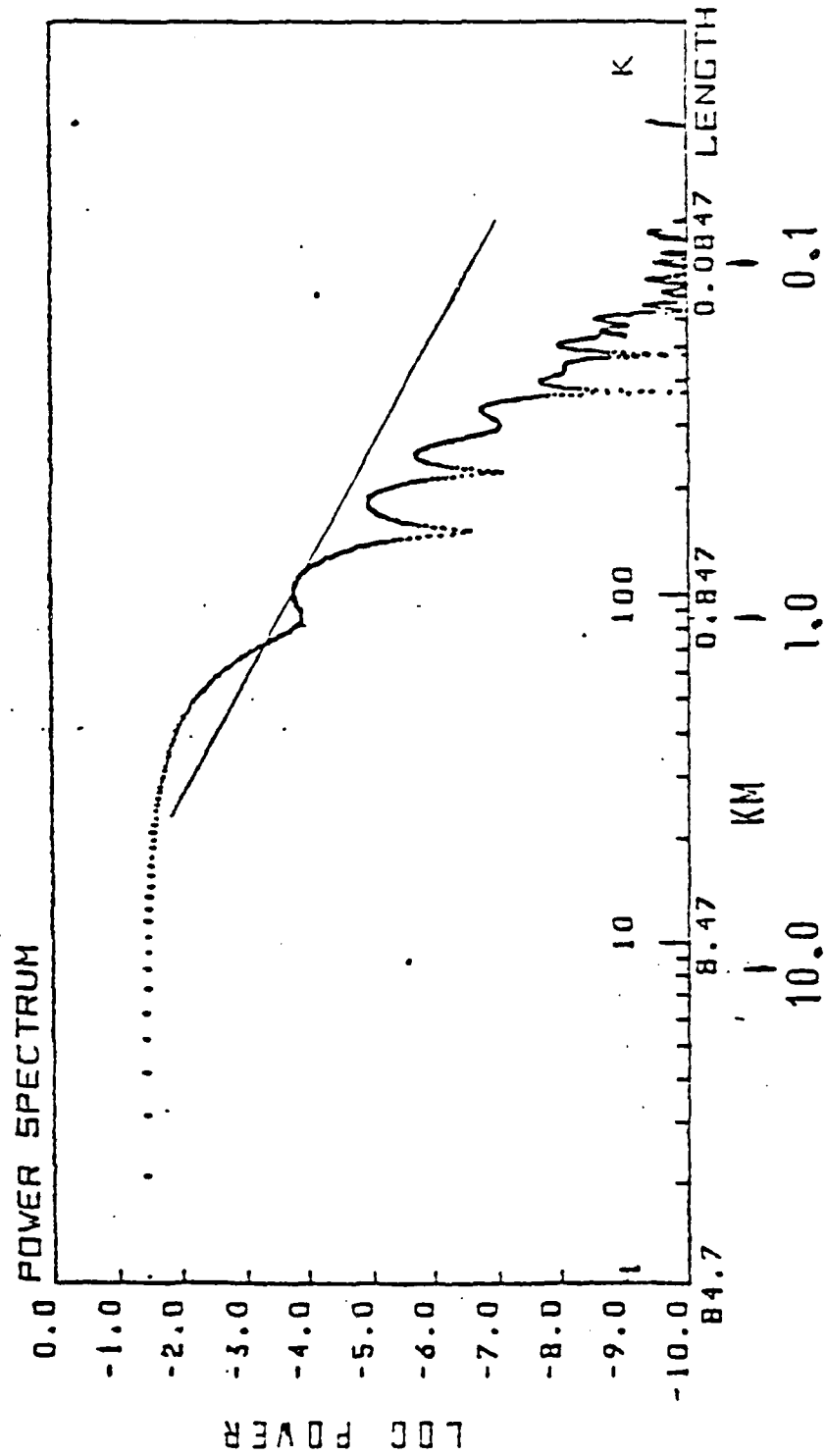
PHI = 9.0000E 01



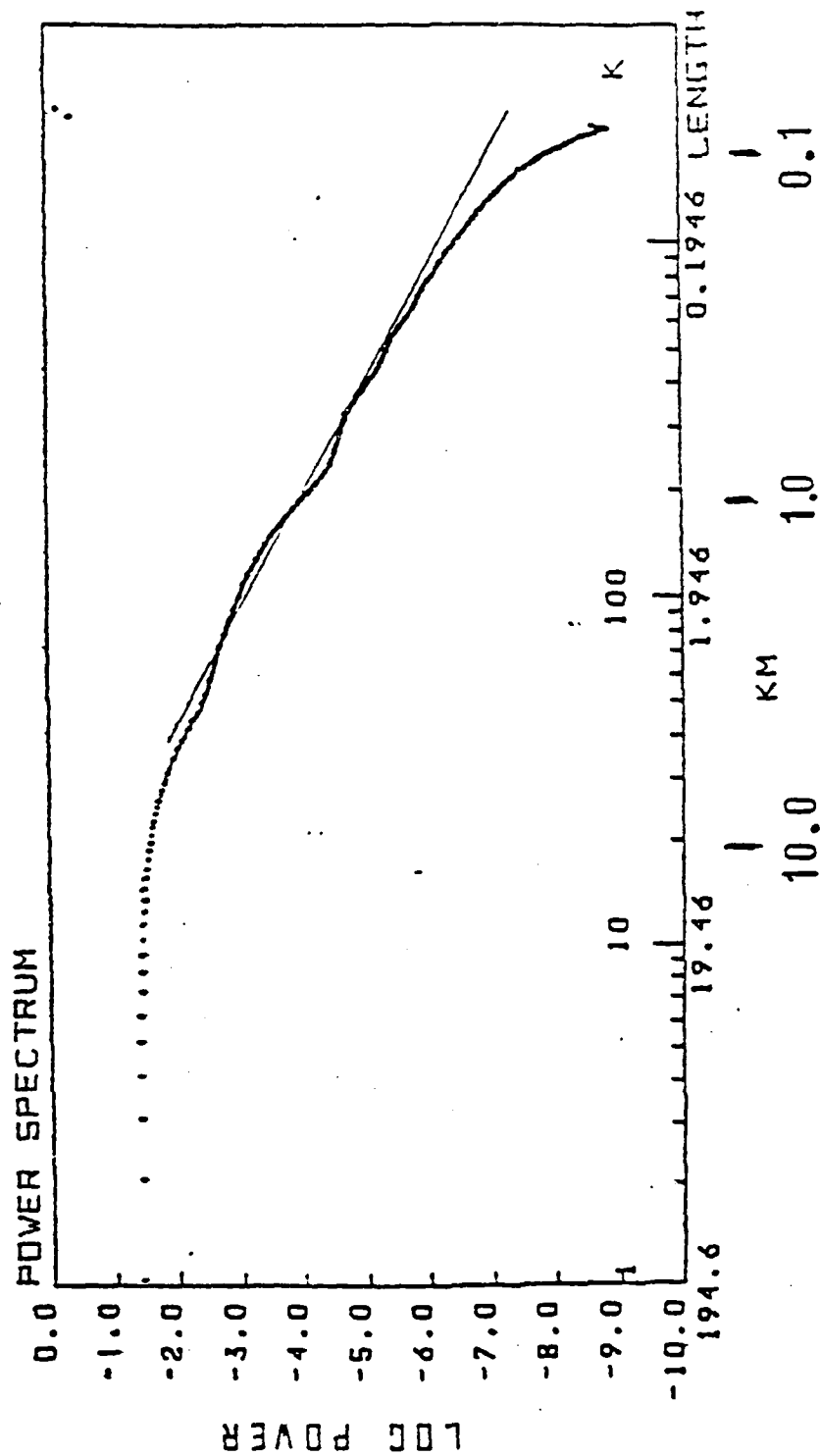
0-17

PRECEDING PAGE BLANK-NOT FILMED

VIEW POSITION THETA=10.00



VIEW POSITION THETA=80.00

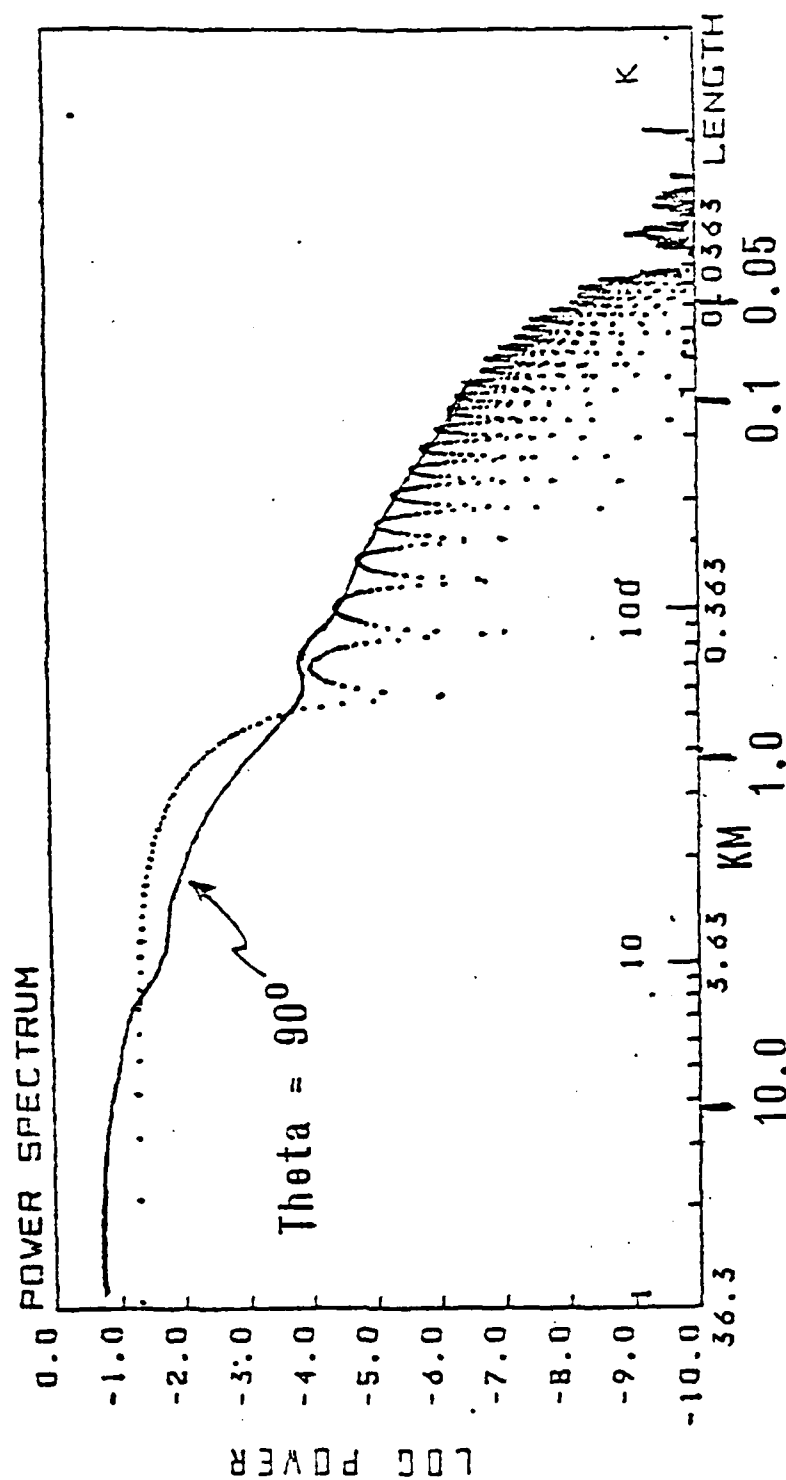


MODEL 901030

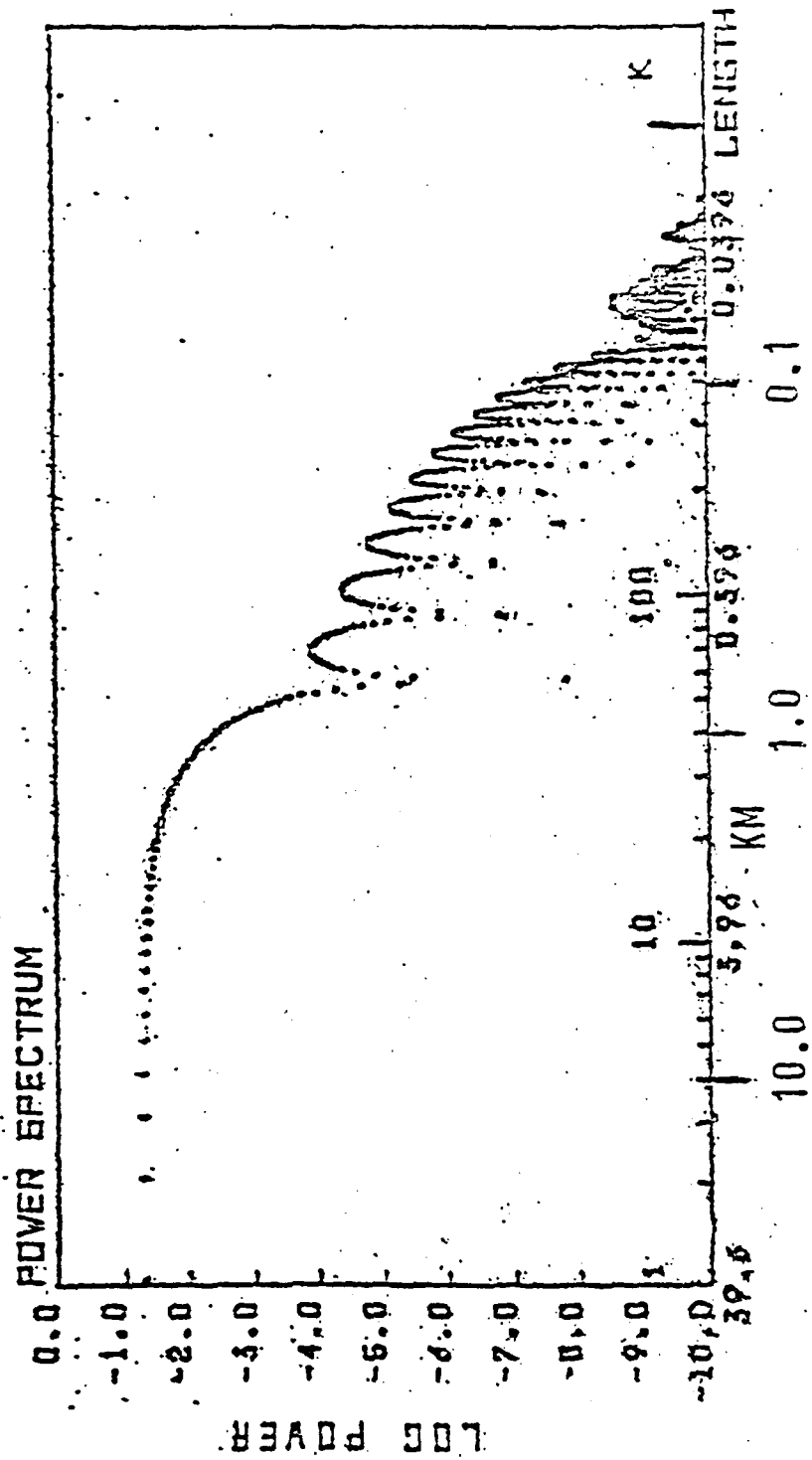
ANGULAR VARIATION IN CLOUD MODEL
(EDGES VARYING BETWEEN 0.1 AND 0.3 KM)

ANGLE	SPECTRAL INDEX FROM LEAST SQUARES FIT	WAVELENGTH OF GAUSSIAN CRIST
0°	~ 6.	NO K ⁻³ REGION
10°	~ 6.	"
20°	4.3	"
30°	3.6	"
40°	3.5	0.45 KM
50°	3.4	0.35 KM
60°	3.5	0.31 KM
70°	3.3	0.26 KM
80°	3.2	0.26 KM
90°	3.2	0.23 KM

VIEW POSITION THETA= 0.00

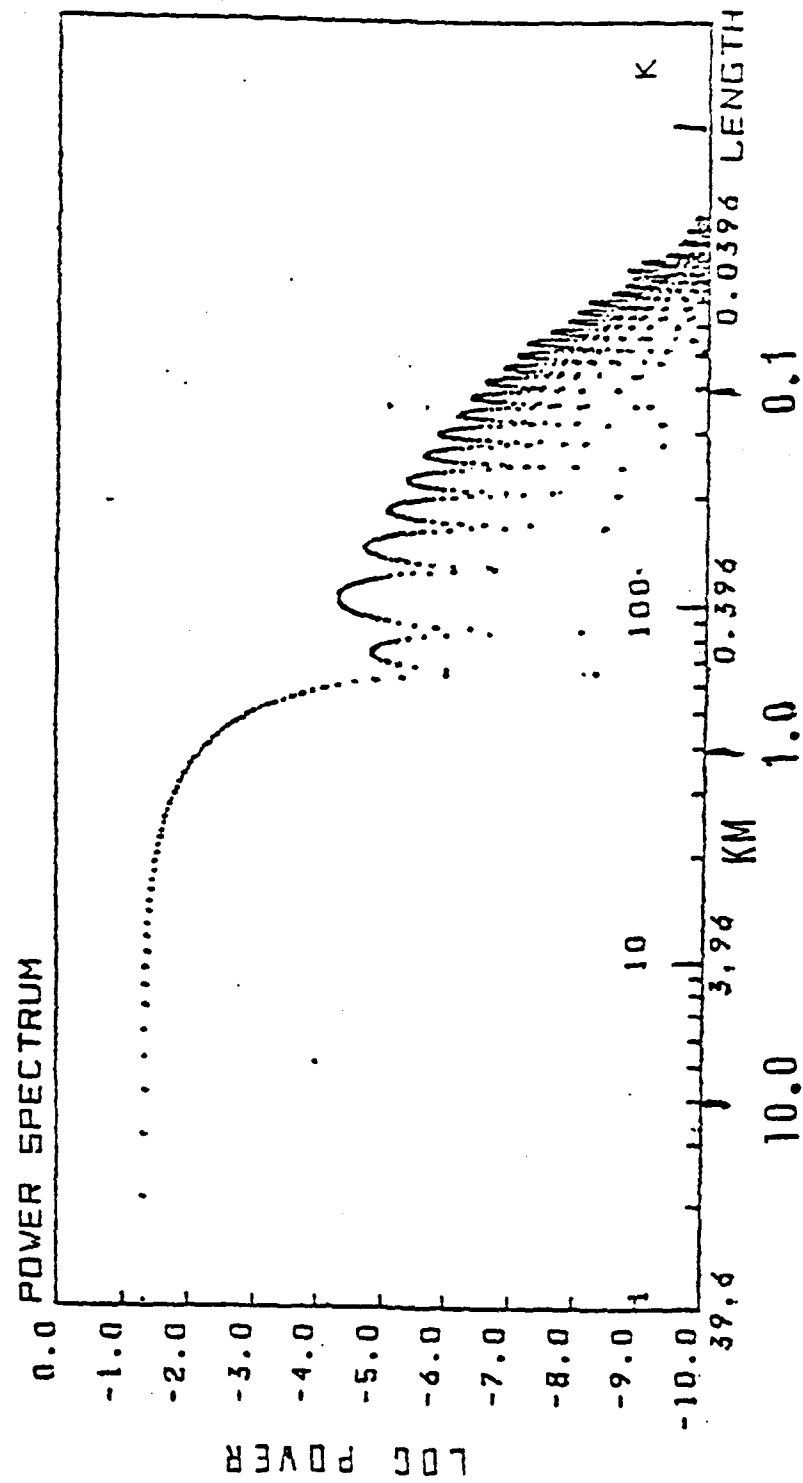


VIEW POSITION THETA= 0.00



MODEL 201010

VIEW POSITION THETA• 0.00



UNCLASSIFIED

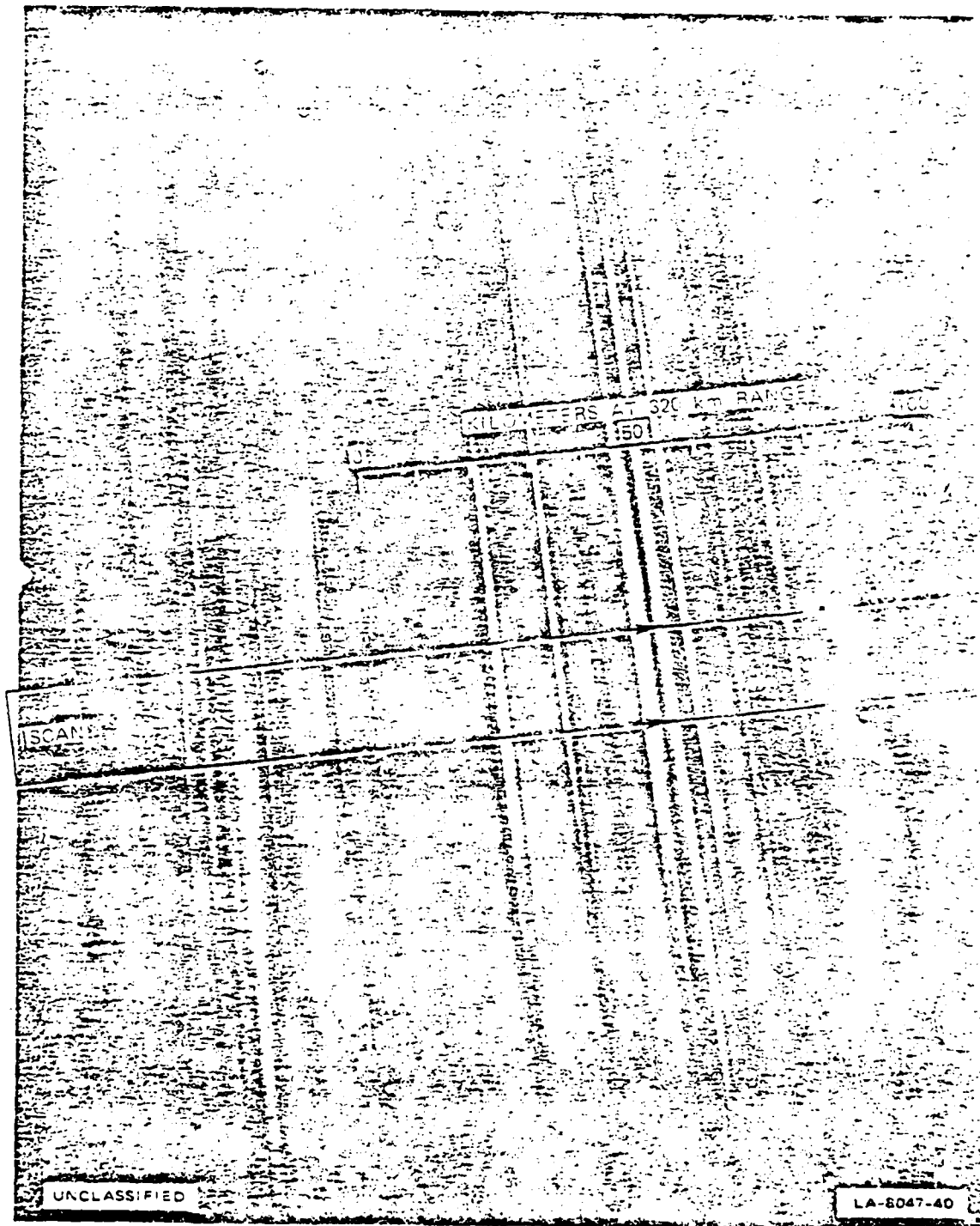


FIGURE 3 PHOTOGRAPH OF CHECK MATE STRIATED FIREBALL AT DETONATION PLUS 384 SECONDS. Area of scan used in analysis is shown. This is Scan 65C from Frame 65 of the CHECK MATE, Johnston Island Praktina film. (U)

VIEWGRAPH 16

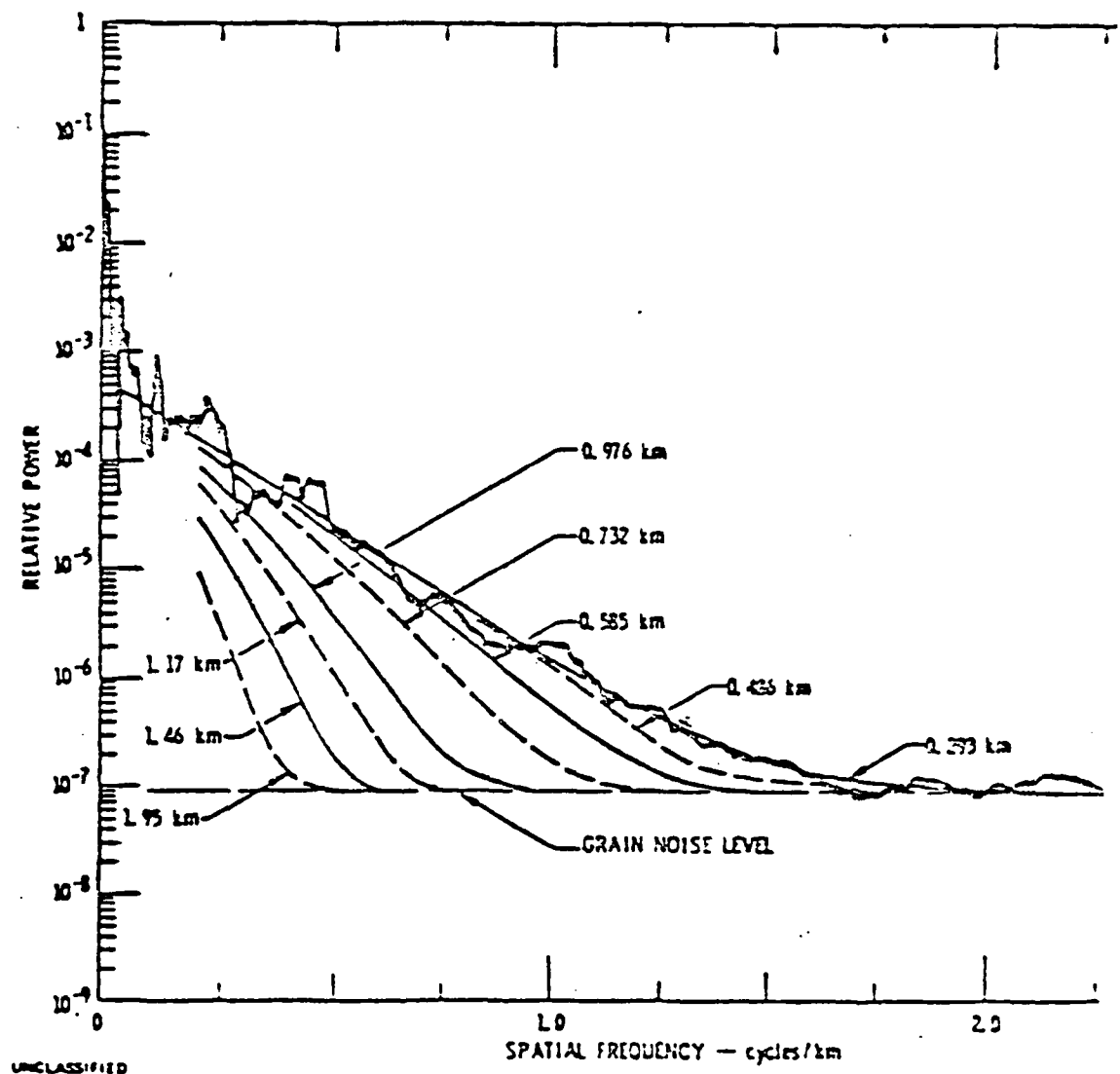
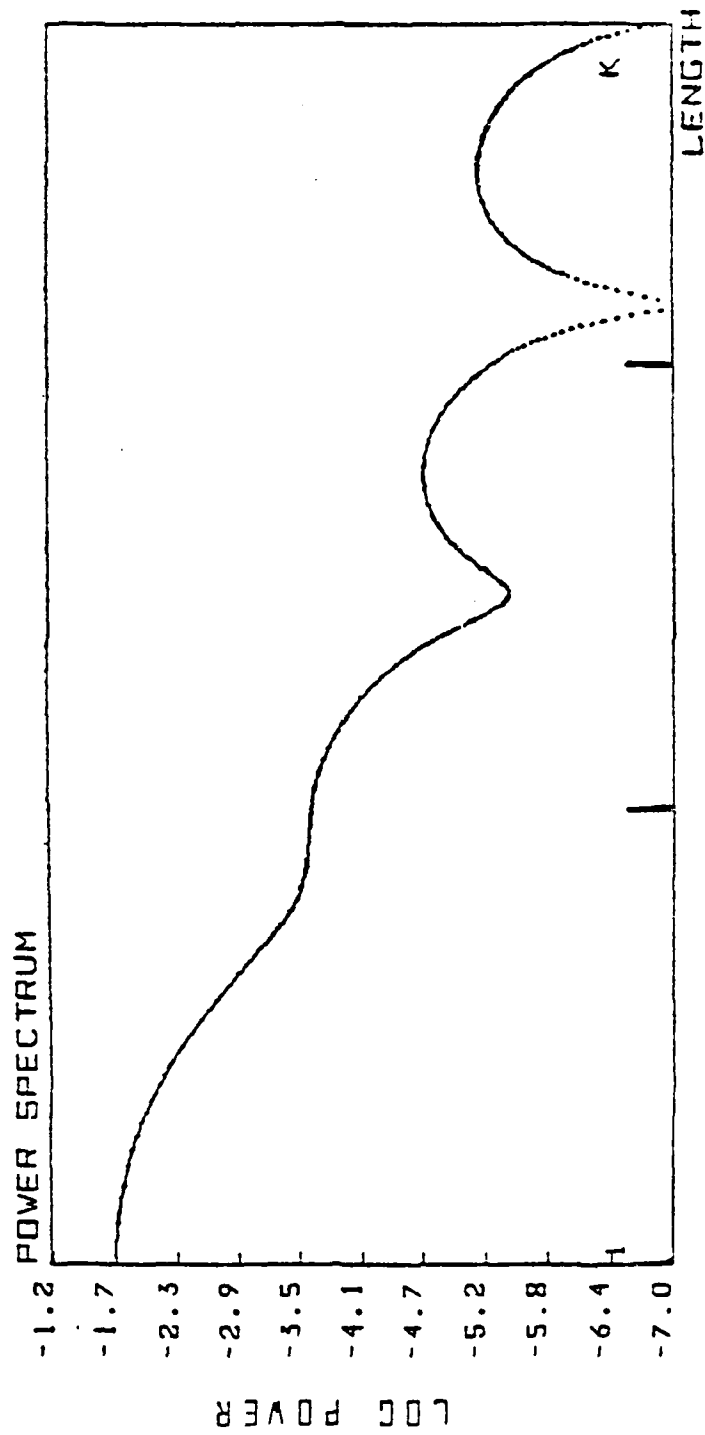


FIGURE 22 MEASURED SPATIAL-FREQUENCY POWER SPECTRUM OF SCAN 1 (FIGURE 3 (Scan 65C)). Also plotted are the computed power spectra that are obtained by truncating the striation size distribution function various radii as shown in Figure 21. (U)

VIEW POSITION THETA=10.00

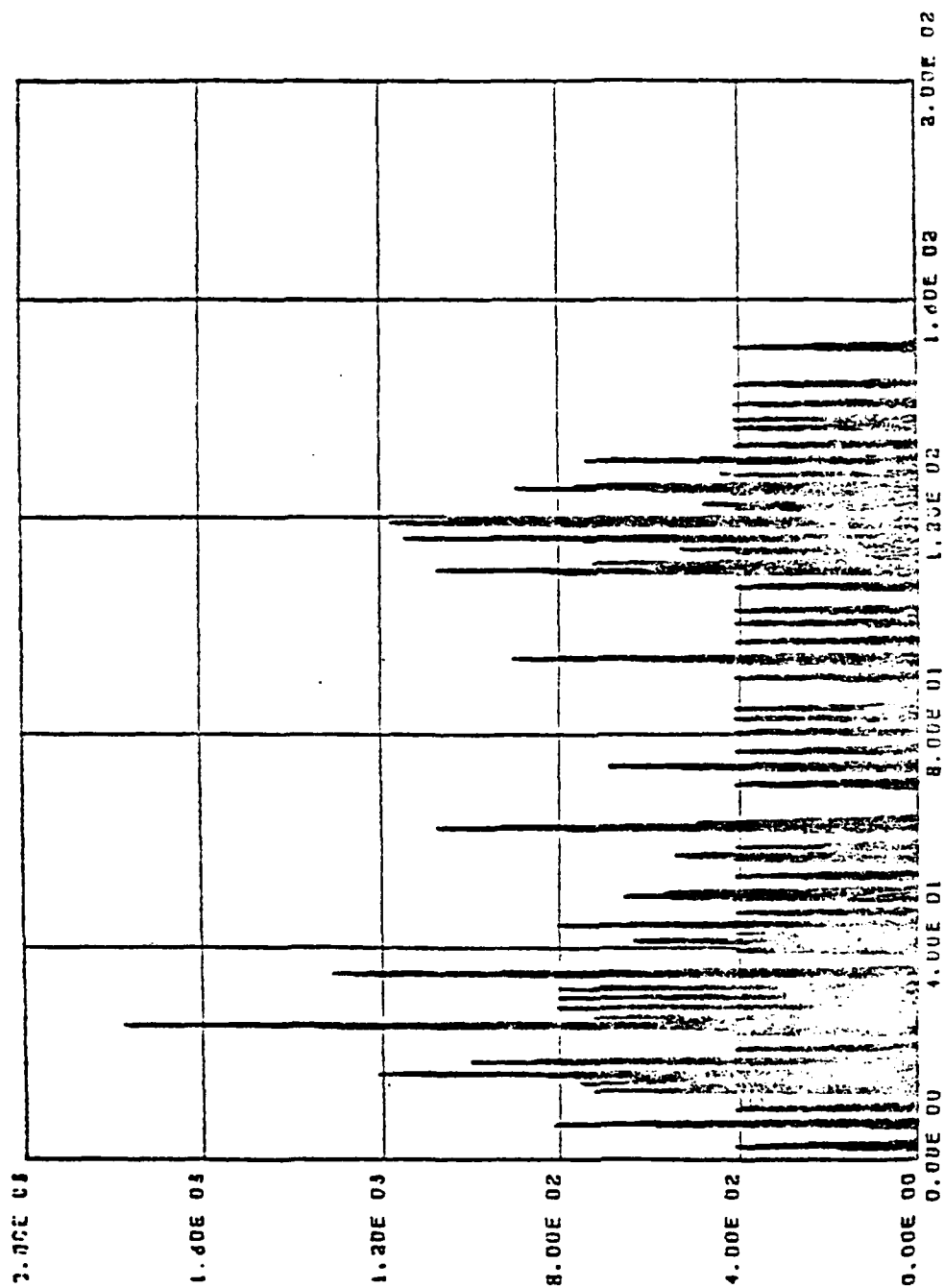


VIEWGRAPH 18

O-26

MODEL 921010

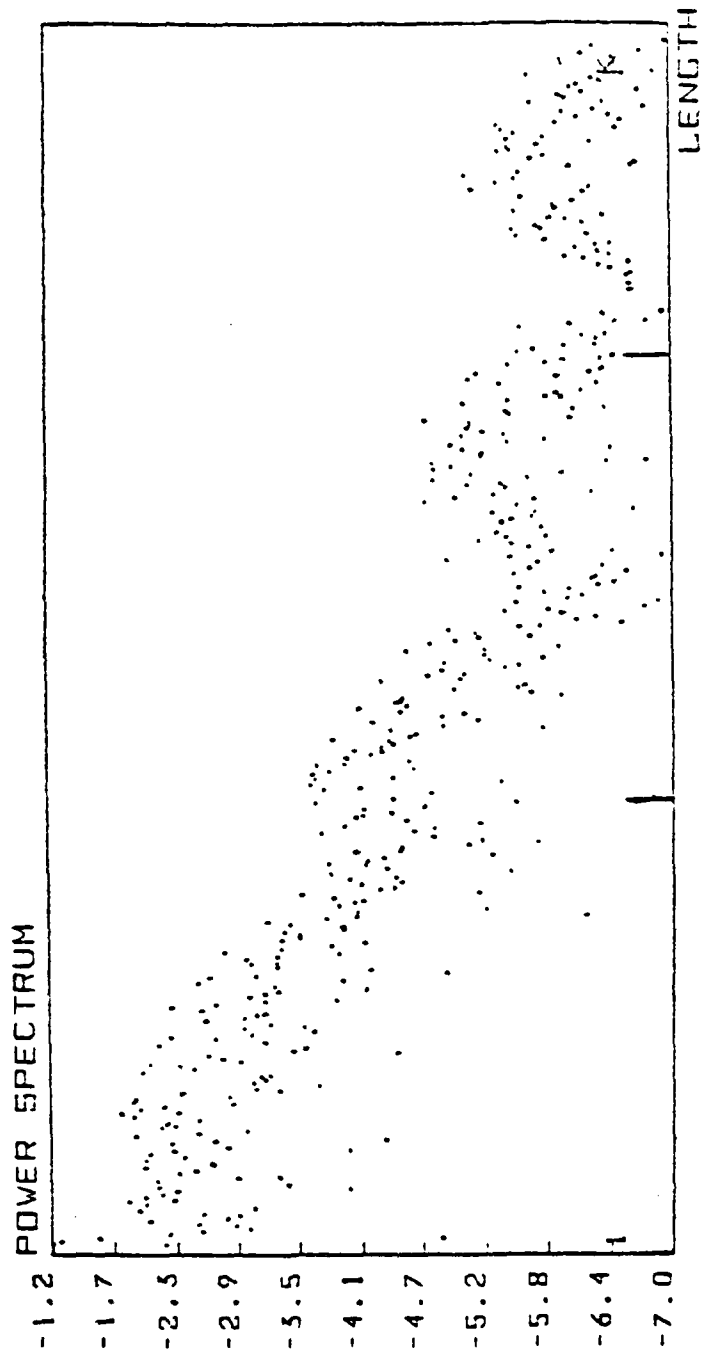
PHI - 1.0000E 01



VIEWGRAPH 19
0-27

PRECEDING PAGE BLANK-NOT FILM

VIEW POSITION THETA=10.00



LOG POWER

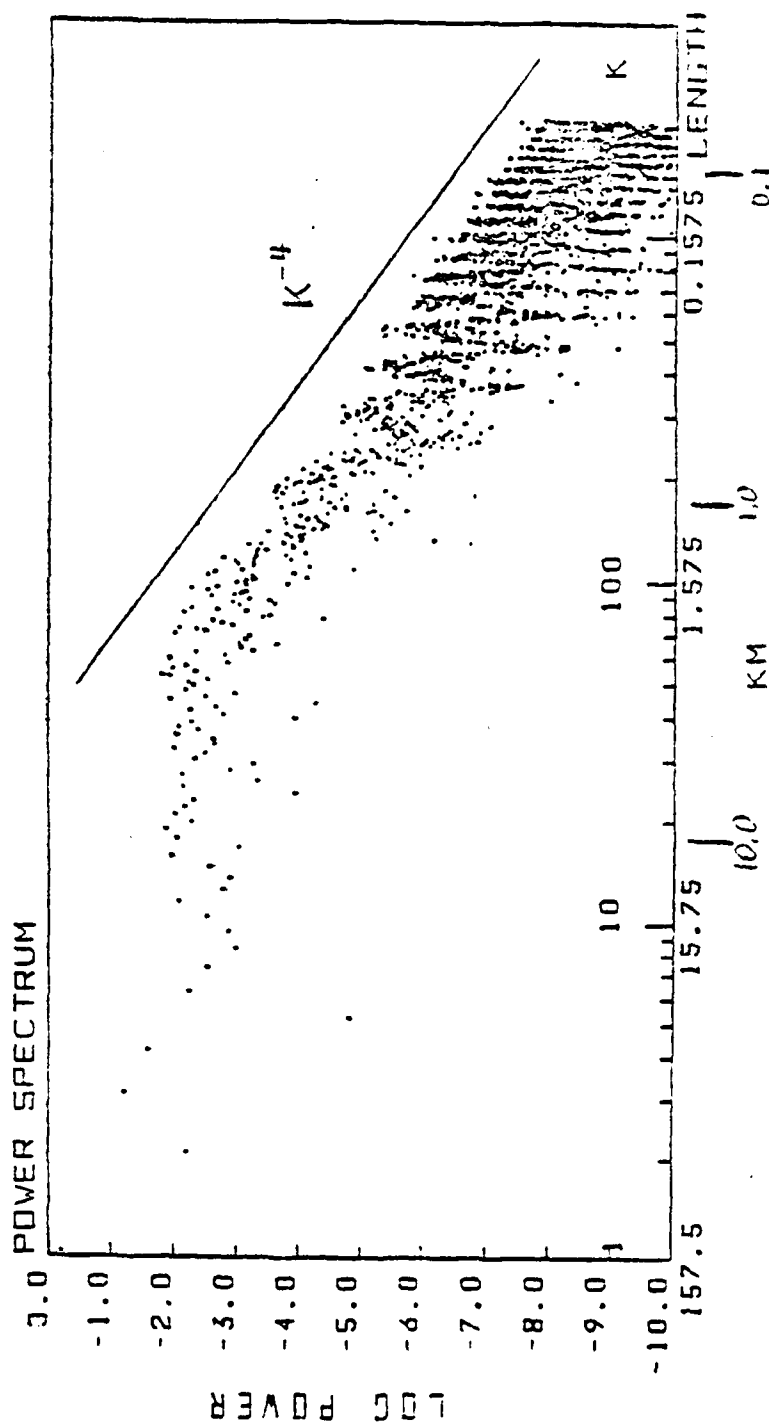
VIEWGRAPH 20

O-28

MODEL 921010

PRECEDING PAGE BLANK-NOT FILMED

VIEW POSITION THETA=10.00



LOG POWER

VIEWGRAPH 21
O-29

MODEL 921010

APPENDIX P
QUASI-STEADY STATE MULTI-PLASMA CLOUD
CONFIGURATION IN THE IONOSPHERE

J. Chen and P. Satyanarayana
Science Applications, Inc.

and

S.L. Ossakow
Naval Research Laboratory

Quasi-Steady State Multi-Plasma Cloud Configuration
in the Ionosphere

J. Chen and P. Satyanarayana
Science Applications, inc.
McLean, VA 22101

and

S.L. Ossakow
Plasma Physics Division
Naval Research Laboratory
Washington, D.C. 20375

December 1983

Synopsis

The morphology of a finite array of plasma density enhancements (multi-plasma clouds) in the ionosphere is studied in order to determine the condition under which the system undergoes a quasi-steady state $\underline{E} \times \underline{B}$ drift. In such a system, the polarization induced self-electric field inside all the plasma clouds must be essentially equal and uniform. The method of image dipoles previously developed for multi-equatorial spread F bubbles is used to calculate the instantaneous electric field exactly. It is found that, even for small separation distances for which the inter-cloud interaction is significant, the electric field inside the clouds can remain uniform for typical ionospheric plasma cloud parameters so that the multiple plasma clouds drift in unison without changing their geometrical shapes. This constitutes a quasi-steady state configuration. The implications on the behavior of late-time plasma cloud striations are discussed.

Table of Contents

	<u>Page No.</u>
1. INTRODUCTION.....	1
2. THEORETICAL FORMULATION.....	5
3. QUASI-STEADY STATE MULTI-CLOUD CONFIGURATION RESULTS.....	9
4. SUMMARY AND DISCUSSION.....	14
ACKNOWLEDGEMENT.....	16
REFERENCES.....	17
FIGURE CAPTIONS.....	19
TABLE 1.....	21
TABLE 2.....	22

1. INTRODUCTION

It has been observed that kilometer-scale size structures can persist in both barium and nuclear cloud striation phenomena (J. Fedder, W. Chesnut and L. Wittwer, 1980, private communication). Beyond a certain point (late times) after the release of such plasma clouds, the bifurcation of clouds appears to stop and there is a tendency for the striations to drift in unison for as long as they can be seen. In addition, the survival for hours of the kilometer scale structures has been evidenced by propagation studies (Prettie et al., 1977). This observed behavior of ionospheric plasma clouds is often referred to as the "freezing" phenomenon.

Recently, some studies have attempted to understand the apparent observed cessation of the bifurcation process at a scale length of kilometers. Modelling the plasma cloud and ionosphere as a single two-dimensional layer perpendicular to the ambient geomagnetic field (B_0) including cross-field diffusion due to electron-ion collisions, McDonald et al. (1981) carried out theoretical and numerical simulation studies. They produced a "U" shaped curve representing the minimum striation scale size (a structure's stability against further bifurcation) as a function of the ratio of the integrated Pedersen conductivity of the plasma cloud to the background ionosphere. However, classical electron diffusivity ($\sim 1 \text{ m}^2/\text{sec}$) produced minimum scale sizes of the order of 10 to 30 m. Consequently, anomalous diffusion ($\sim 100 \text{ m}^2/\text{sec}$) had to be invoked in order to obtain "freeze-up" of kilometer scale sizes. The work of Ossakow et al. (1981) proposed that including a second level for the background ionosphere (see, for example, Scannapieco et al., 1976) would allow image striations to build up and allow the conductivity in a striation to be amplified. This in turn would allow for larger conductivity ratios than if one had

just one cloud level, which in turn, could result in kilometer minimum scale sizes by extrapolating the U shaped curve of McDonald et al. (1981) to higher conductivity ratios.

The above studies have sought the possible mechanisms that may be responsible for the apparent cessation of bifurcation associated with the $\underline{E} \times \underline{B}$ gradient drift instability. However, there is another necessary ingredient for the freezing phenomenon. After bifurcation has stopped, the multiple striation fingers appear to undergo a quasi-steady state $\underline{E} \times \underline{B}$ drift across the magnetic field \underline{B}_0 . It is the latter issue of quasi-steady state solutions that we will address in this paper.

Dungey (1958) and later Perkins et al. (1973) showed that the coupled set of equations for density n and potential ϕ describing the dynamics of plasma clouds have no steady state solutions if the cloud, as described by n , has a finite size (with the gradient of n) in the two dimensions perpendicular to the magnetic field \underline{B}_0 . An exception to this rule is a "waterbag" plasma cloud with a piecewise constant density profile with constant densities n_1 and n_2 inside and outside the plasma cloud, respectively (e.g., elliptic, circular cylindrical, slab plasma clouds). Linson (1972) solved the potential (ϕ) equation using methods such as those found in Smythe (1950). In this approach, the continuity equation for n is automatically satisfied. In this configuration, the induced electric field is constant inside the single waterbag plasma cloud and is anti-parallel to the external (zeroth order) electric field. Thus, the total field inside is reduced. A method similar to that of Linson's was adopted by Ossakow and Chaturvedi (1978) to study the morphology of rising equatorial spread F

bubbles. In this case, the induced electric field is again constant inside the single waterbag plasma bubble but is parallel to the external field so that the total electric field inside is enhanced.

In a previous paper by Chen et al. (1983), hereafter referred to as Paper I, a nontrivial extension of the single bubble model of Ossakow and Chaturvedi (1978) was carried out to study a multi-bubble system. In Paper I, the method of image dipoles was developed to solve the potential equation analytically. In the presence of neighboring bubbles, it was found that the induced electric field inside the multiple waterbag bubbles is not constant and has components perpendicular as well as parallel to the external (zeroth order) electric field. This implies that the bubble contours would deform in the subsequent induced $\underline{E} \times \underline{B}$ drift motion and that no steady-state solution exists.

In Paper I, it was noted that the analytical solution obtained for bubbles (plasma density depletions) was also applicable to multiple clouds (plasma density enhancements) such as one might encounter in plasma cloud striation fingers. It was also shown that the interaction of the neighboring bubbles and clouds is substantial for $x_0/a \leq 3$ (where $2x_0$ is the center-to-center distance between two cylindrical bubbles and a is the radius of the cylinder). In particular, for the multi-bubble case, the induced $\underline{E} \times \underline{B}$ drift velocity is reduced by more than 20% to 40% as x_0/a is decreased from 3 to 1.5. At the same time, a horizontal drift of as much as 50% of the vertical drift (with equatorial F region geometry in mind) is produced and the drift velocity within bubbles can vary by 20% to 40%. This nonuniformity in the field and in the induced $\underline{E} \times \underline{B}$ drift is reduced as x_0/a increases. However, even for $x_0/a \geq 5$, the nonuniformity is still in the range of a few percent.

In the case of the multi-finger configuration, observations (see, for example, Davis et al., 1974) indicate that the late-time striation fingers typically have x_0/a in the range of 1.5 to 2.5. Thus, one important observational constraint on any possible quasi-steady state solution is that the electric field inside each cloud must be uniform even for separation distances x_0/a of 1.5 to 2.5, i.e., even in the regime where the inter-cloud electrical interaction is significant. It was already observed in Paper I that the nonuniformity in the multi-cloud configuration was less pronounced than in the multi-bubble configuration for the same separation distance. In this paper, we will show quantitatively that quasi-steady state solutions do exist for multiple plasma cloud striations even at small separation distances.

In section 2, we briefly review the theoretical formulation of two-cloud and multi-cloud configurations. In section 3, we present the detailed results of the above configurations. In Section 4 we give the summary and discussion.

2. THEORETICAL FORMULATION

In this paper, we consider the instantaneous electric field of a system consisting of a finite number of electrically interacting plasma density enhancements ("fingers") imbedded in a uniform background plasma and neutral gas. Neutral wind effects are not included. In Figure 1, two interacting clouds are shown schematically along with the coordinate system and the external electric and geomagnetic fields. The clouds ("fingers") are modeled by cylinders with circular cross-sections of radius a , and the center-to-center separation distance is $2x_0$. The axes of the cylinders are aligned with the earth's magnetic field ($B_0 \hat{z}$) which is assumed to be uniform. The clouds are immersed in a uniform ambient electric field E_0 as indicated in Figure 1. For the present paper, we adopt the basic theoretical formulation of Paper I, utilizing the dielectric analogy to obtain the polarization induced electric field of the multi-finger system. We give below a brief summary of the relevant theoretical results as applied to F-region ionospheric plasma clouds and refer the reader to Paper I for a more comprehensive treatment and a list of references.

The basic equation describing the instantaneous polarization induced electric field, say, at $t = 0$, is

$$\nabla \cdot (\sigma \underline{E}) = 0 \quad (1)$$

where

$$\sigma \equiv v_{in} \frac{nec}{B\Omega_i} \quad (2)$$

is the Pedersen conductivity for an F region plasma cloud. Equation (1) is equivalent to conservation of the cross-field plasma current arising from ion and electron drifts. The electric field \underline{E} which drives the current consists of the uniform external field \underline{E}_0 and the polarization induced self-field. The electric field \underline{E} satisfies the conditions across the cloud boundaries

$$\begin{aligned} (\sigma \underline{E})_{\perp} &= \text{continuous} \\ (\underline{E})_{\parallel} &= \text{continuous} \end{aligned} \quad (3)$$

and at infinity ($x, y \rightarrow \infty$)

$$\underline{E} \rightarrow \underline{E}_0. \quad (4)$$

The symbols \parallel and \perp refer to the directions parallel and perpendicular to the boundary surfaces, respectively. The above dielectric analogy was noted by Longmire (1970) and Perkins et al. (1973).

In Paper I, we developed the method of image dipoles to solve equation (1) exactly, subject to the conditions (3) and (4). In the interest of keeping the paper self-contained, we repeat the salient results (equations (17), (18), (22) and (23) of Paper I). For the two-cloud system, the total electric field outside the cylindrical clouds has components

$$E_x = -E_0 + \sum_{n=0}^{\infty} 2p_n [f(x + x_n, y) + f(x - x_n, y)], \quad (5)$$

and

$$E_y = \sum_{n=0}^{\infty} 2P_n [h(x + x_n, y) + h(x - x_n, y)], \quad (6)$$

The total electric field \underline{E}^* inside the cloud centered at $x = x_0$ has the components

$$E_x^* = \frac{2}{1+K} [-E_0 + \sum_{n=0}^{\infty} 2P_n f(x + x_n, y)], \quad (7)$$

and

$$E_y^* = \frac{2}{1+K} \sum_{n=0}^{\infty} 2P_n h(x + x_n, y), \quad (8)$$

where the functions f and h are defined as

$$f(x, y) \equiv \frac{x^2 - y^2}{(x^2 + y^2)^2},$$

and

$$h(x, y) \equiv \frac{2xy}{(x^2 + y^2)^2}.$$

For $n \neq 0$, we have

$$P_n \equiv - \left(\frac{1-K}{1+K} \right) \frac{a^2}{b_n^2} P_{n-1},$$

$$b_n \equiv x_0 + x_{n-1}$$

and

$$x_n \equiv x_0 - \frac{a^2}{x_0 + x_{n-1}}.$$

For $n = 0$, we have $x_n = x_0$ and $P_n = P_0$ where

$$P_0 \equiv \frac{1}{2} \left(\frac{1-K}{1+K} \right) a^2 E_0. \quad (9)$$

Here,

$$K \equiv \frac{\sigma_1}{\sigma_2} \quad (10)$$

where σ_1 and σ_2 are the Pedersen conductivities inside and outside the clouds, respectively. In reality, the collision frequency ν_{in} and the number density n vary along the magnetic field so that the conductivity ratio K should be redefined in terms of flux-tube integrated quantities. For the cylindrical cloud centered at $x = -x_0$, the inside field is obtained by replacing x_n with $-x_n$ in the functions f and h . For a $N > 3$ system, a parallel calculation based on the same theoretical formulation yields series expressions similar to equations (5) through (8). Because they are extremely cumbersome and give no new insight, we will show only the results of the two and three cloud systems in this paper. Also, we will present detailed results only for $N = 2$ and $N = 3$ cases since Paper I has shown that $N > 5$ systems exhibit no significant quantitative or qualitative differences from the $N = 3$ case.

3. QUASI-STEADY STATE MULTI-CLOUD CONFIGURATION RESULTS

Equations (5) through (8) and the corresponding equations for a three-cloud system describe the electric field in the frame moving with the velocity $c\mathbf{E}_0 \times \mathbf{B}_0/B^2$ relative to the earth. As a result of the polarization electric field, the plasma clouds undergo induced $\mathbf{E} \times \mathbf{B}$ drift motion with respect to the undisturbed ionosphere. If we define

$$\tilde{\mathbf{E}} \equiv \mathbf{E}^* - \mathbf{E}_0, \quad (11)$$

then the relative drift velocity is

$$\mathbf{V} = c \frac{\tilde{\mathbf{E}} \times \mathbf{B}_0}{B_0^2}. \quad (12)$$

Here, $\mathbf{E}_0 = -E_0 \hat{x}$. In particular, the $\mathbf{E} \times \mathbf{B}$ drift velocity \mathbf{V}_1 of a single isolated cloud is given by

$$V_1 = - \left(\frac{1-K}{1+K} \right) \frac{cE_0}{B_0}, \quad (13)$$

For plasma clouds, $K > 1$ and \mathbf{V}_1 is downward toward the earth (in an equatorial ionospheric configuration). This equation also shows that the plasma elements inside an isolated cloud drift uniformly, maintaining its geometrical shape. Thus, it is a steady-state configuration. Figure 2 shows the field lines corresponding to $\tilde{\mathbf{E}}$ given by equation (11). Inside the cloud, the field and hence the $\tilde{\mathbf{E}} \times \mathbf{B}$ drift are uniform while the field outside the cloud is that of a dipole \mathbf{P}_0 (equation (9)) located at the center of the circle.

In Figures 3(a), (b) and (c), we show a two-cloud configuration with

the separation distance $x_0/a = 1.25$ for three values of the conductivity ratio K . This separation distance is smaller than the typical multi-finger situation where x_0/a is roughly 1.5 to 2.5 (see, for example, Davis et al., 1974). In fact, for $x_0/a < 1.25$, it may be observationally difficult to identify the adjoining clouds as separate. This separation distance is shown in order to maximize the effect of the inter-cloud interaction. Moreover, the $K = 3$ case is shown primarily because this value corresponds to the maximum inter-cloud influence for a given x_0/a . This can be seen by noting that each term in the series in equations (7) and (8) contains a power of the factor $(1-K)/(1+K)^2$. For $K > 1$, the absolute value of this quantity has a maximum at $K = 3$. Thus, Figure 3(a) represents the largest nonuniformity in the inside electric field for $x_0/a = 1.25$. As K increases, the nonuniformity decreases as shown by Figures 3(b) and (c). As a general remark, K is taken to be of the order of 10 for artificial barium clouds and is taken to be of the order of 100 or greater for nuclear clouds.

In Table 1, we show the numerical values of the two-could $\underline{E}_0 \times \underline{P}_0$ drift velocity V (equation (12)) normalized to cE_0/B_0 , along with the values of $V_g \equiv -(1-K)/(1+K)$, the normalized drift velocity (see equation (13)) of an isolated cloud. For $x_0/a = 1.25$, the $K = 3$ case exhibits a variation in V of up to 30% inside the clouds. This variation (i.e., nonuniformity) decreases as K increases. For $K = 10$, the variation is roughly 10% and for $K = 100$, it is 1%. In addition, V approaches the single-cloud value V_g as K increases. Thus, we conclude that, even for a small separation distance of $x_0/a = 1.25$, $K = 100$ is nearly indistinguishable from the single-cloud case. It is of importance to note from Figures 3(a), (b) and (c) that the outside field is significantly

distorted from the single-cloud dipolar field and that the distortion does not change appreciably as K is increased. This implies that the intrinsic inter-cloud interaction is not weakened as K is increased and that only the inside field is affected.

Figures 4(a), (b) and (c) and Figures 5(a), (b) and (c) show two-cloud systems with $x_0/a = 1.5$ and $x_0/a = 2.0$, respectively. Again, three values $K = 3, 10$ and 100 are shown for each value of x_0/a . As x_0/a increases, the inter-cloud interaction decreases. As a result, the inside field is nearly uniform even for $K = 3$. In particular, for $x_0/a = 2.0$ which is a typical separation distance between striations in late times, Table 1 shows that $K = 10$ case has a field variation of roughly 1% and the $K = 100$ case has a variation of 0.1% inside the clouds. In addition, the deviation of the drift velocity from that of the single-cloud case is roughly 1% or less. Such a system of multi-clouds would $\underline{E} \times \underline{B}$ drift in unison while each cloud would maintain its geometrical shape.

Similar behavior is true for the three-cloud and larger N -cloud systems. In particular, Figures 6, 7 and 8 show three-cloud systems with $x_0/a = 1.25, 1.5$ and 2.0 , respectively. For each value of x_0/a , three values of K are shown, viz. $K = 3, 10$ and 100 . In general, the field inside the outer clouds tends to be slightly more nonuniform in magnitude than that in the central cloud. On the other hand, the field in the central cloud tends to be slightly weaker than that in the outer clouds so that the outer clouds drift downward somewhat faster than the central clouds. However, the slight nonuniformity and inequality both decrease with increasing K and vice versa.

Table 2 shows that, for $x_0/a = 1.25$, the variation in the outer cloud decreases from 35% for $K = 3$ to 12% for $K = 10$ and to 1.3% for $K = 100$

while the variation in the central cloud ranges from 19% for $K = 3$ to 6% for $K = 10$ and to 0.1% for $K = 100$. As x_0/a increases, the nonuniformity throughout all the clouds decreases. At $x_0/a = 2.0$, the variation in the field is typically less than 1% for $K = 10$ and $K = 100$. Figures 7(a), (b) and (c) and Figures 8(a), (b) and (c) show the above behavior. Again, as K increases, the drift velocity V inside each cloud approaches that of an isolated cloud, V_g .

We conclude that multi-finger quasi-steady solutions do exist even for small separation distances if K is made sufficiently large. In particular, for $x_0/a = 2.0$, multi-fingers with $K = 10$ and $K = 100$ both constitute quasi-steady state configurations for all practical purposes. Observationally, these systems would be seen to drift across the magnetic field in unison without changing their cross-sectional shapes.

The reason for the quasi-steady state behavior is easy to understand by examining equations (7) and (8). The electric field which determines the relative $\underline{E} \times \underline{B}$ drift motion of the clouds is given by equation (11). Therefore,

$$\tilde{E}_x = - \left(\frac{1-K}{1+K} \right) E_0 + \frac{2}{1+K} \sum_{n=0}^{\infty} 2P_n f(x + x_n, y)$$

From the expressions of P_n and P_0 (equation (9)), we see that P_n and P_0 are not sensitive to K for large K since the factor $(1-K)/(1+K)$ is nearly equal to -1 . However, the factor $2/(1+K)$ multiplying the series in the above expression and in equation (8) is nearly equal to $2/K$ so that the contributions from the neighboring clouds are reduced by a factor of K^{-1} and, for $K \rightarrow \infty$, \tilde{E}_x approaches the single-cloud value $-E_0(1-K)/(1+K)$ with $\tilde{E}_y \rightarrow 0$. Physically, the cloud with a large K is analogous to a

dielectric with a large dielectric constant (see Paper I). Note also that the outside field (equations (5) and (6)) depends only on $(1-K)/(1+K)$. As a result, the outside field is not sensitive to K for large K as has been demonstrated by Figures 3 through 8.

4. SUMMARY AND DISCUSSION

In this paper, we have described the morphology of two-plasma cloud and three-plasma cloud configurations, embedded in an F region ionosphere, in detail using the techniques developed in Paper I. The results are applicable to larger N-plasma cloud systems to a good approximation. The primary objective of this paper is to demonstrate the existence of quasi-steady state multi-plasma cloud configurations in which the electric field inside all the clouds is essentially uniform and equal so that such systems would be seen to drift in unison across the magnetic field while maintaining the overall geometrical shapes.

We have shown that the influence of neighboring clouds on the electric field inside the clouds decreases as K^{-1} for any x_0/a so that the cloud interior is effectively "shielded" from the inter-cloud interactions. Thus, if there is an array of cylindrical clouds with circular cross-sections, each one of which has uniform polarization induced electric field in the absence of neighboring clouds, then the electric field inside each cloud approaches the uniform field of an isolated cloud in the limit as $K \rightarrow \infty$ for any $x_0/a > 1$.

In particular, for $K = 10$, a typical value for barium clouds, the nonuniformity in the magnitude of the drift velocity is approximately 10% for $x_0/a = 1.25$. The drift velocity is also reduced from V_g by approximately 10%. As x_0/a is increased to 2.0, the nonuniformity is reduced to approximately 0.1% and the magnitude of V is also reduced from V_g by a small fraction of 1% (see Tables 1 and 2). Thus, for high- K multi-plasma clouds, deviations from complete uniformity (i.e. an exact steady state configuration) are practically imperceptible.

It has been conjectured (N. Zabusky and E. Overman, 1985, private communication) that one can obtain steady-state solutions for multi-cloud systems by adjusting the contour of each cloud. One cross-section suggested is an ellipse. However, the underlying reason for the quasi-steady state solutions obtained in this paper is the K^{-1} "shielding" effect exhibited by high- K clouds. In fact, since isolated elliptic cross-sections are known (1978) to correspond to steady state configurations (Ossakow and Chaturvedi, 1978), we expect an array of clouds with the same elliptic cross-sections to undergo quasi-steady state $\underline{E} \times \underline{B}$ drift motion if the Pedersen conductivity ratio K is large.

It is not too far-fetched to use a cylindrical waterbag model for evolving plasma clouds and their associated striations. Linson (1972) has shown that evolving (steepening) barium clouds tend to obey a cylindrical rather than a sheet-like model. Also, the results from numerical simulations of steepening equatorial spread F bubbles (with distributed density) show that, at late times, they are best modeled by cylindrical waterbag models (see Ossakow and Chaturvedi, 1978; Ossakow et al., 1979). In the real plasma cloud and attendant striation phenomena, there are continuous plasma density profiles, which subsequently steepen on their backside. As they steepen, at late times, they look like waterbags, except in a thin shell. Thus, the approximation of circular cross sections with piecewise constant density profiles for plasma cloud striation fingers is expected to be applicable in the nonlinear regimes (late times).

ACKNOWLEDGEMENT

This research was supported by the Defence Nuclear Agency and the Office of Naval Research.

REFERENCES

- Chen, J., P. Satyanarayana, and S.L. Ossakow. The morphology of a multi-bubble system in the ionosphere, J. Geophys. Res., 88, 5528, 1983.
- Davis, T.N., G.J. Romick, E.M. Wescott, R.A. Jeffries, D.M. Kerr, and H.M. Peek, Observations of the development of striations in large barium ion clouds, Planet. Space Sci., 22, 67, 1974.
- Dungey, J.W., Cosmic Electrodynamics, p. 161, Cambridge University Press, London, 1958.
- Linson, L.M., Motion of barium ion clouds, Analysis of barium clouds - Semi-Annual Technical Report, RADC-TR-72-103, Vol. I, Avco-Everett Res. Lab., Everett, MA, January, 1972.
- Longmire, C.L., On the motion of artificial ion clouds, Rep., LANC-N-11, Los Alamos Nucl. Corp., Los Alamos, NM, 1970.
- McDonald, B.E., S.L. Ossakow, S.T. Zalesak, and N.J. Zabusky, Scale sizes and lifetimes of F region plasma cloud striations as determined by the condition of marginal stability, J. Geophys. Res., 86, 5775, 1981.
- Ossakow, S.L. and P.K. Chaturvedi, Morphological studies of rising equatorial spread F bubbles, J. Geophys. Res., 83, 2085, 1978.
- Ossakow, S.L., S.T. Zalesak, B.E. McDonald, and P.K. Chaturvedi, Nonlinear equatorial spread F: Dependence on altitude of the F peak and bottomside background electron density gradient scale length, J. Geophys. Res., 84, 17, 1979.
- Ossakow, S.L., S.T. Zalesak, and M.J. Keskinen, A plausible hypothesis for striation freezing in ionospheric plasma clouds, Memo Rep. 4597, Naval Res. Lab., Washington, D.C., Aug. 1981.

AD-A142 573

GEOPHYSICAL PLASMAS AND ATMOSPHERIC MODELING(U) SCIENCE
APPLICATIONS INC MCLEAN VA E HYMAN ET AL. MAR 84
SAI-84/1554 SBI-AD-E001 718 N00014-83-C-2034

6/6

UNCLASSIFIED

F/G 4/1

NL

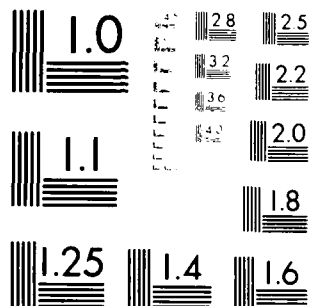
END

DATE

FORMED

8-84

DTIC



MICROCOPY RESOLUTION TEST CHART
NBS 1963-A

- Perkins, F.W., N.J. Zabusky, and J.H. Doles III, Deformation and striation of plasma clouds in the ionosphere, 1, J. Geophys. Res., 78, 697, 1973.
- Prettie, C., A. Johnson, J. Marshall, T. Grizinski, and R. Swanson, Project STRESS satellite communication test results, Tech. Rep. 77-158, Air Force Avionics Lab., Wright-Patterson AFB, Ohio, July 1977.
- Scannapieco, A.J., S.L. Ossakow, S.R. Goldman, and J.M. Pierre, Plasma cloud late-time striation spectra, J. Geophys. Res., 81, 6037, 1976.
- Smythe, W.R., Static and Dynamic Electricity, p. 95, McGraw-Hill, New York, 1950.

FIGURE CAPTIONS

Fig. 1 A schematic drawing of two plasma density enhancements ("clouds") and the coordinate system. The clouds have circular cross-sections of radius a and are infinite in extent along the z direction.

Fig. 2 The field line configuration of \tilde{E} (equation (11)) for an isolated cloud. \tilde{E} is uniform inside the cloud and dipolar outside. The cloud drifts according to equation (12).

Fig. 3 The configuration of the electric field \tilde{E} (equation (11)) in a two-cloud system with $x_0/a = 1.25$ for (a) $K = 3$, (b) $K = 10$ and (c) $K = 100$.

Fig. 4 The configuration of the electric field \tilde{E} (equation (11)) in a two-cloud system with $x_0/a = 1.5$ for (a) $K = 3$, (b) $K = 10$ and (c) $K = 100$.

Fig. 5 The configuration of the electric field \tilde{E} (equation (11)) in a two-cloud system with $x_0/a = 2.0$ for (a) $K = 3$, (b) $K = 10$ and (c) $K=100$.

Fig. 6 The configuration of the electric field \tilde{E} (equation (11)) in a three-cloud system with $x_0/a = 1.25$ for (a) $K = 3$, (b) $K = 10$ and (c) $K=100$.

Fig. 7 The configuration of the electric field \tilde{E} (equation (11)) in a three-cloud system with $x_0/a = 1.5$ for (a) $K = 3$, (b) $K = 10$ and (c) $K = 100$.

Fig. 8 The configuration of the electric field \tilde{E} (equation (11)) in a three-cloud system with $x_0/a = 2.0$ for (a) $K = 3$, (b) $K = 10$ and (c) $K = 100$.

TABLE 1. NORMALIZED $(\underline{E}_o \times \underline{B}_o)_y$ DRIFT VELOCITIES FOR A TWO-PLASMA CLOUD SYSTEM. $V_s = - (1-K)/(1+K)$ IS THE INDUCED DRIFT VELOCITY FOR THE SINGLE CLOUD CASE

x_o	K	A	B	C	V_s
1.25	3	0.3699	0.4548	0.4772	0.5000
	10	0.7316	0.7889	0.8035	0.8181
	100	0.9682	0.9762	0.9782	0.9802
1.5	3	0.4321	0.4701	0.4833	0.5000
	10	0.7755	0.7995	0.8077	0.8181
	100	0.9744	0.9777	0.9788	0.9802
2.0	3	0.4722	0.4844	0.4900	0.5000
	10	0.8016	0.8089	0.8122	0.8181
	100	0.9780	0.9790	0.9794	0.9802

TABLE 2. NORMALIZED $(\underline{E}_0 \times \underline{B}_0)_y$ DRIFT VELOCITIES FOR A THREE PLASMA CLOUD SYSTEM. $V_s = - (1-K)/(1+K)$ IS THE INDUCED DRIFT VELOCITY FOR THE SINGLE CLOUD CASE.

x_0	K	A	B	C	D	E	V_s
1.25	3	0.4069	0.3419	0.3450	0.4405	0.4678	0.5000
	10	0.7560	0.7104	0.7116	0.7781	0.7905	0.8181
	100	0.9715	0.9703	0.9651	0.9746	0.9772	0.9802
1.5	3	0.4391	0.4137	0.4183	0.4612	0.4769	0.5000
	10	0.7395	0.7631	0.7655	0.7932	0.8034	0.8181
	100	0.9750	0.9727	0.9730	0.9768	0.9782	0.9802
2.0	3	0.4673	0.4604	0.4650	0.4792	0.4861	0.5000
	10	0.7981	0.7939	0.7965	0.8053	0.8096	0.8181
	100	0.9775	0.9770	0.9773	0.9784	0.9790	0.9802

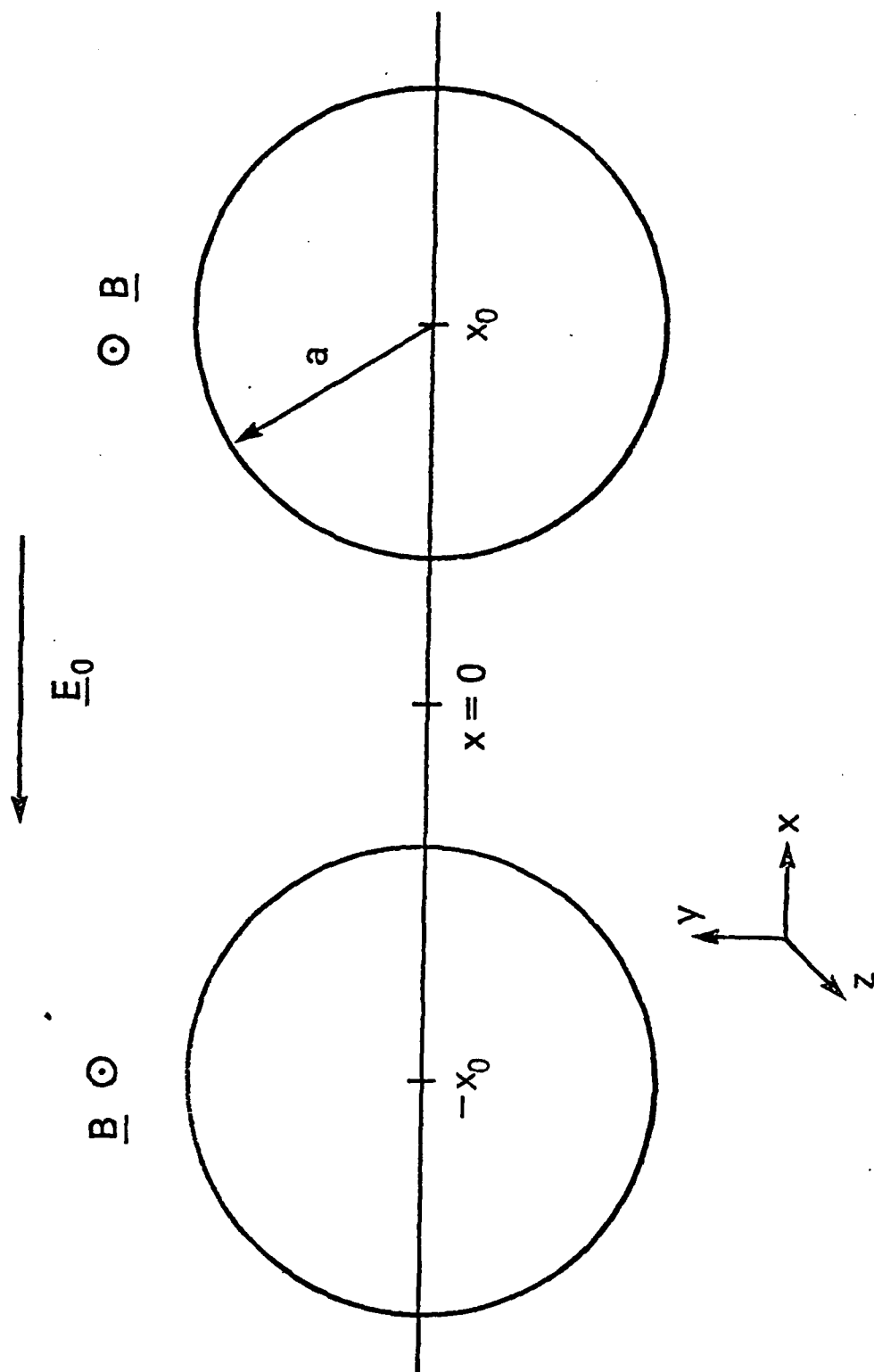


Figure 1

ONE CLOUD

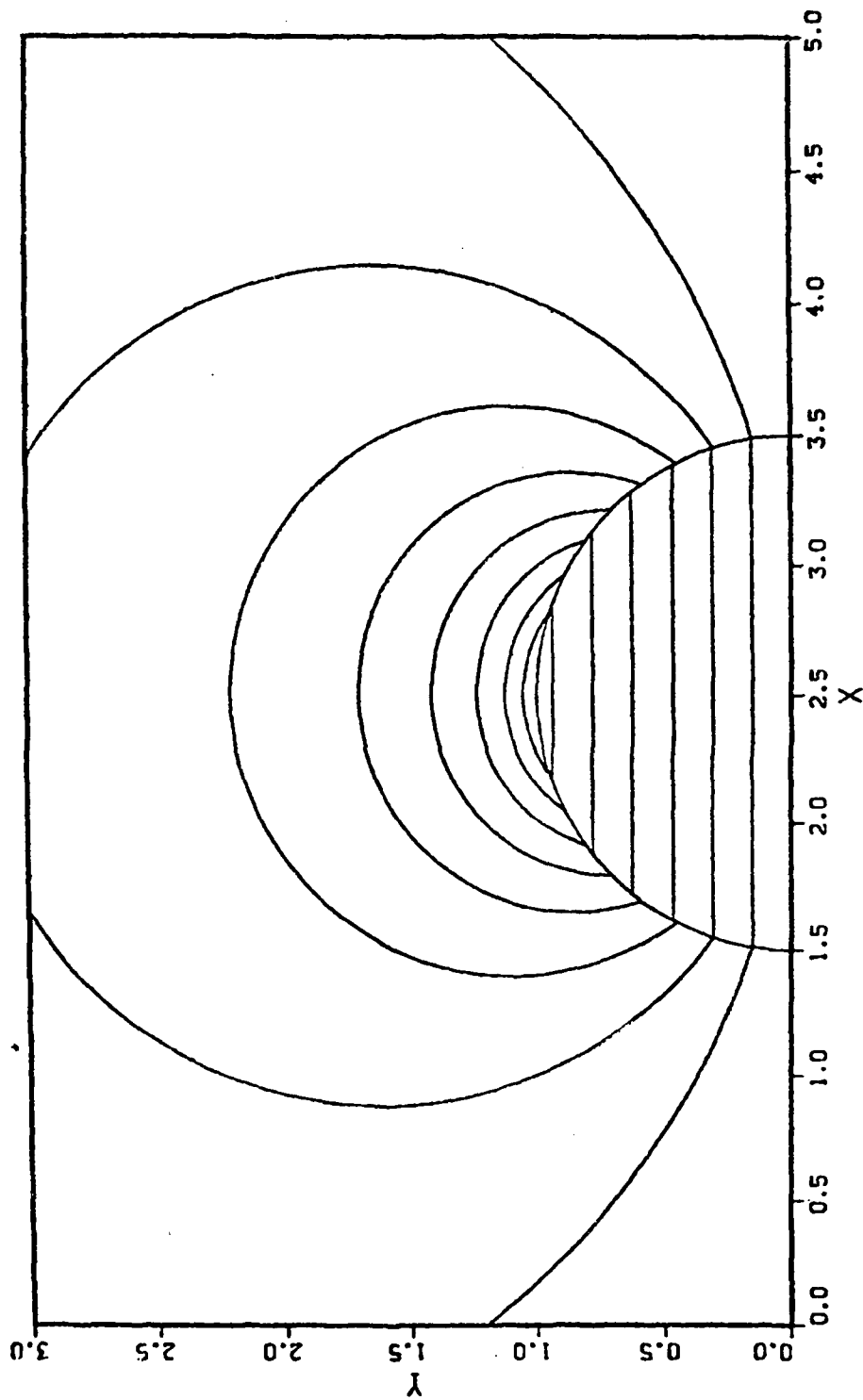


Figure 2 p-30

TWO CLOUDS $K = 3.000 \times 10^{-1.250}$

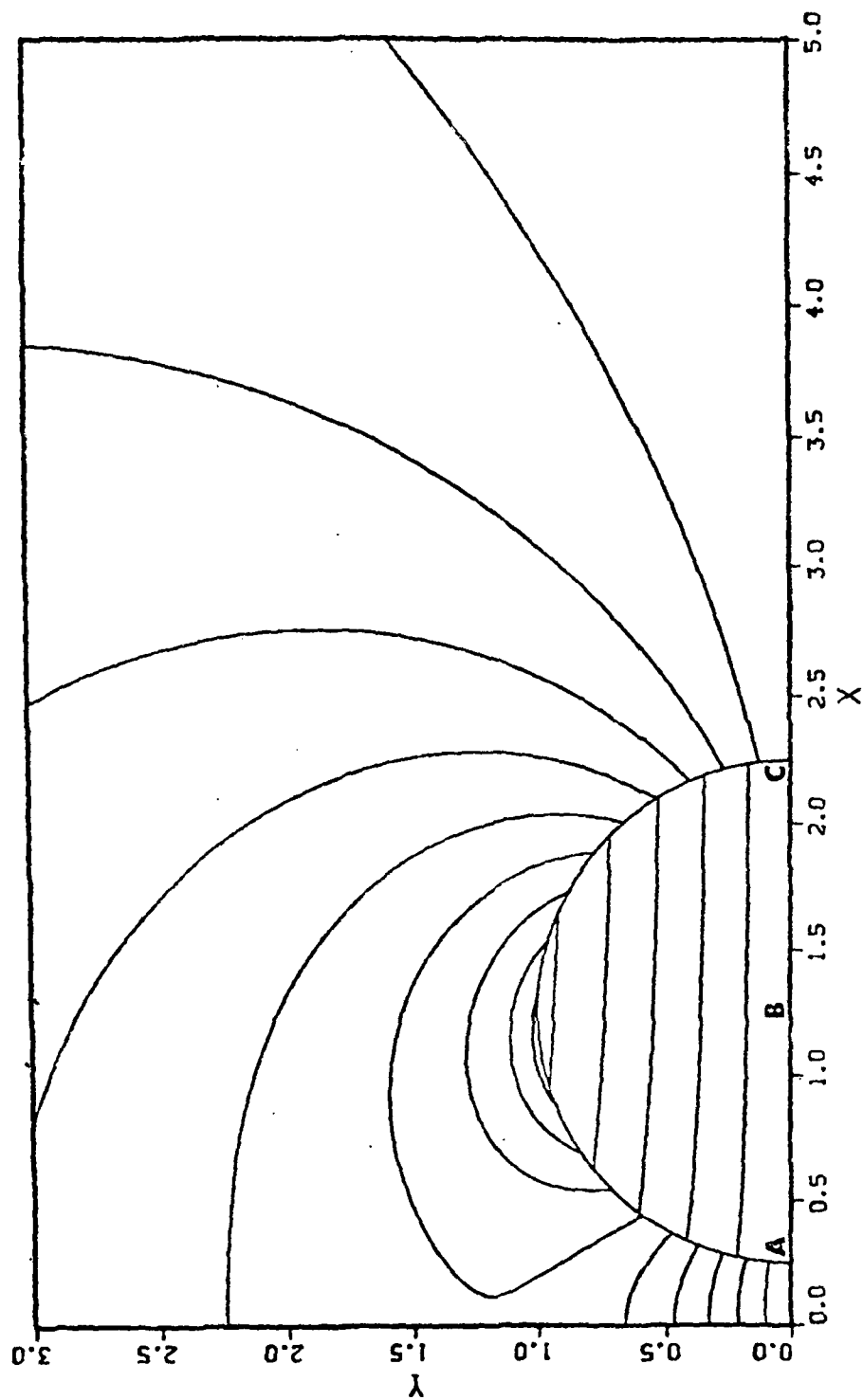


Figure 3(a)

TWO CLOUDS $K = 10.00$ $X_0 = 1.250$

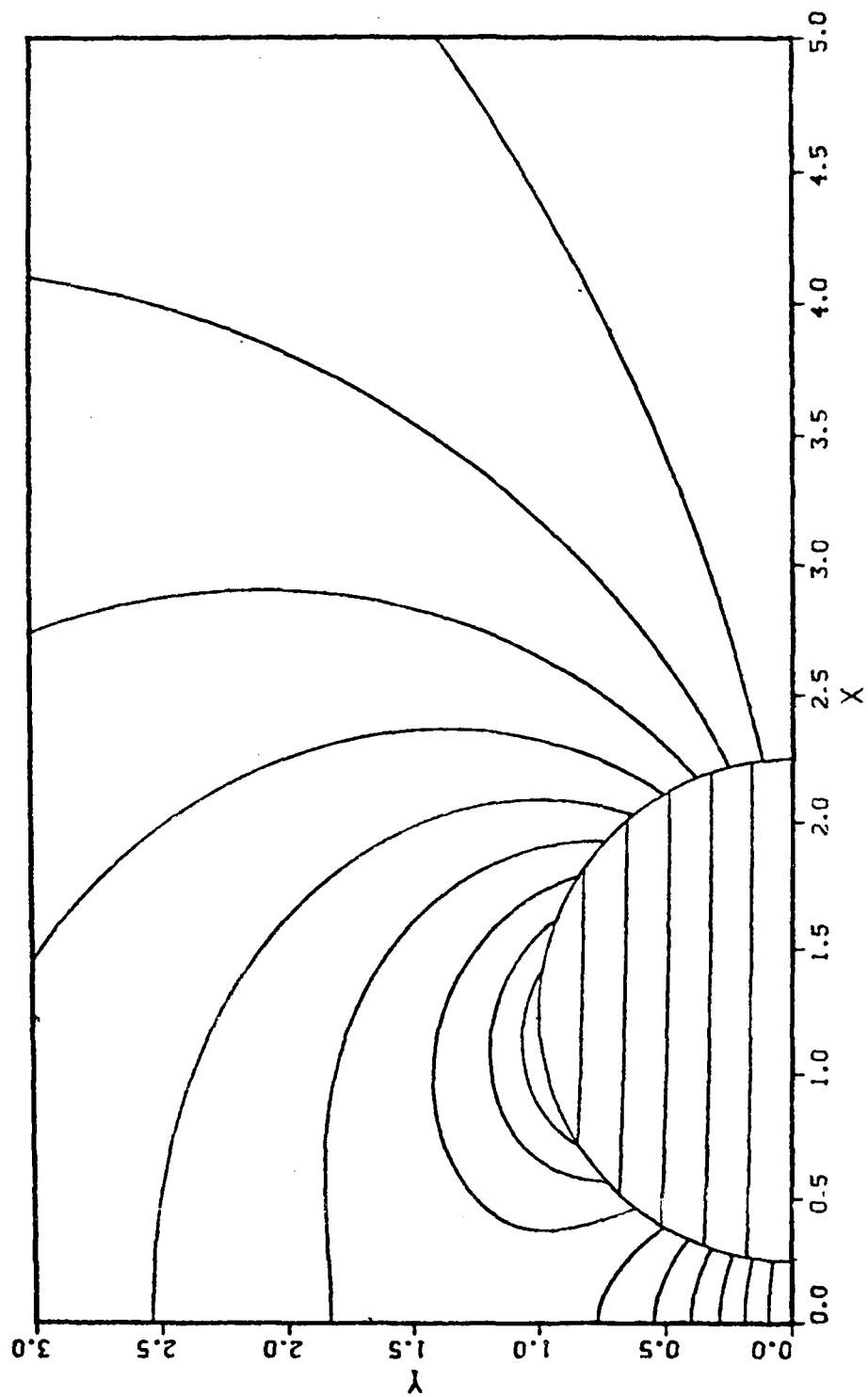


Figure 3(b)

TWO CLOUDS $K = 100.0 \times 0 = 1.250$

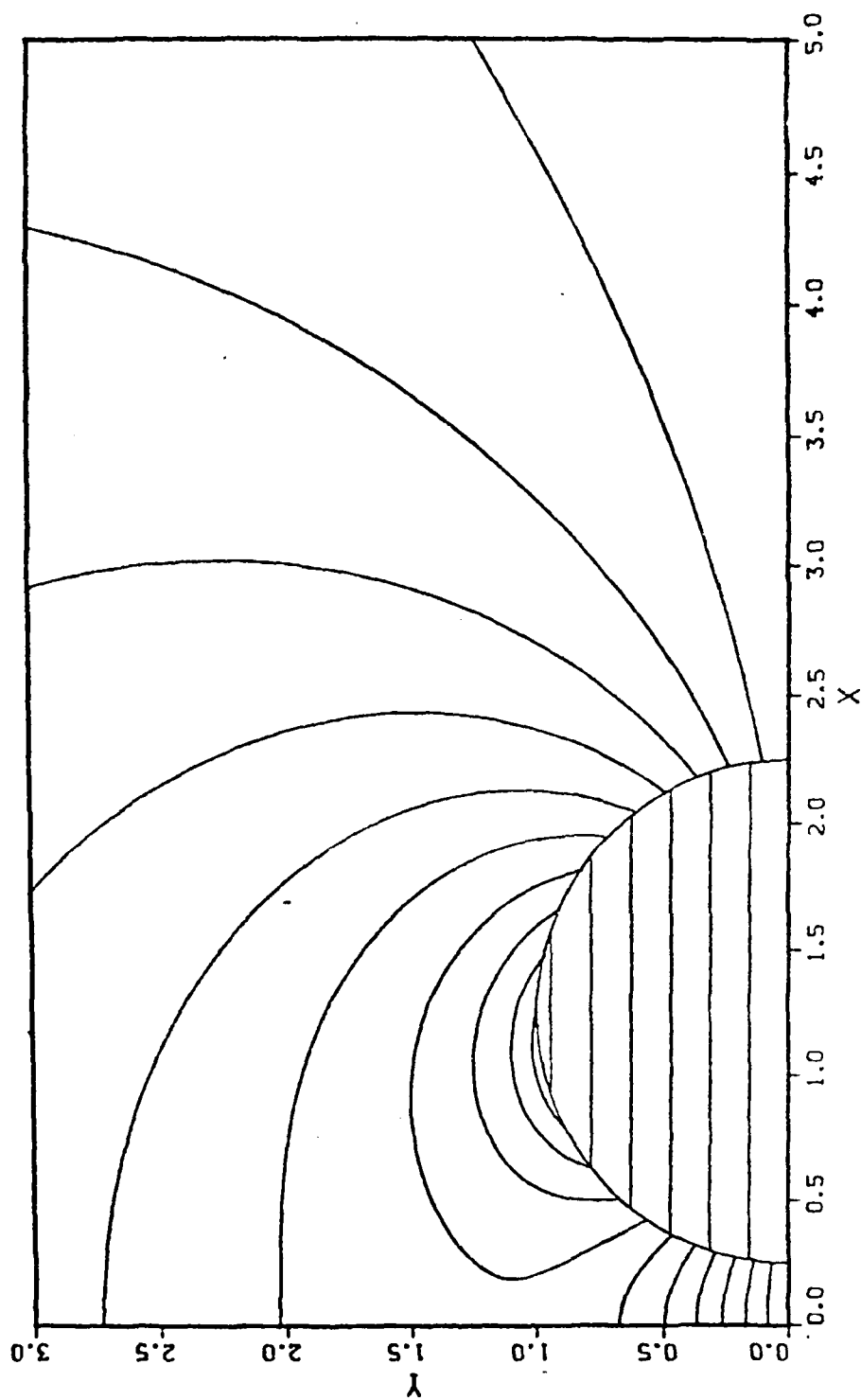


Figure 3(c) P-33

TWO CLOUDS $K = 3.000 \times 10^{-1.500}$

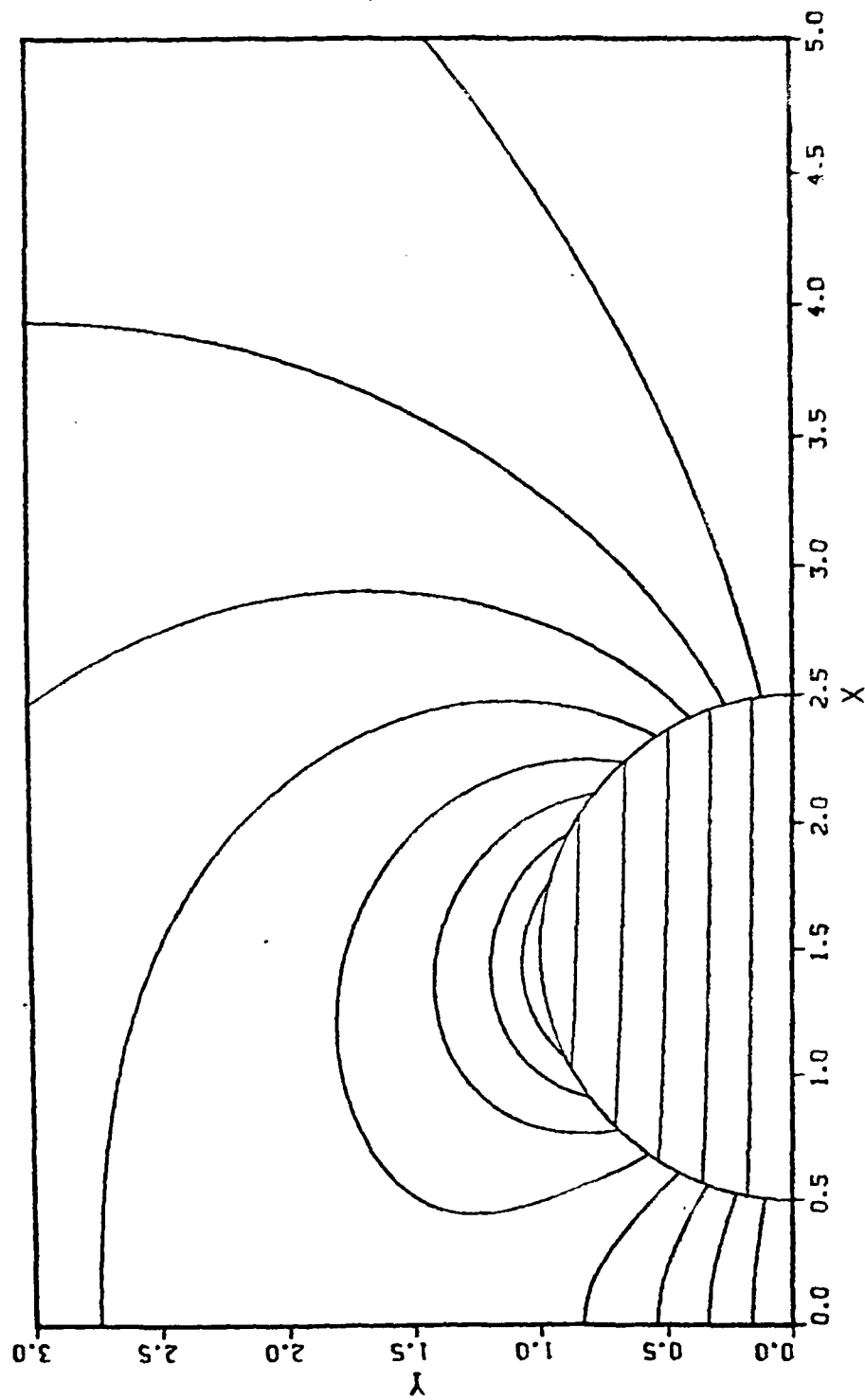


Figure 4(a) P-34

TWO CLOUDS K - 10.00 X0 - 1.500

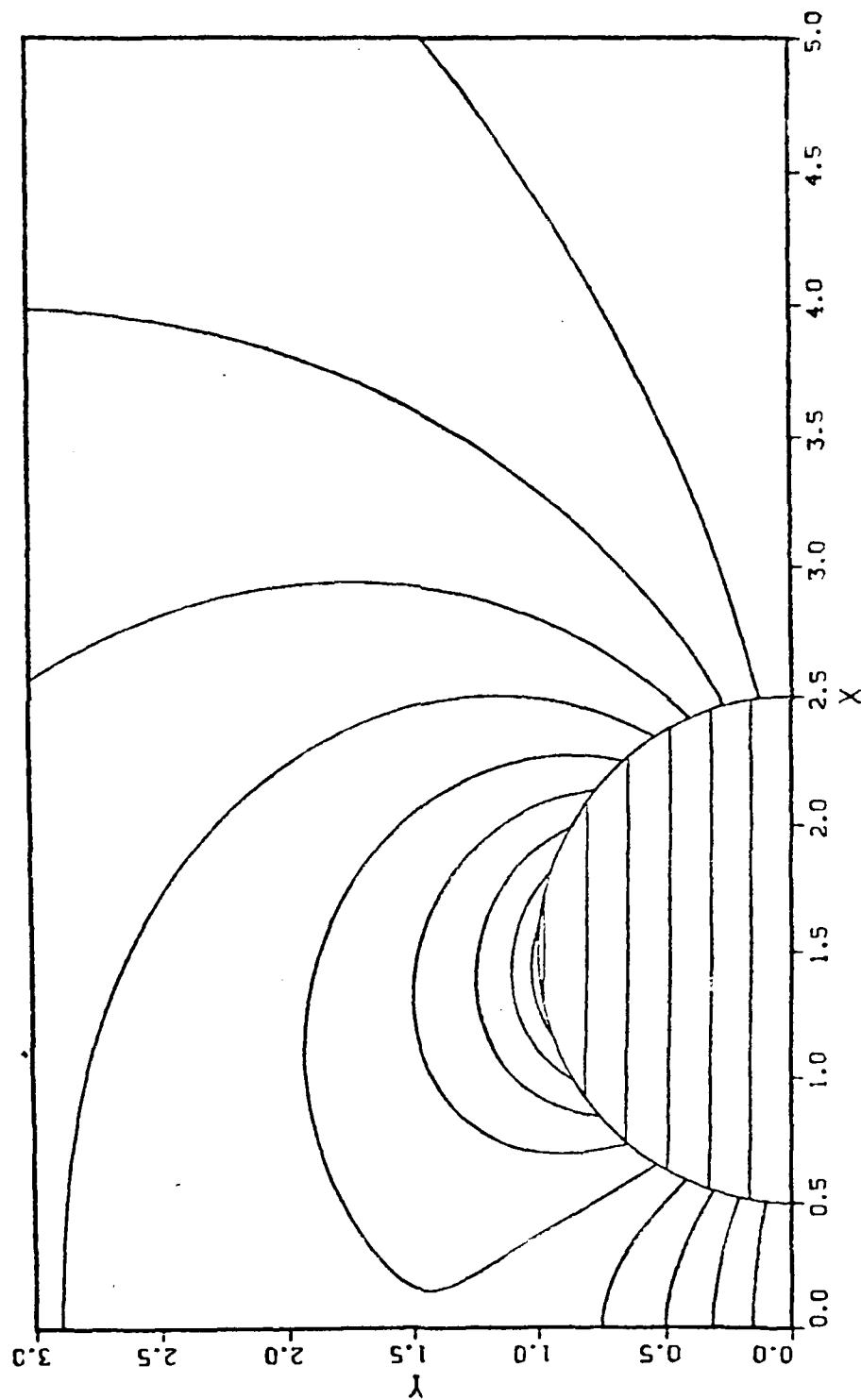


Figure 4(b)

F-35

TWO CLOUDS $K = 100.0 \times 0 - 1.500$

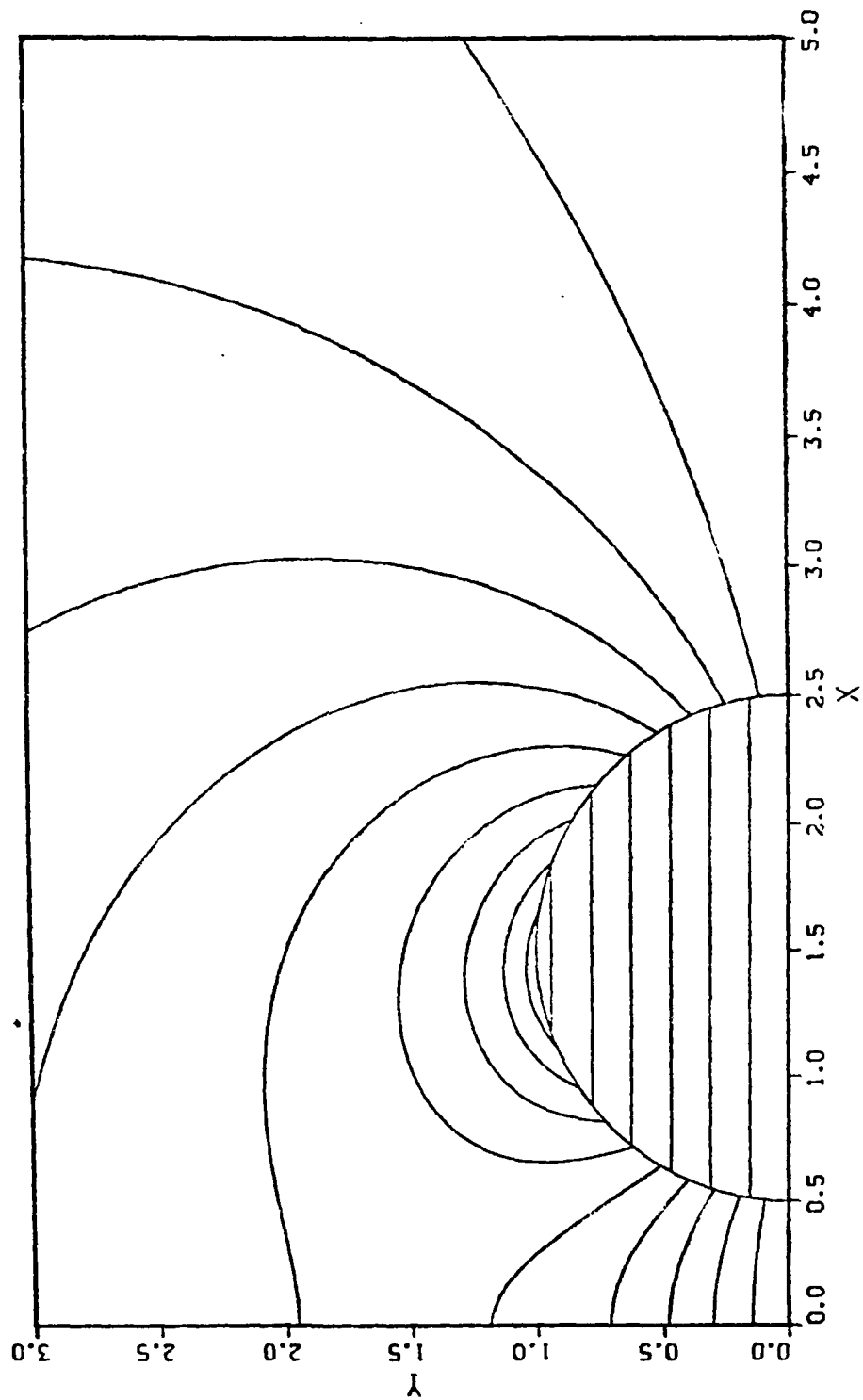


Figure 4(c)

TWO CLOUDS $K = 3.000 \times 10^{-2.000}$

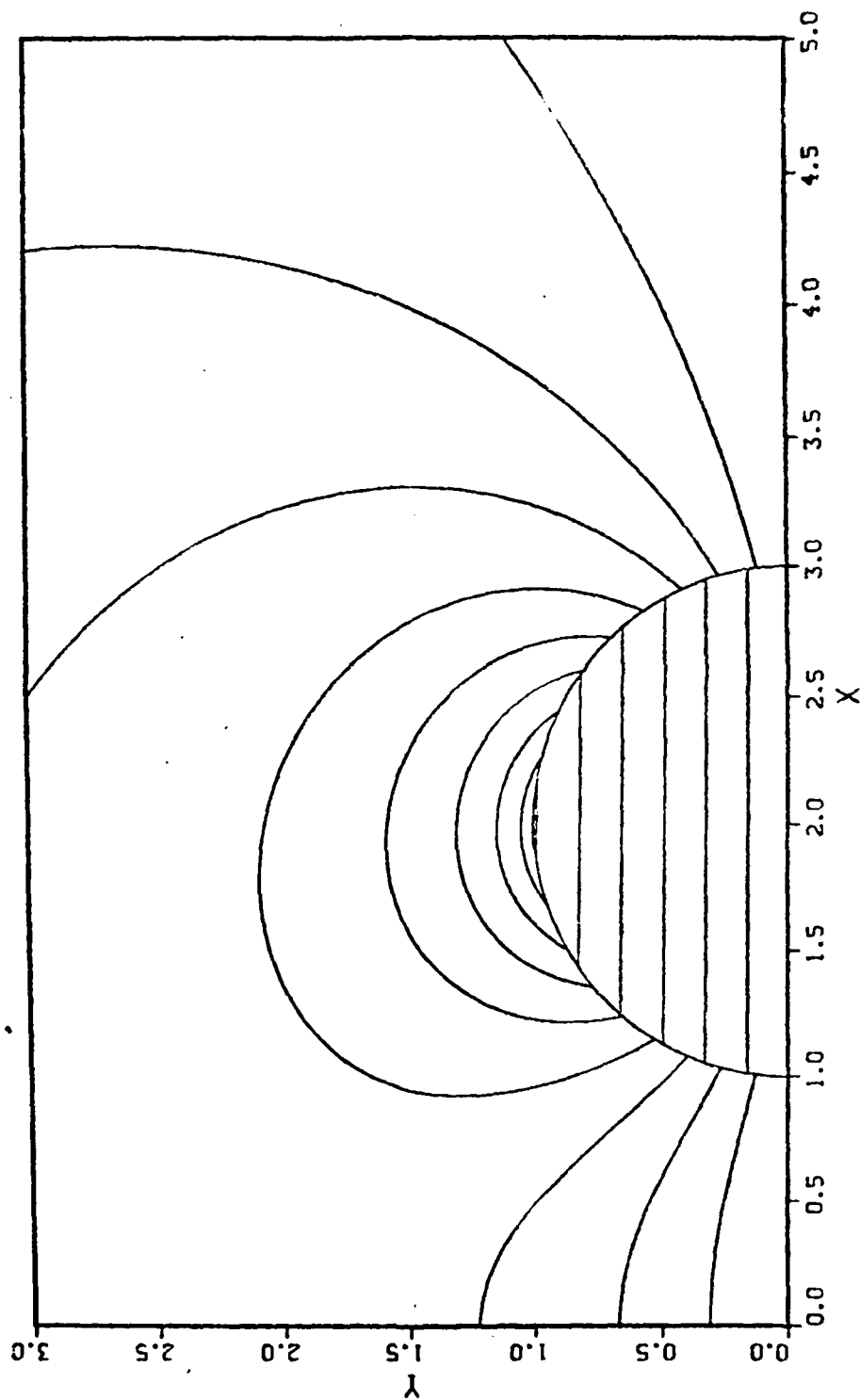


Figure 5(a) P-37

TWO CLOUDS $K = 10.00$ $X_0 = 2.000$

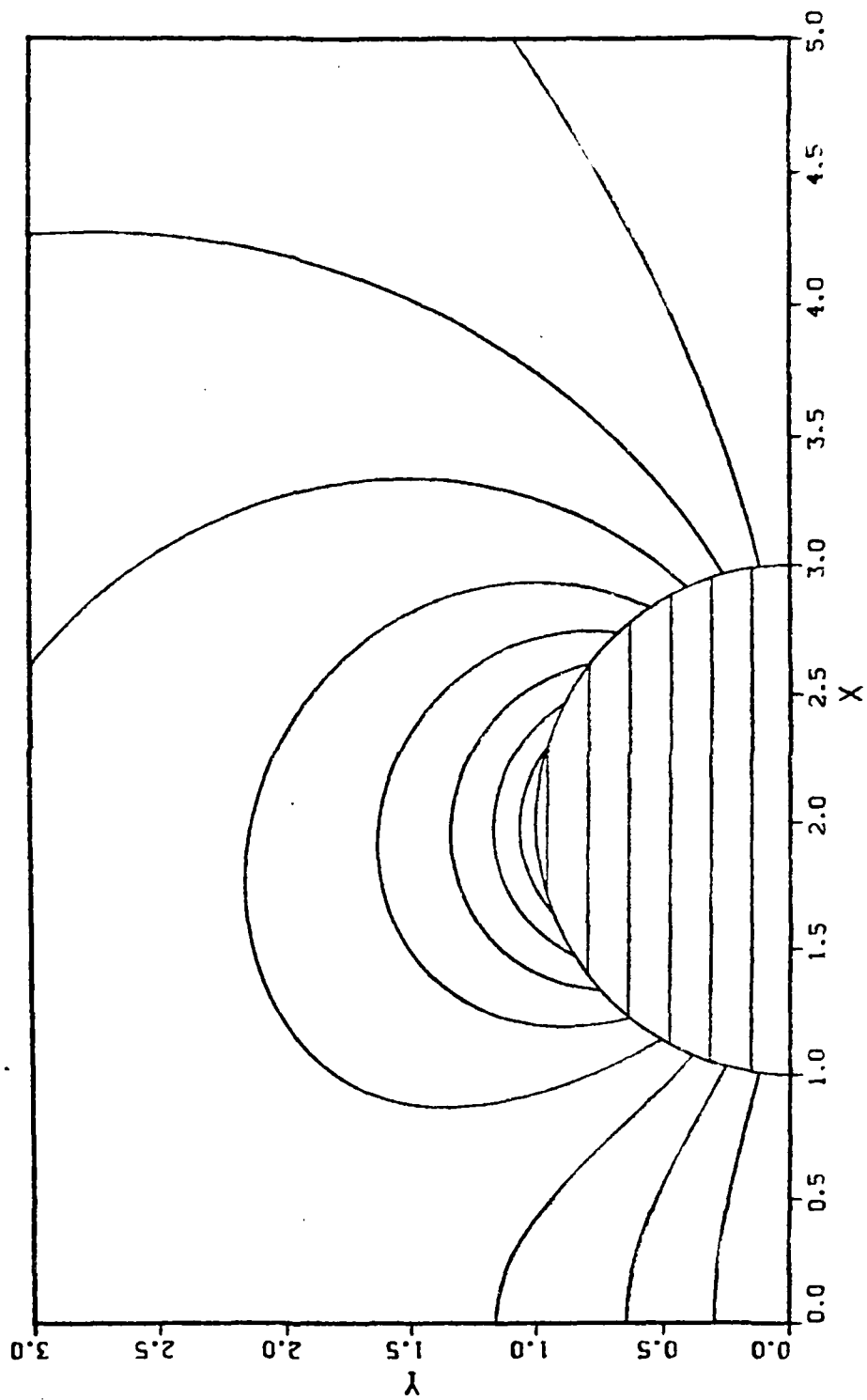


Figure 5(b)

TWO CLOUDS $K = 100.0 \times 0 = 2.000$

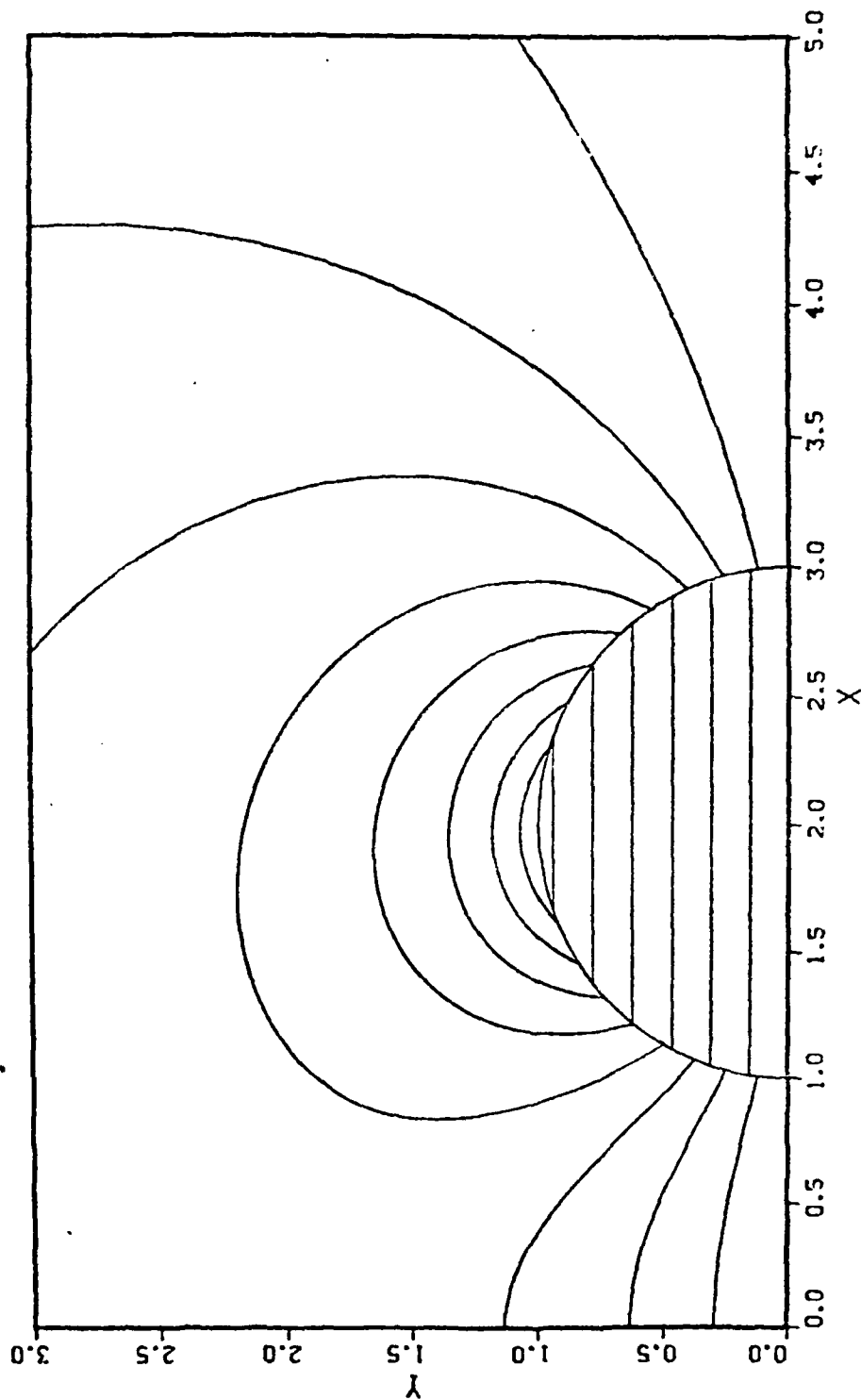


Figure 5(c)

THREE CLOUDS K - 3.000 X0 - 1.250

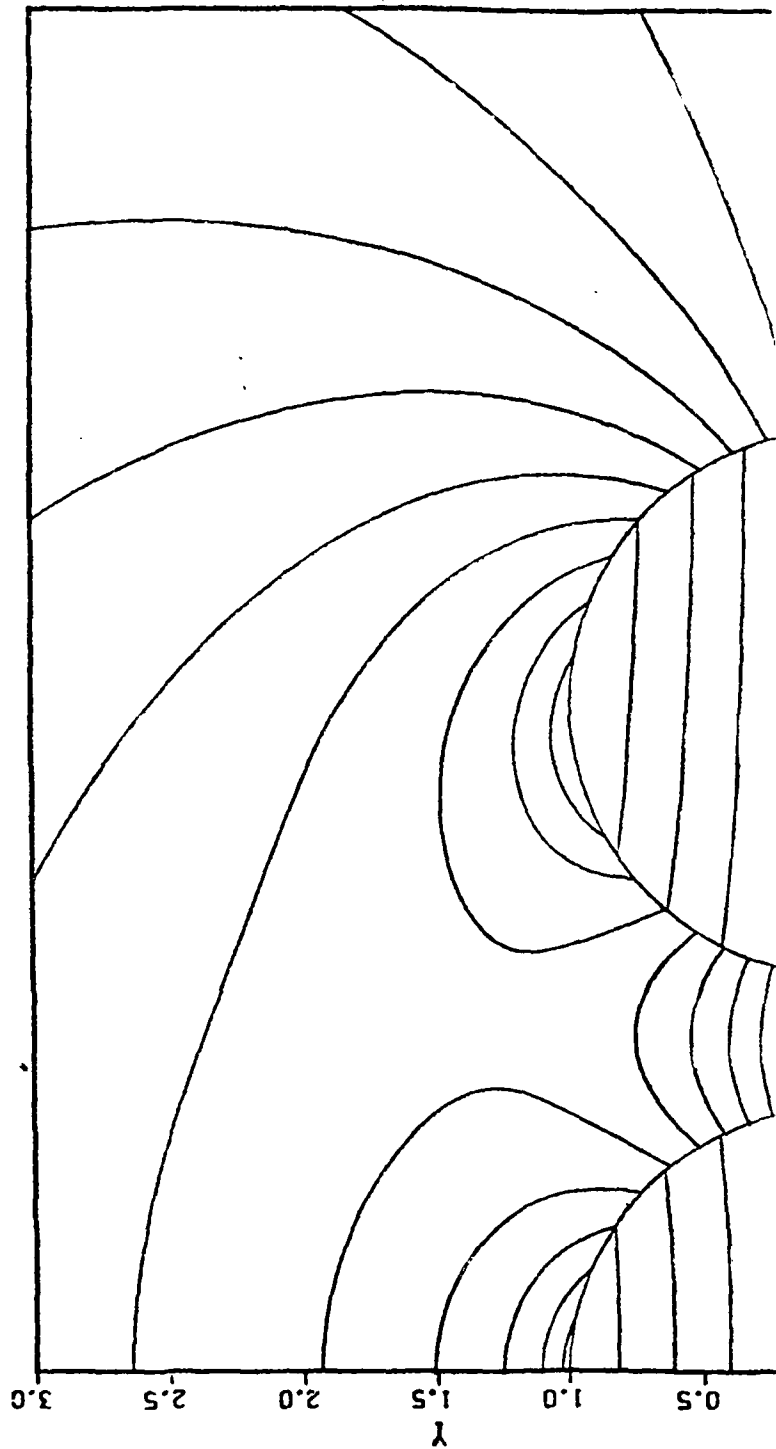


Figure 6(a) P-40

THREE CLOUDS K - 10.00 X0 - 1.250

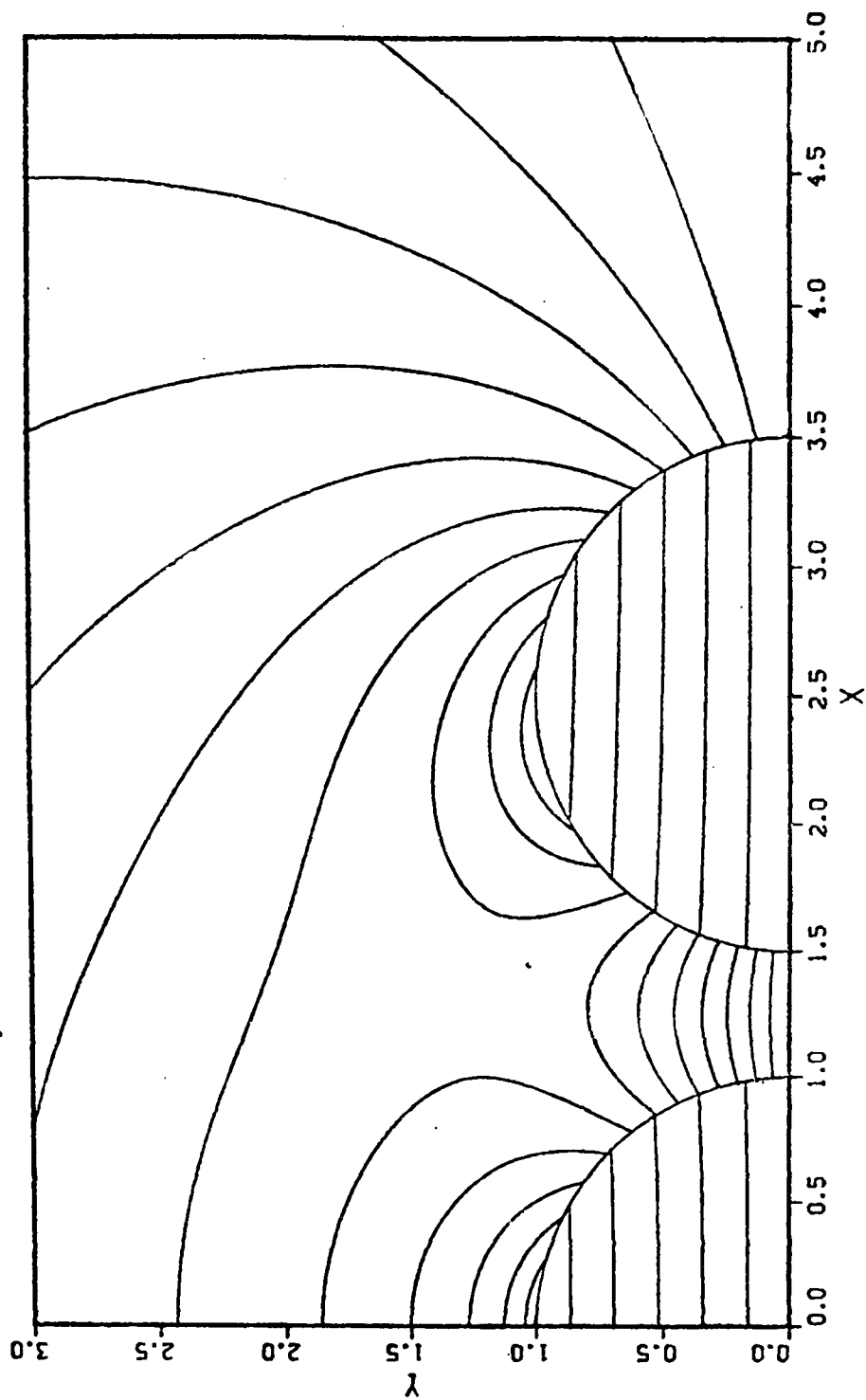


Figure 6(b) P-41

THREE CLOUDS $K = 100.0 \times 0 - 1.250$

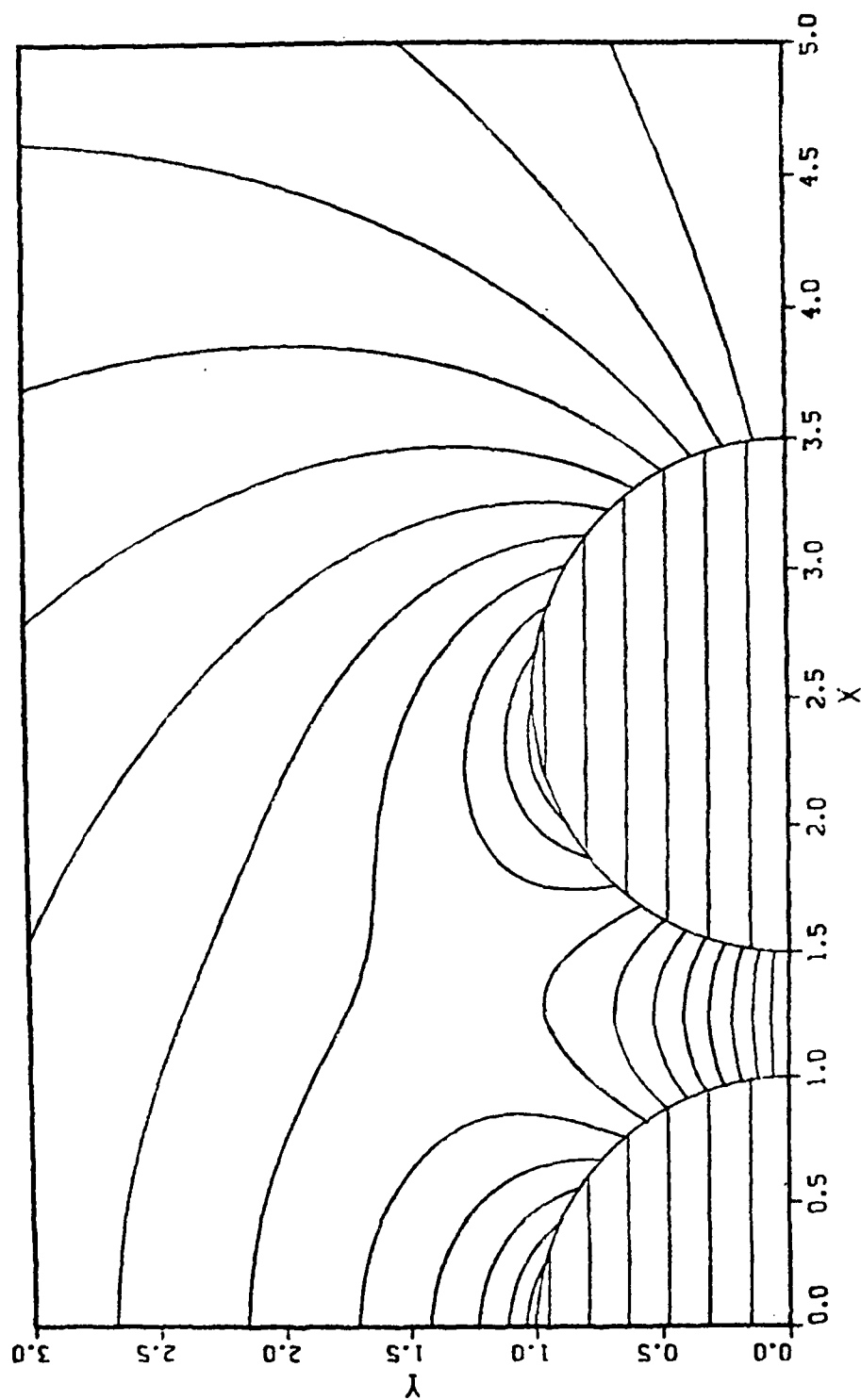


Figure 6(c) P-42

THREE CLOUDS $K = 3.000 \times 10^{-1.500}$

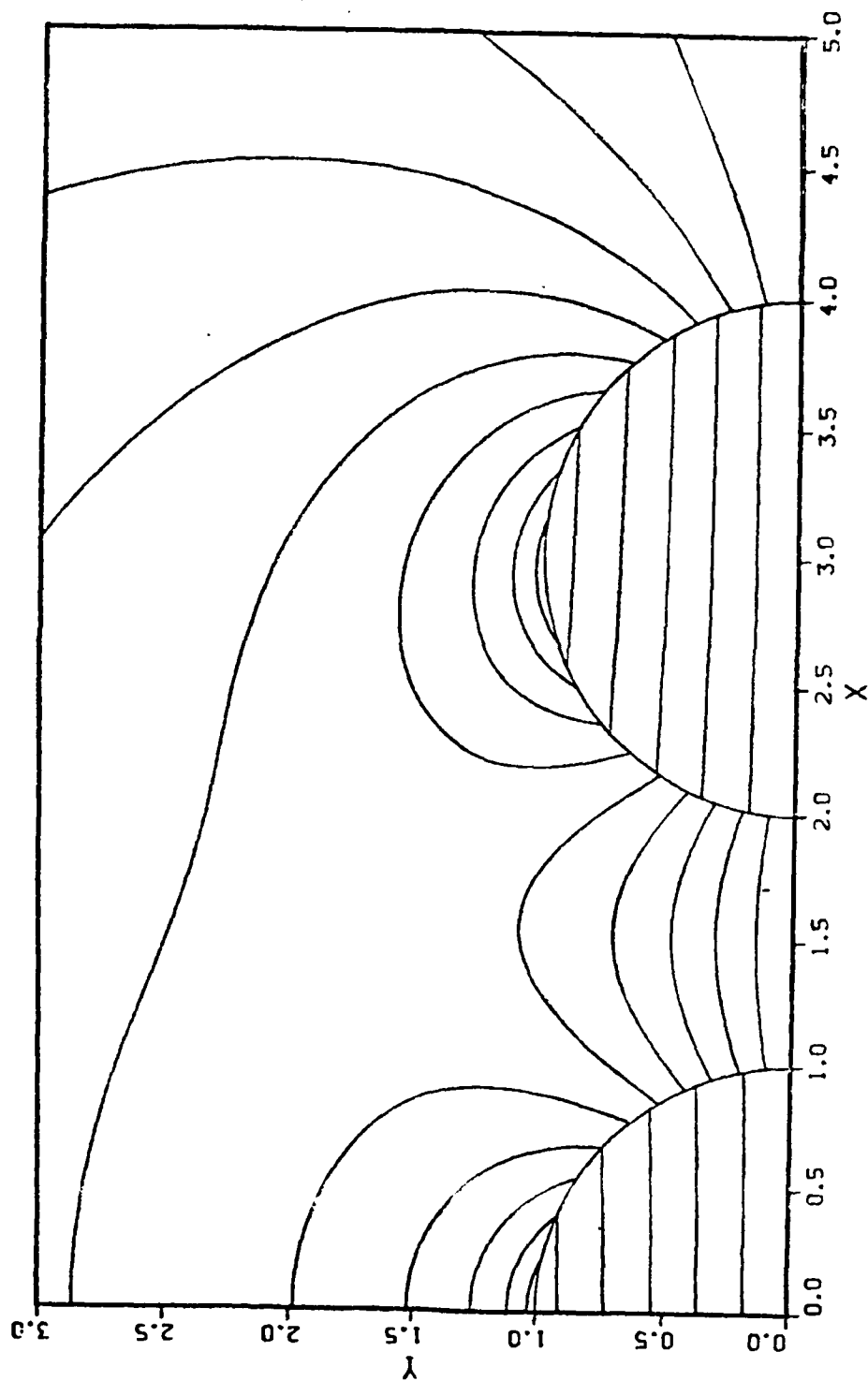


Figure 7(a) P-43

THREE CLOUDS $K = 10.00$ $X_0 = 1.500$

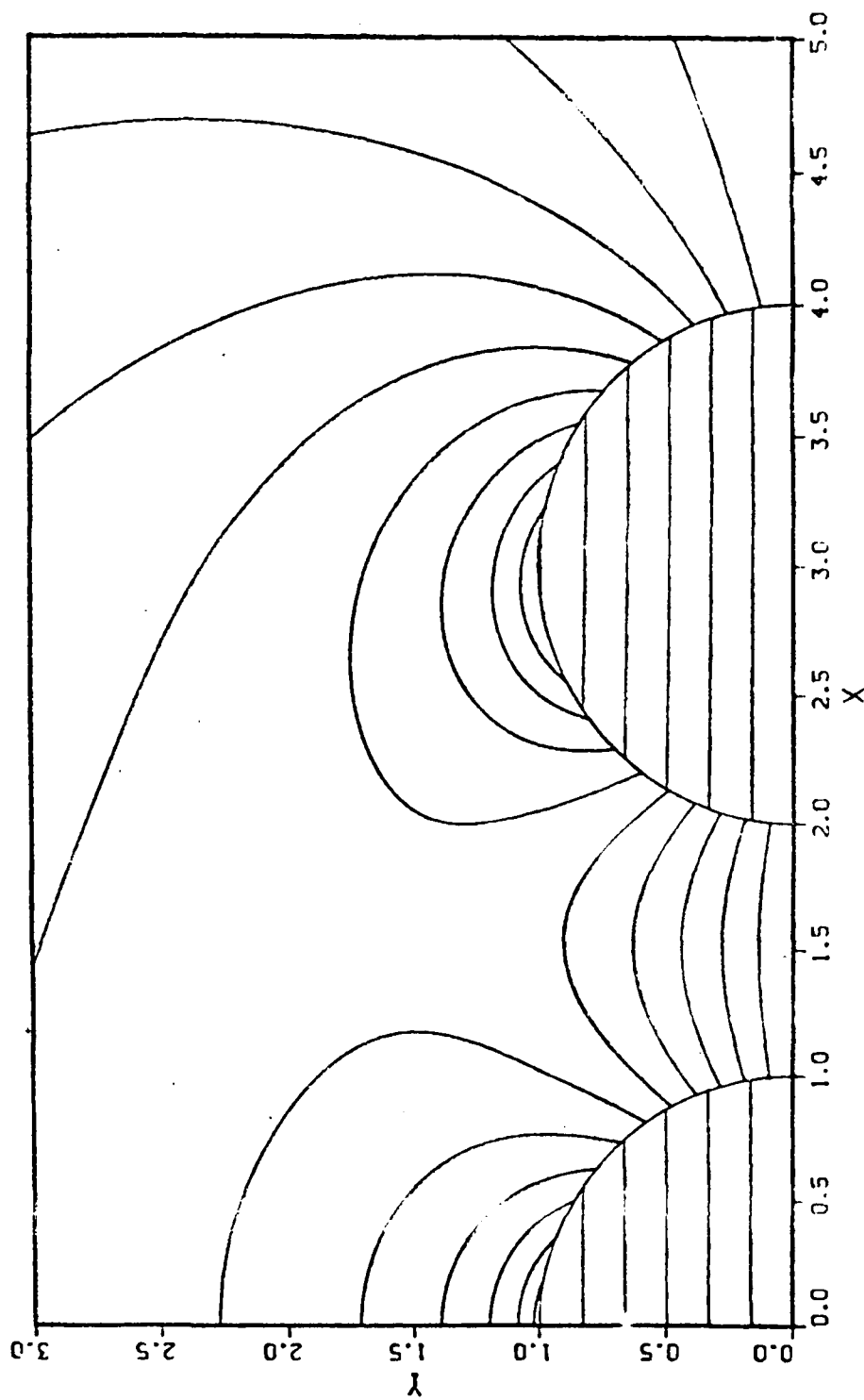


Figure 7(b)

THREE CLOUDS K - 100.0 X0 - 1.500

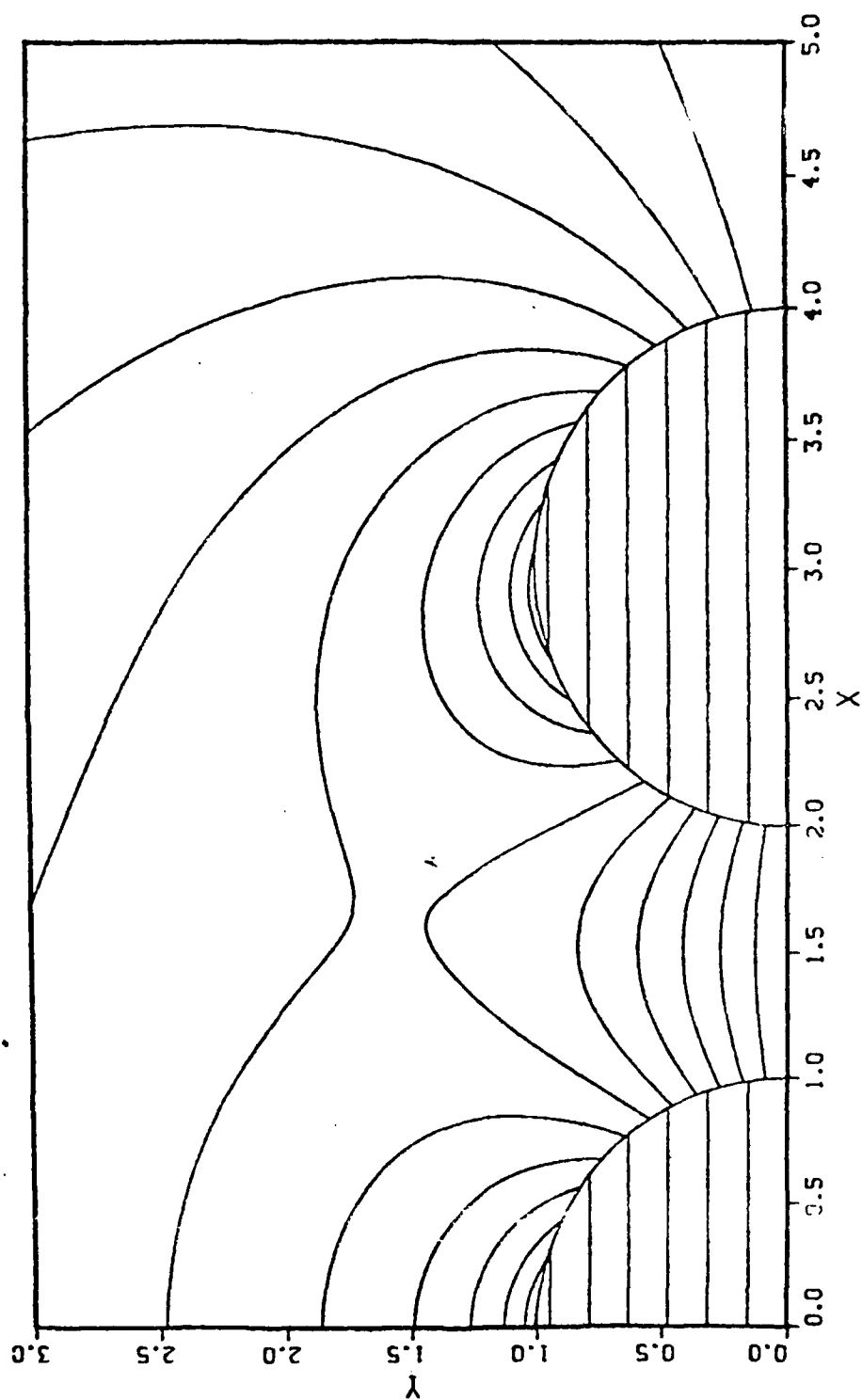


Figure 7(c)

THREE CLOUDS $K = 3.000 \times 10^{-2.000}$

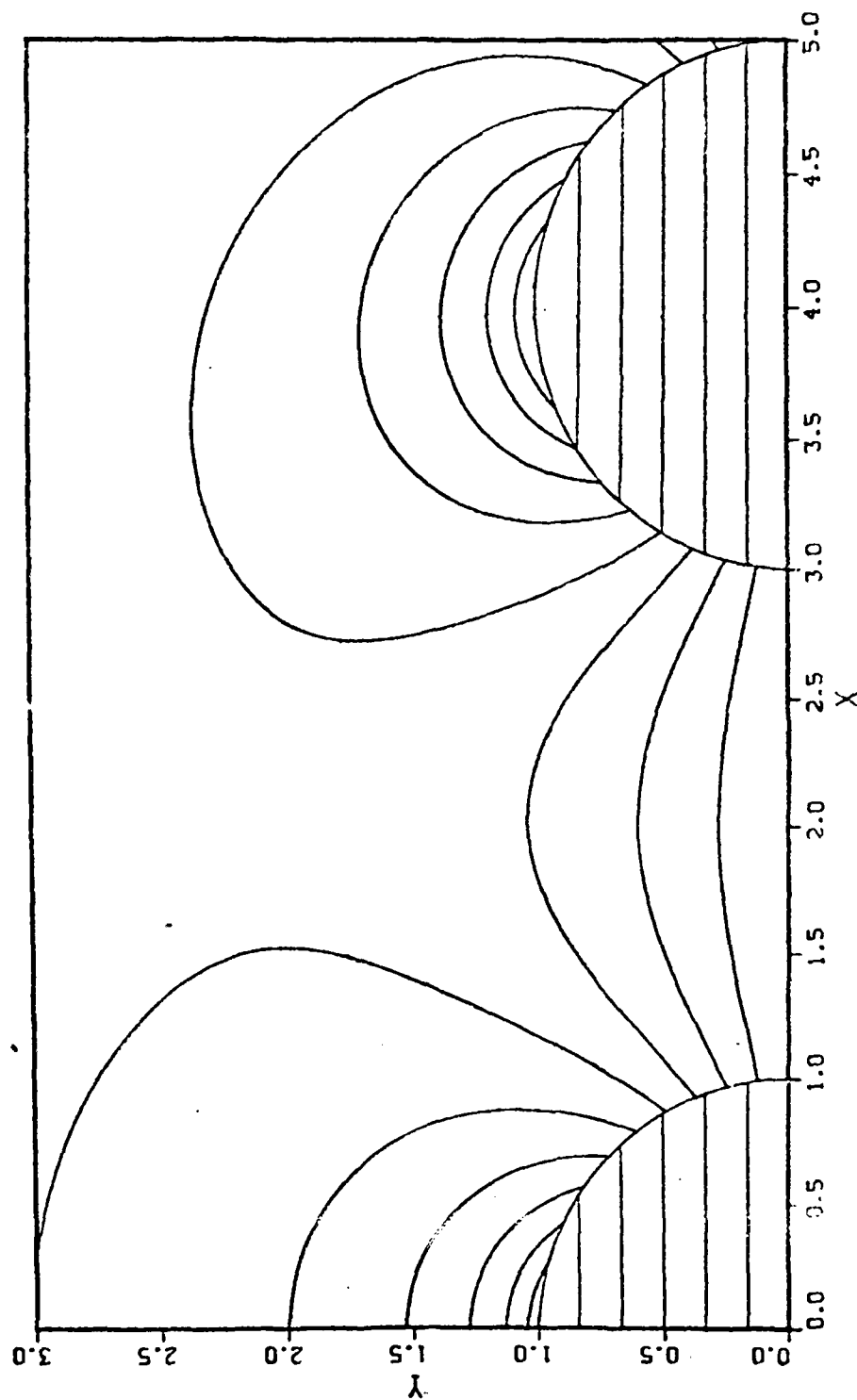


Figure 8(a)

THREE CLOUDS $K = 10.00 \times 0 - 2.000$

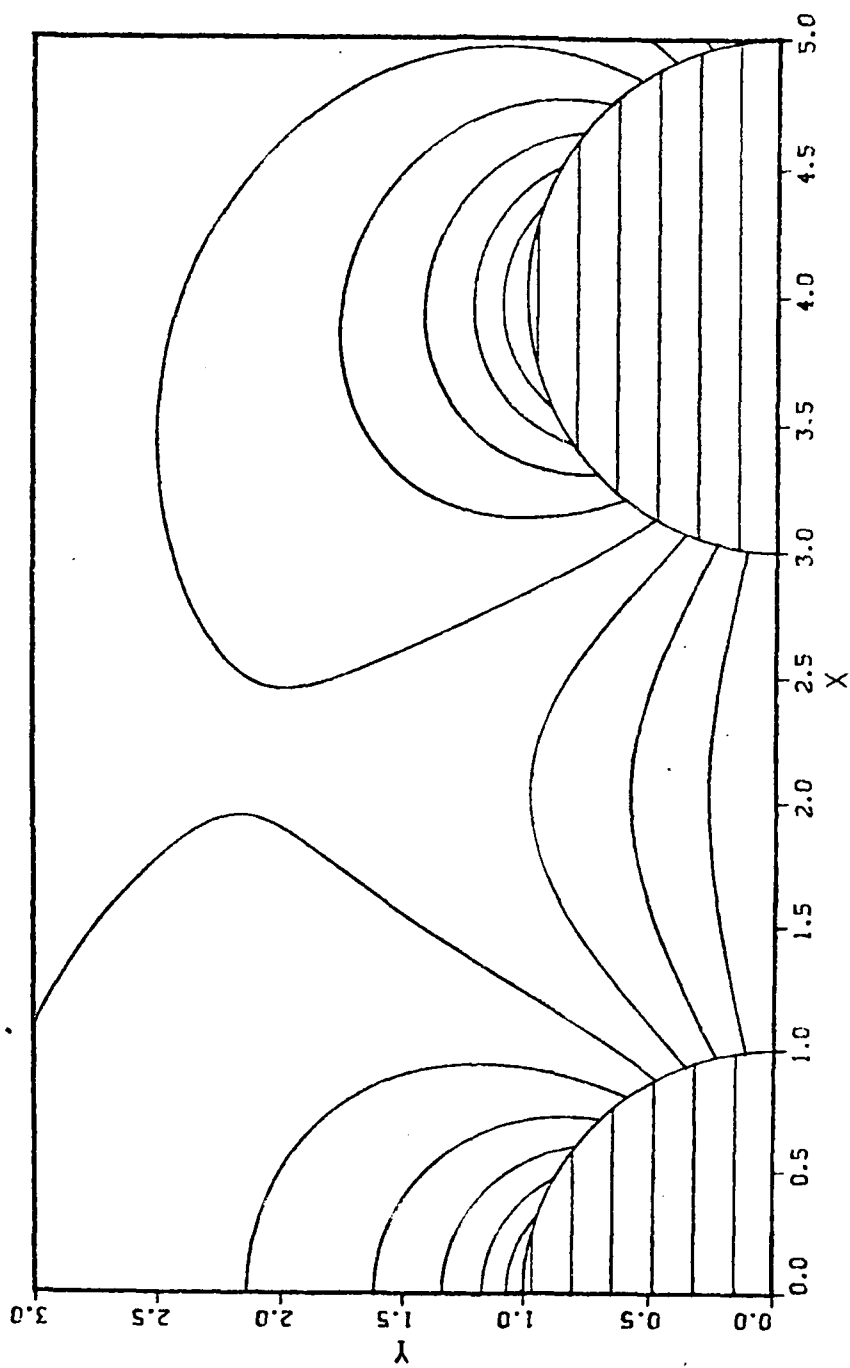


Figure 8(b) p-47

THREE CLOUDS $K = 100.0$ $X_0 = 2.000$

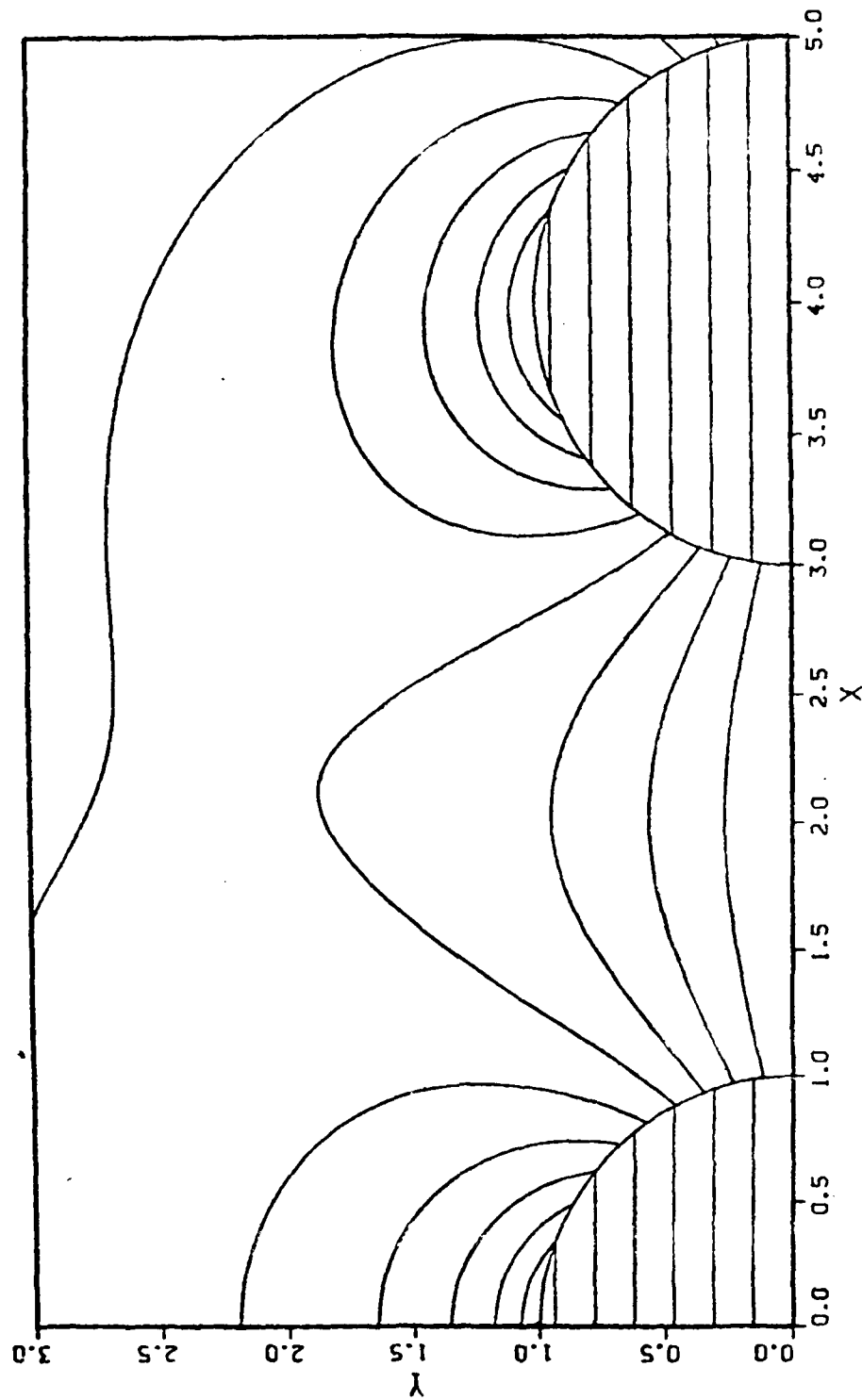


Figure 8(c)

APPENDIX Q
MODEL OF LINEAR RESPONSE TO
TROPICAL HEAT SOURCES

Keith Sashegyi
Science Applications, Inc.

Model of Linear Response to Tropical Heat Sources

The model is a two dimensional linear model in latitude and height which provides the linear response in a stratified atmosphere to prescribed tropical heat sources. The model variables are Fourier decomposed in longitude. The model follows that of Geisler (1981) who modelled the Walker circulation as the linear response of a stratified atmosphere to a prescribed steady latent heat source in a basic state of no motion. Here we use a basic state with a mean zonal flow, which can depend on latitude and height.

1. Model Equations

In the model, the primitive equations on a sphere in log-pressure coordinates are linearized with respect to a basic state with a mean zonal flow, which can be dependent on latitude and height. We are interested in the motion forced by prescribed latent heat sources of given frequency ω . Damping is modelled by Rayleigh friction (coefficient s), Newtonian cooling (coefficient $\bar{\theta}$), vertical eddy viscosity (coefficient K) and by cumulus friction.

The equations are

$$\left[i\omega + \frac{i s \bar{U}}{a(1-y^2)} \right] U - \left(2\omega y - \frac{1}{a} \frac{\partial \bar{U}}{\partial y} \right) V + w \frac{\partial \bar{U}}{\partial z} \\ = -\frac{i s}{a} \bar{\theta} + F_1 \quad (1)$$

$$\left[1 + \frac{1}{a} \frac{s \bar{U}}{(1-y^2)}\right] V + \left[2xy + \frac{2 \bar{U} y}{a(1-y^2)}\right] U$$

(2)

$$= - \frac{(1-y^2)}{a} \frac{\partial \bar{U}}{\partial y} + F_y$$

$$\frac{1}{a} \frac{s \bar{U}}{(1-y^2)} + \frac{1}{a} \frac{\partial V}{\partial y} + e^{z/H} \frac{\partial}{\partial z} (e^{-z/H} W) = 0 \quad (3)$$

$$\left[1 + \frac{1}{a} \frac{s \bar{U}}{(1-y^2)}\right] \frac{\partial \bar{U}}{\partial z} + N^2 W - \frac{fV}{(1-y^2)} \frac{\partial \bar{U}}{\partial z}$$

(4)

$$= \frac{RQ}{c_p H} + F_Q$$

$$\frac{\partial \bar{U}}{\partial z} = \frac{gT}{T_0}$$

Here the vertical coordinate z in this model is given by

$$z = -H \log p/p_0$$

where p is the pressure, p_0 a constant reference pressure (taken at the surface) and H is a scale height defined by

$$H = \frac{RT_0}{g}$$

where R is the gas constant, T_0 a reference temperature and g is the acceleration due to gravity. For $T_0 = 300$ K,

$H = 8.8$ km. In the model N^2 is the Brunt Vaisala frequency, which measures the stability of the stratified model atmosphere,

$$N^2 = \frac{g}{T_0} \left[\frac{d\bar{T}}{dz} + \gamma \frac{\bar{T}}{T_0} \right]$$

where $\langle T \rangle$ is a horizontally averaged temperature over the model horizontal domain and $\gamma = g/c_p$ is the adiabatic lapse rate, with c_p the specific heat at constant pressure. y is the sine of latitude, a is the average radius of the earth and Ω is the earth's rotation rate. U, V, W, ϕ, T are zonal Fourier amplitudes for the perturbation motion field, geopotential and temperature, respectively at zonal wavenumbers S ($S = 0, 1, 2, \dots$). \bar{U} is the zonal motion of the basic state about which the variables are linearized. Here the components U, V of the model horizontal motion are given by

$$U = u' \cos \phi$$

$$V = v' \cos \phi$$

where u', v' are the Fourier amplitudes of the horizontal velocity components and ϕ is the latitude. $W = dz/dt$ is the Fourier amplitude of the vertical velocity field with respect to the log-pressure coordinate Z . The components of the vertical frictional forces in the model are represented by F_x (in longitudinal direction) and F_y (in the

latitudinal direction), while the dissipation of heat is represented by F_Q . Q represents the Fourier amplitude of the heating rate which forces the model.

2. Model Forcing

2a. Cumulus Heating, Q_c

The model is forced by prescribed heat sources Q_c which represent the latent heating caused by large-scale cumulus convection. The vertical structure of the cumulus heating follows that of Stevens et.al. (1977) who used a cubic equation in pressure to represent the vertical structure of the cumulus heating. The functional form is

$$Q_c = Q_0 C (p - p_T)(p - p_n)(p - p_{CB}) B(y, s)$$

where $p_T = 140$ mb is cloud top, $p_{CB} = 900$ mb is cloud base and p_n is chosen to give a maximum heating rate at 400 mb. C is the normalizing constant chosen to give a vertically integrated heating rate that matches a precipitation rate of 1 cm/day. Q_0 is the rainfall rate in cm/day. This functional form of the vertical heating profile, which has a maximum heating rate of $6^\circ\text{C}/\text{day}$ at 400 mb, is close to the heating profiles deduced from budget studies of organized deep convection in the tropics (Yanai et.al., 1973). $B(y, s)$ represents the Fourier amplitude of the horizontal

distribution of the heating rate. The horizontal distribution is specified to match the observed distribution of rainfall rates in the tropics.

2b. Forcing by Prescribed Sea Surface Temperature Anomalies, T_s

A warm sea surface temperature anomaly (SST) is prescribed and the resulting surface sensible heat flux calculated by a drag coefficient formulation. The sensible heating in the boundary layer is modelled by eddy diffusion with a coefficient K given by that for the eddy diffusion of momentum. Deep cumulus convection can form over these SST anomalies in the western and central Pacific. The amount of cumulus heating caused by an SST anomaly is parameterized in terms of the total moisture convergence in the atmospheric layer below the trade wind inversion at 2km. The magnitude of the cumulus heating that is compatible with the warm SST anomaly can be found by an iterative process of many solutions. This method was used by Schneider (1977) in his model of the Hadley cell. The iterative method is now described. An initial solution provides the mass convergence in this lower 2km layer, caused by the sensible heating from the warm SST anomaly. The horizontal distribution of the moisture field q in the tropical boundary layer is specified and

the moisture convergence calculated with the initial solution. The moisture convergence then gives the vertically integrated cumulus heating rate.

$$\frac{1}{g} \int_0^{1000} c_p Q_c dp = \begin{cases} Lq w_I, & w_I > 0 \\ 0 & , w_I < 0 \end{cases}$$

where L is the latent heating of fusion, q the moisture field and w_I the vertical velocity at the level of the trade wind inversion ($z = 2\text{km}$).

Assuming the vertical structure of the cumulus heating given in 2a, the magnitude is found. The response to the addition of this cumulus heating rate is then found with the model, providing the second solution. A new boundary layer convergence can then be calculated and a corrected cumulus heating rate found and the process repeated.

3. Frictional Forces

3a. Eddy Fluxes

The vertical fluxes of momentum and heat we parameterized in this case using an eddy diffusion coefficient K which can be a function of height.

For momentum,

$$F_{xK} = \frac{\partial}{\partial z} \left(K \frac{\partial U}{\partial z} \right)$$

$$F_{yK} = \frac{\partial}{\partial z} \left(K \frac{\partial V}{\partial z} \right)$$

For heat,

$$F_{QK} = \frac{q}{T_0} \left[\frac{\partial}{\partial z} K \left(\frac{\partial T}{\partial z} + \frac{T}{T_0} \right) \right]$$

where the eddy diffusion coefficients of heat and momentum are assumed equal. The eddy diffusion coefficient K is made large (some $K = 5 \times 10^5 \text{ cm}^2/\text{sec}$) in the surface boundary layer and smaller in the interior (some $K = 5 \times 10^4 \text{ cm}^2/\text{sec}$).

3b. Rayleigh Friction and Newtonian Cooling

In the model interior, damping can be modelled by a linear drag (coefficient ϵ) and cooling (coefficient δ) with

$$F_{Xe} = -\epsilon U$$

$$F_{Ye} = -\epsilon V$$

$$F_{Q\delta} = -\frac{\delta q}{T_0} T$$

Near the model upper boundary, the Rayleigh friction coefficient ϵ can be increased in magnitude to suppress spurious reflections of the solution. In the interior of the model domain small values of the coefficients ϵ, δ are used with damping times $\epsilon^{-1}, \delta^{-1}$ of 15 days.

3c. Cumulus Friction

The vertical transport of horizontal momentum by deep convection can have a damping effect on the large-scale flow field. Schneider and Lindzen (1976) parameterized this cumulus friction as

$$F_C = \frac{1}{\rho} \frac{\partial}{\partial h} [m_C (\bar{v} - \bar{v}_{CB})]$$

where h is the altitude, m_C the mean cloud mass flux and \bar{v} the velocity of the large scale wind field at height h . \bar{v}_{CB} is the velocity of the large-scale wind field at cloud base. They showed that decomposing the variables (u, v) into a zonal average \bar{u} and a deviation u' , v' lead to the following linearized form,

$$F_{xC} = \frac{1}{\rho} \frac{\partial}{\partial h} [\bar{m}_C (u' - u'_{CB}) + m'_C (\bar{u} - \bar{u}_{CB})]$$

$$F_{yC} = \frac{1}{\rho} \frac{\partial}{\partial h} [\bar{m}_C (v' - v'_{CB})]$$

We follow their formulation and in log-pressure coordinates we have for the Fourier amplitudes u, v

$$F_{xC} = -g \left(\frac{\partial \bar{m}_C}{\partial p} \right) (U - U_{CB}) - g \left(\frac{\partial m'_C}{\partial p} \right) (\bar{U} - \bar{U}_{CB}) \\ + \frac{gH}{p} \bar{m}_C \frac{\partial u}{\partial z} + \frac{gH}{p} m'_C \frac{\partial \bar{U}}{\partial z}$$

$$F_{yC} = -g \left(\frac{\partial \bar{m}_C}{\partial p} \right) (v - v_{CB}) + \frac{gH}{p} \bar{m}_C \frac{\partial v}{\partial z}$$

The zonally averaged cloud mass flux m_c is a specified function of latitude and height. In latitude its variation is given by that of the observed zonally averaged rainfall in the tropics. In height its variation is taken from Schneider and Lindzen as

$$\bar{m}_c = \bar{m}_{c0} [1 - \exp(-(p-p_T)/p_D)]$$

where $p_T = 140\text{mb}$ is the pressure at cloud top, $p_D = 100\text{mb}$ is the detrainment scale and \bar{m}_{c0} the zonally averaged mass flux at cloud base given by $g\bar{m}_{c0} = 2.5\text{mb/hr}$.

The cloud mass flux m_c for the perturbation field can be related to the perturbation field cumulus heating Q_c . Here we use the result of Yanai et al (1973) who showed in their budget study of the large scale effect of convection that the apparent heating due to cumulus convection can be represented as

$$Q_c = -m_c \frac{\partial S}{\partial p} - Le$$

where $S = c_p T + gh$ is the large scale dry static energy, L is the latent heating of fusion and e the evaporation of cloud droplets. The apparent heating Q_c is then interpreted as consisting of an adiabatic warming due to a component of downward motion which compensates the cloud mass flux m_c (1st term on right) and a cooling due to the re-evaporation of cloud droplets (2nd term on right). The

second term $-Le$ is much smaller than the first and we neglect it. Then in the log pressure coordinates we have

$$Q_c = \frac{M_c}{\rho} \left(\frac{\partial T}{\partial z} + T/T_0 \right)$$

which relates the cumulus mass flux in the perturbation field to the perturbation cumulus heating which is known. ρ is the basic state density field.

4. The Boundary Layer

In the tropical atmosphere a well mixed layer exists in the lowest 500-600 meters. Above the mixed layer is a trade cumulus layer with an inversion around 2km and the free atmosphere above. Following Schneider and Lindzen (1977) we use a large eddy viscosity of $K = 5 \times 10^5 \text{ cm}^2/\text{sec}$ and a reduced N^2 of 10^{-5} sec^{-1} to represent the large mixing and lower stability of the mixed layer. The trade cumulus layer (to 2km) is modelled as a transition layer in which the eddy viscosity decreases to its interior value of $10^4 \text{ cm}^2/\text{sec}$ and the static stability has a value which is 15% smaller than that of the free atmosphere ($N^2 \approx 10^{-4} \text{ sec}^{-1}$). At and above $z = 2 \text{ km}$, the static stability has its free atmosphere value, representing the trade wind inversion.

5. Boundary Conditions

The boundary conditions at the surface are one of

vanishing vertical motion W in log-pressure coordinates with the surface drag parameterized in terms of a bulk drag coefficient c_D . The linearized form of the surface stress is

$$K \frac{\partial u}{\partial z} = c_D U_0 U \text{ at } z = 0$$

where $c_D = 1.5 \times 10^{-3}$ is the drag coefficient and $U_0 = 8$ m/s. The heat flux at the surface is similarly parameterized in terms of a bulk drag coefficient c_H , where

$$-\rho c_p K \left(\frac{\partial T}{\partial z} + T/T_0 \right) = c_H c_p U_0 (T_s - T) \text{ for } T_s > 0$$

where T_s is the prescribed warm sea surface temperature anomaly.

A rigid lid is placed at the upper boundary of the model where $W = 0$ and

$$\frac{\partial U}{\partial z} = \frac{\partial V}{\partial z} = \frac{\partial T}{\partial z} = 0$$

The model domain is global. For non-zero wavenumber, the boundary conditions at the poles are given by zero geopotential and vertical velocity W . For wavenumber zero (the zonal mean solution), a flux boundary condition is used at the poles. That is, the meridional mass flux across the polar cap (at the first grid point of V off the

pole) balances the vertical motion at the pole. The geopotential at the pole then follows from the thermodynamic Equation (4).

6. Finite Differencing

The equations (1) to (4) are finite differenced on a global domain in a staggered grid with grid spacing $\Delta y = 0.1$ and $\Delta z = 1.5$ km. The rigid lid is placed at 22.5 km. The geopotential ϕ and vertical motion W are placed at the grid points in latitude and height, while the horizontal velocity components U and V are placed at the half grid points in latitude and height. The resulting block matrix system is solved using the technique of Lindzen and Kuo (1969).

7. References

- Geisler, J.E., 1981: A linear model of the Walker circulation. J. Atmos. Sci., 38, 1390-1800.
- Lindzen, R.S. and H.L. Kuo, 1969: Reliable method for numerical integration of a large class of ordinary and partial differential equations. Mon. Wea. Rev., 97, 732-734.
- Schneider, E.K., 1977: Axially symmetric steady-state models of the basic state for instability and climate studies. Part II. Nonlinear calculations. J. Atmos. Sci., 34, 280-297.
- Schneider, E.K. and R.S. Lindzen, 1977: Axially symmetric steady-state models of the basic state for instability and climate studies. Part I. Linearized calculations. J. Atmos. Sci., 34, 263-279.
- Schneider, E.K. and R.S. Lindzen, 1976: A discussion of the parameterization of momentum exchange by cumulus convection. J. Geophys. Res., 81, 3158-3160.
- Stevens, D.E., R. S. Lindzen and L.J. Shapiro, 1977: A new model of tropical waves incorporating momentum mixing by cumulus convection. Dyn. Atmos. Oceans, 1, 365-425.
- Yanai, M., S. Esbensen and J. H. Chu, 1973: Determination of bulk properties of tropical cloud clusters from large-scale heat and moisture budgets. J. Atmos. Sci., 30, 611.

APPENDIX R
A LINEAR DYNAMIC MODEL OF THE EAST AFRICAN
JET IN A STRATIFIED ATMOSPHERE

K.D. Sashegyi
Science Applications, Inc.

and

J.E. Geisler
University of Utah

A LINEAR DYNAMIC MODEL OF THE EAST AFRICAN JET IN A STRATIFIED ATMOSPHERE

K. D. Sashegyi
Science Applications, Inc.
McLean, Virginia

and

J. E. Geisler
Department of Meteorology
University of Utah
Salt Lake City, Utah

1. INTRODUCTION

It is thought that the East African Jet is a cross-equatorial flow forced by the summer monsoon and concentrated into a western boundary jet by the north-south topographic barrier of the East African highlands. Various models have been proposed to explain this jet. The one-layer reduced gravity models (Anderson, 1976; Hart, 1977; Bannon 1979a, b, 1982) have shown how much a jet can be formed and described much of its dynamics. However, they are unable to describe its vertical structure or include baroclinic effects of such surface heating contrasts as exist across the coastlines of Somalia and Saudi Arabia. These models have also had problems correctly simulating the horizontal curvature of the jet where it separates from the East African topography and placing the wind speed maximum off the coast of Somalia. The planetary boundary layer model of Krishnamurti et. al. (1982), which is forced by a prescribed vertically varying pressure field obtained from observations, modelled the jet's vertical structure and more realistically simulated the curvature of the jet and the position of the wind speed maximum.

In this study we investigate the linearized response of the jet to prescribed monsoon heat sources in a stratified atmosphere in the presence of a topographic barrier. The pressure field is produced dynamically by the model and the topographic barrier simply modelled as a rigid meridional wall at a longitude of 38°E. The response to latent heating caused by the large scale monsoon convection over India and Indochina is compared to that forced by the differential heating contrast across the eastern coastline of Somalia and Saudi Arabia.

2. THE MODEL

The primitive equations on a sphere in log pressure coordinates are linearized about an isothermal basic state at rest. We are interested in the motion forced by localized tropical heat sources of a given frequency. Damping is simply modelled as Rayleigh friction and Newtonian cooling, with damping times of 5 days each. A rigid lid is placed at 22.5 km and the

vertical structure separated from the equations using the appropriate set of vertical modes, which satisfy the boundary conditions of zero vertical velocity at the surface and at the rigid lid. The forcing, given by the vertical derivative of the heating function, is then projected onto the vertical modes, and the horizontal structure equations solved numerically by the method of Lindzen and Kuo (1969) for each mode. The resulting modal solutions are then summed. The topographic barrier of the East African highlands is modelled as a rigid western wall placed at a longitude of 38°E. The vertical modal technique precludes a more realistic representation of the barrier from being used.

The summer-averaged monsoon latent heating over the region of India was represented by a steady prescribed heat source centered at a latitude of 23.6°N ($y=0.4$) and lying 47° east of the western wall. The horizontal dependence of the heating function was a Gaussian with half-widths of 12° in latitude and 20° in longitude. In the vertical, the heating profile had a maximum heating rate of 6° C/day at 400 mb. The vertically integrated heating rate was normalized to a rainfall rate of 1 cm/day. To resolve the vertical structure of the heating, 16 vertical modes were used. Oscillations in the monsoon heating over India were represented by an oscillating heat source of period 14 days, following the period of the active/break cycle found by Krishnamurti and Bhale (1976), and with an amplitude equal to that of the steady heating.

The summer-averaged sensible heating over the land areas of Somalia and the Saudi Arabian peninsula is represented by a steady low-level heat source, which was placed adjacent to the western wall and centered at latitude 11.5°N ($y=0.2$). In longitude, the heating function was constant in longitude from the wall out to a position (defining an idealized north-south coastline), which lay 500 km from the wall, and where the heating decreased sharply to zero over a distance of 2° of longitude. In latitude the heating function was Gaussian in shape with differing halfwidths of 12° to the north and 6° to the south of the heating center. The heating maximized near the surface with a value of 2°

C/day and was nearly constant from the surface to 2 km. Above 2 km the heating decreased with height to zero at about 4 km. The maximum heating was chosen so that the vertically integrated heating rate matched the daily averaged surface sensible heat flux of 70 watts/m² observed over Saudi Arabia (Blake et al., 1981). For model runs with this heat source, the lid was lowered to 11.25 km and 46 vertical modes used to resolve the vertical structure of the heating. A more realistic orientation of the "coastline", which lay at an angle to the western wall, was also used.

The model horizontal domain stretched pole to pole and 110° in longitude from the western wall to a further rigid wall at the eastern boundary. In latitude, the sine of latitude y was used as the coordinate with a grid point separation of $\Delta y = 0.1$ (about 6° of latitude). A stretched longitudinal coordinate was used to provide a grid separation of 0.45° (about 50 km) at the western edge and about 10° of longitude at the eastern edge of the domain.

3. RESULTS

3.1 Steady Monsoon Latent Heating

The steady monsoon latent heat source described above was placed a distance of 47° in longitude from the western wall (which was at 38°E) and centered at a latitude of 23.6°N ($y=0.4$). The response at the surface is illustrated in Figures 1 and 2. Figure 1 shows the geopotential and wind field in the region from the western wall out to a distance of 75° from the wall. The heating center is indicated by the letter Q and the magnitude of the wind vectors by the labelled arrow.

In Figure 1, a low lies in the interior to the northwest of the heating center, with a strong westerly flow to the south of the low which reaches 10 m/s. Along the western boundary, the flow is concentrated into a northerly boundary jet at the latitude of the low, and a southerly boundary jet which crosses the equator. These two boundary jets separate abruptly from the western boundary at around 14°N ($y=0.25$) to flow eastward into the region of the heat source. The narrow intense flow close to the western wall is shown in Figure 2. The abrupt separation of the flow from the boundary is typical of many one-layer models (Anderson, 1976; Bannon, 1982). The observations however show a more gradual turning of the jet from the topographic barrier (see Findlater, 1977; for example). In the absence of the western wall, the steady response is similar to the interior solution shown in Figure 1 with weak diffuse cross-equatorial flow.

The horizontal structure of the low-level boundary jet that crosses the equator is shown more clearly in Figure 2. Here the surface wind field is shown in the region along the western wall. The intense flow in the boundary jet is maximum at the western wall, and decays exponentially away from the wall, a result of the Rayleigh friction used in the model. The maximum speed in the boundary jet of 35 m/s occurs at the equator, a consequence of the linearity and the northern latitude of the heating. The mass flux crossing the equator in the boundary jet is found to be 22.0×10^{12} gm/sec. The weak cross-equatorial flow in the interior contributes only a further 2.5×10^{12} gm/sec to the

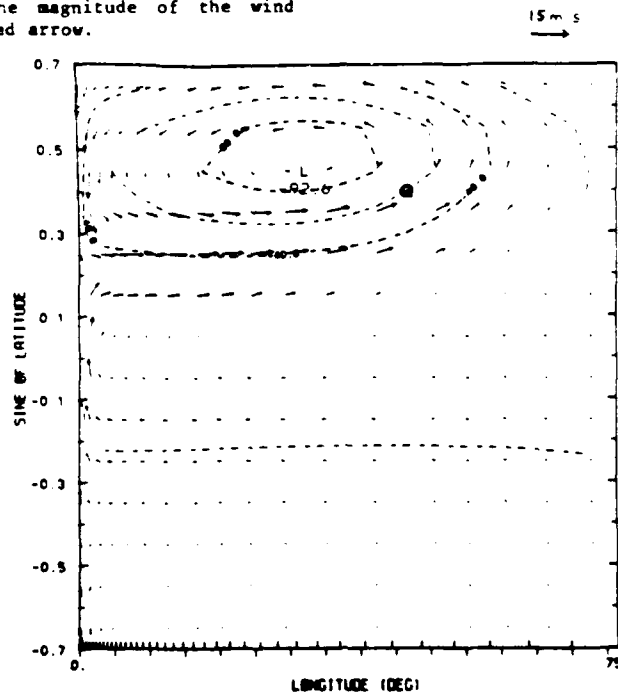


Figure 1. The contours of geopotential (in units of $10^5 \text{ cm}^2/\text{sec}^2$) and the wind field at the surface. Contours every $20 \times 10^5 \text{ cm}^2/\text{sec}^2$.

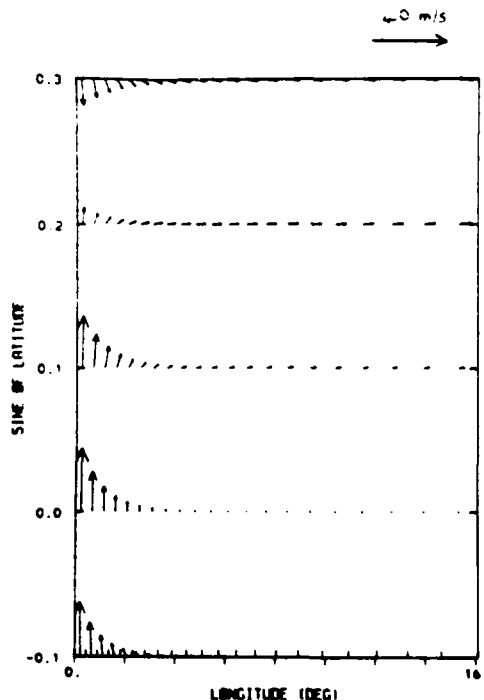


Figure 2. The surface wind field in the western boundary region.

total mass flux crossing the equator. Without the western wall, the total mass flux crossing the equator is 18.0×10^{12} gm/sec. For the month of July, Findlater's (1969) observed mass flux in the low-level jet at the equator was found to be a lot larger, some 89×10^{12} gm/sec. In our model, the addition of a similar heat source over Indochina (centered at 18°N and 67° east of the wall) only increases the mass flux in the modelled jet by a further 50% for a total of 33×10^{12} gm/sec. We next investigate the effect of sensible heating contrasts across the coastline of Somalia and Saudi Arabia.

3.2 Steady Low-Level Sensible Heating

The low-level heat source was placed north of the equator adjacent to the western wall and centered at latitude 11.5°N . In this case the latitudinal resolution was increased with a grid separation given by $\Delta y = 0.05$ (about 3° near the equator). The response at the surface is shown in Figure 3, which shows the same region as Figure 2. The latitude of maximum heating is indicated by the letter Q. Here the surface response is a low adjacent to the western wall and centered at latitude 16°N . A boundary jet is seen crossing the equator along the wall and separating from the boundary around 9°N to flow northwards along the coastline and around the low center. At the surface, the jet is of a similar magnitude at the equator to that forced by the steady monsoon heat source (shown in Figure 2) but it separates from the wall further to the south. In this case the maximum velocity in the jet of 40 m/s occurs just to the north of the equator at 3°N ($y=0.05$), a consequence of

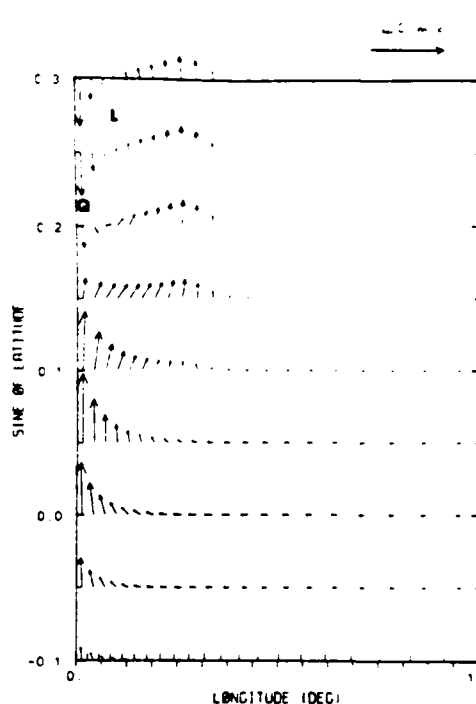


Figure 3. The surface wind field in the case of the sensible heat source.

the significant easterly drift of 4 m/s seen along the equator. A local wind maximum of 15 m/s is found to the southeast of the low center around 14°N ($y=0.25$) at the position of the coastline. The observations of the jet (see Findlater, 1977) however show the major wind maximum just off the coast of Somalia and a secondary wind maximum at the equator.

Our modelled low-level circulation is shallow and lies below 1.5 km in elevation. The low-level circulation decreases in intensity with height above the surface. The average velocities in the layer from the surface to 1.5 km elevation are about half of those shown in Figure 3. A much weaker anti-cyclonic circulation of similar structure is situated above with its maximum intensity at a height of 3 km. In contrast, the steady monsoon circulation modelled in Figure 2 is much deeper, extending from the surface to 5 to 6 km in elevation without much variation over the first 1.5 km in elevation.

For the case with the "coastline" lying along a direction inclined to the wall a similar response to that above is found. Although the surface response is large for both orientations of the coastline, the low-level circulations are shallow and the contribution to the mass flux crossing the equator in the jet is small, some 4×10^{12} gm/sec. We now investigate the effect of oscillations in the monsoon heating, representing the active/break phases of the monsoon.

3.3 Oscillations in the Monsoon Latent Heating

The monsoon latent heat source described above was oscillated at a period of 14 days with an amplitude equal to that of the steady case. The response is shown at the surface in Figure 4 two days after the heating is maximum. A low is found northwest of the heating center (indicated by the letter Q) with a westerly flow of 10 m/s south of the low center. The westerly flow is at its maximum intensity at this time. A broad southerly boundary jet separates from the western wall south of the equator at 12°S ($y = -0.2$) and feeds the westerly flow south of the low. The curvature of the oscillatory boundary jet in Figure 4 is also not as sharp as in the steady case in Figure 3. In Figure 4, the low center west of the heating region, the southerly boundary jet and its associated trough propagate westward with time.

In Figure 5, we show the surface wind field and geopotential 5 days after the heating maximum, by which time the southerly boundary jet has propagated towards the western wall and separates north of the equator at 9°N ($y = 0.15$). The velocities in the boundary jet have increased to 8 m/s near the wall south of the equator. The easterly mass flux to the east of the wall is a maximum at this time. Two days later, at the time of maximum cooling, the velocities in the boundary jet at the equator reach their maximum speed of 8 m/s at the wall.

In comparing Figures 4 and 5, it can be seen that the westward propagating lows and highs produce wave like oscillations along the western wall. On nearing the wall, the trough in the Southern Hemisphere is seen to move northwards along the wall, while weakening in the process and increasing the wind speed on its left flank. Neither the wind speed maximum nor the low itself appear to cross the equator. Anderson (1981) found that in a one-layer linear model, such trapped disturbances propagating along the western boundary cannot cross the equator. Near the equator, our boundary response is also similar to that found in Bannon's (1979b) one-layer model of the jet in which he described the oscillatory boundary wave response as a mixed Rossby gravity wave, whose amplitude decreased in distance from the western boundary. In our case, the boundary wave has a shorter longitudinal wavelength of about 10° (or 1,000 km) for the same period of 14 days, due to the weaker dissipation used.

The mass flux that crosses the equator in the above modelled oscillatory boundary jet was of a comparable amplitude to that for the steady case. The southerly mass flux in the jet was maximum 3 days after the heating maximum, that is nearly a quarter cycle out of phase with the heating. During the positive half cycle of the southerly mass flux for the oscillatory jet, the average mass flux crossing the equator is 14×10^{12} gm/sec.

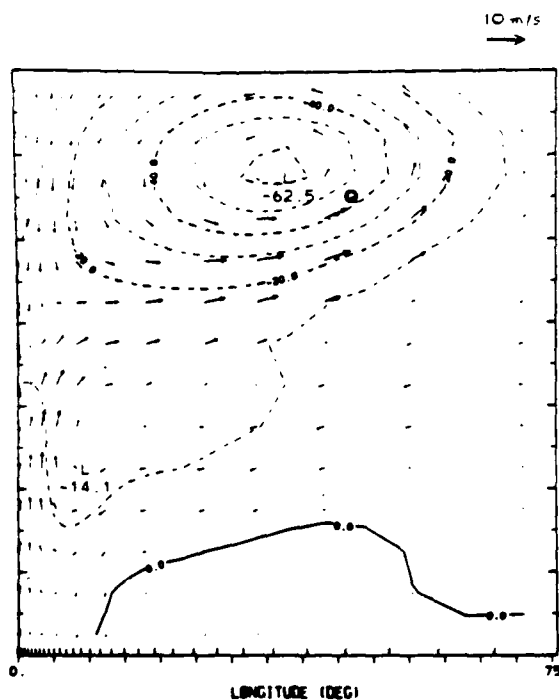


Figure 4. The contours of geopotential (in units of $10^5 \text{ cm}^2/\text{sec}^2$) and the wind field at the surface at day 2 for the oscillatory monsoon heat source. Contours every $10 \times 10^5 \text{ cm}^2/\text{sec}^2$.

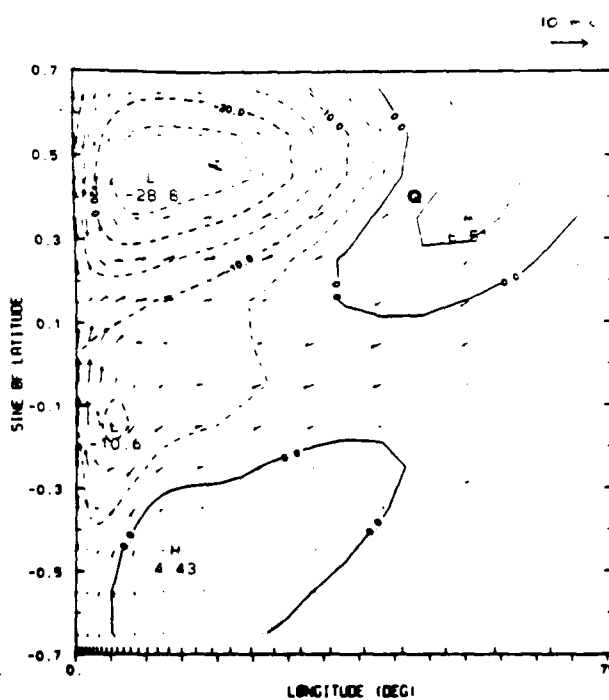


Figure 5. As in Figure 4 except at day 5.

4. SUMMARY AND CONCLUSIONS

The cross-equatorial flow forced by our steady monsoon latent heating was concentrated into a boundary jet by the western wall. The flow was much deeper and separated more abruptly from the western boundary than is indicated by the observations, with the largest velocities found at the western boundary and the surface. With the addition of the baroclinic effect of low-level sensible heating over Somalia and Saudi Arabia, the position at which the monsoon flow separates from the western wall can be shifted further to the south. A local wind maximum along the coastline of Somalia and a more gradual turning of the jet from the topographic barrier can be produced. The observations show the wind maximum further offshore than shown in our model. The upwelling of cold water along the Somalia coast, which was not included in our model, could enhance and possibly move offshore the horizontal heating gradient, shifting the wind maximum further offshore and intensifying it.

Oscillations in the heat source over India at a period of 14 days, representing the active/break cycles of the monsoon, produced westward propagating highs and lows west of the longitude of the heating in both hemispheres. Such fluctuations, incident on the topographic barrier produced oscillations in the boundary jet along the western wall, which can act to broaden the width of the jet and reduce the sharpness of its curvature. The wavelength of the boundary wave response appears sensitive to the magnitude of the dissipation used in these linear models.

The contributions to the mass flux crossing the equator in the jet from the various heat sources above were assessed. The largest contribution was from the steady monsoon latent heat sources over India and Indochina, while the contribution for the low-level sensible heat source was small. Summing the above steady contributions to the mass flux in the jet, we obtain a total of 37×10^{12} gm/sec. Oscillations of the monsoon heating over India produced oscillations in the mass flux in the jet with an amplitude of 20×10^{12} gm/sec. The observed mass flux in the jet (from 35°E to 75°E) is some 89×10^{12} gm/sec (Findlater 1969).

5. REFERENCES

- Anderson, D. L. T., 1976: The low-level jet as a western boundary current. Mon. Wea. Rev., **104**, 907-921.
- _____, 1981: Cross-equatorial waves, with applications to the low-level East African jet. Geophys. Astrophys. Fluid Dyn., **12**, 267-284.
- Bannon, P. R., 1979a: On the dynamics of the East African Jet. I. Simulation of mean conditions for July. J. Atmos. Sci., **36**, 2139-2152.
- _____, 1979b: On the dynamics of the East African Jet. II. Jet transients. J. Atmos. Sci., **36**, 2153-2168.
- _____, 1982: On the dynamics of the East African Jet. III. Arabian Sea Branch. J. Atmos. Sci., **39**, 2267-2278.
- Blake, D., J. S. Fein, T. N. Krishnamurti and S. Low-Nam, 1981: Heat low over Saudi Arabia. Condensed Papers and Meeting Report, International Conference on Early Results of FGGE and Large-Scale Aspects of its Monsoon Experiments, Tallahassee, Jan 12-17, GARP, Session 6, 8-15.
- Findlater, J., 1969: Interhemispheric transport of air in the lower troposphere over the Western Indian Ocean. Quart. J. Roy. Meteor. Soc., **95**, 400-403.
- _____, 1977: Observational aspects of the low-level cross-equatorial jet stream of the Western Indian Ocean. Pure Appl. Geophys., **115**, 1251-1262.
- Hart, J. E., 1977: On the theory of the East African low-level jet stream. Pure Appl. Geophys., **115**, 1263-1282.
- Krishnamurti, T. N., and H. N. Bhalme, 1976: Oscillations of a monsoon system, Part I. Observational aspect. J. Atmos. Sci., **33**, 1937-1954.
- _____, V. Wong, H. -L. Pan, R. Pasch, J. Molinari, and P. Ardanuy, 1983: A three-dimensional planetary boundary layer model for the Somali Jet. J. Atmos. Sci., **40**, 894-908.
- Lindzen, R. S., and H. L. Kuo, 1969: Reliable method for numerical integration of a large class of ordinary and partial differential equations. Mon. Wea. Rev., **97**, 732-734.

APPENDIX S

FINITE GEOMETRY EFFECTS ON THE STABILITY OF A
CHARGED BEAM PROPAGATING THROUGH A RELATIVISTIC
ANNULAR ELECTRON BEAM

G. Ganguli
Science Applications, Inc.

and

P. Palmadesso
Naval Research Laboratory

Finite Geometry Effects on the Stability of a Charged Beam Propagating Through a Relativistic Annular Electron Beam

G. GANGULI* AND P. PALMADESSO

*Geophysical and Plasma Dynamics Branch
Plasma Physics Division*

**Science Applications, Inc.
McLean, VA 22102*

September 28, 1983

This work was supported by the Office of Naval Research.



NAVAL RESEARCH LABORATORY
Washington, D.C.

Approved for public release; distribution unlimited.

S-3

PRECEDING PAGE BLANK-NOT FILMED

REPORT DOCUMENTATION PAGE		READ INSTRUCTIONS BEFORE COMPLETING FORM	
1. REPORT NUMBER		2. GOVT ACCESSION NO	
NRL Memorandum Report 5191		3. REPORTING DATA NUMBER	
4. TITLE and Subtitle		5. TYPE OF REPORT & PERIOD COVERED	
FINITE GEOMETRY EFFECTS ON THE STABILITY OF A CHARGED BEAM PROPAGATING THROUGH A RELATIVISTIC ANNULAR ELECTRON BEAM		Interim report on a continuing NRL problem.	
6. AUTHOR(s)		7. PERFORMING ORG REPORT NUMBER	
G. Ganguli* and P. Palmadesso			
8. CONTRACT OR GRANT NUMBER(s)		9. PROGRAM ELEMENT PROJECT TASK AREA & WORK UNIT NUMBERS	
10. PERFORMING ORGANIZATION NAME AND ADDRESS		11. REPORT DATE	
Naval Research Laboratory Washington, DC 20375		September 28, 1983	
12. CONTROLLING OFFICE NAME AND ADDRESS		13. NUMBER OF PAGES	
Office of Naval Research Arlington, VA 22203		22	
14. MONITORING AGENCY NAME & ADDRESS (if different from Controlling Office)		15. SECURITY CLASS. of this report	
		UNCLASSIFIED	
		16. DECLASSIFICATION DOWNGRADING SCHEDULE	
17. DISTRIBUTION STATEMENT of this Report			
Approved for public release; distribution unlimited.			
18. DISTRIBUTION STATEMENT of the abstract entered in Block 20, if different from Report			
19. SUPPLEMENTARY NOTES			
*Present address: Science Applications, Inc., McLean, VA 22102 This work was supported by the Office of Naval Research.			
20. KEY WORDS (Continue on reverse side if necessary and identify by block number)			
Electron acceleration Collective acceleration Relativistic beams			
21. ABSTRACT (Continue on reverse side if necessary and identify by block number)			
Finite geometry effects on the stability properties of a charged beam propagating through an intense relativistic annular electron beam has been studied. The stability of the system under transverse oscillation has been examined in detail in a parameter domain pertinent to the Collective Particle Accelerator, currently under development at the Naval Research Laboratory. Both the normal mode and the convective aspects of this instability have been investigated. Despite a substantial temporal growth rate as predicted by the normal mode approach this instability does not prevent successful acceleration of a portion of the axial beam. Thus the transverse oscillation is not fatal to the CPA operation.			

DD FORM 1 JAN 73 1473 EDITION OF 1 NOV 65 IS OBSOLETE
S/N 0102-314-6601

SECURITY CLASSIFICATION OF THIS PAGE (When Data Entered)

CONTENTS

I.	Introduction.....	1
II.	Theory.....	2
III.	Results.....	8
IV.	Finite Geometry Effects.....	12
V.	Conclusions	18
	Acknowledgments.....	20
	References	20

FINITE GEOMETRY EFFECTS ON THE STABILITY OF A CHARGED BEAM PROPAGATING THROUGH A RELATIVISTIC ANNULAR ELECTRON BEAM

I. Introduction

The stability properties of systems of intense relativistic electron beams are of considerable interest for many applications. The Collective Particle Accelerator (CPA), currently under development at the Naval Research Laboratory is one such application. The Collective Particle Accelerator is a device in which an intense modulated hollow electron beam propagates along a rippled magnetic field. The interaction of the modulated annular electron beam with the rippled magnetic field produces an axial electric field which consists of both backward and forward waves¹. A solid electron beam can be introduced axially and entrapped by the backward wave potential. There is a transfer of energy from the axial electric field to the axial beam particles which in turn get accelerated to high energies, provided that both beams propagate in a stable fashion. In this paper we examine some stability properties of a solid charged beam propagating through an annular intense relativistic electron beam in the parameter domain pertinent to the Collective Particle Accelerator at the Naval Research Laboratory.

An earlier study² of the coupled transverse oscillation for an intense unmodulated charged particle beam in a straight guiding magnetic field concluded that the transverse oscillation excited by the propagation of a solid charged beam inside a hollow relativistic electron beam is unstable. The growth rate of this instability is a significant fraction of the diocotron frequency of the hollow beam for a solid electron beam and even greater if the solid beam is made up of ions. In this paper we study this instability more specifically in the context of the CPA. As in Ref. 2 we use a fluid model for the hollow electron beam and a kinetic model for the solid beam. In order to

Manuscript approved July 29, 1983.

make the analysis simple, here we ignore the ripples in the axial magnetic field and the beam modulation. The radius of the solid beam R_s is taken to be less than the inner radius R_1 of the hollow electron beam. In order to make this study more relevant to the experiments we have recognized the finite extent of the system in the axial direction. A rigorous study of a finite system involves a two dimensional eigenvalue equation and its solution. This is beyond the scope of this paper and will be addressed in a future paper. Here we solve the wave kinetic equation and show that a successful acceleration is always possible for the beam head. This is because the wave energy of the instability travels at the group velocity V_g which is much smaller than the beam velocity v , which in turn is close to the speed of light. Thus the transverse oscillation is not fatal for the CPA operation as was implied in Ref. 2.

The composition of this paper is as follows: In Section II we review the equilibrium properties, the basic assumptions and the equations governing the system. In section III we solve the dispersion relation in the parameter domain pertinent to the CPA at the Naval Research Laboratory and discuss the results for a solid electron beam. In Section IV we solve the wave kinetic equation and discuss its relevance to a finite device and finally in Section V we give our conclusions.

II. Theory:

The equilibrium configuration is given in figure (1). We follow the treatment as given in Ref. 2. An intense relativistic charged electron beam propagates along the axial magnetic field $B_0 \hat{e}_z$. The inner radius of this annular beam is R_1 while the outer radius is R_2 . A solid beam of radius R_s propagates along the magnetic field. The solid beam radius R_s is smaller than

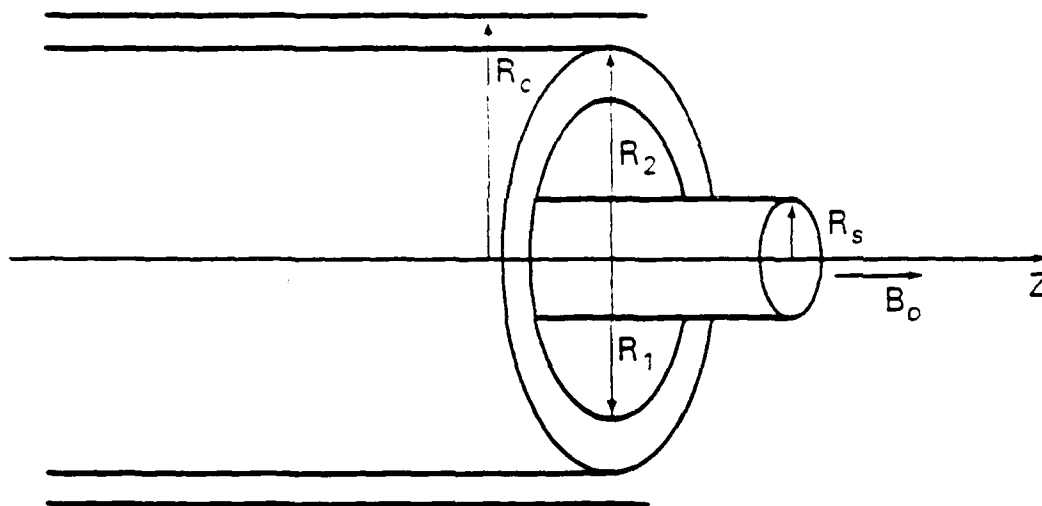


Figure 1a — The equilibrium configuration of the hollow and the solid beams.

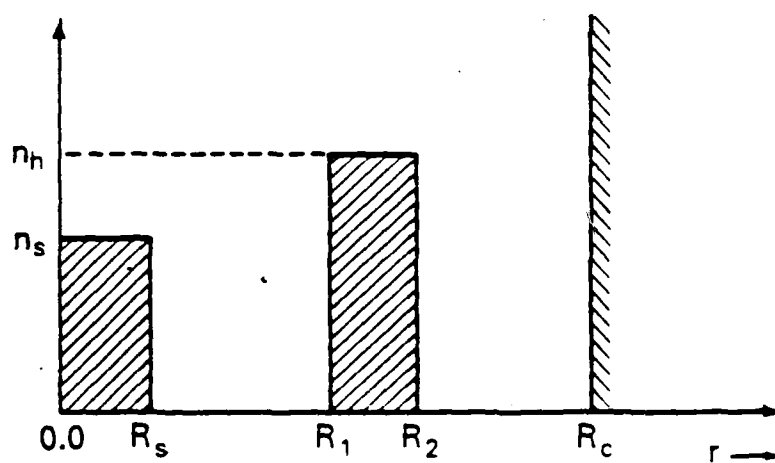


Figure 1b — The density profile for the equilibrium as shown in figure 1a.

the inner radius R_1 of the annular electron beam. The magnetic field confines the beams in the radial direction in equilibrium. Cylindrical coordinates (r, θ, z) is used.

We assume that the transverse velocities are much smaller than the axial velocity i.e., $v_z^2 \gg v_r^2 + v_\theta^2$. The hollow beam is tenuous $\omega_{ch}^2 \gg \omega_{ph}^2$, where $\omega_{ph}^2 = 4\pi e^2 n_h / m_h$ and $\omega_{ch}^2 = eB_0 / \gamma_h m_h c$, $\gamma_h = (1 - \beta_h^2)^{-1/2}$ and $\beta_h = v_h / c$. Further we assume that $v_s / v_s = N_s Z_s^2 e^2 / m_s c^2 \gamma_s \ll 1$, where s denotes the solid beam particles, v_s is Budker's parameter, $N_s = 2\pi \int_0^{2\pi} dr r n_s^0(r)$ is the number of particles per unit axial length, $n_s^0(r)$ is the equilibrium particle density, $-e$ is the electron charge, Z_s is the charge state of the solid beam particles, $v_s m_s c^2$ is the characteristic particle energy for the solid beam and c is the speed of light in vacuum. Since the axial velocity is much greater than the azimuthal velocities ($v_z^2 \gg v_r^2 + v_\theta^2$) the self-magnetic field in the axial direction produced by the azimuthal current can be neglected. The equilibrium is azimuthally and axially symmetric i.e., $\frac{\partial}{\partial \theta} \equiv 0$ and $\frac{\partial}{\partial z} \equiv 0$.

The annular beam electrons are described as macroscopic, cold fluid immersed in an axial magnetic field $B_0 \hat{e}_z$. The equation of motion and the continuity equation for the hollow beam electrons are

$$\left\{ \frac{\partial}{\partial t} + \underline{V} \cdot \nabla \right\} \gamma_h m_h \underline{V} = -e \left\{ \underline{E} + \frac{\underline{V} \times \underline{B}}{c} \right\}, \quad (1)$$

and

$$\frac{\partial}{\partial t} n_h + \nabla \cdot (n_h \underline{V}) = 0, \quad (2)$$

where \underline{E} and \underline{B} are the electric and the magnetic fields respectively, n_s and \underline{v} are the density and the mean velocity, m_s is the rest mass of the annular beam particles (in this case the electrons).

The distribution function for the solid beam particles is given by

$$f_s^0(\underline{x}, \underline{p}) = (n_s / 2\pi\gamma_s m_s) \delta(H - \omega_s P_\phi - \hat{\gamma}_s m_s c^2) \delta(P_z - \gamma_s m_s \beta_s c) \quad (3)$$

where n_s is the particle density at $r = 0$, $H = (m_s^2 c^4 + c^2 p^2)^{1/2} + e_s \phi_0(r)$ is the total energy, $P_\phi = r[p_\theta + (e_s/c)(rB_0/2)]$ is the canonical angular momentum, $P_z = p_z + (e_s/c)A_z^0(r)$ is the axial canonical momentum, $A_z^0(r)$ is the axial component of the vector potential for the azimuthal self magnetic field, and ω_s , β_s and $\hat{\gamma}_s$, are constants. $\phi_0(r)$ appearing in the definition of H is the electrostatic potential for the equilibrium self electric field.

The density profile consistent with the solid beam distribution is given by 3,2,

$$n_s^0(r) = \begin{cases} n_s, & 0 < r < R_s \\ 0, & \text{otherwise.} \end{cases}$$

The fast (+) and the slow (-) laminar rotational frequencies are given by²

$$\bar{\omega}_s = -\frac{\epsilon_s}{2} \omega_{cs} \left[1 \pm \left(1 - \frac{2\omega_{ps}^2}{\gamma_s^2 \omega_{cs}^2} \right)^{1/2} \right], \quad (4)$$

where $\omega_{cs} = eZ_s B_0 / \gamma_s m_s c$, $\omega_{ps}^2 = 4\pi n_s e^2 Z_s^2 / \gamma_s m_s$, $\gamma_s = (1 - \beta_s^2)^{-1/2}$, $\epsilon_s = v_s/c$ and $\epsilon_s = \text{Sgn}(e_s)$. For a valid equilibrium for the solid beam ω_s is

restricted between ω_s^- i.e., $\omega_s^- < \omega_s < \omega_s^+$. The density profile for the annular beam electrons is given by,

$$n_h^o(r) = \begin{cases} n_h, & R_1 < r < R_2 \\ 0, & \text{otherwise.} \end{cases}$$

The density profiles chosen here have sharp boundaries as shown in figure 1b. Consistent with the equilibrium conditions just described the rotational frequency of the annular beam $\omega_h(r)$ is given by²,

$$\omega_h(r) = \omega_D \left(1 - \frac{R_1^2}{r^2} - \gamma_h^2 \frac{\epsilon_s n_s^2}{n_h} (1 - \beta_s \beta_h) \frac{R_s^2}{r^2} \right), \quad (5)$$

where the diocotron frequency of the hollow beam is given by

$$\omega_D = \omega_{ph}^2 / 2 \gamma_h^2 \omega_{ch} \quad (6)$$

For the stability analysis for the coupled transverse oscillation of a intense charged beam travelling through a relativistic annular electron beam a normal mode approach is used. A dispersion relation is obtained by linearizing fluid, Vlasov and Maxwell's equations. All perturbations are assumed to vary in time and space as,

$$\delta \phi(\underline{x}, t) = \hat{\phi}(r) \exp[i(l\theta + kz - \omega t)], \quad (7)$$

where ω is the complex eigen frequency. The azimuthal harmonic number is l and k is the axial wave vector. We further assume that the axial wavelength is long i.e.,

$$|kR_c|^2 \ll (\ell^2 + 1),$$

and the frequencies are low i.e.,

$$|\omega R_c|^2/c^2 \ll (\ell^2 + 1),$$

where R_c is the radius of the conducting wall.

Under these conditions the dispersion relation obtained by Uhm² is given by,

$$\begin{aligned} \Gamma_h(\omega, k) \Gamma_s(\omega, k) &= \gamma_h^2 \gamma_s^2 (1 - \epsilon_s \epsilon_h)^2 \left(\frac{R_s}{R_1} \right)^{2\ell} \frac{S}{2\gamma_s^2} \\ &\left[\frac{H(R_1)}{2\gamma_h^2} \left(1 - \frac{R_1^{2\ell}}{R_c^{2\ell}} \right) \left\{ 1 - \frac{R_1^{2\ell}}{R_c^{2\ell}} + \frac{H(R_2)}{2\gamma_h^2} \left(1 - \frac{R_1^{2\ell}}{R_2^{2\ell}} \right) \right. \right. \\ &\left. \left. \left(1 - \frac{R_2^{2\ell}}{R_c^{2\ell}} \right) \right\} - \frac{H(R_2)}{2\gamma_h^2} \frac{R_1^{2\ell}}{R_2^{2\ell}} \left(1 - \frac{R_2^{2\ell}}{R_c^{2\ell}} \right) \right], \end{aligned} \quad (8)$$

where the dielectric functions of the hollow and the solid beams are,

$$\begin{aligned} \Gamma_h(\omega, k) &= \frac{H(R_1)}{2\gamma_h^2} \left[1 - \frac{R_1^{2\ell}}{R_c^{2\ell}} + \frac{H(R_2)}{2\gamma_h^2} \left(1 - \frac{R_1^{2\ell}}{R_2^{2\ell}} \right) \left(1 - \frac{R_2^{2\ell}}{R_c^{2\ell}} \right) \right] \\ &- \frac{H(R_2)}{2\gamma_h^2} \left(1 - \frac{R_2^{2\ell}}{R_c^{2\ell}} \right) - 1, \end{aligned} \quad (9)$$

$$\Gamma_s(\omega, k) = \frac{S}{2\gamma_s^2} \left(1 - \frac{R_s^2}{R_c^2} \right) - 1, \quad (10)$$

$$\frac{H(r)}{2\gamma_h^2} = \frac{\omega}{\omega - k\beta_h c - \lambda\omega_h(r)}, \quad (11)$$

and

$$S = \frac{\omega_s^2}{(\omega - k\beta_s c - \lambda\omega_s) (\omega - k\beta_s c - \lambda\omega_s) + \epsilon_s \omega_{cs} + 2\omega_s}. \quad (12)$$

In the following sections of this paper we shall use the dispersion relation as given in equation (8) to examine the stability of the transverse oscillations for the NRL CPA. The details of the derivation of the dispersion relation are given in Ref. 2.

III. Results

In this section we solve the dispersion relation given in equation (8) in the parameter range pertinent to the NRL CPA. Here $R_1 = 2.0625$ cms, $R_2 = 2.25$ cms, $R_3 = 0.25$ cms and $R_c = 2.3438$ cms. The injection energy of the hollow beam electrons is one MeV which corresponds to $\beta_h = 0.941$ while the injection energy of the solid beam electron is 0.7 MeV which gives $|\beta_s| = 0.906$. The space charge limiting current for the hollow beam is 20 kilo Amps and 2 kilo Amps for the solid beam giving the ratio $I_s/I_h = 0.1$. Given the ratio of the currents, the velocities and the areas of cross-section of the solid and the hollow beams, the ratio of the densities can be calculated. The expression for the density ratio for the solid and the hollow beams is,

$$\frac{n_s}{n_h} = \left(\frac{I_s}{I_h} \right) \left(\frac{\beta_h}{\beta_s} \right) \left(\frac{A_h}{A_s} \right), \quad (13)$$

where A_h and A_s are the areas of cross-section of the hollow and the solid beams respectively. In all the calculations given in this paper we have used the expression (13) for the density ratio and used $\omega_{ph}^2 = 0.1$.

In figure 2 we plot the real and the imaginary parts of the complex frequency ω against the axial wave vector k , for the azimuthal mode number $\lambda = 1$. The instability exists roughly for kc/ω_D between -0.85 to 0.25 , and achieves a maximum at $kc/\omega_D \sim -0.3$. The growth rate at its peak is about $0.5\omega_D$, which is a substantial fraction of the diocotron frequency of the hollow beam. The instability once again reappears in the range $0.55 < kc/\omega_D < 1.1$, but with much reduced temporal growth rate. This as explained by Uhm^2 , is a residual influence of the familiar diocotron instability. Since the instability is a significant fraction of the diocotron frequency, Uhm^2 concluded that the propagation of the solid beam will be severely limited. In the following section we shall apply the finite geometry restriction in the axial direction and show that despite the substantial temporal growth rate it is possible to achieve successful acceleration.

In figure 3 we provide a plot of the maximized growth rate against the ratio of space charge limited currents (I_s/I_h) for the solid and the hollow beams. In this plot the ratio of the densities n_s/n_h , is calculated self consistently by equation (13). The values of the self consistent n_s/n_h are indicated on the plot at various values of I_s/I_h . The growth rate increases with increasing I_s/I_h . The ratio of the currents, I_s/I_h was varied from 0.01 to 0.2 ; and the corresponding maximized growth rate increased from $0.153\omega_D$ to $0.687\omega_D$. The self consistent density ratio n_s/n_h in the same range increased from 0.134 to 2.69 . The value of kc/ω_D where the maximum occurred moved from -0.15 to -0.45 .

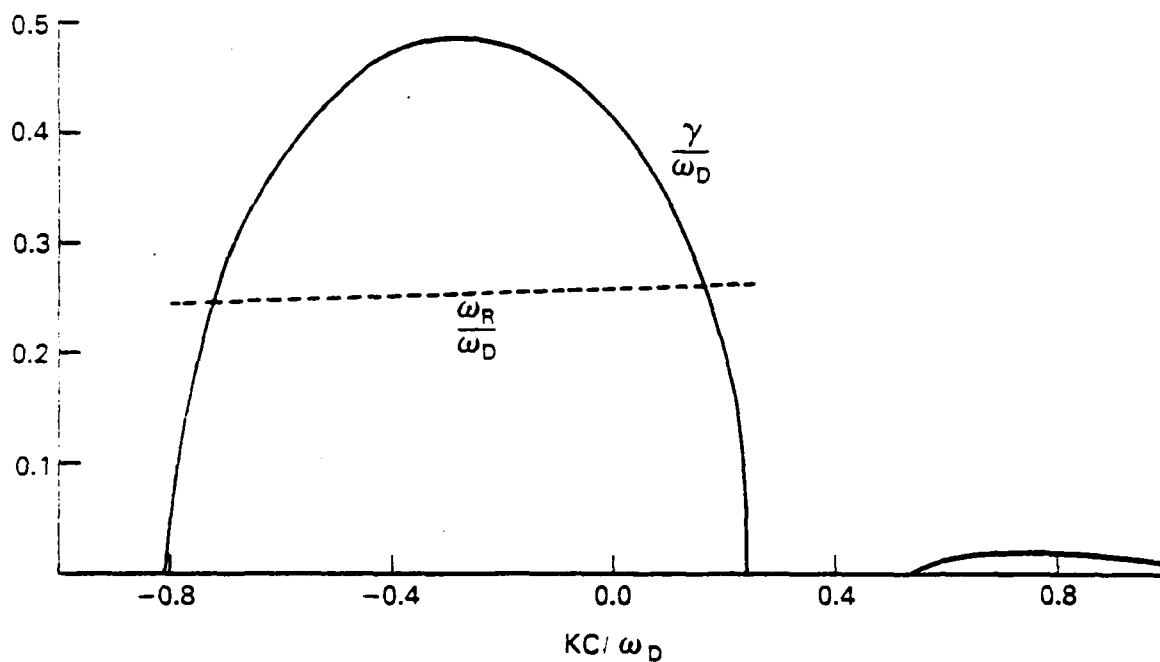


Figure 2 — A plot of the growth rate against the axial wave vector. Here $R_1 = 2.0625$ cms, $R_2 = 2.25$ cms, $R_s = 0.25$ cms, $R_c = 2.3438$ cms. $I_s/I_h = .1$ and n_s/n_h is in accordance of equation (13). $\beta_h = 0.941$, $\beta_s = 0.906$ and the azimuthal wave number $l = 1$.

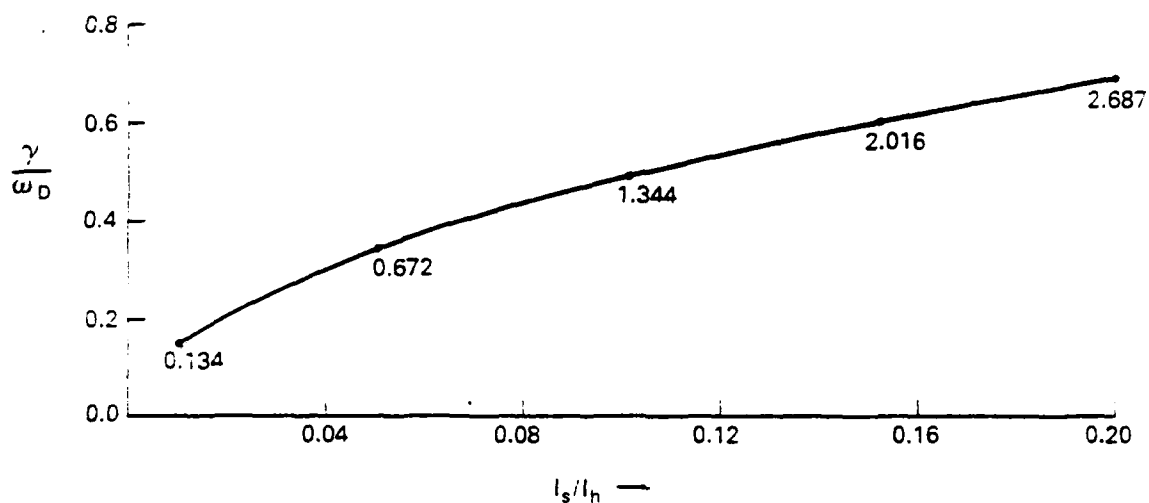


Figure 3 — A plot of the growth rates maximized over the axial wave vector as a function of the ratio of the space charge limited currents in the solid and the hollow beams. The density ratio n_s/n_h is computed self consistently by equation (13) and its magnitude for various I_s/I_h values are indicated on the plot.

Figure 4 is a plot of the maximized growth rate against the velocity of the solid beam β_s . Again the density ratio n_s/n_h is given by equation (13). We see that as β_s becomes small the density ratio n_s/n_h increases thereby increasing the growth rates. Since in the NRL experiment β_s for a solid electron beam is always in the opposite direction of the hollow electron beam velocity β_h , we have restricted our calculations only to negative values of β_s . For $\beta_s < -0.5$ the growth rate becomes more or less constant. This is unlike the nature indicated in the figure 2 of Ref. 2, where n_s/n_h is held constant throughout the range of β_s . Hence the figure 2 of Ref. 2 does not correspond to one particular experimental setup. If we set $\beta_s = \beta_h$, i.e. consider the case where both the hollow beam and the solid beam travels at the same speed the growth rate vanishes.

IV. Finite Geometry Effects:

In the previous section we have shown that a solid electron beam propagating through a relativistic hollow electron beam is unstable to the transverse oscillation. This was the primary reason which lead Uhm² to conclude that the propagation of the solid beam through a hollow relativistic electron beam will be severely limited. In this section we shall study the propagation of the energy density W due to the instability along with the propagation of the beam head itself for finite systems.

The wave kinetic equation for the CPA is,

$$\frac{\partial W}{\partial t} + V_g \frac{\partial W}{\partial z} = \gamma W [1 - H(z - \beta_s ct)], \quad (14)$$

where W is the energy density, V_g is the group velocity of the transverse mode, $H(z - \beta_s ct)$ is the Heavside step function,

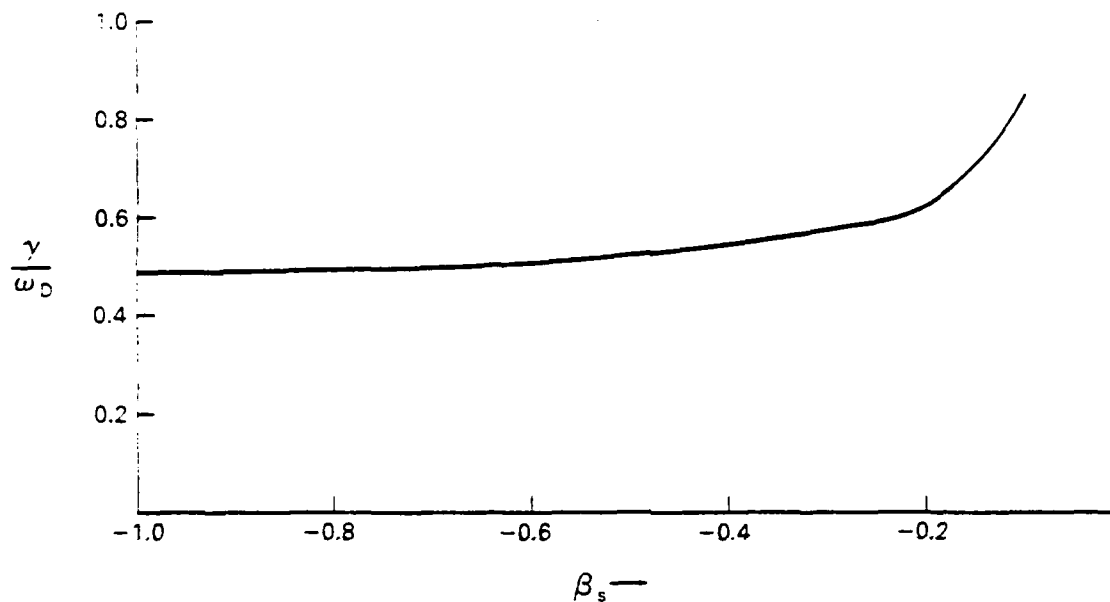


Figure 4 — A plot for the growth rate maximized over the axial wave vector k against the velocity of the solid beam β_s .

$$H(x) = \begin{cases} 1, & x > 0 \\ 0, & \text{otherwise,} \end{cases}$$

and γ is the growth rate of the transverse instability. Fig (5) describes the CPA configuration. The annular beam propagates along the magnetic field $B_0 \hat{e}_z$ between the radii R_1 and R_2 . The solid beam propagates along the axis with a radius R_s and with a velocity $\beta_s c$. If the solid beam particles are electrons then the solid and the annular beam travel in the opposite direction while if the solid beam particles are ions then they travel in the same direction. The position of the beam head at any a time t is given by $\beta_s c t$.

First we shall discuss the case of a solid electron beam propagating through a relativistic hollow electron beam. The configuration is described in figure (5). The general solution of equation (14) can be written as,

$$W(\eta, z) = W_0 \exp \left[\frac{\gamma}{V_g} \int_0^z \left\{ 1 - H \left(1 - \frac{\beta_s c}{V_g} z' + \frac{\beta_s c}{V_g} \eta \right) \right\} dz' \right] \quad (14a)$$

where,

$$\eta = z - V_g t$$

and

$$W_0 = W(0, \eta).$$

Define,

$$\hat{z} = \left(\frac{V}{V - V_g} \right) \eta, \quad (15)$$

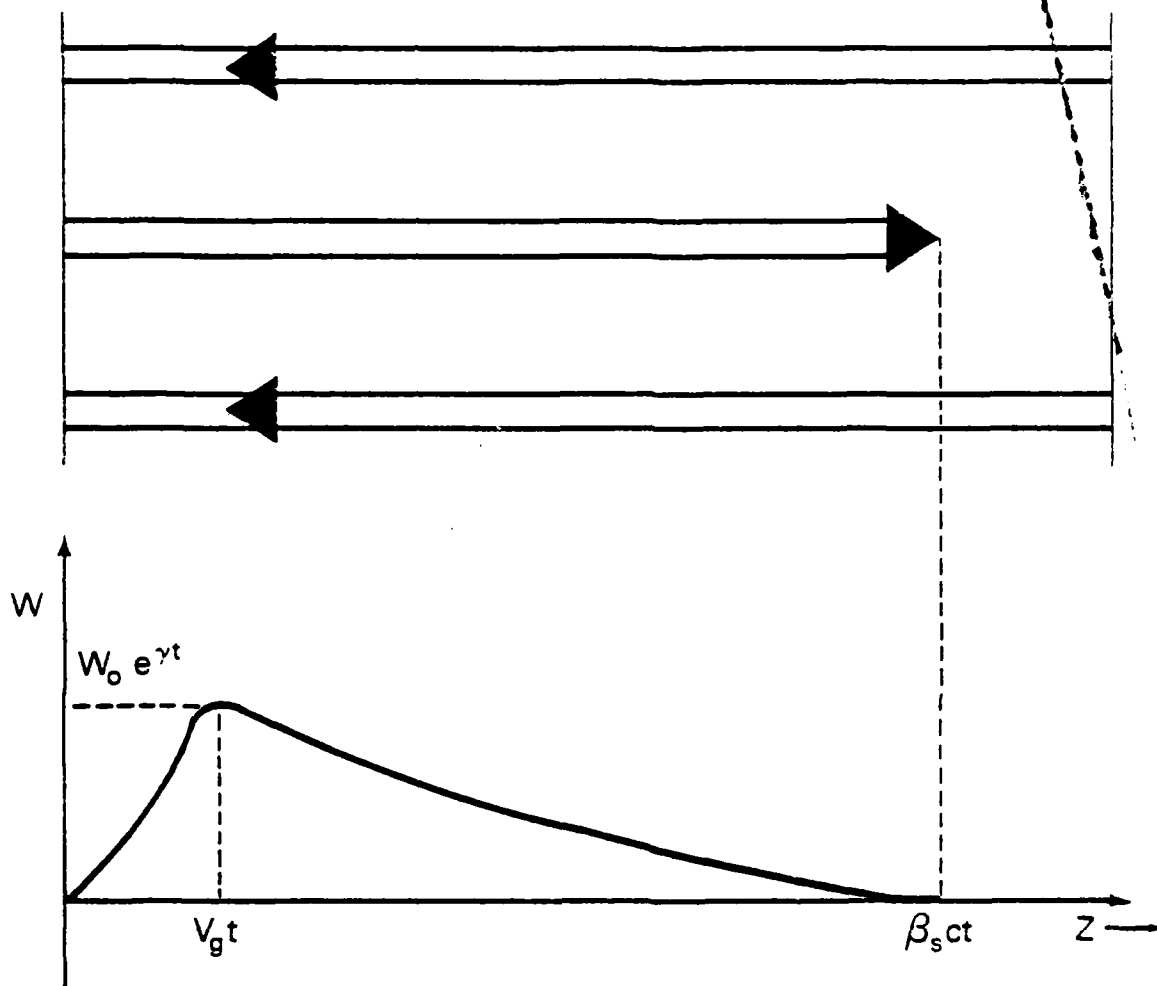


Figure 5 - A schematic diagram of the hollow electron beam and a solid electron beam. Also shown schematically is the solution $W(z,t)$ of equation (14) for this case.

such that

$$\left(1 - \frac{\beta_s c}{v_g}\right) \hat{z} - \frac{\beta_s c}{v_g} z = 0.$$

We shall discuss the solution (14a) in three regions:

(a) $z > \beta_s c t$

This corresponds to the case of $\hat{z} > z$. For $\hat{z} > z$ the argument of H is positive and thus the solution becomes

$$W(z, t) = W_0 \quad (16)$$

The solution implies that the energy of the region where the solid beam has not yet arrived remains unaffected at the initial value W_0 .

(b) $\frac{v_g}{\beta_s c} z < z < \beta_s c t$

This corresponds to the case $0 < \hat{z} < z$. Here the solution is given by,

$$W(z, t) = W_0 \exp\left\{\frac{Y}{\beta_s c - v_g} (\beta_s c t - z)\right\} \quad (17)$$

At $z = \beta_s c t$ it reduces to the previous case where $W(z, t) = W_0$. An observer travelling with the beam head, i.e., with a velocity $\beta_s c$, sees a backward convective growth of W with a growth length L'_g , in the region between the beam head and the point at which $W(z, t)$ reaches its maximum value. In the laboratory frame this growth length is,

$$L_g = \frac{E_s c - V_g}{V_g}.$$

17a

Although from the laboratory frame of reference the instability grows in time, it is stationary in the region between the peak and the beam head when viewed from the beam head. This is illustrated in figure 5. As a consequence of the backward convective nature of the instability near the beam head, there will be a region in which the effects of the instability are nondestructive, regardless of the length of the device. If the initial perturbation energy density (noise level) is 1% of the beam energy density then it takes about five growth lengths for that perturbation to grow to a level such that W is comparable to the beam energy W_B . Thus a portion of the beam of length $\sim 5L_g$ remains only weakly affected by the instability. Since L_g can be controlled by the experimental parameters this distance can in principle be increased.

$$(c) \quad \underline{z < V_g t}$$

This is the region between the origin ($z=0$) and the peak of $W(z,t)$ at $z = V_g t$. In this region the solution is given by

$$W(z,t) = W_0 \exp\left(\frac{V_g z}{V_g}\right) \quad (18)$$

Here the energy density rises exponentially as a function of z and reaches a peak at $z = V_g t$.

We now apply the solution discussed above specifically to the NRL CPA in the parameter range given in the previous section. From figure 2 we see that the maximum temporal growth rate occurs at $kc/\omega_D \approx -0.3$ and has a magnitude of $0.486\omega_D$. Also from the plot of ω_r/ω_D we see that the group velocity V_g given by

the slope is roughly 0.1189c. With $\beta_s = 0.906$ the injection velocity in equation (17a) the growth length is 0.61 meters. The diocotron frequency $\omega_D = 9 \times 10^8$. Now if the perturbation energy density (i.e., noise level) is 1% of the beam energy density, the ratio $\frac{N}{N_B} \lesssim 1$ for about $5L_g = 3$ meters and if the perturbation is 0.01%, then $\frac{N}{N_B} \lesssim 1$ for about $9L_g = 5.49$ meters from the beam head (see figure 5). Thus it is possible to successfully accelerate about 3 to 6 meters (depending on the magnitude of the initial perturbation) of the solid beam despite the substantial temporal growth. Also this estimate was done using $\beta_s \sim 0.906$ which is the injection velocity. In figure 6 we use expression 17a to plot L_g against β_s . As the solid beam gets accelerated β_s approaches unity and L_g increases thereby allowing a larger portion of the beam to be unaffected by the transverse instability. Also note that $\omega_D = \gamma_h^{-2}$, thus raising the velocity of the hollow electron beam β_h will further increase L_g . Similar treatment can be given for the case of a solid ion beam.

V. Conclusions

The stability of the transverse oscillations for a charged beam propagating through a relativistic hollow electron beam was examined in the parameter regime pertinent to the NRL CPA experiment. The ratio of the beam densities n_s/n_h was maintained as a dependent parameter. For the NRL experiment the ratio of the space charge limited currents $(I_s/I_h) = 0.1$, was used to determine the self consistent n_s/n_h . For a solid electron beam the transverse oscillation had a growth of about $0.5\omega_D$. The growth rate was found to increase with I_s/I_h . This was mainly because increasing I_s/I_h increased n_s/n_h . The maximum growth rate increased with decreasing β_s . For β_s in the range of -0.5 to -1.0 the growth rate maintains a fairly constant magnitude.

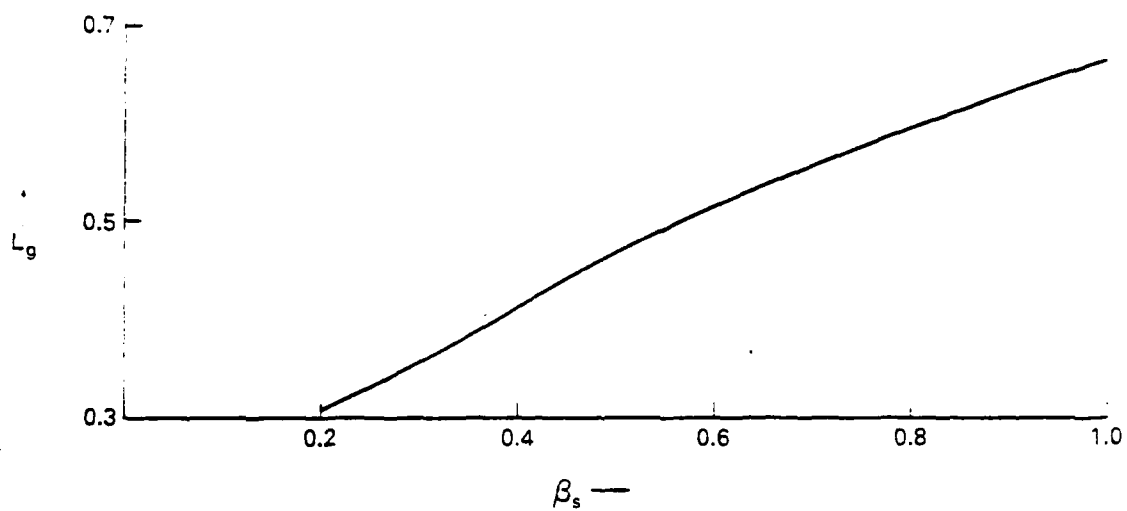


Figure 6 — The magnitude of the growth length L_g , is plotted against the injection velocity of the solid beam, β_s .

Finite geometry effects were examined by solving the wave kinetic equation. It is found that despite the substantial temporal growth rate of the transverse oscillation it is possible to achieve successful acceleration of about 3 to 6 meters of the solid beam length for the present operating parameters. In principle this can be further increased. Thus we conclude that the transverse oscillation will not be fatal to the operation of this device.

A similar conclusion for the case of a solid ion beam can also be made. However it must be pointed out that due to the defocussing of the ion beams this method of propagating a solid ion beam through a relativistic hollow electron beam will fail. Thus the analysis given by Uhm² for the solid ion beam acceleration does not apply to the NRL CPA experiment. A solid ion beam will have to propagate through a solid electron beam and this configuration will make a new formalism necessary. A new formalism dealing with the propagation of a solid ion beam through a solid electron beam is now being developed and will be reported in a future paper.

Acknowledgments

We would like to thank Dr. H.S. Uhm of the Naval Surface Weapons Center and Dr. M. Friedman of the Naval Research Laboratory for useful discussions. This work was supported by the Office of the Naval Research.

References

1. Friedman, M., NRL Memorandum Report, 3724 (1978).
2. Uhm, H.S. Phys. Fluids, 25, 1908 (1982).
3. Uhm, H.S, and R.C. Davidson, Phys. Fluids, 23, 813 (1980).

ATE
LME